



Forschungszentrum Karlsruhe
in der Helmholtz-Gemeinschaft

Wissenschaftliche Berichte

FZKA 7291

EUR 22705 EN

**Nuclear Fusion Programme
Annual Report of the
Association Forschungszentrum
Karlsruhe/EURATOM
January 2006 – December 2006**

Programm Kernfusion

April 2007

Forschungszentrum Karlsruhe

in der Helmholtz-Gemeinschaft

Wissenschaftliche Berichte

FZKA 7291
EUR 22705 EN

Nuclear Fusion Programme
Annual Report of the
Association Forschungszentrum Karlsruhe/
EURATOM
January 2006 – December 2006

compiled by I. Pleli
Programm Kernfusion

Forschungszentrum Karlsruhe GmbH, Karlsruhe
2007

This work, supported by the European Communities under the contract of Association between EURATOM and Forschungszentrum Karlsruhe, was carried out within the framework of the European Fusion Development Agreement. The views and opinions expressed herein do not necessarily reflect those of the European Commission.

Als Manuskript gedruckt
Für diesen Bericht behalten wir uns alle Rechte vor

Forschungszentrum Karlsruhe GmbH
Postfach 3640, 76021 Karlsruhe

Mitglied der Hermann von Helmholtz-Gemeinschaft
Deutscher Forschungszentren (HGF)

ISSN 0947-8620

urn:nbn:de:0005-072916

Introduction

The worldwide energy consumption is mainly covered by fossil energy sources. Their environmental impact, to a certain extent already visible, requires in the long term new ways of energy supply. In addition the worldwide energy demand will substantially increase in the course of this century in particular in populous countries such as China and India. Nuclear fusion offers an option of an environmental benign energy source with favourable safety features and almost unlimited fuel resources.

Nuclear fusion research is aiming to generate the physical and technical basis of a fusion power station which, similar to the sun, gains energy from the fusion of light atoms. In order to attain ignition of the plasma, the fuel, a mixture of deuterium/tritium (isotopes of hydrogen), must be confined by strong magnetic fields and heated up to more than 100 million degrees.

The construction of the experimental reactor ITER which will start in Cadarache/France in the framework of a worldwide project by 2008 marks the next big step on the way to a fusion power station. For the first time a fusion power of 500 Mega Watt will be generated by a long burning plasma and applied technologies will undergo extended tests. The construction costs including personnel are about 5 billion EURO.

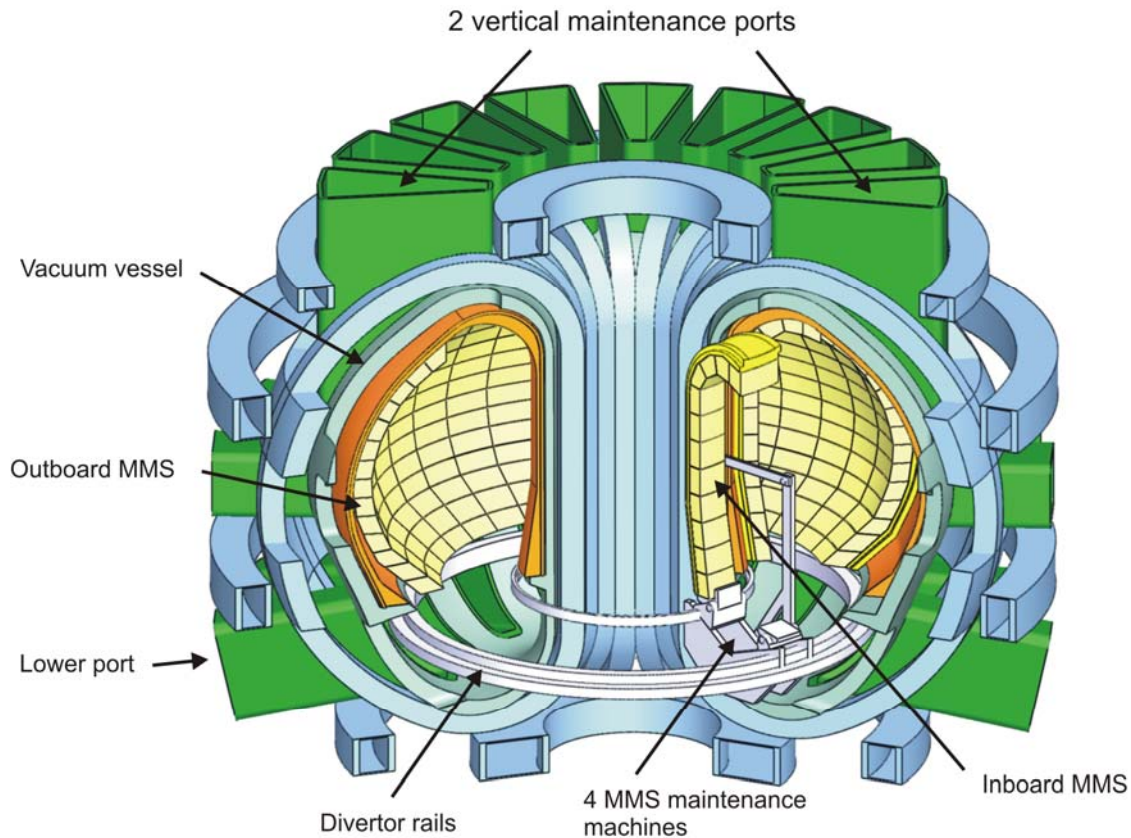
In the framework of the European Fusion Programme the Association FZK-EURATOM is developing key technologies in the areas of superconducting magnets, microwave heating systems (Electron-Cyclotron-Resonance-Heating, ECRH), the deuterium-tritium fuel cycle, He-cooled breeding blankets, a He-cooled divertor and structural materials as well as refractory metals for high heat flux applications including a major participation in the international IFMIF project. Furthermore investigations on plasma wall interactions and core and divertor modelling are carried out and a global plasma model is being developed.

The results from experimental activities such as the tests of high temperature superconducting current leads in the test facility TOSKA, the quasi-stationary gyrotron operation and the operation of fuel cycle subsystems and components with deuterium-tritium have already been utilised for the design work for ITER. In addition large progress has been made in the engineering design of test blanket modules for ITER.

With the construction of ITER new challenges have to be mastered by the EURATOM-Associations. While up to now concepts for components and systems have been developed and their functionality has been tested in laboratory scale or semi-technical scale, now plant components have to be constructed for fabrication and their integration into the plant has to be supported. In order to effectively deploy personal and financial resources consortia of European Association Laboratories are being formed which will bear the responsibility for the realisation of components and systems in accordance with the procurement packages of ITER. This concerns systems in the range of ten up to one hundred millions EURO which require the specific know-how of fusion laboratories. The Association FZK-EURATOM is going to lead a consortium for the construction of the European test blanket module (TBM) systems and a consortium for the construction of the upper port plug ECRH microwave launcher. The negotiations to form these consortia are near to be finalized. In addition the Association FZK-EURATOM is also involved in other consortia such as the fuel cycle and the development and procurement of gyrotrons providing microwaves of 170 GHz and 2 MW output power for ITER. Furthermore the already existing co-operation with industrial companies is being intensified.

The detailed design and construction of ITER components and subsystems needs to be supported by experiments such as prototype testing, validation of scale up factors and additional R&D. For this purpose a helium loop HELOKA is being constructed which not only serves for experimental investigations of the TBM, but also as a pilot loop in view of the loops to be installed in ITER for the cooling of test blanket modules.

The demonstration power station DEMO constitutes the next step beyond ITER which is supposed to be planned after some years of ITER operation. In the framework of a European DEMO study the Association FZK-EURATOM is developing the so-called multi-module blanket concept which promises reduced plant shutdown times during remotely controlled exchange of blankets and thus contributes to an increased plant availability.



Remotely controlled exchange of blanket modules according to the MMS concept.

Furthermore a helium cooled divertor for DEMO is under development. First thermomechanical and thermohydraulic simulations supplemented by experimental investigations have demonstrated that the reference multi-jet concept for the He cooled divertor is able to withstand the heat load in a fusion power reactor.

About 220 professionals and technicians are involved in the fusion programme of the Association FZK-EURATOM with additional support of technical departments.

Progress from January 2006 to December 2006 is reported here. More information is available from the programme management and from the responsible scientists. The website www.fzk.de/fusion offers further access to the fusion activities of FZK.

Contents

Page

Introduction

Plasma Edge	1
EFDA/03-1080 (TW3-TPP/MATDAM) Characterisation of Material Damage for EU W and CFC ITER Divertor Materials under Repetitive Plasma Energy Fluxes by Modelling and Experimental Validation	3
EFDA/05-1305 (TW5-TPP/BEDAM) Modelling of Material Damage to Be-clad and Be-coated ITER Plasma Facing Components under Type I ELMS, Disruptions and Mitigated Disruptions and Scoping Studies for First Experimental Validations	7
TW5-TPP/ITERTRAN Modelling of ITER Divertor Target Damage and Plasma Contamination following ELMs and Disruptions	11
Divertor and Core Plasma Modelling for ITER	15
Heating and Current Drive - Physics	21
EFDA/06-1406 (TW6-TPHE-ECHULB4) Design and Analysis of the Upper Launcher and Port Plug for the ITER ECH&CD System	23
and TW6-TPHE-ECHULA (Subtasks C and D)	
Diagnostics	29
EFDA/06-1417 (TW6-TPDS-WINCOD2) ITER Practice for Non-Metallic Replaceable Window Assemblies	31
TW4-TPDC-IRR CER Irradiation Effects in Ceramics for Heating and Current Drive, and Diagnostics Systems.....	34
Vessel/In-Vessel	37
TW5-TVV-EBWO Demonstration of Overhead E-Beam Welding.....	39
Magnet Structure and Integration	43
EFDA/03-1105 (TW3-TMSC-CRYLAB) Cryogenic Laboratory Tests for V-I Characterisation of Subcable Samples.....	45
EFDA/04-1216 (TW4-TMSC-CRYOLA) ITER Cryogenic Testing Collaboration Task between CEA Grenoble and Forschungszentrum Karlsruhe.....	49
EFDA/05-1274 (TW5-TMSM-CRYTES) Cryogenic Testing of Materials, Welds and ITER Mock-ups for Magnet Structures	55
EFDA/05-1276 (TW5-TEB-CRYO2) Design of the ITER Cryoplant and Cryodistribution System	60
TW5-TMSF-HTSMAG Scoping Study of HTS Fusion Magnets	62
TW5-TMSC-HTSPER HTS Materials for Fusion Magnets	65
Breeding Blanket	69
TW5-TTB-001 Construction of the High Pressure Helium Loop (HELOKA-HP/TB) for Testing of TBMs.....	71
EFDA/06-1393 (TW6-TTB-RFMON1) Technical Monitoring Assessment of the EU/RF Collaborative Task on the Development of Diagnostic Systems for Electromagnetic TBMs.....	74

Breeding Blanket – HCPB Blanket Concept	75
TTBB-001 Helium Cooled: TBM Design, Integration and Analysis	77
TW5-TTBB-001 D 2 Detailed Design of Sub-components and Prototypical Mock-ups for the HCPB TBM Qualification	77
TW5-TTBB-001 D 9 Study with Experimental Verification of the Pebbles Filling in the HCPB TBM	81
TW5-TTBB-001 D 11 Analyses for the HELICA and HEXCALIBER Experiments using the ABAQUS Drucker-Prager Model.....	83
TW6-TTBB-001 D 2 Activation and Decay Heat Analyses of the HCPB TBM	85
TW6-TTBB-001 D 3 HCPB TBM Design and Integration Analysis	87
TTBB-002b Helium Cooled: Blanket Manufacturing Technologies	95
TW2-TTBB-002b D 5 Manufacturing of HCPB Cooling Plates by Diffusion Welding.....	95
TTBB-003 Helium Cooled: Out of Pile Testing.....	99
TW5-TTBB-003 D 1 Manufacturing and Testing of Mock-ups for Investigation of Coolant Flow in the Manifold System of HCPB TBM (GRICAMAN Experiments).....	99
TTBB-006 Helium Cooled: Breeder and Neutron Multiplier Materials.....	105
TW6-TTBB-006 D 1 Development of Beryllium and Beryllium Alloy Pebble Beds with Improved Tritium Release Characteristics	105
TTBB-006b Helium Cooled: Thermo-mechanical Modelling of Pebble Bed Assembly	108
TW2-TTBB-006b D 2 Development of Pebble Beds Models	108
and TW2-TTBB-006b D 3 Validation of Pebble Beds Models	
Breeding Blanket – HCLL Blanket Concept	111
TTBA-006b Water-Cooled: Magneto-Hydrodynamics	113
TW2-TTBA-006b D 1 Test and Modeling of Forces Convection MHD.....	113
TTBC-006 Helium-Cooled Lithium Lead: Magneto-Hydrodynamics and Liquid Metal Materials.....	116
TW5-TTBC-006 D 1 MHD Experiments on a 3D Relevant Mock-up of the HCLL TBM.....	116
Materials Development – Structural Materials	119
EFDA/05-1244 Investigation of Options to Reduce Critical Elements in Low Activation (TW4-TTMS-RedAct) Ferritic/Martensitic Steels	121
TTMS-001 Irradiation Performance	124
TW2-TTMS-001b D 5 Tensile, Charpy and Fatigue Specimen Testing after Neutron Irradiation up to 15 dpa in the Range of 250°C – 450°C	124
TW2-TTMS-001b D 9 Fast Reactor Irradiation up to 30 dpa, at 340°C of Tensile, Charpy and LCF RAF/M Specimens, Completion of the PIE	128
TW4-TTMS-001 D 1 Fabrication and Irradiation of Fe-54 enriched Samples to Study the Influence of He/dpa Ratio on Materials Degradation up to Medium Dose Level.....	132
TW5-TTMS-001 D 2	
TW5-TTMS-001 D 4 TAP (Tomography Atomic Probe) Analysis of EUROFER Material Irradiated in the ARBOR Irradiation Campaign.....	135
TW5-TTMS-001 D 10 Mechanical Post Irradiation Examinations of FZK-Specimens Irradiated in the ARBOR-2 Experiment in the BOR 60 Reactor	139

	Page
TW5-TTMS-001 D 11	Assessment of Irradiations performed on EUROFER 97 140
TW5-TTMS-001 D 14	Assessment of Irradiated Fracture Mechanic Samples on EUROFER, F82H (and OPTIFER) to Study the Size Effect 142
TTMS-002	Metallurgical and Mechanical Characterisation 144
TW2-TTMS-002a D 19	Creep-Fatigue Testing at 550°C on EUROFER, Continuation to Longer Times Preferably under Controlled Atmosphere 144
TTMS-003	Compatibility with Hydrogen and Liquids 145
TW4-TTMS-003 D 1 TW6-TTMS-003 D 3	Development of Modeling Tools to Describe the Corrosion Behaviour of Uncoated EUROFER in Flowing Pb-17Li and their Validation by Performing of Corrosion Tests at T up to 550°C 145
TTMS-004	Qualification Fabrication Processes..... 149
TW4-TTMS-004 D 1 TW6-TTMS-004 D 1-3	Improve Design Limits of Welded Components through Improved Post Weld Heat Treatments, Qualification and Improvement of Welded and Diffusion Bonded Joints 149
TW5-TTMS-004 D 1	Diffusion Welding Techniques..... 153
TTMS-005	Rules for Design, Fabrication and Inspection 156
TW2-TTMS-005b D 1	TBM Design Rules..... 156
TW2-TTMS-005b D 2 and TW5-TTMS-005 D 8	Evaluation of the Material Design Limits for TBM's Application Definition of an Experimental Programme for Validation of HT Creep-fatigue Rules at Fusion Relevant Conditions..... 161
TW2-TTMS-005b D 4	Creep-fatigue Lifetime Prediction Rules for Irradiated EUROFER 167
TW2-TTMS-005b D 7 and TW5-TTMS-005 D 3	Small-scale Fracture Mechanics Specimens SSTT: Model the Ductile Region – Development of Models for Transferability of Small Size Specimens to Standard Size and FW Application
and TW6-TTMS-005 D 12	SSTT: Continuation of the Modeling the Ductile Region – Development of Models for Transferability of Small Size Specimens to Standard Size and FW Applications 169
TW4-TTMS-005 D 2	Mechanical and Structural Characterization of EUROFER 97-2..... 175
TW5-TTMS-005 D 4	Experiments in Support of Modelling Activities on Size Effects 182
TW5-TTMS-005 D 5	High Temperature Fracture Mechanical (creep-fatigue) Rules: Formulation and Implementation 184
TW5-TTMS-005 D 6	Define and Perform Accompanying Experiments to D 5 (e.g. creep crack growth at 550°C)..... 185
TW5-TTMS-005 D 7	General Implementation of HT Rules (including creep fatigue interaction rules) 187
TW5-TTMS-005 D 9	Experimental Programme for Verification of HT Creep-fatigue Rules from Uniaxial Experiments (e.g. LCF tests with long dwell time) and/or Multi-step LCF Tests 190
TW6-TTMS-005 D 4	Experimental Verification and Validation of Newly Implemented HT Creep-fatigue Rules 195
TTMS-006	High Performance Steels 196
TW6-TTMS-006 D 5	Nano Compositied Ferritic Steels for HT Application: Identification of Promising Candidate Allow Compositions and Respective Fabrication Routes According to the Outcome of the 2004 Study. Production of Different Laboratory Batches (14%Cr) 196

	Page
TW5-TTMS-006 D 6	Characterisation of Reference EU ODS-EUROFER Batch (Tensile, Creep and Charpy) 201
TW5-TTMS-006 D 10	Characterisation of Reference EU-ODS-EUOFER Batch: Optimisation of Heat Treatment, Ageing Behaviour and Microstructural Characterisation 203
TTMS-007	Modelisation of Irradiation Effects 206
TW5-TTMS-007 D 5 TW5-TTMS-007 D 10	Defect Microstructure Evolution 206
TW5-TTMS-007 D 7 TW6-TTMS-007 D 10	Production and Characterization of Single Fe-Cr Crystals and Elaboration of a Critical Review of the Physical Metallurgy of EUROFER Alloying Elements and Impurities, Heat-treatment/Phases/Microstructure, Phase Stability, and Segregation 208
Materials Development – Advanced Materials 211
TTMA-002	Divertor and Plasma Facing Materials 213
TW3-TTMA-002 D 3	Mechanical Testing of Improved W Alloys: Tensile and Fracture Toughness Testing 213
TW3-TTMA-002 D 7 TW6-TTMA-002 D 6	Fundamental Studies on Mechanical Properties of W-alloys 216
TW4-TTMA-002 D 2 TW5-TTMA-002 D 2	Development of Improved W-Alloys for Application in a Power Plant with He Cooled Divertor 219
TW5-TTMA-002 D 6	Mechanical Testing of Irradiated W Tungsten Samples 222
EFDA/05-1232 (TW5-TTMA-WCOMP)	Development of Tungsten with Composite Structure for High Temperature Application 224
Materials Development - Nuclear Data 229
TTMN-001	Nuclear Data: EFF/EAF Data File Upgrade, Processing and Benchmark Analyses 231
TW6-TTMN-001 D 3	Test Application of MCSSEN Sensitivity/Uncertainty Calculations for the TBM in ITER using the Track Length Estimator Method 231
TW6-TTMN-001 D 4	Evaluation of Mn-55 Cross-Sections up to 150 MeV for the EFF-3 Library 232
TW6-TTMN-001 D 5	Benchmark Analyses for Revised/Updated EFF-3 Data Evaluations based on Monte Carlo Calculations with MCNP 234
TTMN-002	Nuclear Data: Benchmark Experiments to Validate EFF/EAF Data 238
TW6-TTMN-002 D 2	Design of TBM-HCLL Neutronics Experiment: Design of Measurement Techniques for Tritium Production Rates (TRP) and of Neutron and γ -ray Flux Spectra; Assessment of Uncertainties 238
TW6-TTMN-002 D 3	Design of TBM-HCLL Neutronics Experiment: Monte Carlo (MC) Based Pre-analysis of Design and Optimise the Experimental Set-up for the Measurements of the Flux Spectra and the Tritium Production 242
TW6-TTMN-002 D 5	Pre- and Post-analysis of the Validation Experiments for Cr Cross Sections up to 55 MeV in an IFMIF-like Neutron Spectrum 244
TW6-TTMN-002 D 7	Validation Experiment of Gamma Activities of La Irradiated in Fusion Peak Neutron Field 248

Materials Development – IFMIF		251
TTMI-001	IFMIF – Accelerator Facilities	253
	TW5-TTMI-001 D 3 Studies of End-to-end Transmission and Beam Losses along the Accelerator Facilities Considering the Effects of the Different Sources of Errors on the Transport of the Beam	253
TTMI-003	IFMIF – Test Facility	255
	TW5-TTMI-003 D 8 Tungsten Spectral Shifter: Neutronics Analysis (dpa Evaluation, H, He and other Impurities Generation, Recoil Spectrum, etc.) of Different Positions and Geometries	255
	TW5-TTMI-003 D 9 Automatic Generation of a 3D Test Cell Model for MC Calculations from CAD Data.....	262
	TW6-TTMI-003 D 1 Manufacturing and Procurement of a Complete HFTM Compartment Including the Whole Set of Test Samples and the Qualification of Brazing Procurement for the Heating Systems.....	264
	TW6-TTMI-003 D 3 Development of Activation Foils Dosimeters for Determination of IFMIF-relevant Flux Spectra: Analytical Tools.....	268
	TW6-TTMI-003 D 5 Structural Materials Selection Guideline for In-Test-Cell Components	274
EFDA/05-1291 (TW5-TTMI-003a)	Preliminary Design Description Document for the IFMIF Test Facility.....	275
TTMI-004	IFMIF – Design Integration	276
	TW6-TTMI-004 D 2 Proton and Deuteron Induced Activation and Dose Rates of the EVEDA Accelerator Prototype, including Beam Dump. Proposals for Operational Scenarios of Low Activation.....	276
Fuel Cycle – Vacuum Pumping		279
TW3-TTFF-VP 35	Study of Cryopump Compatibility with Carbon Erosion Products	281
EFDA/04-1173 (TW4-TTFF-VP 41)	Design and Procurement Specification for ITER Prototype Torus Exhaust Cryopump	284
TW4-TTFF-VP 45	Performance Assessment of Mechanical Pumps in Tritium Plant	288
TW5-TTFF-VP 51	Mechanical Tests and Post-operational Examination of TIMO	289
TW5-TTFF-VP 57	ITERVAC Validation Test	294
TW5-TTFF-VP 58	Upgrade of TIMO	299
TW6-TTFF-VP 53	Tritium Test of Ferrofluidic Cartridge Seals for Roots Roughing Pump	301
TW1-TTF/VP 13	Compatibility of Leak Localisation Tracers with Cryopanel	304
Fuel Cycle – Tritium Plant		307
TW1-TFF-TR 11 and TW3-TTFD-TR 31 and TW4-TTFD-TR 41 and TW4-TTFD-TR 43	Gas Processing during in-situ Tritium Recovery from PFC's.....	309
	Improvements to the Mechanical Design of the PERMCAT Component	
	Experimental Investigation of Undesired Side-reactions in PERMCAT	
	Comparison of Batch and Continuous Operation Modes for the Impurity Processing Stage of the Tokamak Exhaust Processing System	
TW1-TTF/TEP 13A and TW3-TTFD-TR 33	Self-assay, Fast Delivery Tritium Storage Bed Development	319
	Determination of Isotopic Effect during Rapid Delivery from Storage Beds	

TW4-TTFD-TR 44	Inactive Tests of Selected Composition Control Loop Performance under Typical ITER Operating Conditions.....	320
TW1-TTF/TR 16	Tritium Recovery from Ceramic Breeder Test Blanket Module.....	321
TW4-TTFD-TR 46	Design, Experimental Plan and Procurement of Cryogenic Distillation System for Isotope Separation Tests for ITER	324
TW4-TTFD-TR 47	Upgrading of LPCE (Liquid Phase Catalytic Exchange) Column for Trade-off Studies between WDS and ISS	326
EFDA/05-1237 (TW5-TTFD-TPI 51)	Development of ITER PRM and Standard Parts Catalogues in CATIA V5 for Tritium-containing Systems and Components	329
EFDA/05-1239 (TW5-TTFD-TPI 52)	Development of a Resource-loaded Schedule for the Overall ITER Tritium Plant Integration	332
EFDA/05-1240 (TW5-TTFD-TPI 53)	Definition of the Interfaces and Supply Limits between Tritium Plant and the Torus Pumping, Fuelling, Neutral Beam and Wall Conditioning Systems	334
EFDA/05-1251 (TW5-TTFD-TPI 54)	Development of a Tritium Manual for ITER.....	336
EFDA/05-1342 (TW5-TTF-TLK)	Documentation of ITER-relevant Experience Gained from Operation of the Tritium Laboratory (TLK) in 2005 and 2006	337
Safety Analysis and Environmental Impact		339
TW5-TSS-SEA 3.5	In-vessel Safety: Mitigation of Hydrogen and Dust Explosions.....	341
EFDA/05-1369 (TW5-TSS-SEA 3.5)	Development of a Dust Explosion Computer Model	345
TW5-TSS-SEA 5.4	Busbar Arcs Behaviour and Consequences	353
	TW5-TSS-SEA 5.4 D 2-4 Experimental Simulation in the VACARC Facility.....	353
TW5-TSS-SEA 5.5	Validation of EU Safety Computer Codes and Models	358
	TW5-TSS-SEA 5.5 D 5 Validation of MAGS: Quench Simulations for the Q3D Coil	358
TW5-TSS-SEP 2	Dosis to the Public and Validation of UFOTRI	361
DEMO Conceptual Studies		363
TRP-001	PPCS He-cooled Divertor Concepts	365
	TW5-TRP-001 D 1 He-cooled Divertor Development: Conceptual Design, TW6-TRP-001 D 1+2 Analysis, and Tests	365
TRP-002	DEMO Physics Studies	375
	TW5-TRP-002 D 2 Analysis of Total Radiation in Tokamak Reactor Scenarios.....	375
	TW6-TRP-002 D 3 Development of an Improved Treatment of Plasma Radiation for Medium- and High-Z Impurities	380
EFDA/05-1283 (TW5-TRP-003 D 1)	Review of Blanket Segmentation and Maintenance	383
EFDA/05-1280 (TW5-TRP-005 D 2)	Review of Blanket Concepts for the DEMO Conceptual Study.....	387
TRP-005	Neutronic Analysis	394
	TW6-TRP-005 D 2 TBR and Shielding Analyses for the HCPB DEMO Reactor	394

	Page
TRP-009	He-cooled Divertor Test Module for ITER..... 395
	TW5-TRP-009 D 2 Testing suitable HEMS/HEMJ Prototypes in ITER 395
TRP-012	Optimisation of a Fusion Power Plants for the Production of Hydrogen 398
	TW6-TRP-012 D 1b Optimisation of a ‘Start-up’ Scenario where the Power is less than 100 MW 398
	TW6-TRP-012 D 2 Assessment of the Impact of a Fusion Power Plant for H ₂ Production on Internal Components 400
Tritium Inventory Control 407	
TW3-TI-VP 31	High Temperature Regeneration Tests of the ITER Model Torus Cryopump 409
Design Support and Procurement 411	
EFDA/05-1279 (TW5-TDS-NSA3)	Nuclear Analyses Service: Part 1 – Enabling-Coordinating Activities..... 413 Del. 5 – Version 1 of the CAD – MCNP Interface Programme and Manual of Use
EFDA/05-1331 (TW5-TDS-CLDES)	Final Design of HTS Current Leads for ITER..... 416
JET Technology 419	
JW5-FT-3.11	Assessment of in-situ Detritiation in JET – OPL Tile Analysis 421
JW5-FT-5.20	Shutdown Dose Rate at JET Tokamak – Code Benchmark 425
JW1-FT-6.1	Impact of Tritium on the Performance of a Prototype Cryosorption Pumping Panel..... 426
Heating Systems Technology Project 431	
EC Coaxial Cavity Gyrotrons and Test Facility:	
TW6-THHE-CCGDS4 D 1b	Design, Support to the Industrial Development and Preparation of Technical Specifications
and TW6-THHE-CCGT1 D 1	Scientific Execution and Co-ordination of the Tests 433
EFDA/04-1185 (TW4-THHN-IITF2)	The First ITER NB Injector and the ITER NB Test Facility: Progress in the Design 437
EFDA/05-1352 (TW5-THHN-MONRF)	Monitoring the EU/RF Collaborative Tasks on the First ITER NB Injector and the ITER NB Test Facility 439
Physics 441	
ECR Heating and Current Drive – Step-Tunable Gyrotron Development 443	
Microwave Heating for Wendelstein 7-X 447	
Underlying Technology 457	
Operation of the Fusion Materials Laboratory 459	
Appendix I	FZK Departments Contributing to the Fusion Programme..... 463
Appendix II	Fusion Programme Management Staff 465
Appendix III	Glossary 467

Plasma Edge

EFDA/03-1080 (TW3-TPP/MATDAM) Characterisation of Material Damage for EU W and CFC ITER Divertor Materials under Repetitive Plasma Energy Fluxes by Modelling and Experimental Validation

1. Introduction

In the future tokamak ITER the divertor armour is going to be covered with tungsten tiles manufactured as so-called W-brushes and with the carbon fibre composites (CFC). During the ITER operation in the ELMy H-mode at repetitive pulses of plasma impacts with an anticipated heat load of $Q \sim 0.5 - 4 \text{ MJ/m}^2$ on a time scale of $\tau \sim 0.3 - 0.6 \text{ ms}$, the armour materials will be eroded due to surface melting (W), brittle destruction (CFC) and surface vaporization (W and CFC). Such large loads are a major concern for a safe and reliable reactor operation, because the erosion restricts the lifetime of the wall components and causes contamination of the confined plasma.

This report summarises joint numerical and experimental investigations of erosion mechanisms of CFC NB31 and tungsten targets manufactured in the EU (Plansee AG, Austria) at ITER relevant conditions. The investigations were performed at FZK, FZ-Jülich and TRINITI¹. The main experimental activities were carried out at the plasma gun facility QSPA of TRINITI, and the FZJ provided precise analyses of the sample damages after hydrogen plasma impacts of QSPA at the conditions relevant to the mentioned ITER heat loads.

The experiments aimed also at the validation of computer codes under development at FZK. Regarding the material behaviour under high heat fluxes predicted for ITER, FZK applied the surface melt motion code MEMOS for modelling the W damage and the brittle destruction threshold code PHEMOBRID. The computer modelling with MEMOS and PHEMOBRID allowed also the interpretation of the processes that cause the damage produced by the plasma gun to the EU samples.

2. Experiments at QSPA

The regimes of the QSPA provided maximum values of impacting energy density equal to 0.5, 1.0, 1.5 MJ/m^2 , with a plasma pulse duration 0.5 ms. The incidence angle of the plasma stream was 60°. Three CFC and three W targets were exposed to 100 plasma pulses. The targets were preheated up to 500°C.

The absorbed energy density Q_{abs} is one of key parameters determining material erosion, both for the tungsten targets and the CFC targets. The distribution of Q_{abs} was accurately measured with a two-dimensional multi channel calorimeter that contains 11 cells. 6 cells were positioned in a longitudinal and 5 cells in cross directions. These measurements indicated that Q_{abs} has a maximum at the centre of the irradiation spot and its value decreases when going away from the centre (Fig. 1). The maximum of Q_{abs} was measured as a function of the voltage applied between the electrodes of the plasma gun.

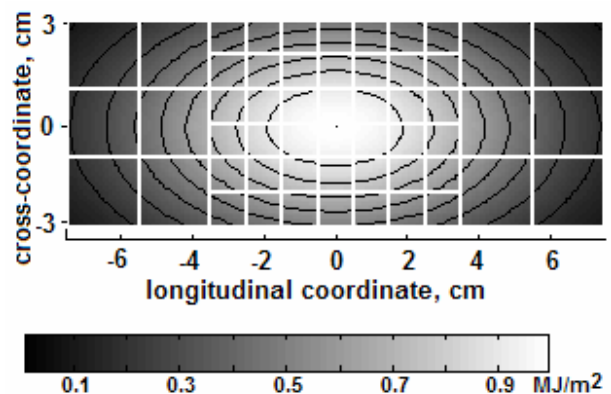


Fig. 1: Q_{abs} on CFC surface in the QSPA.

¹ State Research Centre of Russian Federation Troitsk Institute for Innovation and Fusion Research

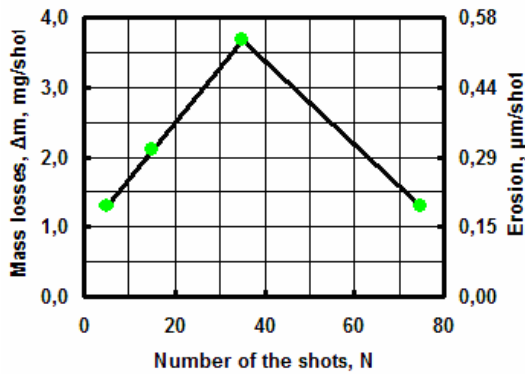


Fig. 2: Mass loss of a CFC sample and its erosion rate as a function of pulse number.

After a total of 100 pulses, the surface profile of each target was measured by a laser profilometer in order to find the value of material losses during a post-mortem characterisation of FZJ. Noticeable mass losses were observed only for the CFC sample that was exposed at the energy density of 1.4 MJ/m^2 (see Fig. 2).

The erosion of CFC samples was determined mainly by erosion of PAN-fibres. The following conclusions have been made based on the results of electron microscope observations, depending on the energy density $Q = Q_{\text{abs}}$. Erosion was observed at $Q > 0.5 \text{ MJ/m}^2$, at first near the plasma facing corners of the tiles.

At $Q > 0.9 \text{ MJ/m}^2$ after 100 exposures the erosion expands over the total surface. At $Q > 1.3 \text{ MJ/m}^2$ a significant erosion of PAN-fibres develops already after 10 exposures.

For tungsten targets, those analyses allowed the conclusion that the erosion of W is determined mainly by the melt layer movement and droplets ejection (see Fig. 3). The following observations were made: At $0.4 < Q < 1.0 \text{ MJ/m}^2$ erosion (melting onset) was observed at the edges of the tiles that face the plasma. At $1.0 < Q < 1.3 \text{ MJ/m}^2$ melting develops up to the total surface. At $1.3 < Q < 1.6 \text{ MJ/m}^2$, the melt accumulates on the plasma shadow edges and after 10 shots melt bridges between the tiles start to form. At $Q > 1.3 \text{ MJ/m}^2$ a droplet ejection was observed, however, its intensity decreases with increasing the number of pulses, which is due to the smoothing of edges after the plasma impacts. At $Q > 1.6 \text{ MJ/m}^2$ small mass losses occur. An averaged erosion of the sample of 0.06 μm/shot was obtained. It is concluded that the main mechanism of tungsten mass losses is the droplet ejection.

W3,R3, 100 exposures

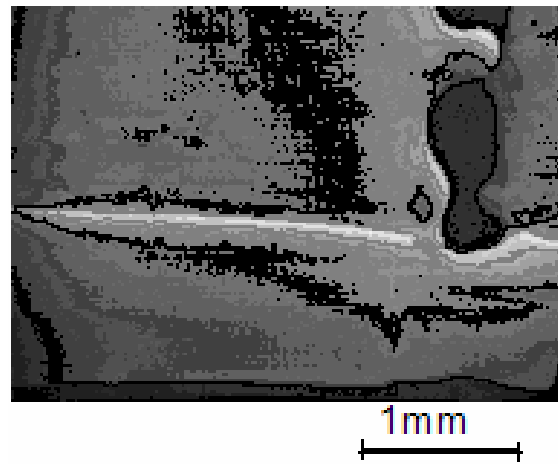


Fig. 3: View of the tungsten tile surface obtained using an electron microscope.

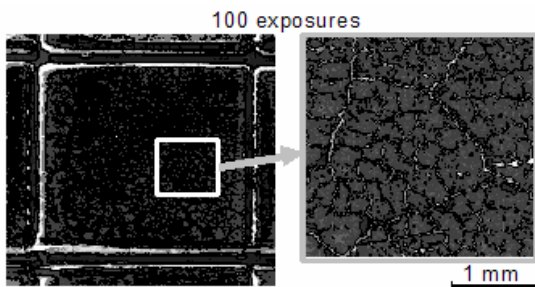


Fig. 4: The images of tungsten tile surface at $Q_{\text{abs}} = 0.9 \text{ MJ/m}^2$.

Crack formation on W surfaces was observed at Q_{abs} larger than 0.8 MJ/m^2 (Fig. 4). At $0.8 < Q_{\text{abs}} < 1.6 \text{ MJ/m}^2$, two types of cracks have appeared forming overlapping grids on the surface. The type 1 cracks have a characteristic size of the grid cells of about $0.1\text{-}0.2 \text{ cm}$; they appeared after 20 pulses. The cell sizes of type 2 cracks are one order of value less: $200\text{-}300 \text{ μm}$; those cracks appeared after 50 pulses. At $Q_{\text{abs}} > 1.6 \text{ MJ/m}^2$ after 100 pulses, the cracks formed an additional, very fine grid (the type 3 cracks) with characteristic cell sizes

significantly smaller than that of type 2 cracks. After each pulse the fine grid melts but it appears again on the resolidified surface. The post-mortem metallographic analysis showed that the depths of the type 1 cracks and the depths of the type 2 cracks are about 500 μm and 50 μm , respectively.

3. Validation of FZK codes by the plasma guns QSPA and MK-200UG

The code MEMOS was mainly applied in two regimes: a) it was validated on the melting threshold in the plasma gun experiments and b) it was used for predictions of melt motion erosion in different arrangements of the ITER design. In addition, the code was validated on the tungsten vaporization threshold at the plasma gun MK-200UG. The former validations of MEMOS have been mentioned in the MATDAM annual report of 2005. The different simulations with MEMOS for ITER are subject of the reports of the EFDA task TW5-TPP-ITERTRAN. Now the code is extended to the three-dimensional geometry which enabled us to take into account the edge effects as well as realistic surface heat load distributions, and to elaborate simulations of the melt motion damage to the W-brush targets. Main achievements relevant to the W-brush geometry are summarized as follows.

The tungsten melting threshold obtained in the experiments on the plasma guns mentioned is in reasonable agreement with the calculations, which justifies the application of the code for the investigation of melt motion damage of the tokamak tungsten armour. The modelling for W-target heating under the QSPA conditions demonstrated melting onset of the brush edges at $Q > 0.7 \text{ MJ/m}^2$ and brush surface melting at $Q > 1 \text{ MJ/m}^2$. The calculations on evaporation erosion profiles are in agreement with experiments (Fig. 5).

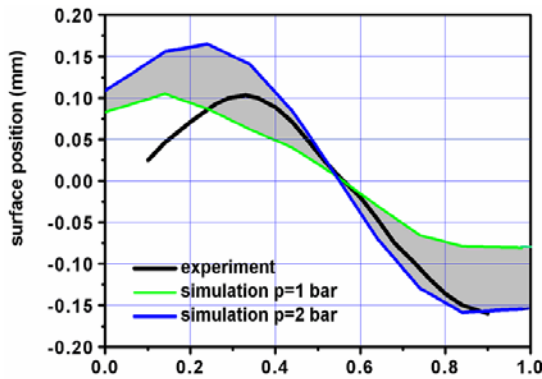


Fig. 5: Comparison of the profiles of W-brushes measured experimentally and obtained in simulations after 100 shots for $Q = 1.5 \text{ MJ/m}^2$.

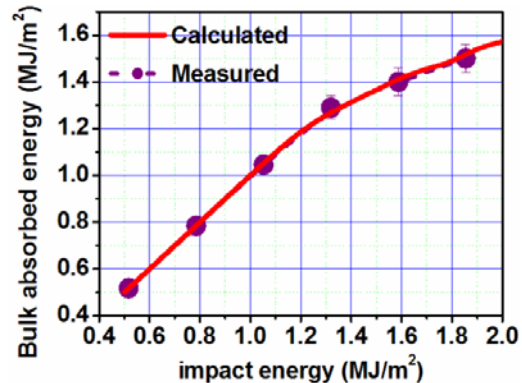


Fig. 6: Q_{abs} vs. impact energy density for the CFC, calculated with PHEMOBRID and measured at QSPA.

The code PHEMOBRID was validated against the plasma guns MK-200UG and QSPA and employed for predictions of brittle destruction caused by the plasma impacts which are expected in ITER. The EU CFC targets features and experimental conditions are implemented, including the preheating of the targets. The dependence of the absorbed energy versus the incident energy calculated for the pitch bundles agrees well with the QSPA-T measurements. A significant erosion of the brush edges and PAN bundles at $Q > 0.7 \text{ MJ/m}^2$ and pitch bundle erosion at $Q > 1.3 \text{ MJ/m}^2$ was obtained. The negligible erosion of pitch bundles and a significant evaporation erosion of PAN bundles at the lateral and frontal edges are simulated. In total, the agreement between the modelling and the experiment seems rather good. The vapour shield effects are preliminary taken into consideration, which allowed a good fitting with the measurements (Fig. 6), but a more appropriate vapour shield model must be implemented in the code.

4. Conclusions

The experimental results obtained at the plasma gun facility QSPA with the tokamak candidate materials W and CFC allowed a validation of the FZK codes MEMOS and PHEMOBRID and thus better computer simulations of material damages for ITER transient loads. A good agreement between the simulations and the experiments is obtained. The joint results of the

experiments and numerical modelling described in this report stimulated further work necessary for reliable predictions of material behaviour in ITER.

Staff:

I.S. Landman
B.N. Bazylev
S.E. Pestchanyi

Literature:

- [1] B.N. Bazylev, G. Janeschitz, I.S. Landman, A. Loarte, S.E. Pestchanyi, "Melt damage simulation of W-macrobrush and divertor gaps after multiple transient events in ITER", 17th International Conference on Plasma Surface Interactions in Controlled Fusion Devices, Hefei, China, May 22-26, 2006. To be published in Journal of Nuclear Materials.
- [2] B. Bazylev, G. Janeschitz, I. Landman, G. Federici, A. Loarte, M. Merola, N. Klimov, V. Podkovyrov, A. Zhitlukhin, J. Linke, J. Compan, T. Hirai, "Erosion of CFC and W macrobrush target after multiple exposures related to ITER ELM. Numerical simulations vs. experiments", 33rd European Physical Society Conference on Plasma Physics, Rome, Italy, June 19-23, 2006. To be issued on CD.
- [3] B. Bazylev, G. Janeschitz, I. Landman, G. Federici, A. Loarte, M. Merola, N. Klimov, V. Podkovyrov, A. Zhitlukhin, V. Safronov, I. Garkusha, "ITER transient consequence for material damage. Modelling vs. experiment", 11th International Workshop on Plasma-Facing Materials and Components for Fusion Applications, Invited lecture, Greifswald, Germany, October 10-12, 2006. To be published in Physica Scripta.
- [4] S. Pestchanyi, J. Linke, "Simulation of cracks in tungsten under ITER specific heat loads", 24th Symposium on Fusion Technology (SOFT-24), Warsaw, Poland, September 2006. To be published in Fusion Eng. and Design.

EFDA/05-1305 (TW5-TPP/BEDAM)

Modelling of Material Damage to Be-clad and Be-coated ITER Plasma Facing Components under Type I ELMs, Disruptions and Mitigated Disruptions and Scoping Studies for First Experimental Validations

1. Introduction

The ITER candidate material beryllium will be located at the main chamber wall in form of Be-clad blanket modules. In addition, Be-coated plasma facing components are likely to appear in both divertor legs, where Be eroded from the main chamber wall may form the deposits covering in a large proportion the CFC and W armour in the areas mostly subject to particle fluxes. A systematic investigation of beryllium surface damage under transient loads of ITER is still absent. Here the computer modelling on Be behaviour carried out in 2006 in FZK-IHM is reported.

Like the main types of erosion of tungsten surfaces in ITER, also the beryllium armour damages are expected to be evaporation, melt motion and melt splashing. For all ITER transient events, in particular the ELMs and mitigated disruptions, the formation of metallic droplets and the splashing of melt layers can play a major role, thus determining the lifetime of the plasma facing metallic armour.

In the computer modelling on Be armour damage the code MEMOS is applied for the ITER ELM-like loads. The melting and evaporation thresholds for the bulk Be only as functions of the heat load duration are calculated. The evaporation from the melt layer is simulated. The evaporation and melt layer thickness under the expected heat loads ranging between 0.2 and 2 MJ/m² for pulse load durations from 0.2 to 0.6 ms are obtained. At the main chamber surface also the radiative transient loads that may occur during disruptions mitigated by massive noble gas injection are assumed.

In addition the main mechanisms of droplet formation under ITER relevant ELM heat loads are estimated, namely the growth of surface waves due to the Kelvin-Helmholtz instability generated by the impacting plasma streams. Preliminary estimations of the rates of mass losses from Be molten surfaces are done. The conditions for intense droplet formation in typical ITER weak ELMs and Type I ELMs (giant ELMs), as well as future experiments on the plasma gun QSPA in Troitsk, Russia, are simulated.

2. The calculations for melting and evaporation thresholds

The code MEMOS has been successfully validated, both on beryllium and tungsten armours, in many experiments performed at the e-beam facility JUDITH in Jülich (on Be and W) and the plasma gun facilities QSPA and MK-200UG in Troitsk (on W only). To apply the code for the new Be issues it was developed further. The thermophysical properties of bulk Be and Be coating on W and CFC armours have been updated and a new model accounting for the radiation screening by the vapor and the reflection from the surface was developed. For the Be coating, the slowing down of impacting ions by the vapour shield was taken into account. Also the properties of the thermal W and CFC contacts with the Be-coating have been implemented in MEMOS.

After that systematic numerical simulations of the erosion for the given parameters started. At first the melting and evaporation thresholds for the bulk Be and the typical thickness of the melt pool as functions of the heat load duration were obtained. It was assumed that the target is heated either by the plasma stream with an ion energy of 100 eV or the electromagnetic radiation with the power deposition density Q varying spatially as a Gaussian profile with a half-width of 4 cm and peak values up to 2 MJ/m². Several scenarios for different heat load durations $\tau = 0.2, 0.3, 0.4, 0.5$ and 0.6 ms with rectangular pulse shape were calculated. The initial target temperature was assumed to be 300K.

As an example, in Fig. 1 the calculated contours of the Be target bulk temperature for the reference scenario with a radiation load duration 0.5 ms are shown. The margin of the melting at the surface corresponds to the heat load of 0.5 MJ/m², which is the melting threshold. A substantial evaporation occurs for heat loads exceeding 1 MJ/m².

For all radiation load scenarios, the maximum depth of the melt pool is achieved at a time that only slightly exceeds the pulse duration τ . The simulations demonstrated that for a given heat load the maximum melt layer thickness depends on the pulse duration and varies in the range between 35 μm ($\tau = 0.2$ ms) and 57 μm ($\tau = 0.6$ ms) (Fig. 2).

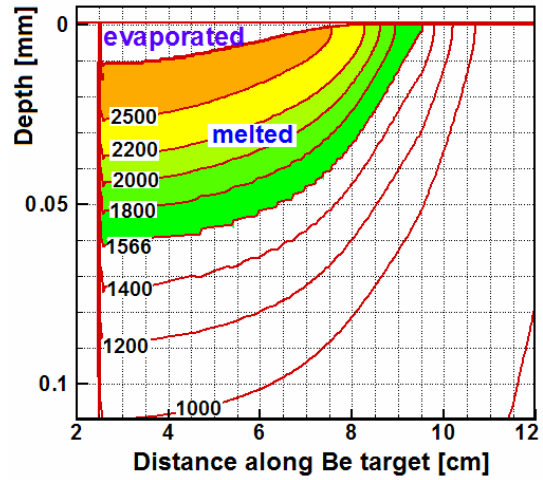


Fig. 1: Volumetric distribution of Be bulk temperature at pulse length of 0.5 ms. The resolidification finishes after 1.1 ms.

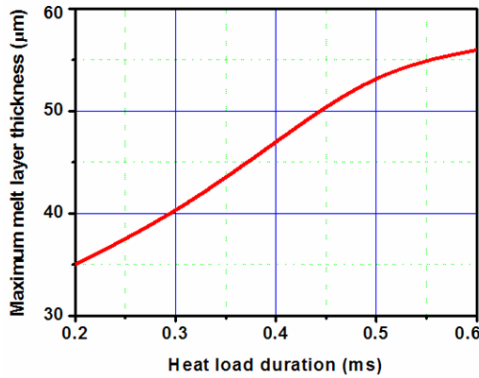


Fig. 2: Melt depth vs. heat load duration.

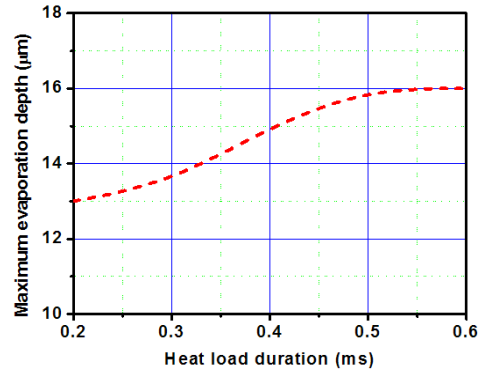


Fig. 3: Evaporation depth vs. heat load duration.

Respectively, the maximum evaporation depth varies between 13 and 16 μm (Fig. 3).

It was found that the vapour shield essentially decreases the evaporation thickness. However, it is insignificant for the melt layer thickness. The dependences of the evaporation depth as functions of the energy heat load for $\tau = 0.2$ and 0.5 ms are shown in Fig. 4. Cases with the radiation heat load and the vapour shielded plasma heat load are compared. In the case of plasma impact of Fig. 1 with the same parameters, the vapour shield influences as follows. The melt pool is fully resolidified after approximately 2 ms and the maximum thickness of the evaporated material is about 2 μm .

The melting threshold is defined as the heat load density of a rectangular pulse of radiation at the surface that corresponds to the onset of melting. Similarly, the evaporation threshold corresponds to the onset of excessive evaporation. The numerical approach of MEMOS assumes the evaporation threshold as the heat load corresponding to the evaporation of 0.1 μm of Be. The dependences of the melting and evaporation thresholds vs. heat load duration for the Be armour are shown in Fig. 5. For the bulk Be target the values of the melting threshold are found to be approximately twice less than that of the bulk tungsten (e.g. 0.4 MJ/m² (Be) vs. 0.8 MJ/m² (W) for $\tau = 0.3$ ms). The simulation information obtained on the thresholds is useful for the future experiments which have to be performed at the QSPA and for further validations of MEMOS.

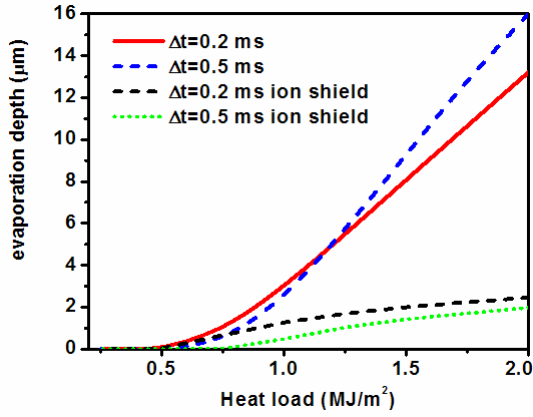


Fig. 4: The vapour shield influence ($\Delta t = \tau$).

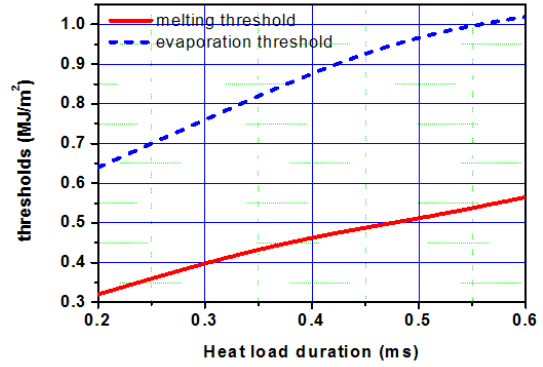


Fig. 5: Be target melting and evaporation threshold vs. load duration.

3. Splashing conditions for Be in future QSPA experiments and ITER ELMs

Formation of droplets and the splashing of the melt layer after ITER transients may be substantial for the erosion of Be coated armour. The cause for droplet formation is a rapid growth and subsequent breakaway of melt at the peaks of unstable Kelvin-Helmholtz- or capillary waves that are generated at the interface between the melt and the incident plasma (in case of weak ELMs) or at the melt-vapor interface (in case of essential evaporation). The surface roughness and the surface edges are responsible for the Rayleigh-Taylor instabilities. In 2006 only the most important mechanism of droplet formation was analysed, namely the one due to the Kelvin-Helmholtz (KH) instability caused by the impacting plasma stream.

The physical process responsible for the KH instability is as follows: A disturbance of the velocity field in the plasma caused by these waves gives rise to pressure variations over the surface. The pressure variations in phase with wave slopes transmit energy from the plasma to the melt layer. Transmission of the kinetic energy from the plasma to the melt leads to the growth of waves. The instability in its non-linear stage leads to droplets formation in the direction perpendicular to the surface.

An analytical consideration of the process in question has been carried out. The following main parameters determine the splashing criterion: the velocity V of the plasma along the melt surface, the plasma density N at the surface, and the time τ of intense plasma motion above the melt layer. An important condition determining the melt splashing is that the characteristic wave length λ remains less than the melt thickness h .

In future QSPA experiments aimed at simulating ITER loads onto Be targets, heat loads Q in the range 0.2 - 1.5 MJ/m² at $\tau = 0.5$ ms and conditions $V < 10^5$ m/s, $N < 10^{22}$ m⁻³ and $h < 50$ μm are to be chosen. For the weak ELMs expected in ITER (no vapour shield, $Q < 1.2$ MJ/m²) it should be $V < 10^5$ m/s, $N < 10^{20}$ m⁻³, $\tau < 0.3$ ms and $h < 80$ μm. Finally, in the case of ITER giant ELMs ($Q > 1.8$ MJ/m²) the vapour shield density may reach the values $N = 10^{24} - 10^{25}$ m⁻³, and $V = 10^3$ m/s. The resolidification time $\tau_{res} \sim \tau$ may exceed 1 ms, and $h \sim 10^2$ μm.

The dependence of λ and the mass loss rate on N for different V was obtained. Thereof, the splashing margins for the different cases are derived. 1) At the QSPA it follows that an intense droplet formation with the droplet sizes ~ 15 μm and the droplet velocity ~ 15 m/s may occur at $Q \sim 0.5-1.5$ MJ/m², and the mass loss rate is in the range 10 to 20 g/(cm²s), which yields a mass loss of 5 to 10 mg/cm² in 0.5 ms. 2) The weak ELMs do not cause the KH instability therefore the melt splashing will not occur. 3) The giant ELMs allow intense melt splashing. For instance, at $V = 10^3$ m/s the droplets of ~ 25 μm size may be splashed away with the velocity ~ 10 m/s, and the expected mass loss for $\tau \sim 1$ ms may reach 10² mg/cm².

4. Conclusions

The improved code MEMOS is applied for the estimation of the melt pool depth and the evaporation erosion of bulk Be for expected ITER ELM heat loads. The dependences of the melting and evaporation thresholds on the heat load duration are obtained. Those dependences can be useful for planning the experiments at the QSPA facility and for predicting the ITER design. Further validation of the code against experimental data should be performed using the QSPA. For a more precise estimation of melt splashing, a better knowledge of plasma parameters in the plasma shield is necessary, which can be calculated using the code FOREV.

Staff:

B.N. Bazylev
I.S. Landman

TW5-TPP/ITERTRAN

Modelling of ITER Divertor Target Damage and Plasma Contamination following ELMs and Disruptions

1. Introduction

It is expected that the Type I ELMs in ITER will primarily result in vaporization erosion at the divertor surfaces. Vaporized carbon plasma can contaminate the SOL and then the confined core plasma, which decreases the fusion power or can even lead to a disruption of the confinement. In 2006, the FZK-IHM computer modelling was targeted at the tolerable ELM frequency in ITER as a function of the ELM size was carried out using the codes FOREV and a newly developed two-dimensional code TOKES.

An improved ELM scenario is implemented in FOREV, which allows more adequate simulations than previously for the hot deuterium-tritium plasma lost from the confinement region. The lost DT plasma hits the surfaces of the divertor and the first wall and the vaporized carbon plasma fills the SOL. Finally FOREV calculates the carbon inflow N_C into the pedestal, and the following carbon penetration into the core was calculated using TOKES. The simulations have been performed for the ELM parameters with $W_{ELM} = 3.5 - 12.1$ MJ total ELM energy and the ELM duration $\tau_{ELM} \sim 0.5$ ms.

Other kinds of ITER wall erosion are surface melting in case of tungsten targets and brittle destruction (BD) for carbon fibre composite (CFC) armour. For modelling these processes the incompressible fluid dynamics code MEMOS was applied to calculate the damage to W surfaces. For the CFC erosion the phenomenological code PHEMOBRID based on well known BD threshold energy 10 kJ/g was used. In 2006 the most important mechanisms of droplet formation were analysed and implemented in MEMOS, namely the growth of surface waves due to the Kelvin-Helmholtz instability generated by the impacting plasma stream. For three-dimensional simulations of the CFC macrobrush damage accounting also for the lateral brush edges, the PHEMOBRID has been significantly upgraded and validated in experiments performed at the plasma gun facility QSPA for heat loads Q from 0.5 to 1.6 MJ/m², which is described in the reports of the task TW3-TPP/MATDAM.

2. Modelling of plasma transport with the codes FOREV and TOKES

Earlier simulations have been done for $N_C = 2.25 \times 10^{20}$ only, with the conclusion that in this case a tolerable ELM repetition period τ is 2 s, which allowed a preliminary estimation of the contamination amount in SOL. The vaporization onset itself and the vaporization rate have been shown to be sensitive to such details of the ELM structure as time- and spatial dependences of the heat flux caused by ELM, rather than to W_{ELM} and τ_{ELM} only.

Therefore, in the last FOREV calculations the divertor power loads during ELMs were simulated using elaborated plasma transport models based on the plasma cross-diffusion coefficient behaviour fitted to the existing tokamaks. As fitting parameters, the pedestal diffusion coefficients D_{ped} and the SOL diffusion coefficient D_{SOL} have been chosen (Fig. 1). After the impact of D-T-He plasma diffusing into the SOL from the pedestal, the vaporized carbon is ionized in the SOL and finally penetrates into the periphery of the confinement region. The calculations showed that the plasma boundary receives so large post-ELM contamination that the carbon density n_C

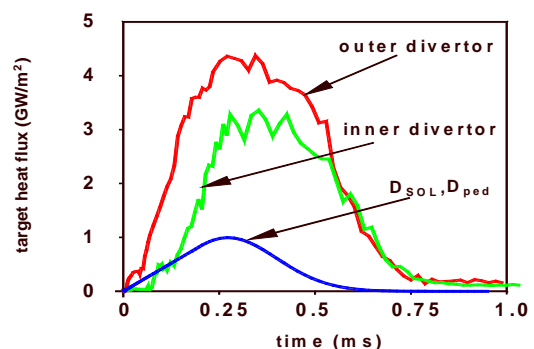


Fig. 1: D_{SOL} and D_{ped} schematically (dimensionless units) and the heat fluxes modelled by FOREV.

drastically exceeds the main species densities n_H (the subscript H stands for D and T). Fig. 2 demonstrates the distribution of the impurity in the SOL.

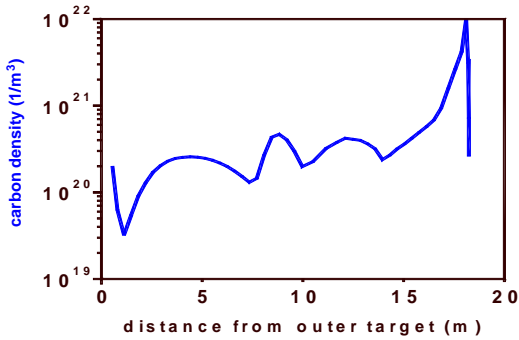


Fig. 2: Separatrix carbon density along the SOL at 1.1 ms after start of ELM ($W_{ELM} = 12.1$ MJ, $\tau_{ELM} = 0.5$ ms).

The models of TOKES simulating multi-fluid plasma transport in the ITER magnetic configuration and the radiation losses in the core during the whole time of the discharge have been generalized for arbitrary ratios n_C/n_H . The temperature of the confined plasma was assumed dropping with parabolic dependence on the poloidal magnetic flux coordinate, from 12 keV at the magnetic axis to 7 keV at the plasma boundary, which in carbon-free plasma corresponds to the α -fusion power of 80 MW foreseen in the ITER design. Plasma contamination by the carbon impurity decreases the fusion power (due to a decrease of the product $n_D n_T$) and increases the

radiation losses. The tolerable ELM repetition period is assumed to be given by the criterion $W_{rad} + \Delta W_{fus} < 40$ MW, with the radiation loss W_{rad} and the fusion power drop ΔW_{fus} calculated by TOKES and being caused by the carbon impurity.

The target vaporisation starts at $W_{ELM} = 4.0$ MJ. At larger W_{ELM} , within a few ms after an ELM the carbon plasma temperature in the SOL may drop down to 1-2 eV, which is due to the radiation loss. Using N_C calculated by FOREV, the core contamination by carbon after multiple ELMs is calculated with the code TOKES. Carbon plasma diffusion inside the core is simulated for the whole ITER discharge. The TOKES simulation starts from initially pure DT plasma, with the fusion reaction switched on and with a stationary fuelling that provides homogeneous sources of D (50%) and T(50%). Within a time period of a few seconds a stationary process establishes, but being interrupted periodically with a period τ by instantaneous injections of N_C carbon ions at the periphery. The Fig. 3 demonstrates the propagation of impurity through the confined DT plasma after the first injection of the amount $N_C = 2.45 \times 10^{20}$. The horizontal coordinate of the figure originates at the tokamak magnetic axis being directed as the radial axis of main cylindrical frame.

The repetitive ELMs produce more and more contamination in the bulk, but due to an entrainment of carbon ions with the DT plasma back into the SOL the carbon caused radiation losses and the fusion power gradually saturates. The dependencies of W_{rad} and ΔW_{fus} on τ are shown in Fig. 4. From Fig. 4 follows that the tolerable ELM wall heat fluxes are below 1 MJ/m².

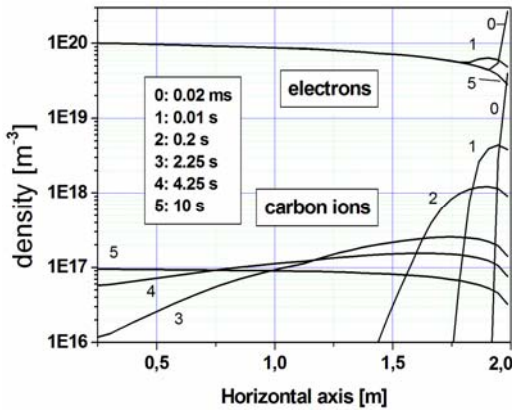


Fig. 3: Electron and carbon densities. The legend gives the time after an ELM.

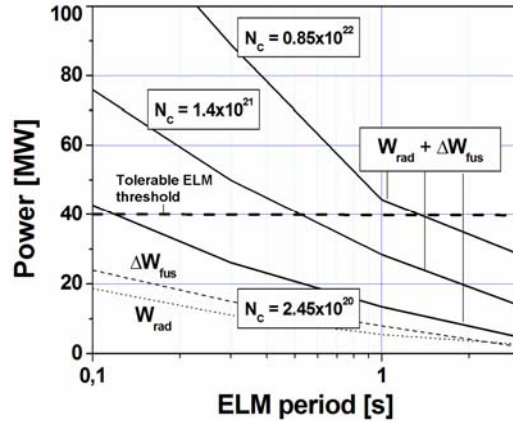


Fig. 4: The radiation and fusion power losses as functions of ELM period.

3. Melting of edge W-brush surfaces and melt splashing criterion

Previous simulations with the code MEMOS demonstrated that a W-brush structure prevents violent melt motion. The most important remaining damage mechanism is the surface melting accompanied by the melt motion driven by the pressure gradient of the impacting plasma stream along the target. The melt layer erosion of the W-brush armour under the transient heat loads was further numerically investigated using MEMOS. The melt motion is described in the “shallow water” approximation, accounting for the surface tension, the viscosity of the molten metal, and the radiative losses from the hot surface. A heat transport equation with two boundary conditions at the moving vapour-liquid- and liquid-solid interfaces describes the temperature inside the target. Typical thickness of melt layers at the edge surfaces is obtained up to 40 μm (Fig. 5). These 3D numerical simulations demonstrate that the melting of the lateral brush edges starts at $Q > 0.7 \text{ MJ/m}^2$ and the melt thickness can be significant. The validations of MEMOS by the experiments at the plasma guns QSPA and MK-200UG (TRINITY, Russia) is already described in the reports of the task TW3-TPP-MATDAM.

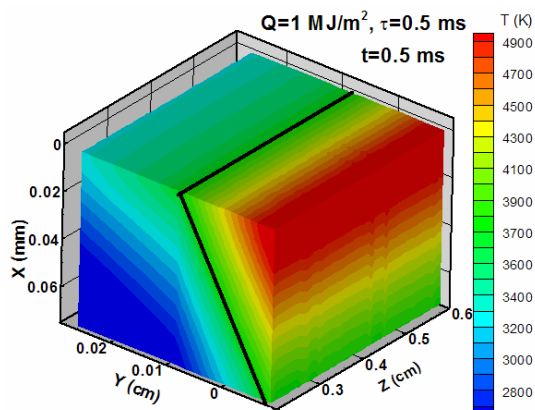


Fig. 5: Temperature distribution calculated with MEMOS for a W-brush. The black line denotes the melt boundary.

The previously estimated criterion of melt splashing at the W-surface was elaborated. In case of strong transient events such as Type I ELMs and disruptions the heat loads produce a significant evaporation at the W surface. Due to formation of a vapour shield the exposed target is essentially protected from the main heat load. But an inhomogeneous distribution of vapour pressure along the target surface generates longitudinal vapour velocities up to 10^4 m/s . The intense directed motion of vapour along the melt generates surface waves. The target material flushes to the edge of the brush, and an erosion crater appears with some mountains at the crater edge and a wavy structure on its resolidified surface. In case of weak ELMs the direct action of the plasma stream impacting on the target surface under a rather low angle of $2\text{-}5^\circ$ produces waves of Kelvin-Helmholtz type at the melt-plasma interface. In case of strong transient processes as those expected in ITER with developed plasma shield, small initial perturbations of the surface heat loads together with a rapid vapour flow along the surface are responsible for the surface perturbations of other types, like the instabilities by Rayleigh-Taylor and the capillary wave instabilities. An analytical consideration was carried out and it is concluded that for the ITER ELMs with heat loads below 2.5 MJ/m^2 the melt splashing due to the droplet formation would not be expected, but in case of ITER giant ELMs with developed plasma shield a violent melt splashing may occur with mass loss rates up to $10^2 \text{ cm}^{-2}\text{s}^{-1}\text{g}$.

4. Conclusions

Carbon ions penetration after Type I ELMs into the periphery of the confinement region of ITER has been analysed using elaborated modelling implemented in the codes FOREV and TOKES. Due to the impurity the plasma thermal energy is significantly re-radiated and the fusion power decreases. The combination of these codes seems a proper tool for estimation of core plasma contamination after ITER ELMs. However, for more accurate predictions the opacity data for radiation transport need to be improved.

The code MEMOS was further developed implementing an arbitrary surface geometry of the W-macrobush, which allowed optimization of the design of W armour. The modelling for W-brush targets heated under the conditions relevant to giant ITER ELMs demonstrated melting onset of the brush edges at $Q > 0.7 \text{ MJ/m}^2$. The calculated evaporation erosion rate is in a

good agreement with the results measured at the plasma gun QSPA. From analytical investigations follows that for ITER ELMs with heat loads below 2.5 MJ/m^2 the melt splashing due to the droplet formation is not expected. However a melt splashing may occur in cases of ITER giant ELMs.

Staff:

B.N. Bazylev
I.S. Landman
S.E. Pestchanyi
R. Kochergov

Literature:

- [1] I.S. Landman, G. Janeschitz, "Numerical simulations of plasma wall interactions for ITER", 17th International Conference on Plasma Surface Interactions in Controlled Fusion Devices, Hefei, China, May 22-26, 2006. To be published in Journal of Nuclear Materials.
- [2] S. Pestchanyi and I. Landman, "ELM induced carbon contamination of ITER core", 17th International Conference on Plasma Surface Interactions in Controlled Fusion Devices, Hefei, China, May 22-26, 2006. To be published in Journal of Nuclear Materials.
- [3] I.S. Landman, G. Janeschitz, "Plasma transport modelling with multiple-mapping magnetic surfaces", 33rd European Physical Society Conference on Plasma Physics, Rome, Italy, June 19-23, 2006. To be issued on CD.
- [4] R. Kochergov, I.S. Landman, G. Janeschitz, "Implementation of plasma diffusion models in the code TOKES", 33rd European Physical Society Conference on Plasma Physics, Rome, Italy, June 19-23, 2006. To be issued on CD.
- [5] B. Bazylev, G. Janeschitz, I. Landman, S. Pestchanyi, A. Loarte, G. Federici, M. Merola, J. Linke, O. Ogorodnikova, A. Zhitlukhin, V. Podkovyrov, N. Klimov, V. Safronov, I. Garkusha, "Modelling of Material Damage of CFC and W Macro-Brush Divertor Targets under ELMs and Disruptions at Plasma Gun Facilities and Prediction for ITER", 21st Fusion Energy Conference IAEA, Chengdu, China, October 16-21, 2006, To be issued on CD.

Divertor and Core Plasma Modelling for ITER

1. Introduction

The goal of the core and divertor plasma modelling program is the development, improvement, and application to ITER of a set of modelling codes which describe the ITER plasma from the core to the divertor plates in a coherent way so as to permit a consistent prediction of ITER plasma operating modes, operating windows, performance, and scenarios. Two separate codes are used for this purpose: the 2D coupled fluid-Monte Carlo code B2-EIRENE for two-dimensional modelling of the ITER divertor and scrape-off layer, and the ICPS model incorporated into the 1D ASTRA transport code for one-dimensional modelling of the ITER core and pedestal. The two codes communicate by means of scaling laws derived for the separatrix parameters from stand-alone runs of the codes. A variant of the model, which uses a simpler two-point model for the scrape-off and divertor plasma, is used to fit results from the experiments. Quantitative predictive modelling of ITER is done with the more complete model.

ITER performance modelling, crucial to establish the expected performance of ITER and to define the operating scenarios to obtain this performance, can be carried out only with such an integrated plasma model which describes in a coherent way the entire plasma from the centre via the pedestal and the scrape-off layer to the divertor plate. Our model has been developed in the framework of a quadripartite collaboration (FZ Karlsruhe, ITER International Team, Hydro-Québec, Varennes, Québec, Canada, and INRS-EMT, Varennes, Québec, Canada), as described in previous Annual Reports.

The previous version of the model and the results obtained were described in the previous Annual Reports and references therein, as well as in [1]. Several contributions described there have now been published [2], [3] or have been accepted for publication [4], [5]. Initial results obtained in 2006 were described in [1]. Advances in ITER 2D divertor modelling were described in [4], [5], and advances in 1D modelling of the plasma core and application of the integrated model were described in [5], [6] for DEMO parameters. Recent work in all these areas and in modelling of DEMO is summarised in [7], and was presented at the 2006 IAEA Fusion Energy Conference [8], [9]. The DEMO modelling is also described briefly in a separate section of this Annual Report [10], [11], and application to startup is described in [12].

2. Divertor Plasma Modelling

Modelling performed this year for a number of devices has extended the approach of determining scaling relations for the divertor and edge plasma parameters from the 2D modelling for several different machine sizes, in particular for DEMO. The results are described elsewhere in this Annual Report [10], [11], and in [5]; here it is important to point out that, at the same SOL power per unit volume of the device, and the same specific pumping speed for ITER and DEMO, the separatrix helium density remains constant, the helium neutral influx decreases, and the peak power loading of the divertor plates remains constant in the transition from ITER to DEMO – all positive results. The sparse results available with the full neutral model indicate that the peak power does not change, but the helium density and influx are a factor 3 lower than from the linear neutral model – a very positive result for both ITER and DEMO.

Continuing optimisation of the design of the divertor cassettes for ITER involves re-assessment of the role of the divertor “dome” and the effect of variations of its shape on divertor performance.

Since pumping is critical for helium removal but the pumping capability of ITER is limited, it was important to refine the definition of the pumping-related parameters, which was now possible in the framework of the nonlinear neutral model, to determine a more precise rela-

tion between the plasma and the engineering parameters. It was found [4] that, whenever in previous work an “effective” pumping speed for ITER of $S_{DT} = 20 \text{ m}^3/\text{s}$ for the linear neutral model was quoted, the corresponding “engineering” pumping speed with the non-linear neutral model is $\sim 60 \text{ m}^3/\text{s}$, which is within the ITER design limits ($75 \text{ m}^3/\text{s}$).

This procedure is applied to a study comparing various dome configurations with a domeless configuration. The primary function of the dome is to increase the neutral pressure in the PFR to make helium pumping more efficient. Besides this, it could be helpful in reducing the neutral reflux to the core through the x-point, in protecting diagnostic equipment in the PFR from plasma, and in neutron shielding of the pump duct. However, it adds to the complexity of the divertor cassette design and to the machine cost. Since most of the dome’s functions are related to interaction with neutrals, whose modelling is improved with the nonlinear neutral model, the effect of the dome on divertor performance was reassessed with the nonlinear model.

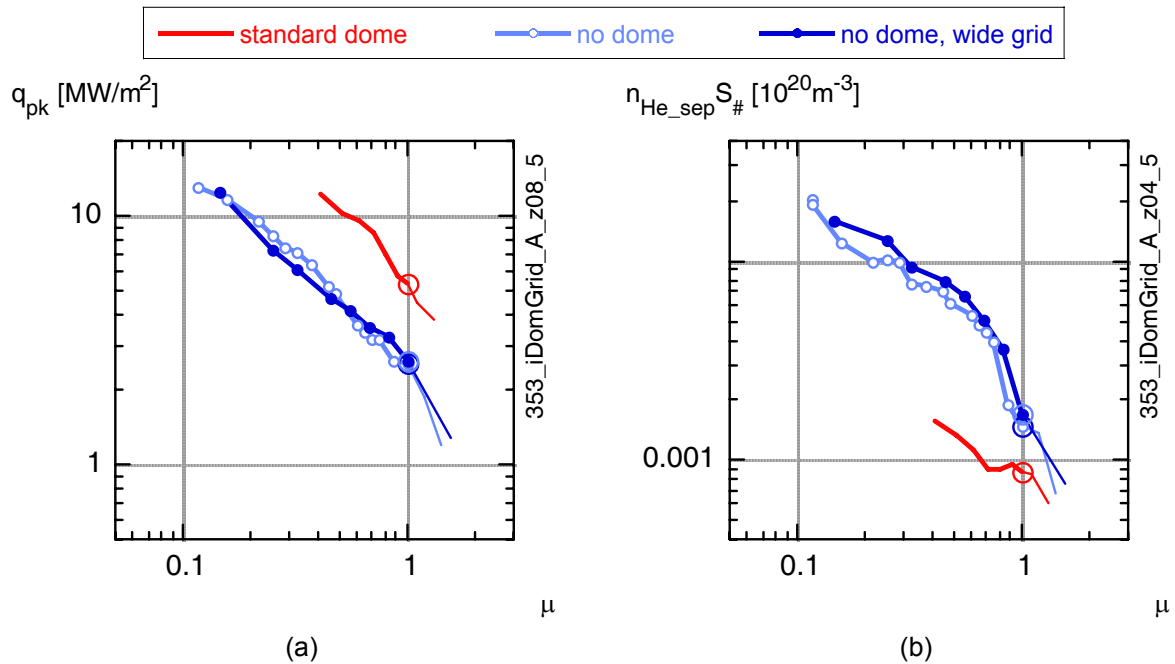


Fig. 1: Peak divertor power load q_{pk} (a) and product of helium separatrix density times normalised pumping speed, $n_{\text{He}_{sep}} S_{\#}$ (b) vs. normalized neutral pressure μ in PFR for the two “domeless” plasma grid options, compared with the standard ITER case. Power input to the SOL $P_{in}=100 \text{ MW}$. The incipient detachment point on each curve is marked with a big circle and corresponds to neutral pressure at the pump duct $p = 9 \text{ Pa}$ for the standard dome case.

The result comparing domed operation with domeless operation (for two different grids, not discussed here) is shown in Fig.1 where the dependence of the peak power loading on the target q_{pk} and separatrix density of helium ions $n_{\text{He}_{sep}}$ times normalized pumping speed $S_{\#}$ on the normalized neutral pressure in the PFR, μ , is compared between the two grid options and with the standard ITER geometry. This selection of parameters allows meaningful comparison in terms of the operational window of the divertor, and the helium related quantities are almost inversely proportional to the pumping speed. Removal of the dome would result in expanding the operating window to about a factor 2 lower peak power on the divertor plate, but the pumping speed needed to maintain the same helium density at the separatrix would have to be increased by a factor of up to 8. Since the technical limits of ITER do not allow such an increase in pumping speed, the effect of higher helium concentration in the core on the reactor flexibility must be assessed, together with other concerns like divertor diagnostic access, neutron shielding, and so on, before a decision on the dome removal could be made.

In separate studies [4] the dome geometry was varied. It was found that the requirement on the transparency of the dome-supporting structures can be relaxed and that therefore the

dome can have stronger supporting structures, and that an increase of the dome length would clearly improve the helium removal efficiency but can be outweighed by the accompanying reduction of the operational window in power loading.

In subsequent work on 2D modelling [7], [8], the computational model of the edge plasma in ITER has been further developed, taking into account particle leaks through the gaps between the divertor cassettes. First results indicate no major negative effect of the gaps on the divertor performance, although the parasitic flows caused by these gaps can be comparable with the pumping throughput. In the presence of the leaks, the dependence of the peak power load on the targets on the neutral gas pressure in the divertor remains unchanged and the core fuelling efficiency remains the same. The helium density at the separatrix decreases when the gaps are present because, at the same pumping speed at the pump, a fraction of the helium flux from the PFR is redirected to the baffle area via the leaks and contributes less to the helium density build-up at the separatrix. However, the helium enrichment decreases by 30%, i.e. the DT throughput is larger by this amount at the same helium production rate. On balance, since the assumed values of the gaps in this study correspond to gaps at least 2 times wider than the design value of 5 mm, and the effects are relatively small, sealing the inter-cassette gaps in ITER may not be a high priority issue.

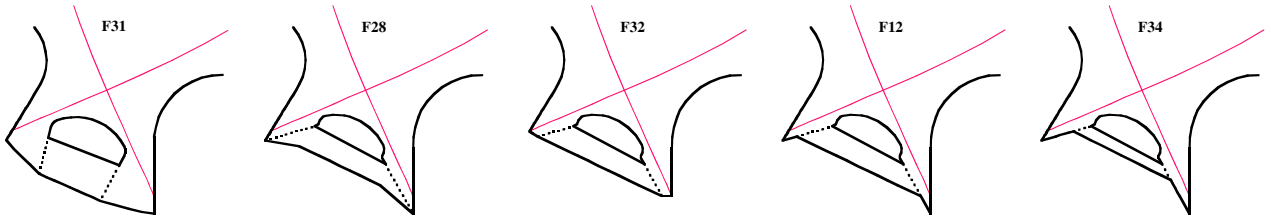


Fig. 2: Variation of divertor geometry used in the re-exploration on the effect of the “V-shapes” near the separatrix strike points. F12 marks our standard modelling configuration, F28, F31, and F32 are more open, and F34 more tight. Dotted lines indicate partially transparent surfaces at the entrance to the PFR..

The calculations reported in [8] confirm the previous observation that the more comprehensive, non-linear model of the transport of the neutral particles leads to much weaker sensitivity of the results to the details of the divertor geometry than the previously used linear model. In particular, it is not as important to maintain tightly sealed, pronounced V-shapes at the corners of the divertor targets close to the separatrix strike points as had been suggested earlier because these geometric effects are attenuated by neutral-neutral collisions. The V-shape has been varied widely in these simulations (Fig. 2).

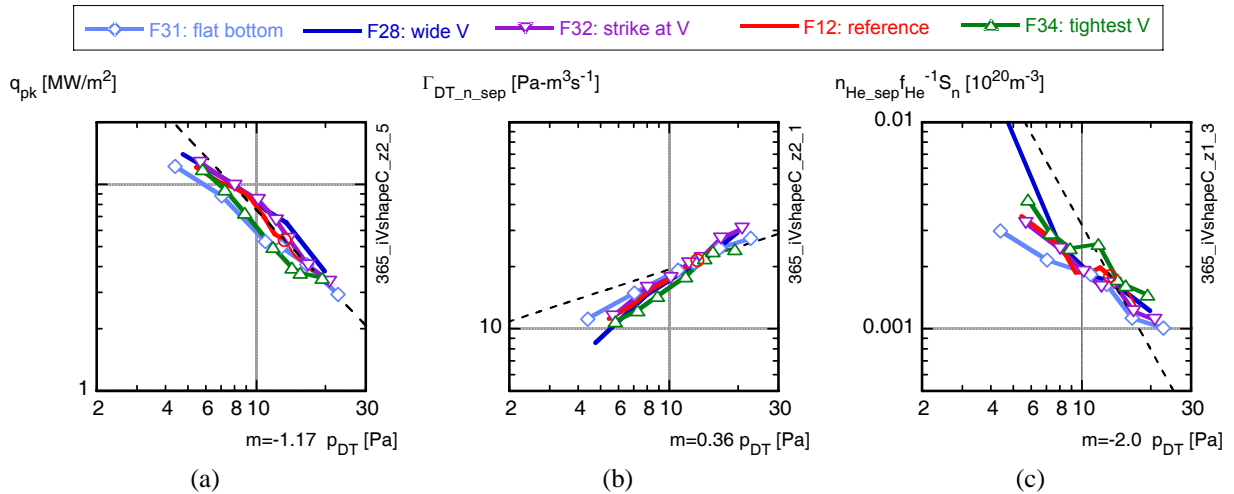


Fig. 3: Peak power (a), D neutral influx into the core (b) and He ion density at the separatrix (c) vs. divertor neutral pressure p_{DT} for different shapes of the divertor bottom (see Fig. 2).

The result is illustrated in Fig. 3. We see no major difference in the parameters determining the core fuelling ($\Gamma_{DT_n_sep}$, n_{DT_sep}), or the helium removal (n_{He_sep} , $\Gamma_{He_n_sep}$). The target power load (q_{pk}) can decrease somewhat, but only by less than 40%, and this can be compensated by ~ 20% increase of the neutral pressure in the divertor. This increases the flexibility, facilitating optimisation of both the divertor design and the plasma configuration in ITER.

Further work was performed [8] on movement of the separatrix strike-points on the targets (20 cm displacement was found to be tolerable) and on comparing the core fuelling efficiency between upper and midplane gas puffs (the efficiency increases moderately for the midplane gas puff but wall erosion by energetic charge exchange neutrals is also expected to increase).

3. Core Plasma Modelling

Pending development of a successor model to GLF by the theoreticians, the MMM model with stabilisation mechanisms has been retained as the reference model for core transport in the simulations (see previous annual reports for a detailed description). Further simulations of hot-ion and hybrid modes, validation with experiment, and extension to ITER has therefore been postponed.

An initial stage of the evaluation of the impact of advanced operation on ITER is the evaluation of the operating window of the device with the present divertor/SOL parameterisation. Initial simulations with the present model have started, with emphasis on determining the effect on the operating window of varying the parameters determining the pedestal and of a decrease of the toroidal field at constant safety factor.

Advances in core plasma modelling in the present period concern mainly DEMO modelling and are described in [10], [11], [12].

4. Perspectives

Work on divertor and core modelling for ITER is continuing, with particular emphasis on:

- In two-dimensional modelling of the ITER scrape-off and divertor plasma with walls having realistic carbon erosion-deposition, extension of the model to include temperature- and flux-dependent variation of the carbon erosion at the target, continuation of the study of variations of ITER geometry with the nonlinear neutral model, further application of the code with both linear and nonlinear neutral models to a highly radiating prototypical DEMO plasma, and initial studies including seeded impurities in the edge plasma.
- In one-dimensional modelling of the plasma core, the work will concentrate on integration of scaling advances from the two-dimensional modelling, variation of the impurity model for present experiments once validated data on impurity transport becomes available, extension of the modelling of ITER and a highly radiating prototypical DEMO to operational modes with longer pulses and initial development of the model toward hybrid operation.

Staff:

H. D. Pacher (INRS-EMT, Varennes, Québec, Canada)
G. W. Pacher (Hydro-Québec, Varennes, Québec, Canada)
A. S. Kukushkin (ITER International Team)
G. Janeschitz
I. Landman
S. Pestchanyi - with the collaboration of G. Pereverzev (IPP Garching).

Literature:

- [1] Pacher H.D., Pacher G.W., in collaboration with ITER IT Garching, FZ Karlsruhe, Max-Planck-Institut für Plasmaphysik Garching, EFDA CSU Garching, "Divertor and core plasma modelling for ITER - Final Report June 2006", INRS Energie, Mat. et Télécom. Report, INRS-EMT-029-0606, June, 2006
- [2] Kukushkin A.S., Pacher H.D., "Critical Evaluation of the Determination of the SOL Transport Mechanism from a Statistical Examination of Experimental Data", *Contrib. Plasma Phys* 7-9(2006)545-550.
- [3] Kotov, V., Reiter, D., Kukushkin, A.S., Pacher, H.D., Börner, P., Wiesen, S., "Radiation absorption effects in the B2-EIRENE divertor modelling", *Contrib. Plasma Phys.* 7-9(2006)635-642.
- [4] Kukushkin, A.S., Pacher, H.D., Kotov, V., Reiter, D., Coster, D.P., Pacher, G.W., "Effect of the Dome on Divertor Performance in ITER", presented at 17th International Conference on Plasma Surface Interactions in Controlled Fusion Devices, Hefei, China, accepted for publ. in *J. Nucl. Mat.* (2007)
- [5] Pacher, H.D., Kukushkin, A.S., Pacher, G.W., Janeschitz, G., Coster, D.P., Kotov, V., Reiter, D., "Effect of the tokamak size in edge transport modelling and implications for DEMO", presented at 17th International Conference on Plasma Surface Interactions in Controlled Fusion Devices, Hefei, China, accepted for publ. in *J. Nucl. Mat.* (2007).
- [6] Janeschitz, G., Pacher, G.W., Pacher, H.D., Kukushkin, A.S., "Simulation of DEMO Core Operation Consistent with Divertor Constraints", presented at 33rd EPS Conf. on Plasma Physics, July 2006, Rome, Italy (2006)
- [7] Pacher H.D., Pacher G.W., in collaboration with ITER IT Garching, FZ Karlsruhe, Max-Planck-Institut für Plasmaphysik Garching, EFDA CSU Garching, "Divertor and core plasma modelling for ITER - Intermediate Report December 2006", INRS Energie, Mat. et Télécom. Report, INRS-EMT-033-1206, December, 2006, in preparation
- [8] Kukushkin, A. S., Pacher, H. D., Kotov, V., Reiter, D., Coster, D., Pacher, G. W. "Effect of Pumped Gas Reflux on Divertor Operation in ITER", *Proc. 21st IAEA Fusion Energy Conf. Chengdu*, paper IAEA-CN-149/IT/P1-16, to be subm. to *Nucl. Fusion* (2006)
- [9] Pacher, G.W., Pacher, H.D., Janeschitz, G., Kukushkin, A.S., Kotov, V., Reiter, D., "Modelling of DEMO Core Plasma Consistent with SOL/Divertor Simulations for Long Pulse Scenarios", *Proc. 21st IAEA Fusion Energy Conf. Chengdu*, paper IAEA-CN-149/FT/P5-42, to be subm. to *Nucl. Fusion* (2006)
- [10] Pacher H.D., Pacher G.W., "Task TW5-TRP-002.D2 DEMO Physics Studies, D2 Analysis of total radiation in tokamak reactor scenarios", this Annual Report (Systems Studies Section)
- [11] Pacher H.D., Pacher G.W., "Task TW6-TRP-002.D3 DEMO Physics Studies, D3 - Development of an improved treatment of plasma radiation for medium- and high-Z impurities", this Annual Report (Systems Studies Section)
- [12] Pacher H.D., Pacher G.W., "Task TW6-TRP-012.D1b, Optimisation of fusion power plants for H2 production, D 1b - Optimisation of a 'start-up' scenario where the power is less than 100MW", this Annual Report (Systems Studies Section)

Heating and Current Drive – Physics

**EFDA/06-1406 (TW6-TPHE-ECHULB4)
and
TW6-TPHE-ECHULA (Subtasks C and D)**

**Design and Analysis of the Upper Launcher and Port Plug for the ITER
ECH&CD System**

Objectives

For the control of plasma instabilities, especially of neoclassical tearing modes (NTMs), it is foreseen to inject up to 20 MW mm-wave power at 170 GHz into the ITER plasma by an Electron Cyclotron Heating and Current Drive (ECH&CD) system. The $q=3/2$ and $q=2$ flux surfaces will be targeted by angular steering in the poloidal direction. Resulting from the previous work under EFDA of the "ECHULA group" of EU associations (ENEA/CNR Milano, CRPP Lausanne, FZK Karlsruhe, FOM Rijnhuizen, IPP/IPF Garching/Stuttgart), an initial reference design for the ECH&CD Upper Launcher was developed on the basis of the remote steering (RS) concept and transferred to the ITER design office in 2004 called the "RS 3/8 launcher model". However, the performance of this design was marginal for the steering ranges required for operation at different plasma scenarios (i.e. ITER plasma scenario 2, 3 and 5) because of adverse consequences for the focalisation of the beams, and therefore reduction of the local density of driven current. Thus, the main emphasis in the design work has been redirected towards the front steering design, as it is at present the only steering option that meets the ITER stabilisation requirements. Beyond the basic front steering concept of the upper launcher ("NTM launcher"), the steering angles can be expanded to cover the plasma range of $\rho_p = 0.40$ to 0.93 . This allows to extend its application down to $q=1$, the latter being of particular importance for sawtooth control ("Enhanced performance launcher (EPL)"). The mm-wave beam lines are integrated into the upper port plug structure, consisting of the blanket shield module closing the gap in the blanket at the port, the port plug frame which houses the internal shield, the closure plate forming primary vacuum boundary, and the launcher back-end following the closure plate (cf. Fig. 1). The launcher design has to provide satisfactory performance as well as to fulfill the criteria of robustness and reliability set for all ITER systems. In particular, the design has to reflect the requirements given by operations in vacuum and in a nuclear environment, with the launcher being actively cooled where necessary and having the required neutron shielding capability to achieve the specified constraints on activation at the port plug closure plate.

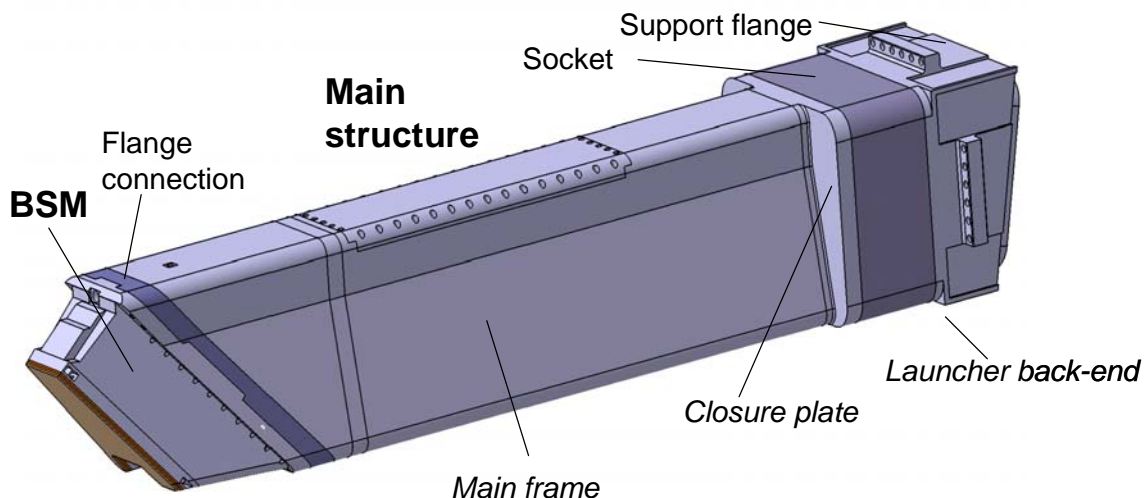


Fig. 1: Location of the main structural components of the ITER EC upper port plug (BSM: Blanket Shield Module).

Structural integration of the Front Steering Launcher

The launcher main structure has to meet in the first place the “environmental” requirements of ITER, i.e. the geometrical constraints in terms of enveloping dimensions and positioning, including the cantilevered fixation of the whole structure to the vacuum vessel port extension. The thermal requirements call for baking and cooling (where needed). Mechanically the structure must be rigid enough to cope with dead weight, vibration and electromagnetic loads, and it must allow remote handling of internals in the hot cell. These requirements led in the initial “RS 3/8 launcher model” to the double-wall design with cooling (or baking) fluid in the inter-space, and allowing axial access to the internals after removal of the BSM. The evolving FS concept, along with striving for communality with diagnostics launchers as well as fabrication and cost considerations, led to the currently pursued slim wall design. It is characterised by a single wall section of the main frame (55 mm wall thickness) with a removable cover that allows vertical access to part of the internal shield. Baking of that section up to about 180 - 200 °C is achieved passively by radiation from the surrounding structures. At the front end, the double wall design has been maintained for cooling, baking and shielding purposes, implying that the BSM fixation and axial removal of parts of the internal shield are unchanged.

The conceptual design of thermal and nuclear shielding components was adopted for the EPL versions of the Front Steering launcher (cf. Fig. 2). The shielding system can be grouped into two major parts: The shield blocks located in the blanket shield module and the internal shield in the main structure.

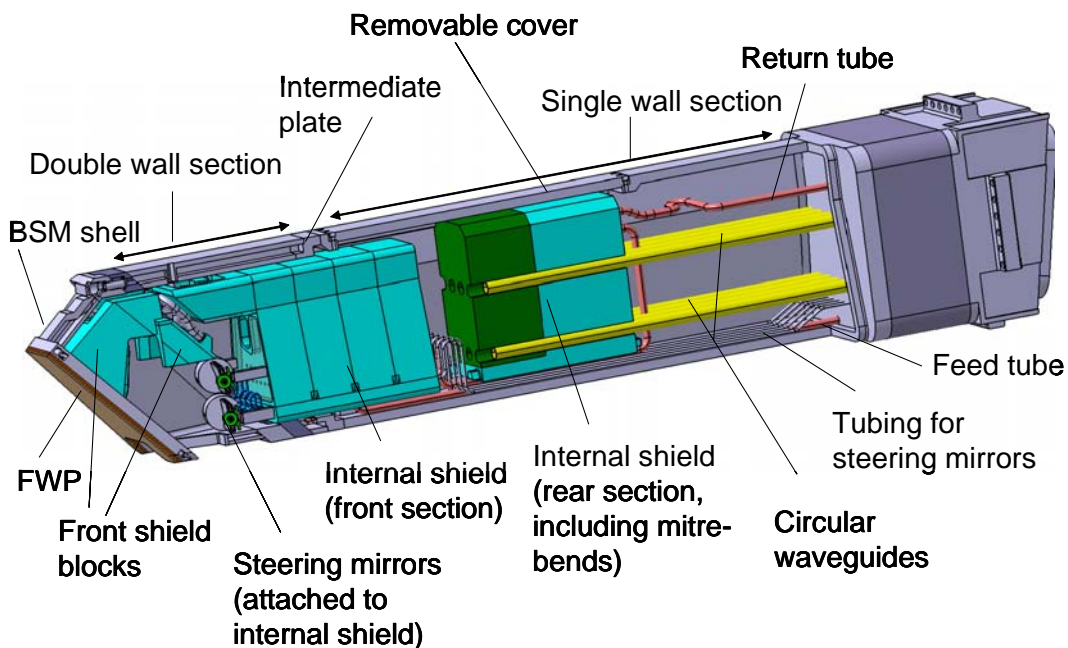


Fig. 2: Components of the ECH&CD Upper Port Plug integrating the Extended Performance Launcher version.

For the shield blocks, two design variants are considered which are distinguished by their size and shape conformity. The “encased shield block” is better suited for large and regularly shaped volumes and consists of a welded stainless steel (SS) casing with stacked SS plates and water interspaces. In the “solid shield block” which offers a more flexible adoption to complex space requests, a two-level arrangement of machined cooling channels provides the proper SS/water composition for the neutron shielding in the high flux area (80/20 vol. %).

The internal shield provides the major radiation protection of the launcher internals up to the launcher back-end and of the surrounding structures, like part of the vacuum vessel and the superconducting coils. For general configurations, three design options have been brought to a conceptual design level: Block, tank and modular design. The most straightforward design, which lends itself most directly to standard welded structures, is the tank design. However, the partitioning of the internal shield, which is inherent to the mm-wave system of the EPL, favours a combination of a modular design formed by a small number of individual plates in the front part and a block design formed by a metal block with machined cooling channels and with potentially fully integrated waveguides (cf. Fig. 2).

Radiation shield analyses for the BSM were performed to determine the arrangements of the shield blocks which have to provide enough empty space for mm-wave propagation. The nuclear heating density was calculated in the BSM structures with detailed distributions in the steering mirror assembly. The 2-D map of the heating distribution based upon the material compositions of the BSM and the Vacuum Vessel (VV) was determined as input for the thermo-mechanical analysis.

Radiation damages of candidate materials envisioned for the steering mirror assemblies have been estimated by the MCNP code. The structural damage levels in terms of displacements per atom (dpa) rates are given in Table 1 for the steering mechanisms and flexure pivots. These two assembly elements are located at opposite sides

Table 1: The neutron induced displacements rate per atom (dpa) modeled for a total of 0.5 full power years (0.5 fpy at a fusion power of 500 MW) in materials of the steering mechanism and the flexure pivots holding the steerable mirror.

Section	SS316 L(N)-IG, [dpa]	Inconel 718 [dpa]	Ni [dpa]	Ti ₆ Al ₄ V [dpa]	Cu [dpa]
Upper steering mechanism	0.164	0.177	0.188	0.162	0.156
Lower steering mechanism	0.126	0.138	0.146	0.128	0.127
Upper pivot	0.340	-	-	0.334	0.314
Lower pivot	0.520	-	-	0.505	0.472

of the steering mirror. The maximum damage of 0.5 dpa is found in the lower pivot where the highest estimated value is obtained in the steel SS316L(N)-IG at the lower pivot side. These values have been obtained for a BSM configuration which is characteristic for the NTM launcher. As the reduced steering angles in the EPL concept result in a smaller cut-out in the FWP, both nuclear heating and structural damage rates obtained in the present analysis can be considered as conservative.

Conceptual design and construction of a launcher handling test facility

A comprehensive validation process of the Upper Launcher would need to address various specific stages in which the complexity of the components under tests and the scale and specialisation of the test beds is progressively increased:

- a) Component tests:
Demonstration of the industrial manufacturing followed by integrity and performance studies for critical components under specific loads
- b) Component handling tests:
Alignment and assembly of key components in subsections of major launcher subsystems
- c) Vacuum vessel docking-tests:
Testing of full size launcher mock-ups at representative vacuum vessel sections

d) Launcher transfer tests:

Upper port plug removal from vacuum vessel and transfer into transport cask for hot cell facilities

e) Hot cell docking tests:

Launcher installation and sealing at hot cell test bed

At the present stage, the tests that are related to components and component handling are most urgent with respect to their implications on the launcher design development and procurement. Therefore, the objectives of the launcher handling test facility (LHT) at FZK are pitched to the first two needs. The conceptual development for the latter three items are being considered in a future sharing of tasks with a port plug test bed and the hot cell facilities at the ITER site.

The most pronounced complexity of the structural components with respect to manufacturing and performance challenges is given for the blanket shield module and for its internals. The FZK launcher handling test facility is proposed to provide the test bed particularly suited for testing these components in conjunction with testing needs for critical components handling requirements. The fabrication of a BSM corner prototype based on hot isostatic pressing (HIP) route was contracted; the tendering actions for two alternative routes (brazing and plate machining/deep drilling) are underway. The design of the cooling loop providing regular and baking operation parameters of the ITER blanket cooling system was finalised and the related cooling system is being manufactured for installation in early 2007. A major testing phase has been defined for the years 2007 – 2009 with respect to component tests (BSM prototypes, inner shield module) and component handling tests (semi-automated and remote handled). They will be performed in close cooperation with the ECHULA partners, in particular with the Dutch partners focusing on positioning tools and processes.

Window development

For the design, procurement and testing activities, major decisions were prepared and agreed for the specific window configurations. For the FS torus window, the required aperture can be reduced from 95 mm to 60 mm, allowing a reduction of the window thickness to 1.11 mm and of the disk diameter to 70 mm (and thus reducing the costs of the CVD diamond disk to 35%). For the FS window, the design of a window prototype with hybrid cooling was developed, in which the conventional edge cooling concept and the particular indirect cooling concept can be studied in parallel.

Dummy window structures were manufactured which were identical to the prototype RS torus window, yet with the CVD diamond disk replaced by a copper disk. Thermo-hydraulic investigations showed that the flat dependence of the cooling efficiency on the water flow rate can be expected for flow rates of 5 l/min and above. In extending the pressure of the cooling system beyond 0.8 MPa (set on grounds of the FEM analysis), no residual deformations in the copper cuffs were observed up to the pressure of 1.6 MPa. This proved the conservative nature of the design analysis.

For semi-automated cutting/re-welding of the window structure to window sockets, commercial tools were studied to determine the procedures which will allow on-torus replacement of the window unit. The cutting was successfully demonstrated with a slightly oversized tool and a dedicated tool was procured (with a working area of 73 – 141.3 mm) which is ideally suited for the RS window design. Successful welding was performed with an adapted tube-to-tube sheet weld head. This specialised weld head was procured for continued handling studies of both RS and FS torus window prototypes.

Outlook towards future R&D activities

The development of the detailed design of the ECH&CD upper port plug will be advanced with the goal of defining technical specifications and detailed drawings for starting the tendering action of the upper launcher system by 2009. On this route, a harmonised time schedule for the iterative R&D activities for the optical system and the structural system has been established along two levels of details: Level 1 is focusing on key interfaces and milestones (design reviews - releases) and level 2 is showing detailed paths to the achievement of the specific deliverables. The R&D strategy consists of advancing the design with two major design reviews.

The first review is planned to be held in March 2007 and to cover the following aspects:

- Primary mm-wave optical system ("UL06") with key structural components designed (Main structure, BSM housing, Shield blocks + Internal shield)
- Electromagnetic and thermophysical loading classification
- Updated data base on structural damage and neutron loads obtained by neutron analysis
- Decision on type of cooling configuration for FS torus window

The second review is planned to be held in March 2008 and to cover the following aspects:

- "Pre-final" mm-wave optical system (UL07c) with key structural components designed (Main structure, BSM housing, Shield blocks + internal shield)
- Manufacturing of BSM corner + BSM housing demonstrated
- "Pre-final" data base on structural damage and neutron loads obtained by neutron analysis
- Thermo-mechanical design with experimentally cross-checked parameters established
- Guiding results from positioning tests of the BSM corner prototype achieved for remote handling process definition

The torus window prototype for the RS launcher was proven for its suitability for the high power (short pulse) operation as well as for performance with respect to vacuum, pressure and thermo-hydraulic specifications. The torus window design for the FS launcher will be validated accordingly including high power/long pulse experiments (together with JAEA) to complete the qualification criteria for a common torus window used for ECH&CD launchers at both the upper and the equatorial port plug.

Staff:

Y. Chen
I. Danilov
U. Fischer
G. Gantenbeim
G. Hailfinger
R. Heidinger
K. Kleefeldt
w. Leonhardt
M. Lux
A. Meier
G. Neffe
A. Serikov
P. Späh
H. Tsige-Tamirat
J. Weggen

Literature:

- [1] R. Heidinger, I. Danilov, A. Meier, B. Piosczyk, P. Späh, M. Thumm, W. Bongers, M. Henderson, F. Leuterer, A.G.A. Verhoeven, D. Wagner; Development of high-power window prototypes for ECH&CD launchers. 24th Symp. on Fusion Technology (SOFT 2006), Warszawa, PL, September 11-15, 2006, to be published in Fusion Engineering and Design
- [2] R. Heidinger, U. Fischer, G. Hailfinger, K. Kleefeldt, A. Serikov, P. Spaeh; Design and Analysis of the ECH Upper Port Plug Structure at ITER; Proc. of 21st IAEA Fusion Energy Conference, 16 - 21 October, Chengdu, China
- [3] R. Heidinger, U. Fischer, G. Hailfinger, K. Kleefeldt, A. Serikov, P. Spaeh, Design and Analysis of the Shielding Structure in the ECH Upper Port Plug at ITER; Workshop on RF Heating of Fusion Plasmas, September 23-26, 2006, Nara (Japan)
- [4] R. Heidinger, G. Hailfinger, K. Kleefeldt, A. Meier, P. Späh, M. Henderson, G. Saibene, A.G.A. Verhoeven; Critical Structural Design Issues of the ECRH Upper Launcher for ITER; Proc. 14th Joint Workshop on Electron Cyclotron Emission and Electron Cyclotron Resonance Heating (EC 14), Santorini, GR, May 9-12, 2006
- [5] I. Danilov, R. Heidinger, A. Meier, B. Piosczyk, M. Schmid, P. Späh, W. Bongers, M. Graswinckel, B. Lamers, and A.G.A. Verhoeven; High power short pulse and thermo-hydraulic tests of the window prototype for remote steering launcher; Submitted to Fusion Science and Technology
- [6] I. Danilov, R. Heidinger, A. Meier, et al; Thermo-hydraulic performance and high power transmission characteristics of the RS torus window prototype; Proc. 14th Joint Workshop on Electron Cyclotron Emission and Electron Cyclotron Resonance Heating (EC 14), Santorini, GR, May 9-12, 2006
- [7] A. Serikov, U. Fischer, R. Heidinger, Y. Luo, H. Tsige-Tamirat; Radiation shielding analyses for the ITER upper port ECRH launcher: Proc of The American Nuclear Society's 14th Biennial Topical Meeting of the Radiation Protection and Shielding Division, Carlsbad, April 2-6, 2006
- [8] P. Späh, R. Heidinger, G. Hailfinger, M. Henderson, K. Kleefeldt, A. Serikov, E. Ciattaglia, G. Saibene, Design and Analysis of the Structural Components in the ITER ECH Upper Port Plug; 24th Symp. on Fusion Technology (SOFT 2006), Warszawa, PL, September 11-15, 2006, to be published in Fusion Engineering and Design
- [9] D. Strauss, G. Gantenbein, R. Heidinger, W. Leonhardt, A. Meier, G. Neffe, P. Späh, J. Weggen; Objectives and Design of the Launcher Handling Test Facility at FZK; Workshop on RF Heating of Fusion Plasmas, September 23-26, 2006, Nara (Japan)
- [10] T. Bonicelli et al; Review of the EU activities in preparation of ITER in the field of EC power sources and NB systems; Proc. 21st IAEA Fusion Energy Conf., Chengdu, China, 2006
- [11] D. Wagner, F. Leuterer, et al.; New frequency step tunable ECRH system for ASDEX upgrade; International Journal of Infrared and Millimeter Waves, 27(2006) S.173-82

Diagnostics

EFDA/06-1417 (TW6-TPDS-WINCOD2) ITER Practice for Non-Metallic Replaceable Window Assemblies

Objectives

ITER diagnostics and heating systems use components with key parts made of non-metallic materials (i.e. flange mounted windows). Especially those components which are part of the primary safety boundary have the function of holding back tritium and possible contaminants from plasma spattering. The primary confinement component, the Vacuum Vessel (VV), is designed and fabricated based on approved industrial pressure vessel codes with special requirements developed to take into account the peculiarity of the ITER machine. Non-metallic materials are generally not allowed in pressure vessel codes, and there is no existing industrial standard that specifies the criteria for the design, the manufacturing, and the testing of these parts and components in way directly applicable to ITER.

It is therefore necessary to recommend additional codes and standards with prescriptive guidelines regarding the design, fabrication, Non Destructive Examination (NDE), testing and, if needed, In-Service Inspection (ISI) of components primarily built of non-metallic parts and belonging to the primary safety confinement. The objective of this task is to propose a set of engineering criteria, to provide the justifications for their selection and to give evidence of their soundness. For this purpose, a set of documents is being prepared at FZK:

- An "Engineering Justification Document" containing a detailed support of the soundness of the criteria contained in the technical specifications.
- A "Supporting R&D and Qualification Document" defining all the R&D required to validate the defined criteria.

To support the preparation of these documents, an investigation of the existing industrial specification and/or practice documents and a review of past experience in relevant fields has to be carried out. The outcome of this research will be the preparation of the "Existing Practice Document" containing a list and a general presentation of other technical specifications or specific norms on non-metallic components used and developed for other purposes, that can be used as a reference for the ITER non-metallic components, and a review of existing and past practices in fusion and in other relevant environments.

Project activities: kick-off meeting and following actions, preparation of the First Intermediate Report

The objectives of the kick-off meeting on 12 October 2006 (Garching, D) were to "Agree on a set of requirements that the task needs to satisfy and establish a work strategy and work procedures which ensure that the required outcome will be achieved". During the meeting, the following actions have been defined for the FZK group:

- Identify the list of materials to be included in the set under study and the required flexibility
- Go through the windows reference document to shortlist possible useful documents and double check with the ITER responsible officer for relevance/validity
- Collect and identify reference documents that describe the design types of the window assemblies that are within the scope of the technical specification
- Contact relevant people from the inertial confinement field to inquire about possible relevant experience

Exploitation of the JET experience on optical windows for diagnostic

JET experience is considered to be a major input for the preparation of the window code in ITER. The following points concerning mainly optical windows for diagnostics were summarized.

1. The choice of the material of the window cuffs with respect to the thermal expansion coefficient of the disk: crystal quartz disk bonded to Inconel, SiO₂ disk bonded to tantalum, sapphire to SS316 etc.
2. The purchase of some natural crystals must be considered in advance in order to avoid shortage of the material later. For instance, natural quartz crystals of a proper size (big enough for preparation of the window disks) are rare. Another point is that usually only about 20% of the whole crystal is suitable for the disk preparation.
3. Failures of the diagnostic windows after a water spill showed that in the case of Al-bonding a disk had only few cracks (Fig.1, type 1) and was water tight and the aluminum bond was generally intact. Although the window design was the same, the Au-bonded disks showed a different behavior (Fig.1, type 2).

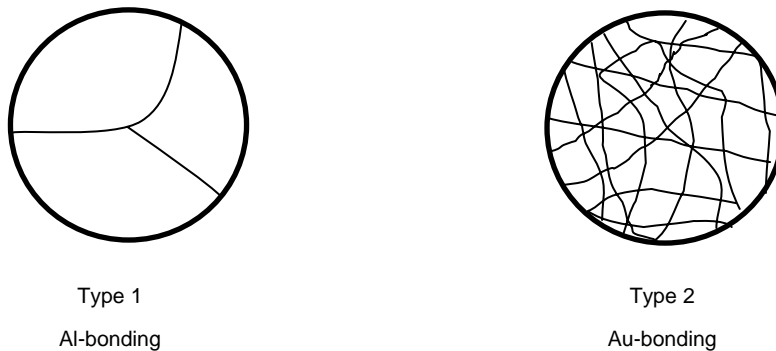


Fig. 1: Schematic image of two types of the cracks.

This fact allowed concluding that high internal stresses were characteristic for the windows manufactured by Au-bonding technique. The modeling of the window design and the choice of the window component materials like ferrules and brazing materials (coupled with temperature of the brazing) should be done in a way that internal stresses in the windows (especially in the disks) are avoided or minimized.

The Type 1 of the window behavior was agreed to be considered as a safety criteria.

4. The definition of the thicknesses of the window disks must be done for room and for operation temperatures, so that an effect of the thermal expansion is taken into account. It will then provide the proper window transparency at resonant frequency (which is coupled with the half wavelength) and operation temperature. For room temperature, the window thickness is to be defined for an easier control during the manufacturing.
5. The locations of all windows must be specified in order to finalize boundary conditions.
6. Quality check: A measurement of the leakage rate should be performed for all windows as the adequate test of the window tightness. Note: the windows on JET were aligned so that the atmospheric pressure forced the window disc on to the ferrule. However, reverse pressure tests were performed for all windows after assembly to confirm the bond strength.
7. Disk flatness/bow: All discs were manufactured to required flatness (a few wavelengths) and to specific thicknesses with very tight tolerances. A specialist firm did this work for JET. All windows were designed to have a small tilt angle to avoid problems with internal reflections. The control of the disk bow however can be considered as a control criterion for internal stresses.

8. Window control: A polarimetry technique should be included for the quality assurance test of the optical windows.

Outlook

By the end of February 2007 the preparation of the following documents must be fulfilled.

No.	Description
1	Existing Industrial Practice Document, including following sub-documents: Fusion Experience document Codes/Standards Review Existing Practice Document
2	Engineering Justification Document
3	Supporting R&D and Qualification Document

Staff:

I. Danilov
R. Heidinger

TW4-TPDC-IRR CER

Irradiation Effects in Ceramics for Heating and Current Drive, and Diagnostics Systems

Objectives

The overall objective of this task is to provide the required irradiation testing and screening of small prototype components, the necessary insulator research, and the database for heating and current drive as well as diagnostic systems for ITER. Especially for the ECRH applications, work was done to assess the effect of tritium on the optical and dielectric (loss) properties of CVD diamond. In order to reduce cost, it was decided to employ deuterium rather than tritium. An important aspect is the impact of radiation on the permeation effect. Thus, diamond specimens are also exposed to deuterium under electron irradiation for radiation enhanced diffusion, including also specimens with significant structural damage (typically 10^{-4} dpa).

Effects of hydrogen isotopes on the dielectric loss and thermal conductivity for CVD diamond ECRH/ECE applications (Deliverable 13)

Specimens for dielectric, thermal conductivity and optical measurements were prepared from a high power CVD diamond window grade to obtain basic indications on the effects of hydrogen isotopes on the relevant properties for ECRH/ECE applications. They were laser cut from a fractured full size window unit which was manufactured by joining the diamond disk "34DB1" (108 mm dia.) to the metallic structure of the window cuff. Dielectric measurements of the 30 mm disk (34DB1a) showed that the dielectric loss was typical for bulk absorption in regular low loss CVD diamond grades. The 20 mm disks prepared (34DB1_20b, 34DB1_20c) were suited exclusively for optical and thermal conductivity measurements because of substantial mm-wave diffraction losses at the edges of the small disks (see Table 1).

Table 1: CVD diamond specimens prepared for the deuterium diffusion/permeation experiments at CIEMAT with dielectric loss determined for the 30 mm disks.

Specimen code	Original disk	Geometry	Measured loss (140 GHz)	Measured loss (90 GHz)
34DB1a	34DB1	30mm dia x 1.81mm	$1.2 (\pm 0.2) \times 10^{-5}$ (effective)	$1.2 (\pm 0.1) \times 10^{-5}$ (GF) $1.5 (\pm 0.2) \times 10^{-5}$ (NF)
34DB1_20b	34DB1	20mm dia x 1.81mm	n/a	n/a
34DB1_20c	34DB1	20mm dia x 1.81mm	n/a	n/a

The specimen 34DB1a was irradiated at the CIEMAT electron irradiation facility with 1.8 MeV electrons covering almost the full area of the specimen (28 mm diameter) [1]. The structural damage accumulated at the end of the irradiation period was $3 \cdot 10^{-6}$ dpa. This is close to the level of 10^{-5} dpa which is reached for the maximum fast neutron fluence of 10^{20} n/m² (E>0.1 MeV) allowed for the torus window of an ECRH launcher. However, the ionising dose rate of 130 Gy/s which was applied during most of the irradiation time (39h out of 42h) was by far exceeding the conditions of a typical torus window ($\approx 10^{-4}$ Gy/h), i.e., the contribution of ionising radiation is being exaggerated in the irradiation. The maximum irradiation temperature was 35.5 °C. The irradiation was performed in the permeation test facility of CIEMAT with the growth face of the specimen exposed to deuterium at 0.9 bar and the nucleation face placed in vacuum ($\approx 10^{-4}$ mbar). No D-permeation was detected at a sensitivity level of the CIEMAT test facility of $3 \cdot 10^{-10}$ mbar·l/s.

The mm-wave measurements of the irradiated specimen 34DB1a (cf. Tab. 2) yielded the same data as obtained before the irradiation within the experimental uncertainties. In particular, no indication of surface loss terms were found in the broadband measurements (90 -100 GHz).

Table 2: The dielectric loss tangent ($\tan\delta$) measured in the CVD diamond disk 34DB1a before and after electron irradiation with the growth face exposed to deuterium (0.9 bar).

Specimen code	Measured loss (140 GHz)	Measured loss (90-100 GHz)
34DB1a pre-irradiation	$1.2 (\pm 0.2) \times 10^{-5}$ (effective)	$1.2 (\pm 0.1) \times 10^{-5}$ (GF) $1.5 (\pm 0.2) \times 10^{-5}$ (NF)
34DB1a post-irradiation	$1.5 (\pm 0.2) \times 10^{-5}$ (effective)	$1.0 (\pm 0.1) \times 10^{-5}$ (GF) $1.1 (\pm 0.2) \times 10^{-5}$ (NF)

The thermal conductivity was measured by the photoacoustic method. For this technique, it is required to apply a thin graphite coating as an absorbing layer for the exciting laser beam on one of the diamond faces. As graphite has pronounced mm-wave absorption, thermal conductivity measurements could only be performed after the mm-wave loss measurements, implying that the specimen 34DB1a could not be measured before irradiation. Representative for the unirradiated state, the 20 mm disk which was not irradiated (34DB1_20c) was taken as a control sample.

Table 3: The thermal conductivity measured in the CVD diamond disk 34DB1a after electron irradiation with the growth face exposed to deuterium (0.9 bar) as compared to an unirradiated control specimen taken from the same original (window) disk.

Specimen code	Original disk	Geometry	Thermal conductivity
34DB1a (irradiated)	34DB1	30mm dia x 1.81mm	1710 (± 100) W/(m·K)
34DB1_20c (unirradiated)	34DB1	20mm dia x 1.81mm	1870 (± 100) W/(m·K)

The thermal conductivity data obtained at ambient temperature (cf. Tab. 3) showed that the unirradiated material is entirely within the characteristic range of high quality CVD diamond material (i.e. between 1800 and 2000 W/(m·K)). The level

observed for the irradiated disk was very close to the low end of this characteristic range, even though still consistent with it within the uncertainty range.

Conclusions and outlook

Specimens from a high power CVD diamond window grade were examined to obtain basic indications on the effects of hydrogen isotopes on the dielectric loss for CVD diamond ECRH/ECE applications. For the typical ECRH torus window grade, electron irradiations were performed at the CIEMAT permeation test facility with 1.8 MeV electrons generating levels of structural damage ($3 \cdot 10^{-6}$ dpa) indicative for the maximum neutron irradiation damage to expected at the torus window of the ECRH launchers. The CIEMAT irradiation experiments, which were performed in a permeation test facility with a sensitivity of $3 \cdot 10^{-10}$ mbar·l/s, did not give any evidence of (radiation accelerated) hydrogen isotope permeation through the CVD diamond disk. Likewise, hydrogen-isotope effects on post-irradiation mm-wave loss could be excluded for the given irradiation conditions.

However, an unresolved aspect remained from the present studies with respect to thermal conductivity. There is the possibility that the onset of the degradation of thermal conductivity which is generally observed with neutrons at a level of 10^{-4} dpa was already reached in this experiment. For clarifying this aspect beyond the present experimental uncertainties, an extension of the irradiation tasks by adding comparable amounts of displacement damage in consecutive steps will be useful.

Staff:

I. Danilov
R. Heidinger
P. Likits
A. Meier
M. Rohde

Literature:

- [1] R. Heidinger, I. Danilov, A. Meier, M. Rohde, E. Hodgson, J. Molla, CVD diamonds windows for ECRH/ECE, Proc. EFDA Ceramic Irradiation Programme: General Progress Report Monitoring Meeting; 6th - 7th of April 2006, Garching
http://efdasgl.ipp.mpg.de/irrcer/IRRCER/IRRCER_info/IRRCER_Meeting/Presentations/ECRH_Window_RH.ppt

Vessel/In-Vessel

TW5-TVV-EBWO Demonstration of Overhead E-Beam Welding

Deep penetration electron beam (EB) welding is an advanced welding method for the joining problem of the vacuum vessel (VV) required in the ITER (International Thermonuclear Experimental Reactor) project. This technique can yield fewer passes (compared to TIG welding) and less distortion. On the other hand, one-path welding of stainless steel plates with a thickness of approximately 60 mm in all positions will lead to a drop-out of the melt, at least in overhead position. This can only be avoided with the aid of a melt support system. The objective of this task is the design and test of an adequate electromagnetic system.

The proposed system is shown schematically in Fig.1. Both the magnetic field \mathbf{B} and the electric current density \mathbf{j} in the molten metal are directed parallel to the surface of the welded plate. The resulting Lorentz force $\mathbf{F}_L = \mathbf{j} \times \mathbf{B}$ is directed perpendicular to the surface and can provide a support of the melt. The developed contactless inductive scheme utilizes eddy currents induced in the workpiece by applying an oscillating magnetic field.

The principal functionality of such a system was already demonstrated in a previous project¹. In that project, the system was tested during laser welding of aluminium. During those experiments with a 4 kW Nd:YAG laser, a magnetic field strength of $B_0 = 0.26$ T and a frequency $f_0 = 779$ Hz were applied generating a pressure of $p_M = 4$ kPa. This is exactly the pressure necessary during welding of 60 mm steel in overhead position.

The next step is the optimal choice of working parameters of the proposed system for single pass pulsed (50 or 100 Hz pulses, duty 50%) electron beam welding of 60 mm thick stainless plates.

Choice of optimal parameters of the EM weld-pool support system

These experiments have to be performed with steel plates instead of aluminium probes, because the required frequencies are material dependent. The reason for this dependency is the electric conductivity of stainless steel (0.74 Si/ μm) which is much lower than the conductivity of Al-alloys. To obtain a large enough electric current density in the workpiece a magnetic field with a frequency up to about 4 kHz is necessary.

During the tests performed in 2006, the magnet system modified in 2005 was used. It was equipped with two pairs of coils having windings made from Cu band designed for welding of steel (see Figure 2, right).

The left part of Figure 2 shows the modified AC-magnet. In order to reduce the heating of the magnet system during operation observed in previous experiments, non-conductive ceramic parts are used to fix the magnet poles and to protect the magnet from the spatter of liquid steel.

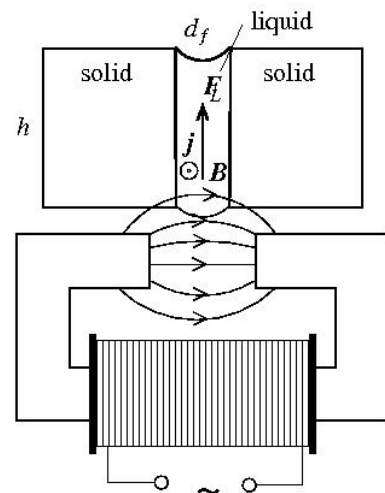


Fig. 1: Schematic view of the inductive EM weld-pool support system.

¹ Avilov, V. V.; Berger, P.; Ambrosy, G.: Simulation of weld-pool support system for power beam welding of VV sector welds. January, 29th 2003. Task TW1-TVV/WELDSP (Contract 01584).

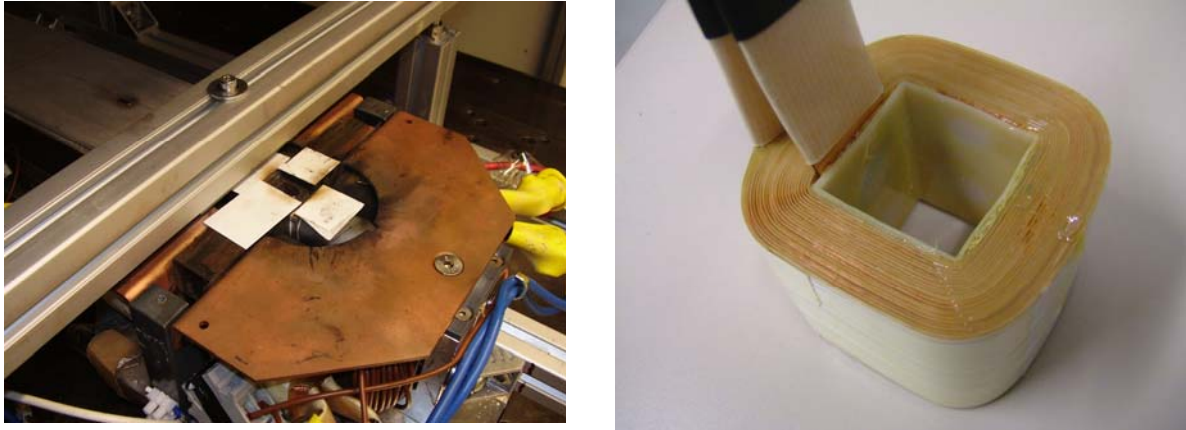


Fig. 2: Left: AC electromagnet for electromagnetic weld-pool support for overhead welding of stainless steel plates. The magnetic field within the workpiece can reach up to 0.4 T at frequencies of about 4 kHz; dimensions: 200 x 230 x 90 mm³, weight: approx. 20 kg, the magnet cores and poles are made from 0.05 mm thick Fe-Si alloy (microsil) band. The magnet poles width is 25 mm and the gap between the poles is 20 mm.
Right: New magnet coils are made of 0.35 mm thick Cu-band.

The most important parameters of EM weld-pool support are the amplitude and the frequency of the oscillating magnet field. The hydrostatic pressure of a 60 mm high column of liquid steel with the density $\rho_l=7.0 \text{ g/cm}^3$ is 4.0 kPa. In accordance with the standard skin-effect theory, the EM-pressure in the workpiece is proportional to the square of the amplitude of the oscillating magnetic field. Hence, the operation parameters can be optimized by 5 kW CO₂ laser-beam welding of 8 mm thick plates of type 304 stainless steel. However, for these relatively thin plates the surface tension effects are comparable with the hydrostatic pressure in the liquid. To estimate the surface pressure in the melt, the curvatures of both sides of the re-solidified weld seams were measured using a light-cut system for surface inspection, see Figure 3. Up to 16 scans per test welding yield the width and heights of the re-solidified metal, the surface pressure and the total pressure in the melt during the solidification. The total pressure measured in this experiment is equal to the EM-pressure of the weld-pool support system.

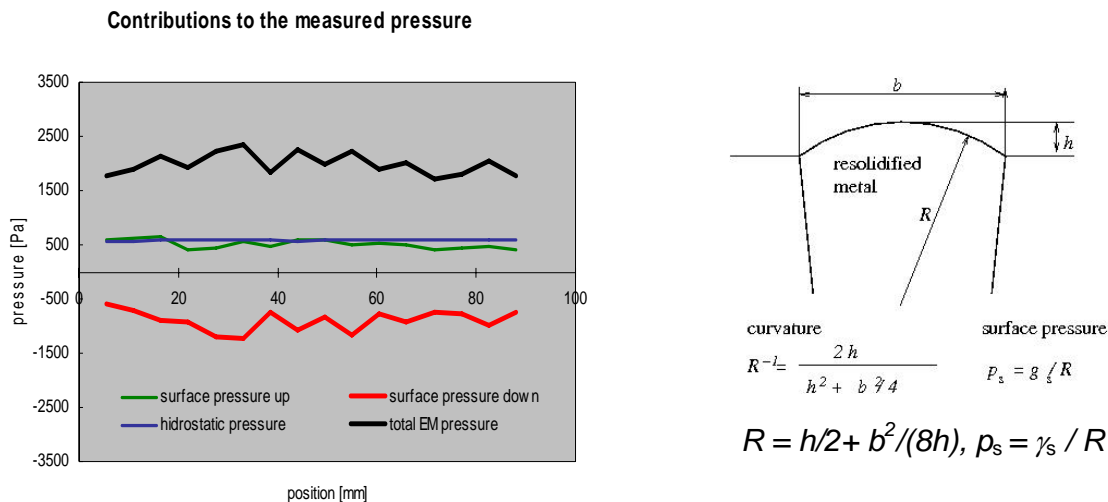


Fig. 3: Estimation of surface tension contribution to the pressure in the melt. The width and the highest of the re-solidified metal determine the curvature of both surfaces.

Figure 4 shows the ratio of the AC magnet supply power in relation to the EM pressure. This value is plotted as a function of the operation frequency of the AC magnet. The optimal value of the frequency corresponds to the minimum on this plot. The AC magnet with 3.3 kHz

needs 0.9 Watt per Pascal of the electromagnetically generated pressure in the melt. For stainless steel with a density of 7.0 g/cm³ it provides 630 Watt per cm of the melt. This means that 3.8 kW are necessary to prevent the gravity drop-out during welding of 60 mm thick stainless steel plates in overhead position.

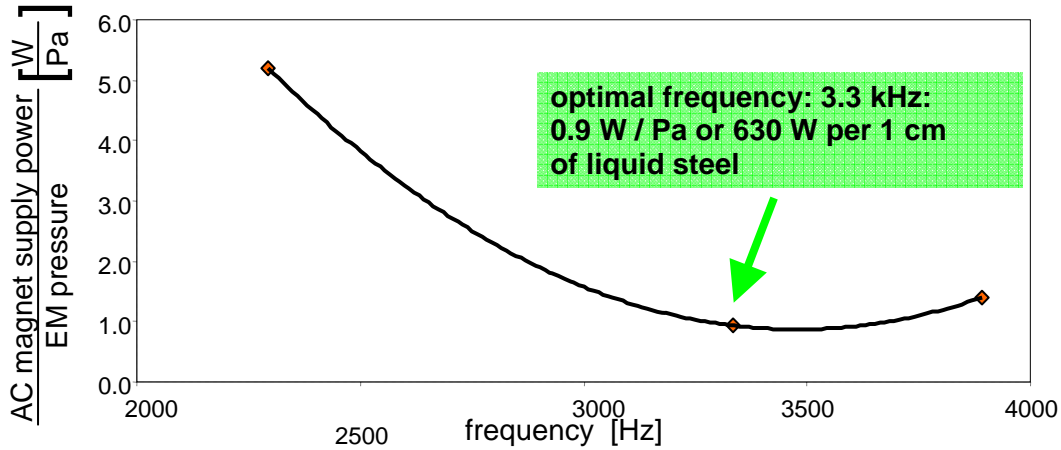


Fig. 4: The ratio of the AC magnet supply power to the EM pressure in the melt as a function of the operation frequency.

Pulsed electron beam welding with EM weld-pool support

The laser-beam welding tests demonstrate huge perspectives of the proposed technology. Note, that the magnetic pressure in the melt is proportional to the square of the amplitude of the applied AC magnetic field. This value is limited by the saturation field of ferromagnetic materials used in the design of the magnet. We use non-expensive laminated Fe-Si alloys with 1.4 Tesla saturation field. Hence, an EM support by single-pass welding of up to a few decimetres thick weld pools is possible.

To verify these properties, a power beam system which can penetrate deep enough in a metallic workpiece is needed. This can only be fulfilled by an electron beam welding system. Therefore, a 5 kW DC-AC converter for EM melt support by 50 Hz pulsed EB welding has been built up, now, Figure 5. Each support phase is starting with rapid increase of the applied magnetic field, Figure 6.

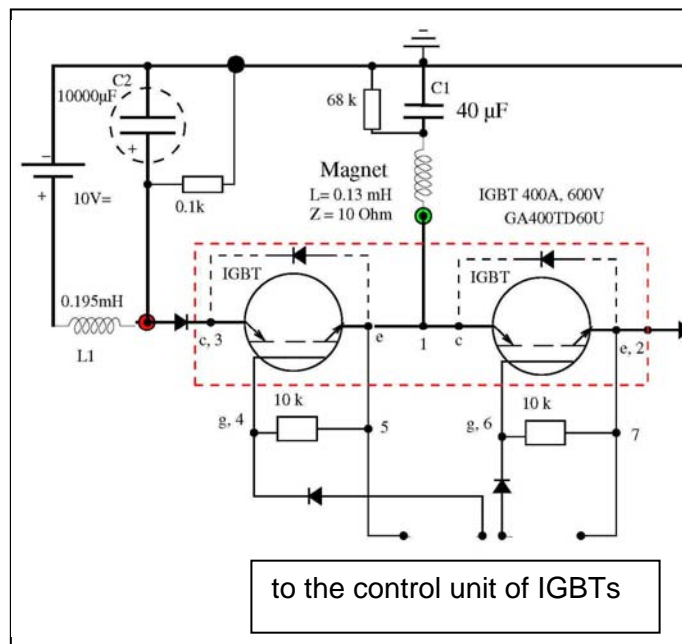


Fig. 5: DC-AC inverter.

Stage 1 “welding”, 10 ms: both IGBT switches are in the position OFF, no current in the magnet coils. However; the capacitor C remains charged.

Stage 2 “support”, 10 ms, the electron beam is OFF. Depending on the polarity of the electric current in the magnet coils either the left or the right IGBT switch is ON. The slow decreasing of the amplitude of oscillations with the characteristic time 1 ms is necessary to provide an effective de-magnetization of the used ferromagnetic magnet cores.

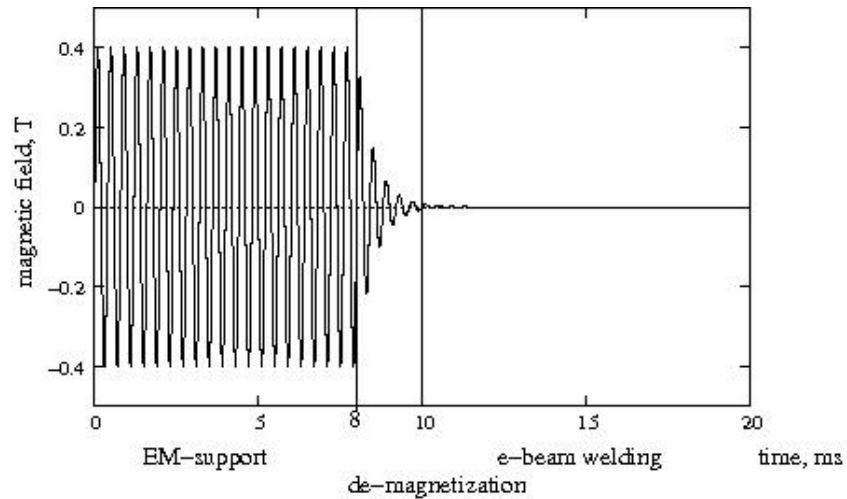


Fig. 6: One period of weld support in 50 Hz pulsed electron beam welding.

Staff:

V. Avilov
P. Berger
R. Moldovan
T. Graf

University of Stuttgart
IFSW
70569 Stuttgart, Germany

Literature:

- [1] Avilov, V. V.; Berger, P.; Ambrosy, G. .: Electromagnetic Melt Support System for Overhead Position Laser and Electron Beam Welding of Thick Metal Plates. In: Proc. of the 5th International Symposium on Electro-magnetic Processing of Materials (EPM2006), Oct. 23-27, 2006, Sendai, Japan, pp. 237-241.

Magnet Structure and Integration

EFDA/03-1105 (TW3-TMSC-CRYLAB) Cryogenic Laboratory Tests for V-I Characterisation of Subcable Samples

The main objective of this work is to perform measurements of the V-I characteristics of Nb₃Sn sub-size (>30 strands) cable-in-conduit conductors (CICC) under applied longitudinal strain in liquid He (T = 4.2K) and high magnetic fields (up to B = 14 T).

Emphasis shall be put on the measurement of the thermal pre-strain of the strands. To this end the experimental set-up shall be capable of performing accurate measurements of specimens having – in particular – different conduit materials, thickness, cables sizes and void fractions [1, 2]. The strain applied to the strand shall be – typically – up to ≈ 1.5%. The instrumentation sensitivity is planned to allow measurements of critical electric fields as low as E = 10 μV/m with a sensitivity better than 1 μV/m.

After the experimental set-up has been completed, instrumented and accurately calibrated, specimen testing shall be started. All specimens will be made available by EFDA. In total, during the contract period, about 25 specimens shall be tested.

To conduct this work the *FBI*-facility at the Forschungszentrum Karlsruhe will be used. This facility is capable to investigate the influence of applied longitudinal strain (*F*) and magnetic field (*B*) on the critical current (*I_c*) at liquid helium temperature. The facility contains two separate experimental setups to cover tests on single superconducting strands and also on CICC's [3, 4].

Within this work the facility was upgraded and is now under use for performance tests of advanced single strands and sub-stage CICC's developed for ITER [5].

Cable-in-conduit sub-stage samples

Table 1: Details of the used OST internal-tin strand.

Diameter of (NbTi) ₃ Sn strand	0.81 mm
Subelements	19
Number of filaments / subelement	~ 150 - 160
Single Ta barrier	
Cu:non-Cu ratio	1
Current density J _c , non-Cu	~ 1200 A/mm ² (Type 1) ~ 1100 A/mm ² (Type 2)
Non-Cu hysteresis losses	900 kJ/m ³ (Type 1) 700 kJ/m ³ (Type 1)

OST Type 1 taken from billet 7730-1

OST Type 2 taken from billet 7878-1

In a first stage of this programme a systematic characterization of the influence on the critical current *I_c* of the main cable parameters, like cable pattern, void fraction and twist pitch was performed. For this purpose several samples were manufactured under the supervision of CEA, France. The details of the used strand is given in Table 1 together with a cross sectional view of the strand shown in Fig. 1. For the different examined CICC sub-size samples the details are listed in Table 2.

In the first column the sample name is given with a number engraved onto the sample for better identification. Because every sample was made with a backup, there are A and B followed by the number of superconducting strands in the first triplet, like A1 for one or A2 two superconducting strands in the first triplet. In case the void fraction deviates from 32% an additional 25 or 45 is added (e.g. A225). For samples with a short twist pitch an S is given at the end.

The second column indicates the strand used for this CICC sample. There are two different billets used from Oxford Superconducting Technology (OST Type 1 from billet 7730-1 and

OST Type 2 from billet 7878-1). Because most samples are made from OST Type 2 we will mainly focus on these for comparison.

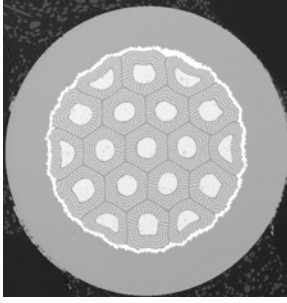


Fig. 1: Cross sectional view of the used internal-tin OST Type 1 strand with 0.81 mm diameter. The OST Type 2 is comparable to this view. Details of the strand parameters are given in Table 1. (Courtesy of J. Parrell from OST, 2005).

The next four columns give details of the number of superconducting and copper strands used in the first triplet, the void fraction and the twist pitch. In Fig. 2 the cross section of the three different cable layouts are illustrated, the smallest with 3x3, the 3x3x5 and the largest layout examined 3x3x5x4. The outer diameter ranges from about 3.3 mm to 15 mm depending on the layout. All samples have an overall length of 1.1 m. Additional cooling holes on both ends of the sample allow liquid helium to circulate through the sample length [5].

All samples were heat treated using following temperature steps: 210°C / 50 h, 340°C / 25 h, 450°C / 25 h, 575°C / 100 h, 650°C / 100 h all steps with 10°C/h.

Table 2: Overview of different cable parameters.

sample	Used strand	Cable pattern	Strands in 1 st triplet	Void fraction	Twist pitch [mm]
n01 A3	OST 1	3x3	3 sc / 0 Cu	32 %	45 / 85
n05 A225	OST 1	3x3x5	2 sc / 1 Cu	25 %	45 / 85 / 125
n06 A245	OST 1	3x3x5	2 sc / 1 Cu	45 %	45 / 85 / 125
n22 A1	OST 2	3x3x5	1 sc / 2 Cu	32 %	45 / 85 / 125
n08 A1	OST 2	3x3x5x4	1 sc / 2 Cu	32 %	45 / 85 / 125 / 160
n14 B2	OST 2	3x3x5	2 sc / 1 Cu	32 %	45 / 85 / 125
n17 A2	OST 2	3x3x5x4	2 sc / 1 Cu	32 %	45 / 85 / 125 / 160
n09 B3	OST 2	3x3	3 sc / 0 Cu	32 %	45 / 85
n11 A3	OST 2	3x3x5	3 sc / 0 Cu	32 %	45 / 85 / 125
n15 B225	OST 2	3x3x5	2 sc / 1 Cu	25 %	45 / 85 / 125
n16 B245	OST 2	3x3x5	2 sc / 1Cu	45 %	45 / 85 / 125
n24 B2S	OST 2	3x3x5	2 sc / 1 Cu	32 %	35 / 65 / 110
n25 A2S	OST 2	3x3x5	2 sc / 1 Cu	32 %	35 / 65 / 110

Experiment

The experiments were performed at 4.2K using the FBI-facility, equipped with a split-coil magnet reaching a maximum magnetic field of 14 T. To measure the strain sensitivity of the critical current I_c the sample can be loaded up to 100 kN by a tensile machine. The determination of the critical current is limited to 10 kA, the maximum of the available current supply. Reaching a critical field of 0.1 μ V/cm was taken as I_c criterion. More details can be found in [5].



Fig. 2: Cross section view of the different sub-stages with the smallest cable layout of 3x3 (OD 3.3 mm), the larger 3x3x5 (OD 7.6 mm) and the largest cable in conduit sample with 3x3x5x4 layout (OD 15 mm).

First the magnetic field dependence of I_c was measured from 14 T down to 10 T, in some cases to 8 T, in one Tesla steps. After this the strain dependence of I_c was measured at a constant field of 12 T.

Because the samples contain different numbers of superconducting strands it is more convenient to normalize the obtained data by dividing I_c by the number of superconducting strands for each sample (e.g. $I_c / 30$ for a 3x3x5 with 2 s.c. strands in the 1st triplet). Regarding the strain measurement the applied strain is shifted to zero at maximum I_c . In the following all data is presented in this form.

A. $I_c(B)$ dependence

In Fig. 3 the magnetic field dependence on I_c of the two different strand types is plotted, normalized to the number of superconducting strands. The data of the measured samples collapses to two main $I_c(B)$ lines: one for OST Type 1 and one for OST Type 2 which is shifted about 10% to lower values.

Here no significant influence of the cable parameters can be seen except the strand origin. This effect is understandable when looking at the different critical current density values for OST Type 1 and Type 2 as given in Table I.

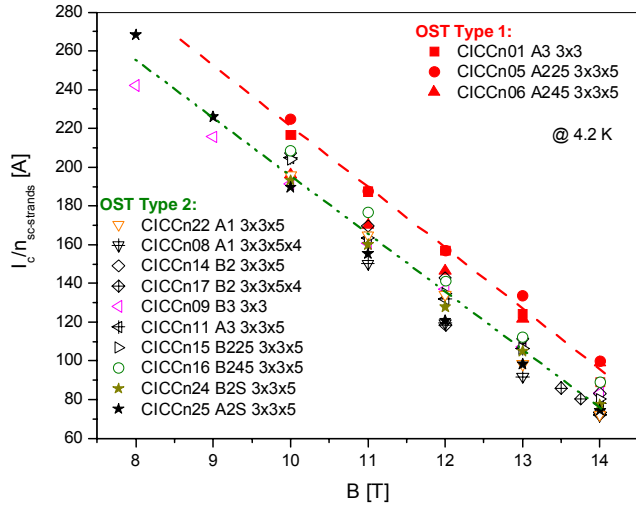


Fig. 3: Summary of the $I_c(B)$ measurements normalized to the number of superconducting strands of all sub-stage CICC's made from OST Type 1 and OST Type 2 strands. The measurements were performed at 4.2K.

B. $I_c(\epsilon)$ dependence

In Fig. 4 and Fig. 5 the strain effect on I_c at 12 T is summarized. The curves show a clear dependence regarding the cable layout of the sample. For the OST Type 1 samples in Fig. 4 the highest I_c is reached as already seen in $I_c(B)$. However, increasing the void fraction seems to decrease I_c .

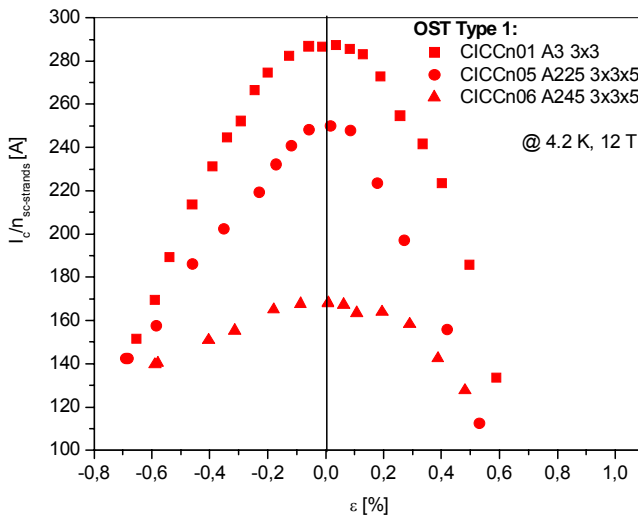


Fig. 4: $I_c(\epsilon)$ for sub-stage CICC's manufactured from OST Type 1 strand measured at 4.2K and 12 T.

Looking at the OST Type 2 sub-stage CICC's the number of samples is sufficient to examine the impact of the different cable layout parameters. The highest I_c values reached (n14-B2-3x3x5) are not influenced by a reduced void fraction (n15-B225-3x3x5), a reduced number of superconducting strands (n22-A1-3x3x5), or a higher cabling stage (n08-A1-3x3x5x4).

Contrary to this, a higher void fraction (n16-B245-3x3x5) or a shorter twist pitch (n24-B2S-3x3x5, n25-B2S-3x3x5) decreases the maximum current of about 20 %. Even the increased number of three superconducting strands in the first triplet tends to decrease the

possible maximum I_c (n09-B3-3x3, n11-A3-3x3x5) for the OST Type 2 sub-stage CICC's.

Conclusion

Examining the results from the samples, it is obvious that the VAMAS strand properties can not be recovered (OST ~ 310 A I_c at 12 T obtained within the single strand test programme [6]). The experiments about $I_c(\epsilon)$ show a clear influence of the cable layout.

There is not such a difference before stretching in the $I_c(B)$ data. This can be understood, because the Lorentz force on the conductor level is not significant. However, the increase of Lorentz force per strand, due to the increasing I_c during stretching, reveals a sensitivity and degradation of some of the samples.

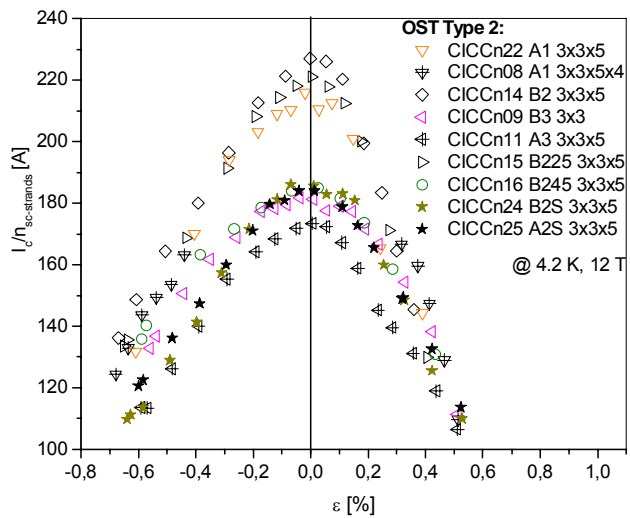


Fig. 5: $I_c(\epsilon)$ for sub-stage CICC's manufactured from OST Type 2 strand measured at 4.2K and 12 T.

As a tendency:

- OST Type 1 behave better than OST Type 2
- 32% and 25% void fraction samples are the best of OST Type 2
- 45% void fraction samples, small twist pitches samples, B3 and A3 (all s.c. strands samples) are the worst
- No clear influence of the cable pattern (size) of the sample is seen.

The results obtained within the first stage of the test programme gives indications for an optimization of an ITER cable layout. In a next stage the sensitivity to strand origin (companies) has to be examined. Therefore, samples from five different manufacturers will be prepared.

Staff:

K.-P. Weiss
H. Kiesel

Literature:

- [1] J.W. Ekin, "Filamentary A15 Superconductors", M. Suenaga, A.F. Clark, Eds. New York and London: Plenum Press, 187 (1980).
- [2] W. Specking, J.L. Duchateau, "Improvement of I_c in Nb_3Sn conductors by reduction of the axial prestrain", Transactions on Applied Superconductivity 5 (2), 845 (1995).
- [3] W. Specking and R. Flükiger, "A compact 5 kN test facility for superconducting conductors carrying up to 1.5 kA in magnetic fields up to 14T", Journal de Physique 45, C1-79 (1984).
- [4] W. Specking, A. Nyilas, M. Klemm, A. Kling, and R. Flükiger, "The effect of axial stresses on I_c of sub-size NET Nb_3Sn conductors", Proceedings of the 11th International Conference on Magnet Technology (MT-11), 1009 (1989).
- [5] A. Vostner, E. Salpietro, K.P. Weiss, W.H. Fietz, A. della Corte, L. Muzzi, "The FBI facility – a test rig for critical current measurements on CICC as a function of strain", IEEE Transactions on Applied Superconductivity 15 (2): 1387, (2005).
- [6] A. Vostner and E. Salpietro, "The European Nb_3Sn advanced strand development programme", Fusion Engineering and Design 75-9: 169 (2005).

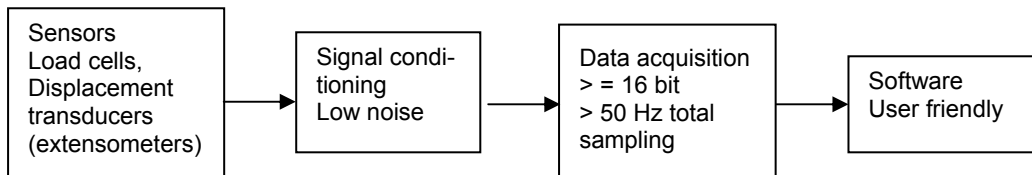
EFDA/04-1216 (TW4-TMSC-CRYOLA) ITER Cryogenic Testing Collaboration Task between CEA Grenoble and Forschungszentrum Karlsruhe

The main objective of this work is to spread and standardize the available know-how on cryogenic mechanical tests across the European laboratories to be prepared for the large number of tests necessary during the ITER magnet procurement action.

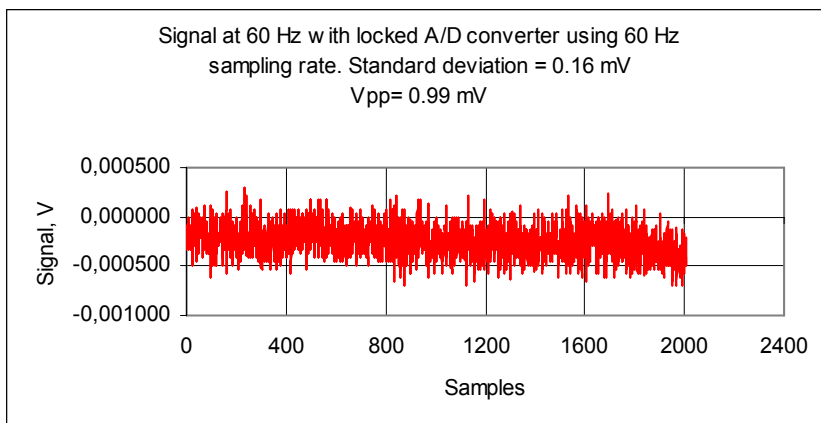
The present report deals with the efforts conducted during the reporting period with the guidelines of measurement techniques with respect to tensile and fracture toughness properties of alloys at 4K. The work, summarized in Table 1, was done in close collaboration between Forschungszentrum Karlsruhe and CEA/Air Liquide, Grenoble. The experiences gained during the last two decades of Forschungszentrum Karlsruhe have been transferred to CEA/Air Liquide, Grenoble. Special attention has been focused on J-tests carried out with small size specimens at 4K. A small round robin test procedure between these two institutions deepened the knowledge techniques. Provided sensing systems of Forschungszentrum Karlsruhe enabled CEA/Air Liquide to carry out sensitive tests resulting in fracture toughness values accepted by the worldwide community.

Background

The following illustration shows the necessary tools and their key requirements for a successful and reliable measurement. Every link in the chain must work properly to ensure a sound measurement quality.



Today it is a top requirement that all recorded data during the measurements should have a digital source. Commercial digital A/D converters with sampling rates > 50 Hz are to date standard tools. These A/D converters should have however, a minimum resolution of at least 16 Bit. The system diagnostics for a quality check can be carried out by shorting the terminal boxes using a ~ 50 Ohm resistance. Figure 1 shows one possible way of the diagnostics after shorting of the A/D converter.



The result given in Fig. 1 shows the quality of the board without any external load. Prior to any measurement this kind of diagnostics gives valuable information about the used data acquisition system.

Fig: 1: Diagram shows the signal (V) versus sample diagnostic test result for circa 30 s static run of an 18 bit A/D converter (differential input) in a laboratory environment with a sampling rate of 60 Hz. A/D channel input is shorted with a 50 Ohm resistance. No mathematical smoothing.

Table 1: Work Programme

Phase	Steps	How to be accomplished	Comments
1	Documentation of the machine upgrade to allow measurements at 4K including the delivery of raw data.	Enable push button change of load direction Reduce voltage for extensometer to ≈ 1 V Enable storage of raw data	
2	Delivery of raw data (ASCII) of the load cell and the used extensometer at RT	Set the machine in start position without specimen loading and acquire the signals (V) versus time for circa 600 s	
	Delivery of raw data (ASCII) of the used extensometer at 4K	Cool down the extensometer within calibration jigs and acquire the signals (V) versus time for circa 60 s	
	Definition and validation of the calibration procedure to be performed. Delivery of calibration raw data (ASCII) at RT	Perform the calibration and acquire the signals versus time	
	Delivery of raw data (ASCII) of the calibration process of the used extensometer at 4K	Move the calibration jig and acquire the readings for about 1 mm displacement. Acquire the extensometer signal versus reference	
	Delivery of the machine property by manual up and down push buttons. Acquire the stroke raw data	Ramp up and down the machine stroke manually and acquire stroke versus time signal	
3	Delivery of the Young's modulus line at RT	Delivery of the raw data load versus displacement as raw data. Delivery of the calibration data of the used extensometers for this measurement. Delivery of the gauge length and the load cell calibration data.	Following procedure validated in phase 2
	Delivery of the Young's modulus line at 4K	Delivery of the raw data load versus displacement as raw data. Delivery of the calibration data of the used extensometers for this measurement. Delivery of the gauge length and the load cell calibration data.	
4	Delivery of the fracture toughness raw material data for a material (ferritic, aluminium e.g.) following the E 399 standard at RT	Raw data of the load versus displacement and the evaluated diagram with the 95% offset secant procedure	
5	Delivery of elastic/plastic raw data of a high strength/toughness material (e.g. 316LN) at 4K	Here especially the determined slopes raw data and the load displacement raw data is necessary for the cross check	
6	Delivery of the fatigue crack growth rate (in Paris regime) data for a 4K test	Delivery of the used slopes for the crack length increment evaluation (in form of ASCII data). Evaluation procedure using the compliance function.	
7	Delivery of thermal expansion from RT to 4K for stainless steel & composite material	Delivery of the raw data from the measurements	Composite material from magnet insulation
8	Delivery of thermal conductivity at 4K for stainless steel & composite material	Delivery of the raw data from the measurements	Composite material from magnet insulation

Figure 2 shows the result of a measurement with an extensometer during the cool down process around 100K. Here the signal of the extensometer is checked for 30 s for a similar type static run diagnostics. As expected the noise is increased almost twofold compared to unloaded A/D converter case. The value is appropriate for the required tests and gives knowledge about the limits of the used experimental set-up. Therefore, at any time of the run it is possible to obtain information about the used transducers performing different cross-checks. This diagnostics should be carried out from time to time, especially at any start of a new measurement task to obtain system healthy check information.

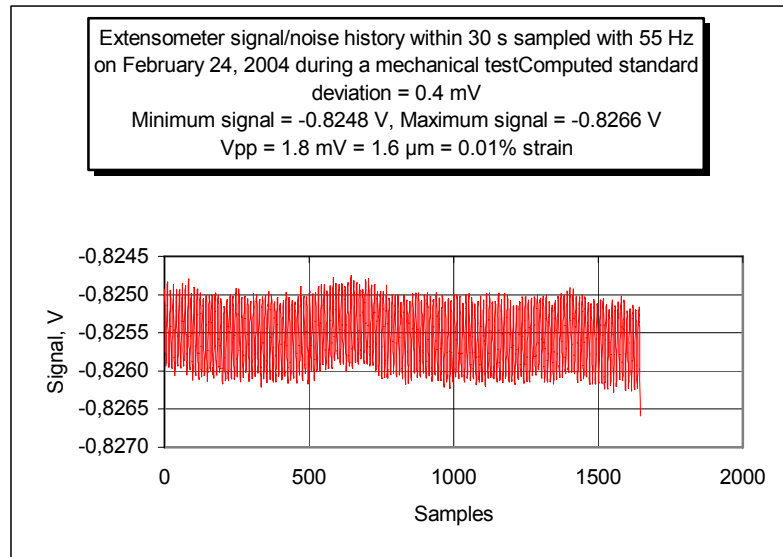


Fig. 2: Diagram shows the extensometer signal versus number of sample diagnostic test result for ~ 30 s run of an 18 bit A/D converter (differential input) in a laboratory environment with a sampling rate of 60 Hz. The scatter gives the noise range of the used extensometer system. Similar type of diagnostics should be made also with the load cell output. No mathematical smoothing

The used extensometers or clip on gauges should have certain criteria and the calibration procedure must meet the ASTM E 83 standard [1]. Before any new measurement task the extensometer must be re-calibrated at ~ 300K using a digital micrometer or LVDT (Linear Variable Differential Transducer). At least once in the lifetime of the extensometer a calibration must be accomplished at the environment, where the measurements will take place later, namely in submerged liquid helium. The determined factor between 300K and 4K is the input data for the later tests.

One source for the increase of the noise at 4K is the power source heat load onto the strain gauges of the extensometers. Therefore, the bridge voltage should be kept lower than 2 V (1 V is ideal) to avoid boiling of the helium at 4K. If otherwise a higher bridge voltage supplies satisfactory results regarding the noise, than the bridge voltage set can be accepted. On requirement calibration chart had to be handled to third parties for the reason of error source clarification. Figure 3 shows a typical calibration diagram and the statistical evaluation of the readings.

Tensile measurements

The mechanical tensile test procedure is standardized for ambient temperature by several standards. Standards such as DIN EN 10 002-1 refer to room temperature measurements and are applicable for large cross section ($>10 \text{ mm}^2$) metallic material specimens, whereas the standards ASTM E 8 [2] and ISO 15579:2000 [3] can be used between room temperature and 77K (-196°C). The gap between 77K and 4K is closed with the new ISO standard, already applicable under the code ISO/AWI 19819 [4]. For small cross section metallic superconducting wires a new standard was recently approved under the framework of IEC (International Electro-technical Committee, code IEC90/63/CDV) [5].

However, all these standards pay little or no attention to the elastic offset line, which determines the important mechanical property known as Young's modulus. This value is a material property useful for calculating the stress distribution by FEM (Finite Element Method) analysis during the design of a component. In addition, the Young's modulus is important,

because an erroneous Young's modulus measurement affects the nominal scale of the stress-strain abscissa, thus influencing the result of the evaluated yield strength.

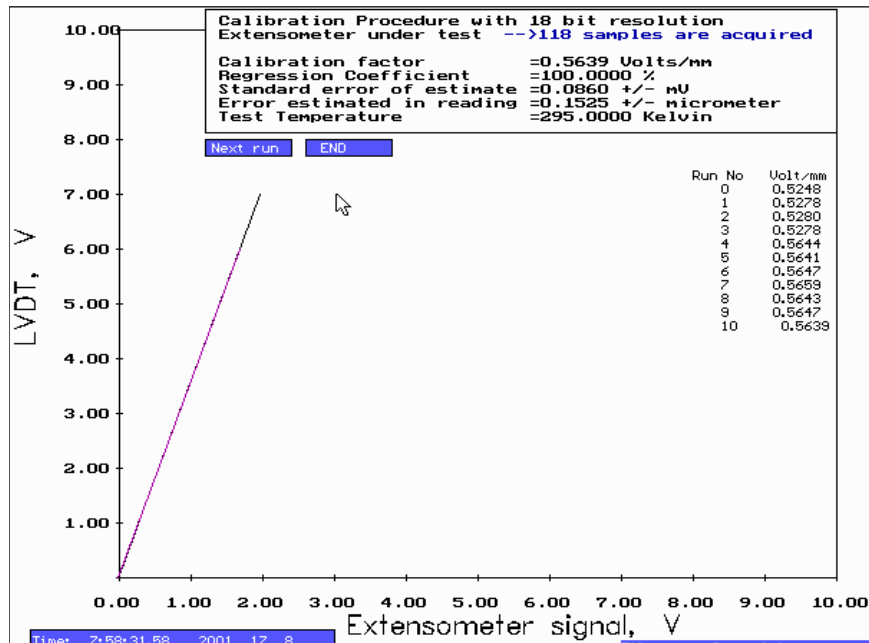


Fig. 3: Calibration procedure of the extensometer plotted as machine LVDT versus extensometer signal. The software determines the calibration factor using a first order linear regression procedure. The diagram gives also information about the statistics of the calibration procedure. The first 4 rows are the results with one extensometer and the following rows are with the second extensometer.

For Young's modulus determination to date only ASTM E 111 standard [6] exists. Although this standard is re-approved in 1988 it does not recommend using the stress-strain curve's initial tangent modulus (slope of the stress-strain curve at the origin) because of the difficulties with the establishing of the zero offset line experimentally. Therefore, until now all evaluations with respect to Young's modulus obtained by different companies and laboratories worldwide are based on different techniques. The determined results are often coupled with large errors (>+/- 40%) as given e.g. in the reference [7]. In this reference the room temperature round robin test results of 91 certified laboratories are published concerning large size specimens of commercial steel. Especially for large cross section specimens a slight bending owing to specimen/machine mismatch can lead in unavoidable bending stresses with the result of a large non-linearity of the initial tangent modulus of the stress-strain curve. This phenomenon is very common as shown by the stress-strain diagrams in several papers [8, 9]. Several techniques based on mathematical polynomial approximations are proposed to evaluate a reasonable elastic line [8] to establish the Young's modulus value. However, a better choice would be to achieve a linear slope from the very beginning of the test. The deviation from the linearity can be easily avoided by averaging the measured strains of two extensometers arranged at equal intervals around the cross section. This technique is also strongly recommended by ASTM E 111 [6] and we use this technique since around more than a decade with great success. In fact, the double extensometer system can average if necessary the specimen/machine mismatch.

Considering the above recommendations, it is possible to obtain ideal strain-stress curves of materials. In fact, the results if taken account of the above considerations confirm so far the sound achievements in the field of materials testing both at room temperature and at cryogenic environment.

Standards on tensile measurements

- *DIN EN 10 002-1*. This standard is applicable for room temperature tests. The standard does not refer to the Young's modulus.
- *ASTM E 8*. This standard is applicable for tests at room temperature but is also used often at low temperatures (-196°C). The standard does not refer to the Young's modulus.
- *ISO 15579:2000*. This standard is applicable for tests, where $T > -196^{\circ}\text{C}$. The standard does not refer to the Young's modulus.
- *ASTM 1450*. This standard is applicable at liquid helium temperature.
- *ISO/AWI 19819*. This is a draft of a standard applicable between 4K and 77K and is approved by ISO. The standard does not refer to the Young's modulus determination, it only recommends the determination of Young's modulus data as an option.
- *IEC90/63/CDV*. This standard refers to NbTi SC tensile tests at 300K. The definition of Young's modulus is given. However, no methodology about the Young's modulus determination is given.
- *ASTM E 111* (Re-approved 1988). This refers to a standard test method for Young's modulus. In 1.2 the terminology is as follows: "*Because of experimental problems associated with the establishment of the origin of the stress-strain curve described in 8.1, the use of either initial tangent modulus (that is, the slope of the stress-strain curve at the origin) or secant modulus is not recommended and their determination is outside the scope of this test method*". Furthermore, the standard recommends in 6.4: "*It is recommended that an averaging extensometer or the average of the strain measured by at least two extensometers arranged at equal intervals around the cross section be used.*"

In general the laboratory should be in a position to handle the raw data upon request for reason of cross check and data verification. The digital file (ASCII or text file) of the raw data (signals) along with the calibration data of extensometers (V/mm), load cell calibration data (N/V), and gauge length of the extensometer are in this sense the important values for third parties. For ITER QA programme the availability of calibration data and sample raw data is a prerequisite.

Work programme

Within Table 1 the required work to be completed for successful measurements are listed. All necessary Phases 1 to 8 are accomplished by CEA/Air Liquide, Grenoble that demonstrated the ability to perform material tests at cryogenic temperature.

Staff:

K.-P. Weiss
M. Schwarz
A. Nyilas
H. Kiesel

Literature:

- [1] ASTM E 83 – 85, "Standard Practice for Verification and Classification of Extensometers", ASTM, Philadelphia, 1985
- [2] ASTM E 8 – 89, "Standard Test Methods of Tension Testing of Metallic Materials", ASTM, Philadelphia, 1989
- [3] DIN ISO 15579, "Zugversuch bei tiefen Temperaturen", DIN Deutsches Institute für Normung e. V. Berlin

- [4] ISO/TC 164/SC 1, "Metallic Materials – Tensile Testing in Liquid Helium", Draft Report of ISO/TC 164/SC1, 2000, Berlin
- [5] IEC 61788-6, "Mechanical Properties Measurement – Room Temperature Tensile Test of Cu/Nb-Ti composite superconductors", IEC 90/63/CDV, IEC 90/63A/CDV, 1999
- [6] ASTM E 111-82, "Standard Test Method for Young's Modulus, Tangent Modulus, and Chord Modulus, ASTM, Philadelphia 1996
- [7] H. F.Recklinghausen, H. J. Kuehn, and T. Fritz, „Der Zugversuch“, Materialprüfung 40 (1998), 11-12, pp 480 - 485
- [8] G. Michalzik, "Normgerecht und Effizient", Quality Engineering 3, (2000), pp. 50-52
- [9] M. Loewe, „Materialprüfung automatisieren – Zugversuch nach DIN EN 10 002-1“, Der Versuchs- und Forschungsingenieur VFI, 2, (2000), pp. 27 – 30

EFDA/05-1274 (TW5-TMSM-CRYTES) Cryogenic Testing of Materials, Welds and ITER Mock-ups for Magnet Structures

The magnet windings and structures of the experimental reactor ITER require materials and welded joints with high mechanical properties to withstand the large electromechanical loads during charge-up of the machine and the operational pulses.

Within this work the fatigue life behavior of a TF cooling inlet mock-up sample is characterized at 4K after having been hydraulically qualified in the OTHELLO test facility at Cadarache. The testing included prior to the fatigue tests the stiffness measurements by special instrumentation and finally the fatigue life performance of the structure for a life time of 30,000 cycles at 4K. In addition, the characterization of fatigue life behavior of candidate structural materials for ITER is performed under compression/tension loading.

Scope of work

The scope of the contract can be briefly described as follows:

- Fatigue life qualification of the cooling inlet areas mock-ups of the TF and CS coils
- Cryogenic mechanical characterization of structural materials and welds according to the task progress
- Tensile strength, fatigue properties and thermal contraction tests for the selected candidate structural materials at cryogenic temperature (4K)
- Fatigue life tests on TF coil case candidate structural materials, here specifically the low cycle properties at $R = -1$ at 295K and at 7K

The static material and component tests are conducted according to the existing standards. For tensile tests the applicable document ISO/CD 19819 "Metallic materials – Tensile testing in Liquid Helium" are the basis of those investigations.

Fracture toughness tests are conducted using the ASTM standards E 813-89 and the newly developed JETT (J-Evaluation on Tensile Test) technique and fatigue life tests according to ASTM standards. Hourglass specimens were prepared for the fatigue life investigations of the base material and butt welds of the candidate CS jacket materials.

Test facilities

The following test facilities are used in the frame of this Contract:

- Cryogenic tensile/compression material cyclic investigation facility, system MTS (+/-25 kN) working between 295K and 7K
- Cryogenic tensile/compression material cyclic investigation facility, system MTS (+/-50 kN) working at 295K and at 77K (LN₂)
- Cryogenic tensile material cyclic investigation facility, system Schenck (630 kN) working at 4.2K (LHe).

Fatigue life qualification of the cooling inlet areas mock-up of the TF coil

The results of the mock-up test are described in [1] and are only briefly summarized here. On a first test day in 2005 a total of 125,000 cycles were conducted within circa 6 hours at 4K. The average strain was around 0.11% at 220 MPa stress. The cycling was done with a peak stress of 320 MPa and minimum of 120 MPa. On the second day a total of 207,797 cycles were conducted within circa 9 hours at 4K with the same parameters for stress and strain as

the day before. This means that at the end of the second day the total cycle number was 332,797 cycles.

Table 1: Results for cyclic testing of CS weld specimen.

Specimen No	Initial static loading MPa	Peak /Valley stress MPa	Cycle number	Comments
1	300	300 - 30	61707	Survived
2	400	300 - 30	62223	Survived
3	608	500 - 50	26411	Failure
4	-	400 - 40	61838	Survived

During the final experimental day a total of 476,117 cycles was achieved at 4K, before the structure collapsed in the region of the heat affected zone near the weld. Therefore, the TF-structure did not survive the envisaged 600,000 cycles (30,000 with a factor of 20). In Figure 1 pictures of the mock-up during cryostat insertion and after failure are shown.

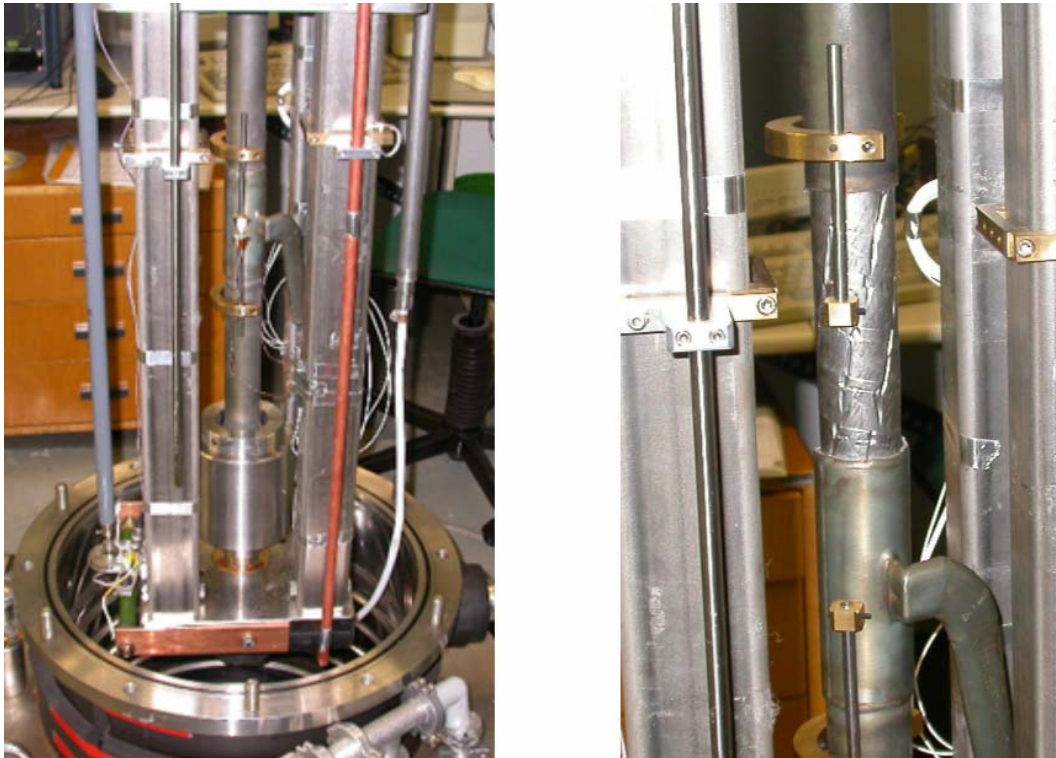


Fig. 1: On the left, the assembled TF-mock-up No II inside the 4K rig is inserted into the cryostat; on the right the structure after failure.

Cyclic loading of CS coil weld specimens at 7K

Cyclic tests were carried out at 7K with specimens machined from the top part of the jacket provided by CEA, Cadarache. The requirement was 300 MPa peak stress at 7K for 60,000 cycles. In Figure 2 the CS coil sample is shown from which the standard specimens were made for cyclic loading. All together four specimens (see Figure 3) were made and tested as follows:

- Specimen 1 and 2
Prior to testing the test both samples were loaded up to 300 MPa for sample 1 and 400 MPa for sample 2. This was done to verify the linear elastic strain behaviour with respect to the envisaged stress range of 300 MPa – 30 MPa.

Sample 1 was cycled for 61,707 cycles without any damage. For sample 2 the total cycle number was 62,223 cycles without any detectable damage.

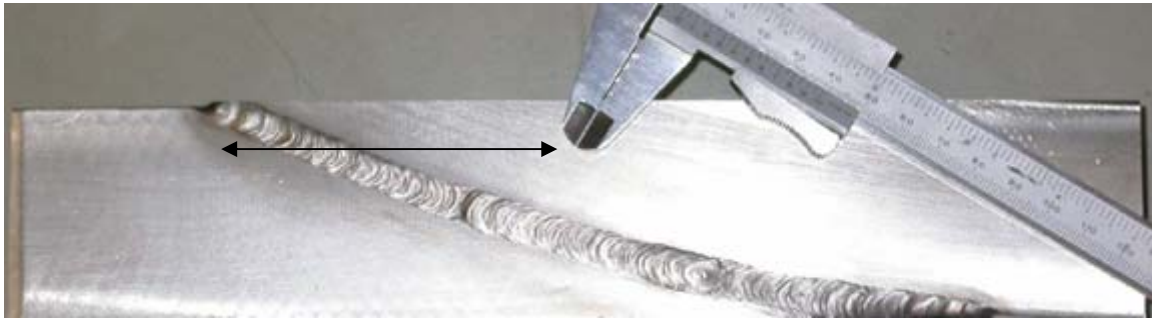


Fig. 2: Sample as provided by CEA. The arrow shows the orientation of the machined four specimens.

- **Specimen 3**
The specimen was loaded initially up to 608 MPa giving a Young's modulus of 168 GPa, significantly lower than the former two specimen with 210 GPa. This sample was cycled between 36 MPa and 500 MPa for 26,411 cycles. At cycle number 26,411 the specimen failed. In Figure 3 specimen 3 is shown after failure. Here one can observe the partly welded section, which is the reason of the early failure. The weld cross section can be estimated according to the present picture to be around 35%.

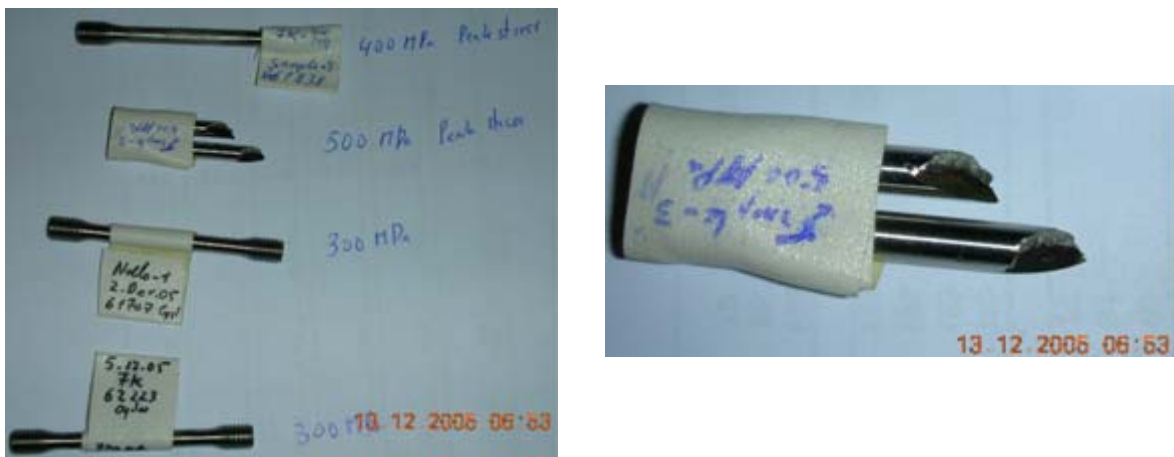


Fig. 3: On the left side the four specimens after cyclic loading tests carried out at 7K and the appearance after the test. On the right specimen 3 which failed after 26,411 cycles with a peak stress of 500 MPa.

- **Specimen 4**
Specimen 4 was cycled at a peak stress of 400 MPa. The specimen could survive the loading for 61,838 cycles.

Tensile and fracture results of aged stainless steel (~Type 316LN) at 7K and at 295K

From the provided tube material specimens were made by EDM (electron discharge method) for tensile and JETT tests. Figure 4 illustrates how the tensile and JETT specimen were taken from the tube.

The specimens were tested at 7K and 295K. However, due to a problem with the machine control sample 3 could not be tested until failure and had to be tested again. Therefore the total elongation is the sum up of the 1st and 2nd test which yields to 43% elongation at fracture.

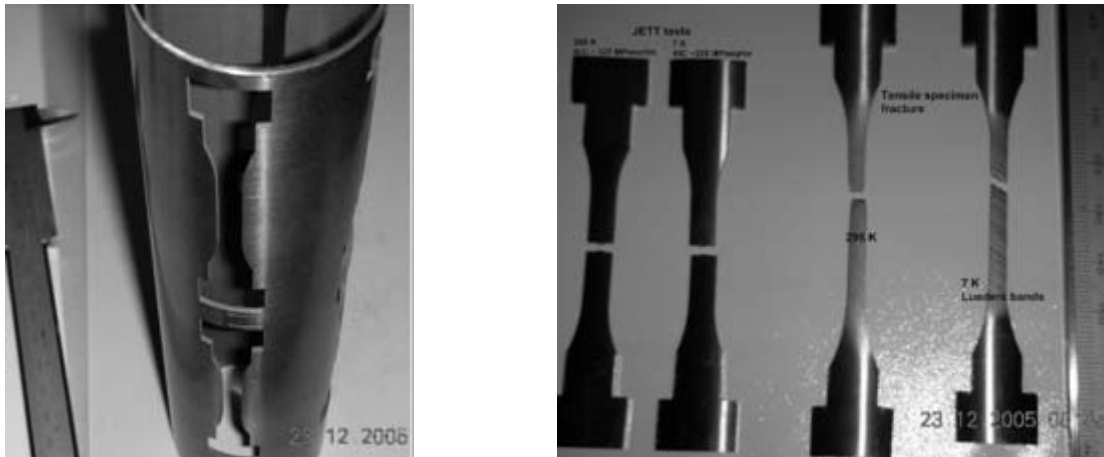


Fig. 4: On the left the provided tube for tensile and JETT specimen. On the right the investigated tensile and JETT specimens at 295K and at 7K showing their fracture status.

In Figure 5 a close up view of all tensile tests is given, the result are summarized in Table 2. The fracture toughness results are shown in Figure 6 and the results in Table 3. Here the JETT procedure was used giving typical results for this kind of material.

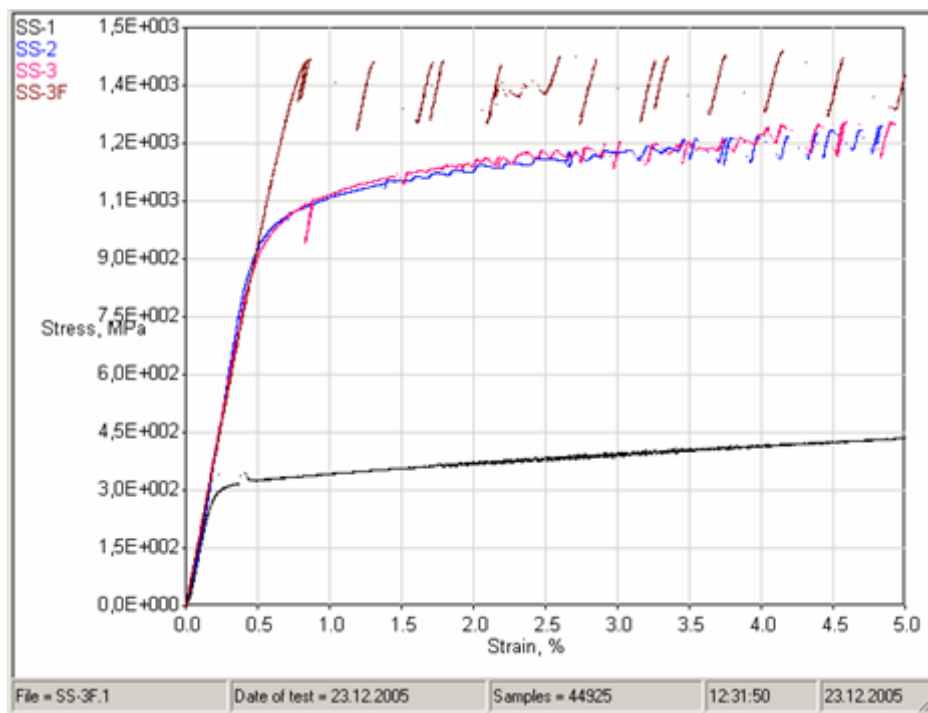


Fig. 5: A close up view of all tensile tests.

Staff:

K.-P. Weiss
A. Nyilas
H. Kiesel

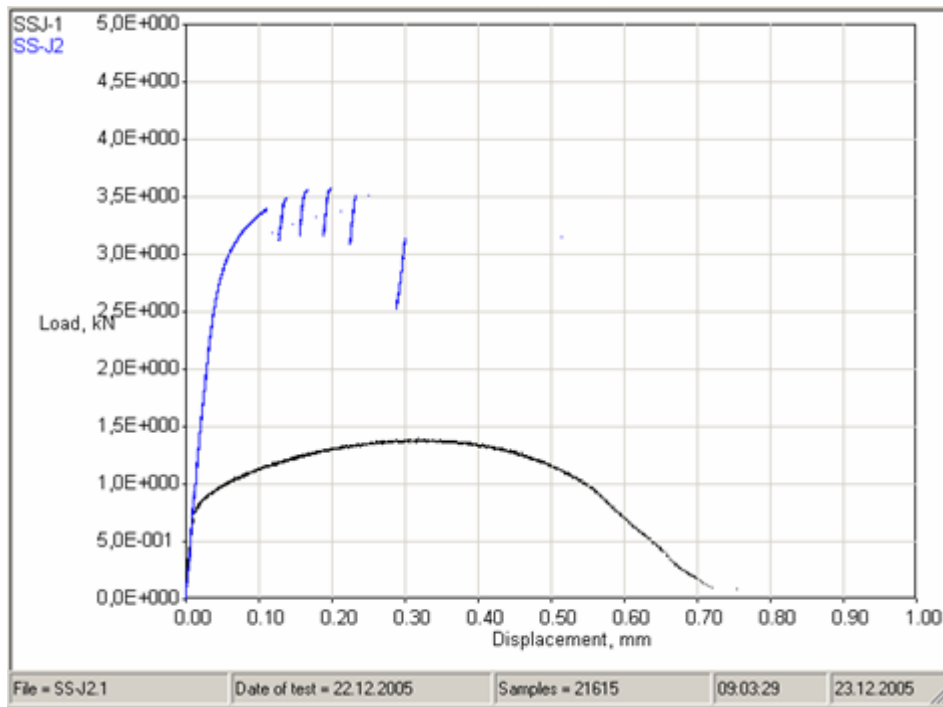


Fig. 6: JETT tests: Load versus displacement curves determined at 7 K and at 295 K (Black curve: 295 K and Blue curve: 7 K).

Table 2: Tensile results of specimens from tube 316 LN:

File & heat	Temperature K	Young's Modulus GPa	Yield Strength MPa	Ultimate Tensile strength MPa	Uniform elongation %	Total elongation %
SS-1	295	178	324	717	44	56
SS-2	7	210	1007	1562	37,5	38,5
SS-3	7	200	1010	1398	-	17,9
SS-3F*	7	195	1358	1575	15,3	24,8

*Second loading of the specimen SS-3

Table 3: Fracture toughness properties of the aged stainless steel material:

File & heat	Temperature K	Critical J N/mm	Fracture toughness converted $K_{IC}(JETT)$ MPa
SSJ-1	295	577	~ 327
SSJ-2	7	260	~ 228

Literature:

[1] Nuclear Fusion Programme, Annual Report of the Association Forschungszentrum Karlsruhe / EURATOM, FZKA 7210 / EUR 22253 ISSN 0947-8620, 65 (2006).

EFDA/05-1276 (TW5-TES-CRYO2) Design of the ITER Cryoplant and Cryodistribution System

Design of a Test Loop to Assess the Mitigation of Pulsed Heat Loads and Validate the Design of ACB for Magnet Structure

Background and Objectives

Several aspects of the design of the cryoplant and cryodistribution system lie on the critical path of the ITER project, due to their impact on layout of key “early installation” buildings and the fact that some components of the cryodistribution system must be delivered and installed during the construction of these buildings. Moreover, the cryoplant and cryodistribution systems are unprecedented in term of their size, a variety of operational modes and a wide range of heat load requirements with large pulsed heat loads.

FZK has to provide, in collaboration with CEA Grenoble, the design of a test loop for studies to mitigate pulsed heat loads, coming from the TF-coils, on the LHe system of the ITER cryoplant (deliverable 2 of the task).

Cooling loop design

According to the present task, a cooling loop to investigate the mitigation of pulsed heat loads from the TF-coil case was designed. The test loop in Fig. 1 consists mainly of a centrifugal pump, two heat exchangers, valves and a test module (short loop and a long loop), which simulates the case cooling channels of a TF-coil.

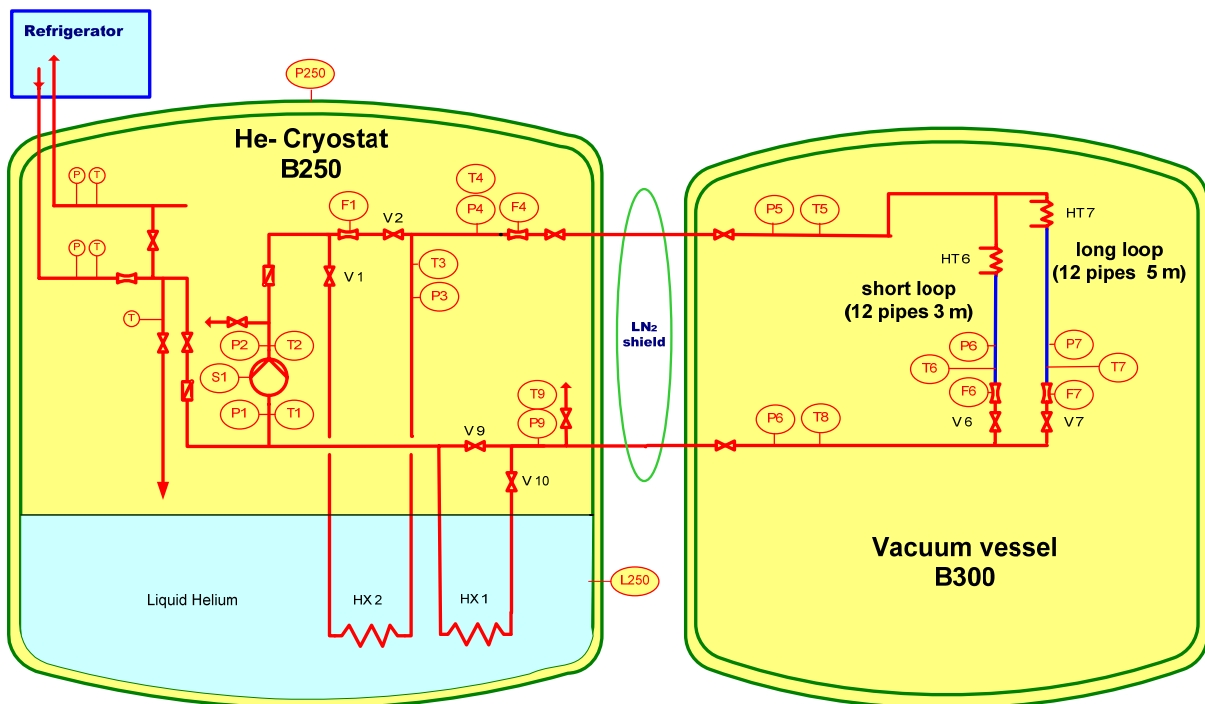


Fig. 1: Simplified cooling scheme of the test loop.

The variable heat load is realized by two heaters at the inlet of the test module. It is made up of 12 parallel pipes with a length of 3 m each to simulate a short loop and 12 pipes with a length of 5 m each to simulate a long loop of the case cooling. The different lengths of the cooling channels together with single heaters offer the possibility to simulate the individual heat load at the inner and outer leg of a coil. In addition, the unequal mass flow distribution after a heat pulse and the flow redistribution during recooling can be studied. In the proposed

test loop, two heat exchangers are integrated. Heat exchanger HX1 is located before and the second heat exchanger HX2 is placed after the pump. By bypassing HX1 it can be investigated, whether the efficiency of a centrifugal pump is influenced by the inlet temperature of the helium.

Two possible test procedures were elaborated, to be able to investigate the mitigation of pulsed heat loads. In a first test, the heat load will be mitigated by bypassing the HX2 in order to reduce the heat load to the refrigerator as foreseen in ITER DDD 34. The disadvantage of this method is that the full heat load of the pump is still transferred to the cooling loop after a heat pulse. In a second test, it is foreseen to mitigate pulsed heat loads by reducing the rotation speed of the centrifugal pump. The advantage of this method is the reduction of the pumping power, resulting in a decrease of the heat load to the cooling loop.

This cooling loop can be integrated in the existing TOSKA facility without major modifications. Most of the existing equipment can be used. As a consequence the investment costs would be low, but the integration in the existing coil test programme for W7-X is difficult. A cost estimate for the installation and assembly as well as for the operation of the test loop will be given in the final task report.

Staff:

R. Lietzow

TW5-TMSF-HTSMAG

Scoping Study of HTS Fusion Magnets

Objectives

After the Forschungszentrum Karlsruhe and CRPP have shown with the 70 kA HTS current lead that high temperature superconducting materials can be used for ITER, these materials should be introduced in other components, primarily in fusion magnets. First a scoping study of HTS fusion magnets shall be performed to check the benefits of using high temperature superconducting materials in fusion magnets including the identification of potential problems.

In collaboration with other associations the Forschungszentrum Karlsruhe assesses different operating scenarios which are:

1. "High field option": Operating temperature at 5K and high toroidal magnetic fields in the range of 15 to 20 T. In this case a comparison LTS vs. HTS shall be included.
2. "Intermediate temperature": Operating temperatures in the range of 20 to 30K and ITER-like magnetic fields, i.e., 10 to 15 T.
3. "High temperature": Operating temperatures in the range of 65K and ITER-like magnetic fields, i.e., 10 to 15 T.

In collaboration with the other associations the work is divided in manageable parts for each Association. The work performed at the Forschungszentrum Karlsruhe focuses on the third operating scenario, i.e., the high temperature option.

Main Results of the investigations for a HTS Fusion Conductor

Following the requirements taken from the reactor studies, the suitable HTS material and a suitable cable design has to be selected according to:

4. 1. High engineering current density in the conductor at the specific temperature and field.
5. 2. Sufficient mechanical strength (stress-strain characteristics) or option for reinforcement.
6. 3. Tolerable hotspot and quench behaviour of the HTS conductor (stabilisation).
7. 4. Optimized current distribution, i.e. feasibility of good joints and optimized inter strand resistance and inductance.
8. 5. Possibilities to limit the AC losses.
9. 6. Compatibility of coolant choice, e.g., nitrogen, helium, neon or hydrogen.
10. 7. Tolerable activation of materials due to neutron flux.

High engineering current density in the conductor at the specific temperature and field

The engineering current density has to be high enough to generate the desired field with a tolerable number of windings because otherwise the inductance of the magnet would be too high and as a consequence the high voltage in case of a fast discharge would be critical. The engineering current density is strongly influenced by the amount of electrical stabilizer and mechanical reinforcement material.

As an example: If using the TF coil dimensions of ITER, i.e., a coil current of $N \cdot I = 9.1 \text{ MA}$, a self inductance of $L = 0.349 \text{ H}$ and a discharge time constant of 12 s, different conductor cur-

rents lead to different discharge voltages resp. discharge time constants. Low currents result in either enormously high voltages of about 160 kV or in unrealistic large discharge time constants of about 190 s. As a result, 30 kA seems to be the minimum acceptable conductor current which is a compromise to limit both the discharge voltage and the discharge time constant.

Sufficient mechanical strength (stress-strain characteristics) or option for reinforcement

The superconductor performance decreases in case of high strain. This is especially critical in the case of a high field operation where the enormous Lorentz forces will cause massive problems that can be hardly handled with today available materials.

Tolerable hotspot and quench behaviour of the HTS conductor (stabilisation)

In case of a quench where superconductivity is lost locally the coil current will deposit a large amount of power due to ohmic heating in this area. Although a fast discharge of the coil is triggered in such a case, the conductor has to be stabilized to withstand the energy deposition until the coil is discharged.

As an example: If using a 4 mm wide YBCO-CC, a critical current density in the 1 μm thick YBCO layer of 2000 A/mm², and a thickness of the copper stabilizer of 50 μm , the resultant hot spot temperature during a discharge ($\tau = 21$ s) will be about 120K. For a critical current density of 10,000 A/mm², the copper thickness of 300 μm would be required to get a hot spot temperature of 130K. So the increase of the critical current density by a factor of five results in an increase of the engineering current density of only a factor of two.

Optimized current distribution, i.e. feasibility of good joints and optimized inter strand resistance and inductance

To load the superconducting cable uniformly with current and to minimize losses on superconductor-superconductor connections good joint have to be feasible with a resistance of only a few nOhms or less. An optimized interstrand resistance helps to allow a current redistribution in case of non conformity.

Possibilities to limit the AC losses

Induced currents caused by field changes will cause massive losses when the superconducting cable is not optimized to deal with AC losses. This is especially critical for the classical tokamak design that uses the field ramping of the central solenoid to drive the plasma current. Goal should be to limit the coupling and eddy current losses to the level of the hysteresis losses.

Compatibility of coolant choice, e.g., nitrogen, helium, neon or hydrogen

The choice of HTS material and the conductor layout depends of course on the choice of coolant.

Tolerable activation of materials due to neutron flux

Due to the high Neutron flux in future fusion machines, HTS and structure material should be chosen to minimize neutron activation as far as possible.

Example for a HTS Conductor Layout

For low T_c superconductors (LTS) the conductor requirements discussed above have lead to sophisticated designed Nb₃Sn or NbTi strands and numerous varieties of optimized cable

layouts depending on the application. The conductor layouts were optimized for tokamak or stellarator designs, e.g. by balancing current distribution, AC losses and cooling capability (transient as well as steady state).

In case of HTS a similar optimization strategy is desirable. The minimization of AC losses surely plays a challenging role because of the large inductive loops present in non twisted superconductors. The coated conductor tapes cannot be twisted easily and technologies like multi-staged multi-filamentary twists are obviously impossible. Other critical properties like current distribution and thermal stability are also an issue because of the structure of the conductor tape.

Staff:

W.H. Fietz

R. Heller

Literature:

G. Janeschitz, W.H. Fietz, W. Goldacker, R. Heller, G. Kotzyba, R. Lietzow, R. Nast, B. Obst, S.I. Schlachter, C. Schmidt, K.P. Weiss, "High Temperature Superconductors for Future Fusion Magnet Systems – Status, Prospects and Challenges", presented at 21st IAEA Fusion Eng. Conf., Chengdu, China, 2006

TW5-TMSC-HTSPER HTS Materials for Fusion Magnets

The global R&D activities on HTS materials have nearly completely changed from the first generation (1G), the BSCCO(2223) conductors with Ag-sheath, to the second generation (2G), the so called coated conductors (ReBCO) which consist of a multilayered thin film composite on metallic substrate tape. This has strong consequences for the application with respect to further material improvement, reliability, performance and the commercial availability in future. Coated conductors, in addition, undergo actually a very rapid improvement and are on a good way to an economic conductor too. Homogeneous conductors up to 427 m with high current of 191 A/cm-width (77K in self field) produced in a single deposition pass at a production speed of 45 m/h (SuperPower) are shown as the best results actually. To decide on the HTS materials, to be the best candidates for HTS fusion coils, it is important to have a measured data set of all commercial available materials. For generating fields of 15 T, 1G HTS tapes need an operation temperature < 30K, whereas 2G coated conductors may be cooled only to around 50K. This gives an enormous potential to save cooling energy using HTS coils.

In this task different BSCCO(2223) tapes from American Superconductor (AMSC), European Advanced Superconductors (EAS), Sumitomo (Japan) and Innost (China) and 3 YBCO coated conductors from commercial sources as SuperPower (USA), American Superconductor (AMSC/USA) and THEVA (Germany) were investigated. The challenge of this task was to assess the data base of physical, electrical and mechanical sample properties. Measurements of the critical currents between 4.2K and 77K with different background fields up to 13 T, investigations of the electromechanical performance under axially applied tensile strains and bending strains and the thermal properties, thermal conductivity and thermal expansion were performed. Of special interest were BSCCO tapes with low thermal conductivity sheath from AgAu alloys for the application in current leads. Such samples were obtained from AMSC and EAS. Improved tapes with better strength or current (high strength or high current version) came from Sumitomo. Sumitomo is the only company with R&D on further improved BSCCO tapes. Investigations on BSCCO tapes which are not available anymore in future (as AMSC tapes) were stopped during the task. Innost from China delivered standard, tin clad and insulated tape pieces.

Table 1: List of samples investigated with measured self field currents

Company	Sample	Measurements	I_c (77K, self field)	J_c (77K, self field)
EAS V3	BSCCO 2223 / AgMg state-of-the-art (V375B4)		99 A	11.06 kA/cm ²
EAS CL Au-1	BSCCO 2223 / AgMg/AgAu-1 current lead tape (old)		64 A	7.3 kA/cm ²
EAS CL V388D	BSCCO 2223 / AgMg/AgAu current lead tape		83.1 A	9.44 kA/cm ²
AMSC	BSCCO 2223 / Ag/SS 4.8 x 0.3 mm cross sect.		121 A	8.17 kA/cm ²
AMSC CL	BSCCO 2223 / AgAu Current lead tape		128 A	14.6 kA/cm ²
Sumitomo HS	BSCCO 2223 / AgMg high strength version (HIP)		110 A	11.39 kA/cm ²
Sumitomo HI _c	BSCCO 2223 / AgMg High current version !		130 A	11.66 kA/cm ²
Innost standa.	BSCCO 2223 / AgMg Standard		106.2 A	11.4 kA/cm ²
Innost Sn clad	BSCCO 2223 / AgMg Standard + Sn coating		88 A	8.32 kA/cm ²
Innost Insul.	BSCCO 2223 / AgMg Standard + Insulation			
AMSC	YBCO-CC MOD 344 on Rabits NiW		65 A	8.1 kA/cm ²
Superpower	MOCVD – CC on Hastelloy		94 A	26 kA/cm ²
THEVA	DyBCO-CC ISD/TCE on Hastelloy		255 A	28.3 kA/cm ²

The properties found, were strongly depending on the specific features of the tapes, which depend on the conductor design as reinforced or alloyed sheaths or the production scheme, in particular for the coated conductors. Extended investigations were done on two suitable coated conductors which actually became real commercial products and will soon surpass lengths of > 100 m for sale. In comparison with the BSCCO tapes, the coated conductors showed several superior properties, high engineering current densities and high mechanical strength. In figure 1 the $I_c(T,B)$ dependence of the SuperPower CC is shown. It is remarkable that the anisotropy is nearly disappearing at 55K which is an indication of a very favourable flux pinning in this material. High absolute currents of 235 A/cm-width and excellent homogeneity over long length > 10 m are outstanding features of this material. Excellent bending properties of this material favour application in high current cables.

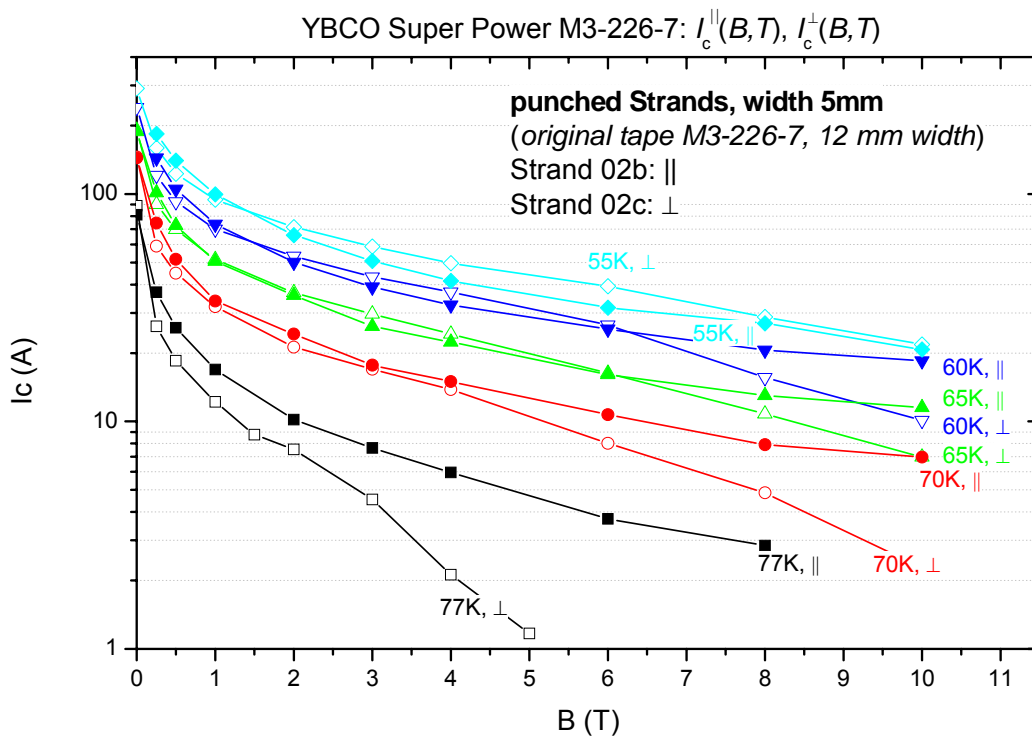


Fig. 1: Critical currents of MOCVD-Superpower Coated Conductor at varied temperatures of $T = 55-77K$ in background fields $B = 0-10 T$ for the two tape orientations B parallel and B perp. to the field.

Figure 2 shows the summary of electro-mechanical investigations measured in the FBI test facility. The critical currents for the mechanical stress and strain limit were defined as 95% of the maximum level. Only the steel laminated AMSC BSCCO conductor shows excellent mechanical performance with > 300 MPa stress value. Current lead materials as EAS-V388D withstands up to 160 MPa due to the inherent AgMg reinforcement, while the high current AMSC AgAu-sheathed material shows very poor mechanical properties. This has big influence on the design strategy of current leads.

Figure 3 shows the equivalent diagram for the coated conductors. Due to the specific boundary conditions of the MOCVD production route, the SuperPower CC has an excellent current and current density and an outstanding mechanical performance which satisfies all occurring stress and strain load in practice of coils and devices and cabling efforts. The relative low processing temperatures of the MOCVD process keep the substrate strong and are the reason for the good mechanical performance. A big advantage is the engineering critical current density of the coated conductors compared to the BSCCO tapes. The stabilising cap layer however, with a thickness of 20 microns (Superpower) is only sufficient for the upper temperature range close to 77K.

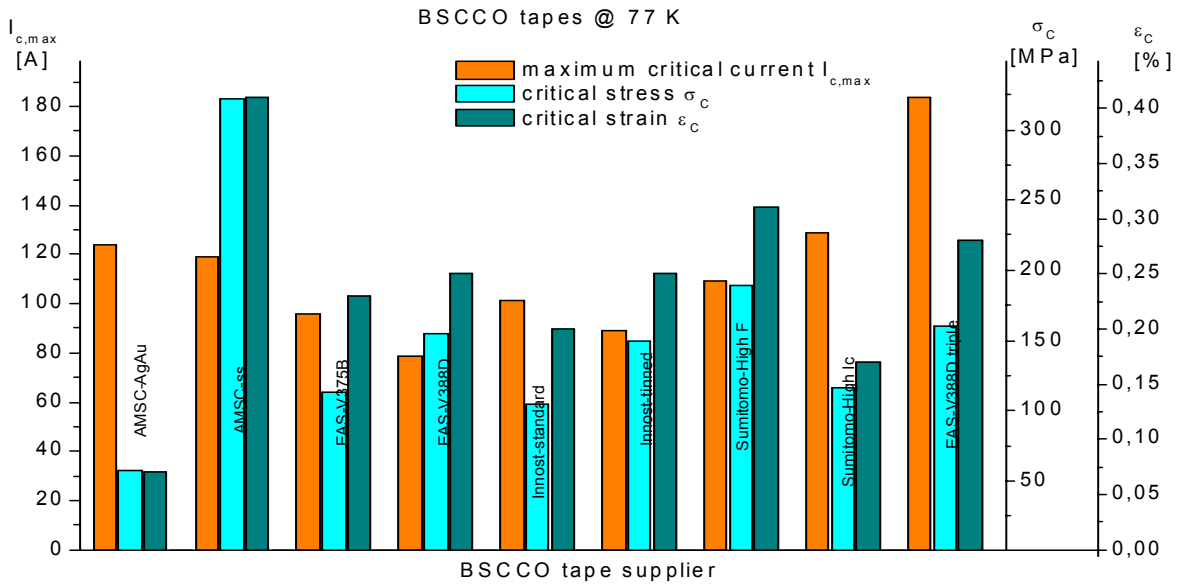


Fig. 2: Electro-mechanical data of BSCCO tapes: Critical Current (95% of maximum), correlated critical stress and strain value.

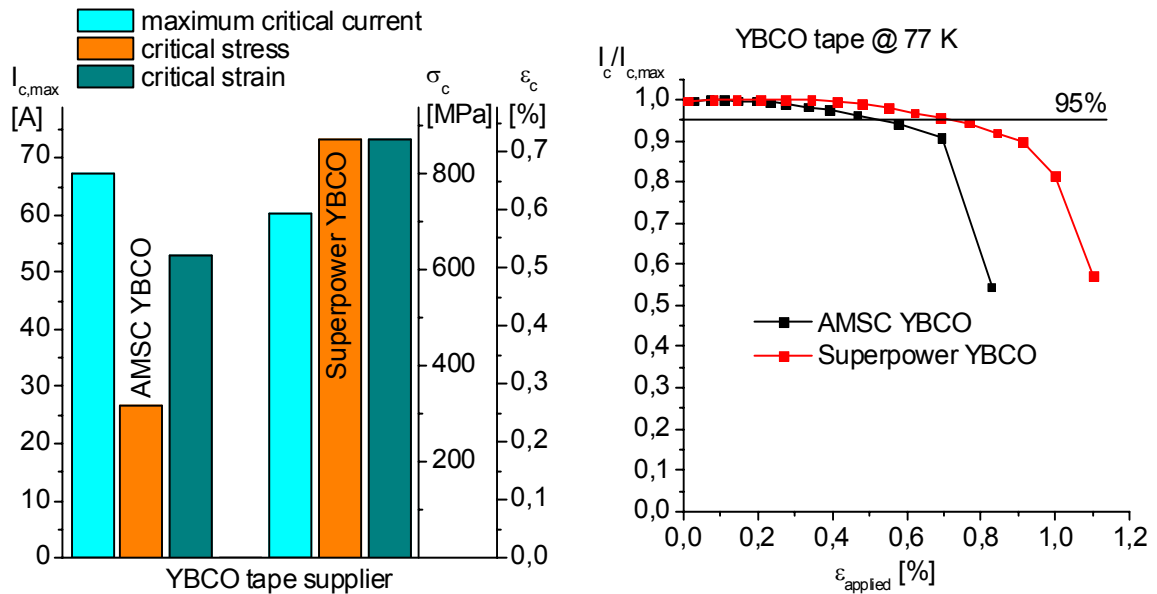


Fig. 3: Electromechanical data of coated conductors from AMSC and Superpower, critical values on the left side, I_c vs strain measurements on the right side.

Operating coils of 15 T at 50K seems a realistic scenario for the future when improved coated conductors become a commercial long length product. The final summary from the data of this task is the selection of coated conductors as the only HTS solution for future DEMO coils, in particular regarding the prospects for the future with the actually demonstrated short sample current carrying values of 700-800 A being 3-4 times higher than the evaluated performance of this task. It is expected that these values can be realized in long lengths. For high current low AC loss conductors, the development of cable systems as a ROEBEL assembled coated conductor cable is absolutely necessary as a logic continuation of this work.

Staff:

W. Goldacker
S. Schlachter
C. Schmidt
A. Frank
B. Ringsdorf
K. Weiss
A. Lampe
M. Schwarz
A. Kling

Literature:

K.P. Weiss, M. Schwarz, A. Lampe, R. Heller, W.H. Fietz, A.Nyilas, S.I. Schlachter, W. Goldacker: "Elektromechanical properties of Bi2223 tapes", presented at the Applied Superconductivity Conference 2006 in Seattle, USA, to be published in IEEE Transactions on Applied Superconductivity 2007

Breeding Blanket

TW5-TTB-001

Construction of the High Pressure Helium Loop (HELOKA-HP/TBM) for Testing of TBMs

Establishment of infrastructures

In June 2005 the Building No. 660 was newly chosen to house the HELOKA high pressure test sections. The existing auxiliary systems (water cooling systems and transformer stations) were analysed and tested in the meanwhile.

The water cooling system available is capable to deliver 430 m³/h of water at 10 bar and about 30°C. The cooling system consists of two loops: a primary circuit which will deliver the needed cooling water for the Helium loop and an open secondary loop with a cooling tower that has a cooling capability of about 7 MW. The mechanical components of the water cooling loop can be used without major refurbishments, while minor modifications are needed to accommodate the necessary manifolds and routing of the pipes in the experimental hall following the HELOKA layout. However, the control system of the water cooling loop and the power supply were outdated and need to be upgraded in order to meet the HELOKA requirements.

Since the TBM experiment planning needs some flexibility a multistage approach was selected for the HELOKA Data Acquisition and Control System (DACCS). The 1st Stage, whose tender was launched at the end of September, includes:

- Modernisation of the control and monitoring of the existing water cooling system including installation and tests of new frequency converters for the existing pumps in the primary and secondary loop, local controls and additional instrumentation.
- Control and monitoring of the existing power supply system with installation and test of local controls and instrumentation.
- Design, installation and commissioning of hardware and software for the Supervisory control, operation, interlock and monitoring of WCS and power supply system.

The tender is now closed and a Supplier has been selected by the end of 2006, while a completion of the execution of the contract before the summer 2007 is foreseen.

The delay of this task is about 6 months, mainly due to the work caused by the newly chosen building.

In addition the HELOKA infrastructure, mainly the construction of the supporting structure of the facility was prepared. For this structure, the official construction authorisation was obtained in May 2006. In the design developed, the areas containing high pressure, high temperature equipment/parts are separated from the working areas. Therefore, the operation of HELOKA facility can be done without restricting the access in the rest of the experimental hall. Furthermore, the possibility to separate the test section hydraulically from the main part of the loop was foreseen to allow working on the installation of the test section in a vacuum tank on the upper platform of the support structure while the loop is pressurised. In view of further developments of the loop (building a secondary test section for Test Divertor Module (TDM) this allows for preparation of one experiment while the other experiment is running. For this purpose tight valves or temporary end caps have to be installed.

In addition, the need for easy access to all main/large equipments was considered, mainly the cooler and the heater, for maintenance or replacement.

In 09/2006 the manufacturing drawings have been finalized and the manufacturing of the parts of the structure was launched. The structure will be build step-by-step once the main components from HELOKA will arrive on site and will be installed.

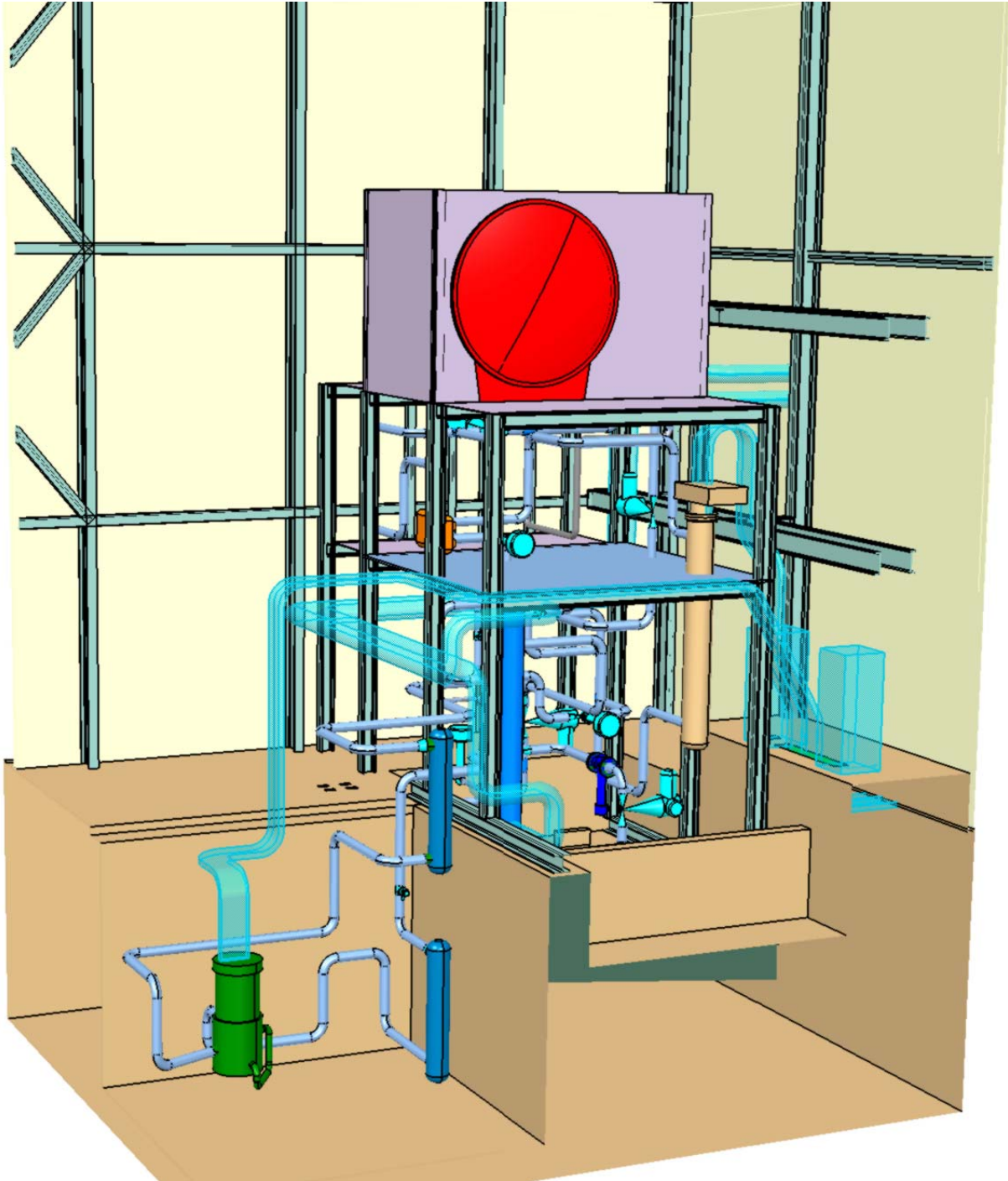


Fig. 1 HELOKA layout: current equipment arrangement and helium piping; water pipe and electrical cables space reservation is shown.

Fabrication of main components

The main components of the loop are circulator (to be delivered by EFDA), heat exchanger, heater, cooler, vacuum tank with heating system, data acquisition and control system, Helium purification system, Helium pressure control system, control valves.

The procurement procedures of the following main components was launched within 2006:

- Helium-Helium heat exchanger (economizer): the call for tender for has been closed (April 2006) and the component has been ordered in May 2006. The technical solution adopted is a compact heat exchanger manufactured by HEATRIC company in Great Britain. This economizer has a high efficiency of over 90% while the space required for its installation is relatively small: 1.2 m × 0.9 m × 0.4 m (see Fig. 2). The manufacturing of the unit was completed and on-shop tests were performed.
- The tender for helium-water heat exchanger (cooler) has been closed and contract negotiation starts by 2007.
- The DACS stage 1 tender was closed, contract negotiation starts by 2007,
- The technical specifications for the heater have been finalized.



Fig. 2: HEATRIC heat exchanger for HELOKA.

Staff:

T. Ihli
M. Ionescu-Bujor
B. Ghidersa
W. Cherdron
V. Marchese
A. Jianu
E. Magnani

EFDA/06-1393 (TW6-TTB-RFMON1)

Technical Monitoring Assessment of the EU/RF Collaborative Task on the Development of Diagnostic Systems for Electromagnetic TBMs

Scope of this task is to support the EU/RF collaborative task on "Development of diagnostic systems for HCPB and HCLL EM-TBMs" (TASK 1 - EFDA/05-994 contract with EFREMOV). In particular, to prepare and check all input technical data necessary for the performing of the task, to perform the technical monitoring and to assess the technical reports.

In September 2006 the task has been started in the frame of the kick off meeting (at FZK) where the technical specifications of the EM- diagnostic systems have been discussed. As concluded in the minutes of the kick off meeting the following technical specifications were presented in the frame of the first deliverable of this task (TW-TTB-RFMON-D1 a, technical specifications, kick off):

- Properties of all relevant materials
- Operational scenarios
- Geometry data of TBM, port plug and vacuum vessel
- Temperature distributions
- Environmental conditions for sensors
- Appendix including minutes of the meeting

In December 2006 the so called "2nd kick off meeting" took place at the FZK. In the frame of this meeting the specifications on mechanical diagnostic have been discussed in detail. The technical specifications for mechanical diagnostics are currently under preparation and will be provided to Efremov as soon as they are finished.

The kick off phase of the project will be completed in the near future and the first intermediate meeting at Efremov institute is scheduled in 03/2007

Staff:

L. Boccaccini
H. Neuberger
R. Roccella

Efremov: A. Alexeev
A. Belov
A. Firsov
M. Sukhanova
E. Privalova

Breeding Blanket HCPB Blanket Concept

TTBB-001 Helium Cooled: TBM Design, Integration and Analysis

TW5-TTBB-001 D 2 Detailed Design of Sub-components and Prototypical Mock-ups for the HCPB TBM Qualification

a) Design Report for the GRICAMAN Mock-ups

Introduction

The coolant routing in Test Blanket Module (TBM) is relatively complex, but each stiffening plate, cap plate and cooling plate in the breeder units have to be cooled sufficiently. The GRICAMAN (GRIdCApsMANifolds) experiments is dedicated to test the mass flow distribution in the TBM. The coolant enters the manifold 1 through the Helium cooling system supply line, from where it is distributed into coolant channels in the first wall (FW channels). The outflow of FW coolant channels is then collected in the manifold 2. In the manifold 2 the coolant is distributed among the stiffening grid channels, the cap channels and the bypass pipes. The mass flow rate of coolant leaving the TBM via the bypass is controlled such that the coolant temperature at the outlet of TBM reaches 500°C. The outflow from the stiffening grid and the cap channels is collected in the manifold 3. The manifold 3 supplies 18 parallel breeding units (BU) with additional cooling plates. From the BU's the coolant is led into the manifold 4 realized in the form of 'ships' from where it, finally, leaves TBM.

Begin of review period

A brief layout of the experiment was done in regard on the design of the plates and adapters necessary to connect the different parts. Preliminary CFD calculations were made to determine the pressure drops in different parts of the manifold, cooling plates and stiffening grid plates. An experiment was designed in detail to determine the flow distribution and the pressure drop in a stiffening plate.

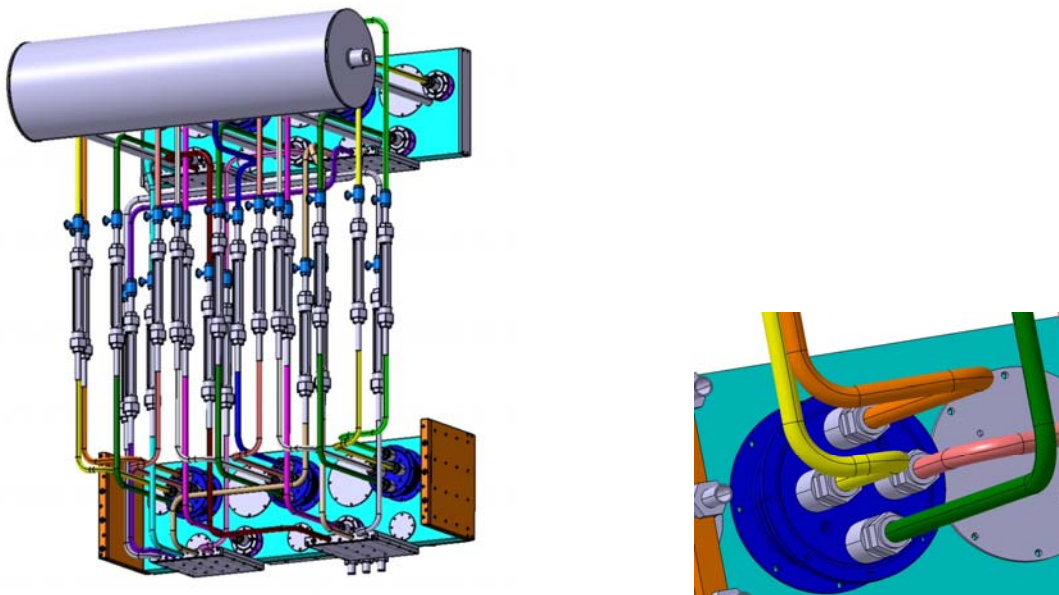


Fig. 1: 3D CAD design of the GRICAMAN C experiment, right side: connection of tube elements.

Results during review period

The design of the experiment was developed in detail. It was adapted to the new smaller size of the horizontal version of a module to be tested in ITER. The measuring technique was chosen and the design of the experiment was adapted to cope with the requirements imposed by the mass flow detectors. The general layout of the measuring system including the data acquisition system was done, while the procurement and programming will have to be performed in the next period.

In Fig. 1 and 2 the detailed CAD design of the test section is shown. The air coming from the permanent distribution of the laboratory is filtered and the pressure is controlled by a regulation valve. The characteristics in each tube connection the different manifold sections can be adjusted by use of a needle valve in combination with mass flow sensors. The pressure distribution in the manifold and the mass flow in all tubes representing stiffening and cooling plates will be detected. As the inlet flow behaviour from the manifold levels into the cooling and stiffening plates could be significantly influenced by the crossflow conditions, the mock-up design for this area was chosen in accordance with the TBM design. In figure 1 the pipe connections at this area is shown while in figure 2 the outlet manifold along with pipe connections is shown. In addition to the valves indicated in the CAD drawing valves and thermal mass flow measuring equipment is arranged between the TBM manifold plates and the manifold vessel of the test section to adapt to the characteristics of the cooling plates and detect the resulting mass flow in each pipe representing a cooling plate.

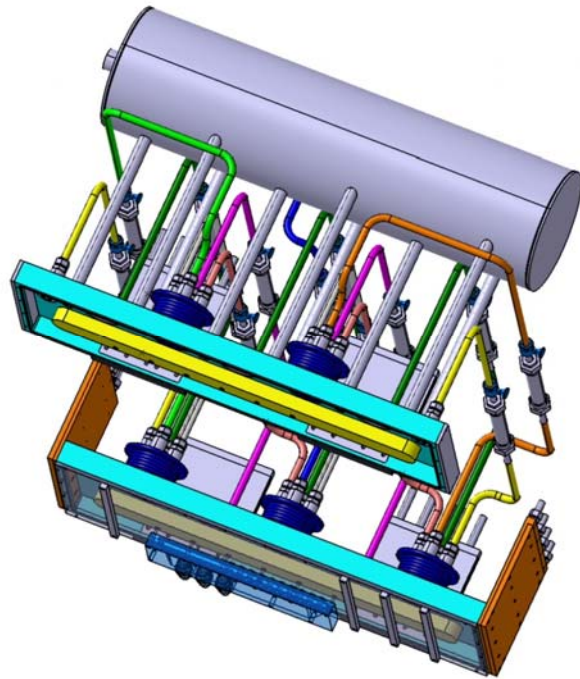


Fig. 2: GRICAMAN experiment top view.

Conclusions

Detailed design development of the GRICAMAN experiment was nearly completed including adaptation to the chosen measuring techniques. The arrangement of pressure measurement points was done, while the according pressure sensors, data acquisition and LabVIEW program will be defined and developed in the next step.

Staff:

T. Ihli
M. Ilic
R. Meyder
H. Neuberger

b) Design Report for the HETRA Mock-up

Introduction

In the frame of the development of the HCPB TBM the validation of numerical simulations especially in the environment of the first wall is required. The HETRA mock up will be used for measurement of pressure drops and heat transfer coefficients in TBM first wall channels to validate numerical (star CD) simulations. From the material point of view there is no requirement on using EUROFER for the HETRA mock up because standard steel will lead to adequate results.

Begin of review period

The numerical simulation of the TBM first wall has already been on an advanced level as described in the respective report (status October 2005). Friction losses as well as heat transfer coefficients already have been calculated for a typical 3 sweep channel of the first wall like shown in figure 3. According to detailed analysis some minor adaptations of the Helium inlet conditions are required for the validation of the CFX computations by using only one sweep of the channel for the HETRA mock up, see figure 4.



Fig. 3: Typical arrangement of one TBM first wall cooling channel.

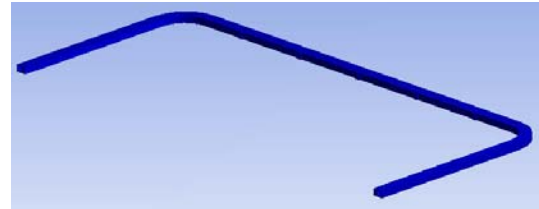


Fig. 4: Only one channel sweep will be used for HETRA.

Results during review period

During this period of review the work on the design of the HETRA mock up has been continued. The facility for the HETRA mock up tests will be the HEBLO Helium circuit of the FZK. HEBLO provides a mass flow of ~ 0.12 kg/s at TBM typical conditions (300°C at TBM inlet

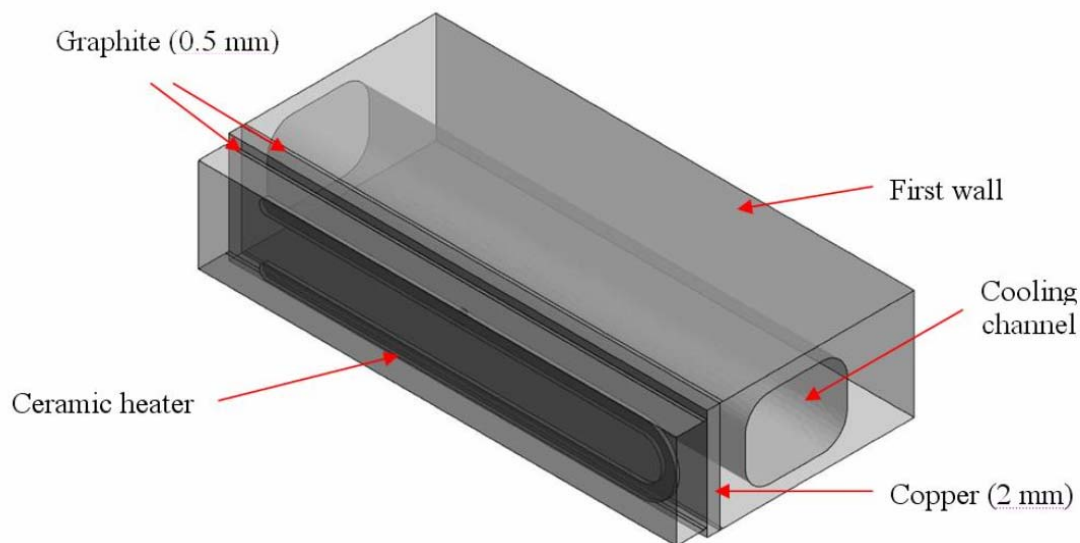


Fig. 5: Section of the HETRA mock up indicating structure of TBM first wall channel.

and 8 MPa coolant pressure). The mass flow provided by the HEBLO facility is adequate for testing of one typically arranged first wall cooling channel including three sweeps. The HETRA mock up will simulate one sweep of a TBM first wall cooling channel in 1:1 scale. Figure 5 shows a section of the HETRA mock up indicating the structure of the simulated TBM first wall channel. The ceramic heater at the opposite side of the first wall will be required to simulate the heat load on the first wall from the rear part of the TBM including the breeding units. The thermal contact between the mock up and the heater will be provided by 2 layers of graphite including a 2 mm copper layer. The surface heating (500 kW/m^2) will be simulated by a total number of 17 ceramic heaters installed in toroidal direction along the cooling channel like shown in figure 6.

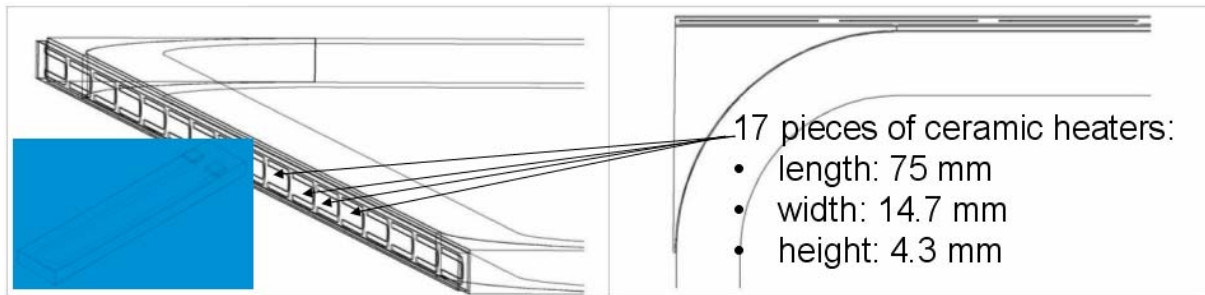


Fig. 6: Ceramic heaters for TBM surface heat flux simulation.

The thermal contact between the first wall heaters and the mock up will be designed in a similar way like at the rear part of the TBM. The ceramic heaters are attached to the HETRA mock up of the first wall channel by several clamps like shown in figure 6 (left). Additionally the whole mock up will require adequate thermal insulation like drafted in figure 6 (right).

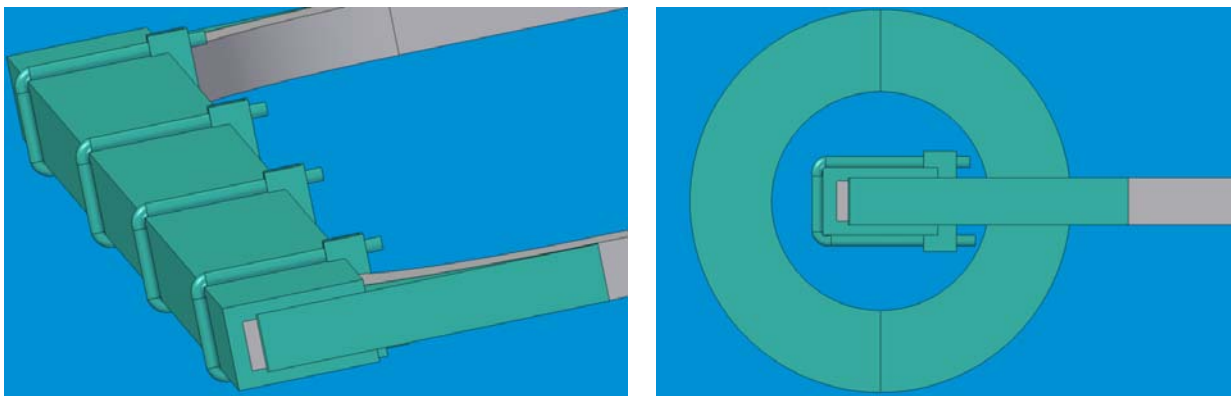


Fig. 7: Assembly drawing of the HETRA mock up including heaters and insulation.

Conclusions

Detailed investigation will be required for the realisation of the arrangement of measurement points of HETRA as they were already proposed. Additionally a concept for installation of the thermocouples into the facility has to be designed.

Staff:

T. Ihli
M. Ilic
R. Meyder
H. Neuberger
B. Kiss (KFKI, Hungary)

TW5-TTBB-001 D 9

Study with Experimental Verification of the Pebbles Filling in the HCPB TBM

Introduction

The assembly of the sub components of the HCPB solid breeder blanket is mainly based on welding. After several welding procedures heat treatments are required. These heat treatment procedures may not be compatible to the presence of the pebble beds inside of the TBM box. Therefore concepts have to be investigated which allow the filling of the pebble beds after the TBM manufacturing process including heat treatment. In the frame of this task the strategies for filling of the ceramic pebble beds as well as for filling of the Beryllium pebble are validated. Therefore two 1:1 mock ups of typical breeding unit designs have been developed to test the filling strategy for Beryllium and ceramic pebble beds with glass pebbles at relevant grain sizes.

Begin of review period

At the beginning of the review period two concepts were presented for the filling of the different pebble beds (see respective report).

Beryllium pebble bed:

- Filling of beds through holes penetrating the caps and one horizontal grid plate to access the beds for filling by a pipe

Ceramic pebble beds:

- For filling of the ceramic pebble beds the outlet collector of the purge gas system was supposed to be used

First CAD designs of two mock ups have been worked out according to the concepts for filling of the Beryllium and the ceramic pebble beds.

Results during review period

During the review period the CAD designs for both mock ups were detailed and 2D drawings have been produced. Subsequently the two different mock ups have been manufactured by Plexiglas in the workshop of the IRS. Figure 1 shows the mock up for Beryllium pebble bed filling.

In the frame of the design progress of the TBM the design of the purge gas system has been changed and therefore the system of filling the ceramic pebble beds which was proposed previously can not be used anymore. Now the filling of the ceramic pebble beds is proposed to be done by pipes penetrating the whole manifold system and accessing the pebble beds directly. Therefore the mock up for the ceramic pebble beds requires adaptation according to the new requirements. The concept for filling the Beryllium pebble beds remained unchanged.

To simulate the filling material glass pebbles have been prepared and sieved to separate them according to their grain sizes to reach typical pebble sizes. Figure 2 shows the glass pebbles used to substitute the Beryllium pebble bed (typical grain size of ~1mm).

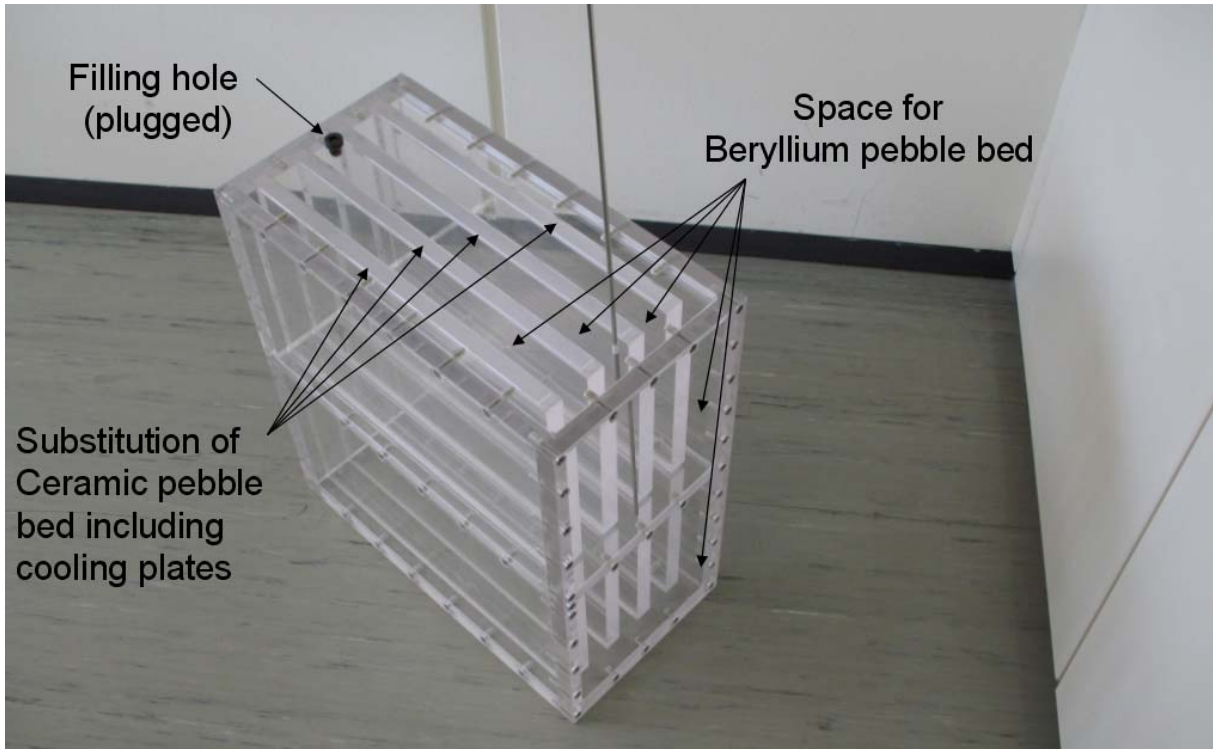


Fig. 1: Mock ups for Beryllium and Ceramic pebble bed filling.

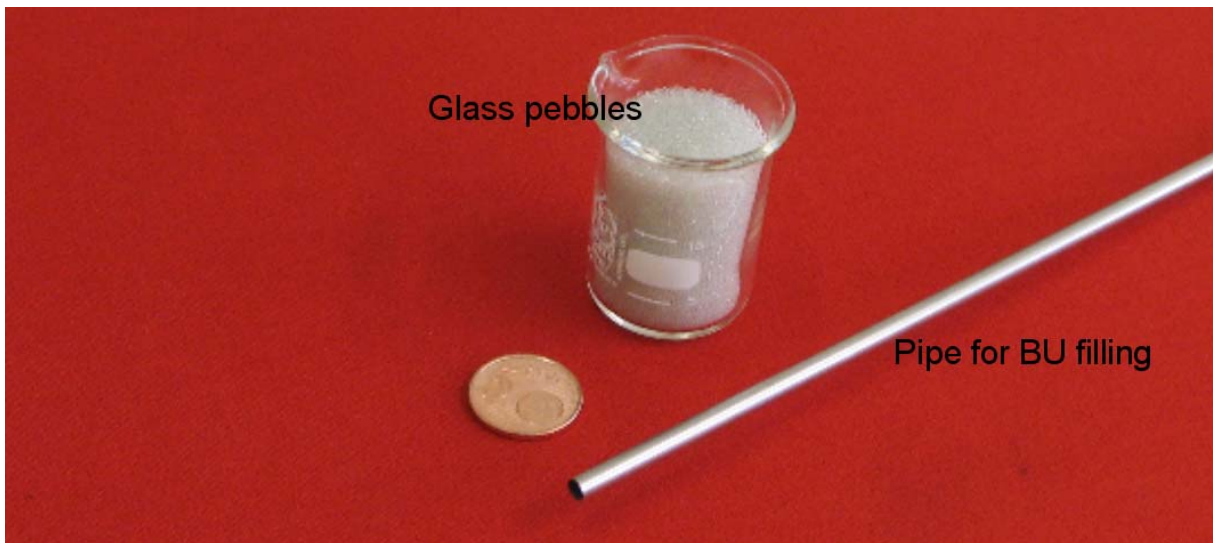


Fig. 2: Glass pebbles used to substitute the Beryllium pebble bed.

Conclusions

The filling experiments are expected to be completed by the end of 2006 and the results of this task will be presented soon in the respective report. Currently no basic problems are expected and the concepts which are proposed for filling of the breeding unit pebble beds are promising.

Staff:

O. Albrecht
K. Lang
R. Meyder
H. Neuberger
S. Stickel

TW5-TTBB-001 D 11

Analyses for the HELICA and HEXCALIBER Experiments using the ABAQUS Drucker-Prager Model

HELICA and HEXCALIBER are mock-ups for performing electrical heating in ENEA Brasimone to study the thermo-mechanical behaviour of ceramic breeder and beryllium pebble beds, in the framework of TBM design. These experiments are also used to perform a benchmark exercise between different material models proposed by different parties [1]. The thermo-mechanical model of pebble beds, developed in task TW2-TTBB-006b D2 [2, 3], has been adopted in this investigation. First, the material model has been calibrated with experimental data from FZK [4], and the results are shown in Fig. 1. For oedometric compression (left plot), the temperature varies from 50 to 850 °C; and only four typical creep testing curves are given in the right plot.

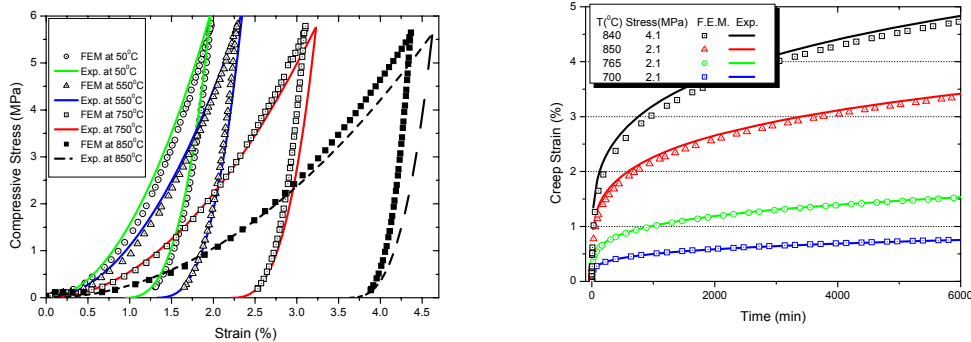


Fig. 1: The comparison between the prediction of the material model and the empirical curves: left, oedometric compression; right, creep tests under different temperature and stress levels.

The HELICA mock-up has been modelled by 2D generalized plain strain elements in this analysis, shown in Fig. 2, taking into account symmetry boundary conditions. The materials used in HELICA are indicated in Fig. 2, and the materials' database is provided by Ref. [5]. Concerning the pebble-wall interaction, a thermal contact conductance (TCC) model has been used to analyse the pressure-dependent heat transfer between contacting surfaces, in order to correctly predict the temperature field during the thermal loading. The effect of beryllium pebble-wall interaction is expected to be more pronounced, although in the analysis of the HELICA mock-up, the analysis shows that it is of importance that the ceramic pebble-wall interaction is taken into account, too.

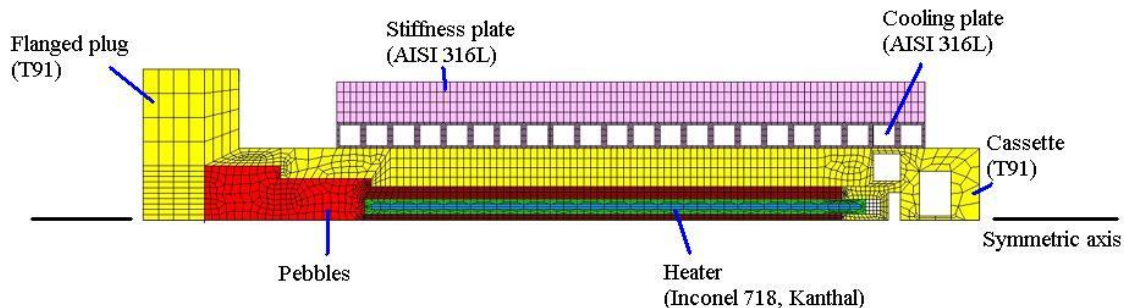


Fig. 2: Finite element mesh of HELICA mock-up.

The obtained results from the finite element analysis are compared with experimental data from ENEA Brasimone during one heating cycle, in Fig. 3. The comparison shows that the current material model, together with the TCC model, gives reasonable results in both tem-

perature and displacement fields. The analysis of two heating cycles has also been carried out to study the irreversible strains inside the pebble layer.

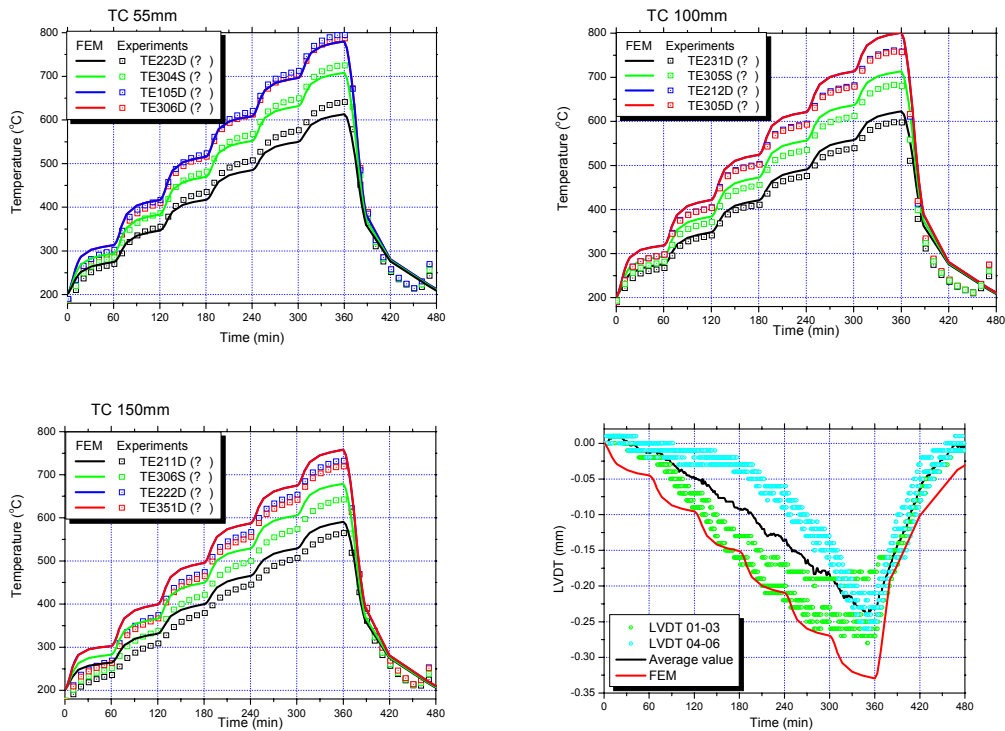


Fig. 3: Comparisons between FE analysis and experimental data: top-left, top-right and bottom-left are at the locations of thermal couples along the symmetric axis, 55, 100 and 150 mm to the first wall respectively; bottom-right, the displacement of cooling plate, measured by LVDTs.

Staff:

Y. Gan
M. Kamlah

Literature:

- [1] G. Dell'orco, A. Malavasi, L. Sansone, P. A. Di Maio, R. Giannusso, G. Vella and A. Tincani, Progress in the benchmark exercise for analyzing the lithium breeder pebble bed thermo-mechanical behaviour, Fusion Engineering and Design 81 A (2006) 169-174.
- [2] Y. Gan and M. Kamlah, Identification of material parameters of a thermo-mechanical model for pebble beds in fusion blankets, Fusion Engineering and Design In press (2006).
- [3] Y. Gan and M. Kamlah, Thermo-mechanical modelling of ceramic breeder and beryllium pebble beds, Internal report on TW2-TTBB-006b-D02, 2006.
- [4] J. Reimann, R. Knitter, A. Moeslang, B. Alm, P. Kurinskiy, R. Rolli, C. Adelhelm, H. Harsch and G. Raeke, Production and characterisation of breeder and multiplier materials in support of the HELICA and HEX-CALIBER experiments, TW5-TTBB-006 D1+D2, 2006.
- [5] J. H. Fokkens, Thermo-mechanical finite element analysis of the HCPB in-pile test element, TW0-TTBB-004-D1, NRG Report 21477/02.50560/P, 2003.

TW6-TTBB-001 D 2 Activation and Decay Heat Analyses of the HCPB TBM

The objective of Task TW6-TTBB-001, Deliverable 2, was to provide detailed activation and afterheat data required for quality assured safety analyses of the Helium Cooled Pebble Bed (HCPB) Test Blanket Module (TBM) in ITER taking into account two different irradiation scenarios.

The afterheat and activity inventories were assessed for the HCPB TBM in ITER making use of a code system that allows performing 3D activation calculations by linking the Monte Carlo transport code MCNP and the fusion inventory code FISPACT through an appropriate interface. To this end, a suitable MCNP model of a 20 degree ITER torus sector with an integrated TBM of the HCPB PI (Plant Integration) type in the horizontal test blanket port was developed and adapted to the requirements for coupled 3D neutron transport and activation calculations (Fig. 1).

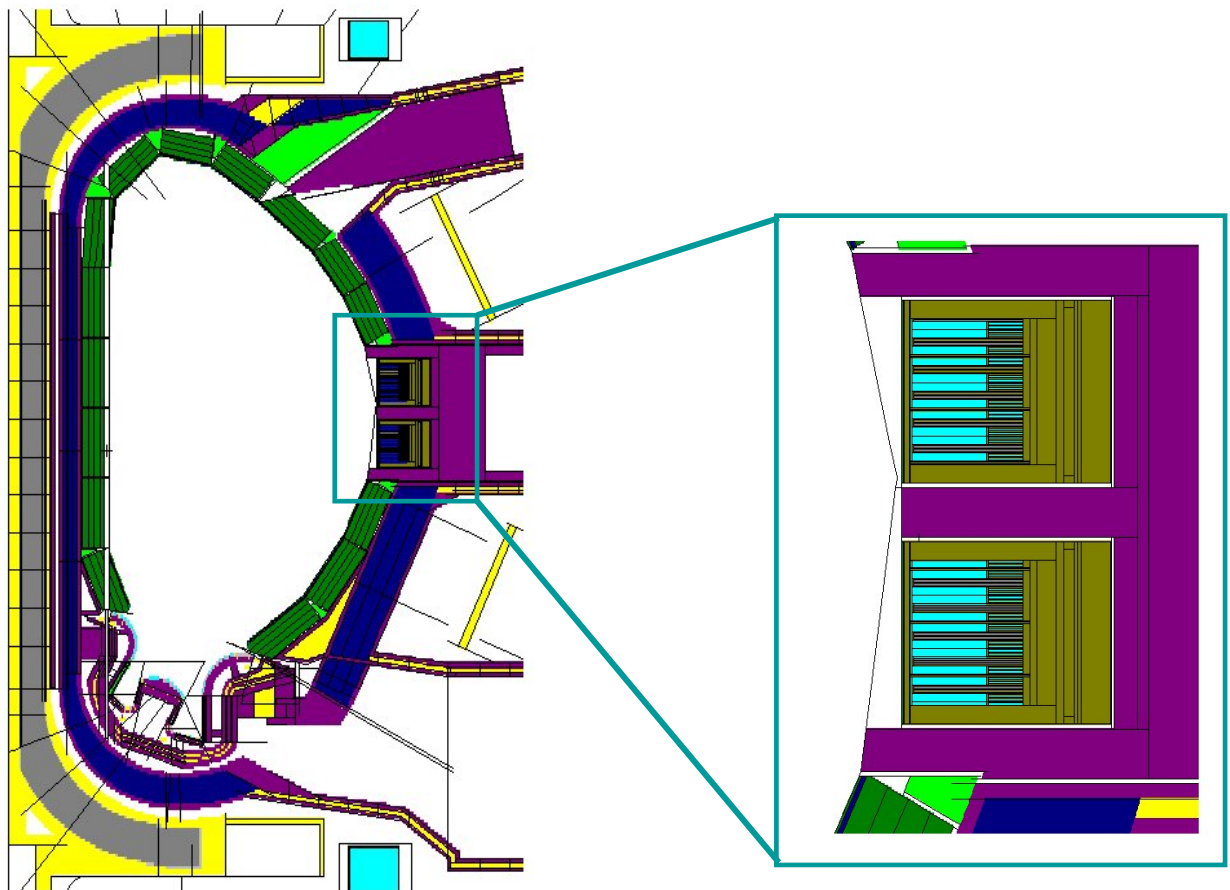


Fig. 1: MCNP model (vertical cut) of ITER 20° torus sector with integrated HCPB test blanket modules.

According to the task specifications, coupled 3D neutron transport and activation calculations have been performed for two different irradiation scenarios. The first one is representative for the TBM irradiation in ITER with a total of 9000 neutron pulses over a three (calendar) years period. It was simulated by a continuous irradiation for 3 years minus the last month and a discontinuous irradiation with 250 pulses (420 s pulse length, 1200 s power-off in between) over the last month. The second irradiation scenario is very conservative assuming an extended irradiation time over the full anticipated lifetime of ITER according to the so-called M-DRG-1 irradiation scenario with a total first wall fluence of 0.3 MWa/m^2 .

For both irradiation scenarios the radioactivity inventories and the afterheat were calculated as function of the decay time as specified in the technical description of the task deliverable. Data were processed for the total activity and afterheat of the TBM, its constituting components and materials. For each decay time, a table of the 20 dominant radio-nuclides was prepared. In addition, profiles of the afterheat power densities in Beryllium, the breeder ceramics and the Eurofer structure were prepared for decay times until 30 days after shutdown. Tables were also prepared for the contact gamma dose rates of the different TBM components including their breakdown into the 20 dominant radio-nuclides at each decay time. The data were provided to CEA, Saclay, and Studsvik Nuclear, Nyköping, for performing the safety analyses and the waste classification, respectively. Figs 2 and 3 show examples of the total afterheat and activity of the HCPB TBM as calculated for the representative irradiation scenario.

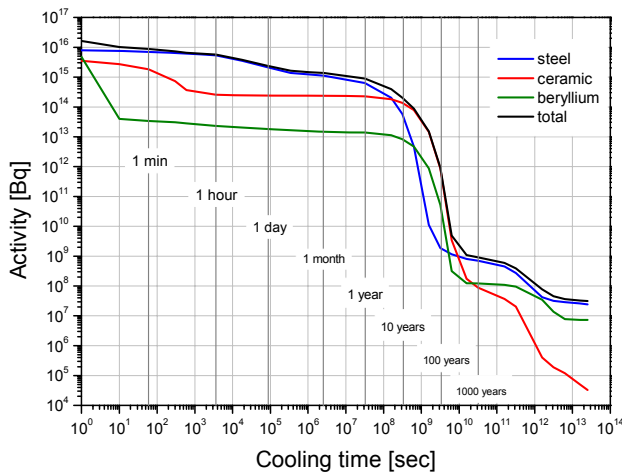


Fig. 2: Total activity [Bq] of the HCPB TBM as function of the cooling time (representative irradiation scenario).

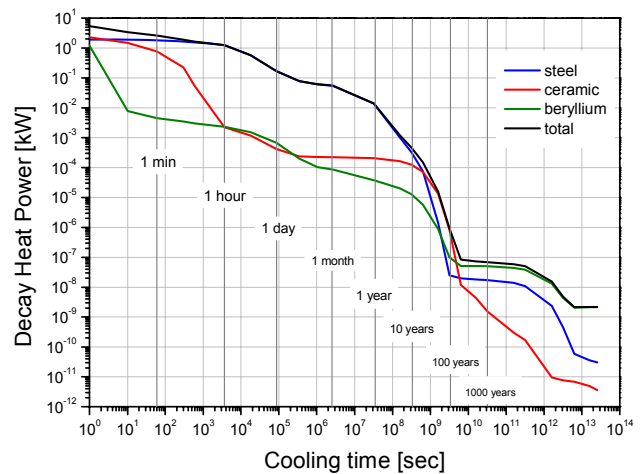


Fig. 3: Total decay heat power [kW] of the HCPB TBM as function of the cooling time (representative irradiation scenario).

Staff:

U. Fischer
P. Pereslavl'tsev

TW6-TTBB-001 D 3 HCPB TBM Design and Integration Analysis

The objective of the task is the continuation of the engineering design work on the HCPB TBM System. In particular the updating of the TBM design, the production of detailed drawing of the TBM, the mechanical integration of the instrumentation, the definition of maintenance sequences, and design and integration of the Helium Cooling System (HCS).

Design analysis and TBM drawings update

An updating of the overall TBM design is necessary as consequence of a recent re-definition of the frame dimensions (agreed in the TBWG-17 in Cadarache).

Due to the new frame design the TBM first wall dimensions changed from 1270 mm x 740 mm (referring to old frame design) to 1208 mm x 710 mm (referring to new frame design) like shown in figure 1.

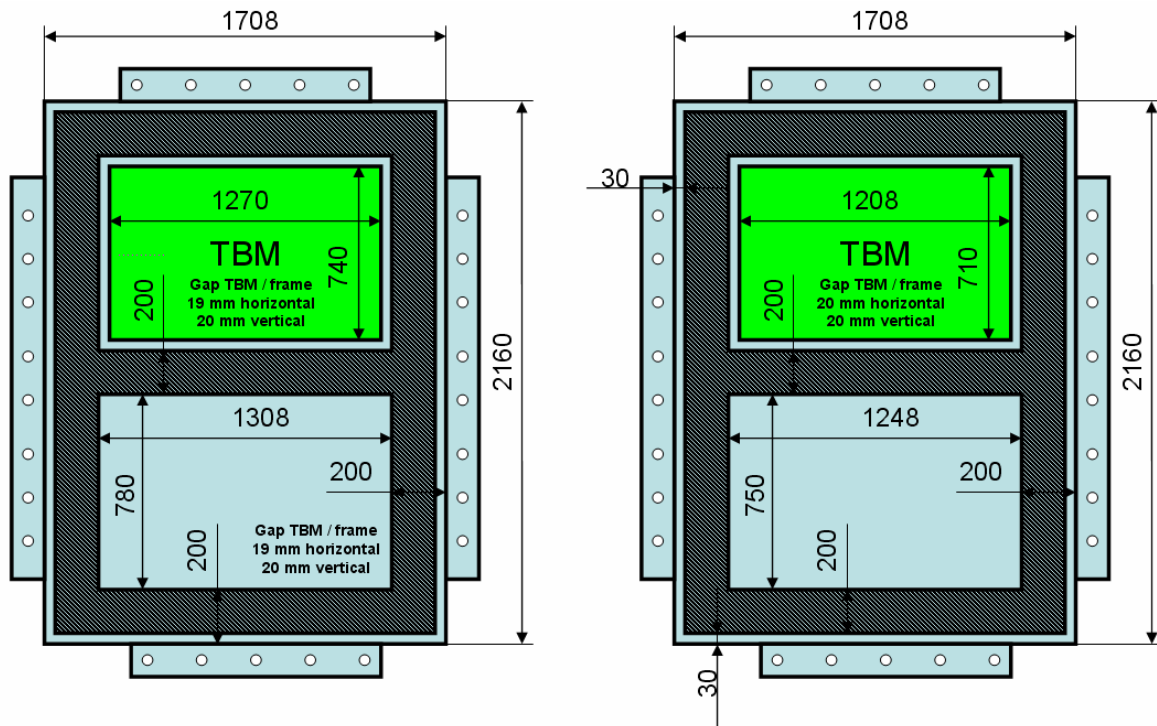


Fig. 1: TBM and frame design, left: old design, right: reference TBWG-17.

This change of dimensions has as major consequence the necessity of a new FW lay-out. The FW design (according to Ref.1.0, documented in the HCPB DDD-2005) has been modified to adapt the cooling channel arrangement to the new first wall dimensions due to the changed frame geometry. Additionally the design of the first wall has been approved according to results of analysis performed for the previous reference design (Ref.1.0).

The new design including the adaptations to the new frame and design improvements is called Ref.1.1. Some major changes in the design are shown in figure 2 - 4. In addition a new feature will be introduced in the design, namely the use of FW channels with square section in order to keep open the possibility to make the fabrication of the FW fully compatible with the HIP fabrication methods starting from square tube or square grooves in plates.

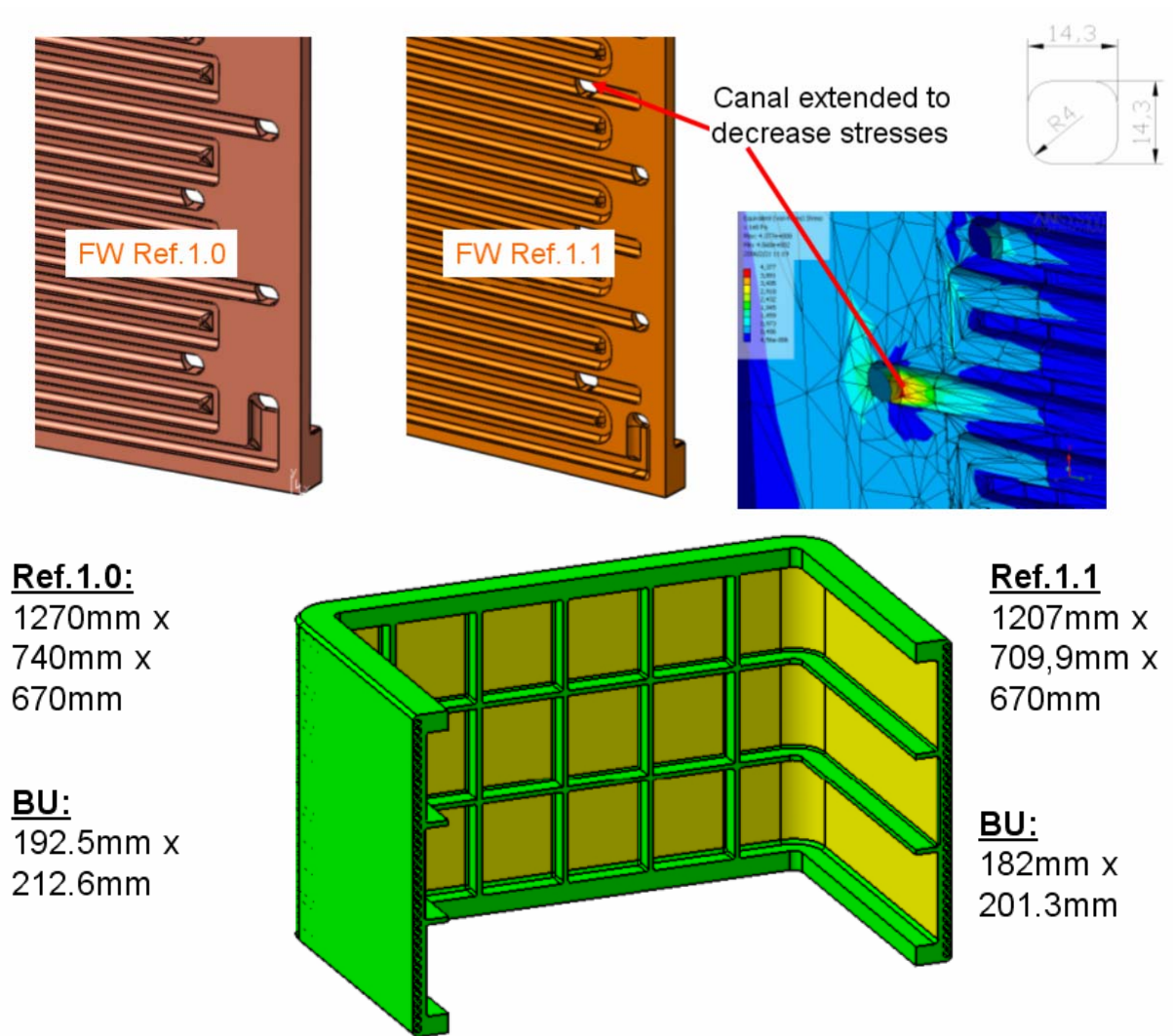


Fig .2: FW designs Ref. 1.0 compared to Ref1.1 (including squared channel cross section 14.3 mm x 14.3 mm and outer dimensions of FW and BU).

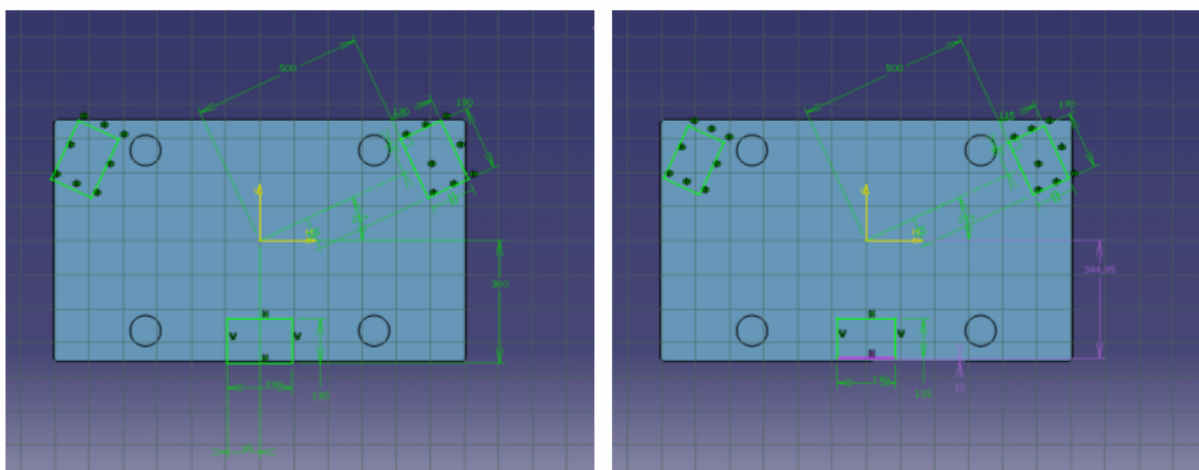


Fig. 3: Location of the attachment components (shear keys) requires adaptation to the new outer dimensions (left Ref 1.0; right Ref.1.1); shear keys will be smaller in the new design.

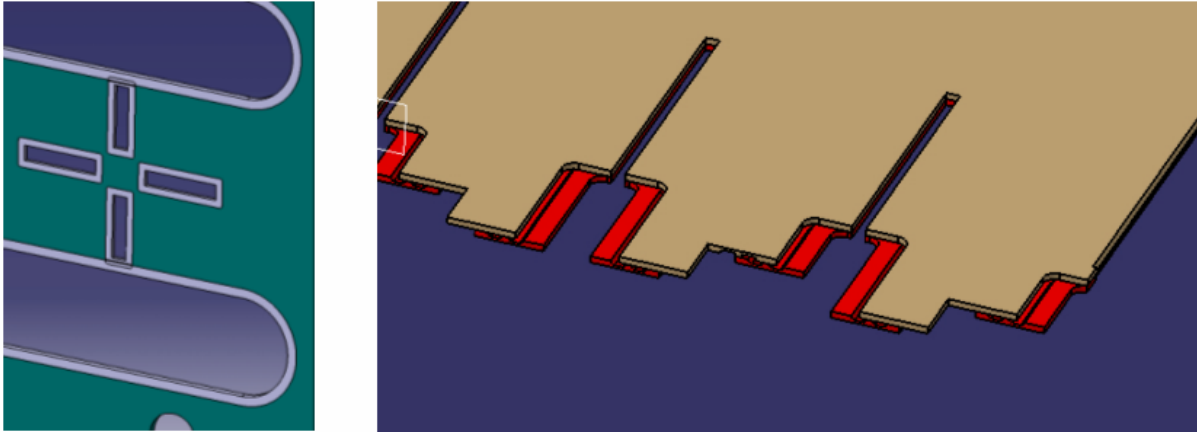


Fig. 4: Left, Ref 1.0: decrease of TBM outer dimensions requires change of the manifold plate design → space for welding between grid and plates is no more sufficient

Right: An alternative design (Alt 1.0) of the grid plates could be used to decrease the space requisition for the welding by combining inlet and outlet of each cooling plate.

Several thermo-hydraulics and structural analyses should be repeated to assess the compatibility to the design requirements basing on a new TBM CAD model which is currently under development.

Definition of a design specification package in support to the fabrication R&D and sub component testing

A complete CAD model and drawings of the TBM and of the necessary sub-component fabrication test samples will be delivered in this task to support the Fabrication R&D. Feedback from the fabrication task (design modifications required by the fabrication processes and testing issues) will be integrated in the current design. In addition, dimensional tolerances of components and acceptance criteria for joint will be specified. Specifications (temperatures, stresses, etc.) related to operating and off-set condition will be delivered, too.

At the beginning of the review period the design of the TBM based on the concept Ref.1.0, documented in the HCPB DDD-2005.

In the frame of the adaptation of the TBM geometry to the new frame requirements (Ref 1.1) an alternative manufacturing concept of the TBM is developed (Alt 1.0). This alternative concept uses several design features to simplify the TBM manufacturing process. The main differences between Ref 1.0 and Alt 1.0 are as follows:

- **Stiffening grid**

A new concept for manufacturing of the grid plates without using diffusion welding process will be tested. The cooling channels of the plate (figure 5 brown part) will be manufactured by Electrical Discharge Machining (EDM, erosion). On the plasma side of the plate the channels will be closed by welding before the connection welding to the first wall is established. The design including EDM machining and welding will be qualified by an adequate mock up which is shown in figure 6.

- **Manifold system**

The manifold system of Alt 1.0 will be designed basing on plates which are separated vertically, one for each column of breeding units (figure 7). The plates of the vertical grid are designed continuously reaching without intersection from the upper to the lower cap. This design means a simplification from manufacturing point of view.

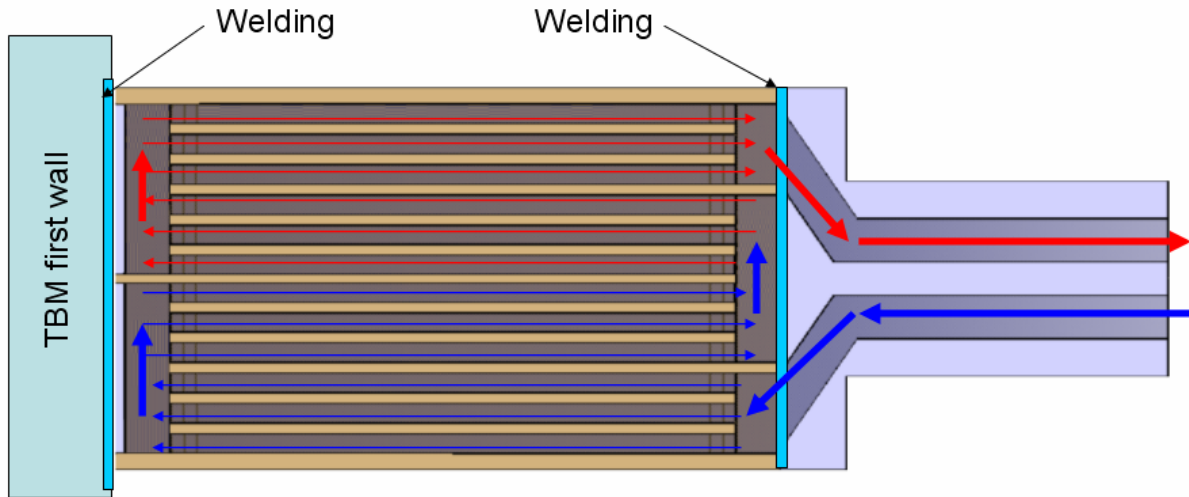


Fig. 5: alternative cooling plate design.

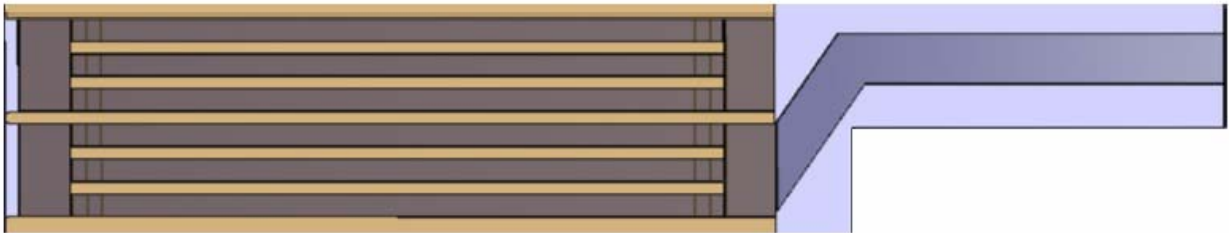


Fig. 6: Simplified mock up to qualify manufacturing technology.

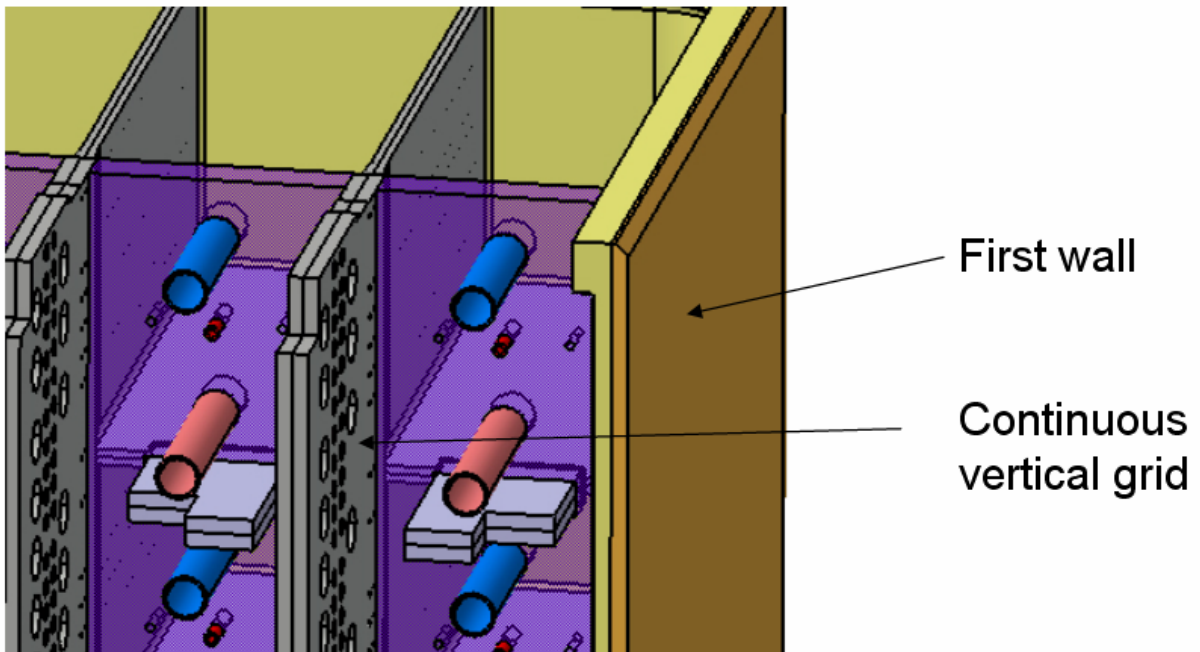


Fig. 7: Alternative manifold design.

- **Breeding units**

The breeding unit cooling plates used for Alt. 1 design will be made from three plates which are equipped with cooling channels manufactured by EDM process. One plate will be bended by an angle of 180 °. Each end of the bended plate will be connected to a straight plate by welding. Subsequently the cooling plates will be connected to the BU

back plate like shown in figure 8. This alternative design of the breeding units will be qualified by adequate mock ups.

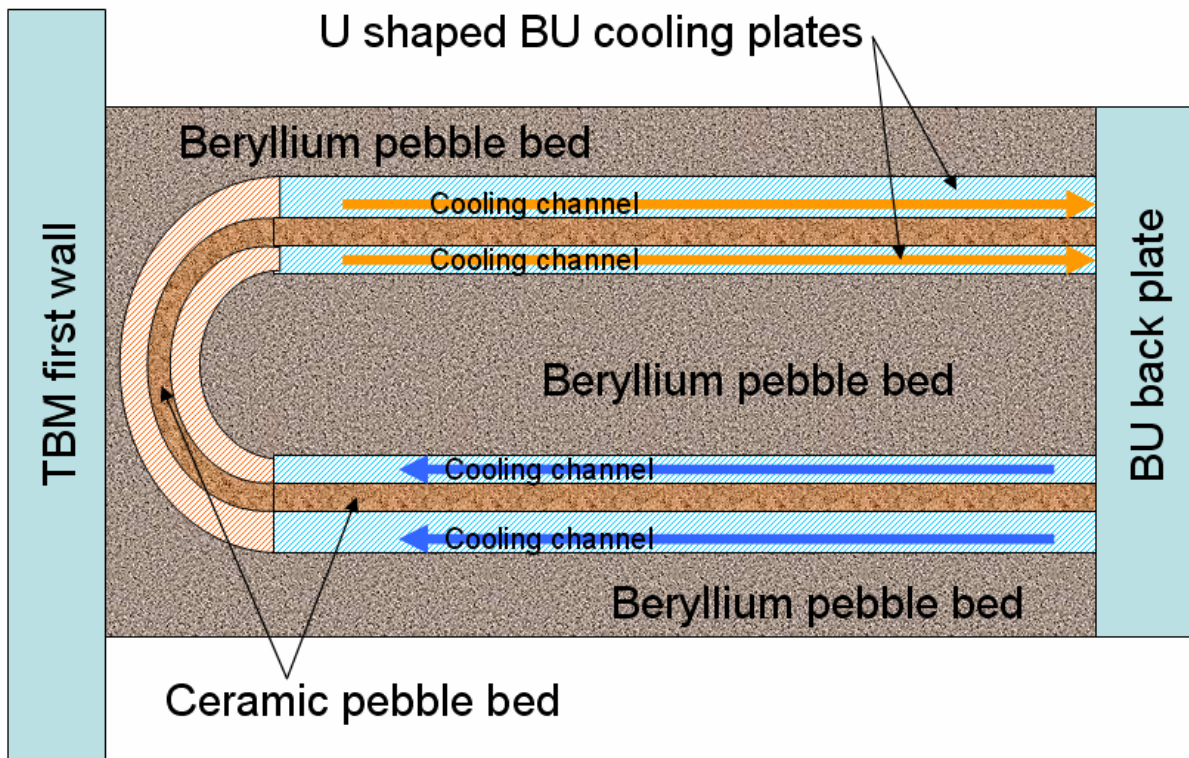


Fig. 8: Alternative BU design.

A CAD model of the “Alt 1.0” design is currently under preparation. Further analysis, discussion with manufacturing experts and the manufacturing of the mock ups will be required.

Mechanical integration of possible instrumentation into TBM (in particular for the EM-TBM)

This activity continues the work already started with task TW5-TTBB-001-D1b. Instrumentation and monitoring systems (that are being developed in other tasks) will be integrated in the EM-design. In particular the impact on the reference design will be analysed, the necessary modifications will be implemented and the compatibility with the remote handling systems in ITER will be checked.

At the beginning of the review period the instrumentation integration system described in TW5-TTBB-001-D1b (figure 9) has been proposed. In this design the sensor extension lines will be connected to the Data Acquisition System (DAS) by an instrumentation pipe (adequate for ~30 sensors) with an interface between the port plug rear side and the integration cask (PIC) in the environment of interface 2.

After discussion with instrumentation experts it turned out that only one pipe used for sensor extension cables will not be sufficient. Probably one instrumentation pipe will be required for the low pressure environment inside of the TBM box (e.g. BU temperatures and grid temperatures), another for the high pressure environment inside the manifold system and a third pipe will be used to combine the sensor extension lines of the diagnostic equipment on the TBM surface.

Detailed investigation is ongoing to determine the number and the positioning of the TBM sensors. Additionally it has to be checked if increasing the number of instrumentation pipes is compatible to the systems and components proposed for remote handling in the environment of interface 2 for TBM exchange.

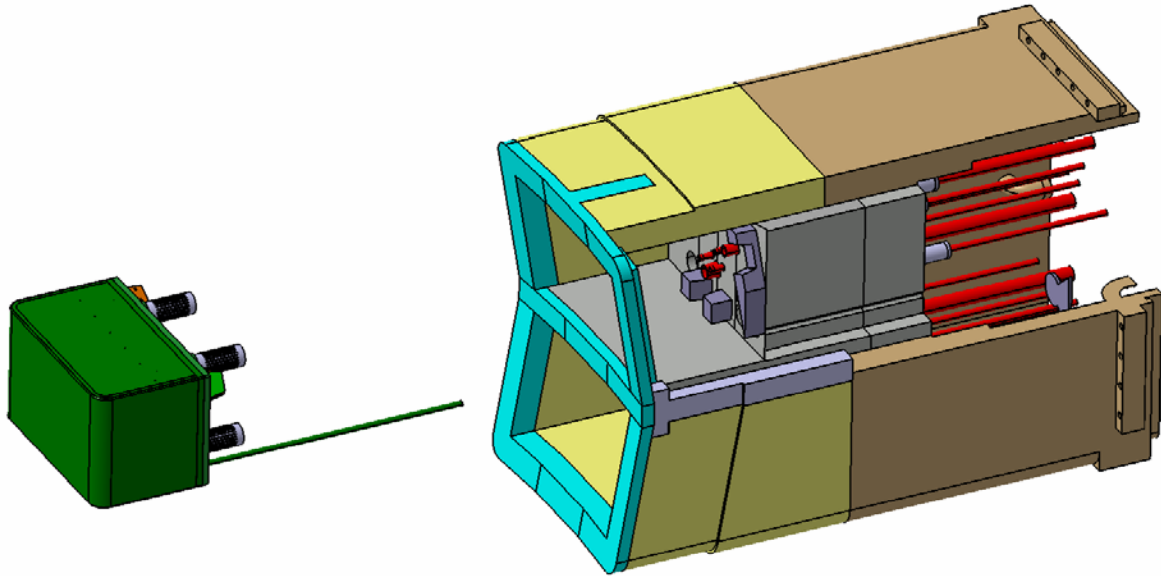


Fig. 9: TBM (including instrumentation pipe) and port plug.

Design and integration analyses of the TBM HCS

A conceptual design for the HCS based on a 8 layout (with recuperator in order to keep the compressor at low temperature, i.e. $<150^{\circ}\text{C}$) has been already developed by FZK in the frame of task TW5-TTBB-001-D1c. The design has to be further developed in order to fulfil ITER requirements, especially space limitations and maintenance, piping lay-out and interface with other ITER systems (e.g. power and cooling water supply). The already implemented RELAP 5 model of the whole TBM system will be updated according to modifications in the TBM design and to a more detailed definition of the loop components.

The status of the HCS for the HCPB-TBM in ITER at the beginning of the review period is described in TW5-TTBB-001-D1c, final report.

In the frame of this task the space requirements of the system have been investigated more detailed, however it turned out that the place dedicated to the EU HCPB TBM HCS inside of the TCWS vault ($\sim 20\text{m}^2$ foot-print) is not sufficient. Figure 10)-1 shows a more realistic estimation of the space requirements ($\sim 60\text{m}^2$).

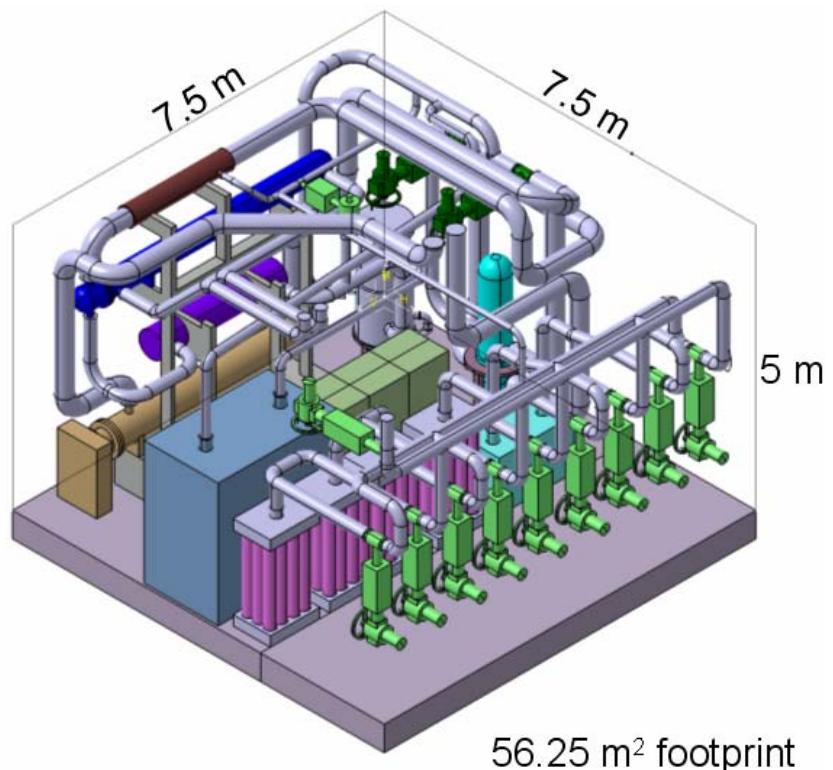


Fig. 10: TBM HCS in ITER including first estimation of CPS and PCS.

Reference concept (Recuperator is installed in vault)

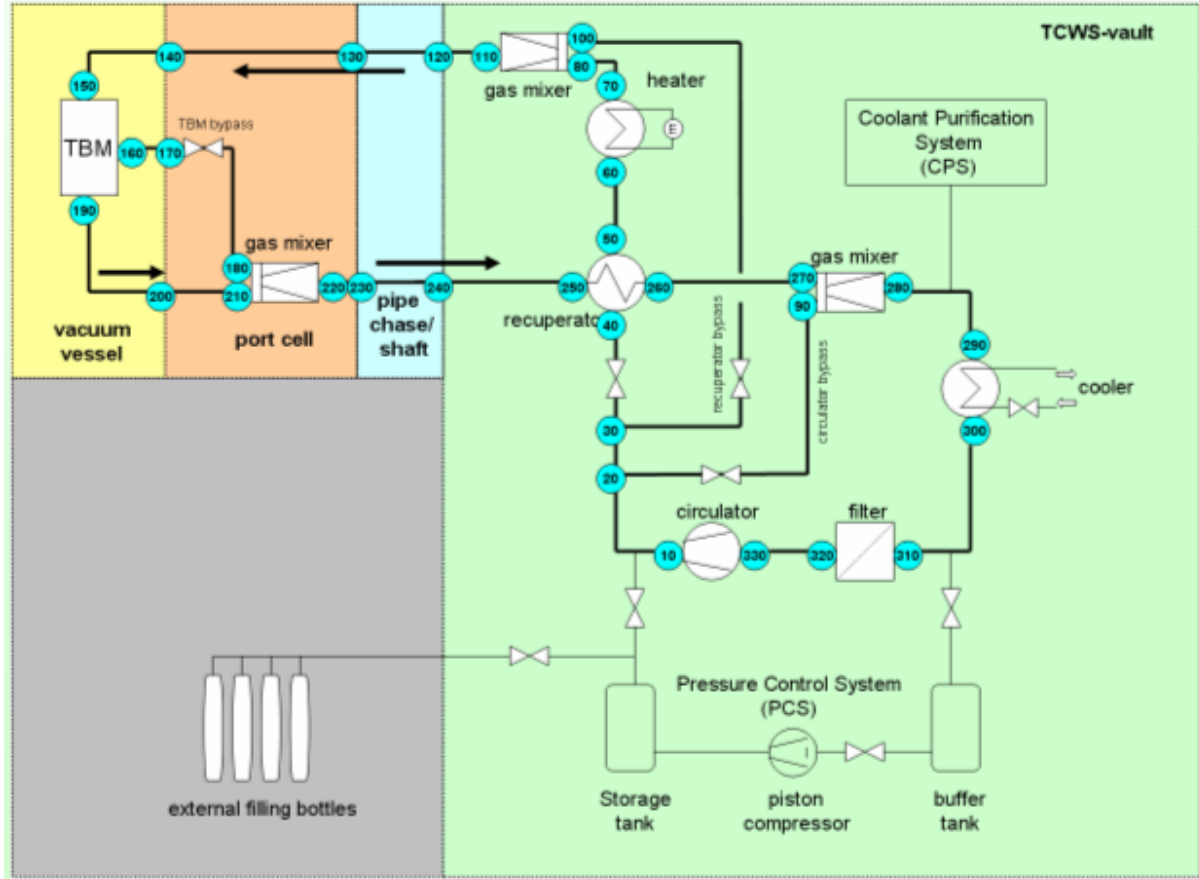


Fig. 11a: Reference concept, hot leg of circuit inside of vault.

Additionally the selection of components used the loop has started (e.g. a compact economizer manufactured by the “Heatric” company will be used). The current selection of the components will be implemented in the RELAP simulation of the circuit.

Additionally an alternative loop design is investigated which bases on the installation of the “hot leg” of the cooling circuit inside of the port cell. Figure 11a and 11b show the “reference” and the “alternative” loop concept.

The investigation of the space requirements for the Helium loop in ITER is ongoing but the value given in the estimation above (60 m²) seems realistic. Further investigation will be required in the selection of components as well as to update the RELAP model accordingly. Additionally the investigation of the loop arrangement (reference/alternative) has to be continued while taking into account the influence on the pressure control system. Detailed work will be required in the field of the development of the coolant purification system.

Alternative concept (Recuperator is installed port cell)

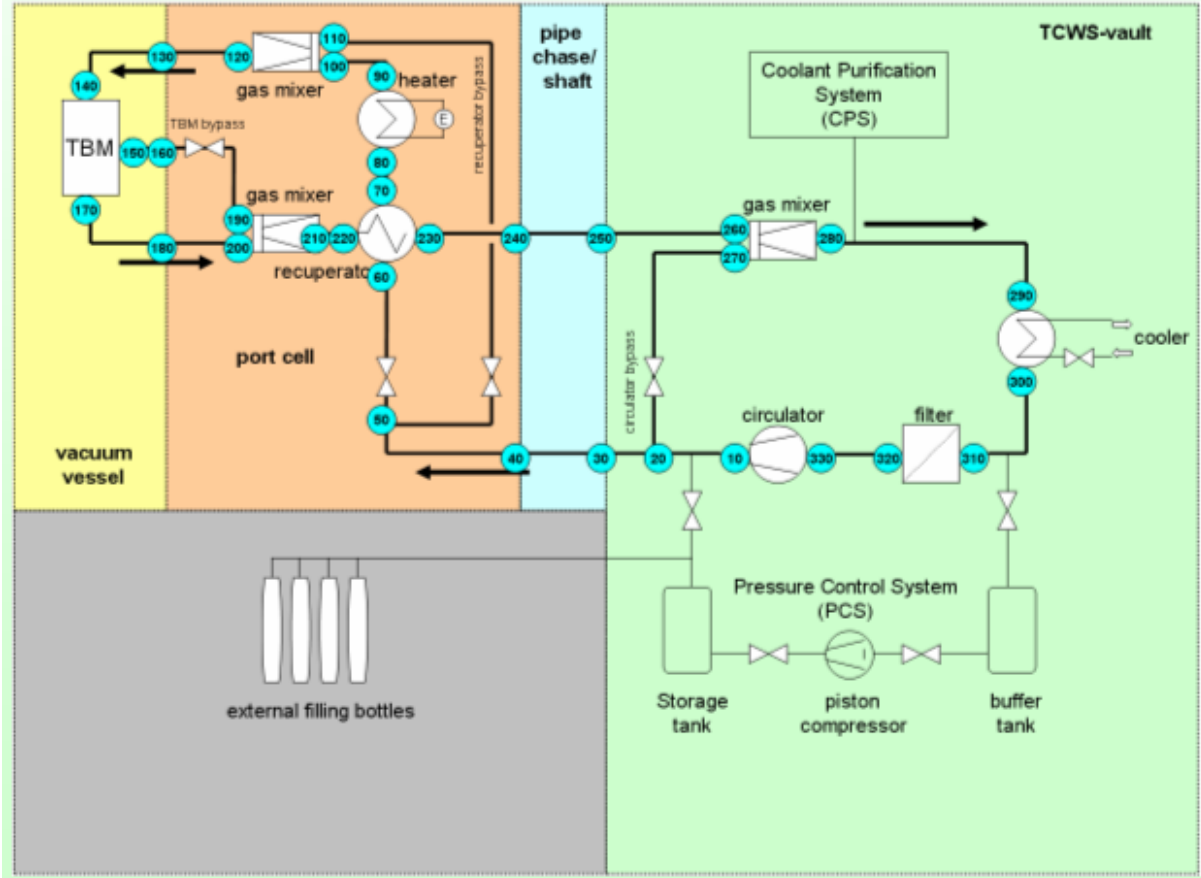


Fig. 11b: Alternative concept with recuperator inside of port cell.

Staff:

L. Boccaccini
B. Dolensky
T. Ihli
X. Jin
R. Meyder
H. Neuberger
R. Polixa

Literature:

- [1] Helium Loop for the HCPB Test Blanket Module, H. Neuberger, X. Jin, L.V. Boccaccini, B-E. Ghidersa, R. Meyder, Poster at Soft 24, Warsaw

TTBB-002b Helium Cooled: Blanket Manufacturing Technologies

TW2-TTBB-002b D 5 Manufacturing of HCPB Cooling Plates by Diffusion Welding

Introduction

The blanket box (BB) of a future fusion power plant will be manufactured by plates with cooling channels. Such cooling plates (CP) will be produced by half pieces with milled cooling channels. The half pieces will then be connected by a diffusion weld process performed by an uniaxial diffusion weld setup (U-DW) or in a hot isostatic pressing setup (HIP).

The task will yield the manufacturing process for CP: Starting with a CP (20 cm x 46 cm) for a breeder unit and then up scaling to large dimension of first wall plate with 2 m x 4 m.

Such a joining process consists of a half piece production with a high speed dry milled weld surface, a cleaning procedure and a diffusion weld process.

The failure of the first industrial transfer with a compact mock up could be clarified as a thermal transient problem. The influence of multiple heat treatments had been investigated. The activities during the year 2006 yield also improvements in the cleaning process and new diffusion weld parameters caused by a new batch of EUROFER 97/2.

Status of first industrial transfer

Fig. 1 shows a first try of an industrial transfer with a self developed boxing device.

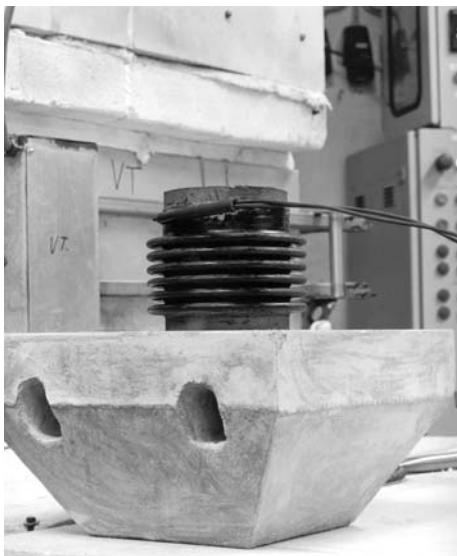


Fig. 1: Photo of a diffusion weld box with a bellow compensating thermal mismatch or plastic compression of the work piece.

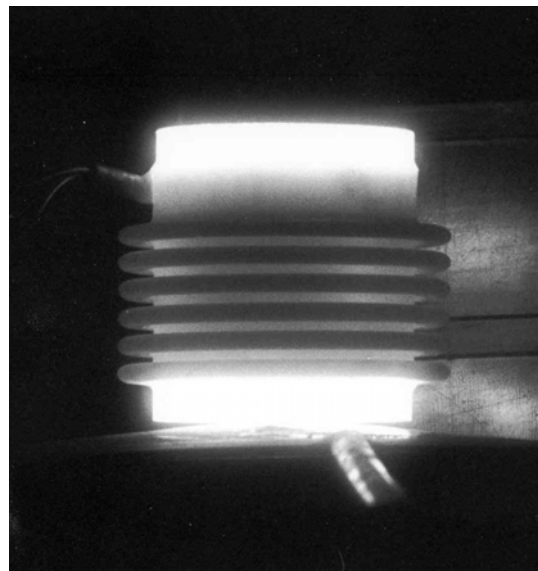


Fig. 2: Infrared photo of the boxing device after taking out of the U-DW setup. Surface temperature about 1000°C.

The box had been leak tight after the diffusion weld process. It had been able to protect the CMU (compact mock up) against oxidation. Unfortunately only a thermal couple in an outer tube had been used. It could not detect the true temperature of the CMU inside.

Fig. 2 displays an infra red photo of the boxing device. It proves with a shadow of the inner getter plates a non homogeneous temperature distribution inside the box. Fig. 3 displays the status compression. The CMU D311 and D312 manufactured at FZK are nearly homogene-

ous and with the same amount compressed. In contrast to those the compression of the industrial CMU varies locally. The amount of compression is smallest in that region of CMU in which region the highest temperature loss (less temperature correlates with less compression) has to be expected by the infrared photo Fig. 2. Fig. 3 displays by the numbers results of tensile properties (yield strength in terms of the base material delivery state). It is well known by other investigation, see next chapter, that the diffusion weld process reduces the tensile strength by about 10%. If the heat treatment would have been correct, yield strength should be by 0.9 in terms of the base material properties. But unfortunately an increase of 20 % has been observed. This proves the temperature measurement together with transient temperature distribution as major reason of failure.

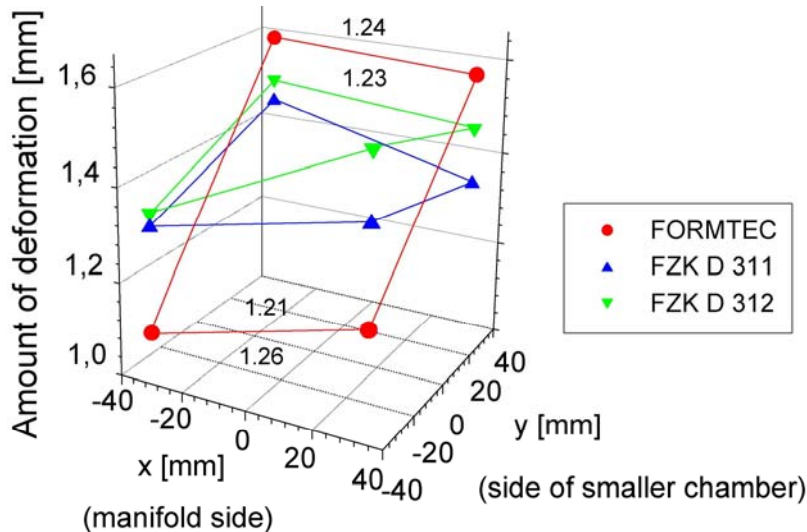


Fig. 3: It displays the local dependency of work piece compression. The industrial FORMTEC CMU is less compressed at the manifold side as the FZK made CMUs.

Multiple heat treatments

Reproaches against the diffusion weld process force a first time investigation on multiple heat treatments. The manufacturing process of a BB needs a five time PWHT (post weld head treatment). The PWHT had been esteemed as fully reversible. The investigation of this task is proofing that a multiple PWHT changes tensile properties and fracture toughness properties. Fig. 4 shows this by the example of the yield strength. A grain coarsening could be observed by micrographs.

This effect should be considered in future investigations: It is necessary to know the final yield strength of EUROFER **after** the complete manufacturing process of a BB.

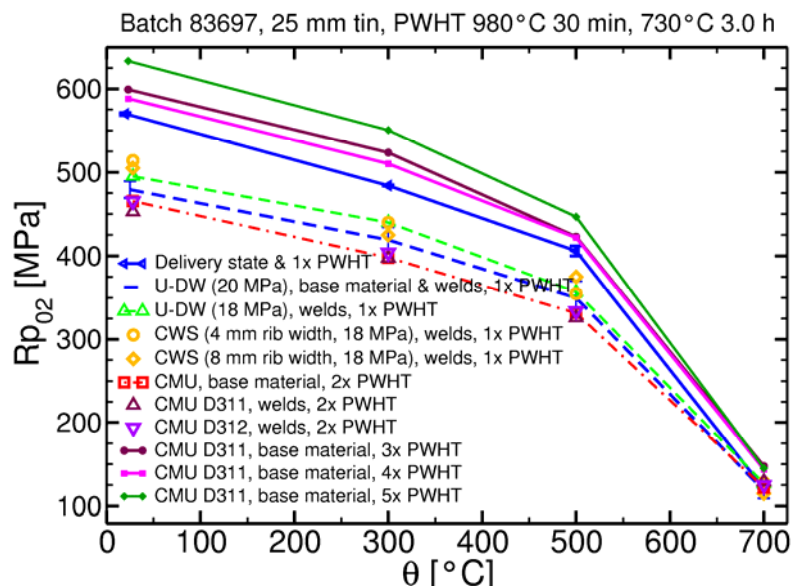


Fig. 4: Tensile property yield strength for different heat treatment states. The yield strength at room temperature is decreased by the heat treatment of the diffusion weld process. The yield strength increases to a higher value than that of the delivery state after a five time PWHT. This proves the normalisation process as non reversible.

Cleaning process

A discussion of the cleaning process starts in this year. The used acetone based cleaning procedure can be applied to small CP dependent on the ultrasonic bath.

A non promising water based process is under discussion needing anti corrosion agents. The IMF-II investigates during this a well promising candidate like cleaning with frozen CO₂ pellets, see Fig. 5. Meanwhile this cleaning procedure yields nearly the same good results (Fig. 6) as the by IMF-II developed acetone based cleaning procedure. The CO₂ pellet cleaning procedure can be well applied to a CP with large dimensions like a first wall plate!



Fig. 5: Cleaning procedure with CO₂ pellets applied to a CMU. CO₂ pellets are accelerated to about twice of sonic speed. They ice pollutions and shave the pollutions by mechanical impact.

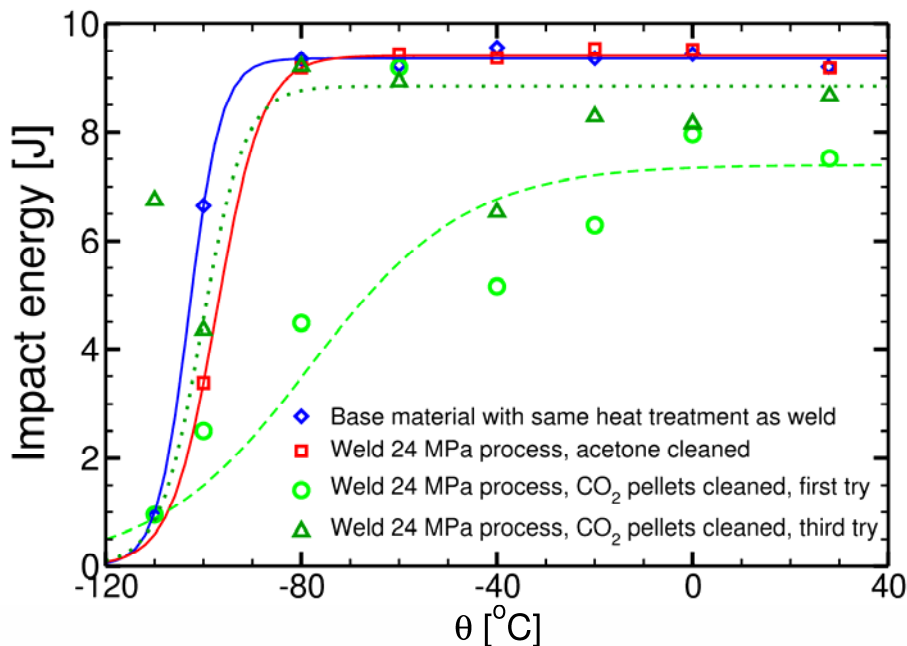


Fig. 6: This diagram compares the results of different cleaning procedures of EUROFER 97/2.

Improvement of the diffusion weld process

The first application of the diffusion weld process with old parameters shows non sufficient result. New process parameters had been evaluated.

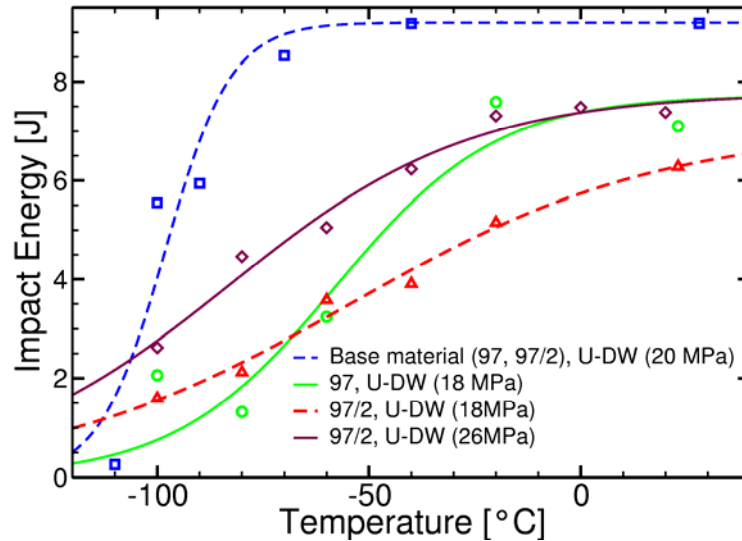


Fig. 7: This diagram compares different diffusion weld process and different batches of EUROFER.

Conclusion

The reasons of failure of the first industrial diffusion weld procedure transfer could be clarified. An improved boxing device is under construction and will be soon transferred to a diffusion weld experiment. Multiple heat treatments (PWHT) generate a coarsening grain. The PWHT had been proofed as a non reversible procedure for the EUROFER steel. A new cleaning procedure had been developed and will be applied for the next mock up attempt. The diffusion weld parameters for the new EUROFER 97/2 could be determined.

Staff:

J. Aktaa
U. Bürkle
B. Dafferner
H. Kempe
J. Rey
A. von der Weth

TTBB-003

Helium Cooled: Out of Pile Testing

TW5-TTBB-003 D 1

Manufacturing and Testing of Mock-ups for Investigation of Coolant Flow in the Manifold System of HCPB TBM (GRICAMAN Experiments)

Introduction

The objective of this task is to contribute to the out-of-pile testing of HCPB TBM. The envisaged activity focuses on out-of-pile testing of a look-alike mock-up of the TBM manifold system, in particular to the optimization of coolant flow.

The flow distribution in TBM coolant system is quite complex. The coolant, helium at 8MPa and 300°C enters the manifold 1 with mass flow rate of 1.2kg/s, from where it is distributed into coolant channels of the first wall (FW channels). The outflow from FW channels is collected in the manifold 2 where the following flow distribution should take place: 0.56 kg/s flows through by-pass pipes out of the system, 0.38kg/s is uniformly distributed through 27 stiffening grids and 0.125kg/s goes into each cap. The mass flow rate through each cap channel is specified. The outflow from grid and cap channels is collected in manifold 3 and from there uniformly distributed among 18 breeding units. The outflow of BU's is led into the manifold 4 designed in the form of 'ships' from where it, finally, leaves TBM. In order to find out whether such a flow distribution can take place, GRICAMAN (GRIdCapsMANifolds) experiments are proposed. The main goals of the experiments are:

1. to investigate whether the mass flow distribution in the manifold 2 among the caps and stiffening grid channels corresponds to the designed one,
2. to investigate whether individual stiffening grid and cap channels are supplied with designed portion of coolant flow and
3. to investigate whether the mass flow distribution among breeding units is uniform.

Using conditions of flow similarity the experiments will be performed with air at 0.3MPa and ambient temperature. The experiments are supported with numerical simulations by the computer code STAR-CD.

Design of GRICAMAN facility

Layout of Gricaman facility is given in Figure 1, while Figure 2 presents the flow diagram with corresponding measuring scheme. The flow rate of 912.6Nm³/h is taken from FZK supply line of pressurized air and led into a buffer tank. After this the air is filtered so that all the particles larger than 0.01µm are removed. In order to keep inlet pressure constant pressure regulator is arranged after the filter. Using an inlet distributor - a cylindrical vessel with diameter 0.35m and length 1.5m the total air flow rate is distributed among 6 FW channels. Each FW channel involves a pipe section of DN 2", a pipe section of DN 1" and a section with real FW cross-section in the length of ~30 hydraulic diameters, what gives the total channel length of ~5m. At the 2" section a ball valve for isolation of the channel and a needle valve for flow regulation are arranged. Needle valves of DN 2" are applied in order to avoid large pressure drops due to high flow rates through FW channels (152.5Nm³/h). At the section of 1" air flow rate is measured with flow meters on calorimetric basis. In front of each flow meter a pressure measuring position is foreseen.

The upper halves of manifold 2 (Mf2) and manifold 3 (Mf3) are for an easier connection rotated by 180°. At the back side of Mf2 by-pass openings are set. Air flow of 425.86Nm³/h is via these openings collected in a header and then through a 2" pipe taken out of the system. The flow rate is controlled via a calorimetric flow meter and needle valve of 2" inserted at

outlet by-pass pipe. Pressure is measured in front of the flow meter. A ball valve of 2" is arranged to keep outlet by-pass pipe closed at the beginning of an experiment. At the front side of Mf2 14 grids are connected. In order to simulate the connection correctly, real cross-section of two inlet grid sub-channels is kept in length of 0.1m. The air flows from the sub-channels join in a circular pipe of DN 3/4". Connection of these pipes to Mf3 is performed in a similar way as to Mf2: air flow from 3/4" pipe is distributed through two parallel sub-channels with cross-section corresponding to grid outlet sub-channels and in the length of 0.045m. At the lower side of Mf2 and Mf3 equivalent cap channels are connected. These channels are designed keeping real geometry of cap channels at sections connected to manifolds (in the length of ~30 hydraulic diameters) and replacing the middle part by circular tubes of DN 3/4". The length and shape of grid and cap equivalent pipes is chosen in order to provide ~2/3 of the total pressure drop in real grid/cap channels. The remaining 1/3 should be performed by local throttling with a valve-like device that is going to be developed (due to low pressure drops in grid/cap channels no real valve can be applied). Air flow rate is measured in each equivalent grid and cap pipe by flow meters with floating body equipped with electrical transducer for electrical data acquisition. For an easy metering of corresponding pressure drop when mass flow rate is known each equivalent grid/cap channel will be calibrated. For isolation of each channel ball valves are foreseen.

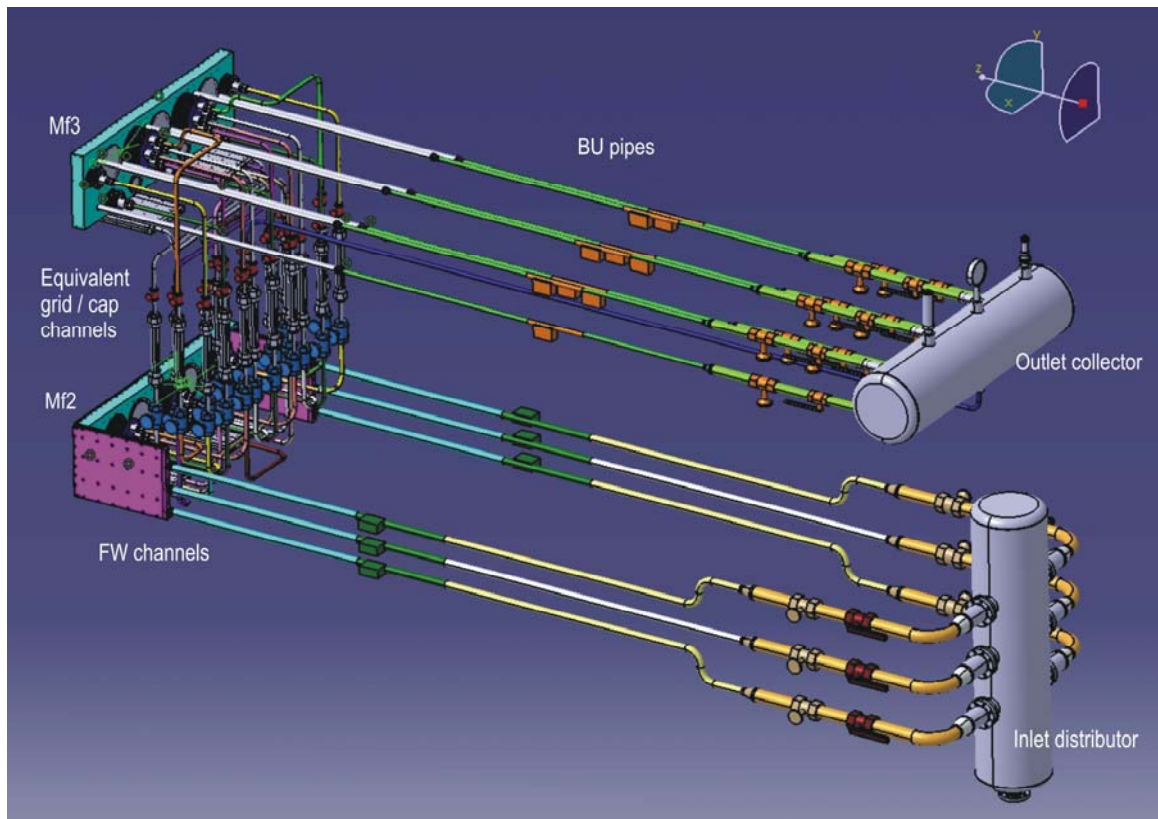


Fig. 1: Layout of Gricaman experimental facility.

From Mf3 air flows into 9 breeding units (BU). The real cross section of BU pipes is kept at their inlets in the length of ~30 hydraulic diameters. After this a section of DN 1/2" is added, which includes calorimetric flow meters. The corresponding hydraulic resistance is in each BU pipe set up with a needle valve DN 1 1/4". For the isolation of a BU pipe ball valves are arranged.

Outflow from BU pipes is collected in a cylindrical vessel with diameter of 0.35m and length of 1.5m. The air flow out of this collector is regulated with a needle valve of DN 2" and measured with a calorimetric flow meter.

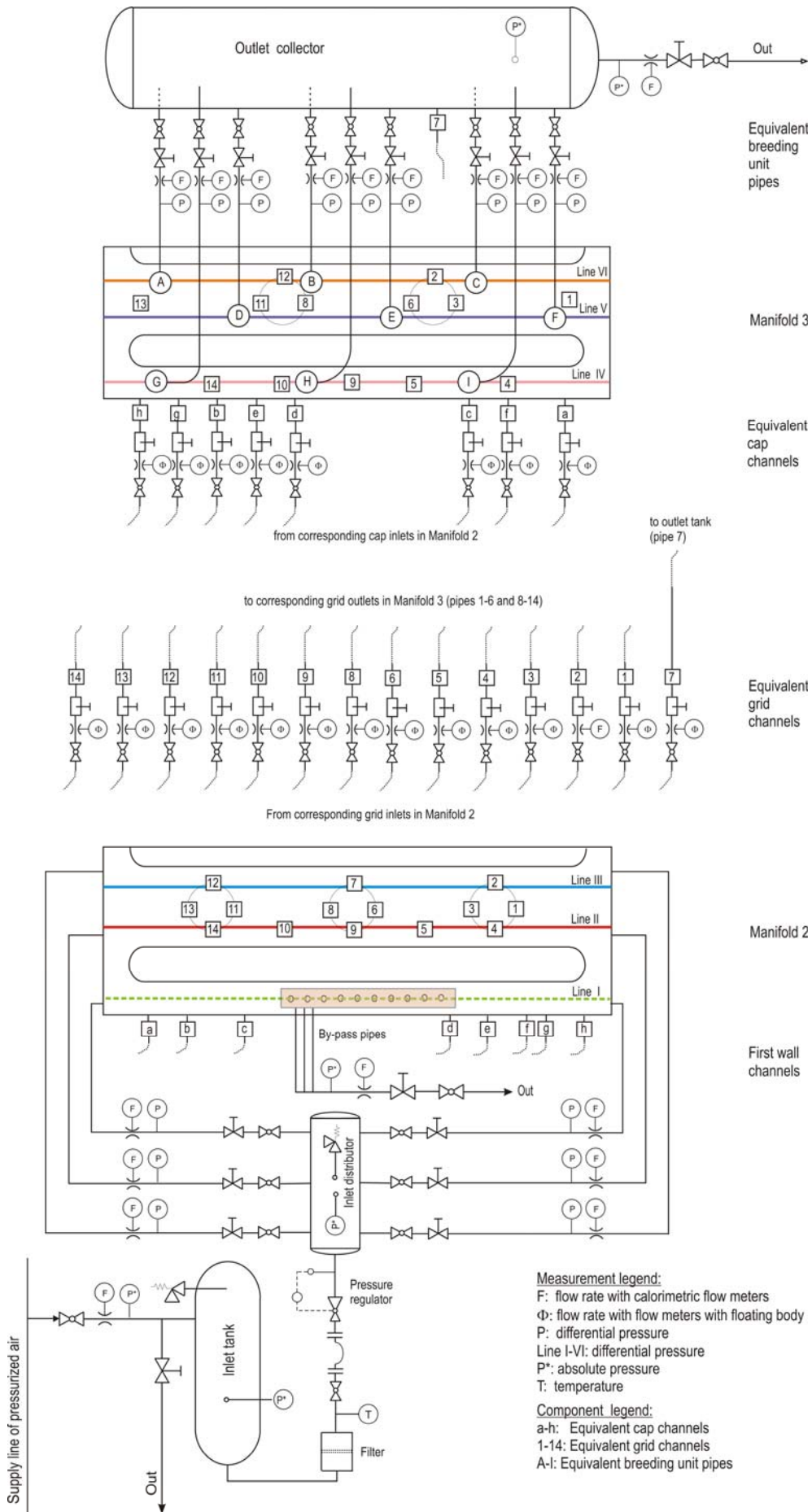


Fig. 2: Flow diagram and measuring scheme of Gricaman facility.

The absolute pressure will be measured in the inlet tank, inlet distributor, outlet collector, bypass outlet pipe and final outlet pipe. At other positions presented in Figure 2 differential pressure measurements will be performed. Especially important are (i) pressure measurements in Mf2, where numerically found strong pressure gradients in domains of FW inlets should be verified and (ii) pressure measurements in Mf3, where flat pressure distribution in front of BU inlets should be confirmed. In relation to this, pressure measurements are foreseen that should provide pressure gradient reconstruction along 3 lines in Mf2 (Line I-III in Figure 2) and 3 lines in Mf3 (Line IV-VI in Figure 2). Differential pressure measurements in FW channels and BU pipes have control character.

The status of the work on Gricaman assembly is: (i) final design is established, (ii) components like filter, pressure regulator, pressure vessels as well as measuring devices are ordered and will be available at the beginning of 2007, (iii) Mf2 and Mf3 with corresponding connections are going to be manufactured at the beginning of 2007, (iv) measurements will start in spring 2007 and (v) numerical model will be improved and verified by the same time.

Investigation of fluid flow in cooling channels of stiffening grids and caps

For a proper dimensioning of equivalent grid / cap pipes in Gricaman facility a detailed investigation of real grid / cap channels has been necessary. This is especially important in the case of stiffening grid plates because of complex channel geometry. In both horizontal and vertical stiffening grid, namely, three characteristic groups of channels can be observed: two parallel inlet channels, three parallel double-U shaped channels (hereafter called 3channel-bundle) and two parallel outlet channels. Inlet channels are connected with 3channel-bundle via an inlet distributor, while the fluid leaving the 3channel bundle is lead to the outlet channels through an outlet distributor. Due to these internal flow distributors the investigations of grid channels had as goals (i) to determine their hydraulic resistance and (ii) to find out whether mass flow distribution through 3-channel-bundle corresponds to the designed one. The investigations are done numerically and experimentally.

In numerical model stiffening grid channels are connected to an inlet and an outlet collector in order to realistically represent the conditions at the grid entrance from Mf2 i.e. exit to Mf3. The pressurized air is supplied to inlet collector through a circular pipe with inside diameter of 0.01m and length of 0.2m and lead from the outlet collector through a pipe with the same dimensions. In experimental facility the pressurized air from FZK supply line, is first filtered, so that all the particles larger than 5 μ m are eliminated. Transfer of possible vibrations to grid facility is prevented inserting a piece of flexible tube between the filter and the inlet pipe. The air flow rate is measured after the exit pipe by a flow meter with floating body. The grid plates are fabricated from Plexiglas and collectors are from steal.

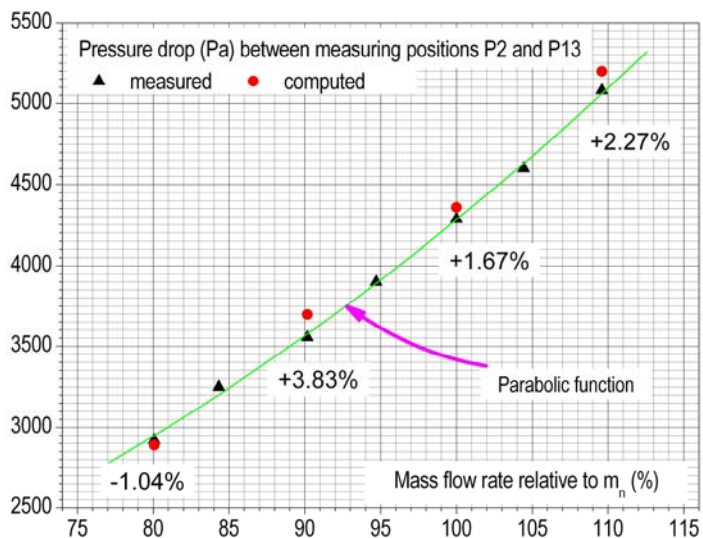


Fig. 3: Computed versus measured pressure losses in horizontal grid channels for different mass flow rates (relative to nominal air mass flow rate, $m_n=8.257 \cdot 10^{-3}$ kg/s). Discrepancy between computational and experimental results is also presented.

The hydraulic resistance of grid channels is determined by measurements of pressure difference between the inlet (position P2) and outlet (position P13) collector for a given mass flow

rate. The results are presented in Figure 3 for the case of horizontal grid channels. A very good agreement between computed and measured pressure drops can be observed.

An experimental determination of mass flow rate distribution in the 3-channel-bundle was a quite difficult question. The classical method with measurement of the velocity in the centre of the channel could not be applied because (i) the cross section of the channels is not circular but a rectangle with rounded corners and (ii) the velocity profiles are deformed due to numerous channel bends. In relation to this we applied two methods to verify the numerical results.

In the first method numerically determined flow distribution through 3-channel-bundle is verified comparing measured and computed velocity profiles. Velocity profiles are experimentally determined through measurements of dynamical pressure with miniature Pitot tubes. Pitot tubes with outer diameter of 1mm, length of 25mm and with step across the channel cross section of 0.25mm are applied. The measurements are done in the cross section of 3-channel-bundle 0.154m far away from the outlet of grid channels. Three velocity profiles are measured in each channel: one along the centreline, one 1.5mm left from the centreline and one 1.5mm right from the centreline. The results are illustrated in Figure 4 through velocity profiles in centreline for horizontal grid channels. While a very good agreement can be observed for inside and outside channel, measured velocities in the middle channel are ~7.5% lower than the computed ones. It is suspected that this disagreement is due to very complicated flow pattern at the inlet of the middle channel that is very difficult to handle computationally. Anyway, the agreement between computational and measured results is considered as acceptable. In relation to this corresponding computed mass flow rates indicate a non-uniform flow distribution in 3-channel-bundle of horizontal grid. In terms of mass flow rate for a perfectly uniform flow distribution, $m_S = m_T/3$ the flow rates through individual channels of 3-channel-bundle are computationally found to be: inside channel, $m_I = 1.059m_S$, middle channel, $m_M = 0.965m_S$ and outside channel $m_A = 0.976m_S$.

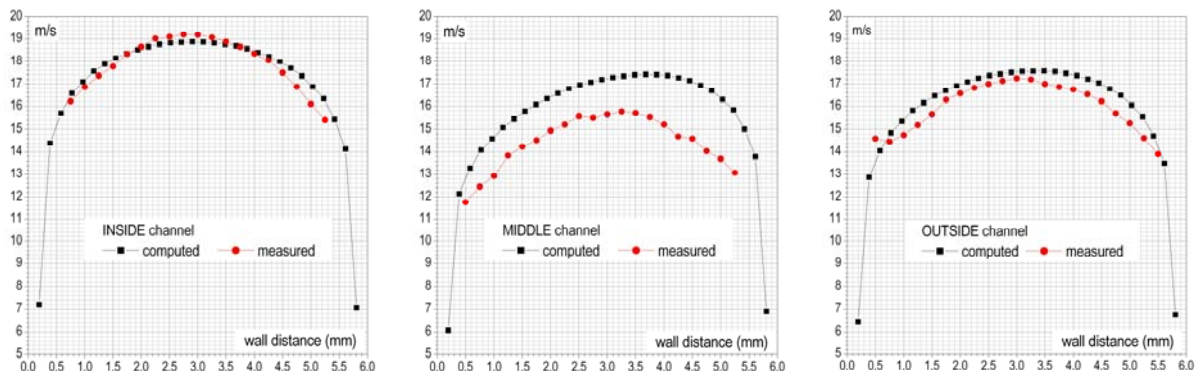


Fig. 4: Computed versus measured velocity profiles in centreline of individual channels of 3-channel bundle of horizontal grid.

In the second method mass flow distribution through 3-channel-bundle is found out indirectly - by means of experimentally determined hydraulic characteristic of each individual channel in the bundle. The hydraulic characteristic of a channel is obtained by blocking two channels and measuring pressure drop in the considered channel for different mass flow rates. When the hydraulic characteristics of all three channels have been known, mass flow rate in through individual channels in normal operation (all three channels free) can be determined on the basis of pressure drops measured from inlet to outlet of individual channels. The obtained relationship between the mass flow rates in the channels of 3-channel-bundle indicates the same trend as the computed one: the inside channel is the best supplied one and the middle channel obtains the less air flow rate. When the magnitude of computed mass flow rates is compared to the measured ones acceptable discrepancies have been found: - 4.8% for inside, +3.9% for middle and +1.36% for outside channel.

A similar test of cap channels is going to be performed, but not before the Gricaman assembly has been tested. The Gricaman tests will namely reveal the magnitudes of flow resistance of individual cap channels necessary to establish corresponding designed mass flow rates. On this basis and with numerical support cap channels will be redesigned and then tested experimentally.

Conclusions

The report deals with Gricaman experimental facility for investigation of flow distribution in the coolant system of HCPB TBM. The considered flow domain is the upper toroidal-poloidal half of TBM bounded at the outlets of FW channels, at the outlets of by-pass pipes and at the inlets of BU's. The facility is designed keeping real geometry of manifold 2 and manifold 3 and replacing complicated grid and cap cooling channels with simple pipes having the same flow resistance as the real channels. The flow resistance as well as internal intern flow distribution within stiffening grids has been investigated in pre-experiments and corresponding numerical models have been verified. The cap channels will be redesigned and experimentally investigated after Gricaman test are performed. The Gricaman assembly is expected to be completed in spring 2007 when the experimental tests and verification of numerical model can be started.

Staff:

O. Albrecht
T. Ihli
M. Ilic
E. Jenes
T. Kuhn
R. Meyder

TTBB-006

Helium Cooled: Breeder and Neutron Multiplier Materials

TW6-TTBB-006 D 1

Development of Beryllium and Beryllium Alloy Pebble Beds with Improved Tritium Release Characteristics

Introduction

The reliable and efficient operation of helium cooled ceramic breeder blankets requires the timely availability of beryllium as appropriate neutron multiplier. In order to overcome some of the disadvantages of existing Be pebbles like tritium release and He embrittlement at blanket operating temperatures, an attempt has been started to investigate relevant properties by producing own and beryllium-based alloys (Be_{12}Ti) on laboratory scale.

According to already available test results, Be_{12}Ti shows, in comparison with metallic beryllium, faster tritium release, much smaller swelling, smaller reactivity with stainless steel, steam and water, therefore, it is becoming interesting also in view of its use in the EU-HCPB blanket.

Due to a high toxicity of beryllium, R&D works on Be and Be alloys has to be performed in a specialized laboratory which has glove-boxes with controlled inert-gas atmosphere (Goraieb Versuchstechnik Company at FZK).

Production of Be_{12}Ti on laboratory scale and its characterization

The main aim of this work was to fabricate samples (consisting mainly of Be_{12}Ti) having different geometric shapes (pellets, electrodes) by means of different methods widely used in powder metallurgy:

- milling of Be-Ti powder mixture in a ball-mill;
- cold uniaxial pressing;
- hot isostatic pressing (HIP);
- heat treatment at different temperatures and in protective atmospheres (vacuum or argon).

Melting of Be-alloyed specimens in argon atmosphere is considered to be an optional method of production. In a few seconds, an electric discharge between an electrode and sample on a copper substrate melts specimen.

Actually, the whole technological chain includes a combination of abovesaid methods of material treatment. All technological equipment is placed in the area of Firma Goraieb Versuchstechnik and includes:

- a ball milling device, NETZSCH MINIZETA 03b made by company NETZSCH-Feinmahltechnik GmbH, for powder production or mechanical alloying which has working speed of rotor $1500 - 3000 \text{ min}^{-1}$, the volume of grinding camera;
- an arc furnace for ingot production of Be-alloys under controlled atmospheres;
- a 20-ton hydraulic press, PW 20 made by company Paul-Otto Weber GmbH, to produce tablets e.g. from Be and Be-Ti powders at temperatures of several hundred degrees;
- fully automatic vacuum oven for annealing tests (vacuum to 10^{-6} mbar at any temperature range up to $1400 \text{ }^{\circ}\text{C}$).

Due to a severe oxidation of beryllium and its alloys at elevated temperatures, all experiments at high temperatures have been performed in protective oxygen-free atmosphere (argon) or in vacuum. This laboratory is also equipped with necessary tools and devices for grinding, polishing and etching of specimens. Plasma Emission Spectrometer allowed us to determine impurity content of different Be-Ti samples (Table 1).

Table 1: Chemical composition of Be-Ti specimens fabricated by methods of an arc-melting in argon atmosphere and powder metal processing.

Element	Arc-melting, wt.%	Powder processing, wt.%
Ti	Bal.	Bal.
Be	29.5	30.7
Fe	0.12	0.19
Al	0.28	0.24
Si	0.11	0.12
Mg	0.068	0.019
Cr	$<2 \cdot 10^{-4}$	$6.7 \cdot 10^{-4}$
Co	$7.5 \cdot 10^{-6}$	$1.0 \cdot 10^{-5}$
U	$5.9 \cdot 10^{-6}$	$4.2 \cdot 10^{-6}$

One should emphasize that the main achievement of Year 2006 was a successful production of Be-Ti rods (Fig. 1) which allows to use them after appropriate machining for more scaleable production of Be₁₂Ti pebbles.

In the frame of this Task, a Precision Cutting Machine which was needed for cutting of samples has been purchased (Fig. 2). At the moment, some preliminary tests are done to adjust the cutting machine to the specific needs of the Beryllium R&D. A special glove-box has been designed and made for this cutting facility to avoid an air contamination with dangerous Be dust. For transportation and storage purposes, Be-containing samples are hold in ambient environment like spirit or tetradecane C₁₄H₃₀. As raw material, we used

- Be pebbles with 2 mm diameter produced by NGK;
- Be powder having 200-300 μm particle size produced by BrushWellman.



Fig. 1: Be-Ti rod consisting of Be₁₂Ti phase fabricated by method of Hot Isostatic Pressing.

Different sorts of titanium powder have been tested to investigate the influence of powder size on formation of intermetallides of type BeTi.

Another part of this work has been performed in IMF I and was aimed to characterize produced specimens using Scanning Electron Microscope (SEM), X-Ray

Diffraction and Transmission Electron Microscope (TEM).

Using of X-Ray Diffraction was necessary to detect Be₁₂Ti phase and to evaluate its quantity (Fig. 3).

Conclusions and future prospective

It was shown that rods containing mainly Be₁₂Ti can be fabricated by method of Hot Isostatic Pressing. Also 15 specimens have been cut out of Be-Ti rod and delivered to Hot Cells (IMF II) for gas release experiments at blanket relevant temperatures.



Fig. 2: Precision cutting machine.

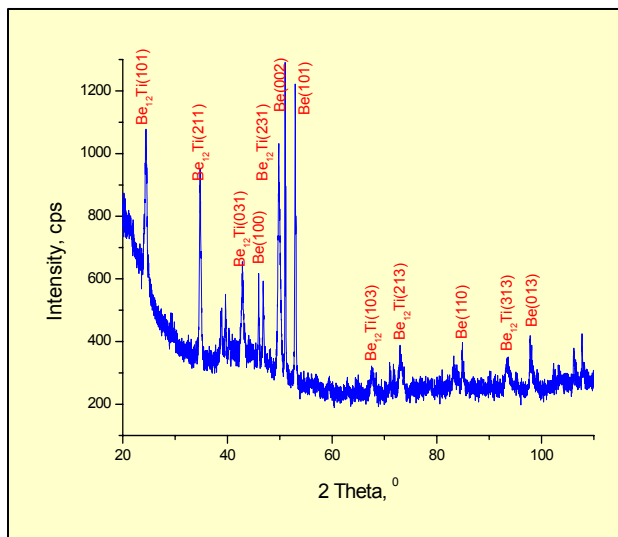


Fig. 3: X-Ray Data of Be-Ti rod produced by method of HIP.

Main aims of the next year are:

- gas release experiments in Hot Cells
- preparation of Be-Ti probes and their investigation by means of Transmission Electron Microscopy;
- further production of Be-containing samples with improved properties (esp. density);
- choice of material revealing better tritium release parameters and its characterisation (microstructure, phase and impurity content, density, etc.);
- design of facilities for production of beryllium and beryllium-based alloys in larger scales.

Staff:

P. Kurinskiy
A. Möslang

Literature:

- [1] P. Kurinskiy, A. Moeslang, M. Klimiankou, A.A. Goraieb, H.Harsch, "Production and characterisation of titanium beryllides", presented at Symposium on Fusion Technologies (SOFT-24), Warsaw, 2006, Sept. 11-15, Proceedings;
- [2] P. Kurinskiy, A. Moeslang, M. Klimiankou and A. A. Goraieb, "Production and characterisation of titanium beryllides for HIDOBE Irradiation", presented at International Conference on Fusion Reactor Materials (ICFRM-12), Santa Barbara, 2005, Dec. 4-9, Proceedings;
- [3] P. Kurinskiy, U. Jaentsch, M. Klimiankou, A. Moeslang, "Fabrication and Analysis of Beryllium and Be₁₂Ti", Final Report on the EFDA Task TW5-TTBB-006 D5;
- [4] A. Möslang, E. Alves, L.V. Boccaccini, J. B. J. Hegeman, P. Kurinskiy, J. van der Laan, E. Rabaglino, J. Reimann, L. Sannen, M. Scibetta, F. Druyts, J. Tiliks; „Beryllium for breeder blankets – status of the European R&D“; Proceedings of 7th IEA Workshop on Beryllium, 29. Nov-2.Dec 2005, Santa Barbara, USA;
- [5] P. Kurinskiy, A. Moeslang, M. Klimiankou, A.A. Goraieb, "Production and characterisation of titanium beryllides"; Proceedings of 7th IEA Workshop on Beryllium, 29. Nov-2.Dec 2005, Santa Barbara, USA.

TTBB-006b

Helium Cooled: Thermo-mechanical Modelling of Pebble Bed Assembly

TW2-TTBB-006b D 2

Development of Pebble Beds Models

TW2-TTBB-006b D 3

Validation of Pebble Beds Models

In task TW2-TTBB-006b D2, a thermo-mechanical model for pebble beds is developed based on experiments at FZK. The current material model of pebble beds consists of a nonlinear elasticity law, Drucker-Prager-Cap theory, a modified creep law and strain-dependent thermal conductivity. In this investigation, a method of identification of material parameters has been proposed and implemented in ABAQUS USDFLD routines [1]. The comparison between experiments (oedometric compression and creep testing) and predictions of current material model has been made. A final report on this task has been submitted to EFDA in February, 2006 [2].

For validation purposes, task TW2-TTBB-006b D3 has been carried out. Two applications have been made in this investigation. The first one is the precompaction of the pebble bed assembly (PBA, NRG Petten [3]). The PBA is subjected to mechanical cycling and thermal cycling, and in the later case, only uniform heating has been considered. The purpose of this analysis is to show the capability of the material model.

The second validation example is the thermo-mechanical analysis of a breeder blanket sandwich structure, composed of layers of beryllium pebbles, EUROFER plates and Li_4SiO_4 pebbles. A non-uniform volumetric heating, according to the profile calculated by a 3300 MW fusion power (results from P. Pereslavitsev and U. Fischer, 2004, IRS, FZK), has been applied in the pebble layers, and the magnitude depending on the distance to the first wall is shown in Fig. 1.

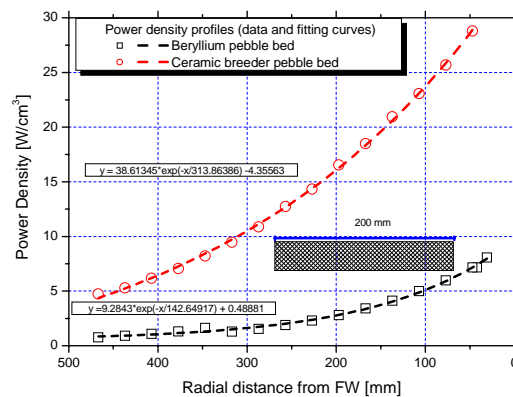


Fig. 1: The volumetric heating profile of the sandwich structure.

The calculation shows the stresses along the upper and lower symmetry axes decrease due to the increasing creep strains, as the sandwich structure is exposed to volumetric heating. Despite the complex distribution of strains, the stresses inside the pebble layers are comparably uniform. This phenomenon is consistent with the fact that the beryllium and ceramic breeder pebble layers are discrete materials, similar to sand and soil.

The final report on this task has been finalized in November, 2006.

Staff:

L.V. Boccaccini
Y. Gan
M. Kamlah
G. Rizzi

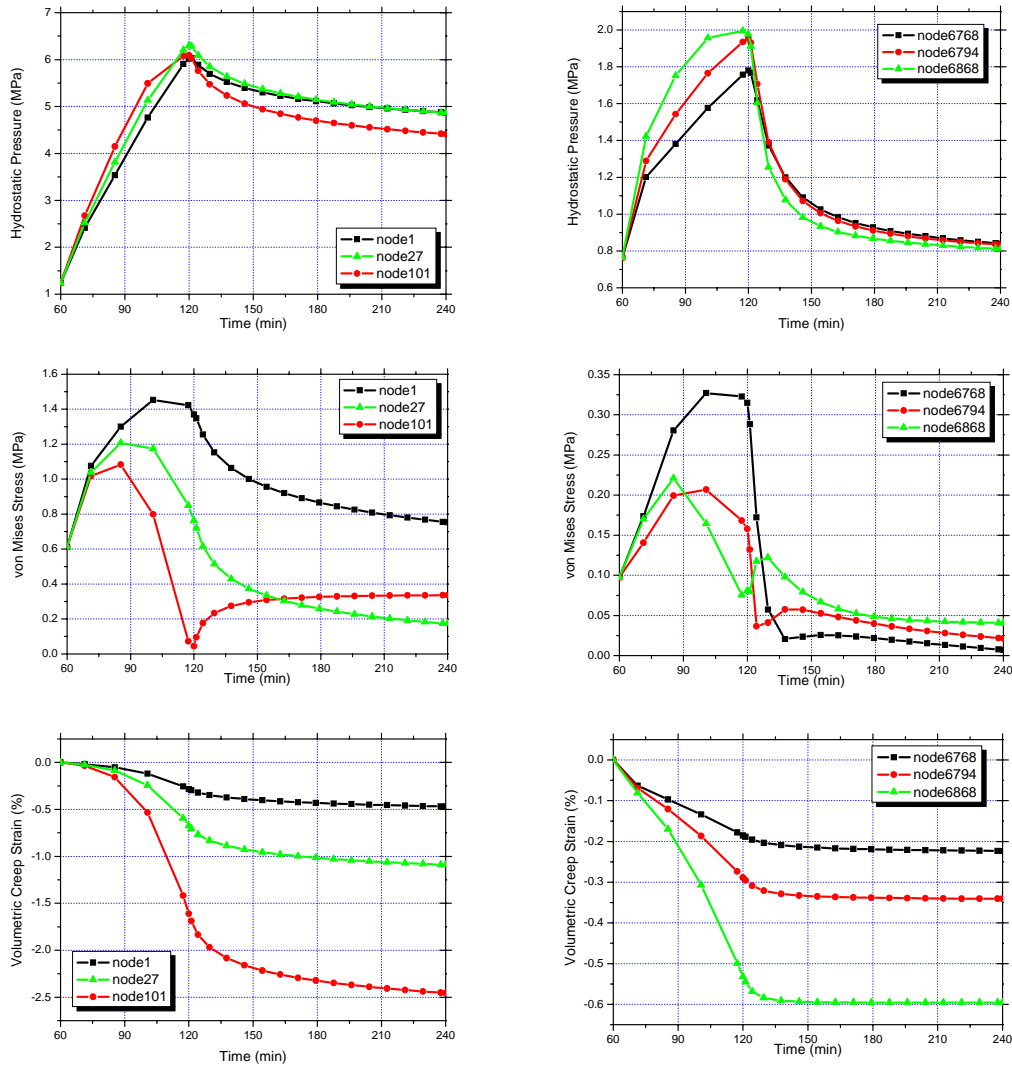


Fig. 2: The variables changing with time (min): nodes in Li₄SiO₄ in the left row and beryllium in right row; the first column, hydrostatic pressure (MPa); the second column, von Mises stress (MPa); the third column, volumetric creep strain (%).

Literature:

- [1] Y. Gan and M. Kamlah, Identification of material parameters of a thermo-mechanical model for pebble beds in fusion blankets, Fusion Engineering and Design In press (2006).
- [2] Y. Gan and M. Kamlah, Thermo-mechanical modelling of ceramic breeder and beryllium pebble beds, FZK Internal Report on TW2-TTBB-006b-D02, 2006.
- [3] [3] J. H. Fokkens, Thermo-mechanical finite element analysis of the HCPB in-pile test element, TW0-TTBB-004-D1, NRG Report 21477/02.50560/P, 2003.

**Breeding Blanket
HCLL Blanket Concept**

TTBA-006b
Water-Cooled: Magneto-Hydrodynamics

TW2-TTBA-006b D 1
Test and Modeling of Forced Convection MHD

The objective of the subtask is the investigation of liquid metal magnetohydrodynamic (MHD) flows in expansions or contractions which are major components of the currently considered HCLL concept. Experiments on MHD flows in a sudden expansion of conducting rectangular ducts have been performed in the MEKKA laboratory of the Forschungszentrum Karlsruhe to get insight into flow redistribution and additional pressure drop, caused by the presence of a strong magnetic field. Measurements of pressure variation along the axis, electric surface potential and local velocity have been performed using the eutectic alloy NaK as model fluid. The detailed results are used as test cases for the validation of computational tools required for a reliable prediction of MHD flows in complex blanket geometries.

Experimental and theoretical results

Electric potentials at the surface of the duct give essential information about the flow pattern inside. It can be shown that the velocity components in a plane perpendicular to the applied magnetic field are related to the potential ϕ as

$$u \approx \frac{\partial \phi}{\partial z}, \quad w \approx -\frac{\partial \phi}{\partial x},$$

i.e. the potential ϕ may serve as approximate hydrodynamic streamfunction of the flow. The distribution of surface potential is measured by more than 300 potential probes mounted on fiberglass plates around the test section. They are connected to a multiplexer that switches the large number of signals to a digital nano-voltmeter. Results have been recorded for various different strengths of the magnetic field, characterized by the non-dimensional Hartmann number Ha and different values of velocity expressed through the interaction parameter N that denotes the ratio of electromagnetic forces to inertia forces. A complete documentation of all results has been given by Bühler & Horanyi (2006). Here as an example, only one result for a high Hartmann number (strong magnetic field) is shown in Fig. 1 and compared with theoretical predictions of an asymptotic theory in Fig. 2.

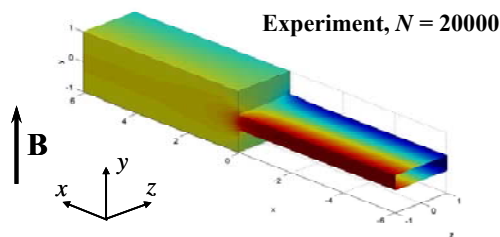


Fig. 1: Colored contours of surface potential measured at $Ha=5000$.

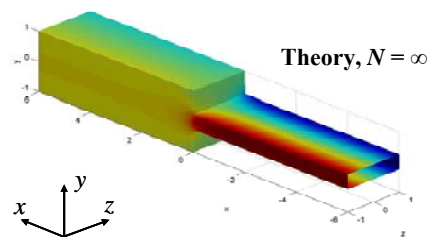


Fig. 2: Colored contours of surface potential calculated for $Ha=5000$.

In the small duct the velocity is higher. This leads to stronger transverse potential gradients in this part of the duct. Downstream the velocity and potential gradient are reduced. Near the expansion the isolines surface potential give a quite good indication how the fluid moves towards the sides.

Near the expansion, at $x=0$, a thin internal layer develops along magnetic field lines that collects all fluid from the upstream duct and transfers most of it also towards the sides. This layer becomes very thin depending on the Hartmann number. Axial and transverse profiles of velocity have been measured in this layer by a local probe that has been traversed through

the duct and results for $Ha=2000$ are shown as an example in Figs. 3-4. One can observe the high axial velocities u in thin layers along the side walls but also the high transverse velocities w along the layer, responsible for the mass transfer between the internal layer and the sides. More details on experimental results have been published by Bühler & Horanyi (2006) and details about numerical simulation have been shown by Bühler (2006) and Mistrangelo & Bühler (2006).

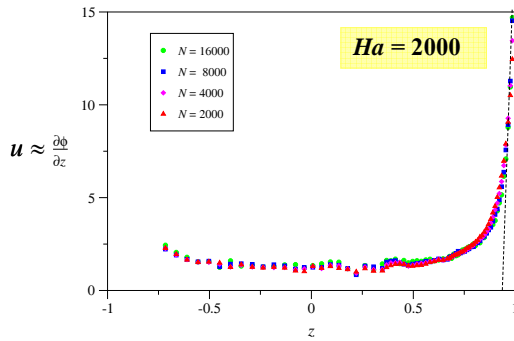


Fig. 3: Axial velocity profiles at $x=0$.

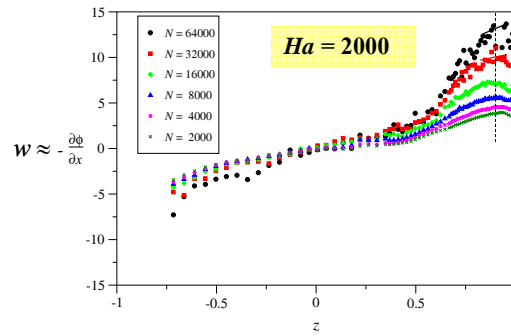


Fig. 4: Transverse velocity profiles at $x=0$.

Conclusions

Experiments on MHD flows in electrically conducting sudden expansions of rectangular ducts have been performed for high Hartmann numbers. The pressure distribution along the Hartmann wall and the distribution of wall potential has been measured up to values above $Ha=5000$. Results for pressure measurements give a clear indication that the total pressure drop contains an inertial contribution that may be quite significant for moderate N but which vanishes asymptotically as $N \rightarrow \infty$. However, even at the highest value investigated here, i.e. $N=39151$, a weak inertial contribution is still observable. For $N \rightarrow \infty$ the measurements confirm quite well the inertialess asymptotic predictions for pressure distribution.

Based on considerations of wall potential it is possible to identify the decreased velocity in the centre of the cores and the increased velocity closer to the side walls, when approaching the expansion. The profiles of side wall potential give further information about the distribution of the local side layer flow rates and indicate a strong side layer jet immediately behind the expansion. A comparison of measured and calculated surface potentials performed here at the symmetry plane of the side wall shows also good agreement.

Staff:

E. Arbogast
L. Bühler
 S. Horanyi
 C. Mistrangelo

Literature:

- [1] Bühler, L.: 2003, Magnetohydrodynamic flows in sudden expansions in strong magnetic fields, 4th International Conference on Electromagnetic Processing of Materials, Proceedings on CD-Rom, Lyon, 14-17 October 2003.
- [2] Bühler, L.: 2003, Inertialess magnetohydrodynamic flows in expansions and contractions, *Forschungszentrum Karlsruhe*, Technical report, FZKA 6904.
- [3] Bühler, L.: 2006, A parametric study of 3D MHD flows in expansions of rectangular ducts, Proceedings of the 17th Topical Meeting on the Technology of Fusion Energy, Albuquerque, November 2006.

- [4] Bühler, L., Arbogast, E. Gnieser, S., Horanyi, S., Stieglitz, R.: 2004, Design and construction of an expansion test section and first experiments, *Forschungszentrum Karlsruhe*, Internal report.
- [5] Bühler, L.; Horanyi, S. 2006, Experimental investigations of MHD flows in a sudden expansion, *Forschungszentrum Karlsruhe*, Technical report, FZKA 7245.
- [6] Bühler, L.; Horanyi, S.: 2006, Experimental investigation of liquid-metal flows through a sudden expansion at fusion-relevant Hartmann numbers, in: *Proceedings of the 6th Symposium On Fusion Technology*, Warsaw, September, 2006.
- [7] Horanyi, S.; Bühler, L.; Arbogast, E.: 2005, Experiments on magnetohydrodynamic flows in a sudden expansion of rectangular ducts at high Hartmann numbers. *Fundamental and Applied MHD: Joint 15th Riga and 6th PAMIR Internat.Conf.*, Riga *Jurmala*, LV, June 27 - July 1, 2005 Proc.Vol.1 p.243-46.
- [8] Mistrangelo, C.; Bühler, L.: 2005, Three-dimensional magnetohydrodynamic flows in rectangular channels under a non- uniform magnetic field. *Jahrestagung Kerntechnik 2005*, Nürnberg, 10.-12.Mai 2005 Berlin : IN-FORUM GmbH, 2005 p.483-86.
- [9] Mistrangelo, C.; Bühler, L.: 2005, Three-dimensional magnetohydrodynamic flows in sudden expansions. *Fundamental and Applied MHD: Joint 15th Riga and 6th PAMIR Internat.Conf.*, Riga *Jurmala*, LV, June 27 - July 1, 2005 Proc.Vol.1 p.239-42.
- [10] Mistrangelo, C.; Bühler, L.: 2006, Numerical and asymptotic analysis of liquid metal flows in rectangular sudden expansions, in: *Proceedings of the 6th Symposium On Fusion Technology*, Warsaw, September, 2006.

TTBC-006

Helium-Cooled Lithium Lead: Magneto-Hydrodynamics and Liquid Metal Materials

TW5-TTBC-006 D 1

MHD Experiments on a 3D Relevant Mock-up of the HCLL TBM

The objective of the subtask is to investigate experimentally the magnetohydrodynamic (MHD) flow in a TBM-relevant test section for a Helium Cooled Lead Lithium (HCLL) blanket, in which a number of breeder units arranged in columns are fed with liquid metal through poloidal manifolds. The breeder units have common, electrically conducting walls, through which an electrical coupling of neighboring flow regions is possible. As a result, the flow in each sub-channel is influenced by the flow in all the other flow regions. A full theoretical description of such electrical coupling is difficult so that major conclusions about 3D MHD flows in a TBM should be drawn from an experiment.

In 2006 a test section for experimental investigations of fusion relevant MHD flows in HCLL breeder units and their poloidal manifolds has been completed and installed into the liquid metal loop in the MEKKA laboratory at the Forschungszentrum Karlsruhe. The test section connected with the liquid metal loop is shown in Fig. 1 in front of the magnet. The available pressure measuring system had to be extended in order to handle the large number of pressure taps. This required severe changes in the whole control system of the facility since an extension of the existing one was not possible. For that reason it was decided to abandon the old system and to install a modern SPS that allows arbitrary extension and access to the control and data acquisition from a PC. Now the new control system is in operation, the test section is ready so that first tests with liquid metal flows can be performed soon.



Fig. 1: MHD mock up connected to the liquid metal loop, here positioned in front of the magnet.

Numerical modeling for the MHD mock-up

The flow in an entire cross section of the MHD module has been modeled for the exact geometry derived from the CEA TBM design. In the analysis 4 breeder units have been considered. They are separated from each other by the so-called stiffening plates (SP). Each breeder unit contains 6 sub-channels created by the presence of the cooling plates. All walls are electrically conducting and have to be properly resolved by the computational grid as well as all viscous boundary layers along the walls.

Results for velocity in the 4 breeder units and in 24 sub-channels are shown in Fig. 2 as colored contours and as velocity profiles in the mid-plane along the poloidal direction. It is found that the presence of stiffening plates introduces strongest deformations on the velocity profile in the outer sub-channels of each breeder unit. The influence by the cooling plates on the velocity profile is also visible but much less pronounced. The deformations in the velocity profile are caused by the disturbance of electric current density due to the presence of the electrically conducting stiffening plates and cooling plates. Results for various parameters and more general orientation of the magnetic field will be published in an upcoming technical report.

Staff:

H.-J. Brinkmann
L. Bühler
S. Horanyi
C. Mistrangelo
C. Polixa
J. Rey
K. Starke

Literature:

- [1] L. Bühler, S. Horanyi, C. Polixa, J. Rey; 2005, Interim Report 2005-1 Design and fabrication of a MHD mock-up for a HCLL TBM, FZK-Internal report 2005.
- [2] Bühler, L. 2005 Magnetohydrodynamic pressure-driven flows in the HCLL blanket, Fusion Engineering and Design, Volumes 75-79, November 2005, 923-926.
- [3] Bühler L. Horanyi S., Polixa C. Rey J. 2005, Design and fabrication of a MHD mock-up for a HCLL TBM, FZK-internal report 2005
- [4] Reimann, J.; Bühler, L.; Molokov, S.: 2005, Magnetohydrodynamic issues of the HCLL blanket. 7th Internat. Symp. on Fusion Nuclear Technology (ISFNT-7), Tokyo, J, May 22-27, 2005.
- [5] Bühler, L.; Wetzell, C.: 2005, Asymptotic analysis of 3D buoyant magnetohydrodynamic flows in strong magnetic fields. Fundamental and Applied MHD: Joint 15th Riga and 6th PAMIR Internat. Conf., Riga Jurmala, LV, June 27 - July 1, 2005 Proc. Vol.1 S.235-38.
- [6] Bühler, L.; Giancarli, L.: 2005, Magnetohydrodynamic flow in the European HCLL blanket concept. Wissenschaftliche Berichte, FZKA-7069.

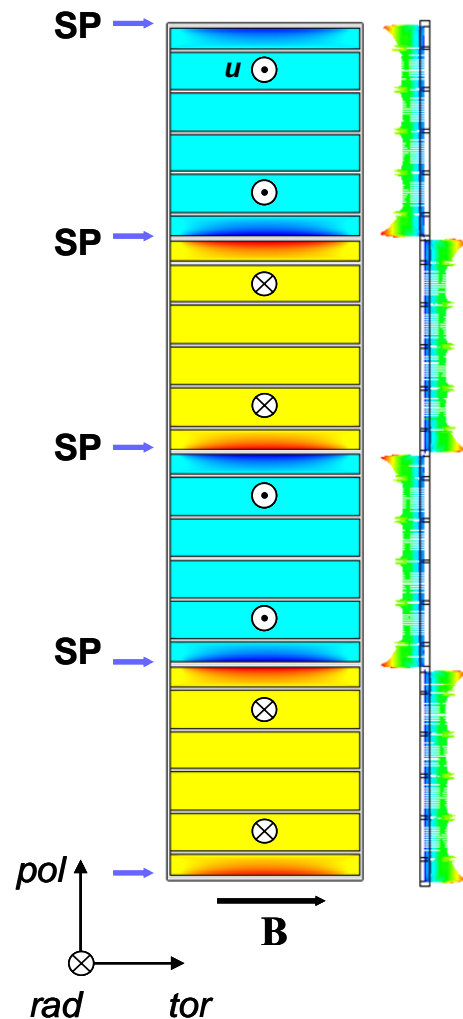


Fig. 2: Contours of radial velocity and velocity profiles (right) for a model with four breeder units.

Materials Development Structural Materials

EFDA/05-1244 (TW4-TTMS-RedAct) Investigation of Options to Reduce Critical Elements in Low Activation Ferritic/Martensitic Steels

In the last few years considerable improvement has been made in the definition and fabrication of 'reduced activation' ferritic-martensitic steels (RAFM). Two batches of a 9CrWVTa-steel called EUROFER 97 and EUROFER 97-2, respectively, and including 10 heats were produced by Boehler in 1999 and by SaarSchmiede in 2003. The production has demonstrated that RAFM steels can successfully be produced at industrial scale. The steels, nominally according to the same specification, actually differ in the detailed contents of minor alloying elements and of impurities. All met the goal of an overall low content of those detrimental elements with respect to the long-term activation behaviour. Thereby, a remarkable step is achieved towards the final goal of the production of 'low activation' steels for the use in a DEMO (demonstration reactor). Studies for further reduction of impurities need to be launched as a generic property of RAFM steels.

The objectives of this task are

- To identify a number of critical elements that should be further reduced to a certain level for the EUROFER 97 technical specification.
- To assess in cooperation with steel producers the technical feasibility.
- To define the specifications of a new heat (or a series of heats) to be produced.
- To determine in cooperation with the steel producers the uncertainty range in the concentrations of the various elements (alloying elements and impurities) in the heat.
- To determine the different and likely increasing costs of the heats with reduced impurity levels.
- To produce this material by industry at the smallest amount that is acceptable.
- To analyse by different laboratories (i.e. the steel producers and qualified EU/EFDA associations) and different methods, the chemical composition of the material produced up to now and from the new melts.

In order to qualify laboratories well in advance, a Round Robin should be organized where a 'blind test' of a laboratory heat is going to be analysed for a list of critical elements to be specified in advance.

Status of work

A comparison of the chemical composition as specified in the technical specification for EUROFER 97 and EUROFER 97-2 and the results achieved in the industrial production of the different products has been performed and the reasons for occurring deviations from the specifications have been analysed. A web-based version of the FISPACT 2005 code has been implemented and numerous calculations with varied compositions of EUROFER have been performed to check the influence of different radiologically undesired elements [1] (Nb, Mo, Al, Ni, Cu, Co) on the activation behaviour of the steel.

Fig. 1 shows a comparison of the activation behaviour of different EUROFER batches with the specified composition and the real composition of the different products as reported in [2]. The calculations of the surface γ -dose rate were performed considering irradiation in a First Wall DEMO spectrum (12.5 MWa/m^2). "EUROFER 97 theor." uses a composition with very low amounts of radiologically undesired elements as suggested in [1].

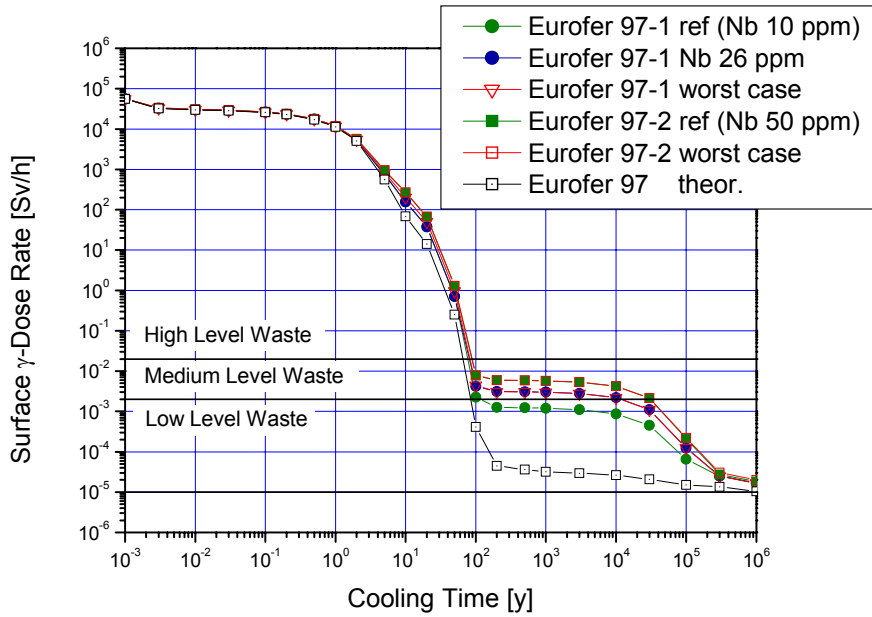


Fig. 1: Calculated γ -surface dose rate of different EUROFER 97-1 and EUROFER 97-2 variants and EUROFER 97 theor. after irradiation in a First Wall DEMO spectrum (12.5 MWa/m^2). Included are also calculations for the max. observed content of elements beyond the specification limits for the two specifications (see [2]).

According to the calculations only EUROFER 97-1 ref, passing the Low Level Waste activation level after about 100 years, can be regarded as reduced activation material. EUROFER 97-2 ref, needs about 30,000 years to fall below this limit. The main originator for that behaviour is niobium, the content of which is 5 times higher for EUROFER 97-2 ref than for EUROFER 97-1 ref, as can be seen also in Fig. 2.

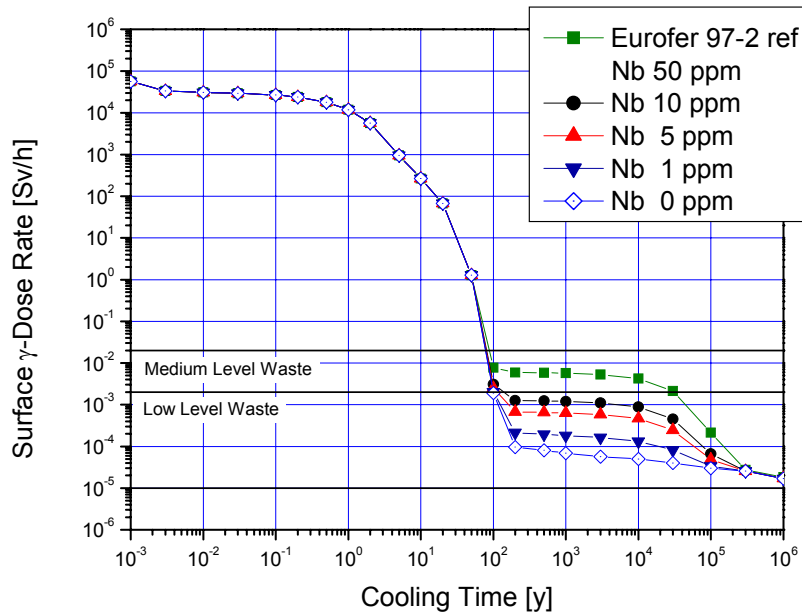


Fig. 2: Calculated γ -surface dose rate of EUROFER 97-2 ref after variation of Nb-content after irradiation in a First Wall DEMO spectrum (12.5 MWa/m^2) - as in Figure 1. Included are also calculations for Nb=zero.

Here the Nb content of EUROFER 97-2 was systematically varied leaving the rest of the chemical composition unchanged. The same calculations were performed with the other undesired elements in the same manner. It turned out, that minimising the Nb content is the most effective way to reduce the activation level for longer times.

On the basis of the above mentioned calculations trial heats can be specified. Input for an Art. 7 contract for the cooperation with steel manufacturers has been given. A call for tender has been launched and a manufacturer, experienced in the production of RAFM steels, was selected as industrial partner for the production of trial heats and performance of the above mentioned study.

Staff:

R. Lindau
C. Adelhelm
T. Kaiser

Literature:

- [1] Lindau, R.; Möslang, A.; Rieth, M.; Klimiankou, M.; Materna-Morris, E.; Alamo, A.; Tavassoli, A.-A. F.; Cayron, C.; Lancha, A.-M.; Fernandez, P.; Baluc, N.; Schäublin, R.; Diegele, E.; Filacchioni, E.; G.Rensman, J.-W.; v.d. Schaaf, B.; Lucon, E.; Dietz, W.; Present Development Status of EUROFER and ODS-EUROFER for Application in Blanket Concepts, Fusion Engineering and Design, 75-79 (2005) p.989-996
- [2] S. Kelzenberg; Berechnung und experimentelle Verifizierung von Materialaktivierungen in D-T Fusionreaktoren, Dr.-Thesis, FZKA Report 5836 (November 1996) p. 48
- [3] Lucon, E.; Benoit, P.; Jacquet, P.; Diegele, E.; Lässer, R.; Alamo, A.; Coppola, R.; Gillemot, F.; Jung, P.; Lind, A.; Messoloras, S.; Novosad, P.; Lindau, R.; Preininger, D.; Klimiankou, M.; Petersen, C.; Rieth, M.; Materna-Morris, E.; Schneider, H.C.; Rensman, J.W.; van der Schaaf, B.; Singh, B.K.; Spätig, P.; The European effort towards the development of a DEMO structural material: irradiation behaviour of the European reference RAFM steel EUROFER. Fusion Engineering and Design 81(2006) S.917-23

TTMS-001 Irradiation Performance

TW2-TTMS-001b D 5 Tensile, Charpy and Fatigue Specimen Testing after Neutron Irradiation up to 15 dpa in the Range of 250°C-450°C

Objectives

Withstanding high neutron and heat flux is a crucial prerequisite for material qualification for future fusion reactors. Reduced activation ferritic/martensitic (RAFM) steels are promising structure materials for the first wall and blanket applications. Although RAFM 10%CrWVTa steels (OPTIFER, F82H) exhibits clearly better irradiation performance compared to the modified commercial 10-11%-Cr-NiMoVNb alloys (MANET), the hardening induced by neutron irradiation accompanied by the embrittlement and by reduction of toughness still remain a main concern, thus indicating a further need of material improvement.

The operating temperatures of conventional RAFM steels are limited to about 550°C. The structure materials with higher operating temperatures, however, are required in order to increase the efficiency of the future power plants. Oxide dispersion strengthened (ODS) RAFM steels are attractive candidates for structure materials with elevated operating temperatures up to approximately 650°C.

Transmutation helium generated in the future fusion reactor structure materials exposed to 14MeV neutrons is believed to strongly influence material embrittlement behaviour. As fission reactors do not provide with fusion adequate He/dpa ratios, the role of He is often studied in different simulation experiments (e.g. doping with boron).

In the SPICE irradiation program the emphasis is put on the investigation of irradiation induced embrittlement and hardening in the newly developed reduced activation steel EUROFER 97 for different heat treatment conditions (EUROFER 97 ANL: 980°C/0.5 h + 760°C/1.5h and EUROFER 97 WB: 1040°C/0.5 h + 760°C/1.5 h) and for HIP powder steels. The embrittlement behaviour of EUROFER 97 is compared with the results on international reference steels included in the SPICE project. A role of He in a process of non hardening embrittlement is investigated in EUROFER 97 based steels, that are doped with different contents of natural boron and the separated ¹⁰B-isotope (0.008-0.112 wt.%).

Work Performed in Previous Reporting Periods

Irradiation was performed in the Petten High Flux Reactor within the HFR Phase-IIb (SPICE) project to a nominal dose of 15 dpa at 250, 300, 350, 400, and 450°C. Three specimen types: Charpy V specimens of KLST type, tensile specimens and fatigue specimens have been loaded into three sodium filled specimen holders coded as 329-01 (SPICE-C), 330-01 (SPICE-T) and 331-01 (SPICE-F), respectively. A total of 130 Charpy, 91 tensile and 160 fatigue specimens were involved. Irradiation at five different target temperatures (i.e. 250, 300, 350, 400, and 450°C) has started on 2001, August 8th, and ended after 771 full power days (31 reactor cycles) on 2004, May 24th. An average dose level of 16.3 dpa in steel has been reached according to HFR-TEDDI calculations (NRG). The specimens have been transported for the second decontamination into the hot cells of the fusion material laboratory of the institute in December 2004. The instrumented impact tests on irradiated KLST specimens (L-T orientation) have been carried out with a newly built impact facility installed in the hot cells.

Irradiation Performance of RAFM Steels

The hardening vs. embrittlement behaviour was quantified in terms of the hardening shift coefficient C defined as $C = \Delta DBTT / \Delta \sigma$, where both $\Delta DBTT$ and $\Delta \sigma$ are obtained by instrumented impact tests. Figure 1 displays this parameter for two test temperatures: a) RT (C_{RT}) and b) 100-120°C (C_{100}). At $T_{irr} \leq 350^\circ\text{C}$, the coefficient C_{100} varies between $0.17 \leq C_{100} \leq 0.53^\circ\text{C}/\text{MPa}$, which is in good agreement with the analysis of 7-9% Cr RAFM steels in the literature ($C = 0.38 \pm 0.18^\circ\text{C}/\text{MPa}$) and indicates that embrittlement is dominated by a hardening mechanism. At these low temperatures hardening is mainly of displacement damage nature. The coefficient C_{100} tends to increase at $T_{irr} = 400^\circ\text{C}$ and suggests a non-hardening embrittlement (NHE) mechanism that primarily occurs under thermal aging conditions. Depending on the nature of the dominating NHE mechanism, the coefficient C may become large, very small or even negative at $T_{irr} \geq 400^\circ\text{C}$ in case of material softening. Such behavior was indeed observed for EUROFER97 ANL, EUROFER97 WB and GA3X in Fig. 1.

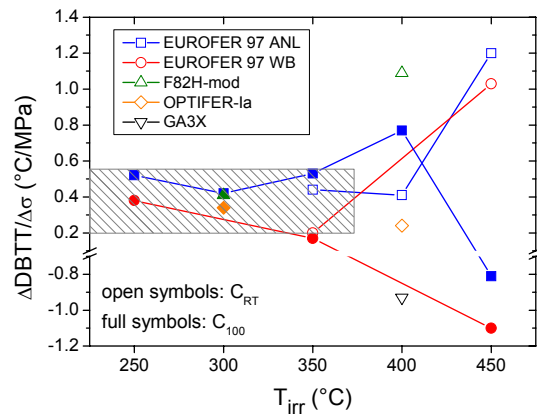


Fig. 1: Hardening shift coefficient C vs. irradiation temperature; open symbols: C_{RT} , full symbols C_{100} , see text for explanation. Dashed area indicates scattering band for $C = 0.38 \pm 0.18^\circ\text{C}/\text{MPa}$ from literature.

Hipped ODS EUROFER with 0.5 wt.% Y_2O_3 showed not satisfying impact properties already in the unirradiated condition characterized by low USE = 2.54 J and large DBTT = 135°C, see Fig. 2. Furthermore, the increase of USE for irradiation temperatures below $T_{irr} \leq 350^\circ\text{C}$ indicates not optimized fabrication process. At low irradiation temperature ($T_{irr} = 250^\circ\text{C}$) neutron irradiation induced shift in DBTT is comparable to that of the base EUROFER steel. At higher irradiation temperatures, however, hipped ODS EUROFER shows larger embrittlement compared to base metal.

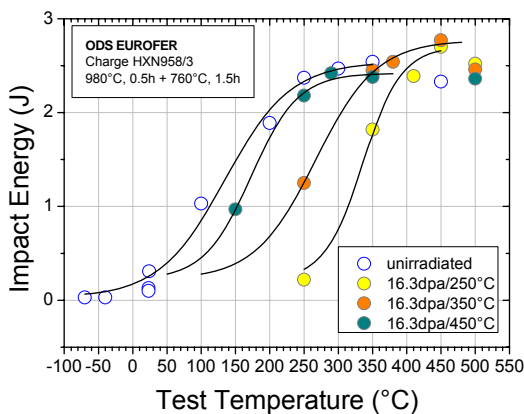


Fig. 2: Charpy impact energy vs. test temperature for unirradiated and 16.3 dpa (average) irradiated ODS EUROFER.

Comparative studies of the EUROFER97 based heats doped with 82 wppm natural boron ($0.2^{10}\text{B} + 0.8^{11}\text{B}$) and with 83 wppm separated ^{10}B isotope proved ^{10}B doped steel to be more susceptible to irradiation embrittlement, see Fig. 3. Boron mediated enhancement of irradiation induced DBTT shift is relatively high at irradiation temperatures below $T_{irr} \leq 350^\circ\text{C}$ and remarkably reduces at $T_{irr} = 450^\circ\text{C}$. Experimental heat doped with 1120 wppm separated ^{10}B isotope showed degraded impact properties already in the unirradiated condition. Irradiation induced DBTT shift of this heat could not be quantified due to large embrittlement found in the investigated temperature range.

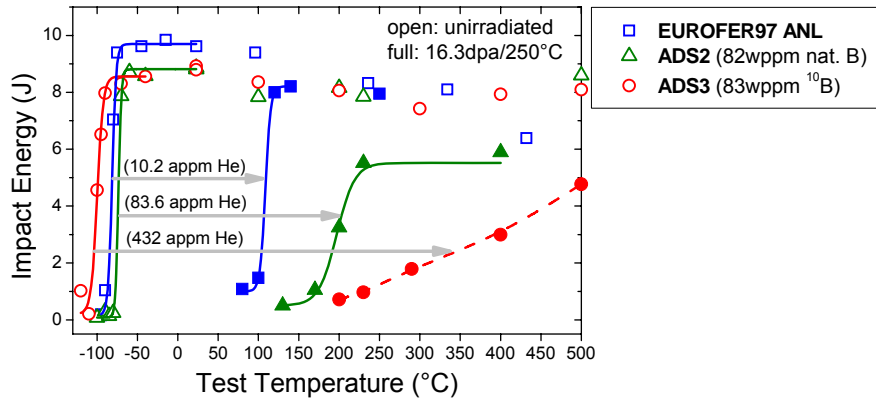


Fig. 3: Charpy impact energy vs. test temperature for unirradiated and irradiated EUROFER97, ADS2 and ADS3 steels. The arrows indicate the irradiation induced DBTT shifts. Produced He amounts due to ^{10}B burn-up are indicated in the parentheses.

Conclusion

Analysis of hardening vs. embrittlement behaviour of RAFM steels indicated hardening dominated embrittlement at $T_{\text{irr}} \leq 350^\circ\text{C}$ with $0.17 \leq C_{100} \leq 0.53$ °C/MPa. Charpy impact testing of EUROFER ODS HIP with 0.5 wt.% Y_2O_3 showed not satisfying results. Improvement of the impact properties will be main prerequisite for material qualification for future fusion reactors.

EUROFER based steels doped with different contents of natural boron and the ^{10}B -isotope (0.008-0.112 wt.%) were investigated in Charpy impact tests with respect to their irradiation performance. Boron doped steels showed up progressive embrittlement and degraded toughness with generated He amount.

The investigations of mechanical properties are continued with tensile tests. First data show in EUROFER ODS HIP a much better behaviour during tensile load. The reduction of ductility is much less than observed in the steel alloys. The analysis of the tensile data begins and will be reported in the next year. The ADS alloys are in this irradiation program to determine the boron distribution in the matrix, the difference between natural boron and the isotope ^{10}B , as the influence on fracture behaviour. The most information will be obtained by post-irradiation examination.

Staff:

J. Aktaa
 B. Dafferner
E. Gaganidze
 S. Lautensack
E. Materna-Morris
 H. Ries
 R. Rolli
 H.-C. Schneider

Literature:

- [1] E. Gaganidze, H.-C. Schneider, B. Dafferner, J. Aktaa, High-dose neutron irradiation embrittlement of RAFM steels, J. Nucl. Mater. 355 (2006) 83–88.

- [2] E. Gaganidze, B. Dafferner, J. Aktaa, Neutron Irradiation Resistance of RAFM Steels, MRS2006 Fall Meeting, Boston, MA, November 27 – December 1 (2006).
- [3] E. Materna-Morris, R. Rolli, H.-C. Schneider, and A. Möslang: Strengthening of Low-Activation 8-10% Cr Steels after Neutron Irradiation at Lower Temperatures. 5th Brazilian MRSMeeting 2006, Florianopolis, Brazil, October 8 – 12, 2006.

TW2-TTMS-001b D 9

Fast Reactor Irradiation up to 30 dpa, at 340°C of Tensile, Charpy and LCF RAF/M Specimens, Completion of the PIE

Objectives

In an energy generating fusion reactor structural materials will be exposed to very high levels of irradiation damage of about 100 dpa. Due to the fact, that fast reactor irradiation facilities in Europe are not available anymore, a co-operation with the Russian institution SSC RF RIAR has been implemented. The irradiation project is named "ARBOR-1" (Latin for tree). Impact, tensile and low cycle fatigue specimens of Reduced Activation Ferritic/Martensitic steels, e.g. EUROFER 97, F82H mod., OPTIFER IVc, EUROFER 97 with different boron contents and ODS-EUROFER 97 have been irradiated in a fast neutron flux (> 0.1 MeV) of 1.8×10^{15} n/cm²s at a temperature less than 340°C up to ~ 30 dpa. Mechanical PIE is under way at SSC RF RIAR

Status end of 2005

The modernized LCF-testing facility and the instrumented Charpy testing facility for KLST specimens under remote handling conditions are installed, calibrated and operating in the hot cells of SSC RF RIAR. All impact tests have been performed and the tensile testing was started.

PIE of ARBOR-1

The mechanical PIE of ARBOR-1 specimens is performed at material science laboratory of SSC RF RIAR. Due to the fact that tensile test results are complete now and low cycle fatigue tests started in December 2005, we concentrate here on tensile and LCF data. The tensile and LCF tests are performed with a modernized tensile and LCF testing facility of INSTRON-DOLI 1362 type, equipped with a 100 KN load cell, a high temperature furnace and a strain measurement system, installed in the K-12 hot cell of the SSC RF RIAR.

The ARBOR-1 tensile tests have been performed on mini-tensile-LCF specimens. But for comparison three different kinds of types were utilized in the different reference irradiations. NRG [1] irradiated cylindrical specimens of 20 mm gauge length and 4 mm diameter and performed the tests with a strain rate of 5×10^{-4} s⁻¹. In the SPICE irradiation [3] cylindrical specimens of 18 mm gauge length and 3 mm diameter are tensile tested under vacuum with a strain rate of 10^{-4} s⁻¹. In the 15 dpa BOR 60 irradiation [4] cylindrical specimens of 15 mm gauge length and 3 mm diameter are tensile tested with a strain rate of 3×10^{-3} s⁻¹.

In the ARBOR-1 irradiation cylindrical specimens of 7 mm gauge length and 2 mm diameter are tensile tested with a strain rate of 3×10^{-3} s⁻¹. From the load-displacement curves strength and strain data are calculated: 0.2% offset Yield Stress ($R_{p0.2}$), Ultimate Tensile Strength (R_m), Uniform Strain (A_g) and Total Strain (A). Since the most considerable changes due to irradiation are found in the ($R_{p0.2}$)- and (A_g)-values only these quantities are reported here. Even if one takes into account that the tensile testing conditions are slightly different, from Figs. 1 and 2 an increase of the Yield Stress and a decrease in Uniform Strain with increasing irradiation damage can be detected.

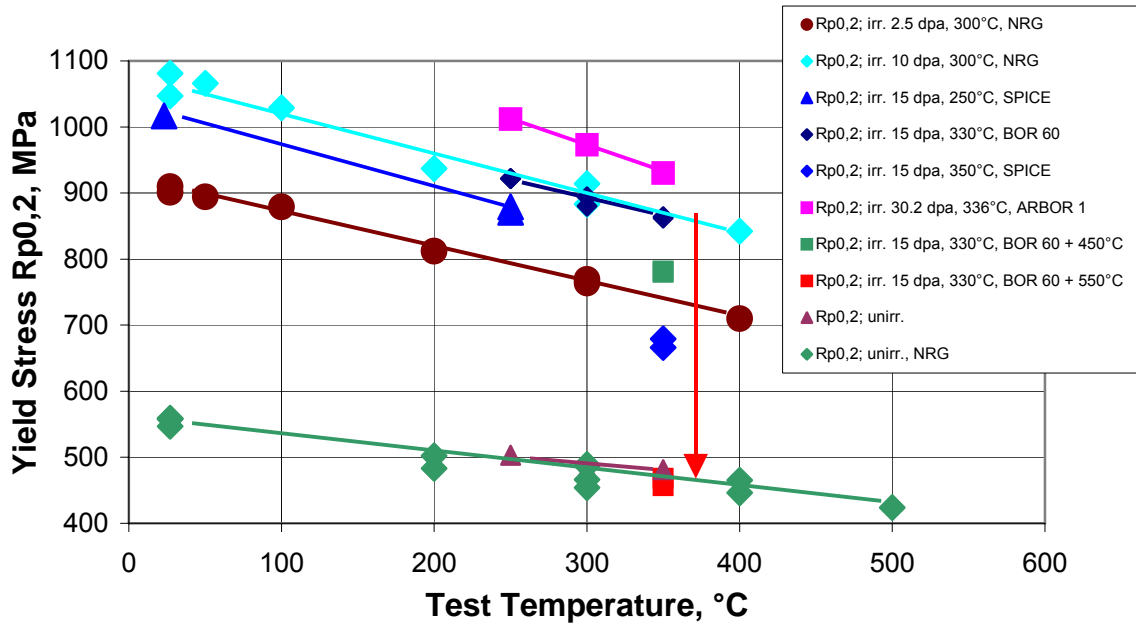


Fig. 1: Yield Stress ($R_{p0,2}$) behaviour of irradiated EUROFER 97 on dependence of test temperature compared to unirradiated data (the temperature in the legend indicates the irradiation temperature).

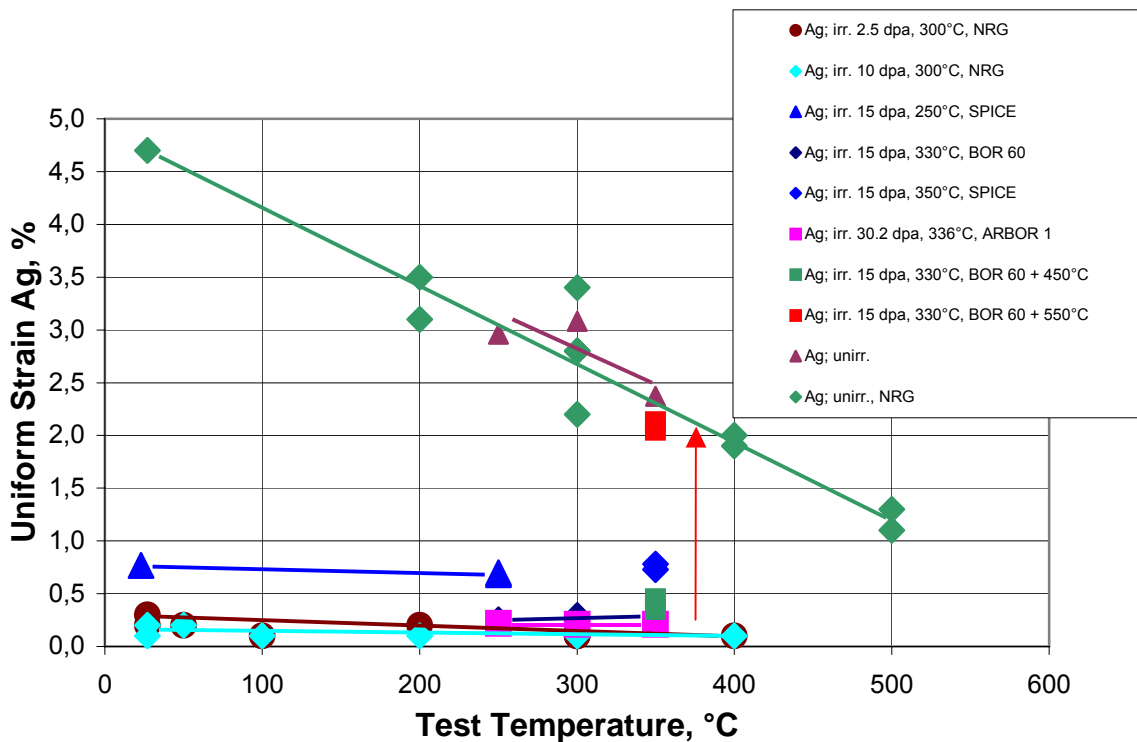


Fig. 2: Uniform Strain (A_g) behaviour of irradiated EUROFER 97 on dependence of test temperature compared to unirradiated data (the temperature in the legend indicates the irradiation temperature).

So the 2.5 dpa damage has the lowest increase of around 300 MPa in Yield Stress and the 30.2 dpa damage the highest increase of around 460 MPa in Yield Stress, that is nearly a duplication of the unirradiated quantity. The effect of the irradiation damage on the Uniform Strain is also considerable - mostly A_g - values below 0.5 % are reached - but does not depend as much on the damage dose as the stress values.

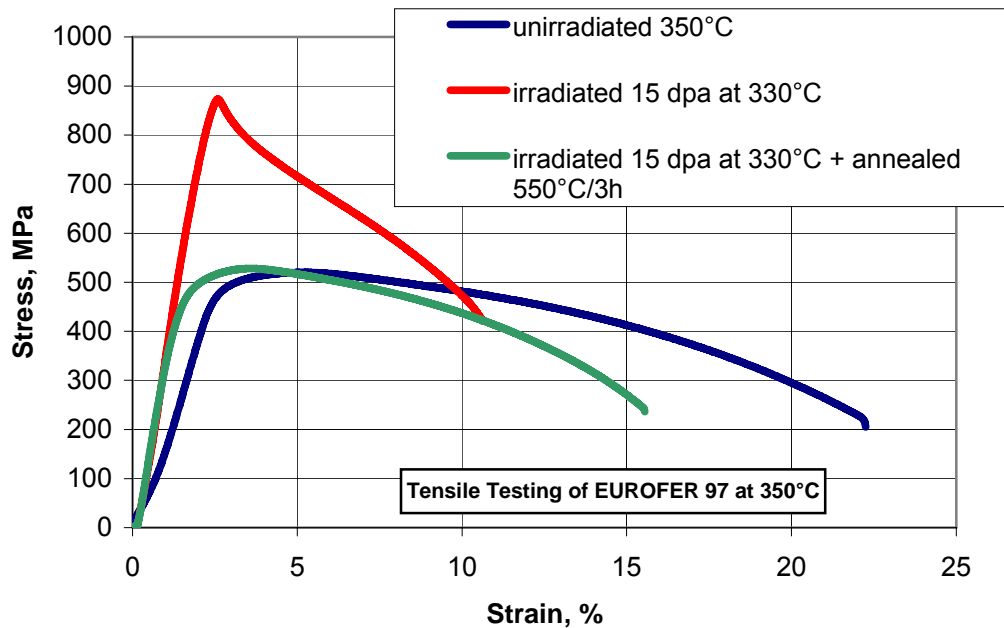


Fig. 3: Comparison of the stress-strain behavior of 15 dpa irradiated EUROFER 97 to unirradiated and postirradiation annealed data.

An exemplary postirradiation annealing experiment after the 15 dpa BOR 60 irradiation for 3 hours at 450°C or 550°C lead to the possibility to heal irradiation damage. But only at 550°C the Yield Stresses and Uniform Strains reached again nearly virgin values (see Fig. 3 and red arrows in Figures 1 and 2).

Staff:

B. Dafferner
M. Klotz
C. Petersen
M. Walter
M. Lerch

Literature:

- [1] Rensman J., et al., "Characteristics of unirradiated and 60°C, 2.7 dpa irradiated Eurofer 97", J. Nucl. Mater., 307 - 311 (2002) 250 – 255.
- [2] Rensman J.W., "NRG irradiation testing: report on 300°C and 60°C irradiated RAFM steels", Final report on the EFDA Tasks TW2-TTMS-001a D 6 and TW2-TTMS-001b D 12, (2005).
- [3] Schneider H.-C., et al., "HFR irradiation programme", Scientific Report FZKA 7117, (2004)
- [4] Petersen C., et al., "The WZ 01/577 Reactor Irradiation in BOR 60", personnel communication, (2004)
- [5] C. Petersen, A. Povstyanko, V. Prokhorov, A. Fedoseev, O. Makarov and B. Dafferner: "Mechanical Property Degradation of Ferritic/martensitic Steels after the Fast Reactor Irradiation "ARBOR 1", to be published in Journal of Nuclear Materials, Special Edition of ICFRM 12.

- [6] O. Makarov, A. Povstyanko, V. Prokhorov, A. Fedoseev, S. Kuzmin and C. Petersen: "Mechanical Testing Methods in RIAR Hot Cells for Sub-Sized Specimens of Fusion Reactor Materials", presented in the plenary meeting of the "European Working Group on Hot Laboratories and Remote Handling", HOTLAB 2006, 19.-21.9,2006, Jülich, Germany.
- [7] C. Petersen, J. Aktaa, E. Diegele, E. Gaganidze, R. Lässer, E. Lucon, E. Materna-Morris, A. Möslang, A. Povstyanko, V. Prokhorov, J.W. Rensman, B. van der Schaaf and H.-C. Schneider: "Mechanical Properties of Reduced Activation Ferritic/Martensitic Steels after European Reactor Irradiations", to be published in the Proceedings of 21. IAEA Fusion Energy Conference, 16.-21.10.2006, Chengdu, China.

TW4-TTMS-001 D 1

TW5-TTMS-001 D 2

Fabrication and Irradiation of Fe-54 Enriched Samples to Study the Influence of He/dpa Ratio on Materials Degradation up to Medium Dose Level

Overview

The structure components of future fusion reactors will suffer from specific irradiation damage, i.e. the ratio of helium production (in appm) to displacement rate (in dpa) varies around 10 appm He/dpa. Due to the lack of appropriate high energy neutron sources there seems to be only one promising way to generate such irradiation damages in a RAFM steel with common in-pile fission reactor irradiation experiments: If the content of natural iron would be replaced by the stable isotope Fe-54, helium production would be stimulated by the according (n, alpha) reactions. A significant advantage over the alternative boron-10 helium production technique would be a uniform helium distribution through the whole matrix.

Therefore, the goal of the task is to produce a heat similar to EUROFER using Fe-54 instead of natural iron. Then miniaturized Charpy and tensile specimens with cores of Fe-54 substituted EUROFER steel have to be fabricated. Finally some of the specimens will be used to perform instrumented Charpy and tensile tests, the remaining specimens will be provided for an according irradiation program which has to be planned and managed. The whole production, processing and testing procedures have to be accompanied by chemical and microstructural examinations.

Initial Status

A number of different pre-tests finally led to a more simplified production of the desired EUROFER plate as was planned initially. Casting the heat into a suitable mould spared further forging or rolling. In a first step all alloy components were molten to pellets in an arc melting furnace. Natural iron was included as powder comparable to the final Fe-54 isotope. The other components were available in form of foliages, small pieces, or powder. Applying this first melting step separates oxide layers and other impurities from the initial alloying components. After that the pellets were molten in a conduction furnace within a ceramic crucible in argon environment. The resulting heat was then cast into a copper mould. Thickness and width were adapted to the desired plate dimensions. Chemical analysis of the first two experimental melts showed that the chromium content was too high while the content of C and N was too low in the experimental heats. Some other elements were slightly out of the specification limits but their level would be still tolerable.

Progress

The chemical composition has been optimized by producing two further melts. With that, the whole production process was tested and verified. In the meantime 391 g of Fe-54 isotope arrived from Russia. The quality of the isotope powder was determined. With an amount of 99.5 wt.% ⁵⁴Fe (0.5 wt.% ⁵⁶Fe, 0.005 wt.% ⁵⁷Fe, 0.002 wt.% ⁵⁸Fe) and with impurities of only 0.37 wt.% O and 0.017 wt.% C the powder is fully within the specifications.

A first melt with about 200 g of the Fe-54 isotope was prepared. But unfortunately, just before casting the heat into the mold the ceramic crucible broke into pieces (Fig. 1 A). Then the valuable heat flowed over graphite isolation and solidified mainly around the cooling coils of the furnace. Most of the material could be restored (see Fig. 1 B) but the chemical composition changed significantly due to the contact with graphite, i.e. the carbon content ended at about 4 wt.%. After that accident a lot of different decarbonization treatments have been tested and analyzed. At the moment it seems that a significant reduction is possible by repeated melting in either normal atmosphere or under hydrogen-argon mix. In addition, we

have tried to find more reliable crucibles and the volume of the melt has been reduced as well.

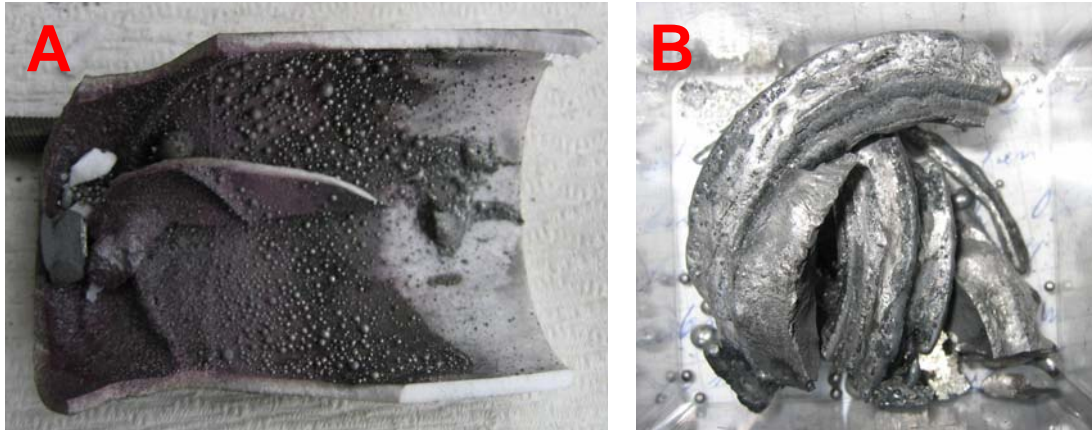


Fig. 1: (A) Broken aluminium-oxide crucible;

(B) Remaining parts of the Fe-54 heat.

With new parameters and with a BN crucible, another Fe-54 EUROFER heat was produced using about 100 g of the isotope. Figure 2 demonstrates the success of the fabrication process. The next steps are a complete chemical analysis and the start of specimen fabrication. For this, welding tests have been performed. The most suitable fabrication method is EB welding, as is illustrated in Fig. 3.



Fig. 2: (A) Crucible and copper mould after casting the heat;

(B) The resulting Fe-54 heat.

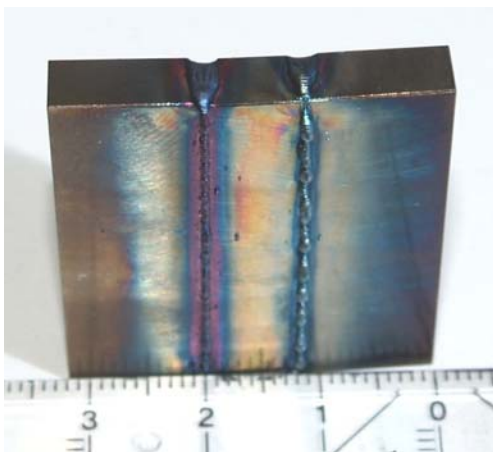


Fig. 3: Test piece of the planned Fe-54 heat specimen fabrication method. To spare the valuable Fe-54 isotope alloy, a centre stripe of the isotope alloy is elongated by two stripes of normal EUROFER. The joints are fabricated by EB welding.

The irradiation is foreseen to take place in the HFIR reactor of ORNL and, if possible, in the Petten HFR. A detailed irradiation program will be elaborated after the specimen fabrication is completed.

Conclusions and Outlook

It has been finally demonstrated that it is possible to fabricate proper Fe-54 EUROFER plates in the proper dimensions by pre-melting, re-melting, and casting. After successful decarbonization of the failed heat, the specimen fabrication may be completed and planning for irradiation campaigns may be started.

Staff:

C. Adelhelm
B. Dafferner
A. Falkenstein
P. Graf
S. Heger
U. Jäntschi
A. Möslang
M. Rieth
P. Vladimirov
H. Zimmermann

TW5-TTMS-001 D 4

TAP (Tomography Atomic Probe) Analysis of EUROFER Material Irradiated in the ARBOR Irradiation Campaign

Introduction

The aim of this task is to investigate the microstructure of EUROFER steel before and after irradiation on atomic level. The ECOTAP (Energy Compensated Optical Tomography Atomic Probe) method seems to be appropriate for this task. This report contains the data for non irradiated EUROFER1 ADS2, ADS3, ADS4, EUROPODShip (EUROF 1+ 0.5%Y₂O₃) steels.

Specimen preparation for TAP

EUROFER based materials produced at FZK were used to prepare needles (0.3x0.3x25 mm). Parameters of electro-chemical erosion cutting method used for preparation were properly selected to avoid any strains in the material. Water cooling and other characteristics of the method prevented the specimens from being heated over 100°C. No volume changes were observed in the prepared needles in contrast to other methods (e.g., mechanical cutting).

The specimens were thinned using the method of anodic etching in electrolyte consisting of 2-butoxyethanol and perchloric acid. The diameters of the specimens varied from 5 nm to 250 nm. To achieve optimal parameters for atom probe investigations (diameter 15 nm – 25 nm, length 100-150 nm), pulsed pickling was used. The shape of the specimens was controlled by TEM.

The final preparations of the needles for atom probe investigation were carried out directly in ECOTAP in the field ion microscope mode. This mode allows adjusting a specimen position, checking the tip shape and improving it by polishing.

Experiment procedures

Atom probe investigations were performed at cryogenic temperatures, 65K-75K. The needles evaporated under 1 kV-12 kV (constant component) and 200-24000 V (pulse component). The average pulse number per evaporated atom was 100. From 1 to 12 hours was required to obtain the data from one specimen.

Data processing

The acceptable data level (the number of events registered) to specify the major impurity peaks in mass spectrums must exceed 15000. The specimens are extremely fragile, so the necessary data were possible to obtain, on average, only from one of 15 specimens, while the others broke during examination. The data from at least 5 specimens were necessary to obtain reasonable statistics. Data processing includes mass spectrums interpretation, elements concentration calculations, 3D image reconstructions which are necessary to look for segregation patterns of each solute type.

Results

Materials of the analyzed samples are presented in Table 1.

Table 1: Non-irradiated materials analyzed by ECOTAP.

ADS2	EUROF 1+82 wppm. nat B (1040°C +760°C)
ADS3	EUROF 1+83 wppm B 10 (1040°C +760°C)
ADS4	EUROF 1+1160 wppm B 10 (1040°C +760°C)
EUROPODShip	EUROF 1+ 0.5%Y ₂ O ₃ (1040°C +760°C)

Samples without ODS particles

In case of ADS2, ADS3, ADS4 samples no impurity segregation was observed. Lower impurity concentrations in comparison with those obtained by chemical analysis could be due to solutes segregations at the grain boundaries or dislocations outside the investigated volume. The obtained spatial distributions are similar for all three kinds of the specimens. It is worth noticing that a significant increase of Cr, B and other elements concentration at dislocations and, as a result, matrix depletion were also confirmed in several publications. However, the probability for the detection of B-rich precipitates in the ATP specimens was too low, as these precipitates are on average much larger than the transversal dimensions of the ATP needles.

Samples with ODS particles

EUROPODShip (EUROF 1+ 0.5%Y₂O₃) specimens were prepared and investigated by the same methods. It was noticed that if dark areas, which are supposed to be oxide particles, were observed on TEM images, early collapse of the specimens took place during the atom probing process due to heterogeneity of particle-matrix interface.

The mass spectrum interpretation reveals evaporation of molecular ions like YO and VO. This finding confirms strong binding between these pairs of elements.

Present tomography atom probe investigations of EUROPODShip specimens showed two types of structure. The first one has more or less uniform solutes distribution in the volume. However, clusters of characteristic size 3×3×3 nm were also observed (p.13). In these clusters increased concentrations of such elements as Y, Cr, C, Mn, Ni, V, O, S, Cu, Si and some molecules were found.

The second type is characterized by layers of increased impurity concentration. These layers have characteristic thickness 2 nm and are situated nearly at right angle to the needle long axis, which goes along the long axis of the cylinder of which the specimens were made. The spacing between the layers varies from 2 to 30 nm in the same specimen. The concentrations of Y, V, O, N, C, Cu, S and Ta in the layers were found to be several times higher than the average concentrations in the volume under investigation.

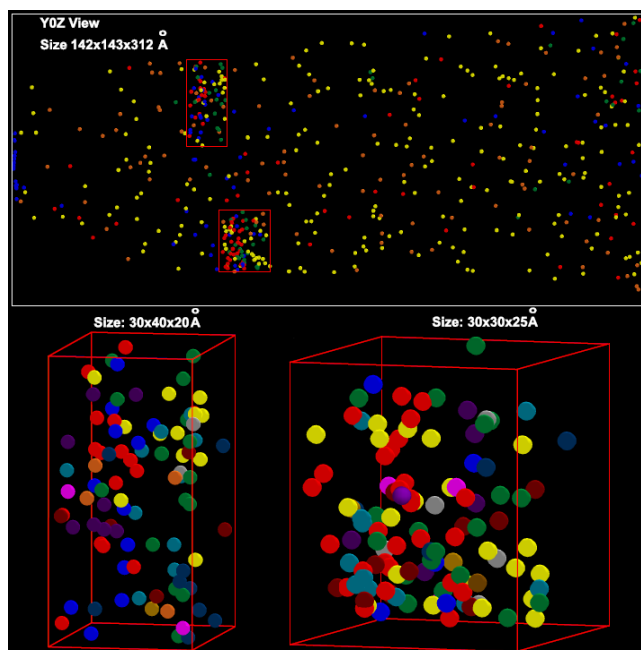


Fig. 1: TAP image of a EUROPODShip sample (first structure type).

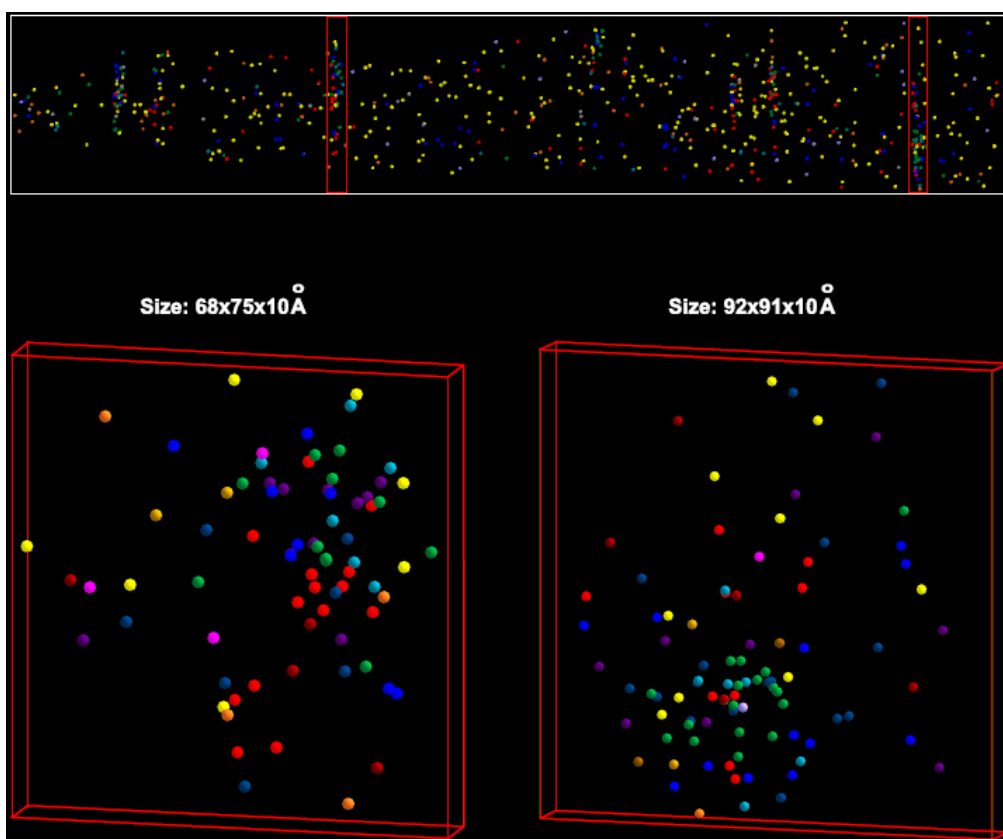


Fig. 2: TAP image of a EUROPODShip sample (second structure type).

In our opinion the presence of these layers can not be ascribed to errors of the method because of the following:

- under identical experimental conditions specimens with and without layers were found;
- the averaged concentrations observed in the layers (with the highest and lowest values taken into account) are higher than in the matrix;
- accumulation of particles on the surface is possible when the evaporation speed is constant and the impurities are distributed homogeneously in the matrix. However, layers with increased impurity concentration either would not appear at all (as saturation on the surface and then further evaporation would happen) or they would be arranged periodically, which contradicts our results: within one specimen the layers spacing can be 2 to 30 nm.

The clusters could be either partly dissolved introduced yttrium particles or segregations of solute elements stimulated by yttrium presence.

Conclusions and preview

Tomography atomic probe experiments were performed on non irradiated samples of EU-ROFER steel with and without ODS particles. Samples without ODS have shown no segregation patterns, while two types of segregations were found in presence of ODS. The first type of segregation is a spherical region about 3 nm in diameter with local impurity concentration increase. This type might correspond to the early stages of ODS particle formation. The second type of segregation pattern is a layer with a thickness of about 1 nm. Physical origin of this type of segregation is not quite clear presently.

Investigation of irradiated samples will be performed after transportation of the samples from RIAR, Dimitrovgrad to ITEP, Moscow.

Staff:

A. Möslang
P.Vladimirov
C. Petersen

A. Zaluzhnyi ITEP
S. Rogozhkin ITEP

TW5-TTMS-001 D 10

Mechanical Post Irradiation Examinations of FZK-Specimens Irradiated in the ARBOR-2 Experiment in the BOR 60 Reactor

Objectives

In an energy generating fusion reactor structural materials will be exposed to very high levels of irradiation damage of about 100 dpa. Due to the fact, that fast reactor irradiation facilities in Europe are not available anymore, a cooperation with the Russian institution: SSC RF RIAR, has been implemented. "ARBOR-2" is the succeeding experiment after ARBOR-1 from FZK and ALTAIR from CEA, to reach irradiation damages up to 70 till 80 dpa.

Status end of 2005

The ARBOR-2 irradiation in BOR 60 of SSC RF RIAR, Dimitrovgrad, with pre-irradiated RAF/M specimens of FZK from the ARBOR-1 irradiation (30 dpa), of CEA from the ALTAIR irradiation (40 dpa) and new RAF/M specimens of FZK and CEA, running up to a damage of 40 to 80 dpa, had been started on 11.2.2003 and finished end of May 2005. The rig was dismantled. The specimens were unloaded in RIAR's hot cells, identified and separately stored in FZK and CEA containers for decay and cooling down.

The irradiation project ARBOR-2

Negotiations for the contract of mechanical PIE of the FZK part of specimens from the ARBOR-2 irradiation are under way and the proposal will be prepared for signature. The aim is to perform the FZK part of ARBOR-2 postirradiation experiments starting January 2007 again at the hot laboratory of SSC RF RIAR under a prolonged ISTC partner contract.

Staff:

B. Dafferner
M. Klotz
M. Lerch
C. Petersen
M. Walter

TW5-TTMS-001 D 11 Assessment of Irradiations Performed on EUROFER 97

Objectives

The structure materials of future fusion reactors have to withstand high neutron and heat fluxes. Although the reduced activation ferritic martensitic (RAFM) 10%CrWVTa steels (EUROFER, OPTIFER, F82H) exhibits clearly better irradiation performance compared to the modified commercial 10-11%-Cr-NiMoVNb alloys, the hardening induced by neutron irradiation accompanied by the embrittlement and by reduction of toughness still remain a main concern. The assessment of impact properties of irradiated RAFM steels (EUROFER, OPTIFER, F82H) will support material database generation and specification of new EUROFER-2.

Data Collection and Assessment

The collection and assessment of irradiated Charpy impact data has been continued. Fig. 1 shows neutron irradiation induced shift in DBTT vs. irradiation dose for EUROFER 97, F82H/F82H-mod and OPTIFER-1a steels for irradiation temperatures (T_{irr}) between 300 and 330°C. The impact testing was performed with KLST type Charpy-V specimens (3x4x27 mm³). Large data scattering observed at low and intermediate doses prevents an unambiguous quantitative description of the embrittlement trend. The lines in Fig. 1 are guides for eye only. For RAFM steels no embrittlement saturation can be observed up to 32 dpa. Slightly better irradiation resistance for EUROFER 97 (ARBOR-I, 31.8 dpa) compared to F82H-mod (ARBOR-I, 32.3 dpa) can be partly attributed to a slightly lower irradiation dose in the former case.

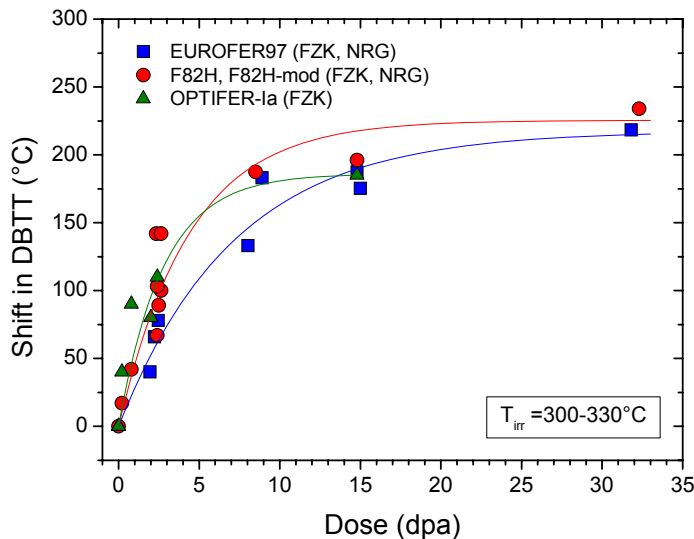


Fig. 1: Irradiation induced shift in DBTT vs. irradiation dose assessed for EUROFER 97, F82H and OPTIFER-1a KLST (3x4x27 mm³) specimens. Irradiation campaigns: MANITU, HFR-Ib, SPICE, WTZ, ARBOR-I (FZK), SUMO02-04, CHARLOT02-04, SINEXT05 (NRG). The solid lines are guides for eye only.

Impact properties of EUROFER 97 were compared with those of reference RAFM steels (F82H-mod, OPTIFER-1a, GA3X) included in the HFR-Phase-IIb (SPICE) irradiation programme (16.3 dpa at 250-450°C). At $T_{irr}=300^{\circ}\text{C}$, the DBTT of all RAFM steels lie between 100-110°C. OPTIFER-1a shows irradiation induced embrittlement and hardening comparable to EUROFER 97 and the best impact toughness at $T_{irr}=300^{\circ}\text{C}$. At $T_{irr} \geq 350^{\circ}\text{C}$ all RAFM steel exhibit good embrittlement behaviour with DBTTs below -20°C and hence well below the steel operational temperatures foreseen in the future fusion reactors.

Conclusion

Collection and assessment of the available Charpy impact data on RAFM steels (EUROFER, OPTIFER, F82H) was performed. Irradiation resistance of the RAFM steels show not satisfactory results for irradiation temperatures below $T_{irr} \leq 330^{\circ}\text{C}$. No embrittlement saturation

can be observed up to 32 dpa. The ARBOR II (~330°C/70dpa) irradiation experiments will shed more light on the high dose embrittlement behaviour. Irradiation resistance of RAFM steels for irradiation temperatures above $T_{irr} \geq 350^{\circ}\text{C}$ are satisfactory up to a (highest available) damage dose of 16.3 dpa.

Staff:

B. Dafferner
E. Gaganidze

Literature:

- [1] E. Gaganidze, H.-C. Schneider, B. Dafferner, J. Aktaa, High-dose neutron irradiation embrittlement of RAFM steels, J. Nucl. Mater. 355 (2006) 83–88.

TW5-TTMS-001 D 14

Assessment of Irradiated Fracture Mechanic Samples on EUROFER, F82H (and OPTIFER) to Study the Size Effect

Objectives

Various fracture mechanics (FM) experiments have been performed on EUROFER 97 and other reduced activation ferritic-martensitic (RAFM) steels (F82H, OPTIFER). Different specimen types and testing methods were used for specimens irradiated at different conditions. The assessment aims at the comparison of DBTT and DBTT shift calculated from different specimen geometries to study the size and geometry effects. Comparison of DBTT from FM against Charpy is also discussed.

Data Collection and Assessment

The collection and assessment of unirradiated and irradiated FM and Charpy impact data obtained on EUROFER97 and other RAFM steels within different irradiation programmes (SUMO-02÷SUMO-07, SIWAS-09, SINAS-80/6, SINAS-80/7, IRFUMA-I ÷ IRFUMA-III, HFIR RB-11J, HFIR RB-12J) has been continued.

ASTM E1921-05 procedure has been applied to the reference thickness ($B_0=25.4$ mm) adjusted fracture toughness data for evaluation of fracture toughness transition temperature T_0 . Alternatively, when ASTM E1921-05 procedure was not applicable, a least square fitting to thickness adjusted fracture toughness data with the Master Curve (MC) was used for evaluation of the reference temperature. Fig. 1 shows the fracture toughness transition temperature vs. irradiation dose for EUROFER97 at irradiation temperature of $T_{irr}=300^\circ\text{C}$. A progressive material embrittlement with irradiation dose is observed with no saturation up to 8.8 dpa. The dose dependence of the transition temperature is well described with $T_0=A+B(1-\exp(-\text{dose}/\tau))$ type function.

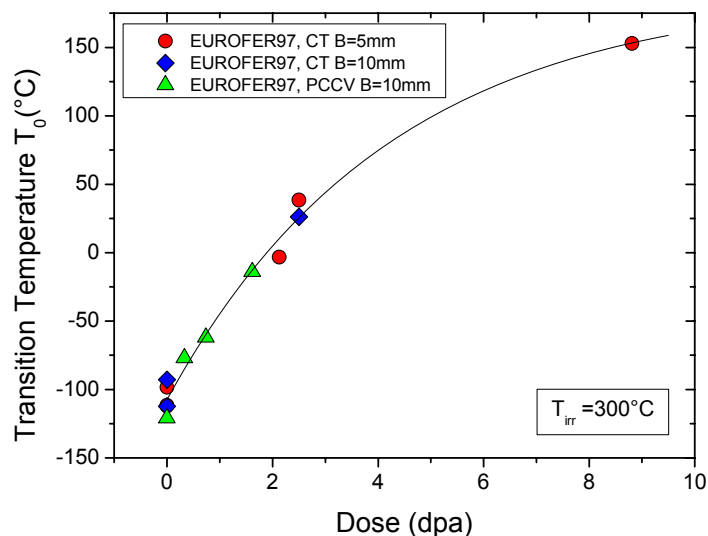


Fig. 1: Fracture toughness transition temperature T_0 on EUROFER 97. Specimen type and thickness is indicated in the legend. Compact Tension (CT) specimens were machined from 8, 14 and 25 mm plates. Pre-Cracked Charpy V (PCCV) specimens were machined from $\varnothing=100$ mm bars. The line is a least square fit to presented data with $T_0=A+B(1-\exp(-\text{dose}/\tau))$ with $A=-107.4^\circ\text{C}$, $B=297.8^\circ\text{C}$, $\tau=4.23$ dpa.

The best fit was obtained with $A=-107.4^\circ\text{C}$, $B=297.8^\circ\text{C}$, $\tau=4.23$ dpa. The transition temperature appears to be independent of specimen type (PCCV, CT) or specimen thickness (5 mm, 10 mm). Good agreement observed on 5 and 10 mm thick CT specimens (NRG) in the unirradiated condition and at 2.5 dpa in Fig. 1 indicates that specimen thicknesses between 5 and 10 mm lead to reliable fracture toughness results.

Fig. 2 shows the irradiation induced shift in fracture toughness transition temperature (ΔT_0) vs. irradiation dose for EUROFER 97 and F82H steels for irradiation temperatures between 60 and 300°C . The observed large difference in ΔT_0 at 5 dpa between NRG and ORNL experiments prevents a quantitative analysis of the embrittlement trend for F82H. At low irradiation

tion doses and at $T_{irr}=300^{\circ}\text{C}$ EUROFER 97 shows better resistance against irradiation compared to F82H-mod.

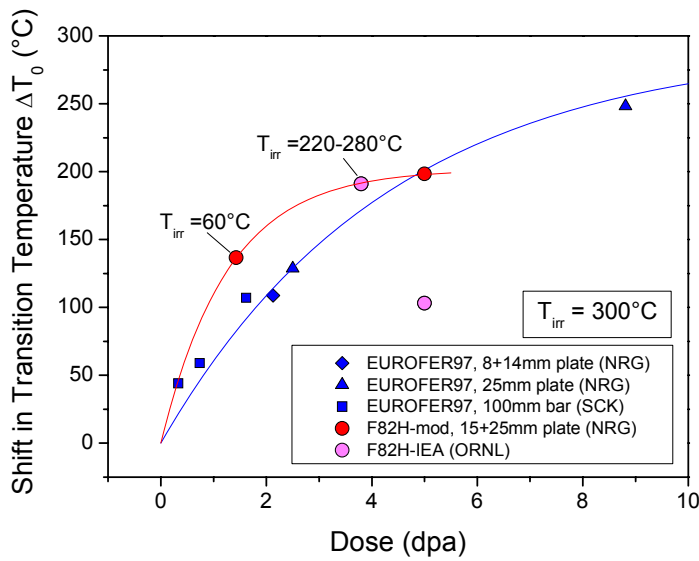


Fig. 2: Irradiation induced shift in fracture toughness transition temperature vs. irradiation dose for EUROFER97 and F82H steels. The lines are eye guide only.

Conclusion

Collection and assessment of the available fracture toughness and Charpy impact data on RAFM steels (EUROFER, F82H) has been performed. The effects of specimen geometry, specimen size, test condition, evaluation method, etc. have been investigated. MC methodology has been applied to normalized fracture toughness data for determination of FTTT. FTTT appeared to be independent of specimen type (CT, PCCV) and size (B=5-10 mm). Progressive material embrittlement observed for EUROFER 97 and F82H indicate

no saturation for the achieved damage doses. The irradiation induced shifts in transition temperatures obtained in FM experiments on EUROFER 97 are consistently and significantly larger than the corresponding shifts quantified by impact testing on KLST specimens.

Staff:

B. Dafferner
E. Gaganidze

Fig. 3 shows irradiation induced shift in fracture toughness transition temperature and in KLST ductile-to-brittle transition temperature vs. irradiation dose for EUROFER97 for $T_{irr}=300-330^{\circ}\text{C}$. Independently of specimen type used, FM experiments show consistently and significantly larger irradiation induced shifts in transition temperatures compared to the corresponding shifts quantified by impact testing on KLST specimens.

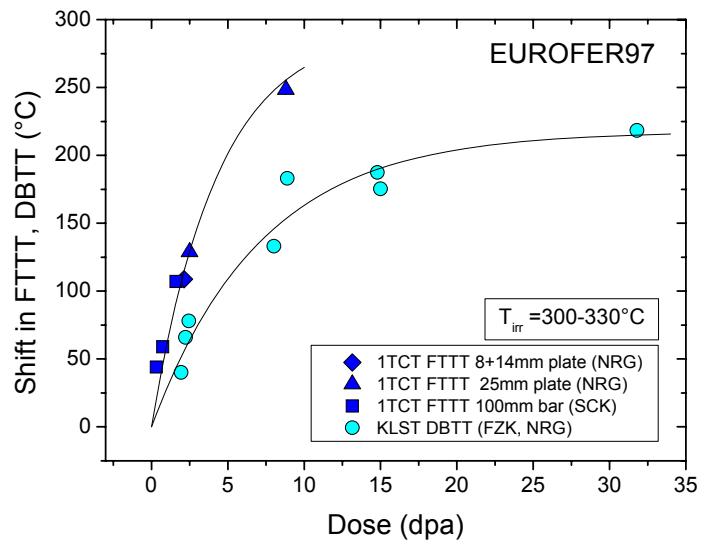


Fig. 3: Irradiation induced shift in fracture toughness transition temperature and in KLST ductile-to-brittle transition temperature vs. irradiation dose for EUROFER97. The lines are eye guide only.

TTMS-002 Metallurgical and Mechanical Characterisation

TW2-TTMS-002a D 19 Creep-Fatigue Testing at 550°C on EUROFER, Continuation to Longer Times Preferably under Controlled Atmosphere

Objectives

A structural component like a Test Blanket Module is subjected during service to alternating thermal and mechanical stresses as a consequence of the pulsed reactor operation. Since the operating temperatures of a future nuclear fusion reactor increase due to economic considerations, the knowledge of the reasons of the creep fatigue endurance of Reduced Activation Ferrite/Martensite (RAF/M) steels like F82H mod. and EUROFER 97 becomes more important.

Status end of 2005

Data of about 500 Thermo Mechanical Fatigue (TMF) experiments, with and without hold times, performed in the last 15 years, have been transferred to modern data storage media as CD and/or DVD. For these data sets reduction programs have been developed to implement proofed results of TMF tests on Ferritic/Martensitic steels, into the Mat-DB, the data bank system of JRC, Petten.

TMF-experiments

After a peer selection process of evaluated TMF-experiments the following data sets had been implemented in the Mat-DB, the data bank system of JRC, Petten:

- EUROFER 97, as received, 6 tests without hold times, 18 tests with 100 s hold times, 16 tests with 1000 s hold times.
- EUROFER 97, heat treated (austenitization 1040°C), 7 tests without hold times, 14 tests with 1000s hold times.
- F82Hmod., as received, 15 tests without hold times, 16 tests with 100 s hold times, 8 tests with 1000 s hold times.

These data sets are available free of charge for the Nuclear Fusion community after registration under <https://odin.jrc.nl> in the ODIN system of JRC.

TMF test results of AISI 316L and other Ferritic/Martensitic steels, including RAF/M modifications will run through the data reduction process and the implementation in the MAT-DB of JRC, Petten is planned for 2007.

Staff:

C. Petersen

Literature:

- [1] L. F. Isern Reali, C. Petersen, A. Armas: Short Fatigue Crack Behaviour of the Reduced Activation Steel EUROFER 97, presented at MRS Meeting, Boston (2006).

TTMS-003 Compatibility with Hydrogen and Liquids

TW4-TTMS-003 D 1 TW6-TTMS-003 D 3

Development of Modelling Tools to Describe the Corrosion Behaviour of Uncoated EUROFER in Flowing Pb-17Li and their Validation by Performing of Corrosion Tests at T up to 550°C

Objectives

The main reasons to execute this activity were that extrapolations of the RAFM-steel corrosion behaviour determined in the past to the new working conditions may be problematic due to large uncertainties at the new working conditions and, additionally, only poor knowledge on transport of dissolved components in the Pb-17Li flow is present. In contrast to earlier investigations, these changes in requirements need the going over from (only) mechanism-based corrosion tests to model supported tests. Furthermore, the whole loop (system) has to be considered in the evaluation of the corrosion tests together with other occurring phenomena and mechanisms as transport effects and precipitations.

Corrosion testing

The alloy EUROFER 97, a 9 Cr W V Ta alloy, which was developed on base of the experience with RAFM alloys of e.g. Optifer type, is at the moment the favoured FM-steel for application in a future fusion system. During the last years the thermal and mechanical behaviour of EUROFER 97 was examined [1] and first corrosion testing in the Pb-17Li loop PICOLO [2, 3] at moderate temperature (480°C) was performed. Under the TW4 task corrosion tests were performed for the first time at 550°C in PICOLO loop with a flow rate of about 0.22 m/s. The planned exposure time of 5000 h was reached under the TW4 task and since end of this year the TW6 is running with an extension of the testing time to 10,000 h. First samples were removed for the TW6 task. All samples are characterized by metallographic tools and corrosion attack is measured. Additionally to the metallurgical investigations SEM and EDX analyses were performed to analyze more in detail the reaction zone EUROFER-liquid PbLi.

Fig. 1 shows the microstructure of the EUROFER exposed for 1025 h to the flowing Pb-17Li at 550°C. The selected picture shows an un-attacked area (left part of the micrograph) and a well wetted and corroded section to the right. The visible step height in corrosion attack is about 80 µm. This value delivers a corrosion rate of about 700 µm/a in comparison to a rate of about 90 µm/a for the 480°C tests. The step height for 1025 h is about twice the value observed after 500 h and this observed height corresponds rather well to the measured reduction in diameter of about 156 µm. No steps or un-uniform corrosion attack could be found for samples exposed longer than about 1000 h. They showed all smooth corroded surfaces and the adherent PbLi scale was in good contact with the matrix as depicted in Fig. 2 for a sample exposed for 3021 h to Pb-17Li. For this sample the corrosion attack was measured to be about 156 µm which is resulting in a corrosion rate of about 460 µm/a.

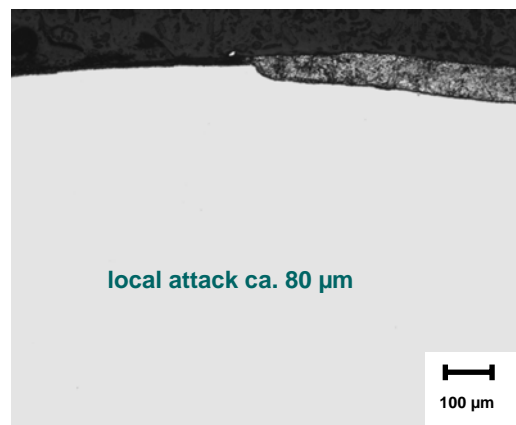


Fig. 1: Sample exposed for 1025 h to PbLi at 550°C with un-attacked and corroded area with adherent PbLi scale (right part of the picture).

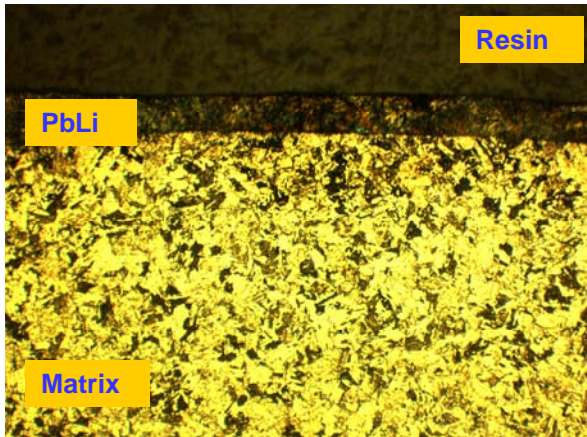


Fig. 2: Sample exposed for 3021 h to PbLi at 550°C with smooth boundary between matrix and PbLi.

Fig. 3 shows the measured corrosion values for the samples exposed up to 5000 h under the TW4 task at a flow rate of 0.22 m/s in the test section at the beginning with a channel width of 4.0 mm in the test section surrounding the cylindrical samples. Depending on the type of extrapolation a forecast of corrosion rates per year can vary between 700 and 400 $\mu\text{m/a}$. The value of 400 $\mu\text{m/a}$ may surely be too small due to channel widening (material take off) during the tests and thus smaller flow velocity in the channel. The 700 $\mu\text{m/a}$ value is based on a rather small exposure time and contains thus a high uncertainty. For entering in the test series (TW6) up to 10,000 h and also for the validation of our modelling tools the 500 $\mu\text{m/a}$ value is

assumed to be the most realistic one. Metallurgical and SEM/EDX analyses confirmed that also at the elevated test temperature of 550°C dissolution is the corrosion mechanism. All microcuts showed a clear boundary between melt and matrix with an uniform attack. The detected corrosion rates confirm also at this new test temperature linear kinetics.

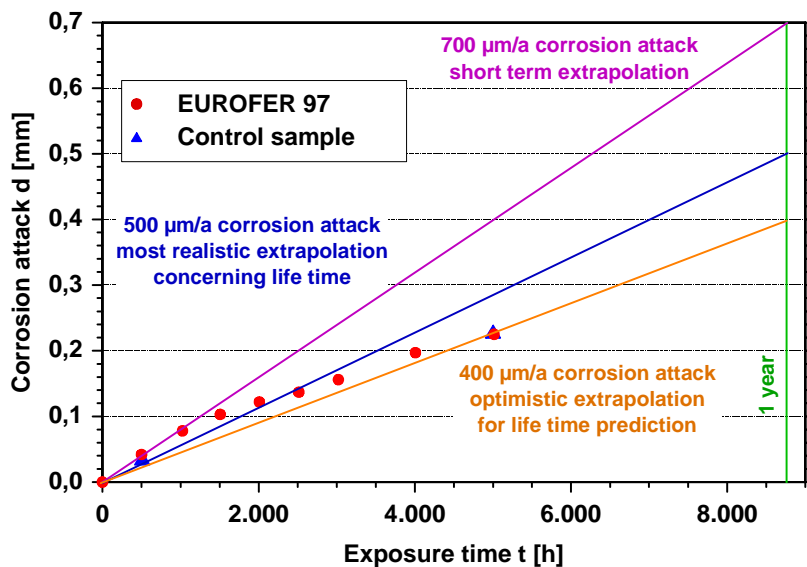


Fig. 3: Corrosion attack of EUROFER vs. exposure time at 550°C and extrapolation of the corrosion rate to one year values.

Modelling

The Pb-17Li alloy is considered as coolant and breeding medium in future fusion reactors which is in contact with the structural components. Under liquid metal flow in a non-isothermal loop system (e.g. also PICOLO loop) beside corrosion in the hot part additional effects as e.g. transport of corrosion products and precipitation of them in cooler parts will take place. In Pb-17Li oxide phases can not be formed on the steel components due to the low O_2 activity of the coolant medium and existing oxide scales will be dissolved. The corrosive attack of the structural alloys, a dissolution process, will be determined mainly by the temperature dependency of the solubility of the steel components in Pb-17Li and by the flow characteristics of the melt. The smaller solubility at lower temperatures leads to precipitations in the cold legs of the system. PICOLO tests performed in the past were looking only at the corrosion attack and the mechanisms but neglected the influence of transport and precipitation phenomena.

Based on these facts the development of modelling tools was performed with the aim to assist the running corrosion testing and to increase reliability in extrapolating results to other test conditions or to predict transport / precipitation phenomena. The developed modelling tools, their theoretical background was described in the previous report, were integrated meanwhile into a computer code called MATLIM. For validation of this code calculations were performed on corrosion rates and precipitations using the physical and chemical properties of the EUROFER, the PbLi melt and applying the typical features of the test loop PICOLO – therefore a parameterization of PICOLO loop (e.g. temperatures, flow velocities, diameters etc.) was performed in dependence of loop position. Both test conditions 480°C (earlier tests) and the actual 550°C tests were used for the tool validation. The flow velocity was assumed to be constant vs. time with 0.22 m/s.

In the TW4 task first analyses were performed to examine the appearance of precipitations in the PICOLO loop. They confirmed that precipitations are formed in the cooler loop section as predicted by the developed modelling tool. However, a valuation of the effects (e.g. amount of precipitations) and tools is too speculative at the moment due to the limited data points (only magnetic trap section of the loop was tested). The TW6 task will continue this topic in more detail.

Fig. 4 shows the dissolution / precipitation rate for the 550°C test scenario in dependence of loop position and corresponding temperature. It can be seen, that the highest dissolution rate (about 500 $\mu\text{m/a}$) is present in the test section – the loop part with high temperature and high flow velocity. All positive values of the (blue coloured) dissolution curve indicate that precipitation takes place. This is the fact for all positions with a loop temperature below about 400°C.

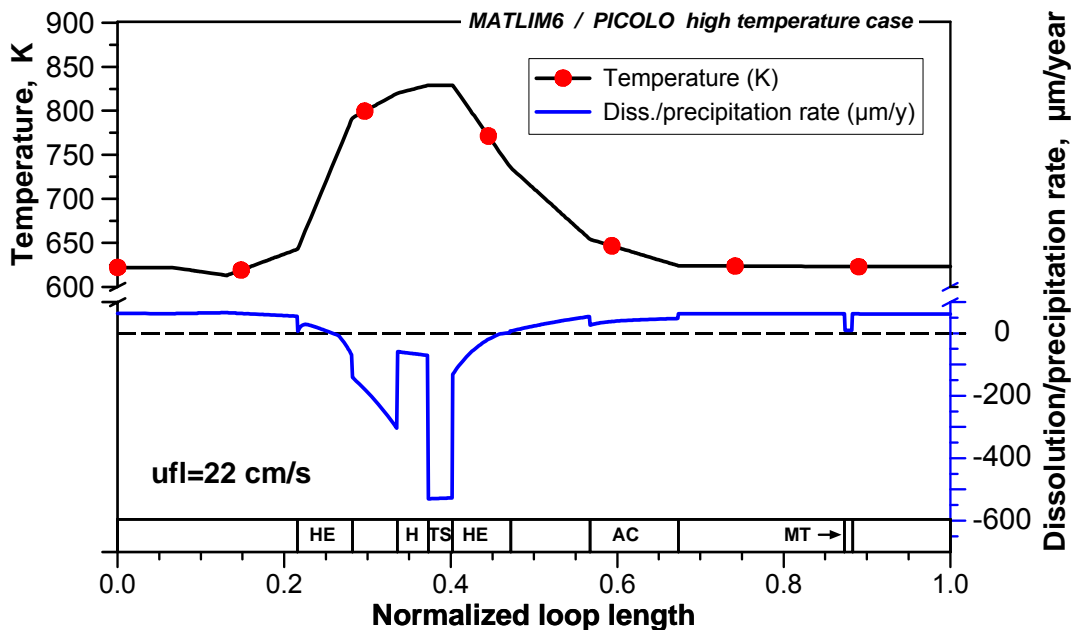


Fig. 4: Predicted corrosion and precipitation behaviour in PICOLO loop at test temperature 550 °C and flow rate 0.22 m/s.

Similar calculations were also performed for the test scenario 480°C. They resulted in corrosion rates of about 80 $\mu\text{m/a}$ using the same physico-chemical properties. The good agreement with the measured data is a rather encouraging result that indicates that the chosen path and the developed modelling tools reproduce correctly the ongoing processes. However, it should be mentioned that the validation was only done for one flow rate (0.22 m/s) and that other regimes (lower velocities) have to be analyzed in the same way to guarantee a global validity of the modelling tools and of the selected properties.

Conclusions

The technological work of upgrading PICOLO-loop for corrosion testing of EUROFER at 550°C was conducted as planned up to 5000 h exposure time under TW4 and first samples were removed from Pb-17Li under TW6. The examination of removed samples indicate, that incubation times as observed in earlier campaigns (480°C testing) are heavily reduced and that corrosion rates are dramatically increased to about 500 µm/a compared to only 90 µm/a at 480°C.

The reliability of extrapolating corrosion rates to TBM relevant durations is low based on the short testing time of only 5000 h and will be increased by new test series going up to 10,000 h and, additionally, by the support of modelling considering the similar behaviour of other RAFM steels e.g. Manet. The performed tests and the results in modelling show clearly that corrosion is a serious problem at high temperatures and will need special measures e.g. corrosion protection by surface coating to reduce the corrosion attack to acceptable limits which guarantee a safe and economic application in TBM's.

Looking on the transport and precipitation effects occurring in a real arrangement first hints are now available due to the results obtained from the modelling work and analyzing first samples cut out of the loop for testing. However, this field requires more additional data for valuation of future measures and estimating the impact on loop operation. Two steps are at least necessary on the short term scale. The first will be the validation of the modelling tools by corrosion rates measured at lower flow rates e.g. at 550°C and, secondly, metallurgical data are urgently required which are describing precipitations at different loop positions for validation of the included dissolution / precipitation tools in modelling.

By combination of experimental and modelling work under the TW4 task a significant progress was realized especially in the change over from only mechanism-based tests to considering the whole loop behaviour under corrosion, transport and precipitation view. This was a necessary step towards interpretation of combined effects in the test loop and for future transfer to analyze a TBM behaviour.

Staff:

J. Konys
W. Krauss
H. Steiner
O. Wedemeyer
J. Novotny
Z. Voss

Literature:

- [1] R. Lindau, A. Möslang, M. Schirra; Thermal and mechanical behaviour of the reduced-activation-ferritic-martensitic steel EUROFER, Fusion Eng. Design., 61-62, 2002, 659
- [2] W. Krauss, J. Konys, Z. Voss, J. Novotny, Corrosion behaviour of EUROFER 97 in flowing Pb-17Li, Corrosion testing in Picolo loop (480°C), TW1-TTMS-003
- [3] J. Konys, W. Krauss, Z. Voss, O. Wedemeyer, Corrosion behaviour of EUROFER steel in flowing eutectic Pb-17Li alloy, J. Nucl. Mat., 329-33 (2004) P.1379-1383

TTMS-004 Qualification Fabrication Processes

TW4-TTMS-004 D 1 TW6-TTMS-004 D 1 – D 3

Improve Design Limits of Welded Components through Improved Post Weld Heat Treatments, Qualification and Improvement of Welded and Diffusion Bonded Joints

Overview

In contrast to austenitic steels untreated welded joints of ferritic-martensitic steels like EUROFER suffer from hardening and embrittlement due to uncontrolled martensite formation in the weld and from softening in the vicinity of the heat affected zones (HAZ). With respect to specific Test Blanket Module design and assembly requirements for DEMO there is a significant discrepancy between the necessary post welding heat treatment and its applicability. Therefore, Tungsten-Inert-Gas (TIG) with EUROFER filler wire, Electron Beam (EB), and Laser welding have been applied to EUROFER plates of different thickness in the condition as received and the influence of different post-weld heat treatments has been thoroughly investigated.

Now the new general objective is to support the fabrication development in the blanket areas and to improve the reliability of the materials and joints according to the test blanket module (TBM) design. The joint quality produced by a low pressure HIP diffusion bonding process has to be investigated with regard to prior surface state conditions. The assessment of fused welding joints' quality will be continued with special emphasis on 40 mm thick welds and their post-weld heat treatments (PWHT). The eventual necessity of a complete heat treatment, that is re-austenitizing plus tempering, to restore microstructure of welds is addressed by investigating fatigue properties.

Initial Status

Prior to specimen fabrication the microstructure of the different welds have been analyzed. All TIG welds show coarse grain formation which is typical for solidification micro structures that form during the welding cycles. Both beam welds didn't show this severe grain coarsening. Also typical for TIG welds were the softened regions in the HAZ. While the width of the beam welds was significantly smaller, softening in the HAZ could only be observed in thicker plates. From these microstructural examinations it was already clear that TIG welds would need a full two-step heat treatment (austenitization plus tempering) in order to recover a uniform distributed fine grain. This was also confirmed by poor Charpy test results. But Charpy tests on beam welded specimens have shown surprisingly good results, even without post-weld heat treatment. Compared to the EUROFER base material, the Ductile-to-Brittle-Transition-Temperature (DBTT) of Laser and EB welds was almost the same. Further advantages and drawbacks of these different welding technologies were discussed in detail based on Charpy, creep, and tensile tests performed on welds with and without applied post-welding heat treatments. The examinations were completed by according microstructural analysis.

Progress

Beside embrittlement due to grain coarsening during the weld process, also degradation of creep strength is a known weak point of ferritic-martensitic alloys. The loss in strength results from fine grain formation in the vicinity of the HAZs. The reason for this is illustrated in Fig. 1.

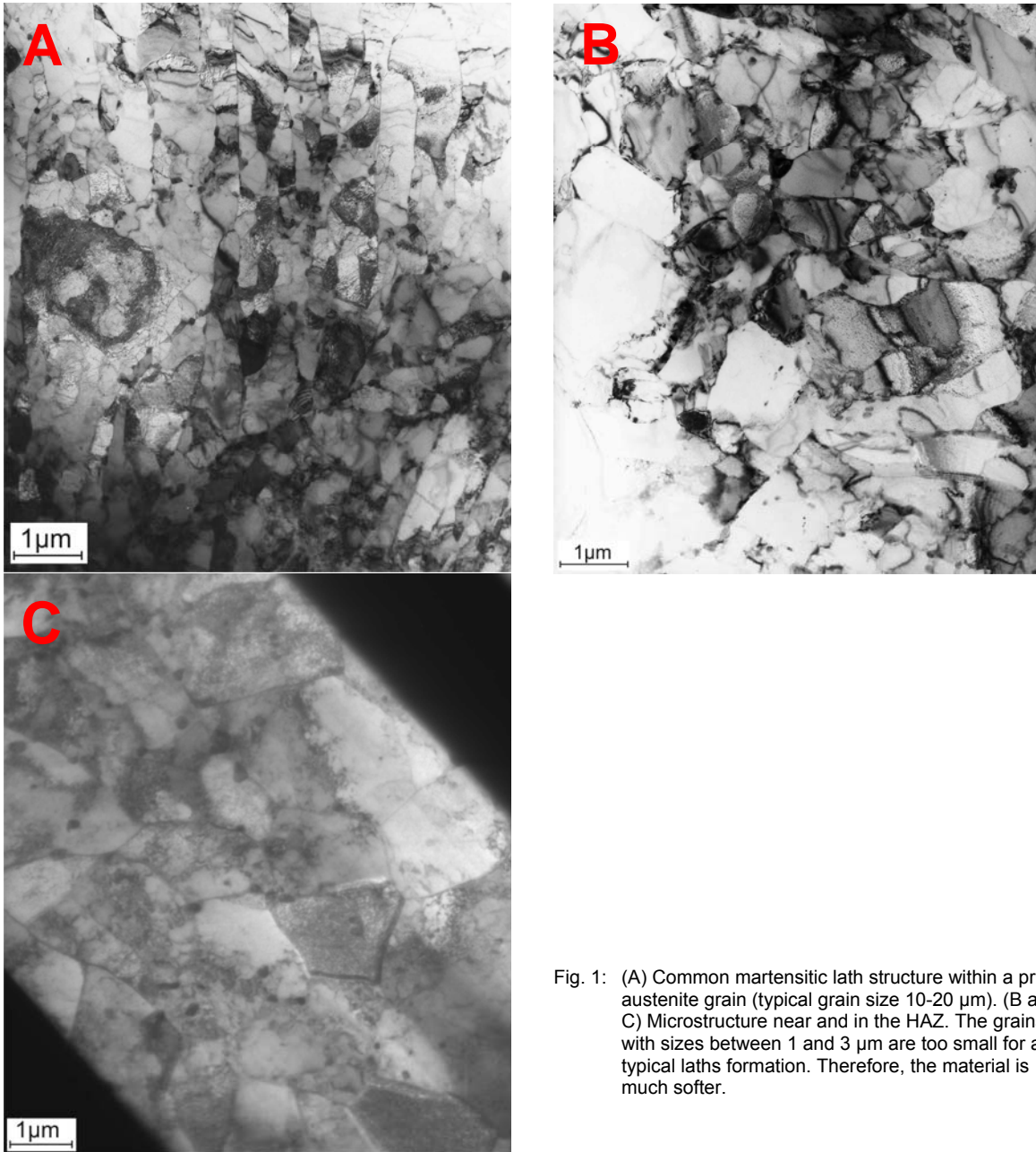


Fig. 1: (A) Common martensitic lath structure within a prior austenite grain (typical grain size 10-20 μm). (B and C) Microstructure near and in the HAZ. The grains with sizes between 1 and 3 μm are too small for a typical laths formation. Therefore, the material is much softer.

For TBM fabrication it is necessary to develop and characterize critical joints. Joining the 40 mm thick upper and lower caps to the first wall (FW) is a typical example. Since EB welds have led to best results in our previous studies, we started with the development of an appropriate EB weld fabrication process on 40 mm thick EUROFER bars (see Fig. 2). As can be seen quite clearly (Fig. 2 C), with properly adjusted parameters the EB beam produces a rather straight and equally narrow fusion zone. There is just a small HAZ and first microstructure examinations have revealed a low defect density of bubbles and micro-cracks. Figure 3 illustrates the according hardness map where the critical soft zones are represented by blue areas. The first mechanical test results are shown in Fig. 4. There is nearly no difference between tests of specimens from the root or from the top of the weld. That is, the properties of the weld are distributed homogeneously. In addition, Fig.4 shows also that this 40 mm EB weld needs a proper PWHT.

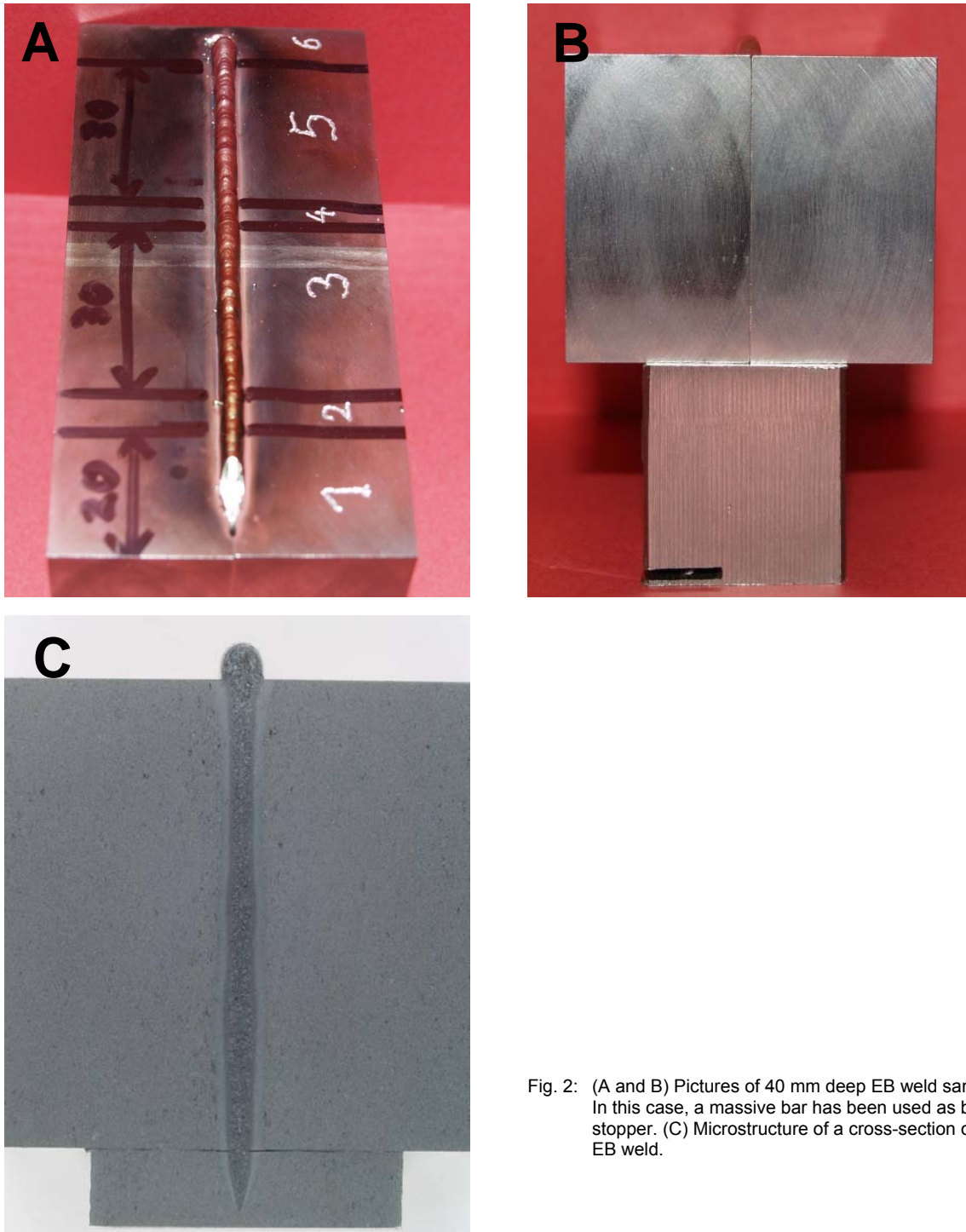


Fig. 2: (A and B) Pictures of 40 mm deep EB weld sample. In this case, a massive bar has been used as beam stopper. (C) Microstructure of a cross-section of the EB weld.

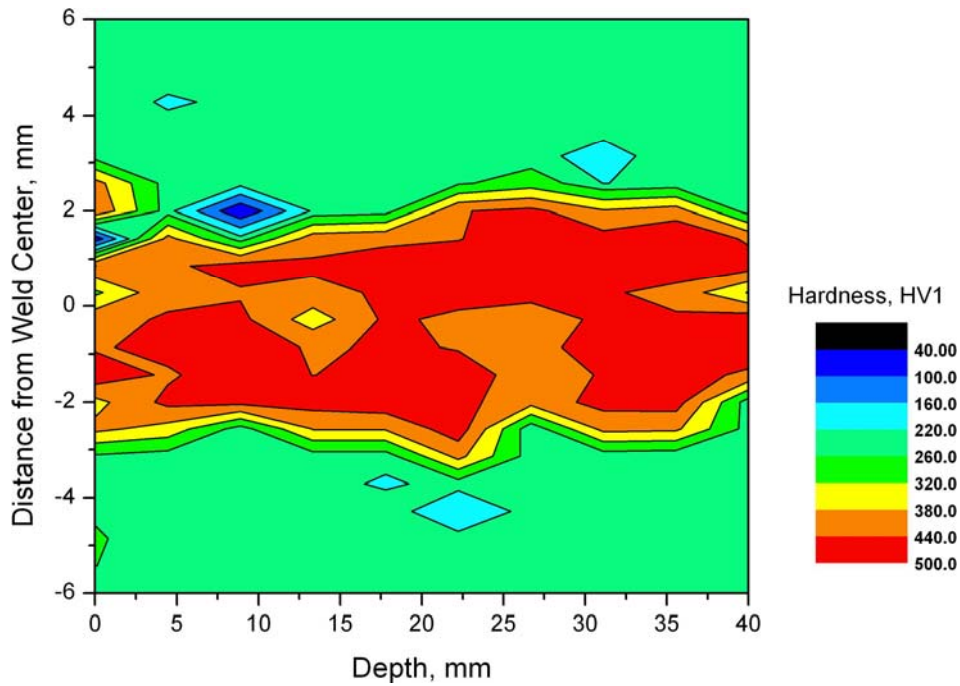


Fig. 3: Hardness map of the 40 mm EB weld cross-section of Fig. 2.

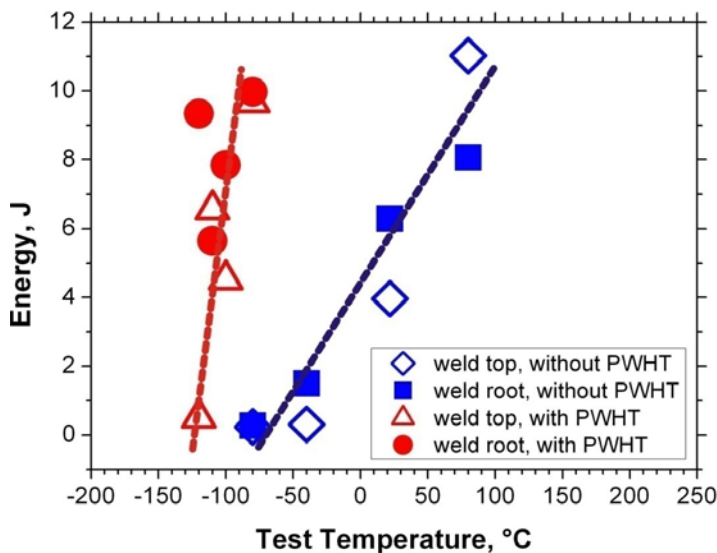


Fig. 4: DBTT of the 40 mm EB weld with and without PWHT of 980°C + 750°C.

For a comprising characterization and evaluation of diffusion welding technologies for the fabrication of first wall components a large number of weld samples and some small mock-ups have been fabricated. The goal is to examine the influence of surface fabrication, contamination, cleaning, and weld processing. This study as well as a low cycle fatigue (LCF) characterization program for welds is still ongoing.

Conclusions

Compared to the base material EB and TIG welds loose creep strength of about 40 MPa at 600°C. Since the maximum operation temperature for EUROFER is 550°C, the reduction in creep strength might still be tolerable. However, the softening problem in the HAZ has to be examined by LCF tests. It has also been shown that tensile test of EUROFER weld specimens are not very instructive. Furthermore, only EB welding seems to be a promising technique for joining the FW and caps of TBMs. Therefore, the discussed 40 mm fabrication method will be further optimized.

Staff:

A. Baumgärtner
 B. Dafferner
 P. Graf
 A. Falkenstein
 S. Heger
 U. Jäntschi

M. Klimiankou
 A. Möslang
M. Rieth
 R. Ziegler
 H. Zimmermann

TW5-TTMS-004 D 1 Diffusion Welding Techniques

Introduction

The industrial scaled blanket box (BB) manufacturing process needs a well defined joining process of the cooling plates (CP). A CP will be manufactured by joining with a diffusion weld process half pieces with milled grooves. The influence of process and material deviations on the weld quality is an open question. This task is related to a two step diffusion weld process. The first step uses a high pressure (typical 15 to 30 MPa) and a low temperature of 1010°C, the second step works at pressures between 5 MPa and 20 MPa at 1050°C.

This activity will consider the following deviations:

- Rolled tins of EUROFER are used as basic material for CPs. The manufacturing process of the rolled tin generates a local varying forming of the material. The task investigates this influence.
- The diffusion weld parameters like time, pressure and temperature will have deviations in a future industrial scaled process. What are the admissible process parameter deviations?

The task started with a material characterisation. Then diffusion weld specimens with different temperature deviations had been produced and investigated by tensile and Charpy impact tests.

Material Characterisation

Tensile tests on base material specimens taken from the edge and the middle of the EUROFER 97/2 plate have been performed. The results of both sample groups agree completely. Charpy impact specimens indicate a difference in the DBTT (ductile to brittle transition temperature). Compression creep experiments exhibited a different compression creep behaviour for specimens taken from the edge region and the middle region. This difference is temperature dependent, note the logarithmic scale of Fig. 1. The knowledge of local varying compression creep behaviour will be fundamental for a FW production. It had been a most important result of this investigation that there is a homogenization procedure later called a pre-stage. The compression creep behaviour of the new EUROFER 97/2 differs completely from that of the old batch. The compression creep speed is nearly constant for constant pressure and temperature. It does not depend on the compression for the new EUROFER 97/2.

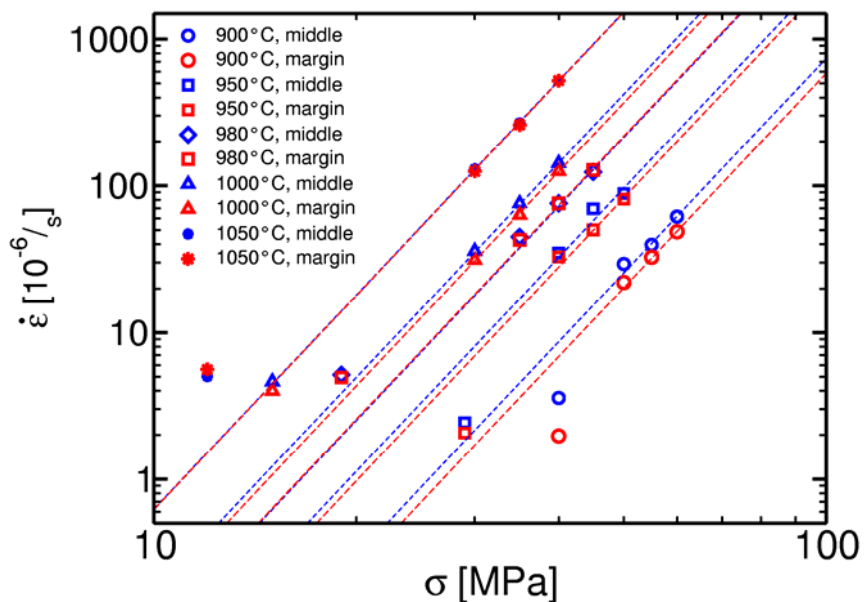


Fig. 1: Results of compression creep experiments.

Diffusion weld experiments

The current status of knowledge entails two kind of experiments: Firstly, the influence of a possible pre-stage on the diffusion weld process has to be investigated with samples taken from the edge and middle region. Secondly, the process parameters have to be varied and their influence on the weld quality has to be investigated.

Results of the pre-stage influence

The use of a pre-stage additionally to the diffusion weld process does not generate an additional grain coarsening. A significant influence on tensile properties, fracture toughness (USE) and DBTT does not have been observed in case of the base material. But the results from Charpy impact experiments of diffusion weld specimens indicate a better weld quality in case of diffusion weld samples taken from the middle region compared to those specimens taken from the edge region, see Fig. 2. An additional pre-stage lowers this difference in the weld quality.

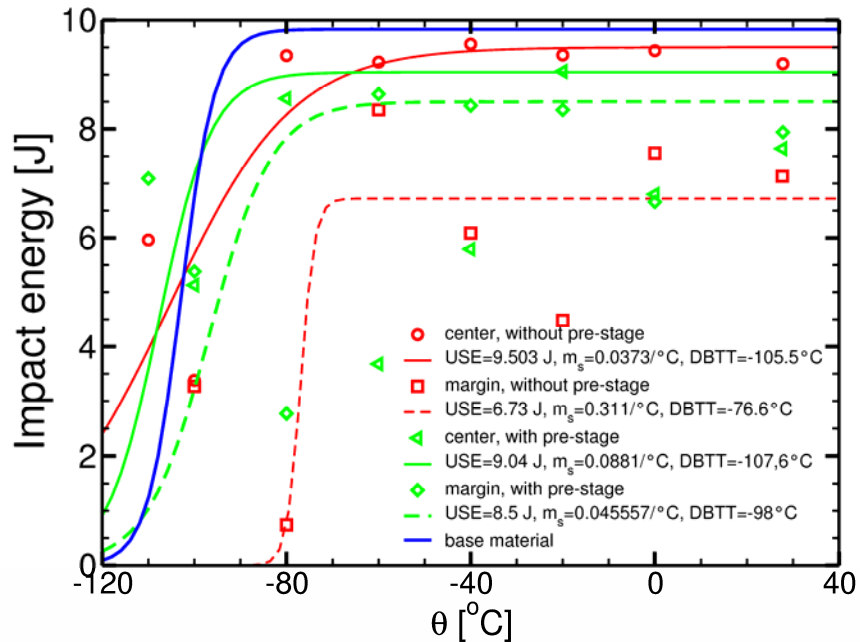


Fig. 2: Results of a diffusion weld serial with specimens taken from the "center" or middle region and the edge region. The same serial had been performed with and without a pre-stage.

An additional pre-stage lowers this difference in the weld quality.

Results of the process parameter variation

Pre-stage and the two step diffusion weld process necessitate a heat treatment at 1050°C. First serial applies in all steps a by 20°C increased process temperature. The results of Charpy impact specimens taken from base material and welds are indicating an up to 30°C increased DBTT. A grain coarsening could be observed. A significant change of tensile parameters does not have been observed.

The decrease of first step parameter pressure and temperature does not generate any influence on tensile parameters. But the results of Charpy impact specimens display a reduced weld quality. A comparison of diffusion weld samples taken from the edge or middle region is showing a drastically increased difference of the weld quality. The diffusion weld process runs easier for a sample taken from the middle region than for a sample taken from the edge region. This is shown in Fig. 3.

There had been some knowledge about process deviations in pressure of the second stage by a former task. Therefore the experimental programme varies only the time of the second stage. But the results do not show a different behaviour. A reduced second step process time reduces the weld quality by a reduced USE and increased DBTT. A drastically increased second step time increase the USE to nearly perfect values. But it increases the DBTT in critical manner. This effect should be investigated again after an applied multiple PWHT.

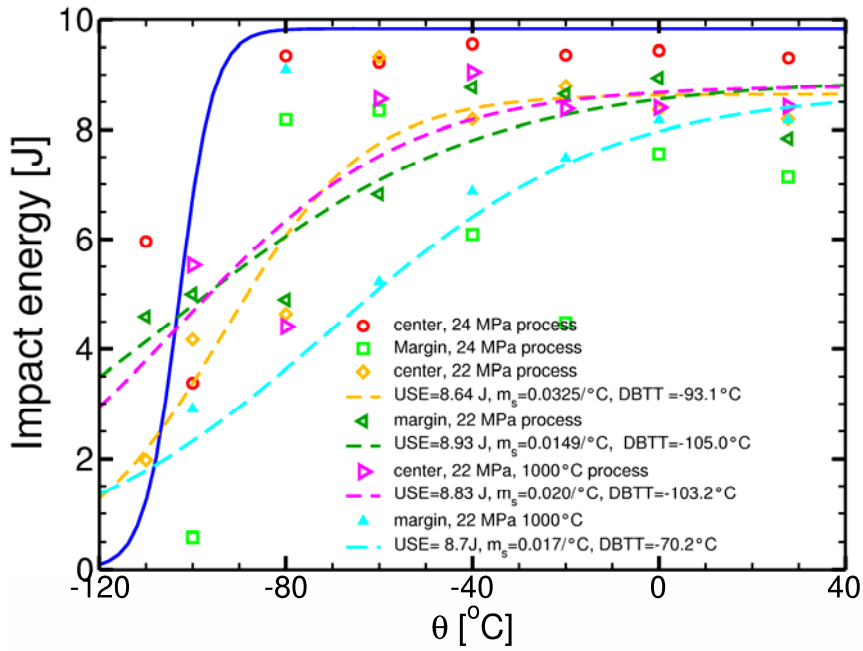


Fig. 3: Results of Charpy impact experiments in diffusion weld specimens produced with flaws during first step. The diffusion weld samples are taken from different regions of the rolled tin.

Conclusion

This task will be closed this year. The task yields a table of allowable diffusion weld process parameters. This will be a first data base to a quality assurance. The task yields the proof for the advantage of a pre-stage procedure. The influence of a locally varying diffusion weld quality and possible counter measures have been investigated.

Staff:

J. Aktaa
U. Bürkle
A. von der Weth

TTMS-005 Rules for Design, Fabrication and Inspection

TW2-TTMS-005b D 1 TBM Design Rules

The objective of this task is the development of design rules for ITER test blanket modules (TBM) built from RAFM steels. The TBM has to be dimensioned against different kinds of failure: ductile, creep and fatigue failure taking into account the influence of irradiation. The design rules will be built up on existing codes for nuclear applications considering the life time prediction approaches that have been developed within TW2-TTMS-005a D4 for RAFM steels and their specific mechanical behaviour. The assessment of the design rules formulated is also a part of this task. Therefore the performance and evaluation of suitable verification experiments, among others isothermal multi-axial fatigue tests at room temperature as well as at elevated temperature, close to the operating temperature, with the reduced activation alloy EUROFER 97 are foreseen.

Within the reporting period the isothermal multiaxial fatigue tests with combined pull-push / alternating torsion loading were completed. As a result of the applied load the directions of the principal stresses and strains are not fixed for non-proportional loading conditions (phase shift between pull-push and torsion $\neq 0^\circ$ or 180°) and rotate during a cycle (rotating principal stresses and strains RPSS). Therefore these tests differ from those reported in the last period, which were performed with fixed principal axis for stresses and strains (FPSS) but at room temperature only.

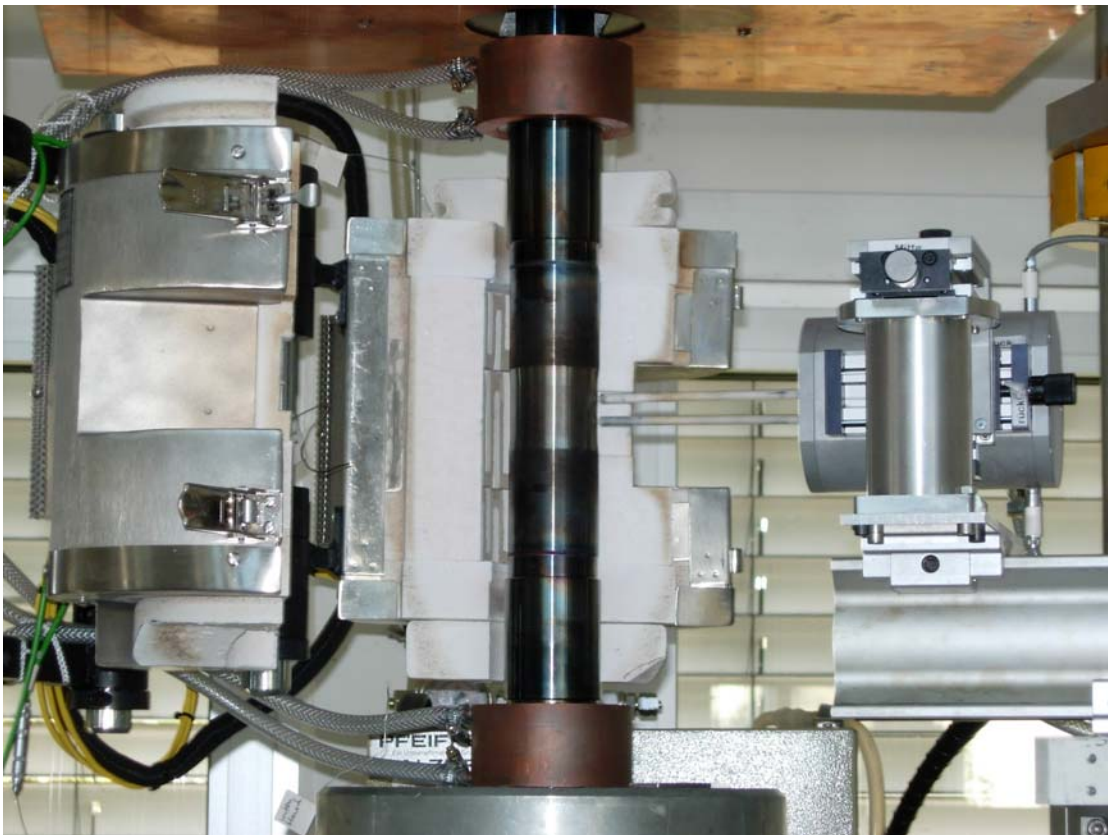


Fig. 1: Biaxial Test Facility.

The combined pull-push / alternating torsion experiments were performed on tube specimens using a biaxial test facility. For the elevated temperature experiments we mounted a resistance furnace (Figure 1) on the pillar of the biaxial testing machine. To ensure that the clamping jaws are not heated, the bolts which are welded with the specimens were ex-

tended, so that it was able to mount cooling sleeves around. Furthermore we used a combined tension/torsion extensometer to measure the axial strain ε_{ax} and the shear strain γ simultaneously. All experiments were fully strain controlled with alternating axial and shear strains which are varied according to sinusoidal courses with a frequency of 0.5 Hz and a shear strain amplitude equal to the axial strain amplitude multiplied by $\sqrt{3}$ for all tests. Beside the temperature the phase shift between the course of axial strain and the course of shear strain as well as the strain amplitudes selected belong to the test conditions which may vary from test to test.

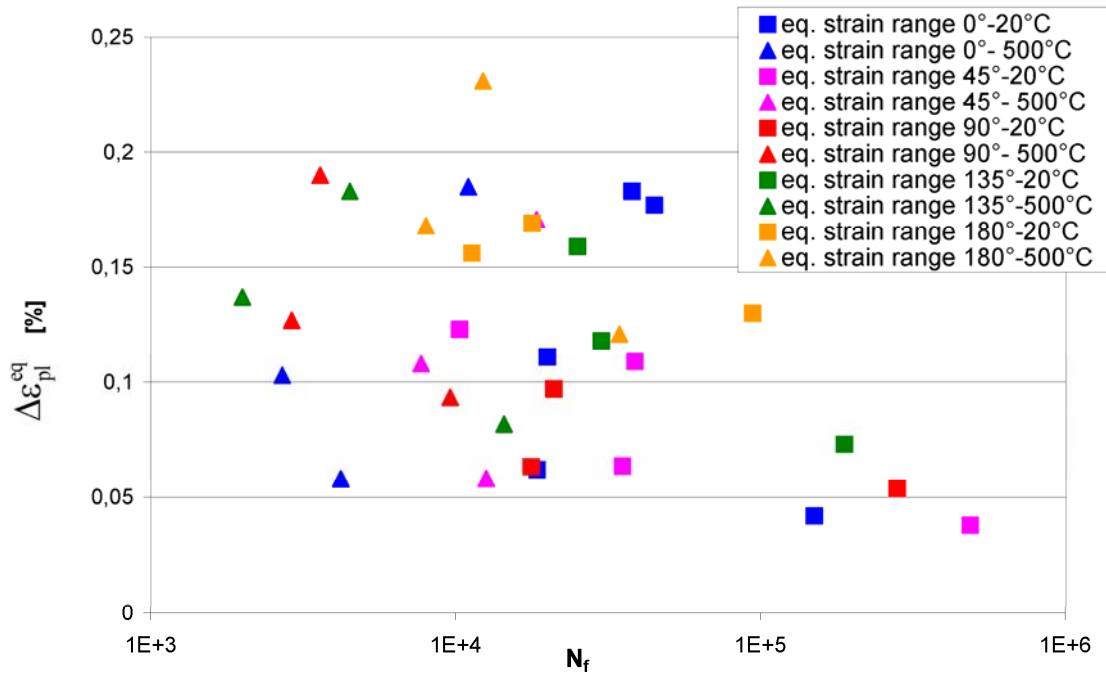


Fig. 2: Correlation between non-proportional fatigue life and the equivalent plastic strain range.

In a first evaluation we plotted in a Manson-Coffin diagram the equivalent inelastic strain range of the cycle at half number of cycles to failure versus number of cycles to failure N_f (see Figures 4-6). The results obtained show no clear monotonic dependence of the equivalent plastic strain range on the number of cycles to failure. In fact a very large scatter band for all phase shifts exists, particularly at low N_f .

Observing the dependence of the equivalent stress range of the cycle at $N_f/2$ on N_f the expected characteristics exist (Figure 3). For higher lifetimes the equivalent stress range decreases for both, room temperature and elevated temperature. At elevated temperature the slope is lower than at room temperature. In this case the influence of the load on lifetime seems to be apparently lower than at room temperature.

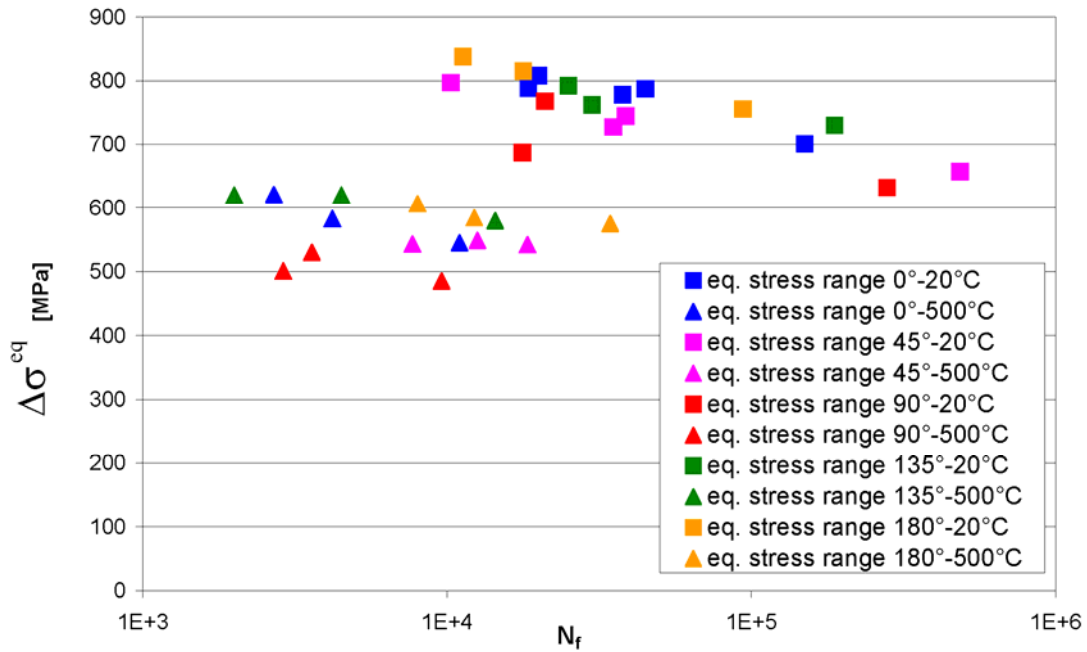


Fig. 3: Correlation between non-proportional life and the equivalent stress range.

Comparing the equivalent total strain ranges of the multiaxial tests with those of the uniaxial tests and those of the design curve derived from the uniaxial tests for the same numbers of cycles to failure (Figure 4) it is obvious that the multiaxial results are more critical. In fact, some multiaxial results are below the design curve. Here for clarity reasons all multiaxial results (for all phase shifts and temperatures) are subsumed.

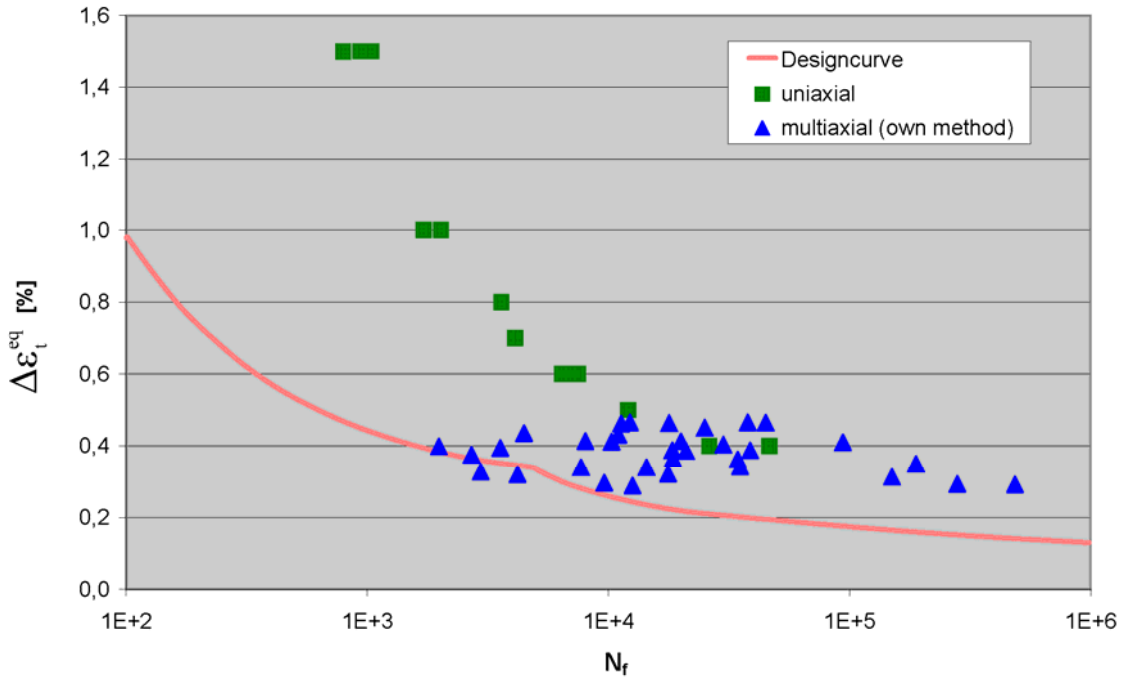


Fig. 4: Total equivalent strains ranges compared to the design curve.

Comparing the equivalent stress ranges to uniaxial stress ranges an affinity is observed (Figure 5). At the same load level the number of cycles to failure is nearly the same.

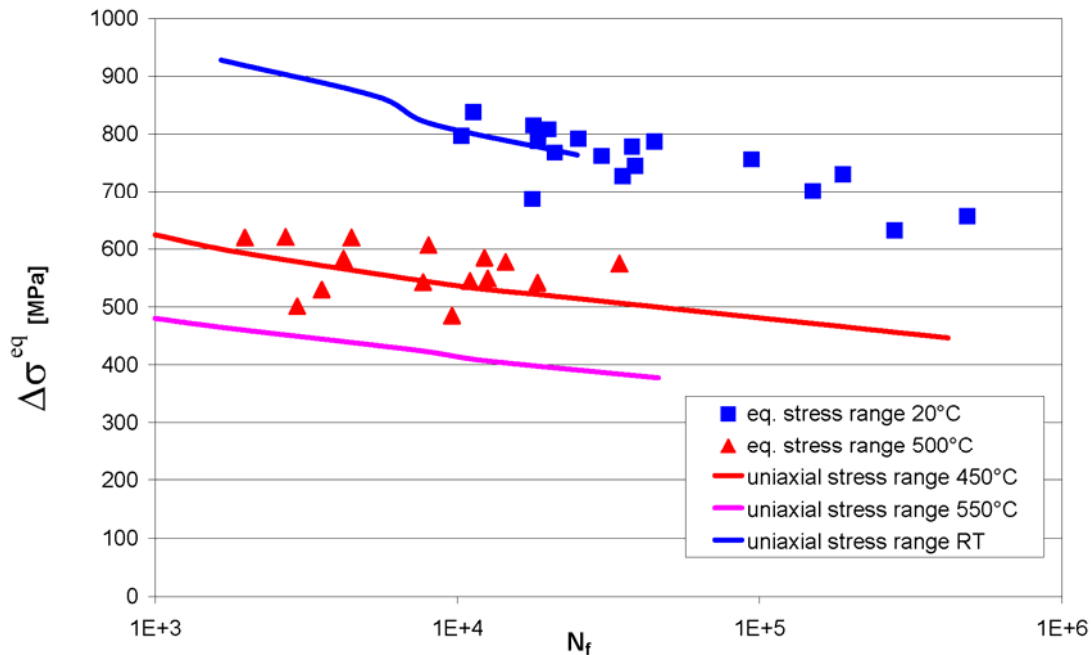


Fig. 5: Equivalent stress ranges compared to uniaxial stress ranges.

So our investigations show the following results:

1. The equivalent total strain ranges are clearly lower than the uniaxial ones at the same number of cycles to failure;
2. The equivalent stress ranges are nearly the same as the uniaxial ones at the same number of cycles to failure.

These differences in strain and the consonance in stress leads to the conclusion that the multiaxial cyclic loading leads to additional hardening and in total reduced softening compared to uniaxial cyclic loading. To verify this assumption we plotted the stress-strain curves at room temperature for multiaxial and uniaxial cyclic loadings and compared the values with the monotone loading curve obtained from tensile test (Fig. 6). The uniaxial cyclic results are clearly below the uniaxial monotone curve. This is in accordance to the well known cyclic softening of EUROFER. In the multiaxial case the behaviour is different where an additional effect must be existent. This effect is probably the additional hardening, which appears under non-proportional cycling loading and leads to higher stresses, compared to the uniaxial case. So for multiaxial cyclic loading both effects, cyclic softening and additional hardening are apparently mutual annulled.

Hence, a pure strain based design curve seems not to be meaningful. The design curve should also consider the stress which has been however taken into account in the lifetime prediction models developed so far under TTMS-005.

A final report including the results of all verification tests performed within this task and their evaluation as well is now in preparation and will be shortly published.

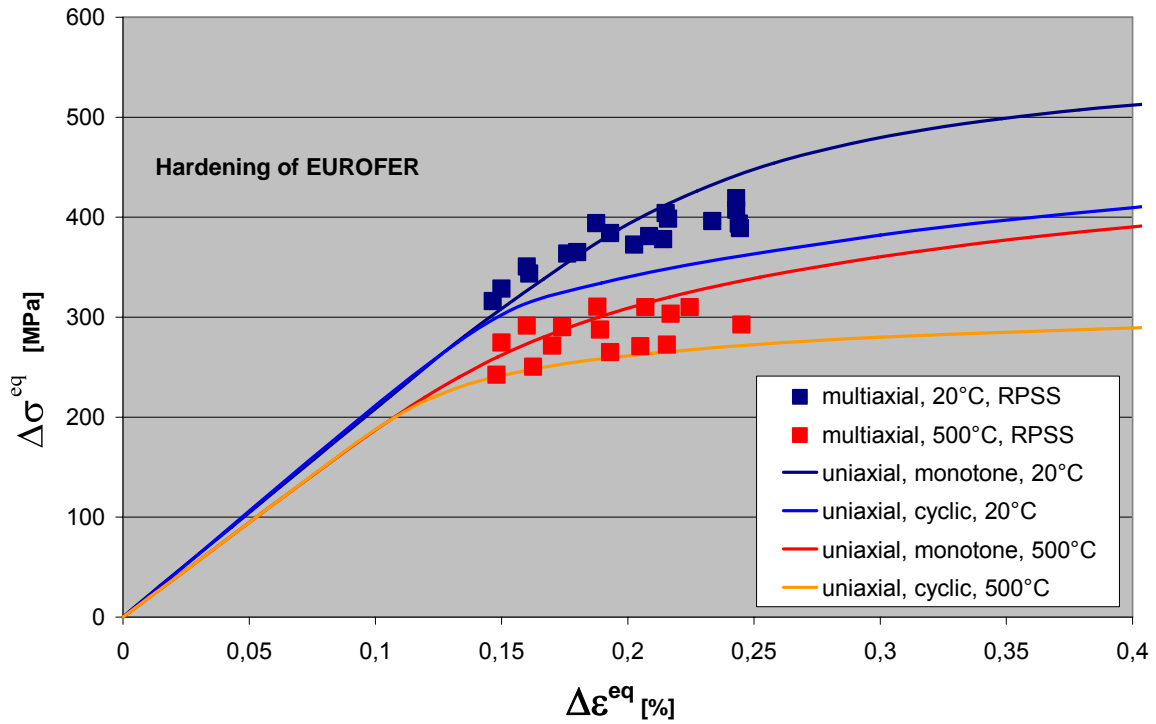


Fig. 6: Hardening of EUROFER at uniaxial (monotonic and cyclic) and multiaxial cyclic loading in comparison.

Staff:

J. Aktaa
M. Weick
S. Knaak

Literature:

- [1] M. Weick, S. Knaak & J. Aktaa, "Multiaxial Fatigue Behaviour of EUROFER 97," ICFRM 12, Santa Barbara, CA, USA, Dec. 2005
- [2] J. Aktaa, M. Klotz, C. Petersen, "Deformation and Damage of RAFM Steels under Thermomechanical Loading: A Challenge for Constitutive Equations," ICFRM 12, Santa Barbara, CA, USA, Dec. 2005
- [3] J. Aktaa and R. Schmitt, "High temperature deformation and damage behavior of RAFM steels under low cycle fatigue loading: Experiments and modeling," Fusion Engineering and Design, 81 (2006) 2221-223

TW2-TTMS-005b D 2

Evaluation of the Material Design Limits for TBM's Application

TW5-TTMS-005 D 8

Definition of an Experimental Programme for Validation of HT Creep-fatigue Rules at Fusion Relevant Conditions

Objectives

In the first line, the aim of the activity represented here is an application of two advanced material models for simulation of the test blanket module (TBM) undergoing cyclic thermal and mechanical loadings. The first model is thereby the ABAQUS standard combined non-linear isotropic-kinematic hardening model whereas the second is a viscoplastic material model considering material damage and being newly implemented by J. Aktaa as an ABAQUS user material (UMAT).

Material parameters for both models are adjusted using results of isothermal tensile and cyclic experiments performed at FZK on EUROFER 97. As is generally known, EUROFER 97 is an important blanket material for the future fusion reactor and belongs to reduced activation ferritic-martensitic steels (RAFM), which soften under cyclic loading in contrast to austenitic steels exhibiting cyclic hardening.

Moreover, the work is focused on the application of some existing design rules considered for austenitic steels and further evaluation of the rules by comparison of their predictions with results of cyclic simulations using the advanced material models mentioned above. Thereby, some important allowable stress limits are calculated under consideration of the cyclic softening of RAFM.

Finally, we aim at a detailed proposition of the mock-up experiment allowing us to verify the advanced material models used within the activity and to assess a capability of the actual TBM design. The propositions include precise definitions of the component geometry as well as optimized thermal and mechanical boundary conditions and loads.

Activity status at the beginning of 2006

Up to the end 2004:

- Adjustment of material parameters required for the ABAQUS-own non-linear kinematic/isotropic hardening material model (see ABAQUS/Standard User's Manual, Vol. II, Ch. 11.2.2) on the basis of the data stemming from a life time study of EUROFER 97 at 450°C, 550° and 650°C performed by J. Aktaa & R. Schmitt [1];
- Creation of a 2D finite element (FE) model of a ¼ of the test blanket module (TBM) according to current TBM design.

Up to the end 2005:

- Enhancement of material parameters determined in 2004;
- Computation of the temperature distribution in the ¼ of TBM due to various thermal loadings;
- Determination of the elastic limit i.e. of the minimum coolant pressure causing an inelastic response after the 1st cycle as a function of the plasma heating and the temperature of cooling channels T^{CC} using both material models;

- Simulation of the cyclic behaviour of TBM using the UMAT for the first 600 cycles under consideration of the following loads: $T^{\text{cc}} = 600^{\circ}\text{C}$ (873 K); the plasma heating of 750 kW/m^2 and the coolant pressure $P = 50\text{ MPa} = 500\text{ bar}$;
- Calculation of the allowable membrane stress intensity labelled as S_m^* under consideration of the cyclic softening of ferritic-martensitic steels;
- Application and verification of some low-temperature design criteria.

Results achieved in 2006

In this section, we represent results of our activity in 2006.

Calculation of allowable stress intensities

We have enhanced and extended the definition of S_m^* introduced in 2005, see fig. 1, for the following reason: It is unfortunately not straightforward to compare directly cycles in tensile experiments carried out at constant temperature on small specimens with operating cycles of a component including mechanical pressure in cooling channels and possibly high temperature gradients. We have thus calculated only one S_m^* value for each temperature and labelled it as S_m^C , whereby the subscript C denotes that the value should be applied if C-type loadings appear in contrast to S_m values valid for M-type loadings. This value corresponds to a cycle number $N_f/2$ highlighted in fig. 1 and is representative for the given temperature. S_m^* becomes therewith a transient value and is not applied below.

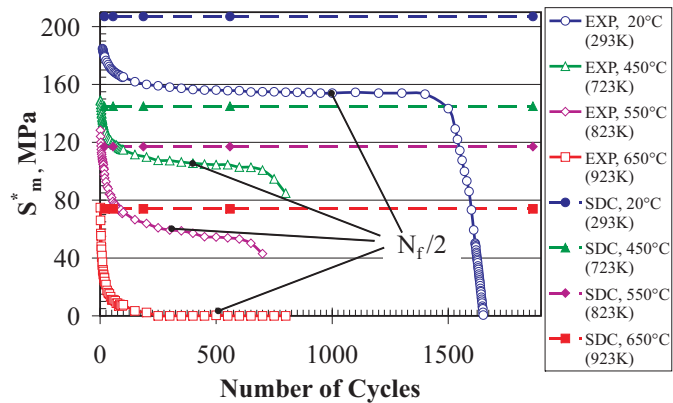


Fig. 1: Change of S_m^* under cyclic loading at RT, 450°C (723K), 550°C (823K) and 650°C (923K); available data for these temperatures S_m are also given for comparison.

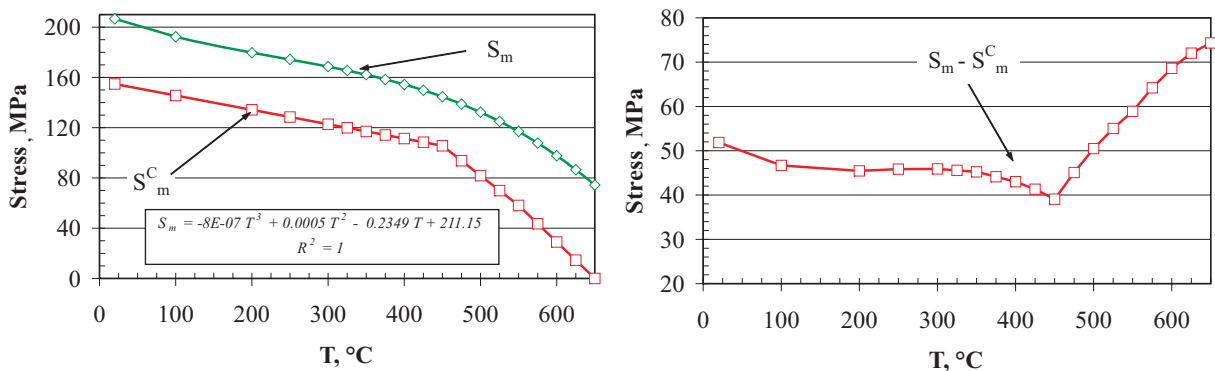


Fig. 2: On the left: the change of S_m^C with temperature up to 650°C (923 K); available data for these temperatures S_m are also given for comparison; the polynomial $S_m(T)$ exhibits a very good agreement with the experimental S_m curve. On the right: the difference between S_m^C and S_m

As follows from the left-hand side diagrams in fig. 2, S_m^C and S_m values exhibit a very similar behaviour as functions of temperature. A gap between the curves increases with increasing temperature as shown again in fig. 2, on the right. Thereby, the gap increases almost linearly at HT beginning with 450°C (723K). The reduction of the allowable stress intensity due to the

cyclic softening should definitely be accounted in design estimations if C-type loadings are considered.

In the same manner, we have also introduced and calculated the allowable primary plus secondary membrane stress intensity S_e^C as well as the allowable total stress intensity S_d^C , see FZKA 7241 (2006).

Evaluation of design rules

We have applied design rules based on the elastic-plastic analysis and being also valid for HT additionally to design rules chosen for evaluation in 2005. Thus, the following design rules have been evaluated:

- Rules for prevention of immediate plastic collapse and plastic instability (M-type damage):

$$\overline{P_m} \leq S_m ; \quad \overline{P_m + P_b} \leq K_{eff} S_m$$

- The rule for prevention of immediate plastic flow localization (M-type damage):

$$\overline{P_m + Q_m} \leq S_e \text{ (elastic)} ; \quad \varepsilon_{m1}^{pl} \leq \varepsilon_u(T_m)/2 \text{ (elastic-plastic)}$$

- The rule for prevention of immediate local fracture due to exhaustion of ductility (M-type damage):

$$\overline{P_m + P_b + Q} \leq S_d$$

- The rule for prevention of progressive deformation or ratcheting (C-type damage):

$$\overline{P_m + P_b} + \left[\overline{\Delta P_{max}} + \overline{\Delta Q_{max}} \right] \leq 3 S_m \text{ (elastic)}$$

$$\varepsilon_{m1}^{pl} \leq 0.5 \lambda_1 \min_{T_m} \{ \varepsilon_u(T_m) \} \text{ (elastic-plastic).}$$

- Creep effects

$$U_t(\overline{P_m}) \leq 1 ; \quad U_t(\overline{P_m + P_b / K_t}) \leq 1 \text{ (elastic)}$$

with the creep usage fraction for primary stress U_t , see ITER SDC subsection IC 2764 [2], and the creep bending shape factor $K_t \equiv [K_{eff} + 1]/2$. Thereby, all overlined expressions above mean the von Mises norm. For other notations used here, we refer to FZKA 7241 and to ITER SDC-IC. Results of the evaluation of the low-temperature rules within the elastic route are collected in table 1.

Thus, the chosen design rules predict (a) plastic collapse and plastic instability, (b) probable plastic flow localization, (c) local fracture due to the exhaustion of ductility as well as (d) probable accumulation of plastic deformation. The prognoses confront however with simulation results using the viscoplastic material model including damage. The simulations show rather a non-ratcheting behaviour at least for the first 600 cycles. To obtain a more definite result, cyclic simulations should be continued up to the component failure. An extrapolation method proposed by [3] allows for instance such simulation. On the other hand, all design criteria should be checked according to the scheme given in ITER SDC-IC, subsection IC 3030.

Table 1: Maximum absolute values of the categorized stress components and their combinations among all values for the chosen paths together with the corresponding values of the available S_m and calculated S_m^C stress intensity limits; the units are MPa.

$\overline{P_m}$	S_m^{898K}	$S_m^{C 898K}$	S_m^{873K}	$S_m^{C 873K}$
117.0	87.0	14.5	98.0	29.1
$\overline{P_m + P_b}$	$K S_m^{898K}$	$K S_m^{C 898K}$	$K S_m^{873K}$	$K S_m^{C 873K}$
179.7	130.5	21.8	147.0	43.6
$\overline{P_m + Q_m}$	S_e^{898K}	$S_e^{C 898K}$	S_e^{873K}	$S_e^{C 873K}$
129.9	86.6	61.8	97.7	68.4
$\overline{P_m + P_b + Q}$	S_d^{898K}	$S_d^{C 898K}$	S_d^{873K}	$S_d^{C 873K}$
260.9	173.1	123.6	195.3	136.8
$\overline{P_m + P_b + \Delta Q_{\max}}$	$3 S_m^{898K}$	$3 S_m^{C 898K}$	$3 S_m^{873K}$	$3 S_m^{C 873K}$
179.7 + 215.8 = 395.5	261.0	43.6	294.0	87.2

Definition of the mock-up experiment

According to our proposition, a box-shaped model of TBM has three separated cooling channels as depicted in fig. 3. Thereby, we have used the first wall geometry proposed by TBM designers. The coolant pressure P is firstly assumed to be constant and equal to 100 bar = 10 MPa. The coolant temperature should vary from channel to channel in accordance with the design of the TBM. In the study, we firstly consider the following four load cases:

- $T_1 = 300^\circ\text{C}$ (573K) & $T_2 = 350^\circ\text{C}$ (623K)
- $T_1 = 350^\circ\text{C}$ (623K) & $T_2 = 300^\circ\text{C}$ (573K)
- $T_1 = T_2 = 300^\circ\text{C}$ (573K)
- $T_1 = T_2 = 350^\circ\text{C}$ (623K)

The cycles are chosen similar to the working cycles of the TBM: (1) heating and application of the pressure, 30 s; (2) holding at the high temperature (HT) t^{HT}_{hold} , (3) cooling to RT, 100 s and, finally, (4) holding at RT for 600 s. Thereby, t^{HT}_{hold} is evidently relevant for the amount of inelastic deformation and has for this reason been chosen as the 1st design parameter. The outer wall thickness (OWT) has been chosen as the 2nd design parameter and changes in the range of 1 mm to 5 mm.

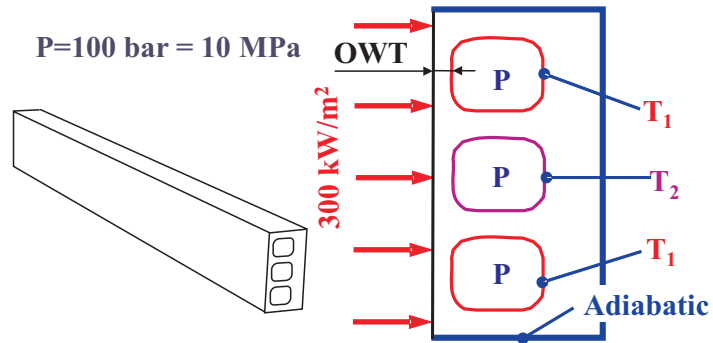


Fig. 3: The geometry of the proposed mock-up model together with the mechanical and thermal loads (on the right).

Thus, within the frame of the work presented we have simulated first 50 cycles using the coupled deformation-damage material model mentioned above for $OWT = 1.0$ mm, 2.0 mm; 3.5 mm, 5.0 mm and $t^{HT}_{hold} = 600$ s, 1800 s, 3600 s, 7200 s on the basis of a 2D FE model. The temperature distribution as well as the linear-elastic behaviour has been simulated however on the basis of a 3D FE model.

Further simulations considering a variation of the coolant pressure and the temperature difference between the cooling channels allow us to formulate the following conditions for the mock-up experiment:

- Case 2 for the surface temperature of the cooling channels i.e. $T_1 = 450^\circ\text{C}$ (723K) & $T_2 = 300^\circ\text{C}$ (573K); (Evidently, higher $T_1 = 550^\circ\text{C}$ (823K) results sufficiently in a reduction of the number of cycles up to the failure of the model. The temperature should be however realizable experimentally.)
- The outer wall thickness $OWT = 5.0$ mm;
- The hold time at the high temperature $t_{hold}^{HT} = 1800$ s;
- The coolant pressure P at least 10 MPa i.e. 100 bar.

If $T_1 = 450^\circ\text{C}$ (723K) is not realizable and only $T_1 = 350^\circ\text{C}$ (623K) can be reached experimentally, P should be increased up to at least 15-20 MPa i.e. 150-200 bar.

For the modelling, we have used geometrical parameters corresponding to actual propositions of TBM designers. Among all these parameters, we have varied only the outer wall thickness OWT . The heating of the front side is considered to be constant and equal to 300 kW/m². We recall also another model simplification concerning the constant temperature over the total surface of a cooling channel. Thereby, surface temperatures in different cooling channels are not equivalent as shown in fig. 3. We also found out that t_{hold}^{HT} influences damage amount only slightly in contrast to OWT and P and, on the other hand, ΔT influences damage more sufficient than P .

Summary and Outlook

In the present work, material parameters required for the non-linear kinematic-isotropic hardening ABAQUS standard material model have been determined. These parameters have been used together with a coupled deformation-damage viscoplastic material model to determine the coolant pressure causing plastic deformation as a function of the temperature in the cooling channels and the plasma heating. Furthermore, the cyclic behaviour of the TBM has been simulated using both material models. It turned out that the ABAQUS standard material model used is not appropriate enough to describe behaviour of components undergoing different loadings at HT for a longer time. However, this time-independent material model can be involved for simulations under monotonic loadings to verify the low-temperature rules for the M-type damage requiring a pure plastic strain part without the creep part.

On the other hand, some important design rules have been applied to the model and their predictions have been compared with results of the cyclic simulations. It turned thereby out that the criterions are not fulfilled, even if the conventional limit values of stress intensities are used. The newly calculated values of allowable stress intensities s_m^C , s_e^C and s_d^C accounting for the cyclic softening of the EUROFER 97 steel lead to a larger gap between the target and actual results.

An investigation of the temperature dependence of the allowable stress intensities shows that cyclic loadings lead to a reduction of conventional values of e.g. s_m by approximately 40 - 80 MPa. For this reason, we recommend to use the available values to design a component underlying to monotonic loadings and the proposed values s_m^C if cyclic loadings occur.

The results of the cyclic simulations exhibit neither plastic collapse nor ratcheting after the first 600 cycles. This discrepancy could mean that the criterions could be possibly too conservative for EUROFER 97 and should be revised. The suggestion, however, requires a further in-depth study including a verification of all (elastic and elastic-plastic) design rules pre-

venting both the M-type and C-type damage as well as the possible changes in the actual TBM geometry.

Further design propositions concerning the mock-up experiment can occur due to a variation of other geometrical parameters, plasma heating, a simulation of more cycles using both the RESTART option and the extrapolation method mentioned above. Moreover, the temperature on the surface of the cooling channels is not constant and should be determined on the basis of a thermo-hydraulic simulation.

Staff:

R. Sunyk

Literature:

- [1] J. Aktaa and R. Schmitt „Creep-fatigue Lifetime Prediction Rules for Ferritic Martensitic Steels“, FZKA 6931 (2004)
- [2] ITER Structural Design Criteria for In-vessel Components (SDC-IC), ITER Doc. G 74 MA 8 01-05-28 W0.2 (internal project document distributed to the ITER participants)
- [3] H. Kiewel, J. Aktaa and D. Munz „Application of an extrapolation method in thermocyclic failure analysis“, Comput. Methods Appl. Mech. Engrg. , 182 (2000), pg. 55-71
- [4] R. Sunyk, J. Aktaa, “Evaluation of ITER design criteria applied to RAFM steels”, , Wissenschaftliche Berichte FZKA 7241, 2006, Forschungszentrum Karlsruhe GmbH, Aug. 2006
- [5] R. Sunyk, J. Aktaa, “Determination of design limits for a test blanket module under ITER operating conditions”, IEEE Catalog No. 05CH37764C, ISBN 1-4244-0150-X, Library of Congress 85-654749 (2005)
- [6] R. Sunyk, J. Aktaa, “Verification of Design Rules for EUROFER under TBM Operating Conditions”, Journal of Nuclear Materials, corrected proof (2006)
- [7] R. Sunyk, J. Aktaa, “Optimization of a Mock-Up Experiment for the ITER Test Blanket Module using Finite Element Analysis”, submitted to Fusion Engineering and Design, 2006
- [8] R. Sunyk, J. Aktaa, “Enhancement of Allowable Stress Intensities by Consideration of Cyclic Softening of Ferritic-Martensitic Steels”, submitted to Int. J. Press. Vessels & Piping, 2006

TW2-TTMS-005b D 4 Creep-fatigue Lifetime Prediction Rules for Irradiated EUROFER

The objectives of this task are the modification of the lifetime prediction model developed in TW2-TTMS-005a D4 for RAFM steels under creep fatigue conditions taking into account the irradiation influence and the verification of the modified model by applying it to EUROFER 97 in the post-irradiated state.

During the reporting time period the post irradiation investigations of EUROFER 97 were in progress however no sufficient data were available for application of the modified life time prediction model on EUROFER 97. Instead, the coupled deformation damage model, which was implemented in the finite element code ABAQUS, has been used to simulate thermo-mechanical fatigue tests performed on EUROFER 97 in the reference (unirradiated) state.

The finite element simulations of the thermo-mechanical tests showed that at the middle of the specimen a mechanical strain range higher than the value measured as an average for the gauge length in the real test can be calculated. However, this maximum mechanical strain range is still lower than that corresponding to the experimentally observed fatigue life predicted on the base of isothermal fatigue data (Figure 1).

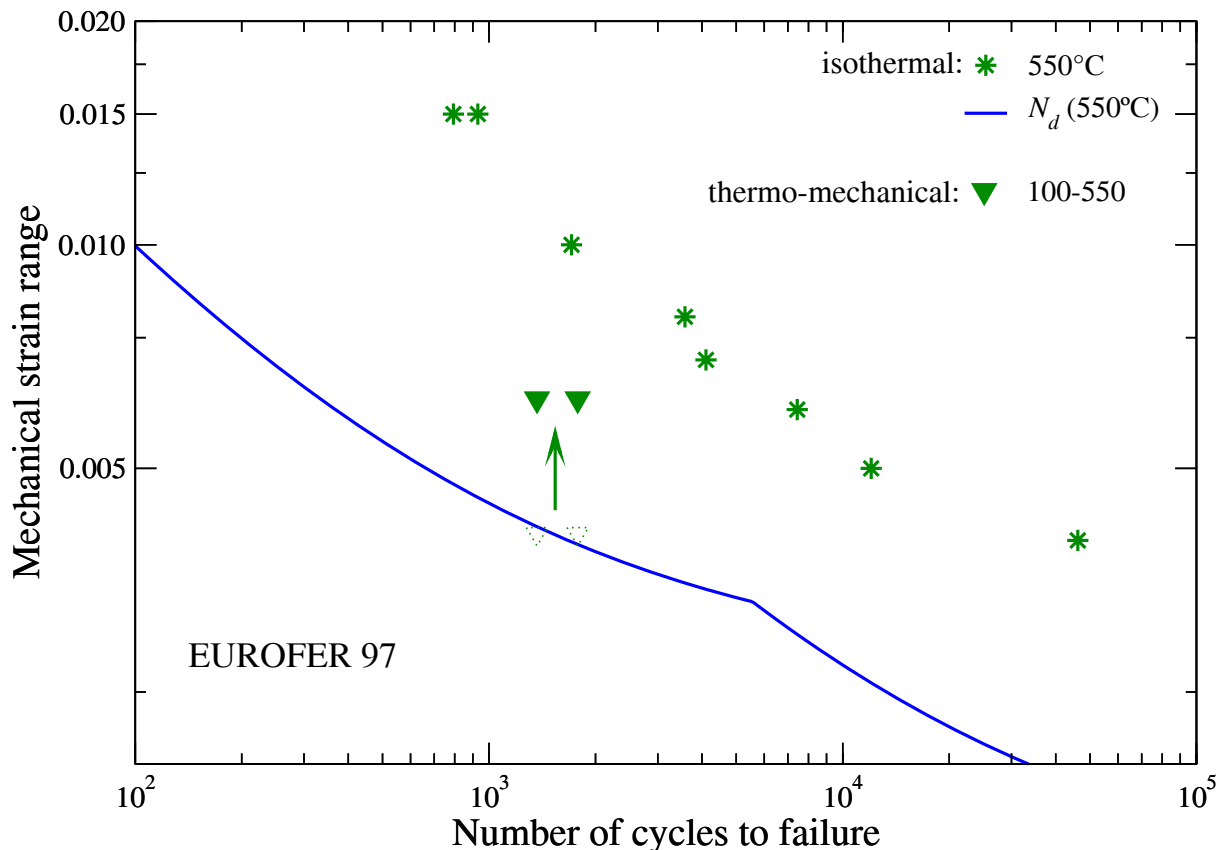


Fig. 1: Maximum mechanical strain range at the half number of cycles to failure calculated using finite element simulations versus number of cycles to failure for thermo-mechanical fatigue tests in comparison to those measured for the entire gauge length (symbols with dotted outline) and to those of isothermal fatigue tests and the design curve derived there from.

Accordingly one may conclude that thermo-mechanical cycling of EUROFER 97 yields more fatigue damage than isothermal cycling with the same mechanical strain range. But before doing so, it should be ruled out that the progressive strain localization calculated at the middle of the thermo-mechanical fatigue specimen, caused by both temperature gradients in the specimen and cyclic softening behaviour of the material, would yield deformation instabilities and locally even higher fatigue loads. These deformation instabilities and the resulting higher

local fatigue loads can not be correctly modelled by the geometric linear finite element simulations performed. However, they can be investigated performing either geometrically nonlinear simulations, which require development of additional tools, or thermo-mechanical fatigue tests with specimens of different geometries and buckling behaviour, respectively.

Staff:

J. Aktaa

Literature:

- [1] J. Aktaa, M. Klotz, C. Petersen, "Deformation and Damage of RAFM Steels under Thermomechanical Loading: A Challenge for Constitutive Equations," ICFRM 12, Santa Barbara, CA, USA, Dec. 2005
- [2] J. Aktaa and R. Schmitt, "High temperature deformation and damage behavior of RAFM steels under low cycle fatigue loading: Experiments and modeling," Fusion Engineering and Design, 81 (2006) 2221-223

TW2-TTMS-005b D 7 Small-scale Fracture Mechanics Specimens

TW5-TTMS-005 D 3

SSTT: Model the Ductile Region - Development of Models for Transferability of Small Size Specimens to Standard Size and FW Applications

TW6-TTMS-005 D 12

SSTT: Continuation of the Modeling the Ductile Region - Development of Models for Transferability of Small Size Specimens to Standard Size and FW Applications

Objectives

The main objective of the activity is to find a save approach for transferring of the FM parameters, in the first line the crack resistance curves $J(\Delta a)$ obtained at small scale specimens to standard-sized specimens and whole components.

Activity status at the beginning of 2006

First test simulations using the micromechanics-based material model implemented by Dr. F. Reusch (University of Dortmund) as a user material (UMAT) in the commercial FE code ABAQUS have been performed in the end of 2005. As described in the previous reports, the modified GTN material model is chosen for the implementation.

Furthermore, the concept for scaling of crack resistance curves proposed in [1] has been studied and chosen as a possible main tool in the current activity. The aim of the further activity is to validate this concept with respect to firstly the GTN material model and secondly to ferritic-martensitic steels.

Achieved results

In this section, we give a short description of results achieved in 2006.

Simulation of the crack propagation in the SE(B) FM probe

The UMAT has been applied to the simulation of the crack propagation in the 3PB specimen depicted in fig. 1. Thereby, simulations have been performed for five different lengths a_0 of the initial crack: 1.0 mm, 1.5 mm, 2.0 mm, 2.5 mm and 3.0 mm. Due to convenient partition shown in fig. 2, a_0 could be controlled exactly by changing of the nodal sets containing the net section of the specimen.

The full integrated 4-nodes plain strain elements CPE4 have been used for the simulation. Three meshes with different (0.075 mm, 0.100 mm and 0.150 mm) lengths of elements along the ligament have been generated to investigate a mesh dependence of J-integral. The discretized FE model is shown in fig. 3 for the element length of 0.100 mm.

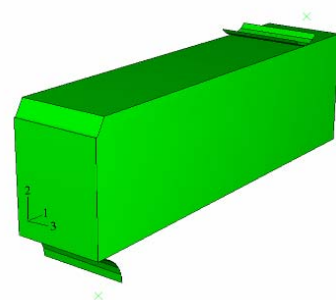


Fig. 1: The half of the 3PB sample (KLST) with the fin and bearing.

Study of the dependence of J-Integral on the definition of the crack-tip region

According to recommendations of [2], a nodal set defining a crack tip region should contain not only the single crack tip node but rather all nodes in the neighborhood of the crack tip, however under the following restrictions:

3. They contain the crack tip node;
4. They form a closed domain;
5. They may not lie on the boundary of the structure.

To verify this proposition, we have defined the crack tip region using three different nodal sets as shown in fig. 2. Thereby, the nodal set cracktip1 contains only the single crack tip node; the cracktip2 contains other nodes (the hatched area in fig. 2 for $a_0 = 1.5$ mm) apart from cracktip1 and, finally, cracktip3 contains all nodes in the pink- and green-colored areas depicted in fig. 2. Note that the set cracktip3 is common for all values of a_0 .

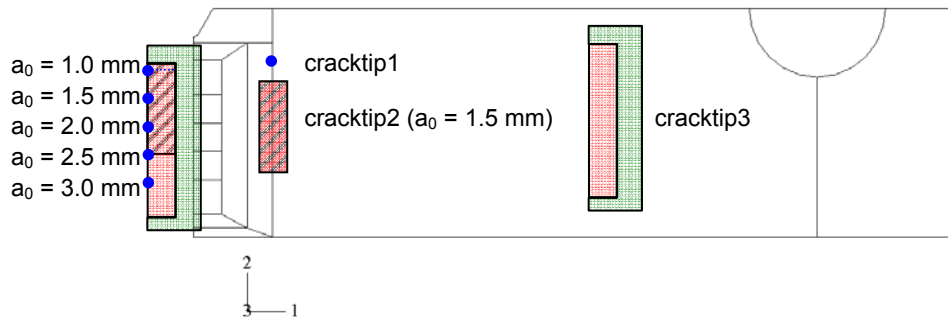


Fig. 2: Partition of the 2D FE model and 3 definitions of the crack-tip region.

Simulations show a good agreement of J-values obtained using cracktip1 and cracktip2 at least up to $a_0 = 2.0$ mm, see fig. 4. For $a_0 > 2.0$ mm as well as for the set cracktip3, the structure boundary should influence the result. For this reason, only results obtained using cracktip1 are discussed below.

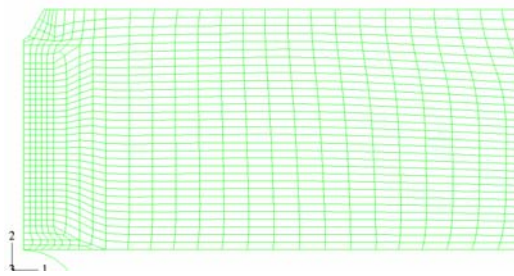


Fig. 3: FE discretization along the ligament with the element length of 0.100 mm.

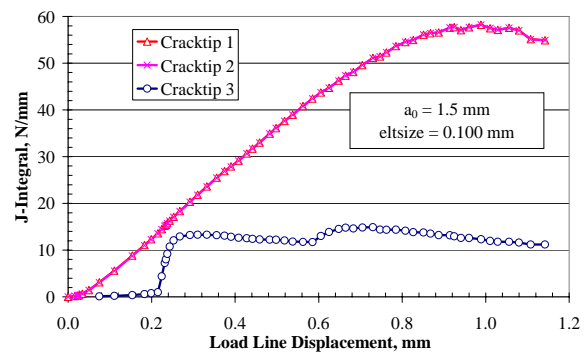


Fig. 4: Comparison of J-Integral-vs.-LL-displacement curves computed by different definition of the crack tip region.

Study of the mesh dependence of the J-Integral

Due to the locality of the material model used for the simulation, the computed J-Integral is dependent on the element size along the ligament. Such mesh dependence is shown in fig. 5 on the left for the case $a_0 = 1.5$ mm. All the meshes lead to the same result up to the load line displacement U_{LL} of approximately 0.43 mm corresponding to comparable crack propagation Δa , which is relevant for an experimental representation of crack resistance curves.

On the right-hand side diagram in fig. 5 is shown the change of J-values in dependence of the element size calculated for U_{LL} of 0.43 mm and 0.83 mm. Unfortunately, the results exhibit only a slight convergence in the case of $U_{LL} = 0.83$ mm. It means that only J-values corresponding to $U_{LL} < 0.5$ mm should be accounted to avoid the mesh dependence. Below, we discuss the results obtained using $eltsize = 0.100$ mm.

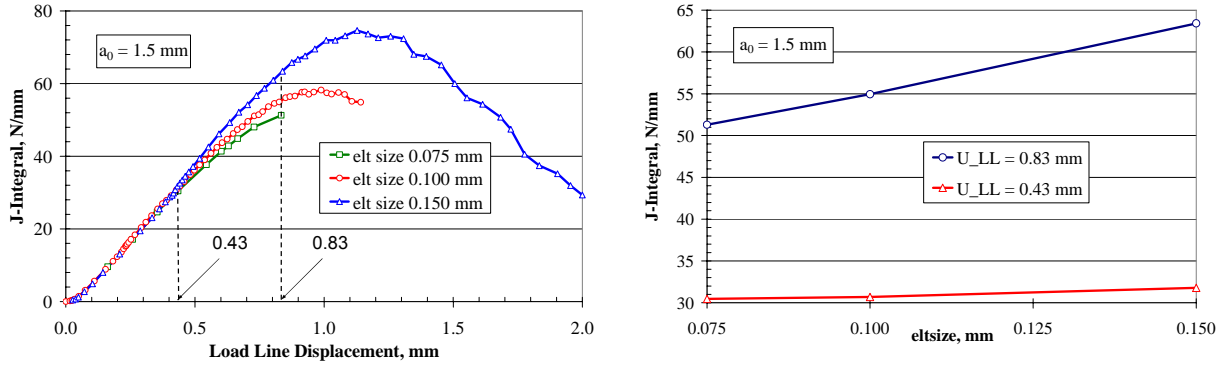


Fig. 5: On the left: comparison of J-Integral-vs.-LL-displacement curves computed with different element sizes along the ligament; on the right: convergence of J values for two values of the LL displacement: 0.43 mm and 0.83 mm (cf. to the left-hand side diagram).

Study of the dependence of J-Integral on the initial crack length

The left-hand side diagram in fig. 6 represents J-values as functions of U_{LL} computed for five different initial crack lengths. The diagram on the right-hand side shows the cross section of the left-hand side diagram for two chosen values of U_{LL} . Both diagrams exhibit a decrease of the J-value as a_0 increases.

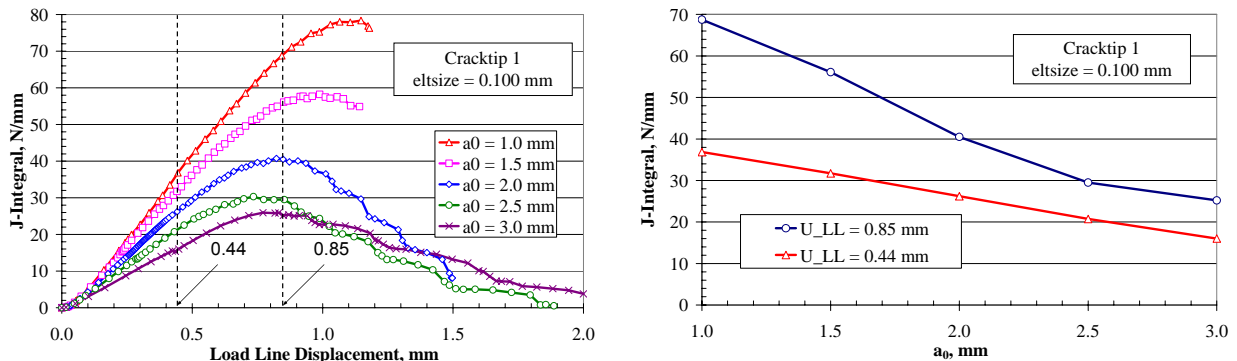


Fig. 6: Comparison of J-Integral-vs.-LL-displacement curves computed for different initial crack lengths.

Representation of advance in the crack propagation

We aim at the calculation of crack resistance curves i.e. in the representation of J-integral as a function of the advance in the crack growth Δa . Whereas J-integral is calculated automatically, convenient criteria for the visualization of the crack propagation should be found out.

According to assumptions of the material model used, material failure occurs i.e. a crack propagates if VVF reaches 0.18 (The final VVF is a material parameter and should be adjusted with accordance to experimental data.). Elements concerned are thereby not eliminated and lose only in stiffness. We propose the following three criteria allowing representation of the crack propagation:

1. VVF (corresponds to the internal model variable SDV7) becomes greater than 0.18;
2. von Mises equivalent stress becomes less than a predefined value (here 10 MPa);

3. Horizontal component of the reaction force at the ligament becomes less than a predefined value (here 10 N).

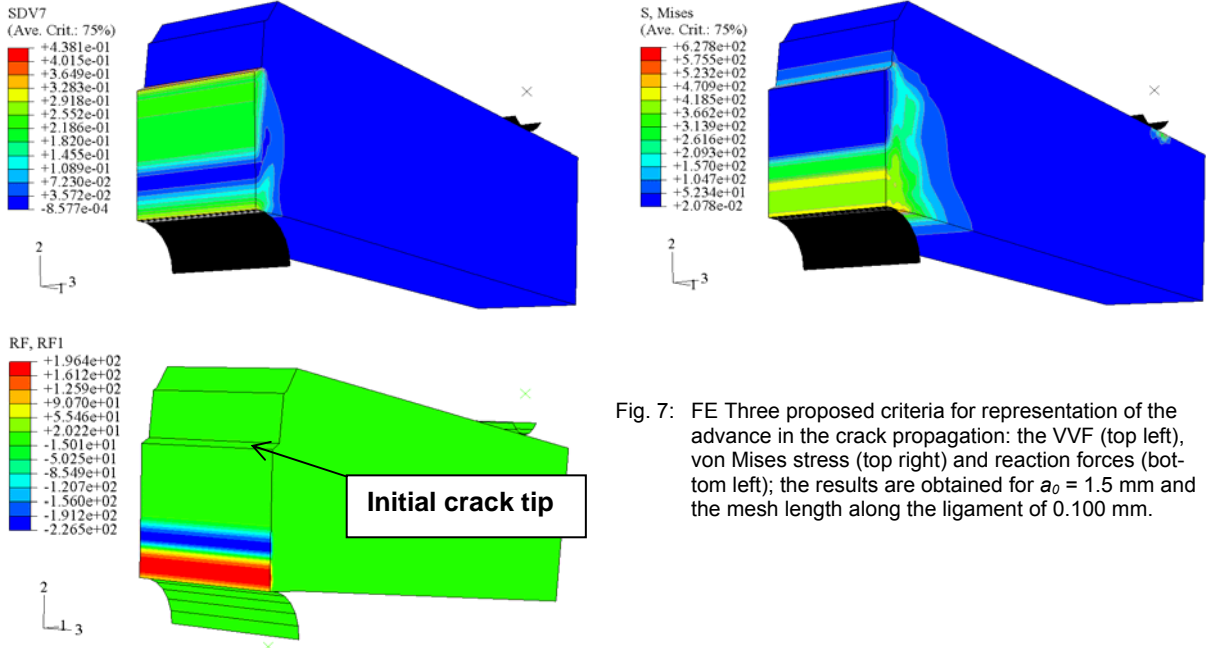


Fig. 7: FE Three proposed criteria for representation of the advance in the crack propagation: the VVF (top left), von Mises stress (top right) and reaction forces (bottom left); the results are obtained for $a_0 = 1.5$ mm and the mesh length along the ligament of 0.100 mm.

Contour plots in fig. 7 illustrate an application of the criteria. An additional illustration to the last criteria is shown in fig. 8. The deformed mesh can also be recognized in this figure (cf. to fig. 3).

Calculation of the $J(\Delta a)$ curves for all computed initial crack lengths

Using one of the criteria described above, a $J(\Delta a)$ curve can easily be calculated according to the following flow chart:

- Save $J_n(t)$ ($n \in [1, N]$) is the current contour number; N is the number of contours in the ABAQUS command line *CONTOUR INTEGRAL), COORY(t), SDV7(t) for all ligament nodes;
- Define $J(t)$ as maximum over all contours: $J(t) = \max\{ J_n(t) \}$ among all $n \leq N$;
- Check one of the crack propagation criteria (CPC) for each node along the ligament and find the critical time t_{cr} for each node if the criterion chosen is fulfilled;
- Define the current Δa as the difference between the current y coordinate of the initial crack tip (ICT) and the current y coordinate of the node K, where the CPC is fulfilled:

$$\Delta a(t_{cr}^K) = \text{COORDY}(\text{ICT}(t_{cr}^K)) - \text{COORDY}(K(t_{cr}^K))$$
- $(\Delta a(t_{cr}^K), J(t_{cr}^K))$ is thus one point of the $J(\Delta a)$ curve.

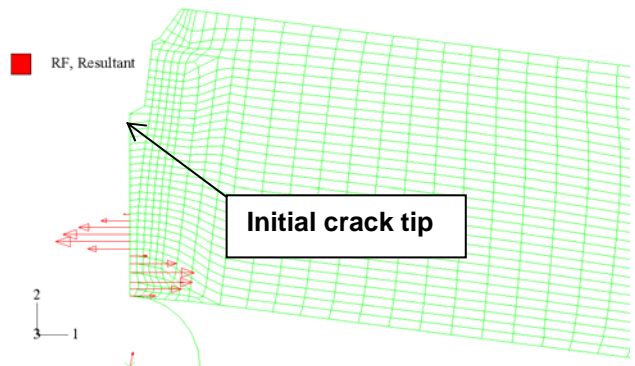


Fig. 8: Deformed mesh after the last simulation step with the resultant horizontal component of the reaction force; the results are obtained for $a_0 = 1.5$ mm and the mesh length along the ligament of 0.100 mm.

Blunting Δa^0 can be also considered as follows. Assume that the CPC at the initial crack tip is fulfilled at t_{cr}^{ICT} . The blunting can then be defined as the difference between the y coordinate of the rigid fin i.e. U_{LL} at t_{cr}^{ICT} and the y coordinate of the ICT also at t_{cr}^{ICT} :

$$\Delta a^0 \equiv \Delta a(t_{cr}^{ICT}) = \text{COORDY}(\text{fin}(t_{cr}^{ICT})) - \text{COORDY}(\text{ICT}(t_{cr}^{ICT}))$$

Δa^0 should be then added to each $\Delta a(t_{cr}^k)$ defined above. $J(\Delta a)$ curves for $a_0 = 1.5$ mm calculated using the proposed criteria are shown in fig. 9. The 2nd and 3rd criteria yield thereby quite similar results, whereas the 1st criterion is more conservative. Below, only the 1st criterion is discussed.

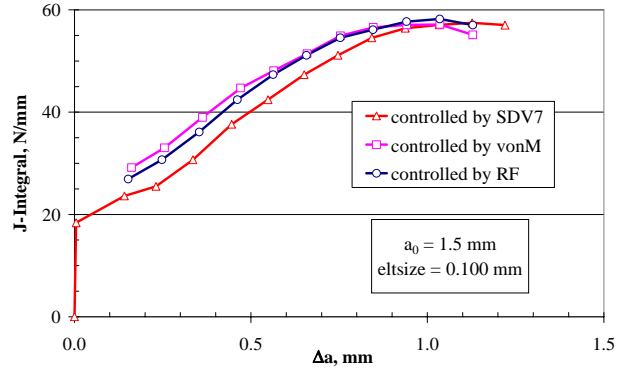


Fig. 9: Comparison of $J(\Delta a)$ curves computed using different criteria of the crack propagation for $a_0 = 1.5$ mm.

All $J(\Delta a)$ curves calculated using the 1st criterion are represented on the left-hand side diagram in fig. 10. The curves should be used for validation of the method proposed by W. Brocks mentioned. The right-hand side diagram in fig. 10 illustrates consideration of blunting described above. Note that blunting increases with increasing a_0 .

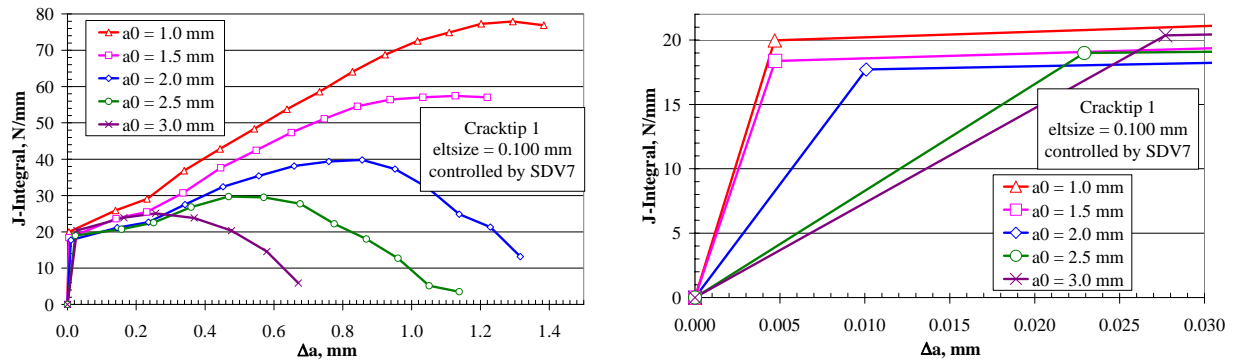


Fig. 10: On the left: comparison of $J(\Delta a)$ curves computed using the VVF criterion for different a_0 ; on the right: increase of the blunting with increasing a_0 .

Outlook

Based on FE simulations:

- Calculation of the stress dissipation rate in dependence on the crack propagation i.e. $R(\Delta a)$ curves using simulation results represented above;
- Scaling of the $R(\Delta a)$ curves and transfer of $J(\Delta a)$ curves shown in fig. 10, on the left, using the approach mentioned;
- Simulation of the crack propagation in a C(T) specimen and validation of the scaling approach by transferring $J(\Delta a)$ curves between C(T) and SE(B) probes.

Based on experimental data:

- Validation of the scaling approach by transferring $J(\square a)$ curves between C(T) and SE(B) probes based on the experimental data listed in FZKA 7252 by E. Gaganidze for SE(B) specimens and obtained from NRG Petten (J.-W. Rensman) for C(T) probes.

Based on both simulation and experiment:

- Study of sensitivity of the local GTN material model with respect to variation of material parameters;
- Adjustment of material parameters for EUROFER by simulation of convenient experiments;
- Validation of the scaling approach of W. Brocks or derivation of an own scaling approach by simulation of the crack propagation in a component (for instance in the TBM mock-up model described in FZKA 7241) and transferring the corresponding $J(\Delta a)$ curve into the $J(\Delta a)$ curve of the KLST FM specimen.

Staff:

R. Sunyk

Literature:

- [1] W. Brocks, P. Anuschewski and D. Hellmann "A concept for scaling J_R -curves by plastic constraint factors", Int. J. Fracture 130: 455-469, 2004
- [2] W. Brocks and I. Scheider „Reliable J-Values“, MP Materialprüfung 45 (2003) 6, pg. 264 - 275.

TW4-TTMS-005 D 2 Mechanical and Structural Characterization of EUROFER 97-2

During the development work of RAFM steels further structural and mechanical characterization on the EUROFER 97-2 batch was performed [1, 2]. This 8 ton batch was delivered in round forgings and plates. The technical and chemical specification of the batch was based on the experience gained with the first EUROFER 97 batch and various RAFM 9CrWTaV-alloys. The use of carefully selected raw materials was essential to achieve high cleanliness and low contents of undesired elements or impurities as Nb, Mo, Ni, Cu, Al, Co, and others, which produce long-living radio-active isotopes under neutron irradiation. One important goal of the procurement was to achieve a good reproducibility of the satisfying properties of the former EUROFER 97 alloy. This additional EUROFER 97-2 material was needed for technological tests and further fabrication trials, particularly to build the Test Blanket Modules (TBM) mock-ups.

The material was melted in a 16-ton vacuum induction furnace, remelted in a vacuum arc device and forged to billets, necessary for the production of round bars, plates, and tubes. The last heat treatment was normalizing 960°C 1.5 h/oil and tempering 750°C 4 h/air. At the beginning of 2004, material structural investigations began with the first round forgings with a diameter of 100 mm, later in the middle of 2005 the investigations began at the plates, tab.1.

Table 1: Delivery forms of the EUROFER 97-2 batch.

Heat	Delivery form	Dimension
993378	round forging	Ø100 mm
993394	round forging	Ø100 mm
993394	plate	8 mm
993393	plate	14 mm
993391	plate	25 mm
993402	plate	25 mm

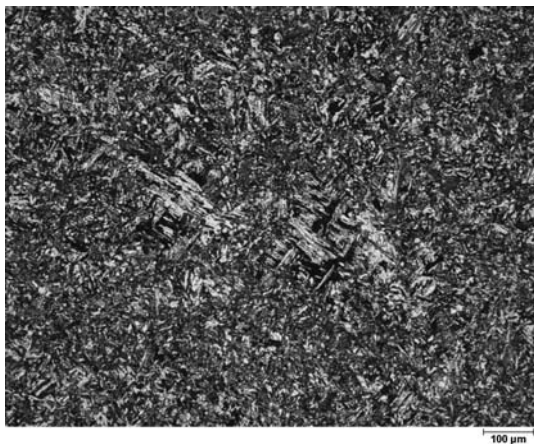


Fig. 1: Micrograph of heat 993402, plate material.

Metallographic cuts were prepared in different orientations and near the material surface of the as-received state. All materials were δ -ferrite free. A very fine grain could be observed up to 200 μm from the surface, due to the last mechanical surface treatment. In the centres of the bars and plates, there were some areas of coarse grains, but there was no anomaly in hardness to other basic material, fig. 1. The hardness in the examined heats was between 216 and 229 HV 30. No difference was found in average grain shape, grain size (ASTM 10-11), and hardness due to the orientation of the samples and forming direction. One's attention was turned to the inclusions. There were few orientation dependence in the shapes of the inclusions. By EDX-analysis, the desoxidation

detergents could be analyzed mainly as Ce and some Al. The important low contents of sulphur and phosphorus could be confirmed by chemical analysis. The specified elements could be essentially analyzed and confirmed, but there was one exception, the nitrogen content in plate heat 993378 was with 0.011 wt.% lower as demanded 0.015 – 0.045 wt.%.

Hardening behaviour was determined in all heats, fig. 2. Specimens were heated between 850 and 1150°C for 30 min and quenched, hardness and grain sizes were measured. Plate materials exhibited some more hardness than the round forged materials. This behaviour accords with the tendency to smaller grain sizes of the plate material, which can be observed in the upper scatter band of the ASTM grain size graph, fig 2. At 850°C, in all heats could be

arisen δ -ferrite due to the low hardening temperature. At higher temperatures there was not any δ -ferrite.

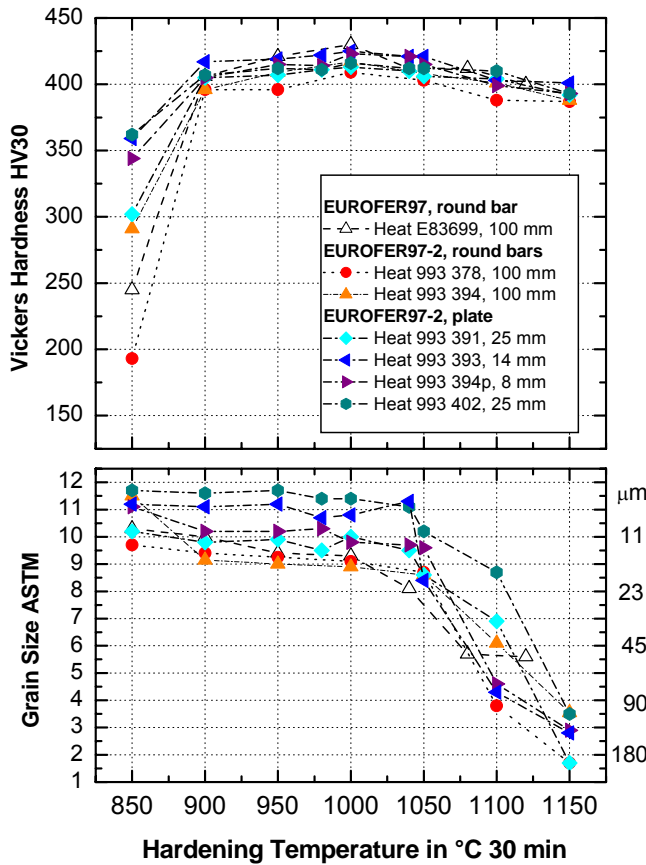


Fig. 2: Hardening behaviour of EUROFER 97-2.

Further series of specimens were hardened at 980°C 30 min or 1040°C 30 min and tempered between 300 and 900°C 2 hours to determine the tempering behaviour, fig. 3. Up to 500°C 2 hours, there was no hardening observable, but at 550°C 2 hours occurred in the most heats the typical secondary hardening of this type of alloys. The hardness decreased again due to the increasing of tempering temperature by diffusion processes and precipitation development. The increase of hardness at 800°C 2 hours can be explained by the beginning of α - γ -conversion. There was observed one exception, again heat 993378, there was no secondary hardening at 550°C 2 hours due to the low nitrogen content. Chemical extractions were performed in the as received condition and after the basic heat treatments. The carbide content of the alloys was 2.9 – 3.1 wt.%.

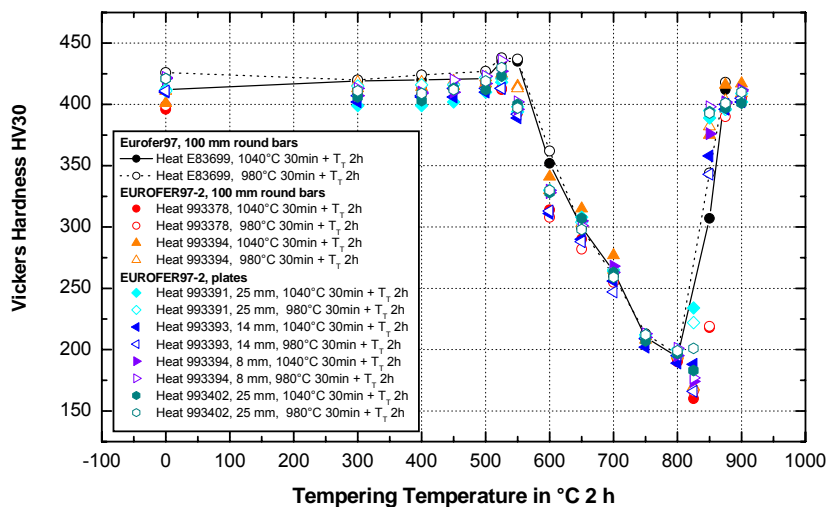


Fig. 3: Tempering behaviour of EUROFER 97-2.

Mechanical Properties

Tensile tests

All tensile specimens (38 x M5) were fabricated parallel to the main direction of deformation of the as received material. An universal testing machine was used to determine tensile strength R_m , yield strength $R_{p0.2}$, uniform elongation A_g , total elongation A , and reduction of area Z at RT, 300, 400, 500, 600 und 700°C. The preset of tensile strength $R_m > 600$ MPa at RT could be achieved of all heats, but against yield strength of $R_{p0.2} > 500$ MPa at RT was achieved just by plate materials, fig. 4. The good strength behaviour of the plate materials could be decided at higher temperatures, too, even better than the first EUROFER 97. Total elongation was specified $A > 15\%$ at RT; these data were better in all heats, fig. 5. Fractures of the broken specimens were examined, too, - all tensile fractures were ductile.

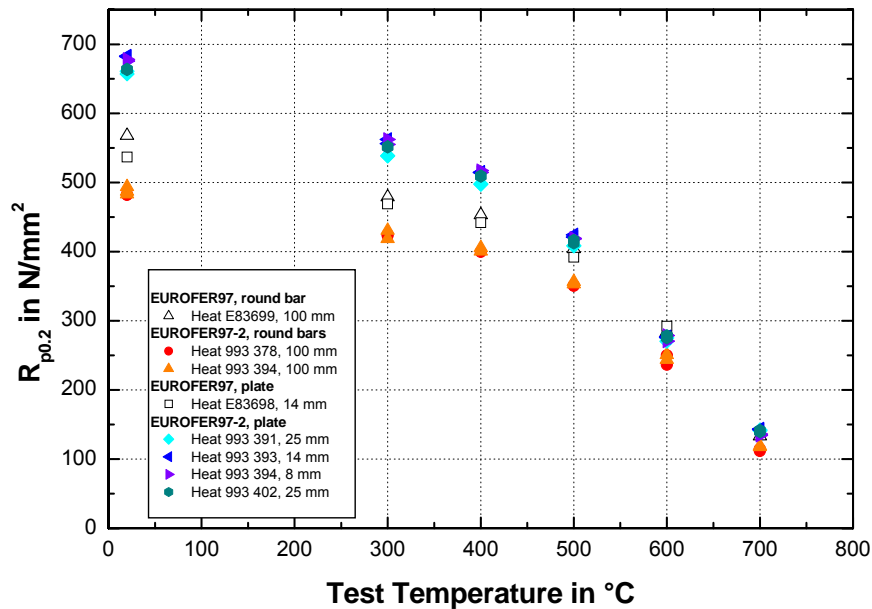


Fig. 4: Yield strength, $R_{p0.2}$.

Impact tests

Two different specimen sizes were fabricated for the impact tests. Large ISO-V specimen (55 x 10 x 10, and 55 x 10 x 5 of 8 mm plate) as standardized testing method, and the KLST size (27 x 3 x 4) for irradiation relevant intercomparison tests, fig. 6. The ISO-V specimens were taken longitudinal, L-C of the round forgings and L-T of the plate materials. Tests were performed in a conventional impact testing apparatus with a 50 J pendulum impact hammer. DBTT and upper shelf energies are listed in Table 2. The best DBTT and USE data was analyzed in heat 993402, but generally all impact data are is the common scatter of technical material.

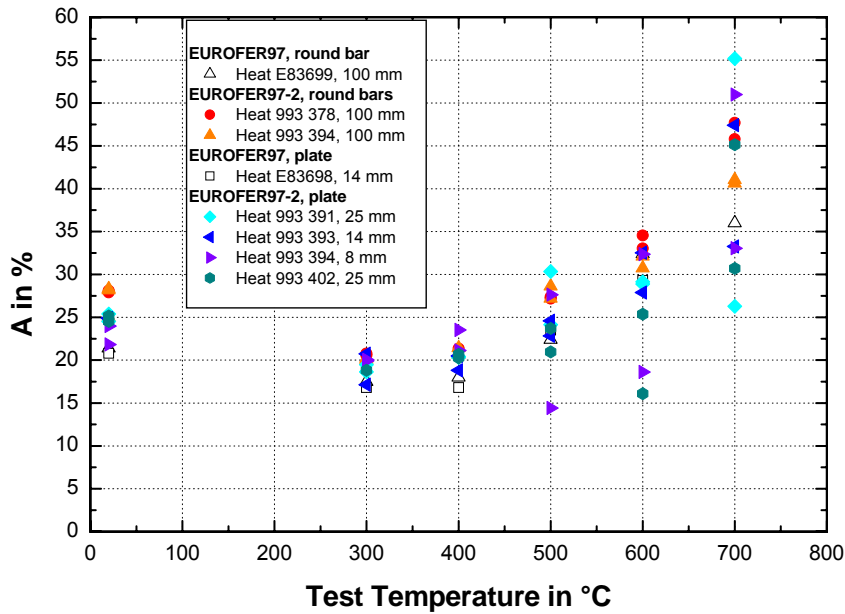


Fig. 5: Total elongation, A.

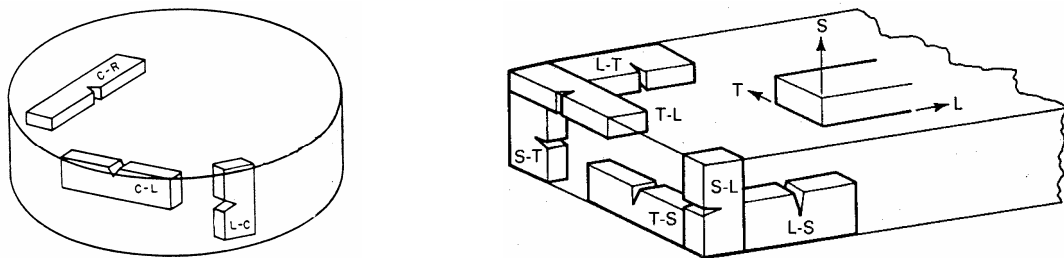


Fig. 6: Specimen orientation of ISO-V and KLST impact specimens.

Table 2: DBTT and USE of ISO-V specimens.

Heat	Orientation	DBTT in °C	USE in J
993378, Ø 100 mm	L-C	-55	286
993394, Ø 100 mm	L-C	-45	285
993391, Platte 25 mm	L-T	-50	290
993393, Platte 14 mm	L-T	-40	270
993394p, Platte 8 mm	L-T	ISO-V half specimen -70	108
993402, Platte 25 mm	L-T	-80	290

KLST impact test specimens were fabricated in different orientations. The specimens of the round forgings have the L-C, C-L, and C-R orientation and of the plate materials L-T and T-S, fig. 6. Important is the alignment of the notch to detect any orientation dependence to deformation directions, but, the determined data of all DBTT and USE did not confirm any orientation dependence of the round or plate material, tab. 3. In general, there was not such clear difference in the quality of impact behaviour between round forging or plate material as e. g. seen by tensile tests. To average, most impact data are in the same distribution band as seen in the ISO-V tests, but with a small tendency to better DBTT in the plate material. The

lowest DBTT is determined in the round forging heat 993394, and, as observed at the ISO-V specimens, the best DBTT has heat 993402.

Table 3: DBTT and USE of KLST specimens.

Heat	Orientation	DBTT in °C	USE in J
993378, Ø 100 mm	L-C	-95	9.8
993378, Ø 100 mm	C-L	-100	9.7
993378, Ø 100 mm	C-R	-90	9.6
993394, Ø 100 mm	L-C	-70	9.7
993394, Ø 100 mm	C-L	-55	9.2
993394, Ø 100 mm	C-R	-60	9.5
993391, plate 25 mm	L-T	-85	9.7
993391, plate 25 mm	T-S	-95	9.5
993393, plate 14 mm	L-T	-90	9.6
993393, plate 14 mm	T-S	-100	9.2
993394p, plate 8 mm	L-T	-105	9.3
993394p, plate 8 mm	T-S	-115	9.4
993402, plate 25 mm	L-T	-120	9.5
993402, plate 25 mm	T-S	-110	9.6

Creep tests

A long term program was started by creep tests at 450, 500, 550, 600, and 650°C and covered estimated test-times up to 8000 h. All creep specimens (56 x M8, and 94 x M12) were prepared parallel to the main deformation direction. The data of 1% strain limit (fig. 7) and time to rupture (fig. 8) show a clear better creep behaviour of the plate material.

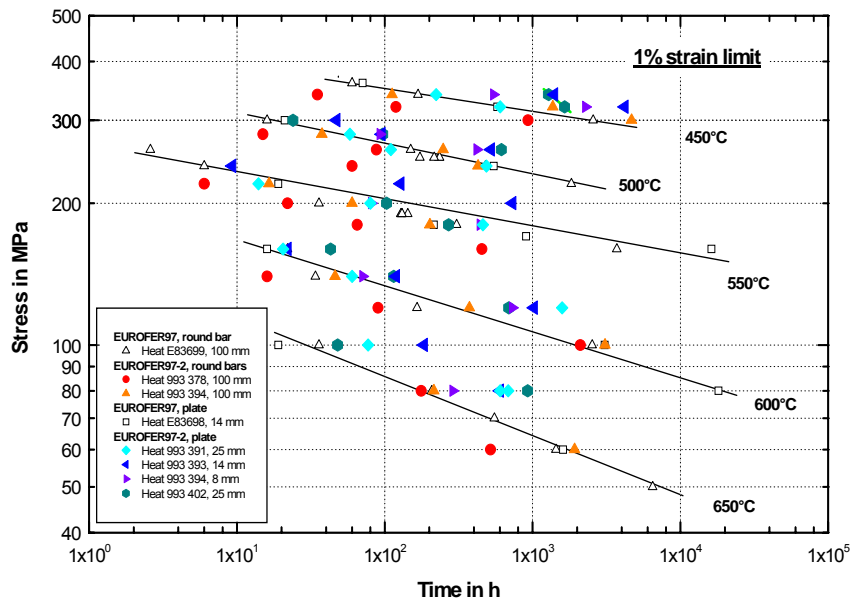


Fig. 7: Creep properties at 1% strain limit.

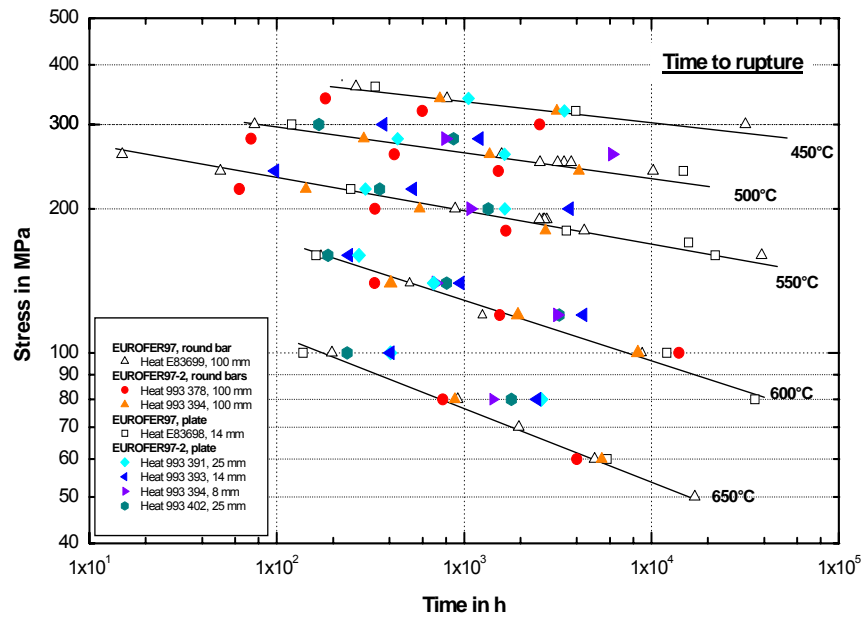


Fig. 8: Creep properties of time to creep-rupture.

Conclusion and Outlook

EUROFER 97-2 batch reveals good accordance to the former EUROFER-alloys. Only the round forging materials had marginal properties. Against this, the plate materials have better results than the first EUROFER 97 alloy. They have higher strength and ductility, and better long time behaviour as compared in the graphs.

These new RAFM-steels are a further step of optimization of material properties targeted on the development of components for fusion reactors [2, 4]. The results obtained form the basis for design and construction of components and will serve for comparing results for future irradiation tests.

Staff:

Ch. Adelhelm
 B. Dafferner
 M. Klimiankou
 P. Graf
 A. Falkenstein
 U. Jäntschi
 R. Lindau
E. Materna-Morris
 C. Petersen
 D. Preiningger
 H. Zimmermann

Literature:

- [1] Materna-Morris E.; et. al.: TW4-TTMS-005D2 Mechanical and structural characterization of EUROFER97-2. FZKA 7117, EUR 22253 EN, Nuclear Fusion Programme Annual Report of the Association Forschungszentrum Karlsruhe / EURATOM, January 2004 – December 2004.

- [2] Materna-Morris E.; et. al.: TW4-TTMS-005D2 Mechanical and structural characterization of EUROFER97-2. FZKA 7210, EUR 21526 EN, Nuclear Fusion Programme Annual Report of the Association Forschungszentrum Karlsruhe / EURATOM, January 2005 – December 2005.
- [3] Möslang, A.; Diegele, E.; Klimiankou, M.; Lässer, R.; Lindau, R.; Lucon, E.; Materna-Morris, E.; Petersen, C.; Pippin, R.; Rensman, J.W.; Rieth, M.; van der Schaaf, B.; Schneider, H.C.; Tavassoli, F.: Towards reduced activation structural materials database for fusion DEMO reactors. Nuclear Fusion, 45 (2005) S.649-55.
- [4] Lucon, E.; et al.: The European effort towards the development of a DEMO structural material: irradiation behaviour of the European reference RAFM steel EUROFER. Fusion Engineering and Design 81(2006) S.917-923.

TW5-TTMS-005 D 4 Experiments in Support of Modelling Activities on Size Effects

Objectives

The development of a convenient model for fracture mechanics (FM) experiments on structure materials is a huge challenge. Finding of scaling factors, which would allow prediction of a crack resistance curve of a standard specimen on the basis of the results obtained on miniaturized specimens, is of vital importance for qualification of structure materials of future fusion reactors. To support modelling work on size effects in the ductile and ductile-to-brittle transition region of structure materials several fracture mechanics experiments are needed.

Fracture Mechanics Experiments on Sub-size Specimens

The Fracture Mechanics (FM) experiments have been performed on EUROFER 97 steel specimens. Mini-bar specimens of KLST type (3x4x27 mm³) have been chosen for quasi-static fracture toughness tests. In order to improve the constraint state near the crack tip selected specimens were side-grooved to a net thickness of 2.33 mm. Room temperature quasi-static three-point-bend (3PB) testing was performed with a servo-hydraulic testing machine Hydropuls®-VHS®-50 (Schenk/Instron). Displacement controlled bending of the specimens were performed with displacement rates of 2-5 mm/min.

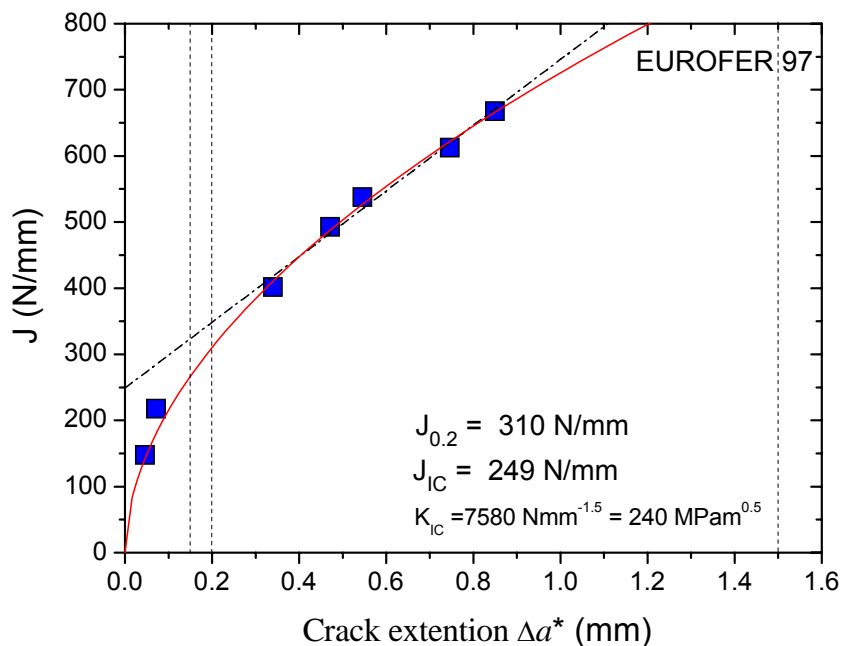


Fig. 1: J - Δa curve for EUROFER 97. The solid line is a least square fit according to $J=C(\Delta a)^\rho$ for data points fulfilling $0.15 \leq \Delta a \leq 1.5$ mm criteria; the best fit was obtained with $C=726$ and $\rho=0.53$. Estimated $J_{0.2} = 310$ N/mm; the dashed dotted line is a linear fit to data points fulfilling $0.15 \leq \Delta a \leq 1.5$ mm criteria; estimated $J_{IC} = 249$ N/mm. (Δa – crack growth, J – J-integral, $J_{0.2}$ – J-integral at 0.2mm crack growth, J_{IC} – critical J-integral at modulus I, J - R – crack resistance curve, K_{IC} – fracture toughness at modulus I)

All EUROFER 97 (980°C/0.5 h + 760°C/1.5 h) specimens exhibited ductile failure at RT. Complex three dimensional fracture surfaces with significant inhomogeneous plastic deformation was observed for the specimens with initial crack lengths of $0.22 \leq a_0/W \leq 0.24$. The examination of the surface profile revealed a complex zig-zag crack-propagation that prevented a quantitative assessment of the stable-crack extension. Neither variation of the

starter notch type (i.e. "U" or "V" type) nor side-grooving of the specimens led to elimination of the zig-zag crack-propagation. Pre-cracking of the specimens up to initial lengths of $a_0/W \sim 0.34-0.36$ and subsequent side grooving, however, considerably improved the crack growth picture, thus allowing a quantitative assessment of the in plane crack extension (Δa^*). A multi-specimen method has been applied for determination of the critical J -integral. Figure 1 shows the crack resistance curve along with a least square fit with $J=C(\Delta a)^p$. The best fit was obtained with $C=726$ and $p=0.53$. Critical $J_{0.2}$ value of 310 N/mm was obtained by analyzing J - Δa curve. The determination of a critical value of J integral at the onset of stable crack growth yielded $J_{IC}=249$ N/mm. $K_{IC}=240$ MPa·m^{0.5} determined this way agree well with the literature data on larger specimens.

The validity of the failure assessment procedure R6 has been verified for a number of EUROFER 97 specimens. For this purpose selected pre-cracked EUROFER 97 specimens with and without side-grooves have been deformed to load levels leading to a macroscopic appearance of crack initiation. K_{IC} values calculated under assumption of option 1 curve of R6 procedure are sensibly independent of specimen geometry (i.e. "U" and "V" starter notches), constraint state (with and without side grooves) and initial crack length ($0.20 \leq a_0/W \leq 0.36$) and agree well with fracture toughness results obtained on EUROFER 97 Mini-bar specimens.

Conclusion

Critical J -integral and fracture toughness has been determined for EUROFER 97 showing ductile failure at RT. The validity of the failure assessment procedure R6 has been verified for a number of EUROFER 97 specimens.

Staff:

J. Aktaa
B. Dafferner
E. Gaganidze
R. Sunyk

Literature:

- [1] E. Gaganidze, B. Dafferner, J. Aktaa, Fracture Mechanical Experiments on EUROFER97 and MANET II Mini-bar Specimens, Forschungszentrum Karlsruhe, FZKA 7252 (2006).
- [2] E. Gaganidze, B. Dafferner, J. Aktaa, Neutron Irradiation Resistance of RAFM Steels, MRS2006 Fall Meeting, Boston, MA, November 27 – December 1 (2006).

TW5-TTMS-005 D 5

High Temperature Fracture Mechanical (creep-fatigue) Rules: Formulation and Implementation

The objectives are the development of the high temperature part of a design code for fusion reactor components built from EUROFER which includes reliable fracture mechanical rules for the assessment of detected defects under creep and creep-fatigue conditions.

Within the reporting time period the high temperature fracture mechanical rules of the R5 and PD6539 (British Standards) have been implemented in a computer code which allows a fast evaluation of detected defects in EUROFER components subsequent to a finite element analysis the parameters of the creep crack growth relation for EUROFER are known. These parameters will be determined in fracture mechanical tests to be performed on EUROFER under deliverable 6, which are now in progress.

To verify the validity of appropriate relations estimating crack loading parameter C^* finite element simulations using standard constitutive equation for creep have been performed, with which the crack loading parameter is calculated using the appropriate algorithm provided by the finite element code and then compared with that estimated by the R5 rules. The fracture mechanical finite element simulations have been extended considering the viscoplastic deformation model developed under TW2-TTMS-005a D4 and implemented in the finite element code ABAQUS within TW2-TTMS-005a D4 which describes the viscoplastic behaviour of EUROFER better than the standard constitutive equations for creep provided by ABAQUS. These simulations are now in progress.

Staff:

J. Aktaa
M. Weick

Literature:

- [1] J. Aktaa, M. Klotz, C. Petersen, "Deformation and Damage of RAFM Steels under Thermomechanical Loading: A Challenge for Constitutive Equations," ICFRM 12, Santa Barbara, CA, USA, Dec. 2005
- [2] J. Aktaa and R. Schmitt, "High temperature deformation and damage behavior of RAFM steels under low cycle fatigue loading: Experiments and modeling," Fusion Engineering and Design, 81 (2006) 2221-223

TW5-TTMS-005 D 6

Define and Perform Accompanying Experiments to D 5 (e.g. creep crack growth at 550°C)

Background and Objectives

For TBM's licensing, in order to establish design rules for the materials, joints and specific sub-components, a broad set of R&D activities have been launched within the WP 2002. These activities will continue with emphasis on implementation in DSCD (Demo structural design code) and verification and validation experiments. Additional rules for HT (high temperature) fatigue-creep interaction need to be formulated, in particular for fracture mechanics.

The low ductility of EUROFER (in particular after irradiation) gives very conservative limits for design against fast fracture and local flow localization. Some experiments are required in support of special design code activities that could lower very conservative assumptions in existing frameworks.

Development of small scale test techniques in fracture mechanics will continue including transferability of the small size specimens tests to the behaviour of the TBM's sub-components.

Subtask: The objective is to perform creep crack growth experiments from EUROFER to determine the da/dt (crack velocity) - C^* (C^* -integral)- behaviour at the temperatures 500°C and 550°C. The results are needed to fit material parameters in HT fracture mechanical rules. Therefore long time tests must be done.

Status January 2006

The design and fabrication of specimens and the assembling of the experimental set-up was nearly finished. Preliminary tests with the set-up for the DC potential method were running in order to determine the correct correlation between voltage and crack length.

Status

The individual parts (holder etc.) for the modification of the long period creep testing machines have been designed and fabricated. CT specimens have been designed (their size depends on the space in the furnace) and fabricated. Since the average grain size of the latest delivered charge of EUROFER is oversized, the material has been cut into pieces a little larger than the CT specimens to do a new heat treatment. After that a 2-step fabrication of the specimens started. In the first step the specimens have been fabricated (a little larger width) with side-notches to get a nearly straight crack front during creation of the incipient fatigue crack. Afterwards the side-notches will be removed for the main experiments (so that the geometry of the specimen is in agreement with the ASTM-norm). In preliminary tests, one can clearly see that this method leads to a nearly straight crack front during the incipient crack creation, also after removing the notches and continuing the fatigue crack propagation.

At the moment preliminary tests with the set-up for the DC potential method are still running in order to determine the correct correlation between voltage and crack length. At higher temperatures ($> 500^\circ\text{C}$), because of oxidations processes, it was a problem to figure out the right correlation with the standard material for the cables etc. (copper). Thus, the material for the conductors was changed (pure nickel), also as the connection of the cables with the specimens (laser welding). Since this, the set-up is working well and the first results show, that one can determine the correct correlation now also at higher temperatures [Fig. 1].

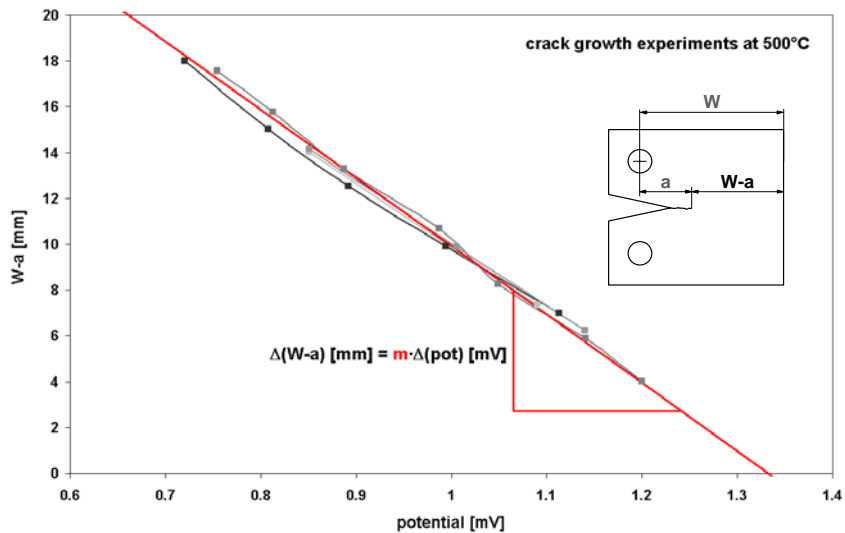


Fig. 1: Results from crack growth experiments at 500°C to determine the crack growth- potential change-correlation.

Parallel to these experiments, preliminary tests to determine the suitable load cases for the long term experiments are under way.

Conclusion and Outlook

The design and fabrication of specimens and the assembling of the experimental set-up has been finished. Preliminary tests with the set-up for the DC potential method are running in order to determine the correct correlation between voltage and crack length in the relevant temperature area. Tests to determine the suitable load cases for the long term experiments are under way. After finishing the pre-tests, the main experiments will start.

Staff:

M. Walter
M. Lerch

TW5-TTMS-005 D 7

General Implementation of HT Rules (including creep fatigue interaction rules)

The objectives are the development of the high temperature part of a design code for fusion reactor components built from EUROFER 97 which includes reliable simplified rules for the assessment of creep, fatigue and creep-fatigue interaction.

Within the reporting time period creep-fatigue evaluation rules based on the rules of the ASME-BPV (Code Case N-47, T-1400) and RCC-MR (RB 3262.12) code used for design against creep, fatigue and creep-fatigue interaction have been formulated. To use these rules for the evaluation of components built from EUROFER 97 the necessary design fatigue and stress-to-rupture curves were determined for this material. In addition, a creep-fatigue damage envelope which provides the allowable total damage values for EUROFER 97 has been proposed.

The design fatigue curves were constructed according to the criteria of the ASME (Section III, Division 1 – Appendices, III-2200) and the RCC-MR (A3.GEN.23) codes. They were obtained from fatigue lifetime (number of cycles to rupture) data of uniaxial strain-controlled fatigue (low cycle fatigue, LCF) tests performed with a strain rate in the order of 10^{-3} s^{-1} . A best fit to experimental data is obtained by applying the method of least squares to the logarithms of the strain range values. The design fatigue curves are then deduced from the best fit curve by applying a factor of 2 on strain range or a factor of 20 on cycles, whichever is the more conservative at each point. These factors are intended to cover effects such as those of the environment, the scale (between the material and the test specimen), surface finish and data scatter [1]. They in no case constitute a safety coefficient. The so determined design fatigue curves for EUROFER 97 are described by the following formula:

$$\Delta \varepsilon = \min \left\{ 0.5(a_1 + a_2 N_d^{a_3}), a_1 + a_2 (20 * N_d)^{a_3} \right\} \quad (1)$$

The resulting values of the temperature dependent parameters a_1 , a_2 and a_3 for EUROFER 97 are listed in Table 1 and the design fatigue curves of EUROFER 97 obtained accordingly are plotted in Figure 1.

Table 1: Parameters of equation 1 determined for EUROFER 97

Temperature in °C	a_1	a_2	a_3
20	3.38×10^{-3}	0.75	-0.56
450	3.84×10^{-3}	1.06	-0.68
550	2.65×10^{-3}	0.70	-0.60
650	2.88×10^{-3}	1.92	-0.73

The stress-to-rupture curves are already determined in [2] on the base of creep lifetime data. Therefore the following relation between the minimum stress value S_r and the Larson-Miller-Parameter P is deduced (S_r in MPa)

$$S_r = 1936 - 88.452P + 0.888324P^2 \quad (2)$$

where

$$P = (30 + \log(T_d)) * (\theta + 273) / 1000$$

with T_d and θ denoting the allowable time in h (hours) and the temperature in °C, respectively. Figure 2 shows the stress-to-rupture curves of EUROFER 97 determined using equation 2 for different temperatures.

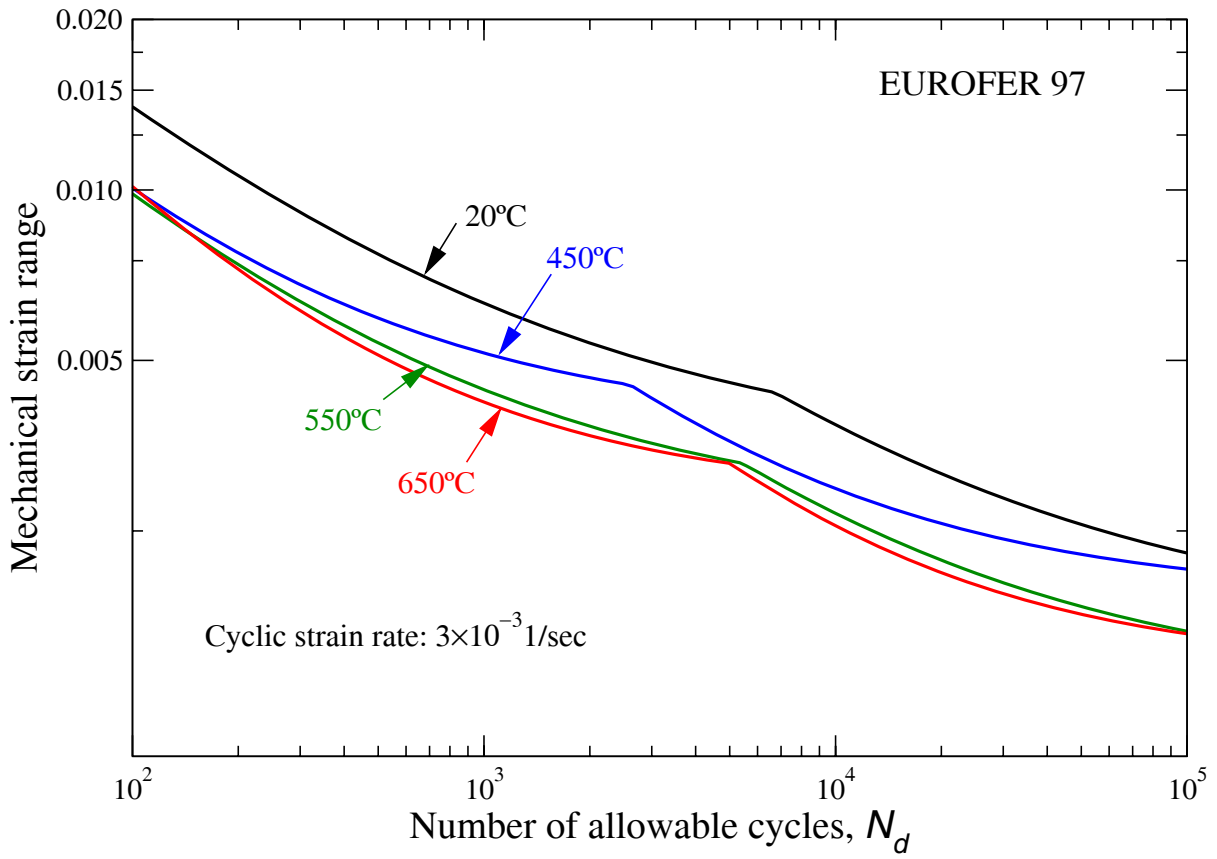


Fig. 1: Design fatigue strain range for EUROFER 97

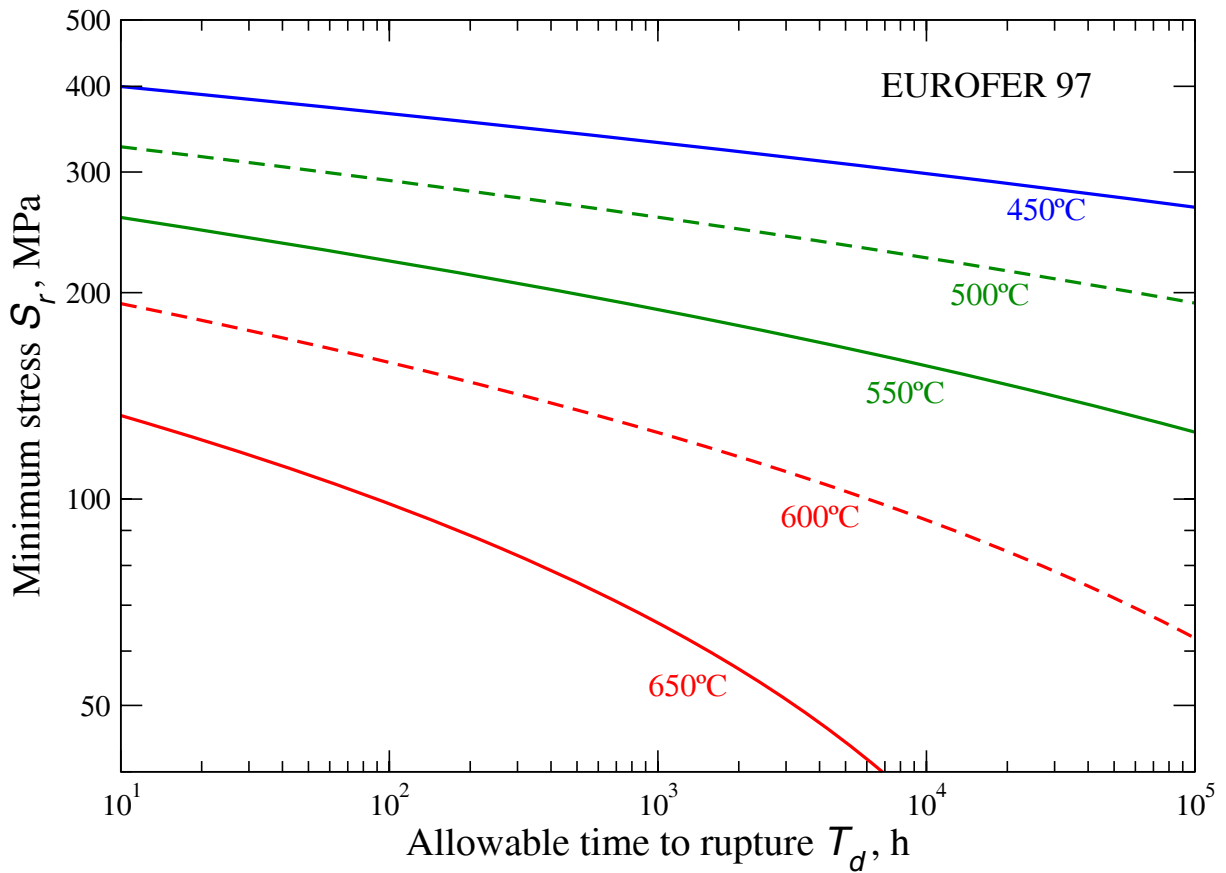


Fig. 2: Stress-to-rupture curves for EUROFER 97

The creep-fatigue damage envelope suitable to EUROFER 97 has to be determined on the base of lifetime data of tests with different creep and fatigue damage fractions, like low cycle fatigue tests with different dwell times. Since the data available from this type of tests are not sufficient further tests, particularly with long dwell times will be performed in current activities in the EFDA Technology Workprogramme (TW5-TTMS-005 D9). However, as long as a creep-fatigue damage envelope for EUROFER 97 can not be determined, one might assume the most conservative envelope specified in the ASME Code for 2-1/4 Cr – 1 Mo and Ni-Fe-Cr Alloy 800H (see Figure 3) to be valid for EUROFER 97.

A final report including a draft of the formulated creep, fatigue and creep-fatigue evaluation rules for EUROFER 97 is now in preparation and will be shortly published.

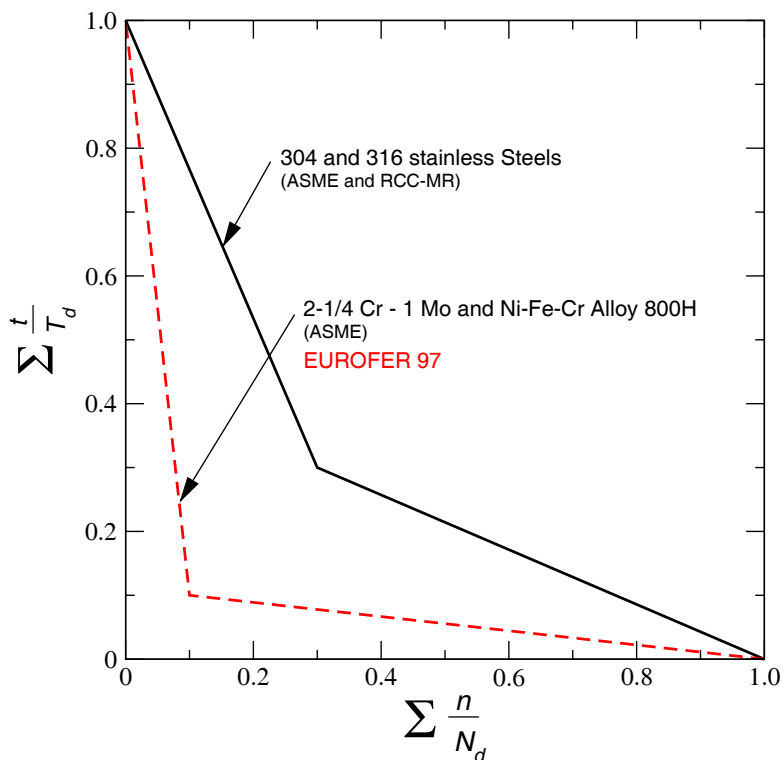


Fig. 3: Creep-fatigue damage envelopes.

Staff:

J. Aktaa

Literature:

- [1] B.F. Langer, Design of pressure vessels for low cycle fatigue, J. Basic Eng., Vol. 84, 1962, p. 379.
- [2] F. Tavassoli, Fusion Demo Interim Design Criteria (DISDC) / Appendix A: Material Design Limit Data / A3.S18E Eurofer Steel, DMN Technical Report, DMN/DIR/NT/2004-000/A, 2004.
- [3] J. Aktaa, M. Klotz, C. Petersen, "Deformation and Damage of RAFM Steels under Thermomechanical Loading: A Challenge for Constitutive Equations," ICFRM 12, Santa Barbara, CA, USA, Dec. 2005
- [4] J. Aktaa and R. Schmitt, "High temperature deformation and damage behavior of RAFM steels under low cycle fatigue loading: Experiments and modeling," Fusion Engineering and Design, 81 (2006) 2221-223

TW5-TTMS-005 D 9

Experimental Programme for Verification of HT Creep-fatigue Rules from Uniaxial Experiments (e.g. LCF tests with long dwell time) and/or Multi-step LCF Tests

Background and Objectives

For TBM's licensing, in order to establish design rules for the materials, joints and specific sub-components, a broad set of R&D activities have been launched within the WP 2002. These activities will continue with emphasis on implementation of DSCD (Demo structural design code) and verification and validation experiments. Additional rules for HT (high temperature) fatigue-creep interaction need to be formulated, in particular for fracture mechanics.

The low ductility of EUROFER (in particular after irradiation) gives very conservative limits for design against fast fracture and local flow localization. Some experiments are required in support of special design code activities that could lower very conservative assumptions in existing frameworks.

Development of small scale test techniques in fracture mechanics will continue including transferability of the small size specimens tests to the behaviour of the TBM's sub-components.

Subtask: The objectives are to evaluate the mechanical properties of EUROFER in the region of creep-fatigue. Therefore suitable uniaxial Low Cycle Fatigue experiments in the temperature range 550°C +/- 50°C must be done (multi-step experiments, experiments with higher dwell times). The results are needed for the verification of high temperature creep-fatigue lifetime rules.

Status

3-step experiments and dwell time experiments have been finished. As shown in the following Palmgren-Miner diagram [Fig. 1], a non linear damage accumulation was found in the multi-step tests.

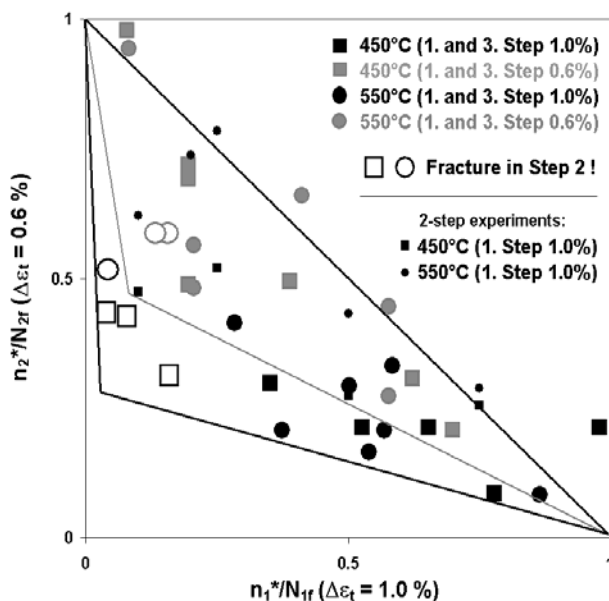


Fig. 1: Results of the multi-step experiments, plotted in a Palmgren-Miner diagram:

$\Delta\epsilon_t$ is the total strain amplitude,
 N_{xf} is the number of cycles to failure from a single-step experiment,
 n_x^* is the number of cycles in one step at 2-step experiments, or the sum of number of cycles from steps with the same total strain amplitude at 3-step experiments.

Generally, it is observed that when starting with a low total strain amplitude, normalised total lifetimes are longer than when beginning with a high total strain amplitude. The following elucidations will explain this behaviour.

In single-step experiments, the material shows strong softening at the beginning and afterwards, a continuously linear softening up to the initiation of a macro-crack. Irrespective of the load case, nearly the same stress level will always be reached in the linear area. This causes an increasing softening potential with an increasing total strain amplitude and decreasing lifetimes due to higher stresses and plastic deformations during one cycle.

When comparing single step experiments with 2-step experiments as shown in Figure 2, it is obvious that a change from the high total strain amplitude (1.0%) to the low total strain amplitude (0.6%) leads to a smaller slope in the linear area compared to the single-step experiment with $\Delta\epsilon_t = 0.6\%$. This behaviour depends on the fact that the total softening potential in the second step is clearly

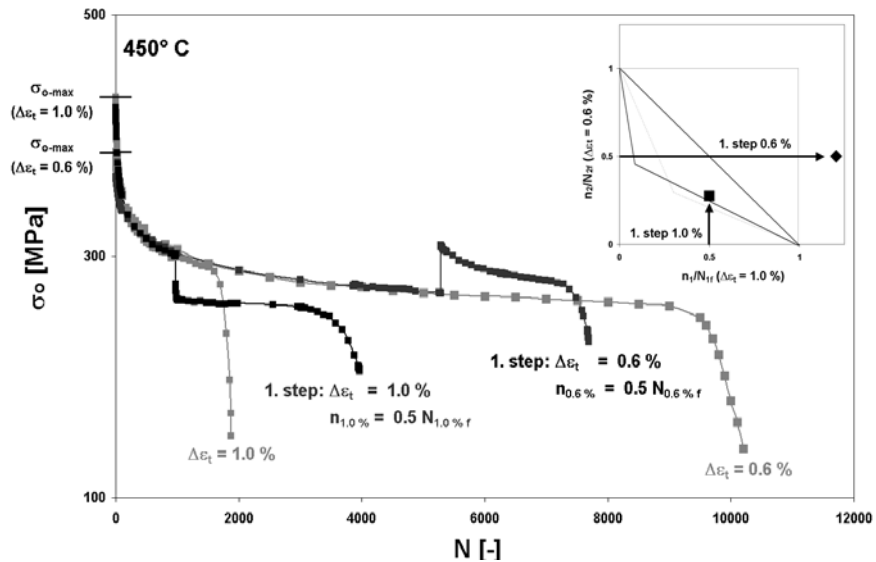


Fig. 2: Comparison of the stress amplitudes as a function of different load conditions in single-step and 2-step experiments.

smaller than the potential in the respective single-step experiment because of the pre-load history in the first step. A change from the low total strain amplitude to the high total strain amplitude also leads to a smaller slope in the linear area compared to the respective single-step experiment, but it is clearly higher than the slope in the single-step experiment with the low total strain amplitude. The reason is the same as in the first case. On the other hand, the softening potential increases depending on the higher loading conditions in the second step. This means that the higher the softening potential is in the second step, the higher is the number of cycles to macro damage. From this, it can be concluded that the change from higher load conditions to lower conditions generally leads to lower normalised total lifetimes than in the opposite case.

The influence of the number of cycles in the first step under the respective load conditions on lifetime is illustrated by the following diagrams of different 3-step experiments. To compare the respective tests, the number of cycles in the second step was fixed to 25% of the number of cycles to damage (N_d is the number of cycles when macro damage starts) obtained from the respective single-step experiment. In general the lifetime increases with a decreasing number of cycles in the first step of experiments with high total strain amplitude in the first and third steps [Fig. 3]. This can be explained by higher softening potentials in the second step due to lower number of cycles in the first step (as reflected by the change of the slope in the linear area of the individual experiments). In contrast to this, experiments with a low total strain amplitude in steps one and three show decreasing lifetimes with decreasing number of cycles in the first step (Exception: experiment with $n_1 = 0.5N_{0.6\% d}$ and $n_2 = 0.25N_{1.0\% d}$. Here, the lifetime is shorter than in the experiment with $n_1 = 0.4N_{0.6\% d}$, but this can be explained by the scatter of the material parameters) [Fig. 4]. The result is due to a higher decrease of the softening potential in the second step, the earlier the step change takes place (this becomes

obvious when comparing the progress of stress amplitude in the second step of the experiment at $n_1 = 0.2N_{0.6\%}$ with the other two tests).

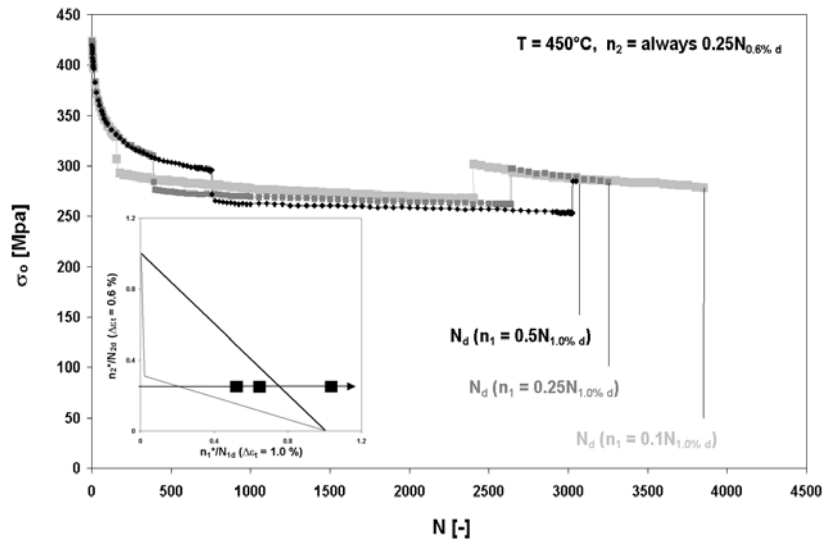


Fig. 3: Comparison of the progress of the stress amplitudes in dependence of the number of cycles in the first step of 3-step experiments with a $\Delta\epsilon_1 = 1.0\%$ in the first and third step.

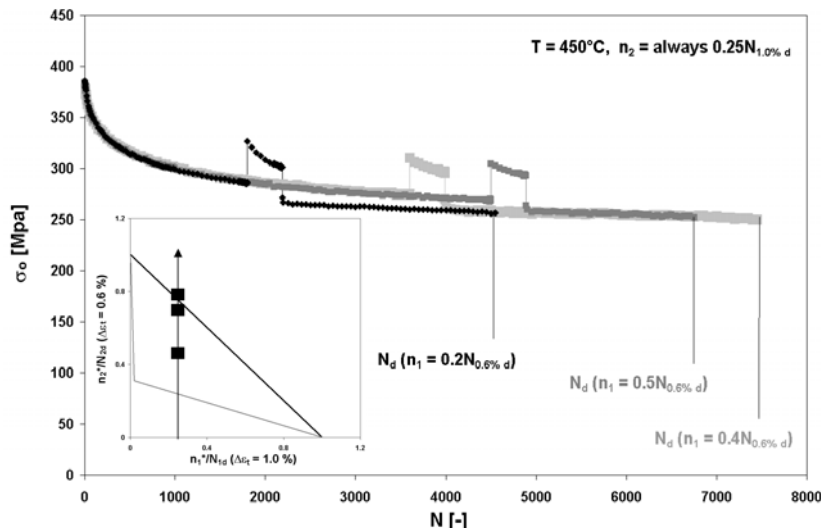


Fig. 4: Comparison of the progress of the stress amplitudes in dependence of the number of cycles in the first step of 3-step experiments with a $\Delta\epsilon_1 = 0.6\%$ in the first and third step.

The diagrams above also reveal that, irrespective of the pre-load history, the same stress level will be reached in the third step of experiments with the same step change (identical n_2). This is due to an equal decrease of the total softening potential at that number of cycles, when the curves meet each other in the last step. That behaviour also results when comparing the hysteresis at these points. They are located directly on top of each other.

In case of the low total strain amplitude in the first and third steps, the stress level clearly is lower than it would be without an amplitude change in the second step. This is the consequence of a higher softening in the second step under higher load conditions. In general, the lower the number of cycles in the first step and the higher the number of cycles in the second step are, the lower is the stress level in the third step.

In case of the high total strain amplitude in the first and third steps, the stress level is a bit higher than it would be without an amplitude change in the second step. This is the consequence of a lower softening in the second step under lower load conditions. Here, no significant change can be observed as a function of the step width.

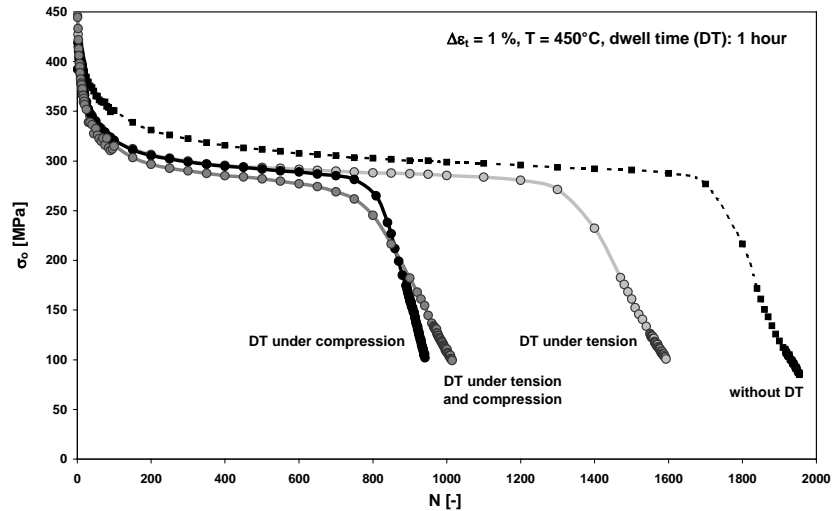


Fig. 5: Results of experiments with a dwell time of 1 hour and a total strain amplitude of 1.0% at 450°C

In contrast to the behaviour of other ferritic or austenitic steels (shortest life-times at dwell times under tension), LCF experiments on EUROFER with longer dwell times (1 hour) in principle show, that dwell times under compression lead to the shortest lifetimes [Fig. 5 and 6]. This was also observed in previous experiments with shorter dwell times. To detect the reason therefore, more experiments are necessary. One possible explanation may

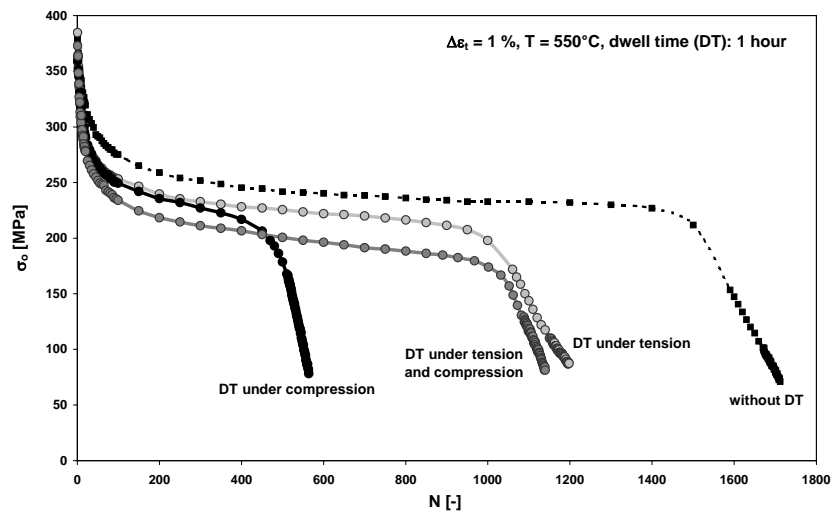


Fig. 6: Results of experiments with a dwell time of 1 hour and a total strain amplitude of 1.0% at 550°C.

be, that orientation processes of the special microstructure during the loading are responsible for it. Thus, also accompanying metallographic analyses should be done.

The positions of the 3-step results (including the 'worse' 2-step results) and the dwell time results relative to the design curve (ASME Code Case N47-29) are illustrated in the last diagram [Fig. 7]. It can be seen, that there is more than enough distance to be on the safe side for calculations of constructions. On the basis of these results it is accordingly possible, to modify the design code towards less conservative assumptions.

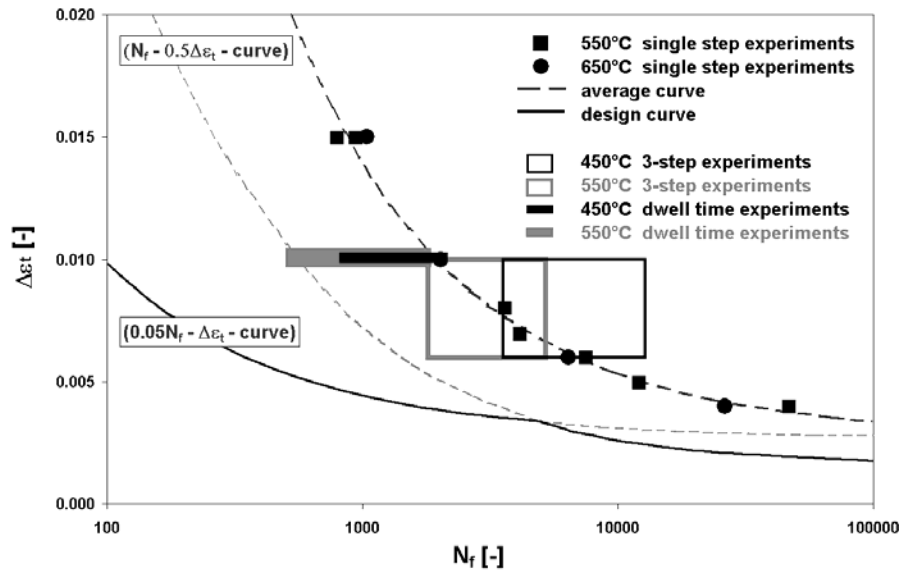


Fig. 7: Comparison of 3-step - and dwell time results with design curve (ASME Code Case N47-29).

Conclusion and Outlook

The main finding from the multi-step experiments is that softening may be understood to be the ability of the material to counteract the evolution of micro damage. The consequences on the material behaviour after a step change are understood and with the rules found, the life-time under the chosen load conditions can be estimated qualitatively. This allows to modify established models or to develop new ones for the mathematical description of the material behaviour in the future.

Experiments with dwell time in general show, that dwell times under compression lead to shorter lifetimes than dwell times under tension and dwell times under tension and compression. This is in contrast to the behaviour of other ferritic and austenitic steels. To detect and understand the reason therefore, more experiments are necessary. They will be done inter alia in task TW6-TTMS-005 D4.

Staff:

M. Walter
M. Lerch

Literature:

- [1] M. Walter, J. Aktaa, M. Lerch, Studies of the Influence of Variations of the Load Conditions on the Failure Behaviour of EUROFER 97 in LCF- Experiments, International Journal of Fatigue (paper submitted under review)

TW6-TTMS-005 D 4

Experimental Verification and Validation of Newly Implemented HT Creep-fatigue Rules

Background and objectives

For the licensing of ITER-TBM a broad set of R&D activities have been launched within the FP VI in order to establish design rules for the materials, joints and specific sub-components. These activities will be continued with emphasis on implementation in SCD (Structural design code) and verification and validation experiments. Additional rules for HT (high temperature) fatigue-creep interaction need to be formulated, in particular for fracture mechanics and subsequently validated within experiments with increasing complexity in loading history and (mock-up) geometry.

The low ductility of EUROFER (in particular after irradiation) gives very conservative limits for design against fast fracture and local flow localization. Investigations are required to define improved fatigue rules that could lower very conservative assumptions in existing frameworks. Development and qualification of NDT (non destructive detection techniques) should get more attention and need to be launched. In particular, NDT will provide the information needed on the minimum detectable crack-size as function of location in the TBM, which is essential for any reliable crack analysis.

Development of small scale test techniques (SSTT) in fracture mechanics will be continued including transferability of the small size specimens tests to the behaviour of the TBM's sub-components.

Subtask:

The objectives are to evaluate the mechanical properties of EUROFER and EUROFER diffusion welded joints in the region of creep-fatigue. performing suitable

- Uniaxial isothermal LCF-experiments with dwell time at 500/550°C on EUROFER
- Uniaxial isothermal LCF-experiments with different total strain amplitudes at 500/550°C on EUROFER diffusion welded joints
- Thermo-mechanical fatigue experiments in the temperature range 100-550°C with dwell times on EUROFER.

Status

The LCF-experiments with dwell times (1, 3 and 10 min; dwell time under tension, under compression and under tension and compression at 500/550°C) have begun. The fabrication of specimens for the thermo-mechanical fatigue experiments and the LCF-experiments on EUROFER diffusion welded joints has started.

Outlook

Continuation of the dwell time tests and after finishing the specimen fabrication (for the thermo-mechanical tests and the LCF-tests on diffusion welded joints), these tests also will start.

Staff:

U. Bürkle
M. Lerch
M. Walter
A. von der Weth

TTMS-006 High Performance Steels

TW5-TTMS-006 D 5

Nano Compositated Ferritic Steels for HT Application: Identification of Promising Candidate Alloy Compositions and Respective Fabrication Routes According to the Outcome of the 2004 Study. Production of Different Laboratory Batches (14%Cr)

The operation temperature of RAFM ODS steels like ODS-Eurofer for application as structural material in advanced blanket concepts like the Dual-Coolant Concept is limited to about 650°C. More advanced blanket concepts like the Advanced HCPB (Model C) or the use as backbone material in gas cooled divertors, require allowable operational temperatures of 700 to 750°C or even more. Reduced activation ferritic (RAF) ODS-steels could fulfil these requirements but are not commercially available at the moment and must be developed. Fe-(12-14)Cr-(2-3)W-(0.2-0.5)Ti-(0.2-0.5)Y₂O₃ being developed in USA and Japan for fission and fusion application seems to be promising and is presently also considered to form the basis for EU efforts.

Within this task, two master alloys containing 13-14% Cr and 1.0-1.2% W and varying Ti contents were ordered and inert gas atomised. These steel powders formed the basis for the production of different ODS steels with varying Y₂O₃ and Ti contents by mechanical alloying in a high-energy attritor mill. Hot-Isostatic-Pressing was applied to consolidate the MA powder. Powders and hiped samples of the different alloys were screened by appropriate methods like metallography, SEM, XRD, HRTEM, and chemical analyses. Tensile and Charpy tests on miniaturised specimens are used for the mechanical characterisation of these alloys. The main goal of this task is the screening of composition, production parameters and heat treatments on microstructure and mechanical properties of RAF 13-14Cr1.1W(Ti, Y₂O₃) ODS steels. In a further developmental step the influence of thermo-mechanical treatment and recrystallization will be determined.

First results of the alloy development are presented as follows: The powders (FeCr13 ferritic masteralloy, Y₂O₃ and Ti) were ball milled in the ZOZ high energy attritor Simoloyer CM01-2I. During the milling process all powders are exposed to impact-, shear-, friction- and compression forces. This leads to continuous deforming, breaking and rewelding of the particles. Finally a wide range of different mechanically alloyed particle sizes is created. The production process depends on certain milling parameters like milling time t_m , speed of milling rotor n_m , powder-milling ball ratio P:B, process temperature T_m , alloy composition, milling atmosphere and abrasion sources (e.g. oxygen incorporation...). Starting with a basic milling run those parameters were systematically altered in follower runs to detect possible changes in powder characteristics. Figure 1 a)-d) shows the original FeCr13, Y₂O₃ powders, as well as the resulting particles of the mentioned basic- and a variable run, which had a shorter milling time. The attritor speed variation in five minute time intervals was carried out to prevent powder adhesion on the inner grinding container.

The spherical FeCr13 powder (a) has been transformed to almost irregular shaped "flakes", (c)/(d) after the milling procedure. This is characteristic for all conducted runs. When applying the shorter milling time in Nr. 23, most of the final particles become coarser than in Nr.18, even one not alloyed spherical particle remained. The yttria powder (b) is very fine (about 1 µm in size) and agglomerates easily to larger groups. In addition to those qualitative studies several quantitative analyses using the EDX system at the REM have been accomplished: The decisive elements Fe, Cr, Y and Ti had amounts [in wt-%] of 82, 14, 1 and 0.4 for the basic run Nr.18 and 83, 13, 1 and 0.3 for the variable run Nr.23. So these measurements are quite similar. Furthermore, remarkable tungsten values of 3-4 wt-% could be detected in both runs, indicating abrasion, coming from the attritor rotor.

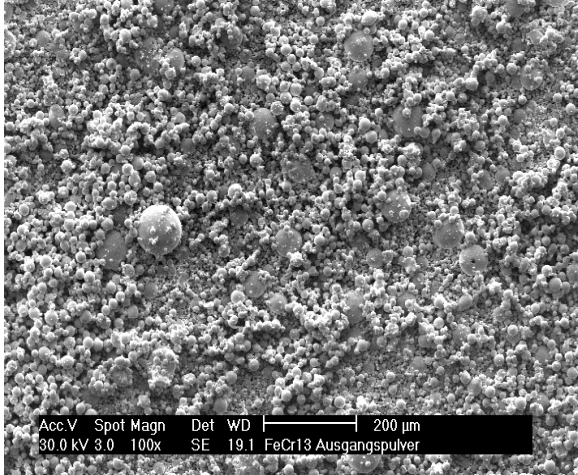


Fig. 1 a): FeCr13 original powder

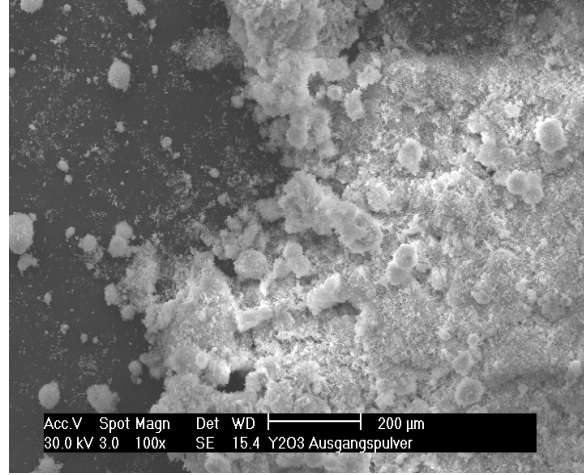


Fig 1 b): Y₂O₃ original powder

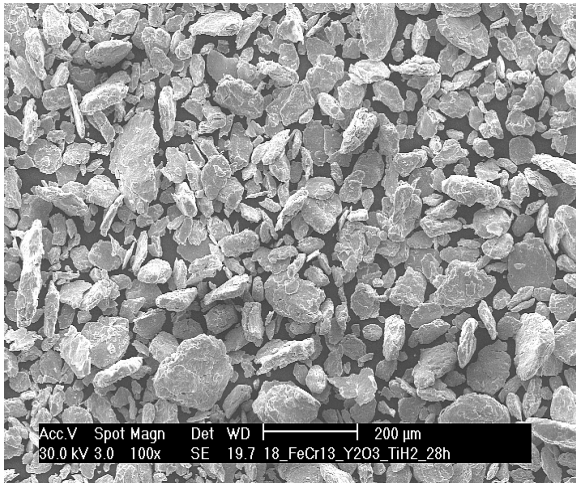


Fig. 1 c): Basic run Nr.18



Fig. 1 d): Variable run Nr. 23

Another analysis performed is the particle size distribution, gained through sieve analysis, depicted in Figure 2. Generally these curves demonstrate, that altering any of the mentioned milling parameters has great influence on the final particle shape. The blue and red curves represent long milling runs, while the orange line stands for a significantly shorter run. The curves with the long runs create maxima in the 45-75 µm area, the orange line is relatively flat. It is evident, that particles do not become smaller above a certain milling time, which means that from this point an equilibrium of particle breaking and rewelding is established. The green line shows an altered powder to ball ratio.

Fewer balls have been used in this run, all other parameters remained unchanged. It leads to much coarser powder, that is why this line remains flat too.

After the MA process all powders were filled in specially designed cans, degassed for 4 h at 400°C and sealed by certain closing procedure. Then Hot Isostatic Pressing could be applied to consolidate the powders. They were hipped for two hours at a temperature of 1150°C and a pressure of 1000 bar. Figure 3 contains metallographic results of the first HIP cycles: A relatively high porosity (23%) occurred, meaning that the compression was not sufficient. Inadequate can sealing and density during HIP proved to be the most probable reasons for this phenomenon. This underlines again the importance of all pre-HIP preparation procedures.

Comparison of particle size distributions from different grindings with variable milling parameters (t_m ; P/B;)

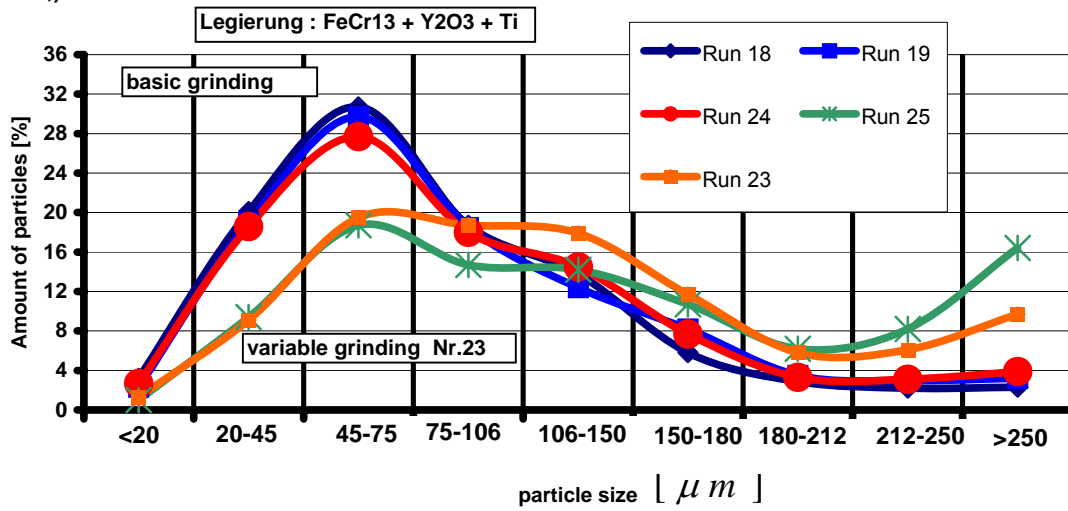


Fig. 2: Comparison of particle size distributions from different milling runs.

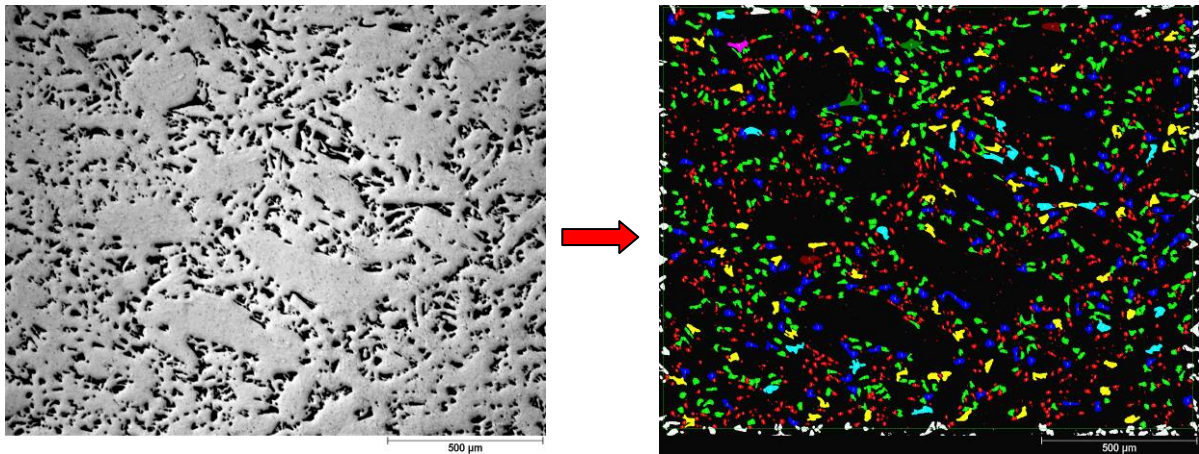


Fig. 3: Result of first HIP cycle with insufficient powder consolidation and porosity (23%).

Through several constructive measures in the HIP can design and filling methods these problems could be solved and a dense material with a comparably low porosity (0.2%) was acquired. This is shown in Figure 4.

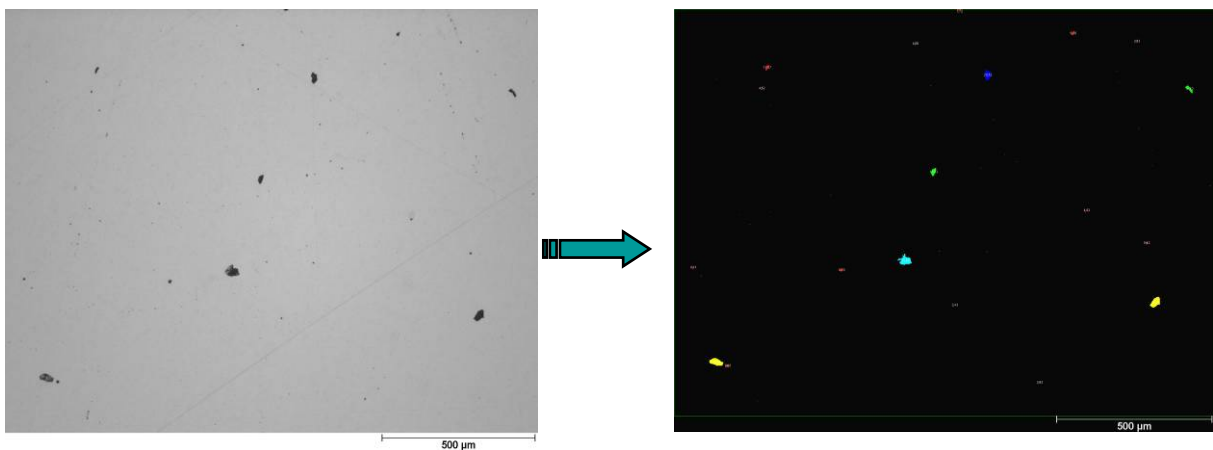


Fig. 4: Result of HIP cycle after constructive changings – better consolidation, lower porosity (0.2%).

The Vickers hardness HV30 was also determined: For the porous specimens it is around 150 – 200 HV, the better consolidated parts have values around 360 HV. The grain size for this ferritic ODS material is around 10-12 ASTM, indicating a very fine grain structure which is quite common for ODS steels.

Beyond all these analyses the alloys were characterized using HRTEM. Figure 5 a)-e) contains some pictures.

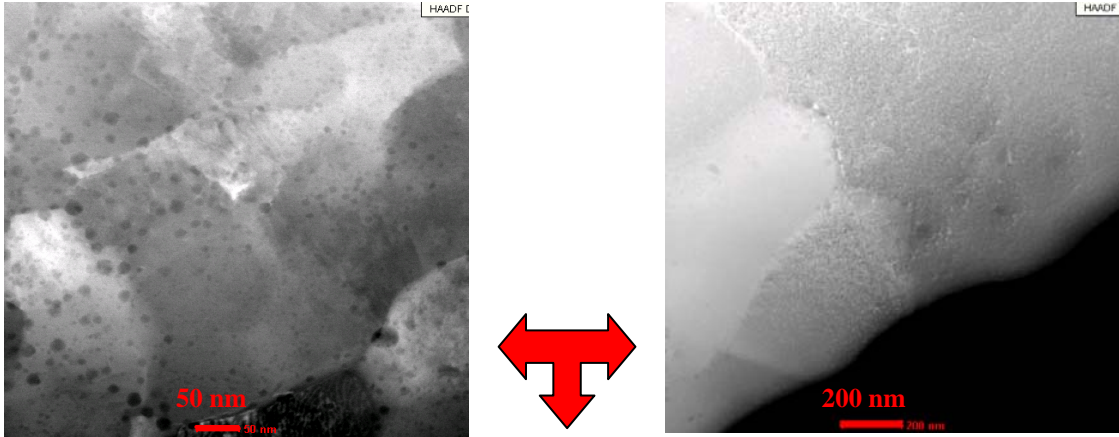


Fig. 5 a): Region with “more” ODS particles.

Fig. 5 b): Region with no ODS particles.

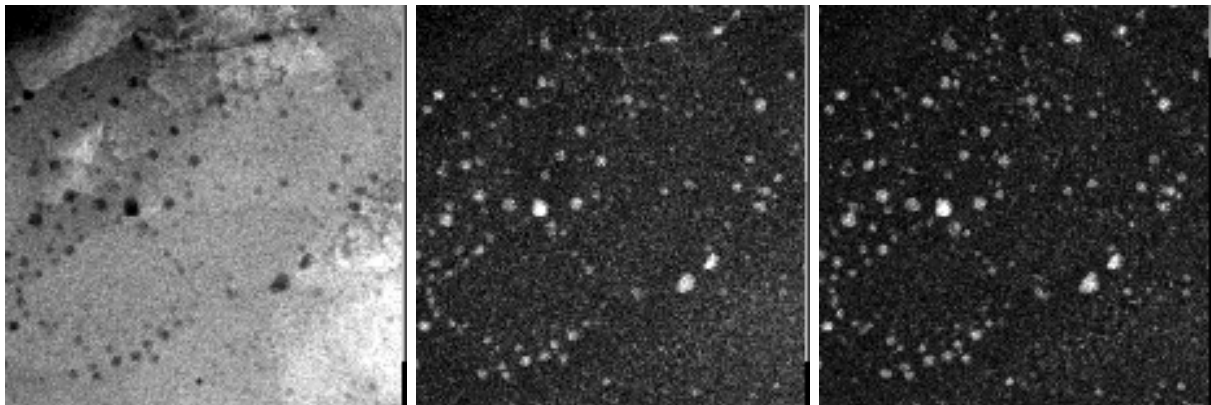


Fig. 5 c): TEM mapping Fe.

Fig. 5 d): TEM mapping Y.

Fig. 5 e): TEM mapping Ti.

Pictures a) and b) show two different regions of the produced ferritic ODS steels. The black dots indicate the ODS particles. By now the distribution of ODS is not homogenous. The reasons for that and steps for a better homogeneity have to be clarified in future studies. Pictures c) till d) contain an element mapping procedure for the decisive elements Fe, Y and Ti. Here white colour means high concentration and black colour low concentration of the screened element. It demonstrates the important fact, that yttria and titan get together and form a complex compound: The white dots in d) and e) are nearly equally distributed. Further analyses have to be carried out for a deeper understanding of these characteristics.

Finally some tensile tests were done. Figure 6 shows the curve:

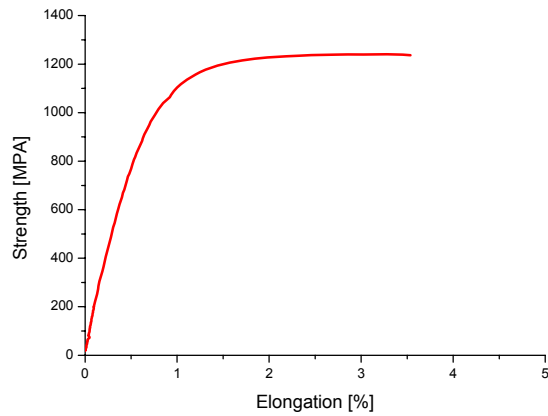


Figure 6: First tensile tests of the ferritic ODS alloy.

These tests showed a high strength but the elongation remains too small, especially if this material is compared to ODS Eurofer. Further heat treatments have to be applied to observe effects on both parameters to optimize these values.

Altogether these works create a promising basis for further developments of these ferritic ODS alloys. In addition to the tensile tests impact test will follow soon. All observations will continue to reach the optimum production parameters and material attributes.

Staff:

C. Adelhelm
S. Baumgärtner
C. Eiselt
P. Graf
M. Klimenkov
T. Kaiser
R. Lindau
A. Möslang
U. Jäntschi
R. Ziegler
H. Zimmermann

TW5-TTMS-006 D 6

Characterisation of Reference EU ODS-EUROFER Batch (Tensile, Creep and Charpy)

In the past different associations, i.e. FZK, CEA and CRPP, have produced several developmental ODS-alloys on the basis of the RAFM steel EUROFER. Results of mechanical tests revealed good tensile, creep and LCF properties of the hipped ODS but poor DBTT ($\sim 100^\circ\text{C}$) compared to EUROFER. Applying special thermo-mechanical treatments, i.e. mechanical deformation plus subsequent heat treatment, lead to a substantial shift of DBTT to temperatures well below 0°C without negative effect on the tensile properties. Moreover the total elongation was increased at higher temperatures compared to only hipped ODS. This fabrication route, developed by FZK in cooperation with PLANSEE, was chosen for the fabrication of a 50 kg EU-ODS-EUROFER reference batch in 4 different product forms, i.e. 2 rolled plates ($t = 6$ and 17 mm) and 2 extruded rods ($\varnothing 12.5$ and 20 mm).

After first heat treatment trials (TW5-TTMS-006 D10) a reference heat treatment (normalising + tempering) of 1100°C 30 min air-/waterquenching + 750°C 2 h air-cooling was chosen. Since the impact properties are most sensitive, impact tests on KLST specimen, applying these two different heat treatments, were performed. Fig. 1 shows the results of these tests in comparison to the precursor alloys and standard EUROFER. It turned out, that the new EU-reference batch (green diamonds) did not reach

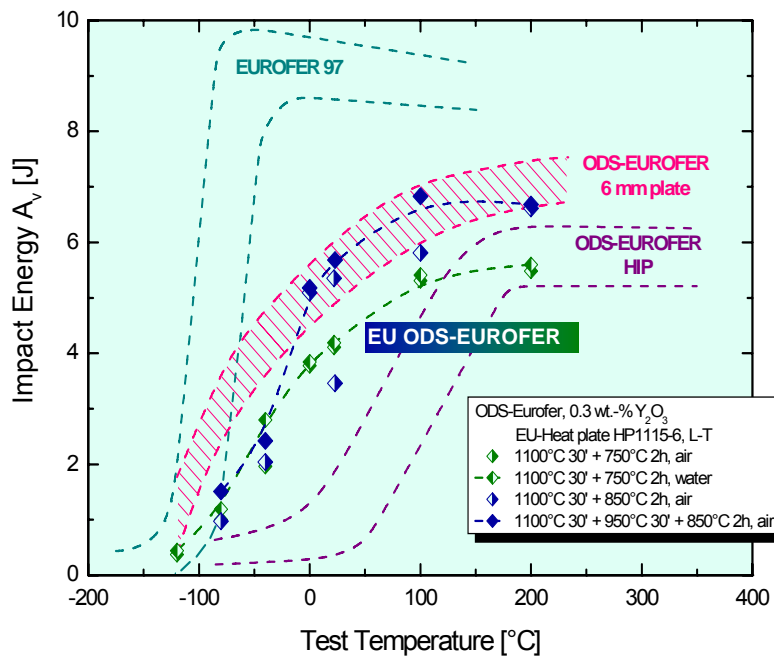


Fig. 1: Test temperature dependence of total absorbed energy of EU ODS-EUROFER in comparison with former ODS-EUROFER and EUROFER 97 (KLST specimens).

the good values of the thermo-mechanically treated plate material produced earlier (pink hatched area). As the tempering diagram (TW5-TTMS-006 D10) shows, the tempering temperature can be raised to 850°C . Two additional heat treatments were performed applying a one or two-step austenitisation treatment followed by a tempering treatment at 850°C . The idea behind the two-step austenitisation was to dissolve as much carbides as possible during the high temperature austenitisation at 1100°C and to refine the grain size in the second austenitisation treatment at 980°C . These two heat treatments (blue diamonds) lead to higher upper shelf energy values (USE) compared to the initial heat treatment, but the ductile to brittle transition temperature (DBTT) was not improved.

The results of tensile tests on the EU ODS-EUROFER 6 mm plate material after standard heat treatment (1100°C 30 min aircooling + 750°C 2 h aircooling) and with a higher tempering temperature (850°C) are shown in Fig. 2 and 3. The blue dotted lines give the scatter band of the tensile results on the FZK ODS plate material. The ultimate tensile strength of EU ODS-EUROFER with the standard heat treatment is superior to that of FZK ODS plate material in the temperature range from RT to 600°C . Applying a higher tempering temperature leads to a decrease of strength below 500°C testing temperature. The uniform elonga-

tion A_g is slightly increased below 600°C while an increase of the total elongation A was observed below 400°C. The two-step austenitisation treatment followed by a 850°C tempering, not shown here, leads to a higher strength but lower ductility below 600°C compared to the one step heat treatment.

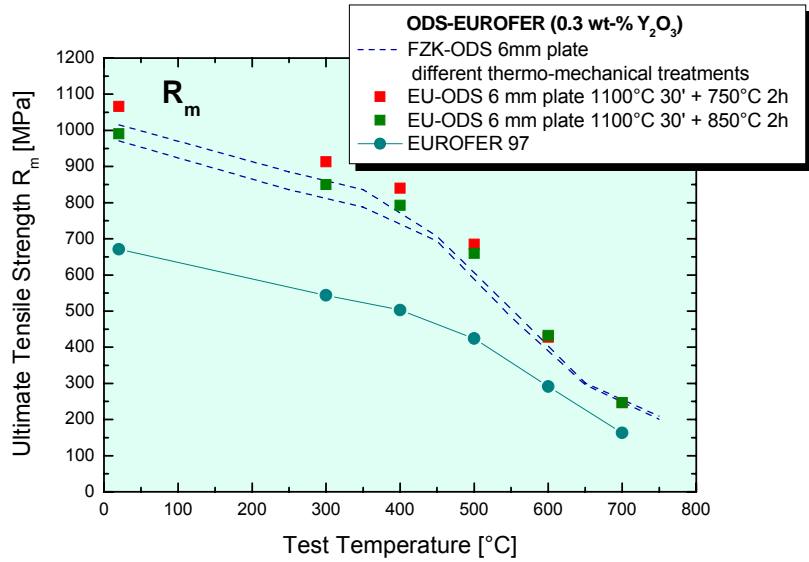


Fig. 2: Ultimate tensile strength R_m of EU ODS-EUROFER in dependence of the test temperature compared to standard EUROFER 97.

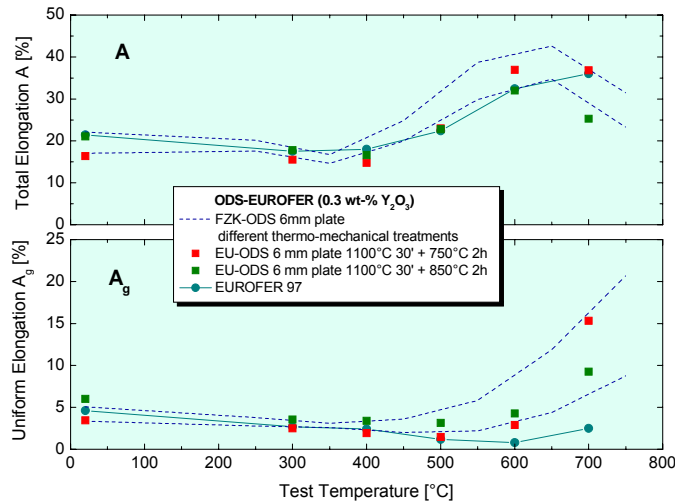


Fig. 3: Uniform and total elongation of EU ODS-EUROFER in dependence of the test temperature compared to standard EUROFER 97.

Staff:

S. Baumgärtner
B. Dafferner
A. Falkenstein
S. Heger
M. Klimenkov

R. Lindau
A. Möslang
U. Jäntsch
M. Rieth
H. Zimmermann

TW5-TTMS-006 D 10

Characterisation of Reference EU-ODS-EUROFER Batch: Optimisation of Heat Treatment, Ageing Behaviour and Microstructural Characterisation

The efficiency of future fusion reactors will strongly depend on the operating temperature allowed by selected structural materials. With this respect, ODS steels are attractive candidates since they would allow to increase the operating temperature by approximately 100°C. The reduced activation martensitic steel EUROFER-97 (8.9 Cr, 1.1 W, 0.2 Ta, 0.42 Mn 0.11 C wt%), which is currently considered as a European reference for structural application, has been selected as a base material. Based on the experience with a precursor a 50 kg EU-ODS-EUROFER batch has been specified and produced (TW3-TTMS-006 D1a). Within this task an optimum heat treatment should be determined. The influence of different heat treatments on microstructure was also investigated.

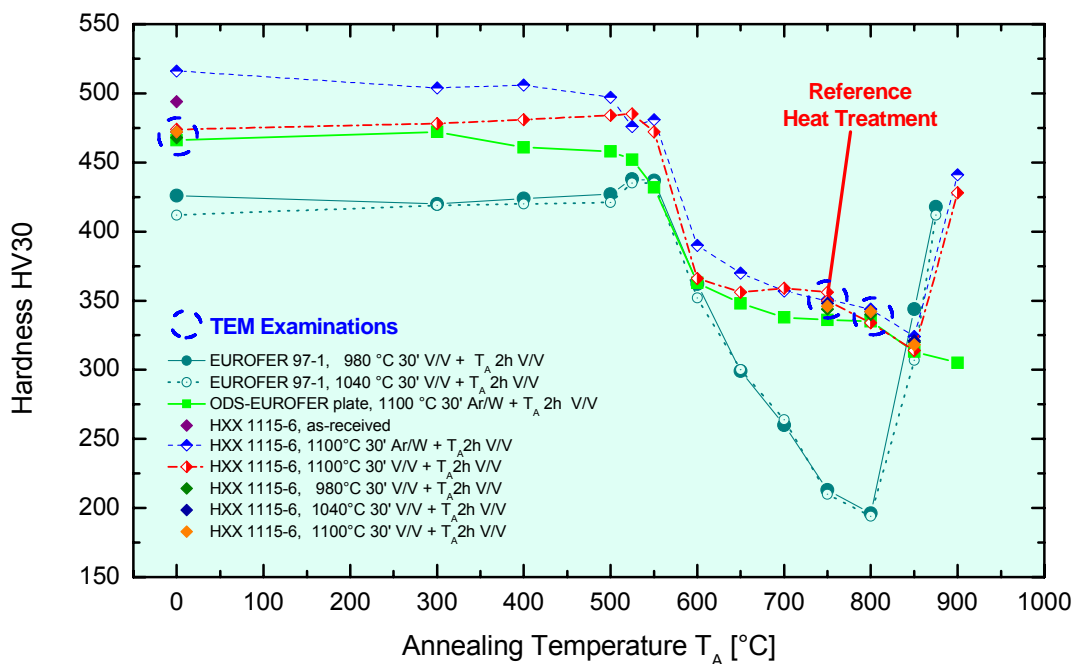


Fig. 1: Vickers hardness HV30 in dependence of the annealing temperature.

First heat treatment trials on the EU-ODS-EUROFER material were performed to define a reference heat treatment. The samples were normalized at 1100°C for 30 min following a tempering treatment at temperatures between 300 and 850°C for 2 hours. The cooling to room temperature after austenitisation was performed either by air- or water- quenching. Fig. 1 gives the development of hardness HV30 in dependence of the annealing temperature. The tempering treatment was performed in a tubular 3-zone furnace. The cooling was performed by withdrawal of the furnace from the vacuum quartz recipient. Due to the small specimen size, the cooling rate is equivalent to air-cooling. The tempering behaviour of the EU-batch (HXX 1115-6, blue and red diamonds) is compared to the precursor alloy (green squares) and standard non-ODS EUROFER steel (full and open dark cyan circles). The Vickers hardness of all ODS alloys in the interesting temperature range between 550 and 850 °C is very similar. According to the good mechanical behaviour of the precursor ODS-EUROFER steel, 1100°C 30 min air-cooling + 750°C 2 h air-cooling was chosen as reference heat treatment. Due to a higher C-content (0.13 wt.-%) of the EU-batch compared to the precursor alloys, the material was air-hardening. This reference heat treatment was recommended for the characterisation work to be performed by different EU associations. In the

course of the mechanical characterisation (TW5-TTMS-006 D6) it turned out, that the impact behaviour was inferior to that of the precursor alloy. As Fig. 1 indicates, the tempering temperature could be raised up to 850°C. Additional heat treatment experiments were performed and it was possible to reach the good impact behaviour of the FZK ODS-EUROFER plate material.

Selected heat-treated samples (blue circles in Fig. 1) were examined by TEM using an analytical FEI Tecnai 20 FEG microscope equipped with HAADF detector for scanning TEM. The investigations should show the influence of austenitisation and tempering treatments at variable temperatures on the microstructure of the alloy. Fig. 2 shows two bright field micrographs of samples austenitised at 980°C for 30 minutes. The sample on the left side (Fig. 2a) has besides austenitisation no further thermal treatment, whereas the sample on the right (2b) was additionally tempered at 800°C for 2h. A characteristic feature of both microstructures is the appearance of a martensitic lath structure.

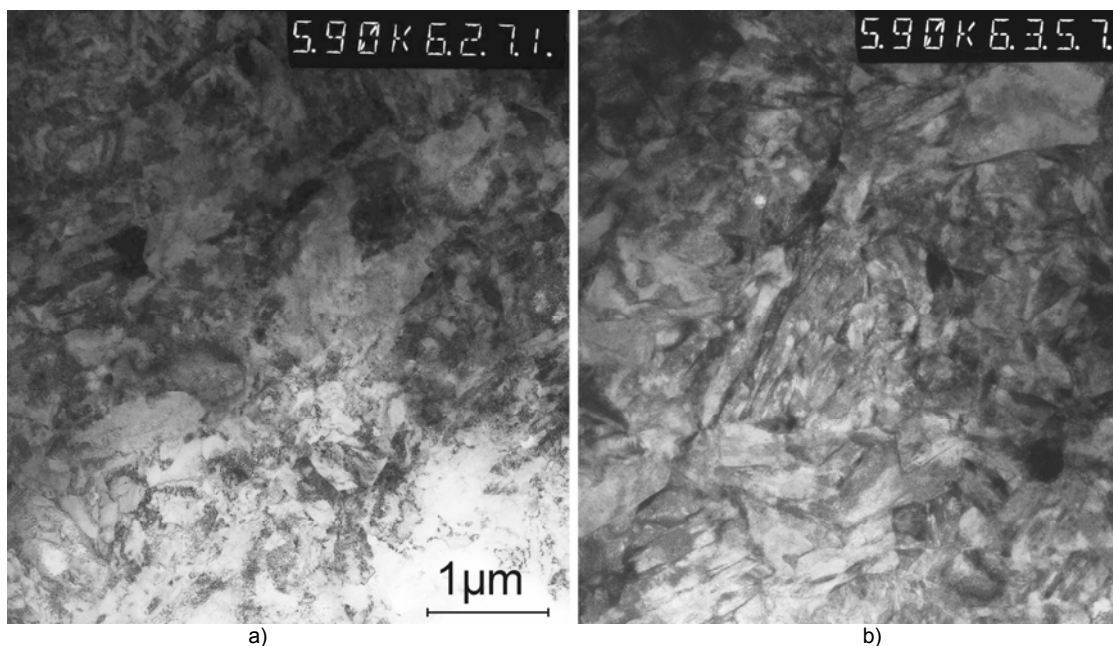


Fig. 2: The bright field images of samples, which were austenitised at 980°C for 30 min. Part (a) shows the image obtained from the sample without further tempering treatment and part (b) with additional tempering treatment at 800°C for 2h.

Besides the martensitic laths small ferrite-like sub-grains of 0.5-1.0 μm in size can be found. The high defect density inside the sub-grains makes the identification of primary austenite grain boundaries and consequently the grain structure itself very difficult. The comparison of sub-grain and laths structures shows no significant differences between both samples within the scope of error. The sub-grain structure of the samples austenitised at different temperatures up to 1100°C was found to be similar to the structure after austenitisation at 980°C as shown in Fig. 2a.

The spatially resolved analytical TEM investigations were used for the imaging of carbide precipitates und herewith for studying their formation depended on the thermal treatment. The carbide precipitates were found to be absent in the samples without tempering treatment. This result has been expected based on the hardness measurements. The carbide precipitates were detected in the samples after tempering treatments at 750°C and 800°C. In Fig.3 the results of elemental analysis in the sample after 800°C treatment for two hours are presented. The carbide precipitates, which are almost invisible in the HAADF image, show a bright contrast in the Cr EDX map and dark contrast in the Fe map. The carbides are statistically distributed in the sample, however in some cases the carbides decorate some grain (or sub-grain) boundaries (Fig. 3b,c). As it can be clearly seen by comparing the HAADF image with the elemental maps not all grain boundaries serve as preferable nucleation sites for car-

bides. The questions, why some boundaries have a good decoration and some boundaries not, cannot be answered reliably.

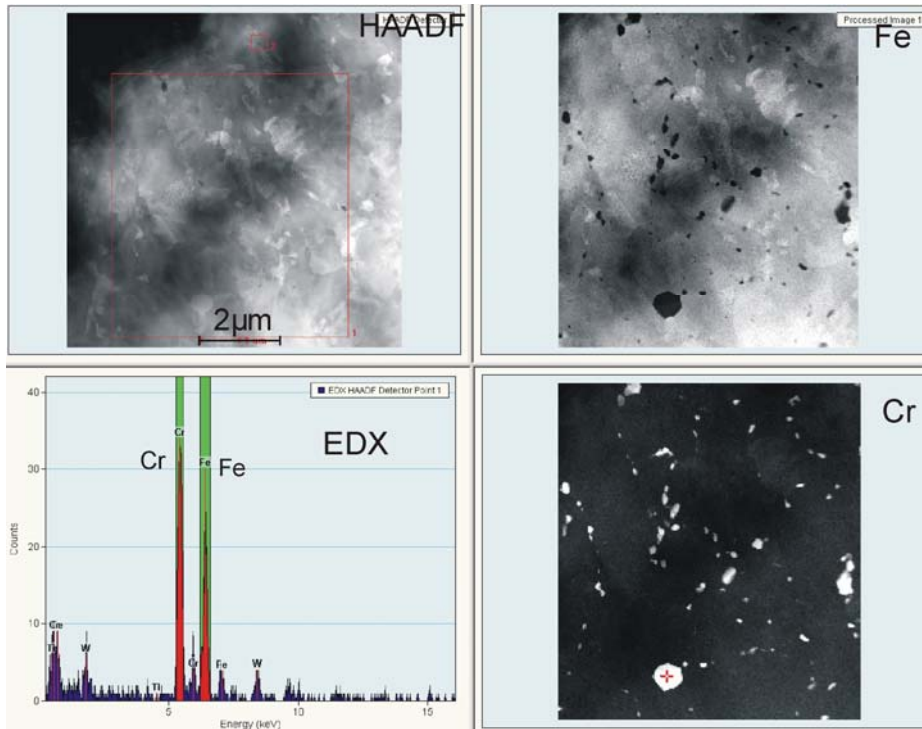


Fig. 3: Analytical investigations of the sample after austenitisation at 1100°C for 30 min followed by a tempering for 2 h at 800°C.

In Fig. 4 two histograms that reflect the size distribution of the carbide precipitates in the samples after tempering for 2 hours at 800°C and 750°C are shown. In both cases the distribution shows a maximum at 100-130 nm and a decreasing tail till the size of about 250-300nm. The size of carbide precipitates is in the average 30% larger after tempering at 800°C then after 750°C.

The micro structural investigations will be continued.

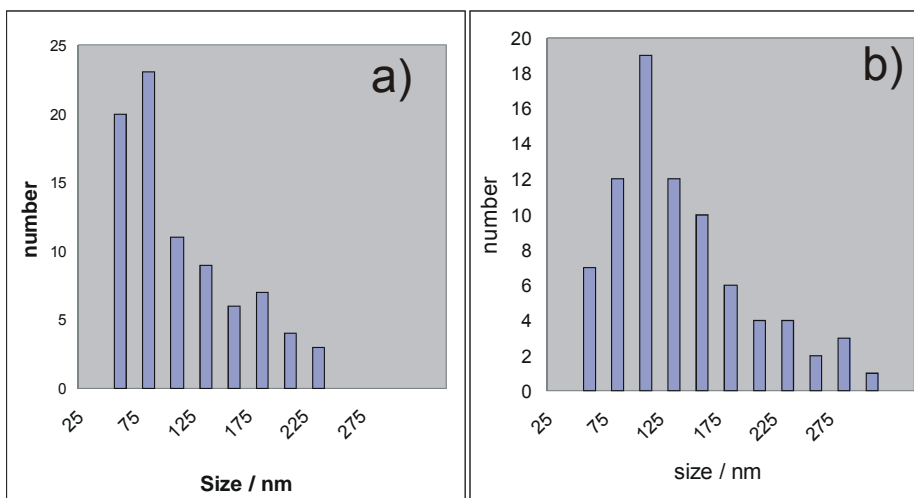


Fig. 4: The size distribution histograms obtained from the samples austenitised at 1100°C and normalised at 750°C (a) and 800°C (b).

Staff:

H. Zimmermann
P. Graf
U. Jäntsch
M. Klimenkov
R. Lindau

TTMS-007 Modelisation of Irradiation Effects

TW5-TTMS-007 D 5 TW5-TTMS-007 D 10 Defect Microstructure Evolution

To improve modelling of irradiation effects in FeCr steels there are still answers needed to a lot of open questions, e.g. the interaction of Cr with dislocation loops, the chemical composition at the border of loops and the morphology of the loops formed after ion irradiation. Answers to these questions can be given (at least partly) by microstructural investigations of single crystal specimens after according ion irradiation experiment performed at HMI. The results will be used for validation of existing modelling techniques and as direct input to the potential development activities.

Two FeCr and two Fe single crystal specimens were prepared for the study. The specimens were cut in form of disks with 3 mm diameter and 0.2 mm thickness. They were implanted with Au⁺ ions of 350 MeV energy. The implantation area has 2 mm diameter in the middle of the discs. Two specimens (that mean one FeCr and one Fe discs) were implanted with a fluence of $5 \cdot 10^{14} \text{ cm}^{-2}$

another two with $3 \cdot 10^{15} \text{ cm}^{-2}$. The calculations show that the distribution implanted Au ions shows a maximum at the 12 μm under the specimens surface (Fig. 1). The maximal damage of 2.1 dpa and 12.6 dpa (for different implantation fluences) is expected to be in the range from 10 μm to 12.5 μm (Fig. 1). In this range of maximal damage is also expected the most possible formation of dislocation loops.

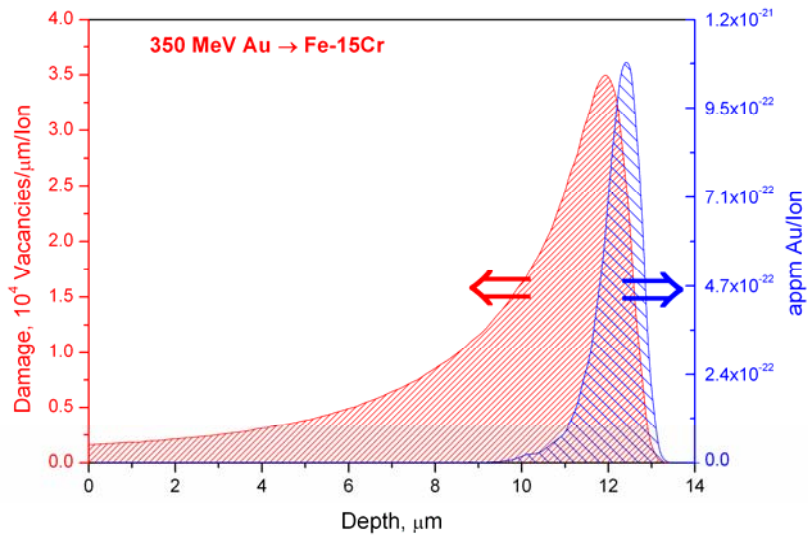


Fig. 1: Depth distribution of implanted Au atoms and damage of the target.

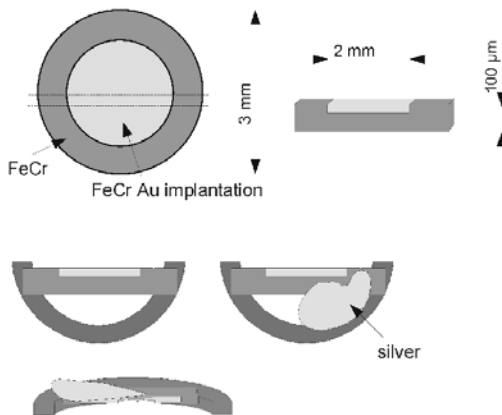


Fig. 2: Preparation steps of TEM specimens by means of FIB.

The specimens preparation for TEM investigations was performed using FIB. The whole procedure is shortly explained in Fig. 2. The implanted discs were cut along the marked lines and then the bars were polished from the both sides till the thickness of 40 μm . After that the bars were affixed on the half cooper ring with the conducting adhesive. Finally the specimens were thinned in the FIB using Ga ion beam of 3 nm diameter. The thinning procedure is usually performed in several steps and takes about 12-24 h. The successfully prepared lamellas for TEM investigations show the homogenous thickness of 100-150 nm

through the depth of about 13 μm . That quality ensures suitability of lamella for TEM investigations. The first TEM investigations show that dislocation loops in the irradiated specimens have a size of 10-25nm. The imaging of such small loops appears very sensitive to the specimen thickness. The best TEM results were obtained with the lamella where by mechanical deformation causes the formation of small holes in the 10-13 μm depth. The thickness of the specimen achieves 20-40 nm on the edge of the hole, that allows the contrast-reach imaging of the loops.

In Fig. 3 is presented the image of dislocation loops in the FeCr single crystal with 12.6 dpa irradiation dose. The dislocation loops have been imaged with enhanced contrast using [110] vector. They have a size of 15-25 nm and the density of $(5\pm 3)\cdot 10^{16}\text{ cm}^{-3}$.

The TEM investigations show that the prepared lamellas have slight deformation. The deformation becomes perceivable by the performing of tilting experiments. The reason for such behaviour could be the impact of magnetic field inside the microscope as well as the mechanical tensions in the specimen. The deformations make the performing of tilting experiments and following, the precise determination of Burgers vector as well as dislocation types difficult. The determination of these parameters requires additional experiments.

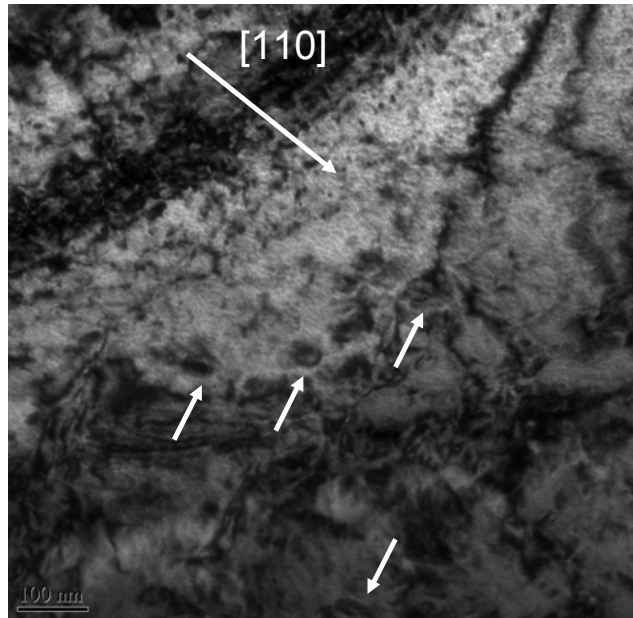


Fig. 3: TEM micrograph of FeCr single crystal with imaged dislocation loops.

The further preparation of specimens and their TEM investigation should be performed within the scope of this sub-task. It should be tried to prepare TEM lamellas with minimal mechanical deformations.

Within the scope of TW5-TTMS-007 D10 sub-task neutron irradiation of FeCr and Fe single crystals was performed. The first specimens were investigated by TEM at SCK.CEN after irradiation of 0.25 dpa. The investigation reveals that the density of created defects is insufficient for the reliable TEM analysis of irradiation effects. The next irradiation dose we will be targeted over 1 dpa. The comparison of formation of irradiation induced defects in FeCr and Fe single crystal samples will be performed.

Staff:

U. Jäntschi
M. Klimenkov
A. Möslang
M. Rieth
P. Vladimirov

H. Hofmann (HMI)

TW5-TTMS-007 D 7

TW6-TTMS-007 D 10

Production and Characterization of Single Fe-Cr Crystals and Elaboration of a Critical Review of the Physical Metallurgy of EUROFER Alloying Elements and Impurities, Heat-treatment/Phases/Microstructure, Phase Stability, and Segregation

Overview

Until today there is still a lack of physical and mechanical data for Fe-Cr single crystals (SC) with a low Cr content. But it would be most desirable for the development of Fe-Cr potentials to know the real elastic constants and thermal expansion coefficients. These data could be directly used to adjust the according fits. Therefore, Fe-Cr single crystals have been produced containing 15 % chromium. Provided the crystal production succeeds, elastic constants and thermal expansion data could be produced on different orientations each.

Initial Status

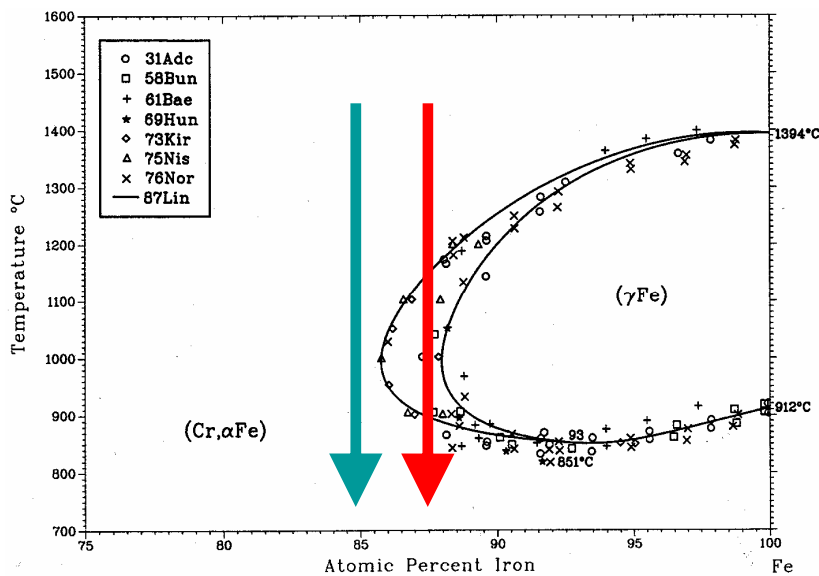


Fig. 1: Fe-Cr binary phase diagram. The difficulty with drawing single crystals from the melt is to avoid the γ -nose during cooling. With Cr contents of 12% (red arrow) it was not possible to get a SC. Only at higher contents (green arrow for 15% Cr) the SC production succeeded.

First the production of Fe-Cr SCs with low chromium content has been tested. But the production failed for Cr contents lower than 15%. The difficulty with drawing single crystals from the melt is to avoid the g-nose during cooling (see Fig. 1). Therefore, the current task had to be restricted to examinations of pure iron SCs and Fe-15%Cr SCs. From these SCs TEM specimens with [100], [110], and [111] oriented surfaces were fabricated. In addition, multi purpose specimens (6 mm x 4 mm x

4 mm) with [100], [110], [111], and [211] surfaces were produced. In all cases the quality of the specimens has been controlled by x-ray and chemical analysis. Both, purity and degree of orientation are well within the acceptable tolerances.

TEM specimens have been provided to HMI for irradiation at 300°C to damage levels of 2.5 dpa and 15 dpa, and to SCK.CEN Mol for neutron irradiation in the BR2 reactor at 300°C. The accumulated damage will be more than 1 dpa. Other than the ion irradiated specimens they will be activated and therefore, preparation and TEM examination has to take place in hot cell facilities.

Progress

After fabrication and quality assurance of the SCs, nano-indentation tests have been planned, prepared, and performed (see Fig. 2 and 3). For the measurement and evaluation

the test-equipment of IMF-II has been used. For the calculation of Young's Modulus there are two methods. One is based on the calculation from the average of the nearly constant part of the load curve. The other method is based on data of the unloading curve. For a higher accuracy, the results have been averaged over ten indentation tests. As can be seen from Fig. 4, both methods lead about to the same results (within a certain deviation). Compared to pure iron, Fe-15%Cr shows a higher modulus for each orientation. The (100) surfaces have the lowest and the (110) surfaces the highest modulus. The difference between (111) and (211) orientation is too small for this method and could therefore not be determined.

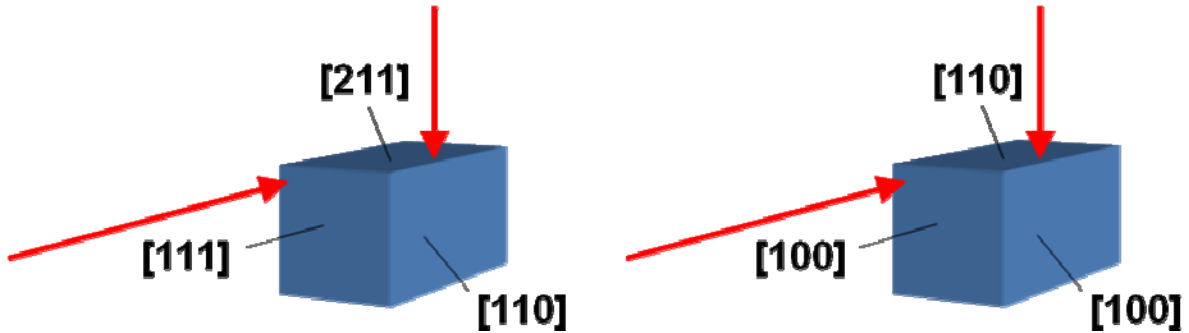


Fig. 2: There are two types of multi-purpose specimens which have been used to perform the nano-indentation tests on four different oriented surfaces. The red arrows indicate the indentation direction.

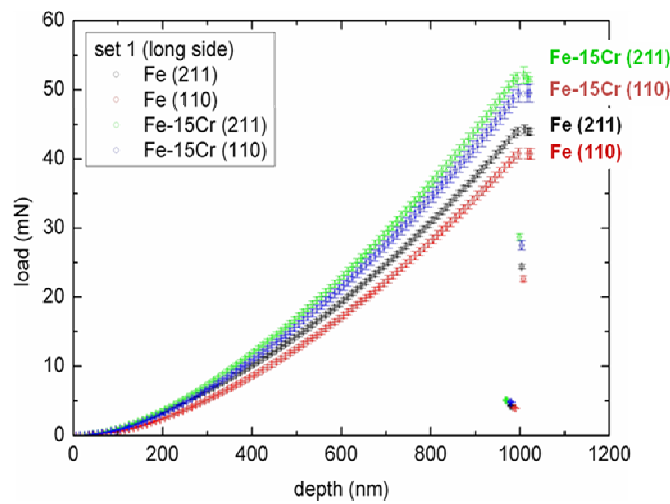


Fig. 3: Typical load curves of nano-indentation tests on different oriented surfaces of single crystals.

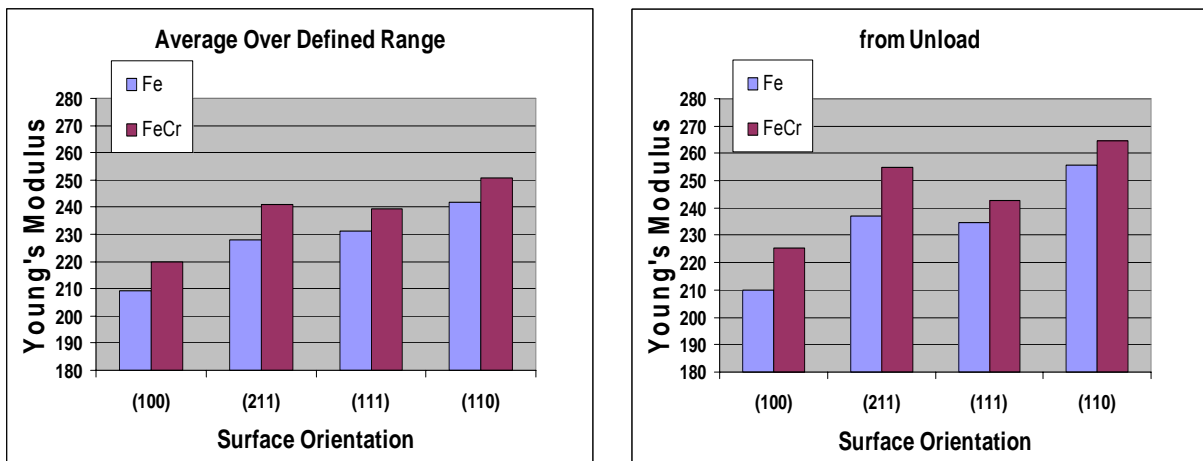


Fig. 4: Test results for Young's Modulus from two different evaluation methods.

It was planned to use the multi-purpose specimens for a determination of the thermal expansion coefficient. Unfortunately, the measurements failed due to the unforeseeable play of the extensometer of the testing device. For an accurate measurement the specimens are too short.

Conclusions

It was not possible to prepare larger Fe-Cr single crystal parts with less than 15 % Cr. But at least Fe-15%Cr SCs could be fabricated with a rather good quality which could be used (together with pure Fe SCs) for irradiations and TEM examinations. The multi purpose SC specimens have been prepared and used for nano-indentation. With the presented results it is now possible to calculate the elastic constants and use these values for a fine adjustment of the interaction potentials which are needed for atomistic simulation methods such as molecular dynamics.

Since the specimens are too small for an accurate determination of thermal expansion coefficients, the task is finished. But the specimens will be further used for destructive tests.

Staff:

C. Adelhelm
P. Graf
A. Falkenstein
S. Heger
U. Jäntschi
M. Klimiankou
A. Möslang
M. Rieth
R. Schwaiger
P. Vladimirov
H. Zimmermann

Materials Development Advanced Materials

TTMA-002 Divertor and Plasma Facing Materials

TW3-TTMA 002 D 3 Mechanical Testing of Improved W Alloys: Tensile and Fracture Toughness Testing

Objectives

A structural component like the divertor is subjected during service to very high heat loads and also to alternating thermal and mechanical stresses as a consequence of the pulsed reactor operation. Even for helium cooled ITER divertor concepts the operating temperatures override the recrystallization of pure tungsten or tungsten alloys. Due to the cyclic operation under service conditions, the knowledge of the reasons of fatigue endurance of these materials becomes more important.

Status end of 2005

The new high temperature high vacuum furnace, with the pull rods for tensile- and LCF-testing, has set into operation in October 2005. After having performed tensile tests on both reference materials, which was pure tungsten and W-La₂O₃, in the high temperature range between 700°C and 1200°C at a strain rate of $3 \times 10^{-3} \text{ s}^{-1}$ pure tungsten has shown at 1200°C a considerable dynamic recrystallization whereas W-La₂O₃, did not recrystallize in the temperature range examined.

Low Cycle Fatigue testing

After the installation of the modified high temperature pull rods, consisting of a Finite Element designed stronger half shell of the gripping system made of W-La₂O₃, the control parameter for the strain controlled LCF tests had been adjusted.



Fig. 1: Temperature calibration arrangement of the tungsten LCF specimen.

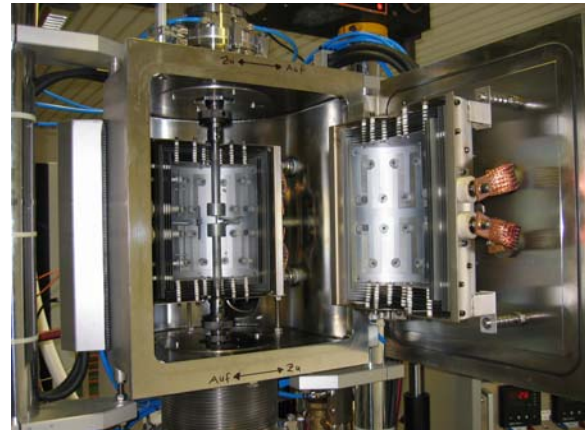


Fig. 2: Overview of the high temperature testing facility with pull rods for LCF-testing.

Also the temperature calibration was optimized by laser welding the Pt-RhPt-thermocouple onto a calibration specimen (Fig. 1). This preceding calibration step is necessary because we cannot damage the specimen surface by a welding spot during LCF testing.

The rigid clamping of the specimen for push-pull LCF experiments still has to be improved, but since these clamping effects on cyclic damage are very low, we performed first experiments on tungsten LCF specimens, successfully.

Since the scatter of numbers of cycles to failure N_f in LCF tests is rather high one has to perform at least three to five tests with the same parameter set. Under the cyclic strain controlled loading, we applied to the rigid clamped specimen, tungsten shows at 800°C at a total strain range of $\epsilon_{tot} = 0.5\%$ a typical appearance of the hysteresis loops.

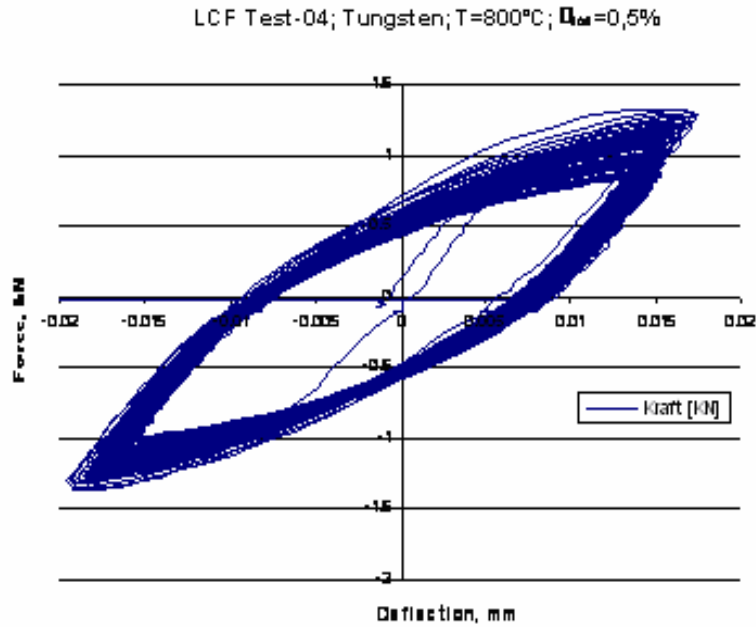


Fig. 3: Hysteresis loops of tungsten LCF-testing.

The number of cycles to failure N_f are ranging according to four experiments performed from 3,220 to 11,480 cycles and fit well to literature data from R.E. Schmunk and G.E. Korth. From Fig. 4 can be depicted a similar cyclic softening behaviour as it is also known from the Ferritic Martensitic Steels.

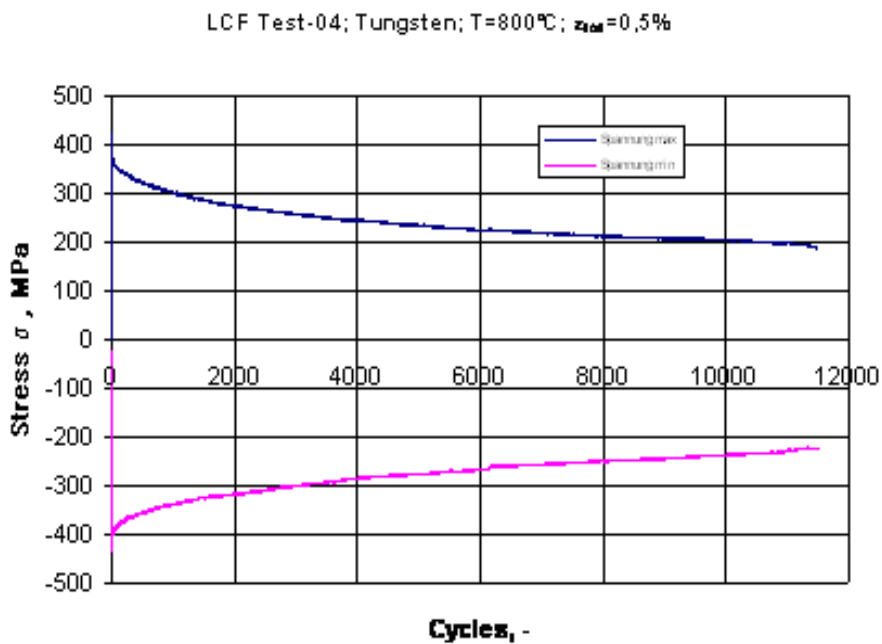


Fig. 4: Cyclic softening behaviour of tungsten.

The W-La₂O₃ specimens show at the same conditions a similar behaviour. Only the stress level is higher during cyclic softening compared to pure tungsten.

Staff:

U. Bürkle
M. Klotz
C. Petersen

Literature:

R.E. Schmunk and G.E. Korth, "Tensile and Low Cycle Fatigue Measurements on Cross-Rolled Tungsten", Journal of Nuclear Materials, 103 – 104 (1981), pp. 943-948

TW3-TTMA-002 D 7
TW6-TTMA-002 D 6
Fundamental Studies on Mechanical Properties of W-alloys

Overview

Tungsten and selected W-alloys are considered to be the primary candidates for armour and structural materials of ITER and of even more ambitious DEMO divertor designs. For the later, present design outlines are based on a structural material with temperatures up to about 1300°C. The most critical issues are ductile-to-brittle transition and recrystallization. The first defines the lower, the second the upper operation temperature limit. Another problem consists in the fact that the microstructure of these refractory alloys depend strongly on the manufacturing history. But mechanical properties are defined by the microstructure, and therefore, refractory alloys can behave quite different, even if their chemical composition is the same.

The goal of this task is a systematic screening of mechanical properties of commercial refractory alloys to determine the influence of microstructure characteristics like grain size and shape, anisotropy, texture, and alloy composition.

Initial Situation

In the previous years a special creep testing facility has been developed and implemented successfully. From Plansee pure tungsten and W-La₂O₃ rods (D8 mm x 1000 mm) were purchased. From these, standard size creep specimens (M8 x 56 mm) have been fabricated and the materials were completely tested at 1100°C and 1300°C for up to 5000 hours.

According to the divertor design, the structural material should have maximum DBTT values of about 300°C in the unirradiated condition. To characterize the DBTT behaviour sub-size Charpy specimens (3 mm x 4 mm x 27 mm) have been fabricated from the W and WL10 rods with L-R orientation (notch root perpendicular to the rod axis). For the Charpy tests temperatures of up to 1050°C were necessary which could only be reached by the use of gas burners. The measured DBTT values at 1/2 upper shelf energy (USE) was about 800°C for W and 950°C for WL10. This is far more than specified by the design criterion. However, for a better reproducibility another testing procedure should be developed for future characterization studies.

Progress

Figure 1 shows the latest Larson-Miller plot of all completed creep test results. From this plot extrapolations are possible in a more accurate way. However, obviously the test results from literature (grey triangles) lead to a significant overestimation of the lifetime which is mainly due to their short testing period (max. 300 hours). Present divertor designs are based on a structure material with creep strength of more than 55 MPa for a time-to-rupture of 20,000 hours at 1200°C. According to our tests, only WL10 fulfils this design criterion.

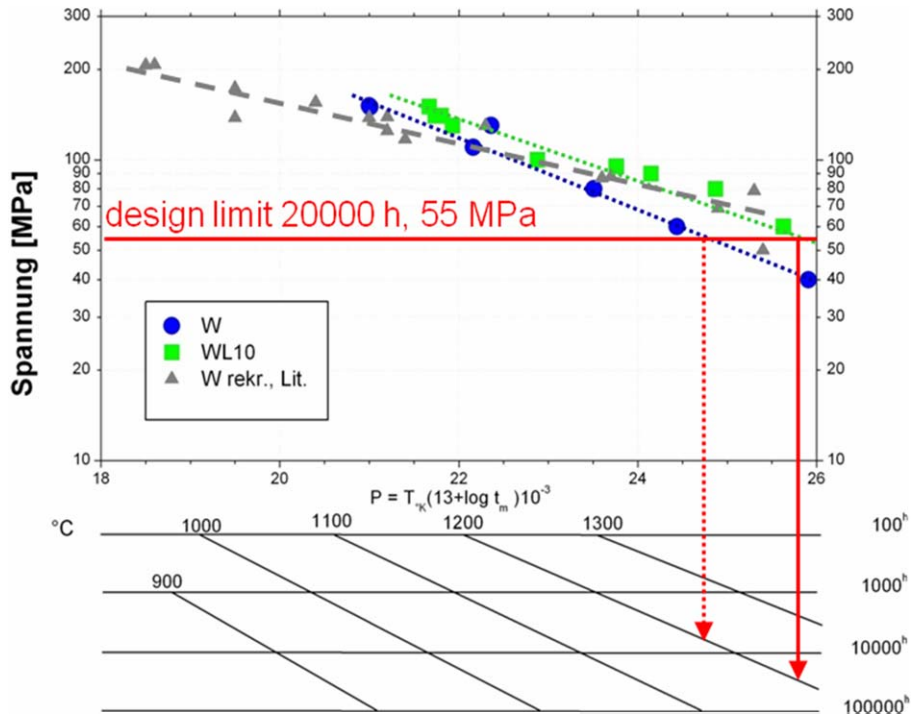


Fig. 1: Larson-Miller diagram of the creep test results. It can be seen quite clearly that the short time creep test results from literature (grey triangles) lead to a significant overestimation of the lifetime. In present divertor designs, the structure material should show creep strength of more than 55 MPa for a time to rupture of 20,000 hours at 1200°C. Only WL10 fulfils this design criterion.

For a more reliable and reproducible method to perform Charpy tests at high temperatures a new test equipment was developed and installed (Figure 2). The new Charpy testing device was then used to examine the embrittlement behaviour of a Ta-10%W alloy. As can be seen in Figure 3, this material is completely ductile and shows much more strength at the same time, compared to pure Ta. But whether this material class is applicable for divertor applications has still to be verified.

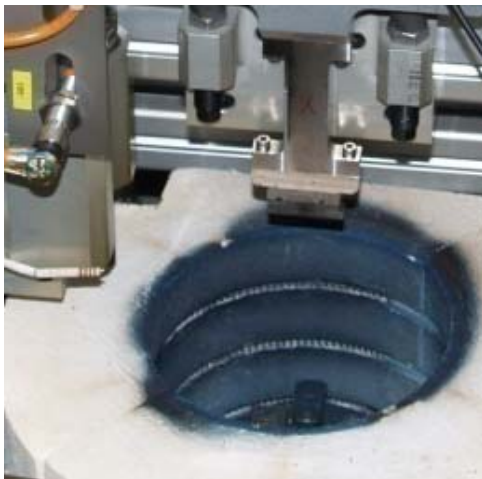


Fig. 2: Instrumented Charpy tests on refractory alloys are performed in-situ within a vacuum furnace. With this newly developed configuration DBTT can be determined reproducibly and with high accuracy.

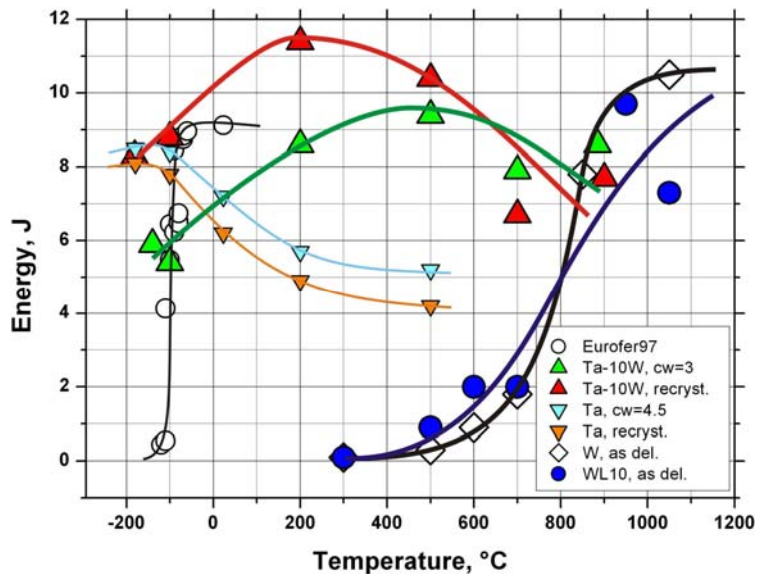


Fig. 3: Brittle-to-ductile transition of tungsten and WL10. Determination of DBTT at 0.5 USE leads to $800 \pm 50^\circ\text{C}$ for tungsten while a conservative estimate for WL10 leads to DBTT of $950 \pm 50^\circ\text{C}$ (both materials were tested with gas burners). For comparison, the transition of the EUROFER steel is also illustrated which clearly demonstrates the extraordinary brittleness of the tungsten materials. The new high-temperature Charpy testing device was used for the examination of Ta-10%W alloys.

Conclusions and Outlook

Oxide dispersion strengthening tungsten with La_2O_3 increases the possible operation temperature by approximately 70-90 °C with the material at hand for a given life-time and load. For a given temperature WL10 compared to pure tungsten may be stressed more by at least 15 MPa to reach the same life-time. That is, WL10 meets the current divertor creep design criterion for time-to-rupture at 1200 °C.

But Charpy tests have shown that the used W and WL10 rods are too brittle to meet the divertor DBTT design criterion. The screening and characterization studies will therefore be continued with other commercially available tungsten alloys.

Staff:

S. Baumgärtner
B. Dafferner
A. Falkenstein
P. Graf
S. Heger
U. Jäntschi
M. Klimiankou
A. Möslang
M. Rieth
R. Ziegler
H. Zimmermann

Literature:

- [1] Rieth, M.; High-temperature creep of pure and dispersion-strengthened tungsten. Jahrestagung Kerntechnik 2005, Nürnberg, 10.-12.Mai 2005, INFORUM GmbH, S.455-58, CD-ROM.
- [2] Rieth, M.; Dafferner, B.; Limitations of W and W 1% La_2O_3 for use as structural materials. Journal of Nuclear Materials, 342 (2005).
- [3] Rieth, M.; Creep and Recrystallization of Pure and Dispersion Strengthened Tungsten; EUROMAT, Prague, 5-9 September 2005.
- [4] Rieth, M.; Evaluation of the mechanical properties of W and W-1% La_2O_3 in view of divertor applications; ICFRM-12, Santa Barbara, 4-9 December 2005.

TW4-TTMA-002 D 2

TW5-TTMA-002 D 2

Developing of Improved W-alloys for Application in a Power Plant with He Cooled Divertor

Objectives

Within these tasks intense R & D work will be carried out on testing commercially available W alloys to create a data base with reliable properties acting as a reference point for the development of W alloys with improved properties for future application of these alloys in a helium-cooled divertor. The performed testing work of state-of-the-art products showed that they will not fulfill the requirements which are deducted from the actual divertor design indicating an application in the temperature range of 600°C to 1500°C. The most critical features will be the ductile to brittle transition and the recrystallization behavior which are also affected by fast neutrons.

The technological work under the tasks TW4-TTMA 002 and TW5-TTMA 002 is directed to the development of new tungsten alloys with improved properties. Based on our experience on the behaviour of refractory alloys and their processing we selected for performing this work program the method of mechanical alloying to synthesize improved ODS-W precursors with nano-scale features. During the subsequent adopted compaction steps (e.g. HIP) the powders will be consolidated to compacts with interlinked grains and controlled morphology. The properties of the improved W-alloys will be compared to standard, commercially available WL10 grade.

Actual status

Determination of tungsten alloy properties (tensile properties, microstructure) was continued by applying raw materials (rods) in the usual (state of the art) way. The tested alloys, pure W and WL10 (W-1%La₂O₃), exhibit large longitudinally elongated grains partially with a rather big diameter of approx. 20 µm for W grains. This is a result of the processing route. The ODS particles are not homogeneously dispersed in the WL10 quality. The performed tests [1] indicate that DBTT of both materials, pure W and WL10, lays at higher levels than claimed by the lower boundary of 600°C, as a result from design analyses. The detected microstructure implies that the grain structure and the ODS distribution is not optimized adequately for a structural material and affects the properties. Thus finer grains and a more homogeneous ODS distribution should improve mechanical and physical properties.

For synthesising improved W powders with a homogeneous distribution of ODS particles an attritor ball milling system was build up and successfully tested with EUROFER steel powder. However, during the processing of first W alloys the milling container was heavily damaged, due to the special and unique behaviour of W powders e.g. feed through failure or overheating, which never occurred, when producing the ODS steels. After redesigning and repairing a modified version was introduced in the middle of 2006. Some difficulties, which were caused by W powders and observed during the first tests, could be reduced or eliminated. The new test series were performed with smaller vessel filling and a reduced powder to ball ratio of 1 to 10 compared to earlier tests. The milling container and the balls were fabricated from Cr-steel. Fig.1 shows the SEM pictures of a W-1%La₂O₃ mixture and after 10 h ball milling. The particle shape changed during processing to the morphology known from milling of other refractory alloys. The performed EDX analyses showed that the La₂O₃ addition is still present in the milled powder at a level of about 1% and may point to a homogeneous dispersion which has to be proven by future TEM analyses.

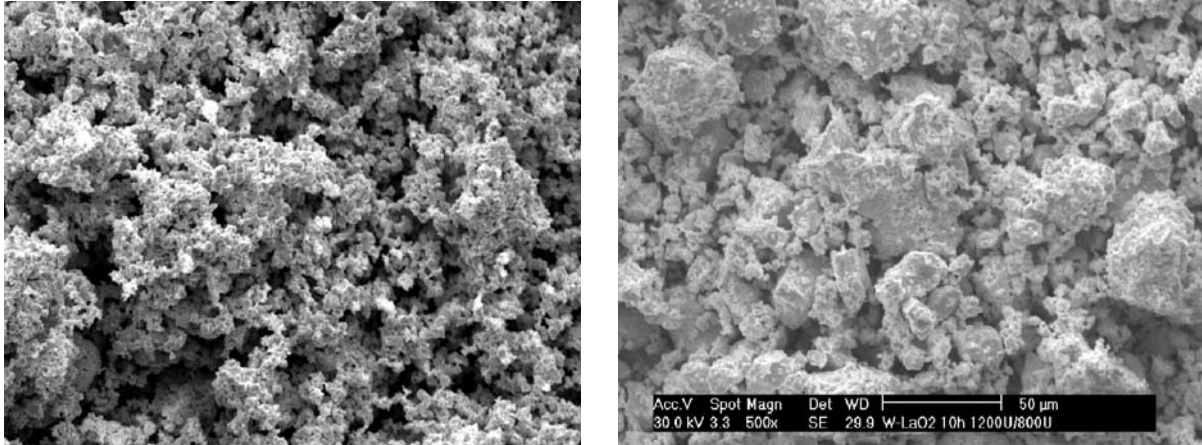


Fig. 1: SEM pictures of W-La₂O₃ powder before (left) and after (right) mechanical alloying for 10 h. Magnification of both pictures 500 x.

At the moment an interval milling is used to keep the heating of the device in acceptable limits. The inspection of the milling system after the first tests showed that abrasive problems inside the container are visible and remarkable. This observation is confirmed by the EDX analyses which showed a contamination of the processed W-powders by the steel components Cr and Fe. Fig. 2 shows the analyses for the elements W, La, Cr and Fe. Similar analyses were also performed at the surface of the milling balls which may indicate that no protective coating was formed during W processing on the balls as expected. More detailed analyses on powder characterization and on consolidation experiments inclusive thermal treatments are under way as planned earlier.

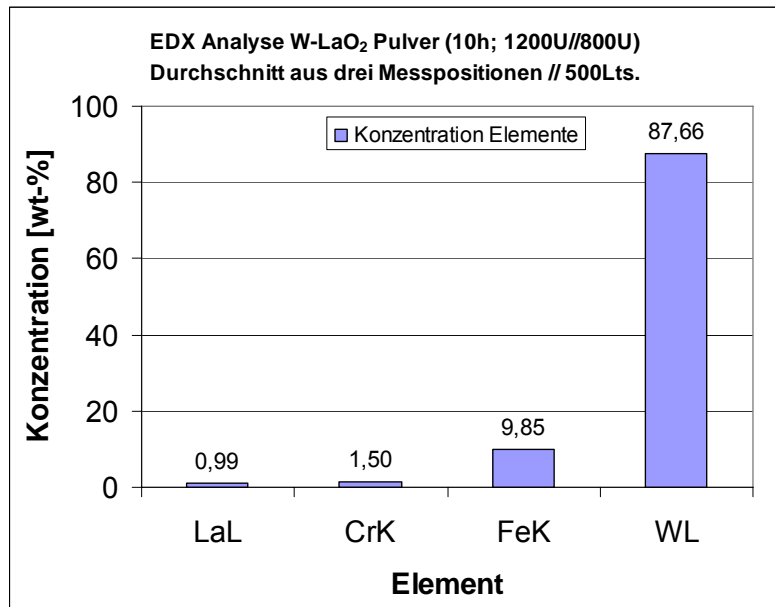


Fig. 2: EDX analyses of W-La₂O₃ ball milled for 10 h.

Staff:

W. Krauss
J. Konys
A. Möslang
M. Rieth
R. Lindau
S. Baumgärtner
C. Eiselt

Cooperation:

With Plansee AG, Reutte, Austria a cooperation agreement for a joint development of improved W-alloys was settled. Plansee delivered first improved W alloys by industrial standards end of 2006 for testing mechanical and physical properties.

Literature:

- [1] M. Rieth, B. Dafferner, Limitations of W and W-1%La₂O₃ for use as structural materials, J. Nucl. Mat. 342 (2005) 20 - 25
- [2] W. Krauss, N. Holstein, J. Konys, Development and fabrication aspects regarding tungsten components for a He-cooled divertor, Fus. Eng. Design 75-79 (2005) 775 - 778
- [3] W. Krauss, N. Holstein, J. Konys, I. Mazul, Investigation of the impact of fabrication methods on the micro-structure features of W-components of a He-cooled divertor. Fus. Eng. Design, 81 (2006) 259 - 264.

TW5-TTMA-002 D 6 Mechanical Testing of Irradiated W Tungsten Samples

High temperature alloys (such as tungsten) are assumed to be primary materials candidates for structural application in the divertor. However, these materials suffer from irradiation-induced embrittlement at “low” temperatures. The DBTT strongly depends on the irradiation dose and probably depends on the material processing. Tungsten furthermore is also considered as a plasma facing material, i.e. as a first wall coating for DEMO-related blankets and as armour material for gas-cooled divertors. Appropriate techniques for mechanical characterisation are to be investigated.

Specimens of WL10 (Tungsten and 1% of La_2O_3) are included in an irradiation experiment in the OSIRIS reactor. KLST-type bend bar specimens and mini tensile specimens (flat bar, T19-type) are to be irradiated at temperatures of 600 and 1000°C up to 5 dpa - equivalent in steel. The specimens are 3 x 4 x 27 mm³ Charpy-specimens [KLST] and 5 x 1 x 19 mm³ flat bar mini tensile specimens [T19] with a centre area of 1.5 x 1.0 mm², cf. Fig. 1.

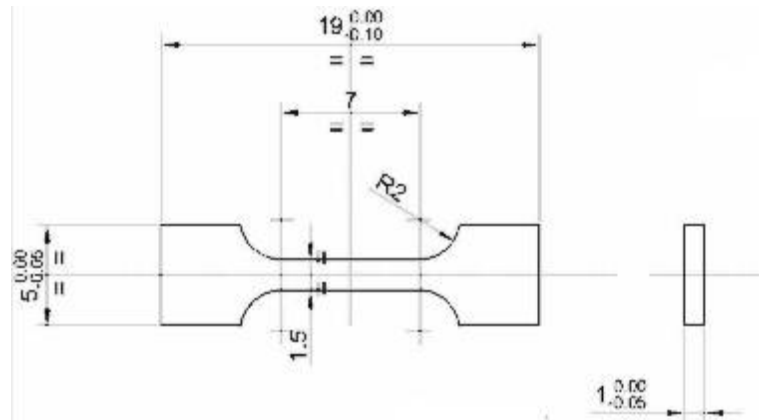


Fig. 1: Tensile specimen (T 19-type), drawing by CEA.

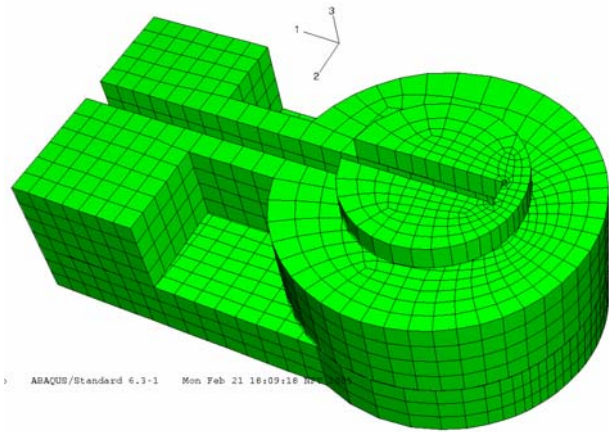
Tensile and KLST-specimens are foreseen for PIE in Karlsruhe after end of irradiation. 56 KLST- and a to be defined number of tensile specimens will be transported to the Fusion Materials Laboratory. They will be tested at different elevated temperatures to define the ductile-to-brittle-transition and the irradiation effect on it. Fractographic analysis of the tested specimens will be done by light microscopy and by SEM, including three-dimensional stereographic analysis.

As soon as specimens are available, unirradiated reference tests will be performed during the irradiation. The PIE will be finished 12 months after availability of specimens.

The Charpy specimens will be tested with an instrumented pendulum to define the transition region, the transition temperature, the upper- and lower shelf energy for every irradiation parameter. For every specimen, force-versus-deflection-curve is recorded, impact energy and dynamic yield stress are derived. The pendulum's energy and impact speed can be varied if necessary.

Tensile tests will be performed accompanying the impact tests as well as at irradiation temperature to give a full dataset of tensile results. A universal testing machine with vacuum-furnace (up to 1200°C) is used for force- and strain-controlled tensile tests. For the T19-type tensile specimens, a special mounting device adapted for the thin foil specimens (5 x 1 x 19 mm³) has been developed (Fig. 2). It serves for clamping of the specimen and for centring of the package in the testing machine's standard fixations.

The device serves as well for the transport of the fragile specimens by fixing an additional bracket. The design of the mounting device, based on Finite-Element-calculations, ensures that the maximum stresses take place in the reduced area of the specimen and not in or near the clamping jaw.



In addition, non-destructive testing by indentation can be done on both specimen types before or after they are tested in the pendulum or in the tensile machine. This method was presented in the annual report of last year, TW4-TTMA-002 Del. 3. It allows the determination of the complete tensile and cyclic material behaviour from multi-stage indentation tests. Meanwhile, this method successfully had been applied to different tungsten-alloys and it offers useful additional information about the material's characteristics at room temperature.

Fig. 2: Mounting device for specimen (lower part, specimen clamped in the round area).

Staff:

H.-C. Schneider
S. Lautensack

EFDA/05-1232 (TW5-TTMA-WCOMP) Development of Tungsten with Composite Structure for High Temperature Application

Introduction

Tungsten alloys are the primary materials candidates for high temperature divertor structural application. Gas cooled divertor concepts have been intensively studied during the past three years using tungsten as structural material. Any of the designs lead to very ambitious requirements with respect to the temperature window, i.e. approximately 700-800°C at the lower limit and more than 1200-1300°C at the higher end, as well as considerable high admissible stress limits, that originate from high pressure helium cooling and from high temperature gradients. In addition, excellent heat conduction properties are mandatory to keep temperature and secondary stresses within acceptable limits. The operation temperature window of tungsten alloys as structural material is determined by the ductile-brittle-transition temperature at the lower and the re-crystallization temperature at the upper end. To enhance the operation temperature window of tungsten different alloys have been proposed. Nevertheless, any of these materials are inherent brittle and show low fracture toughness at lower temperatures. A possibility to circumvent this problem may be the use of tungsten composites. In designing the new material, limitations as acceptable activations and good waste properties at the end of life are mandatory. In particular, vanadium is a candidate for reinforcing a tungsten matrix. Alternatively, materials with low stress carrying capacity at high temperatures might be reinforced with tungsten particles or fibers. In the present study, the potential of tungsten-vanadium composites for high temperature application with a wide range design window is studied numerically. In addition, a first trial heat of the proposed composite material is processed and tested for its fracture toughness at ambient temperature and its creep response in the high temperature range.

Effective material response

In a first approach, the effective thermo-mechanical properties of different types of tungsten-vanadium-composites are studied numerically using an energy based homogenization approach in conjunction with finite element analyses. Three different types of composites are investigated in this numerical screening analysis, including particle reinforced composites, short fiber composites with random fiber orientation as well as unidirectional infinite fiber composites. In all cases, different volume fractions of the two bonded phases are considered ranging from 10% up to 84% volume fraction of the tungsten phase. Both, tungsten and vanadium matrix composites are considered. In Figure 1, the meshes for the representative periodic volume elements and the plastic strain distribution for the tungsten particle, short fiber and UD fiber composites at approximately 30% tungsten volume fraction are presented after cooling down from the assumed stress-free temperature of 1200°C to ambient temperature. For reasons of a more distinct presentation, the two individual phases are shown in a separated manner.

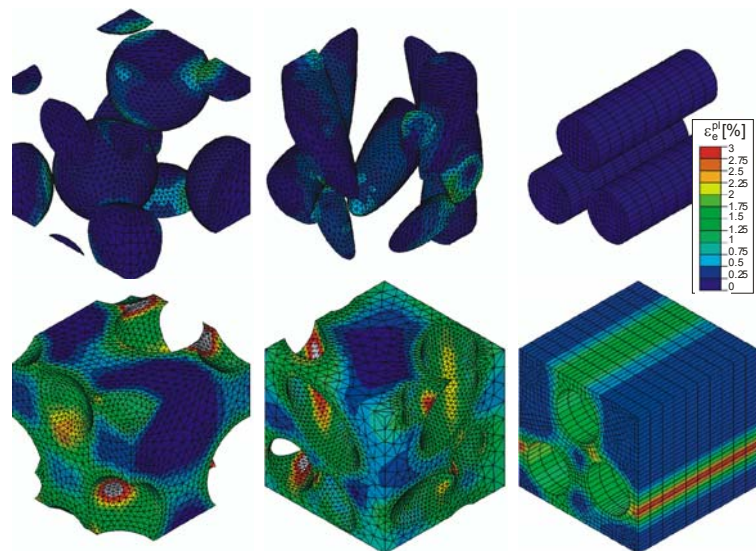


Fig. 1: Finite element meshes and plastic strain distribution after first cooling down from 1200°C.

Both, tungsten and vanadium matrix composites are considered. In Figure 1, the meshes for the representative periodic volume elements and the plastic strain distribution for the tungsten particle, short fiber and UD fiber composites at approximately 30% tungsten volume fraction are presented after cooling down from the assumed stress-free temperature of 1200°C to ambient temperature. For reasons of a more distinct presentation, the two individual phases are shown in a separated manner.

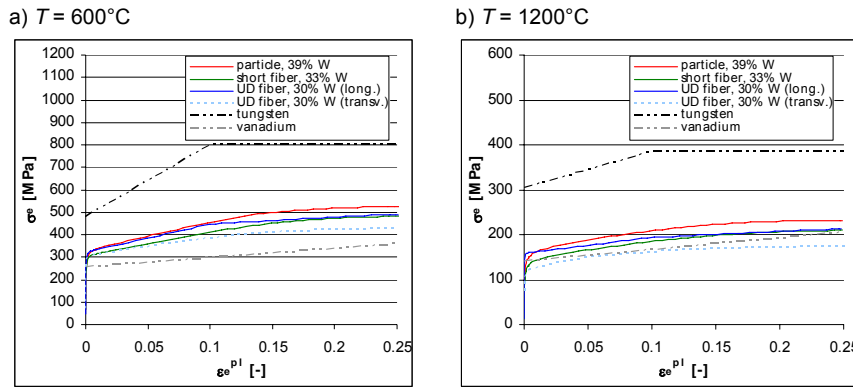


Fig. 2: Macroscopic yield curves for different composite types at 30% inclusion volume fraction.

The finite element models are used to determine the effective thermal conductivity, the effective coefficient of thermal expansion, the effective elastic constants and the effective yield curves of the different composite types at different tungsten and vanadium volume fractions. As an example, the macroscopic yield curves for the tungsten

particle, short fiber and UD fiber reinforced vanadium matrix composites are presented in Figure 2. It is observed that the macroscopic material response is mainly governed by the volume fraction of the different phases with only minor differences between the different composite types. Nevertheless, due to internal straining caused by the mismatch in the thermal expansion of the two bonded materials, the rules of mixture do not apply. Depending on the composite type, the thermal mismatch may result in the development of high local eigenstress levels, which may limit the effective ductility of the material. The best performance in this context is observed for the UD fiber reinforced composite type. Regarding the effective thermal conductivity, it is observed that a tungsten content of 50% or higher is required to meet the requirements of an excellent macroscopic thermal conductivity exceeding 80 W/(m K).

Creep behavior

In order to explore the upper end of the design window of the proposed composite materials, the effective creep response is analyzed. For this purpose, the finite element models for the different composite types are subjected to effective uniaxial stress states and the creep response is computed. In Figure 3, the resulting creep rates after 100 h are presented. The results are normalized with the creep rate of pure vanadium at the corresponding load level. For both load levels, nearly vanishing creep rates are observed for tungsten contents exceeding 50%, even for vanadium matrix composites. The distinct creep constraint for these composite types is caused by internal re-distribution of the local stresses towards hydrostatic stress states which respond purely elastic. Again, the best performance is obtained for the tungsten UD fiber reinforced composite, provided that the material is loaded longitudinally to the fiber direction.

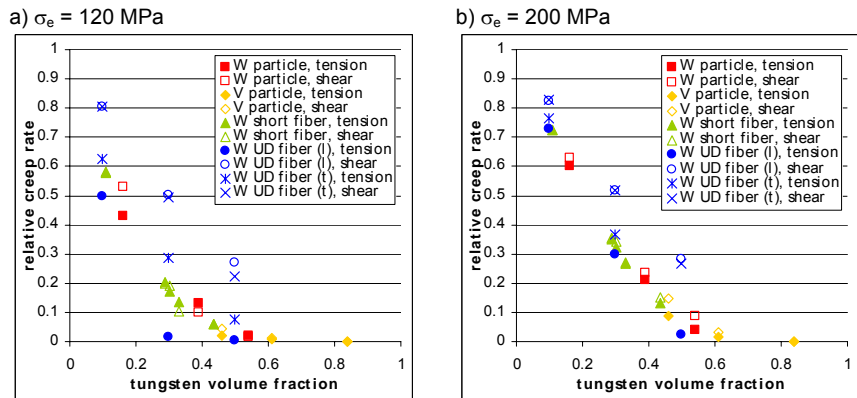


Fig. 3: Normalized effective creep rates after 100 h.

Fracture toughness enhancement

The possible fracture toughness enhancement is studied numerically using a cohesive zone model (see Figure 4), assuming that the ductile phase forms bridges across the crack surfaces in an otherwise brittle material. The effect of the crack bridges is modeled in a smeared manner in terms of the cohesive law $\sigma_{coh} = \sigma_{coh}(2 u_{coh})$ which is estimated from finite element analyses assuming complete failure of the brittle phase on one of the surfaces of the representative volume elements. The maximum theoretical fracture toughness enhancement for the different composite types is presented in Figure 5. In this context, it should be noticed that the results presented in this figure are based on the assumption of an ideal material with excellent conductivity of the ductile phase and perfect bond between the different phases. Therefore, and since the cohesive law relies on an assumed failure strain for the vanadium phase, the results given in Figure 5 are only of qualitative character for a comparison of the different composite options. No distinct differences are observed between the different composite types. An apparent increasing fracture toughness enhancement with decreasing volume fraction of the ductile phase is caused by increasing internal deformation constraints which result in the development of high hydrostatic stress levels and thus may lead to an early brittle failure of the ductile phase at lower load levels.

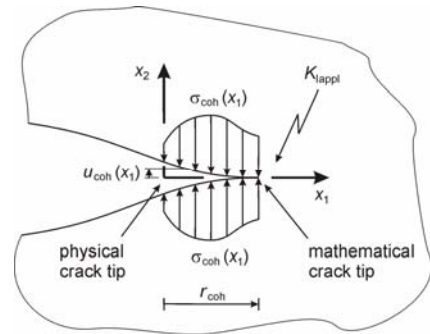


Fig. 4: Cohesive zone model.

Therefore, and since the cohesive law relies on an assumed failure strain for the vanadium phase, the results given in Figure 5 are only of qualitative character for a comparison of the different composite options. No distinct differences are observed between the different composite types. An apparent increasing fracture toughness enhancement with decreasing volume fraction of the ductile phase is caused by increasing internal deformation constraints which result in the development of high hydrostatic stress levels and thus may lead to an early brittle failure of the ductile phase at lower load levels.

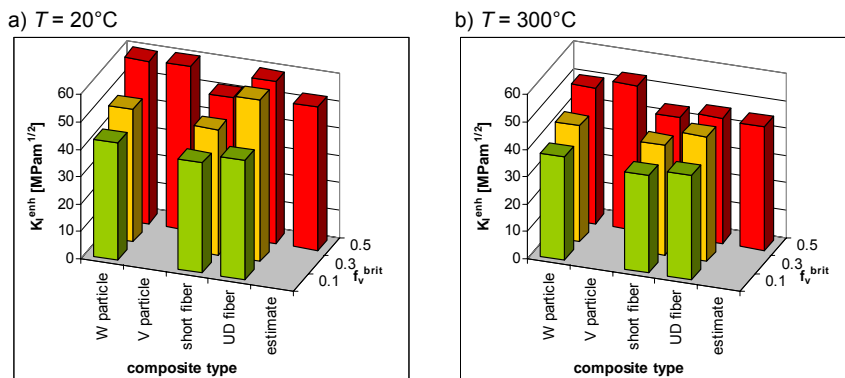


Fig. 5: Maximum theoretical fracture toughness enhancement at low temperatures.

Experimental investigation

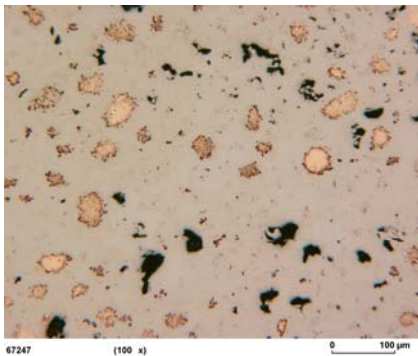


Fig. 6: Optical micrograph.

For a first experimental investigation of the potential of the proposed tungsten-vanadium composite material, a trial heat consisting of 50 vol. % of each of the materials has been produced. The material has been processed by a powder metallurgical route by mixing the powders and subsequent hot isostatic pressing. Figure 6 shows an optical micrograph of a section where dark spots are voids whereas the brown spots are tungsten particles. Distinct spatial variations of the void and particle volume fractions were observed. In an X-ray microanalysis, the matrix was found to consist of tungsten-vanadium mixed crystals rather than of pure vanadium due to diffusion processes during the sintering procedure. From the manufactured

plates, SE(B) 5x10 specimens were machined and tested for the fracture toughness at ambient temperature. A fracture toughness of approximately $K_{Jc} \approx 12 \text{ MPam}^{1/2}$ was obtained. Although this result is within the range reported in the literature for pure tungsten, it indicates

that a fracture toughness enhancement due to the presence of the ductile phase is possible since lower fracture toughness values would be expected for pure tungsten with porosities as observed for the present heat of the tungsten-vanadium composite. For an investigation of the upper end of the design window, creep experiments on tensile specimens were performed at 1000°C in a nitrogen atmosphere. Compared to the creep response of pure vanadium a distinct improvement of the properties was achieved.

Conclusions

The objective of the present project was an exploration of the potential of tungsten-vanadium-composites for high temperature application with a wide-range design window in future fusion power plants. In a theoretical-numerical screening analysis considering particle, short fiber and unidirectional infinite fiber reinforced composite types, a high potential was observed since compared to pure vanadium, the creep response at high temperatures could be improved significantly whereas the presence of the ductile vanadium phase results in a distinct enhancement of the fracture toughness below the ductile-to-brittle transition temperature of pure tungsten. An experimental investigation of the creep response at high temperatures and the fracture toughness at low temperatures on a first trial heat of the proposed composite material qualitatively confirms the theoretical findings. From the quantitative point of view, the produced trial heat proves to be still suboptimal due to its high porosity with inhomogeneous void distribution.

Staff:

M. Aberham
M. Burdack
P. Gumbsch
E. Haas
J. Hohe
M. Rieth
C. v. d. Wehd

Materials Development Nuclear Data

TTMN-001

Nuclear Data: EFF/EAF Data File Upgrade, Processing and Benchmark Analyses

The European Fusion File (EFF) and Activation File (EAF) projects aim at developing a qualified nuclear data base and validated computational tools for nuclear calculations of fusion reactors. The related Task TTMN-001 of the EFDA technology work programme is devoted to the evaluation, processing, application, and benchmarking of the required nuclear cross section and uncertainty data as well as to the development of computational tools for uncertainty calculations. The FZK contribution to Task TTMN-001 is on the evaluation of EFF-3 data, on the qualification of new and updated EFF data evaluations through computational benchmark analyses including sensitivity/uncertainty analyses and on the development of advanced computational schemes for sensitivity calculations based on the Monte Carlo technique.

TW6-TTMN-001 D 3

Test Application of MCSEN Sensitivity/Uncertainty Calculations for the TBM in ITER using the Track Length Estimator Method

The overall objective was to develop the computational tools that allow the calculation of sensitivities and uncertainties of neutron fluxes and nuclear responses in the ITER Test Blanket Module (TBM) on the basis of the Monte Carlo technique. To this end, algorithms were developed (TW3-TTMN-001, Deliverable 4) and implemented (TW4-TTMN-001, Deliverable 3) into the MCSEN code for the efficient calculation of sensitivities with the track length estimator (MCNP tally F4). First tests were performed through the application to the TBM mock-up neutronics experiment (TW5-TTMN-001, Deliverable 2). The objective of the 2006 task deliverable was to test the new feature of the MCSEN code for applications to the TBM in ITER and thereby demonstrate its suitability for sensitivities/uncertainty calculations of nuclear responses in the real 3D reactor configuration.

The standard 3D MCNP model of ITER (20 degree torus sector) with integrated TBM of the Helium-cooled Pebble Bed (HCPB) type was used for the MCSEN test application calculations. Sensitivity profiles and integrated sensitivities were calculated for the total Tritium production in the HCPB TBM using the track length estimator approach. Sensitivities were calculated with respect to the cross sections of Be-9, Li-6, -7, O-16, Fe-56 and H-1 employing the VITAMIN-J group structure with 175 energy groups. The associated uncertainties of the Tritium production due to nuclear data uncertainties were assessed by making use of available co-variance data from different sources (EFF-2, -3, FENDL-2, JENDL-3.3 and IRDF-90) [1].

Integrated sensitivities and cross section induced uncertainties of the total Tritium production with respect to the main reactions of several isotopes are displayed in Tab. 1. Note that the sensitivities and uncertainties shown include contributions of the specified isotopes from all materials, i. e. those in the TBM itself and the surroundings such as the TBM walls, the frame, and the ITER shield blanket modules. The major contribution to the sensitivities, however, comes from the materials contained in the TBM, in particular the Be neutron multiplier (positive contribution) and the breeder ceramics constituents Li-6 (negative contribution) and O-16 (negative contribution). The negative contribution of Li-6 is due to the fact that the neutron absorption by the ${}^6\text{Li}(n,\alpha)t$ reaction causes a reduced low energy neutron flux. For the total Tritium production in the TBM this (indirect) effect dominates the positive (direct) contribution to the sensitivity by the ${}^6\text{Li}(n,\alpha)$ Tritium production reaction. With the calculated sensitivity profiles and the available co-variance data, the cross-section induced uncertainty of the Tritium production has been assessed to be at a level of 2.8 %. This is the weighted sum of the uncertainties obtained for Be-9, Li-6, -7, and O-16, yet with missing contributions for Fe-56 and for H-1 (see Table 1).

Table 1: Integrated sensitivities and cross section induced uncertainties of the total Tritium production with respect to the main reactions of several isotopes.

Isotope	Sensitivity (%/%)	Main reactions	Cross-section induced uncertainty (1σ)
Be-9	0.332	(n,2n), elastic scattering	0.68%
Li-6	-0.701	elastic scattering	2.06%
Li-7	-0.073	elastic scattering	0.29%
O-16	-1.827	elastic scattering	1.71%
Fe-56	-0.038	inelastic scattering	--
H-1	-0.227	elastic scattering	--

The calculation of sensitivities based on the track length estimator approach with the MCSSEN code thus has been successfully applied for assessing nuclear data related sensitivities and uncertainties of nuclear responses of the TBM in ITER. Further upgrading of the MCSSEN code, however, is necessary to allow a more efficient calculation of the sensitivities for those applications where a specific nuclide is contained in many materials in different reactor components. With the current methodology it is necessary to run separate MCSSEN sensitivity calculations for all materials containing the nuclide considered and post-process the sensitivity results afterwards to obtain one single sensitivity profile for this nuclide.

sary to allow a more efficient calculation of the sensitivities for those applications where a specific nuclide is contained in many materials in different reactor components. With the current methodology it is necessary to run separate MCSSEN sensitivity calculations for all materials containing the nuclide considered and post-process the sensitivity results afterwards to obtain one single sensitivity profile for this nuclide.

TW6-TTMN-001 D 4

Evaluation of Mn-55 Cross-Sections up to 150 MeV for the EFF-3 Library

The overall objective is to develop during FP6 a general-purpose nuclear data library up to 150 MeV by adopting existing high-energy evaluations, up-grading and adapting them to the EFF/JEFF data and performing new evaluations as required. According to the priority list elaborated in 2003 to satisfy, in particular, the data needs of the IFMIF project, the objective of the 2006 work programme was to provide a complete 150 MeV data evaluation for Mn-55 [2].

In the evaluation process use was made of the codes ECIS96 for optical model calculations and GNASH for nuclear reaction cross section calculations. Recent high energy experimental data were taken into account for evaluating the total cross section. Global optical potentials for neutrons, protons, deuterons and α -particles were used. Global optical model potentials for tritons and He-3 were newly elaborated. To improve the neutron emission spectra, collective excitations were included in the GNASH calculations. Double-differential cross sections of the emitted particles were calculated on the basis of the Kalbach systematics. A complete ENDF data file was finally prepared for ^{55}Mn covering the full energy range up to 150 MeV.

Fig. 1 shows the flowchart of the evaluation process. Total, reaction, elastic and inelastic scattering cross sections were calculated with ECIS96 applying a spherical optical model potential. Nuclear model calculations were performed with the GNASH code utilizing the Hauser-Feshbach theory for multiple particle equilibrium and the exciton model for pre-equilibrium particle emissions up to 150 MeV.

Measurements of the total cross-sections performed at Los Alamos for Manganese were used to validate the high energy neutron optical model potential. The global potential of Koning & Delaroche appeared to be the most accurate one over the entire energy range from 1 to 150 MeV. It was also used for the proton exit channel. For the deuterons and α -particles the global potentials by Bojowald and Avrigeanu & Hodgson, respectively, were applied. For tritons and He-3, new optical model potentials were invented. Figs. 2 a,b give a comparison of evaluated and measured total cross-sections and elastic scattering angular distributions for ^{55}Mn . Note the perfect agreement of the new evaluations (red curves) with the measured cross-sections over the entire energy range.

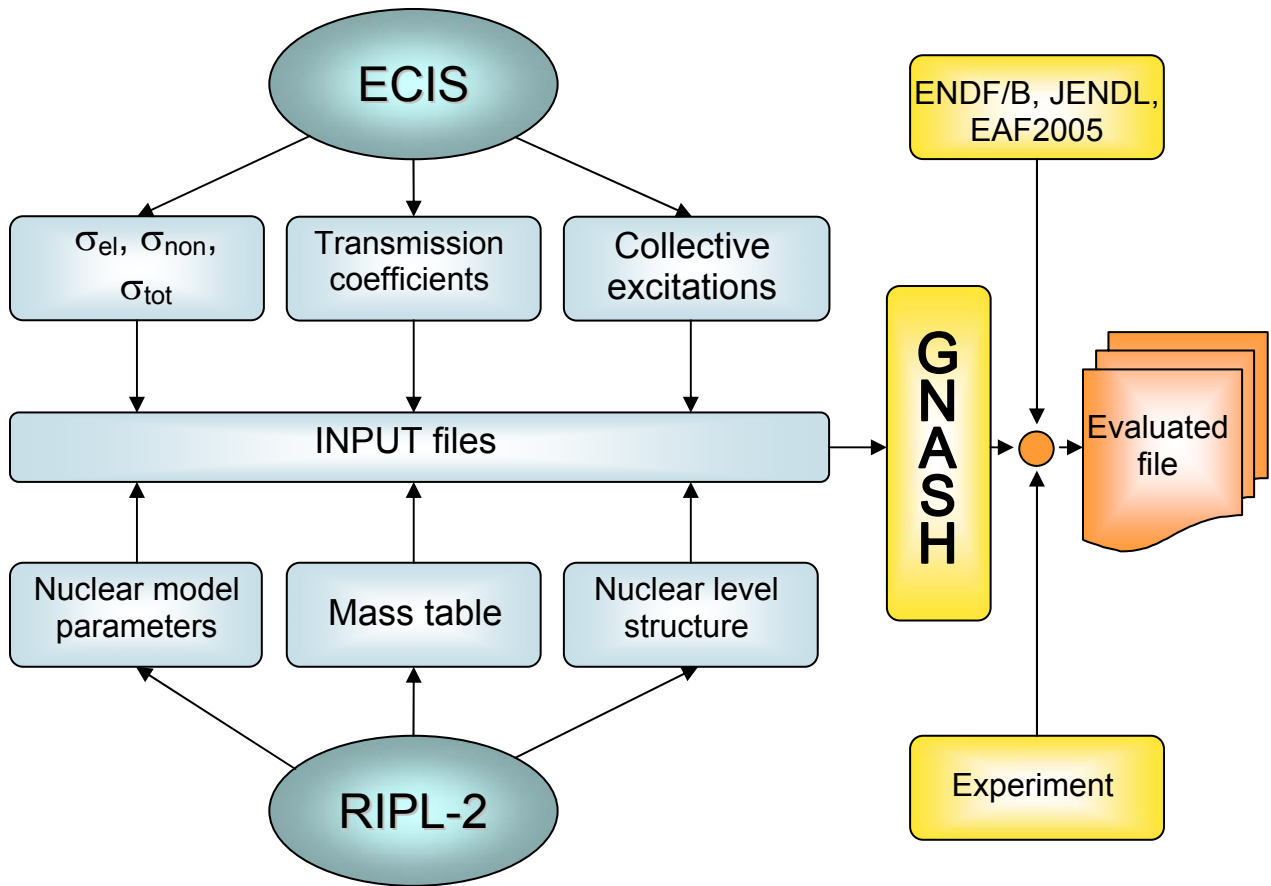


Fig. 1: Flowchart for the evaluation of neutron cross section data of the ^{55}Mn isotope up to 150 MeV neutron energy.

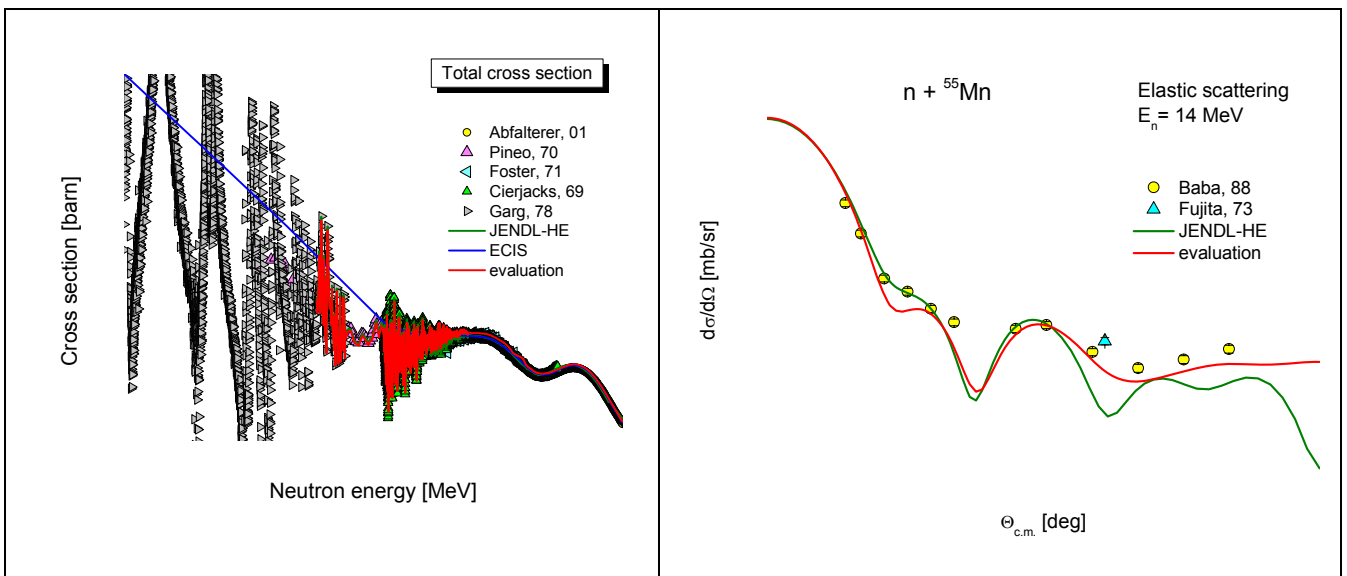


Fig. 2a: Total cross-section for $n + ^{55}\text{Mn}$.

Fig. 2b: Elastic scattering angular distribution for 15 MeV $n + ^{55}\text{Mn}$.

Examples of neutron emission spectra calculated with GNASH are shown in Fig. 3. The good agreement of the new evaluation with the measured emission spectra at higher secondary energies is due to the fact that collective excitations and direct reactions have been taken into account.

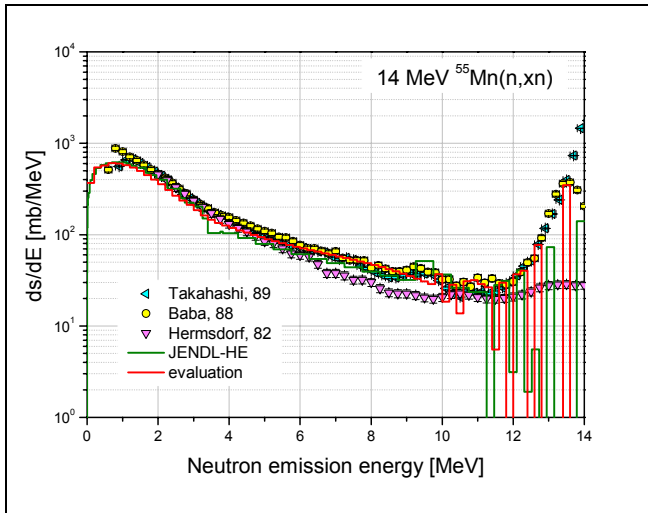


Fig. 3a: Neutron emission spectrum for 14 MeV neutron incidence energy.

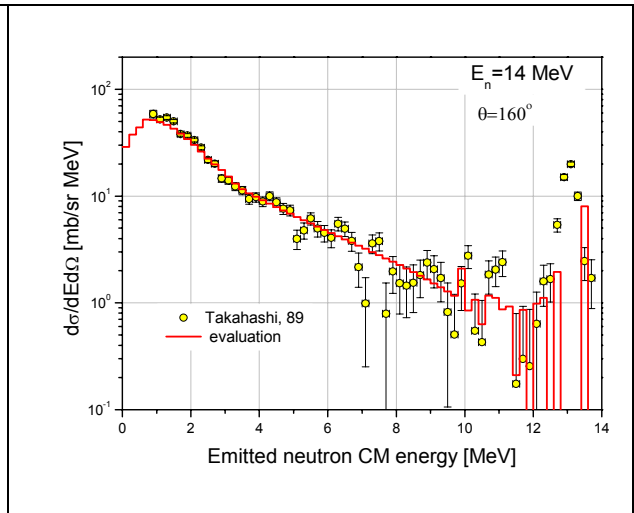


Fig. 3b: Double differential neutron emission spectrum for 14 MeV neutron incidence energy.

The final ENDF data file includes entire new evaluations in the MF=3 file section for the total and elastic scattering cross sections (MT=1,2), the (n,2n), (n,np), (n,nα), (n,p), (n,d), (n,t), (n,He3), (n,α) activation cross sections (MT=16,22,28,103,104,105,106,107) and the inelastic scattering cross sections (MT=51-91). Differential neutron emission data were newly evaluated for the reactions MT=2, 51-61 in MF=4 (angle distributions). Neutron emission spectra as well as angular distributions were evaluated with GNASH for MT=16, 22, 28, 91 and stored in the MF=6 file section. Above 20 MeV, the files contain complete new evaluations. The high energy data are stored in the file sections MF=3 (MT=2, MT=5), MF=4 (MT=2) and MF=6 (MT=5). The MT=5 cross-section accounts for all reactions with the emission of secondary particles. MF=6 contains particle emission spectra in the centre-of-mass frame and photon and recoil spectra in the laboratory system.

TW6-TTMN-001 D 5 Benchmark Analyses for Revised/Updated EFF-3 Data Evaluations based on Monte Carlo Calculations with MCNP

The objective of this sub-task is to check and validate the new EFF-3 data evaluations for a reliable use in design calculations and provide feed-back to the evaluators.

The focus of the recent benchmark analyses was on the cross-section data of Pb [3], V [4] and Ta [5,6]. The presently available evaluated cross section data files for Vanadium and Lead are listed in Tables 2 and 3.

Table 2: Evaluated cross section data files for Vanadium.

File	JEFF-3.1 (V-51)	ENDF/B-VII, beta 3 (V-00)	JENDL-3.3 (V-00)	FENDL-2.1 (V-00)
Release	2005	October 2006	2002	2004
Origin & Comments	ENDF/B-VI, + calculated n- & γ-DDX + angul. distr. discr. lev. from JENDL-3	ENDF/B-VI, with revised (n,np), (n,t), (n,n'cont)	JENDL-3.2, and FF with minor modification	JENDL-3.3

Table 3: Evaluated cross section data files for Lead.

File	JEFF-3.1	ENDF-B6.8	FENDL-2.1
Release	2004	1996	2004
Upper Energy	E < 200 MeV	E < 150 MeV	E < 150 MeV
Origin & Comments	Pb-204 Pb-206 Pb-207 Pb-208	- Pb-206 (mod 2) Pb-207 (mod 3) Pb-208 (mod 3)	- Pb-206 = ENDF-B6.8 mod 2 Pb-207 = ENDF-B6.8 mod 3 Pb-208 = ENDF-B6.8 mod 3

Benchmarking of the data evaluations for V and Pb has been performed against available 14 MeV neutron transmission experiments conducted at different laboratories (FNS, IPPE, JAERI, KIAE, OKTAVIAN and TUD) on pure metallic shells, cubes and slabs.

The JEFF-3.1 Vanadium evaluation was shown to better reproduce the measurements of the neutron flux spectra (Figs. 4a and b) than other libraries do. Nevertheless the photon production is overestimated by 20-80%, whereas ENDF/B-VI or B-VII and JENDL-3.3 only slightly underestimate (Figs. 5a and b). The beta 3 version of the ENDF/B-VII data library shows an unphysical jump in the neutron emission spectrum at 14 MeV incidence energy.

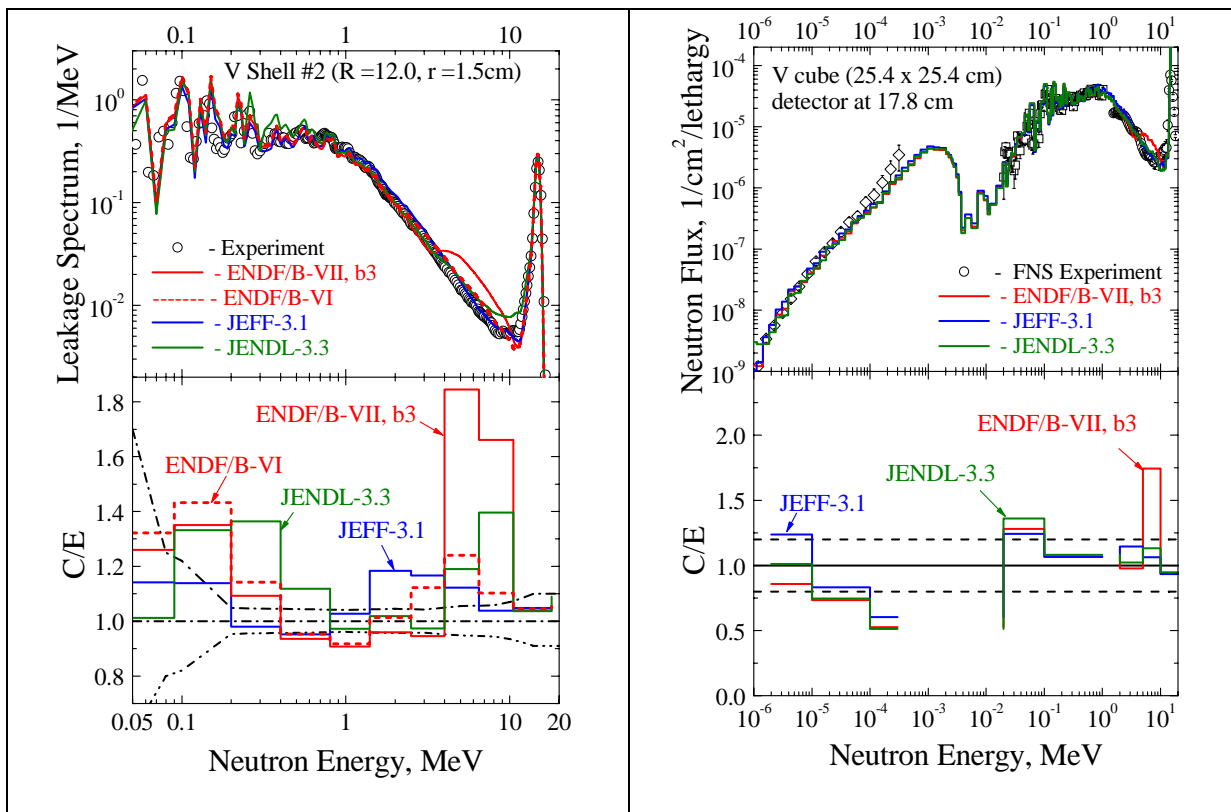


Fig. 4a: V shell with 10.5 cm radial thickness.

Fig.4b: V cube, detector at 17.8 cm from the front surface.

Fig. 4: Comparison of measured and calculated neutron leakage spectra for two V assemblies irradiated with 14 MeV neutrons.

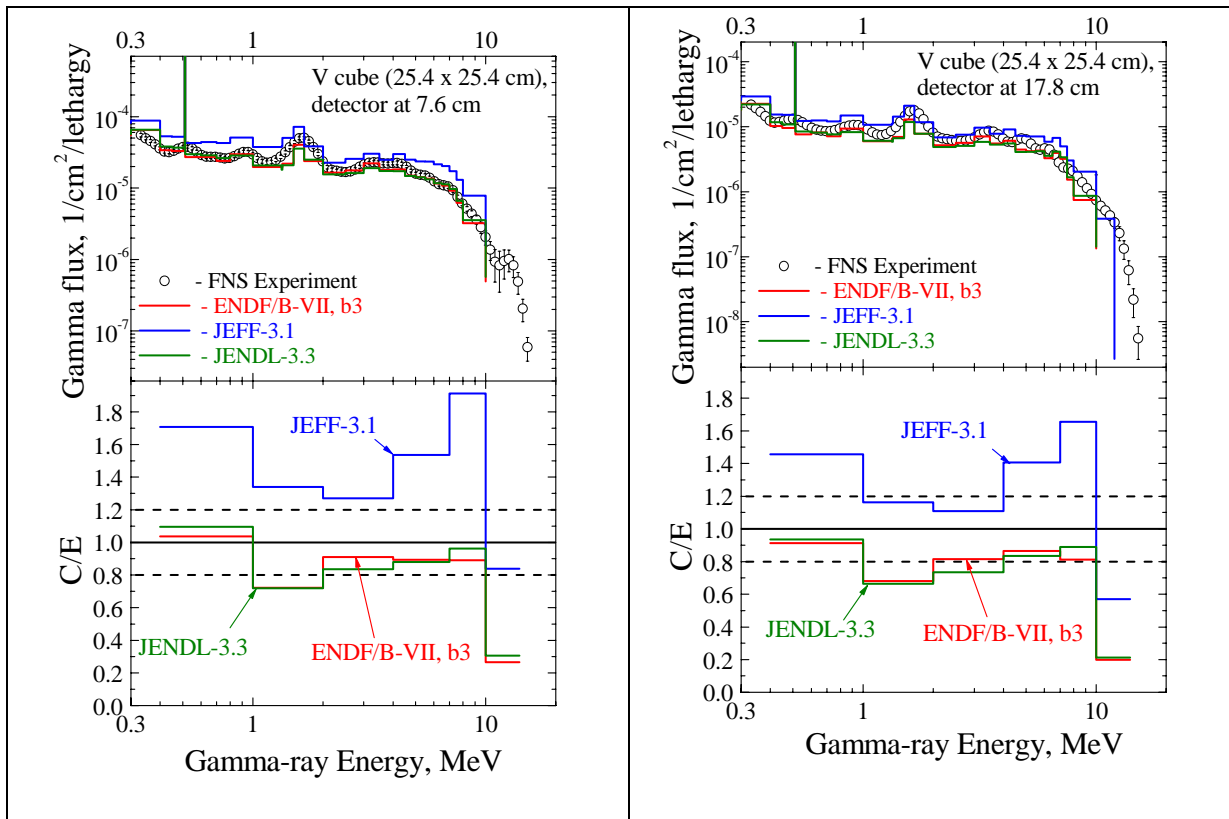


Fig. 5a: V cube, detector at 7.6 cm from the front surface.

Fig. 5b: V cube, detector at 17.8 cm from the front surface.

Fig. 5: Comparison of measured and calculated photon leakage spectra for a V cube irradiated with 14 MeV neutrons.

The new JEFF-3.1 isotopic Lead evaluation was benchmarked against fusion relevant integral experiments and compared to FENDL-2.1 which is identical to ENDF/B-VI.8 for Lead. The neutron leakage spectra from the shells with different radial thicknesses were reproduced within 20% by both independent files. The angular neutron leakage fluxes measured from the slabs at a set of angles are underestimated by typically 10-20%. The measured neutron multiplication was found to be underestimated by up to 15%. A significant underestimation was obtained for the photon leakage spectra above 5 MeV.

Benchmark analyses on Ta have been conducted for the new Ta-181 data evaluation provided by FZK in the frame of the 2005 work programme. Only two other independent Ta evaluations up to 20 MeV do exist which are included in the American ENDF/B-VI and the Japanese JENDL-3.3 data library, respectively. With regard to experimental data, there are available 14 MeV neutron transmission experiments of the Lawrence Livermore National Laboratory (LLNL) on two Ta spherical shells with shell thicknesses of 3.4 and 10.2 cm, and an integral experiment performed at the Lewis Research Centre (LRC) in 1974 on a 9 cm thick Ta shell with a central Am-Be source. Furthermore, neutron emission spectra measured for 14.1 and 7.94 MeV neutron incidence energies were available for comparison with the evaluated data. Satisfactory agreement was found for the new Ta evaluation of FZK while the other available evaluations (ENDF/B-VI and JENDL-3.3) show severe discrepancies with the measured neutron emission spectra.

With the new Ta evaluation of FZK also good agreement was obtained for the neutron leakage spectra measured in the LLNL and the LRC neutron transmission experiments. In particular, significant improvement was found for the LLNL experiments, where the ENDF/B-VI and JENDL-3.3 data fail to reproduce the shape of measured neutron leakage spectra. In case of the new Ta evaluation, the calculated neutron spectra scatter within 10-20% around

the measured data. Thus the new Ta data evaluation constitutes a clear improvement over the deficient ENDF/B-VI and JENDL-3.3 data evaluations for Ta.

Staff:

U. Fischer
D. Leichtle
R. Perel (Hebrew University of Jerusalem)
P. Pereslavtsev
S. P. Simakov
I. Schmuck

Literature:

- [1] R. L. Perel, Test application of MCSEN for sensitivity/uncertainty calculations of the TBM in ITER using the track length estimator method, EFF-DOC-991, NEA Data Bank, Paris, November 2006.
- [2] P. Pereslavtsev, U. Fischer, Evaluation of Mn-55 cross-sections for the EFF data library up to 150 MeV, EFF-DOC-993, NEA Data Bank, Paris, November 2006.
- [3] S.P. Simakov, U. Fischer, Benchmark analyses of Pb JEFF-3.1T data for fusion applications, EFF-DOC-929, NEA Data Bank, Paris, May 2005
- [4] S.P. Simakov, U. Fischer, Benchmarking of Vanadium evaluated data for fusion neutron transport calculations, EFF-DOC-999, NEA Data Bank, Paris, Nov 2006
- [5] S. P. Simakov, U. Fischer, First benchmark analyses of Ta evaluated data for fusion neutron transport calculations, EFF-DOC-952, NEA Data Bank, Paris, November 2005.
- [6] S. Simakov, U. Fischer, I. Schmuck, Benchmark analyses of Ta evaluated data for fusion neutron transport calculations, EFF-DOC-973, NEA Data Bank, Paris, May 2006

TTMN-002

Nuclear Data: Benchmark Experiments to Validate EFF/EAF Data

The objective of Task TTMN-002 is to provide the experimental data base required for the validation of the nuclear data libraries EFF (European Fusion File) and EAF (European Activation File) developed in the frame of Task TTMN-001 of the EU Fusion Technology Programme. According to the FP6 programme orientation towards ITER (TBM) and IFMIF, the focus is on the experimental validation of TBM design calculations by means of a neutronics mock-up experiment and cross-section validation experiments relevant for IFMIF.

TW6-TTMN-002 D 2

Design of TBM-HCLL Neutronics Experiment: Design of Measurement Techniques for Tritium Production Rates (TPR) and of Neutron and γ -ray Flux Spectra; Assessment of Uncertainties (TU Dresden)

Objectives

With the objective to validate the nuclear design parameters of the EU Test Blanket Modules (TBM), a neutronics experiment shall be performed in 2007 for the Helium Cooled Lithium Lead (HCLL) TBM, as carried out in 2005 for the Helium Cooled Pebble Bed (HCPB) TBM. A sketch of the HCLL mock-up is presented in Fig. 1 [1].

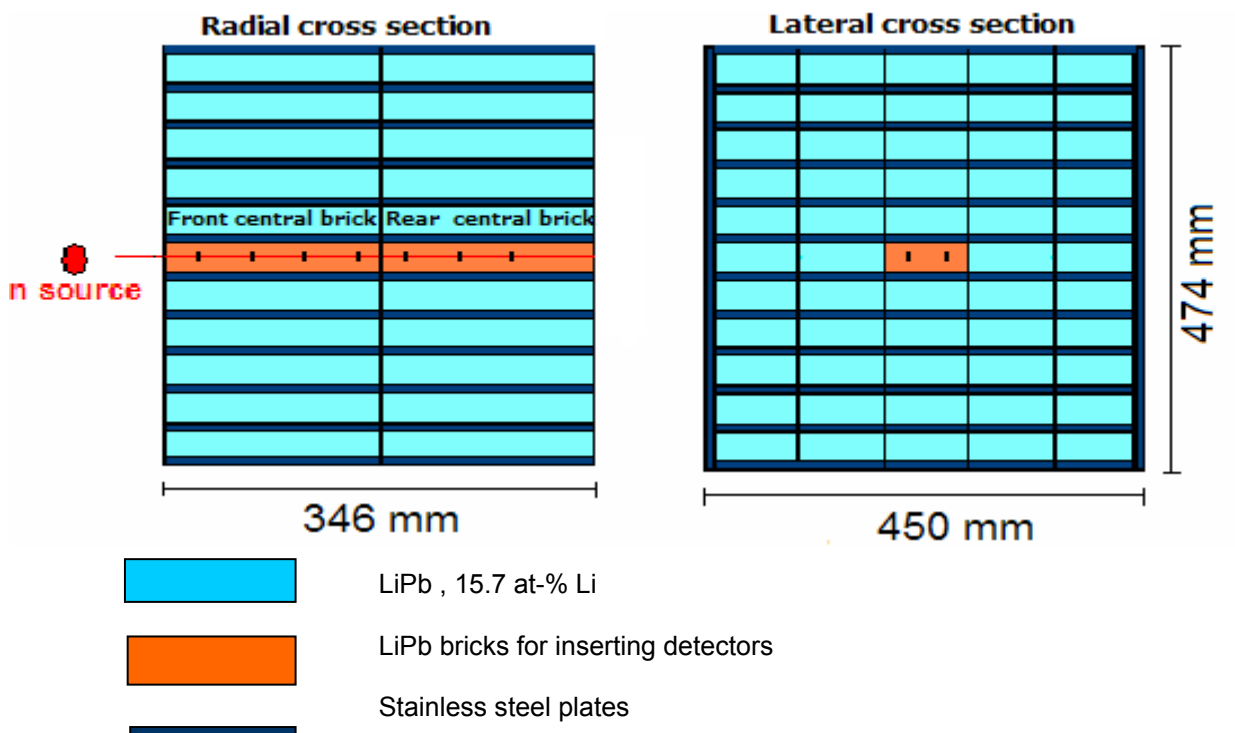


Fig. 1: Vertical sections through the mock-up.

Calculations showed that flux spectra of the fast neutrons and of γ -rays can be measured by pulse-height spectroscopy with an NE213-detector, and the flux distribution of the slow neutrons by time-of-arrival spectroscopy with a ^3He -detector, as in the case of the HCPB mock-up [2]. For inserting these detectors the "rear central brick" (left hand in Fig. 1) must be removed.

Also the Li_2CO_3 -method used for measuring the tritium production rates (TPR) in the HCPB mock-up [3] is available. However, a detailed calculation revealed that the density of the trit-

ium production is significantly lower in the HCLL mock-up [4]. Table 1 gives the TPR at four positions in the “central bricks” (Fig. 1) for one d-t source neutron and for the number of source neutrons produced during the HCPB experiment and planned for the HCLL experiment. With the Li_2CO_3 -method the β -activity of the tritium is measured. The specific activities corresponding to the TPR are given in the last line of Table 1. For comparison, the specific activities measured in the HCPB mock-up were in the range of 60-180 Bq/g [5,6]. Benchmarking the Li_2CO_3 -method [3], it was concluded, that the specific activity should be at least 10 Bq/g. That shows the necessity for applying additional, more sensitive methods for the TPR measurements in the HCLL mock-up.

Table 1: Number of tritium atoms (N_T) produced in Li_2CO_3 probes ($\rho = 1.1234 \text{ g/cm}^3$) at four positions on the central line of the HCLL mock-up and the corresponding tritium activities per unit mass.

Distance from the front plate [cm]	5	13	21	29
N_T / m for 1 source neutron [T-atoms/g]	$3.2 \cdot 10^{-6}$	$1.0 \cdot 10^{-6}$	$4.7 \cdot 10^{-7}$	$2.7 \cdot 10^{-7}$
N_T / m for $5.83 \cdot 10^{15}$ source neutrons [T-atoms/g]	$1.9 \cdot 10^{10}$	$6.1 \cdot 10^9$	$2.7 \cdot 10^9$	$1.6 \cdot 10^9$
A_T / m for $5.83 \cdot 10^{15}$ source neutrons [Bq/g]	33	11	4.9	2.8

In the present work, detectors are tested which could be used to measure the number of tritium producing reactions, instead of the tritium activity. Using LiF thermo-luminescence dosimeters (TLD), the dose induced by neutrons is dominated by the energy deposition of the tritons and α -particles from the reactions on Li. The contribution of other neutron reactions on LiF and those of the photons to the total dose must be eliminated. For this purpose TLDs of different ^6Li -content, BeO dose meters and solid state track detectors (CR-39) were combined in two irradiation experiments with an assembly of similar performance as the HCLL mock-up.

Experiments

The Monte Carlo model of the assembly is shown in Fig. 2. The front block (within a polyethylene shield) consists of Pb bricks and of two layers with the breeder material LiAl. The rear block is made of LiAl. The total number of Pb and Li atoms is the same as in the HCLL mock-up. The distance of the neutron source to the assembly was chosen in such a way that the expected TPR per one source neutron (Table 2) is in the same order of magnitude as the lowest values in the HCLL mock-up (Table 1).

Two experiments with different detectors arranged within the assembly along the x-axis were carried out:

- A. TLD packages were placed at intervals of 4 cm. Each package consisted of 3 TLD-100 (7.5 at-% ^6Li and 92.5 at-% ^7Li , natural isotopic abundance of Li) and of 2 TLD-700 (0.07 at-% ^6Li and 99.93 at-% ^7Li , depleted in ^6Li). In order to demonstrate the high sensitivity for TPR measurements, only $5.9 \cdot 10^{14}$ source neutrons were produced during the irradiation, i. e. one order of magnitude less, than it is planned for the HCLL mock-up experiment ($5.8 \cdot 10^{15}$ source neutrons).
- B. The detector packages at intervals of 4 cm consisted of TLDs and BeO detectors placed on CR-39. The number of source neutrons produced was $1.57 \cdot 10^{13}$ for some of the probes and $8.2 \cdot 10^{13}$ for the other.

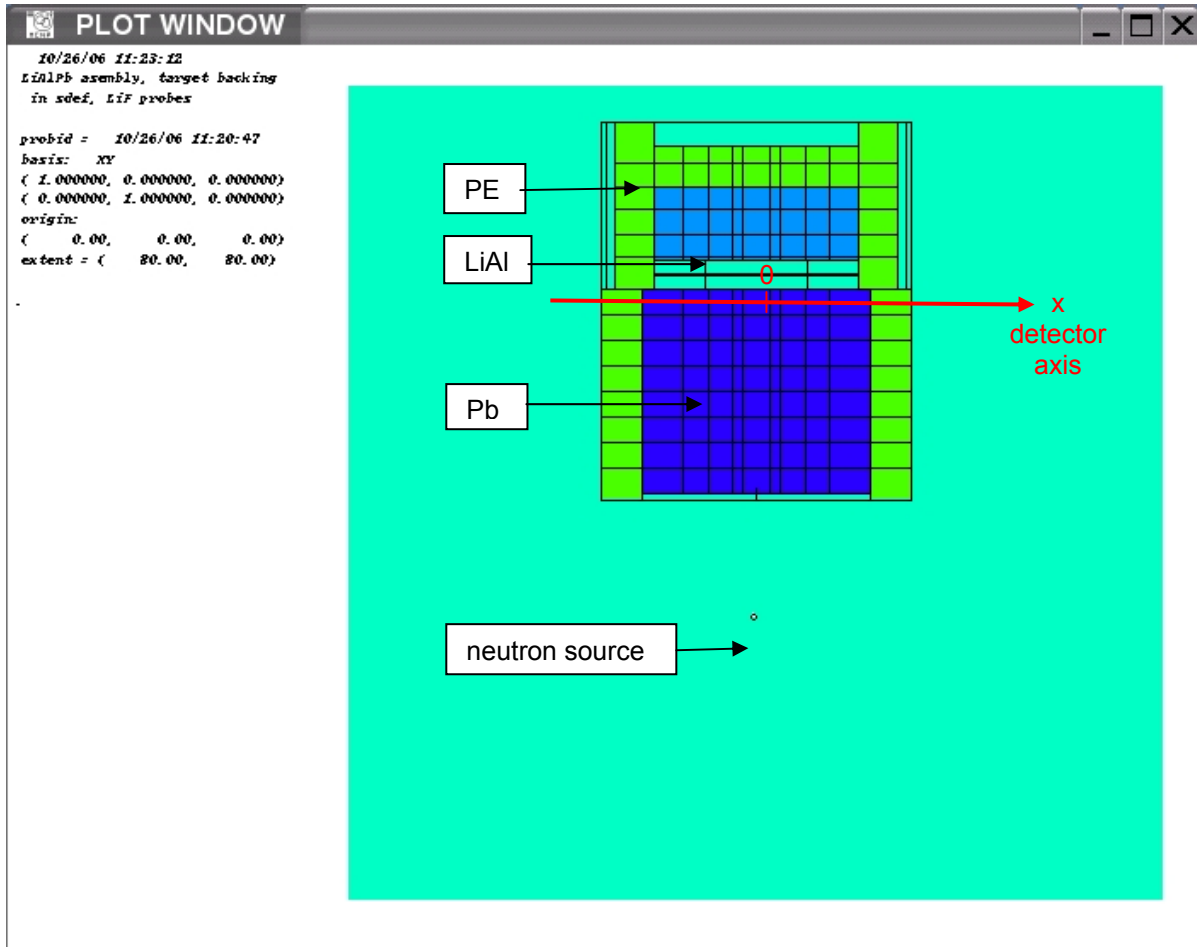


Fig. 2: Horizontal section through the assembly.

Table 2: Calculated TPR in TLD-100 at different positions on the x-axis in the assembly (Fig. 2) as number of tritium atoms (N_T) produced per one d-t neutron and for the number of source neutrons produced during experiment A.

TLD position x [cm]	0	4	8	12	16
N_T / m for 1 source neutron [T-atoms/g]	$3.1 \cdot 10^{-7}$	$3.2 \cdot 10^{-7}$	$3.7 \cdot 10^{-7}$	$4.7 \cdot 10^{-7}$	$8.2 \cdot 10^{-7}$
N_T / m for $5.91 \cdot 10^{14}$ source neutrons [T-atoms/g]	$1.8 \cdot 10^8$	$1.9 \cdot 10^8$	$2.2 \cdot 10^8$	$2.8 \cdot 10^8$	$4.9 \cdot 10^8$

Results

Fig. 3 shows, for the experiment A, the TPR in the TLD-100 calculated with the Monte Carlo code MCNPX (Table 2). They are compared with the differences of the TLD signals from the TLD-100 and TLD-700 probes. The TLD-700 signals are widely independent of the x-positions and are attributed to the photon dose of the TLD. The TPR in the TLD-700 is only about 3% of that in the TLD-100, as calculations show. The experimental TLD signals were multiplied with a factor of $1.75 \cdot 10^7$, which results in a minimum χ^2 to the calculated TPR. For the determination of the absolute response of the TLD-100, the calibration in a well-defined

neutron field shall be combined with the results of experiment B. The number of tracks of tritons and α -particles in the CR-39 foil gives an independent measure of the TPR in the TLD, and the photon dose is measured with the optical stimulated luminescence of the BeO probes.

The evaluation and analysis of the data from experiment B is in progress.

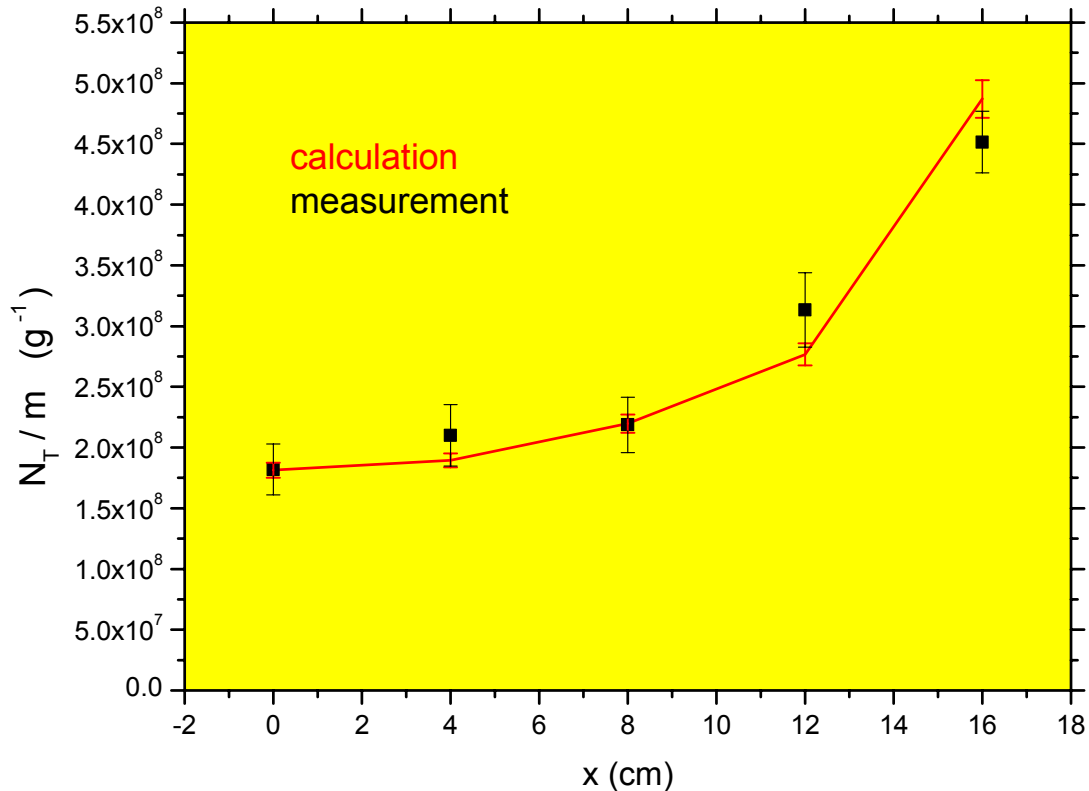


Fig. 3: Calculated specific tritium production at several positions on the x-axis of the assembly for experiment A and measured thermo-luminescence multiplied by $1.75 \cdot 10^7$.

Conclusions

It was demonstrated that the TPR can be measured by TLD-probes with a sensitivity that is at least one order of magnitude better than that needed for the HCLL mock-up experiment. The uncertainty bars of the measured values in Fig.3, which are dominated by systematic uncertainties, give an impression of the lower limit of the sensitivity for the TPR measurements. Experiment B will be used for checking the separation of different dose components and for the calibration.

Staff:

H. Freiesleben
J. Henniger
A. Klix
K. Seidel
M. Sommer

Literature:

- [1] P. Batistoni, private communication.
- [2] K. Seidel, et al. Symp. on Fusion Technology, Warsaw (Poland), Sept. 2006.
- [3] P. Batistoni, et al., Fusion Engineering and Design 75-79 (2005) 911.
- [4] U. Fischer and A. Serikov, Report FZKA 7210, p. 278, FZ Karlsruhe, April 2006.
- [5] K. Seidel, et al., Report TUD-IKTP/01-06, TU Dresden, Febr. 2006.
- [6] P. Batistoni, et al., Symp. on Fusion Technology, Warsaw (Poland), Sept. 2006.

TW6-TTMN-002 D 3

Design of TBM - HCLL Neutronics Experiment: Monte Carlo (MC) Based Pre-analysis to Design and Optimise the Experimental Set-up for the Measurements of the Flux Spectra and the Tritium Production

The neutronics mock-up experiment on the HCLL (Helium-Cooled Lithium Lead) blanket concept aims at validating the capability of the neutronics codes and nuclear data to predict the nuclear performance of the HCLL TBM in ITER in terms of important nuclear responses such as the neutron flux spectra, the tritium production rate and the nuclear heating. Thus, it is necessary to demonstrate that the essential nuclear features of the HCLL TBM can be replicated by the experiment. This can be achieved by analysing the TBM in ITER and using the results as reference for designing and optimising the TBM mock-up configuration.

The objective of TW6-TTMN-002, Deliverable 3, was to provide the data, by means of pre-calculations, required for preparing the design of the HCLL TBM mock-up experiment. To this end, MCNP Monte Carlo calculations were performed for the flux spectra and the tritium production in the HCLL TBM mock-up assembly that will be irradiated at the Frascati Neutron Generator (FNG). The results were compared to those obtained for the HCLL TBM in ITER in the frame of the previous task TW5-TTMN-002, Deliverable 9a.

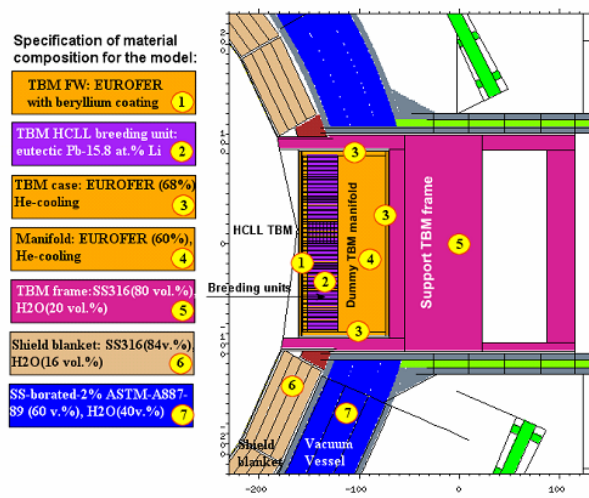


Fig. 1 a: HCLL TBM in ITER

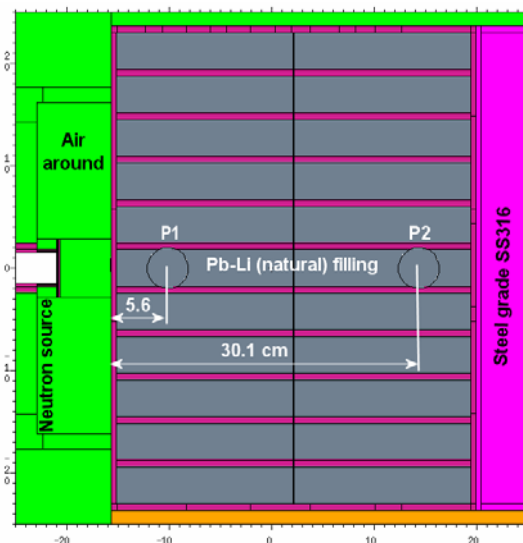


Fig. 1b: HCLL TBM mock-up assembly

Fig. 1a, b: Vertical cuts of the MCNP models employed for the analyses of the TBM assemblies in ITER and the FNG experiment.

Suitable MCNP models were developed for the HCLL TBM mock-up assembly at FNG and the HCLL TBM in ITER, see Figs. 1 a and b.

Calculations were performed with the MCNP5 Monte Carlo code and nuclear cross-section data from the Fusion Evaluated Nuclear Data Library FENDL-2. The neutron flux spectra and tritium production distributions in the TBM were calculated for ^6Li enrichment levels of 90 at%, which is representative for the HCLL fusion power reactor blanket, and 7.5 at%, which will be used in the mock-up experiment. Analogous calculations were performed for the HCLL mock-up experiment employing only naturally enriched Lithium. Detailed comparisons were made for positions P1 and P2 in the TBM mock-up located at 5.5 and 30.1 cm, respectively, from the front surface.

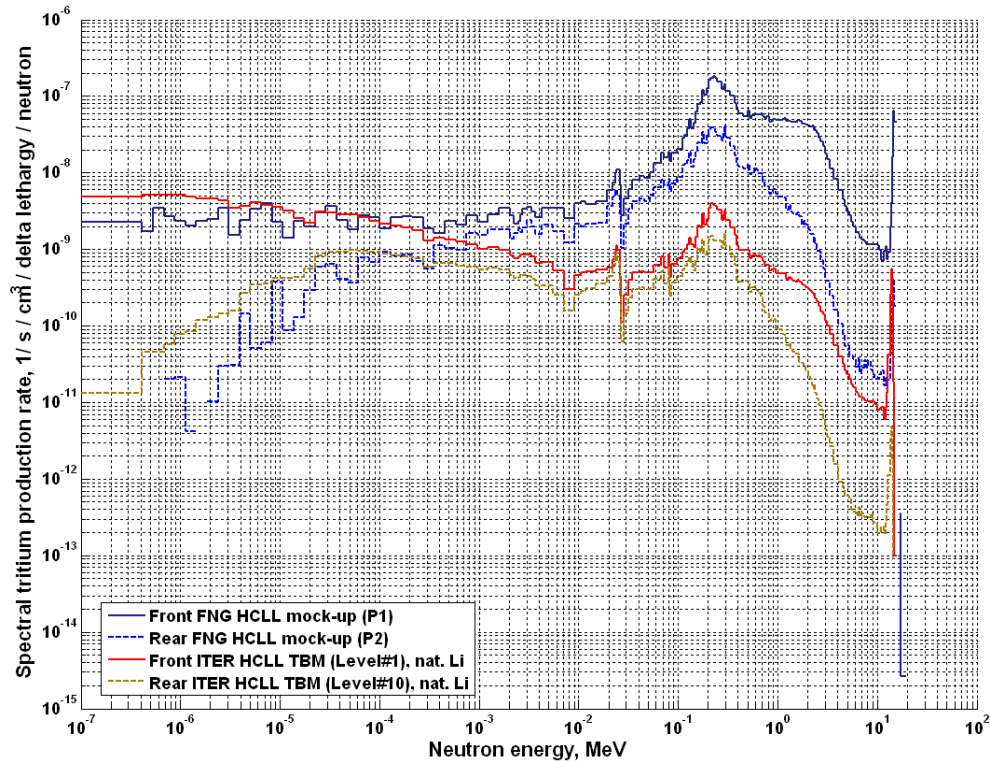


Fig. 2: Neutron spectra calculated for positions P1 and P2 in the HCLL TBM mock-up and the corresponding locations in the ITER HCLL TBM (normalized to one source neutron).

The neutron spectra in the HCLL TBM mock-up were shown to be significantly harder than in the HCLL TBM in ITER, see Fig. 2. This is mainly due to the fact that the TBM in ITER is surrounded by shield modules made of a steel/water mixture thus resulting in a comparatively soft spectrum impinging onto the TBM. The mock-up assembly, on the other hand, does not contain any neutron moderator. In addition, it does not contain a strong neutron absorber since the lithium of the Pb-Li alloy is not enriched. Together with the high neutron scattering power of lead this results, first of all, in a rather high neutron leakage out of the TBM assembly and, secondly, in a rather hard neutron spectrum. As a consequence, Tritium generation in the mock-up mainly takes place in the high energy range above 0.1 MeV, while in the TBM a significant amount of Tritium is produced in the low energy range (down to a few eV), see the cumulative distributions of the tritium production rates in the TBM and the mock-up (Fig. 3). Thus, the HCLL mock-up assembly does not represent an act-alike material configuration of the HCLL TBM in ITER. This could only be achieved by surrounding the TBM mock-up with a large sized reflector/moderator material assembly (such as polyethylene) and enriching the lithium of the Pb-Li alloy.

Staff:

U. Fischer
A. Serikov

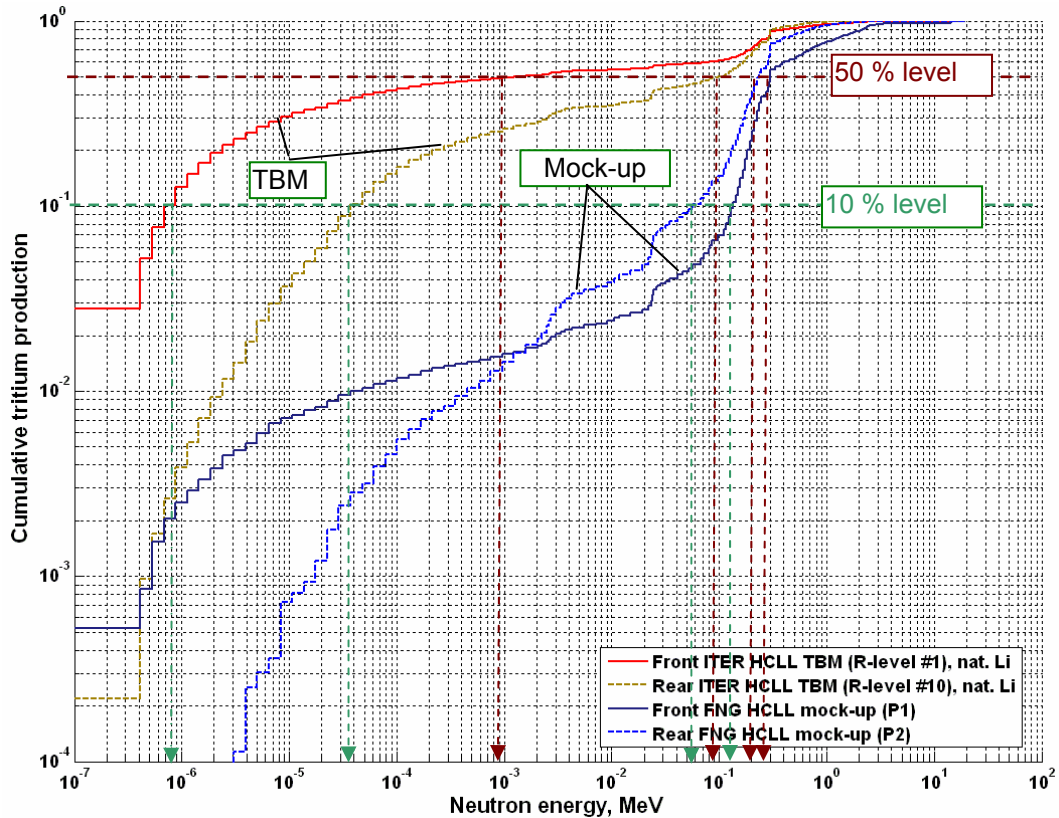


Fig. 3: Cumulative tritium production calculated for positions P1 and P2 in the HCLL TBM mock-up and the corresponding locations in the ITER HCLL TBM (normalized to unity).

TW6-TTMN-002 D 5

Pre- and Post-analysis of the Validation Experiments for Cr Cross Sections up to 55 MeV in an IFMIF-like Neutron Spectrum

In the frame of Task TW6-TMN-002, Deliverable 6, an activation experiment on Chromium was performed at the cyclotron of the Nuclear Physics Institute (NPI), Řež, with the objective to provide the experimental data base for validating the activation cross-section data in the energy range relevant to the International Fusion Material Irradiation Facility (IFMIF) [1]. The objective of Task TTMN-002, Deliverable 5, conducted by FZK, was to perform the computational pre-analysis required for optimizing the experimental set-up and the measurements and to conduct the post-analysis to check and validate the high-energy cross-section data for neutron activation calculations. The computational analyses comprised transport calculations with the MCNPX Monte Carlo and SAND-II unfolding codes for the neutron source characterization [2,3] and activation calculations with European Activation system EASY-2005 (FISPACT/EAF-2005) [4, 5]. Previous efforts to check and validate IAEA-2001 activation cross-section data were performed for Eurofer-97, SS-316, F82H steels and Tungsten [6-8].

Neutron source spectrum characterization

A 37 MeV proton beam impinging on a heavy water target has been used to produce a neutron spectrum up to 35 MeV similar to that of the IFMIF neutron source which employs the d-Li reaction. The objective of the present task was to reproduce the experimental neutron spectrum at the position where the Cr foil was irradiated. The MCNPX Monte Carlo code with the Los Alamos proton library LA-150h and in-built Bertini model was used to model the experimental set-up (Fig. 1) and calculate the differential neutron yield at the points of interest. These calculations were checked against measurements of the neutron spectrum at large distance from the D₂O target using a scintillation detector. As shown in Fig. 2, MCNPX calculations with LA-150h data fail to reproduce both the absolute yield and the energy distribution of the source neutrons. By investigating the reason for the observed large discrepancy it was shown that the LA-150h library does not properly reproduce the double differential cross sections for the D(p,n)2p reaction.

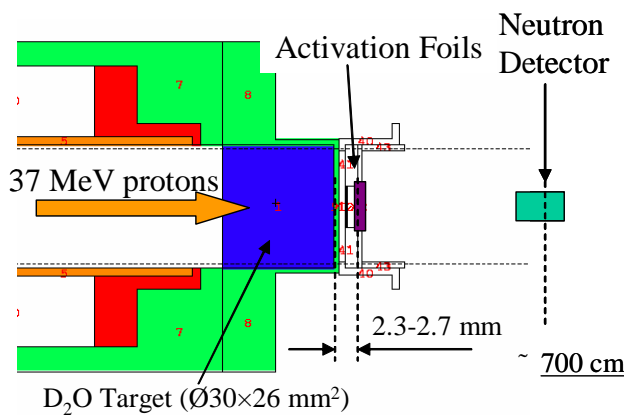


Fig. 1: MCNPX model of the experimental configuration with proton beam indicated.

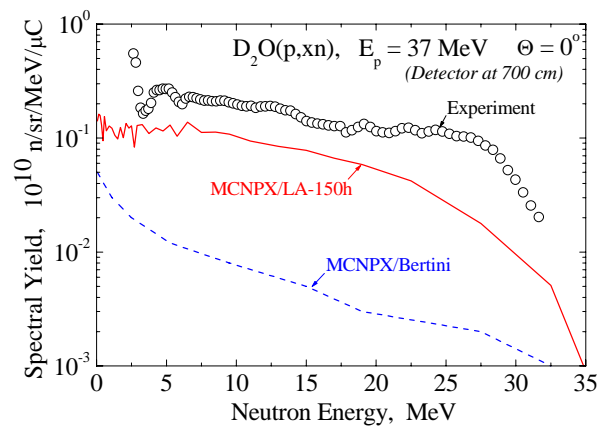


Fig. 2: p-D₂O neutron spectrum at large distance from the heavy water target as measured and calculated by MCNPX.

To determine the neutron flux spectrum at the positions of the Cr sample, the dosimetry foil activation method was applied. For this purpose a stack of pure metallic foils (Al, Au, Co, Fe, Lu, Nb, Rh, Y, Ti, Zr, In and Bi) was located behind the Cr sample and was simultaneously irradiated. The γ -ray activities detected in the dosimetry foils were used for the determination of the neutron flux spectrum by a modified version of the SAND-II code. To accomplish this procedure, the cross section data for the relevant dosimetry reactions need to be extended to the energy range of above 20 MeV. The details of this procedure are described in Ref. [2].

In the experiment, the Cr foil (containing 99.9%) has been irradiated 11.3 minutes at a distance of 2.95 mm from the D₂O target bottom. The irradiation history was derived from the proton beam current recorded as a function of time during the irradiations and was represented in the activation calculations by the one pulse approximation (Fig. 3). Re-normalization of the neutron flux from the dosimetry foils to the Ta spot has been performed by using the measured yield of ²⁴Na generated in the Al monitoring foils (Fig. 4).

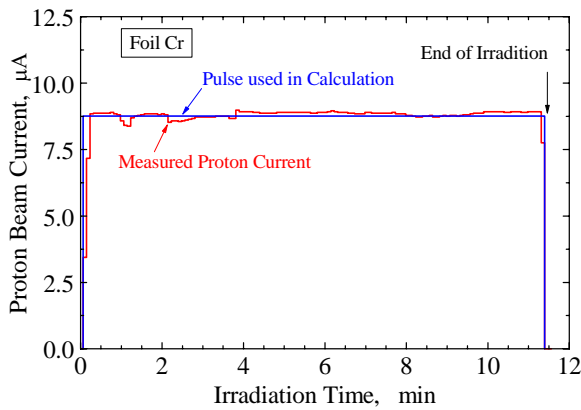


Fig. 3: The Cr irradiation time profile as measured and approximated for activation calculations.

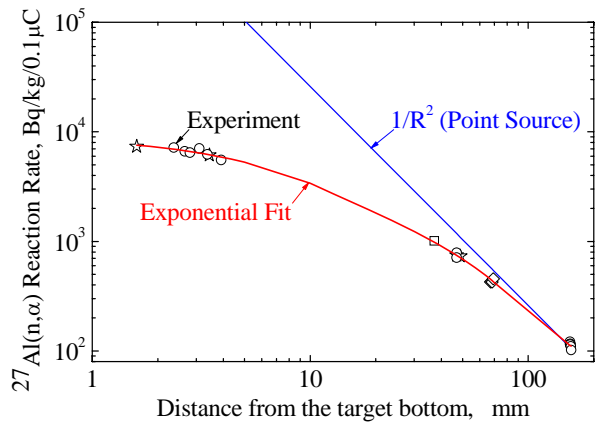


Fig. 4: $^{27}\text{Al}(n,\alpha)^{24}\text{Na}$ reaction rate as a function of distance from the D_2O target bottom.

Validation of the EAF-2005 activation cross-section data.

The activation calculations have been performed with FISPACT/EAF-2005. In Fig. 5 and Table 1, calculated and measured activities (in terms of C/E ratios) for the 7 radio-isotopes detected in the irradiated Cr sample are compared.

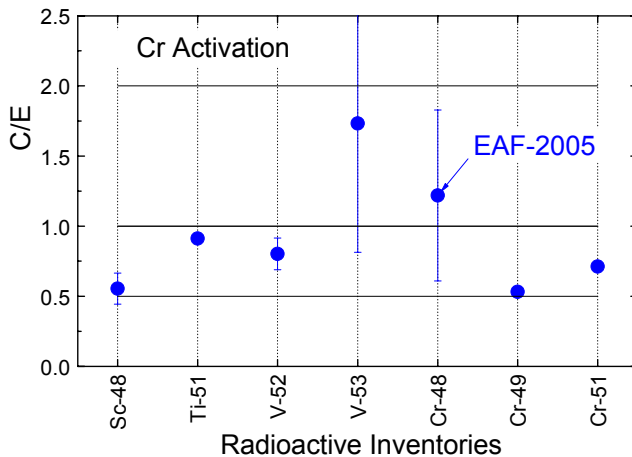


Fig. 5: C/E ratios for specific γ -activities induced in Tantalum calculated with EAF-2005 and IFAF-2001 activation libraries.

It can be seen that the EAF-2005 activation libraries satisfactorily predict (within experimental and calculation uncertainties) the yield of ^{51}Ti , ^{52}V , ^{53}V and ^{48}Cr , but fails to reproduce the other radioactive inventories. Pathway analyses for the production of the specific radio-nuclides have been performed to identify the dominant reactions and the reasons for the observed discrepancies. The results are displayed in Table 1 showing that the generation of the radio-activity products in each case is dominated by one

single reaction. Several examples of the relevant cross sections from IFAF-2001 [9] and EAF-2005 libraries are displayed in Figs. 6 and 7. It is noted that they essentially disagree. The cross sections have a maximum above 20 MeV where no measurements with mono-energetic neutron sources are available.

It is thus concluded that the chromium activation cross sections need to be updated both in the IFAF-2001 and the EAF-2005 data libraries.

Staff:

U. Fischer
S.P. Simakov

NPI/ Řež:

P. Bém
V. Burian
M. Götze
M. Honusek
V. Kroha
J. Novák
E. Šimečková

Table 1: C/E ratios for Cr (weighted mean at several decay times) and dominant reactions.

Nuclide	$T_{1/2}$	Reaction Pathway	C/E	C/E Uncertainty
			FISPACT/ EAF-2005	
^{48}Sc	43.670 h	$^{52}\text{Cr}(n,\alpha) + ^{50}\text{Cr}(n,3p) - 100\%$	0.55	0.11
^{51}Ti	5.800 m	$^{52}\text{Cr}(n,2p) + ^{54}\text{Cr}(n,\alpha) - 100\%$	0.91	0.03
^{52}V	3.745 m	$^{52}\text{Cr}(n,p) - 88\%; ^{53}\text{Cr}(n,d+) - 12\%$	0.80	0.11
^{53}V	1.620 m	$^{53}\text{Cr}(n,p) - 82\%; ^{54}\text{Cr}(n,d+) - 18\%$	1.73	0.92
^{48}Cr	21.561 h	$^{50}\text{Cr}(n,3n) - 100\%$	1.22	0.61
^{49}Cr	41.900 m	$^{50}\text{Cr}(n,2n) - 100\%;$	0.53	0.03
^{51}Cr	27.7060 d	$^{52}\text{Cr}(n,2n) - 98\%; ^{53}\text{Cr}(n,3n) - 1.4\%$	0.71	0.01

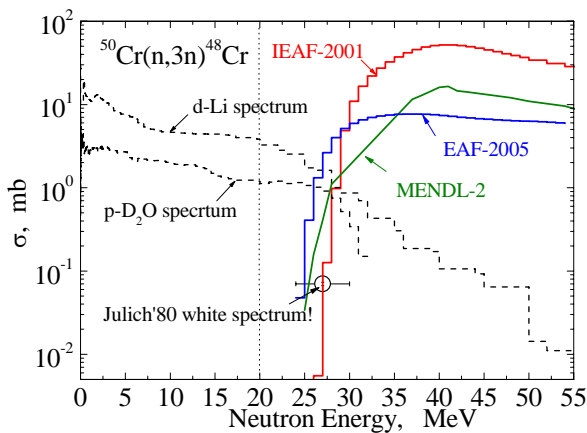


Fig. 6: $^{50}\text{Cr}(n,3n)^{48}\text{Cr}$ reaction cross section as evaluated in IFAF-2001 (red) and EAF-2005 (blue).

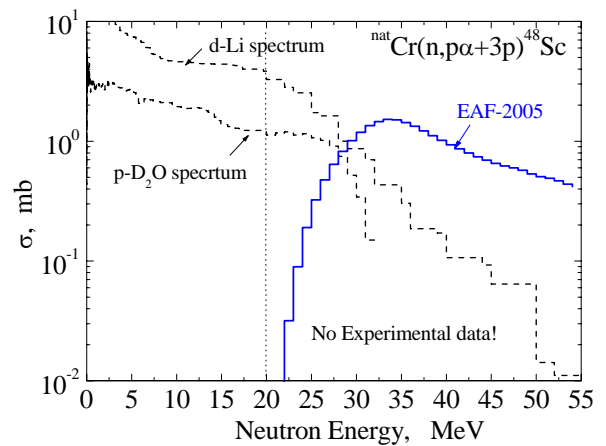


Fig. 7: $^{nat}\text{Cr}(n,p\alpha+3p)^{48}\text{Sc}$ reaction cross section as evaluated in EAF-2005 (blue).

Literature:

- [1] P. Bém, V. Burjan, M. Götz, M. Honusek, V. Kroha, J. Novák, E. Šimečková, U. Fischer, S.P. Simakov, R. Forrest, J. Kopecký. Activation cross section benchmarks at NPI cyclotron, EAF-2007 Workshop, Prague, Oct. 2006.
- [2] S.P. Simakov, P. Bém, V. Burjan, M. Götz, M. Honusek, U. Fischer, V. Kroha, J. Novák, E. Šimečková. "Development of activation foils method for the IFMIF neutron flux characterization", contributed paper at SOFT-24 (Sep. 2006, Warsaw).
- [3] S.P. Simakov, P. Bém, V. Burjan, U. Fischer, M. Götz, M. Honusek, V. Kroha, J. Novák, E. Šimečková. "Determination of the white neutron spectra up to 60 MeV by dosimetry detectors", EAF-2007 Workshop, Prague, Oct. 2006
- [4] R.A. Forrest, "The European Activation System: EASY-2005 Overview", Report UKAEA FUS 513 (January 2005).
- [5] R.A. Forrest, J. Kopecky and J-Ch. Sublet, "The European Activation File: EAF-2005 cross section library", Report UKAEA FUS 515 (January 2005).
- [6] P. Bém, V. Burjan, M. Götz, M. Honusek, U. Fischer, V. Kroha, U. von Möllendorff, J. Novák, S. Simakov and E. Šimečková, Activation of Eurofer in an IFMIF-like neutron field, Fusion Eng. and Des, v. 75-79 (2005) p. 1169

- [7] S.P. Simakov, U. Fischer, U. v. Möllendorff, I. Schmuck, H. Tsige-Tamirat, P.P.H. Wilson, Validation Analyses of IEAF-2001 Activation Cross-Section Data for SS-316 and F82H Steels Irradiated in a White d-Li Neutron Field, Int. Conf. on Nuclear Data for Science and Technology, Santa Fe (2004), AIP Conference Proceedings, 769 (2005), p. 117; see also: EFF-DOC-922, NEA Data Bank, Paris, November 2004.
- [8] R.A. Forrest, J. Kopecky, M. Pillon, K. Seidel, S. P. Simakov, P. Bém, M. Honusek, E. Simeckova. "Validation of EASY-2005 using integral measurements", Report UKAEA FUS 526, Culham 2005
- [9] U. Fischer, D. Leichtle, U. v. Möllendorff et al., Intermediate Energy Activation File IEAF-2001, NEA data bank Programme Library Package NEA-1656/01 (2001), RSICC Oak Ridge, DLC-217/IEAF-2001 (2002).

TW6-TTMN-002 D 7

Validation Experiment of Gamma Activities of La Irradiated in Fusion Peak Neutron Field (TU Dresden)

Objectives

The activation induced by neutrons in the materials of fusion power plant projects represents a central safety related topic. Reduced activation materials with acceptable radiological safety performance and low long-term radiation level have been developed for first wall and breeding blankets [1]. The activation of the materials is mainly caused by neutrons of the d-t fusion peak energy range, where the number of reaction channels is a maximum, and by thermal neutrons because for some reactions the cross section is large in this energy region.

Lanthanum is used as La_2O_3 in the heat shield of divertors. In the present work, a sample of pure La was irradiated with d-t neutrons, and the γ -activities, measured after the irradiation, were analysed with the European Activation System EASY [2] in order to test the relevant data of the European Activation File EAF.

Experiment

For planning the irradiation parameters and in order to determine the time range for measurements of the γ -activities, a calculation with EASY was carried out. La was assumed to be irradiated at power plant conditions; i.e., with a flux of the d-t neutrons corresponding to a power density of 1.0 MW/m^2 , for a period of one year. The results obtained for the contact dose rate as a function of the decay time after irradiation are shown in Fig. 1. The recycling limit of the irradiated La would be reached after about one year. There are only few nuclides that contribute significantly to the total dose rate within this time range.

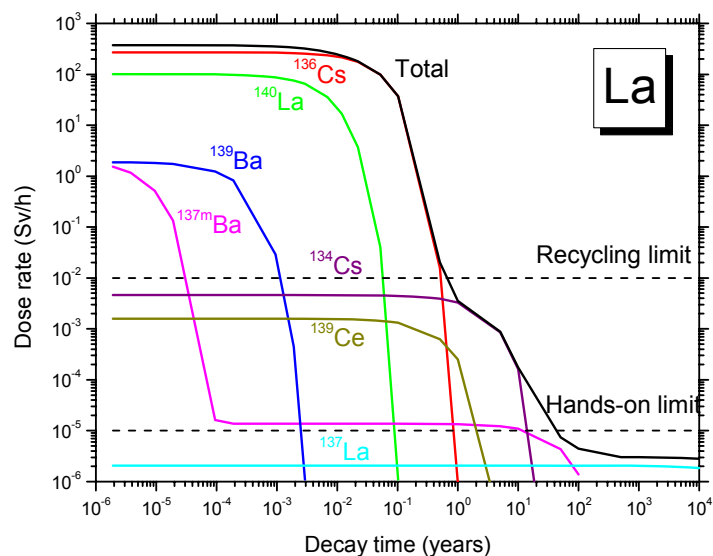


Fig. 1: Calculated total contact dose rate and contribution of the different nuclides after irradiation of La with fusion peak neutrons of 1.0 MW/m^2 power density for one year as a function of the decay time.

In order to investigate the activities of ^{136}Cs , ^{140}La and ^{139}Ba , a fluence of $5.96 \cdot 10^{13}$ d-t neutrons/cm² was applied. The irradiation was performed at the neutron generator of TUD at the FZ Rossendorf. The fluence was determined by simultaneous activation of niobium foils and evaluating the activity induced by the $^{93}\text{Nb}(n,2n)^{92\text{m}}\text{Nb}$ reaction. The time dependence of the neutron production was recorded by two detectors, a ^{238}U fission chamber and a Si-detector for the α -particles of the source reaction. The La sample had a purity of 99.9%, a diameter of 25 mm and thicknesses of 0.62 mm.

γ -ray spectra were taken with an HPGe-spectrometer at decay times in the range from 4 hours to 9 days. The γ -activities identified by energy and half-life were used to determine the nuclide activities, using γ -yield data from EASY. The attenuation of the neutron and of the γ -ray fluxes in the sample as well as the geometry factors (neutron source – sample; sample – γ -ray detector) were determined by 3D Monte Carlo calculations.

Results

The experimental data were analysed with the recent version of the European Activation System, EASY-2005. The results are presented in Table 1. The uncertainties of the experimental values ($\Delta E/E$) are including all possible errors of the γ -activity measurement, of the sample mass, of the γ -yield data and of the neutron flux monitoring. The uncertainty of the calculated activities ($\Delta C/C$) includes both cross section and half-life errors as estimated by EASY. The deviations of the three ratios of calculated-to-experimental activity (C/E) from unity are smaller than the $\Delta E/E$ or $\Delta C/C$. A detailed discussion can be found in Refs. [3 - 5].

Table 1: Results obtained for the activity of nuclides; nuclide identified, its half-life and γ -rays with yield data used to determine the activity, the experimental uncertainty of the activity ($\Delta E/E$), the ratio of calculated-to-experimental activity (C/E), uncertainty of the calculated activity ($\Delta C/C$) and the neutron reaction producing the activity.

Nuclide	Half-life	E (keV)	Y	$\Delta E/E$	C/E	$\Delta C/C$	Reaction	Contr. (%)
^{136}Cs	13.0 d	340.6 1048 1235	0.422 0.798 0.200	0.08	1.02	0.31	$^{139}\text{La}(n,\square)$	100
^{139}Ba	1.38 h	165.9	0.245	0.24	0.97	0.18	$^{139}\text{La}(n,p)$	100
^{140}La	1.68 d	751.8 867.8 925.2	0.044 0.056 0.070	0.07	0.81	0.42	$^{139}\text{La}(n,\square)$	100

Conclusions

For the three dominant activities resulting from La irradiation with fusion peak neutrons in the decay time range until the recycling limit is reached, the EASY-2005 data have a good quality. The experimental uncertainties obtained ($\Delta E/E$ in Table 1) suggest, that the measurements can contribute further to improve the EAF data base [6].

Also the C/E for the production of ^{140}La by neutron capture of fusion peak neutrons is reasonable. In fusion reactors this activity is mainly produced by thermal neutron capture and should also be validated in an appropriate neutron field.

The expected recycling limit of one year for La, irradiated with fusion peak neutrons at power station conditions is confirmed by the present experiment.

Staff:

H. Freiesleben
A. Klix
K. Schomburg
K. Seidel
S. Unholzer

Literature:

- [1] R. Andreani, E. Diegele, R. Laesser, B. van der Schaaf, The European integrated materials and technology programme in fusion, J. Nucl. Mater. 329-333 (2004) 20.
- [2] R. A. Forrest, The European Activation System: EASY-2005 overview, Report UKAEA FUS 513, Culham Science Centre, Abington (U.K.), Jan. 2005.
- [3] A. Klix, R.A. Forrest, H. Freiesleben, K. Schomburg, K. Seidel, S. Unholzer, Validation experiment of gamma activities of La and Er irradiated in a fusion peak neutron spectrum, EFFDOC-971, NEA Data Bank, May 2006.
- [4] A. Klix, R.A. Forrest, H. Freiesleben, K. Schomburg, K. Seidel, S. Unholzer, Measurement and analysis of activation induced in Ta, La and Er by fusion peak neutrons, SOFT-24, Warsaw (Poland), Sept. 2006.
- [5] K. Seidel, Validation experiments at TU Dresden, Workshop on Activation Data – EAF 2007, Prague (Czech Rep.), Oct. 2006.
- [6] R. A. Forrest, J. Kopecky, M. Pillon, K. Seidel, S.P. Simakov, P. Bem, M. Honusek, E. Simeckova, Validation of EASY-2005 using integral measurements, Report UKAEA FUS 526, Culham Science Centre, Abingdon (U.K.), Jan. 2006.

Materials Development IFMIF

TTMI-001 IFMIF – Accelerator Facilities

TW5-TTMI-001 D 3

Studies of End-to-end Transmission and Beam Losses along the Accelerator Facilities Considering the Effects of the Different Sources of Errors on the Transport of the Beam

Objectives

The IFMIF linac must be capable to accelerate a 125 mA cw beam of deuterons to a total energy of 40 MeV. Particle losses can lead to activation of accelerator components. Due to the required hands-on-maintenance losses have to be kept extremely low along the linac. Extensive beam dynamics simulations are necessary to study the influence of fabrication and of alignment errors on beam halo generation and losses. This includes a large number of macro particles. The beam dynamics code LORASR has been optimized with respect to time efficient calculation of space charge forces which is required when using up to 1 million macro particles.

Status of the work before the time period

The number of macro particles was limited to about 20000. This number is high enough for an accelerator layout but not sufficient to study extremely low losses and halo generation. Additionally, not all possible errors had been implemented in the code. Although many RF linacs have been designed and built using the LORASR code but no benchmarking with other common codes has been performed so far.

Results and achievements obtained during the time period

New routines have been implemented or further improved for the beam dynamics code LORASR, in order to allow time-efficient simulations with up to one million macro particles routinely, as well as machine error settings for loss profile investigations.

Furthermore, additional error types have been added to the LORASR routines and the available data analysis tools have been extended: the local resolution of the particle loss prediction has been improved by taking into account the exact shape of the resonator apertures along the linac.

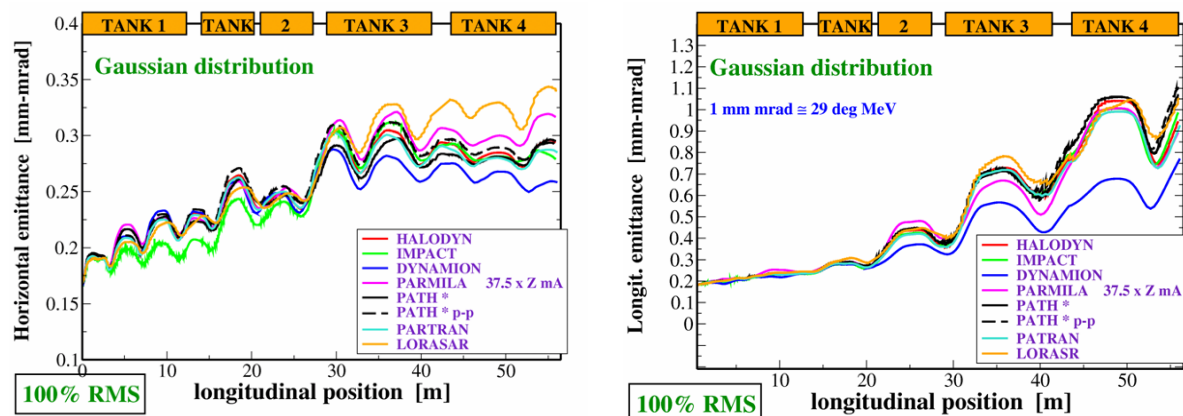


Fig. 1: Horizontal 100% rms-emittance along the GSI-Alvarez calculated by different codes including LORASR (left) and longitudinal 100% rms emittance. The input beam is Uranium 28+, 37 mA, 1.4 AMeV.

All updated routines had to be carefully validated. A good opportunity for code benchmarking was given within the framework of the European network activity 'High Intensity Pulsed Pro-

ton Injector' (HIPPI). The LORASR code was included to the Poisson solver and the UNILAC Alvarez section tracking benchmarking and validated against other well-established linear accelerator beam dynamics codes like 'IMPACT', 'HALODYN', 'DYNAMION' and 'TOUTATIS' (Fig. 1). The achieved degree of accordance between the codes is promising. For further information please refer to the note 'Linac Code Benchmarking in Preparation of the UNILAC experiment' (CARE-Note-2006-011-HIPPI).

Now we are confident in the results of the loss profile and machine error studies made by LORASR on the IFMIF room temperature linac (Alvarez structure) and on the superconducting linac (CH structure).

For the activation and dose-rate study of the normal conducting reference DTL form Alvarez-type with the particle tracking code PARMILA® from Los Alamos the cell geometry from Saclay must be implemented in Superfish® and the calculated gap electric field distribution and transit time factors were used from PARMILA® for the beam dynamics simulations. The cell geometry of the Alvarez-DTL is successfully transformed in Superfish and the transit time factor tables are overtaken in Parmila. The first tank with the given quadrupole parameter-sets are generated. The same for the following 9 cavities will be made. Then first beam dynamics calculations of the complete Alvarez-DTL will be performed. A comparison with the Saclay calculations will also be done. In a last step a Monte-Carlo tolerance study with 100 different linacs and 10^6 macro particles will be made.

In the same framework a Monte-Carlo tolerance study of the H-type linac layout from Figure 2 with the new LORASR code was performed. 100 different runs with 10^6 macro particles for each run were used. This leads in sum to 10^8 particles for 100 different linacs with different RF and quadrupole error configurations. The assumed static errors of the cavities and their internal elements were Gaussian-distributed along the H-type linac. As tolerance-limits, we used for a first validation of the LORASR code standard rf and quadrupole misalignment intervals, e.g. $\pm 1\%$ electric field amplitude error of tanks and each gap, $\pm 1^\circ$ of tank-phase and gap-phase error and ± 0.1 mm transverse misalignment of each magnetic quadrupole. A crosscheck with other multi-particle codes like PARMILA® from Los Alamos or TraceWin® from Saclay is foreseen. First results have been sent to the collaboration partners at FZK and ENEA who use the particle losses along the linac for calculation of the resulting activation after different operation times. For the front end part (RFQ) of the linac first results have been already achieved.

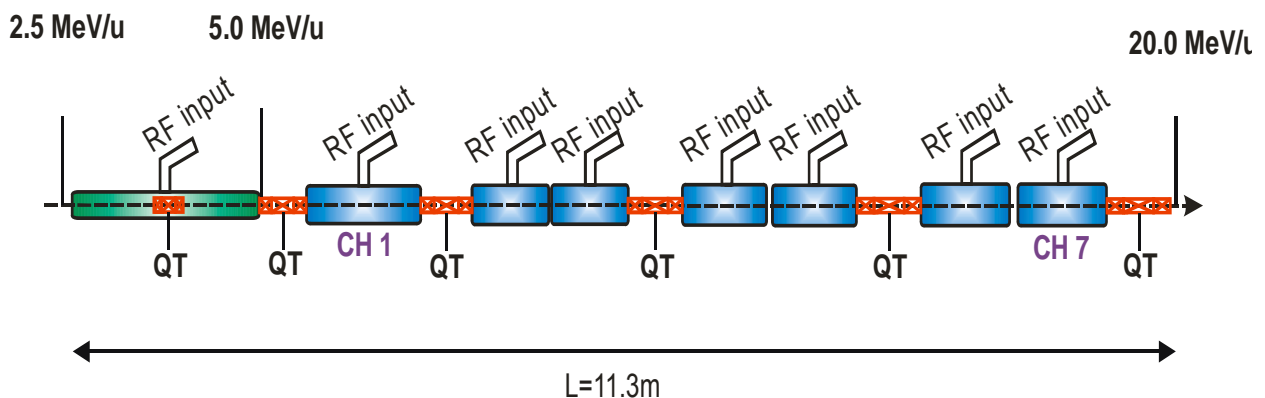


Fig. 2: Layout-scheme of the H-type linac for IFMIF used for preliminary tolerance studies in Monte-Carlo method.

Staff:

H. Klein
U. Ratzinger
H. Podlech
A. Sauer
R. Tiede

Johann Wolfgang Goethe-Universität
Institut für Angewandte Physik (IAP)
Robert-Mayer-Str. 2-4
60486 Frankfurt am Main

TTMI-003 IFMIF - Test Facilities

TW5-TTMI-003 D 8

Tungsten Spectral Shifter: Neutronics Analysis (dpa Evaluation, H, He and other Impurities Generation, Recoil Spectrum, etc) of Different Positions and Geometries

The objective of this task is the optimization of (i) the tungsten irradiation conditions in IFMIF to closer represent those in the divertor of the power fusion reactors and (ii) the tungsten spectral shifter plates position in front and behind the Creep-Fatigue testing machine (CFTM) to adjust the primary knock-on atom spectrum in the in situ creep-fatigue samples. This study is an extension of the IFMIF neutronics analysis performed earlier [1- 3].

Tungsten nuclear response parameters in power fusion reactor divertor

For the comparative tungsten irradiation conditions analyses the nuclear responses in the W tiles covering the divertor of fusion power reactor (Fig. 1) were calculated. This was done for a 4000 MW power reactor with helium cooled lithium lead blanket (HCLL) investigated in the Power Plant Conceptual Study (PPCS) [4]. The tungsten nuclear responses were calculated by the MCNP4C Monte Carlo code using a three-dimensional 20 degrees torus sector model and FENDL-2 cross section data for the neutron transport.

The results presented in Table 1 show that each tungsten atoms will be displaced 2.4 times from its lattice node during 1 full power operation of fusion reactor. The gas generation in tungsten will be dominated by hydrogen and helium production caused by neutrons at the levels of 2.3 appm and 0.7 appm, that give the gas to dpa ratios 1.0 and 0.3, correspondingly.

Tungsten irradiation parameters in IFMIF

The aim of this subtask is a search of location for the tungsten specimens in the IFMIF test modules or close to them, where the atom displacement rate and gas production ratio will optimally reproduce the ones expected in fusion power reactor.

In the IFMIF facility the High, Medium and Low Flux Test Modules (HFTM, MFTM, LFTM) are located just behind Li-jet target to house the specimens for long term irradiations. As a first step we have estimated nuclear responses in the tungsten specimens located there, supposing that they will partly replace the steel samples in the HFTM or can be easily allocated between pull-push rods of Universal Test Machine (UTM), which is a front part of MFTM (see Fig. 2). To perform such neutronics calculations the McDeLicious code [5] with recently updated and validated d-Li cross sections data (task TW4-TTMI-003, D9) [6] were employed. For the representation of current IFMIF test cell design the global MCNP model developed in the frame of task TW4-TTMI-003, D5a (TEKES, Finland) was used.

The results listed in the Table 1 show that atom displacement rate 3.6 dpa/fpy in tungsten could be achieved in UTM, if the specimens will be located between the push-pull rods. This already exceeds the dpa rate in the fusion power divertor. On other hand for the proper rep-

PPCS/HCLL Fusion Reactor
(vertical cut)

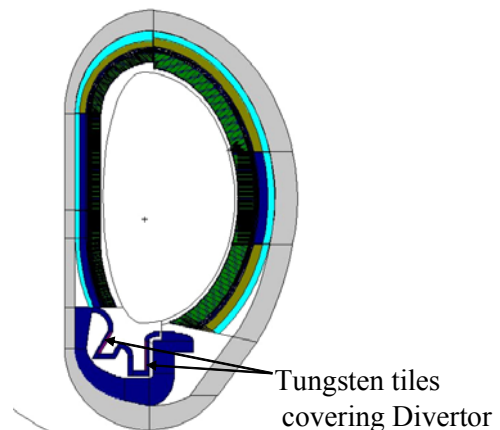
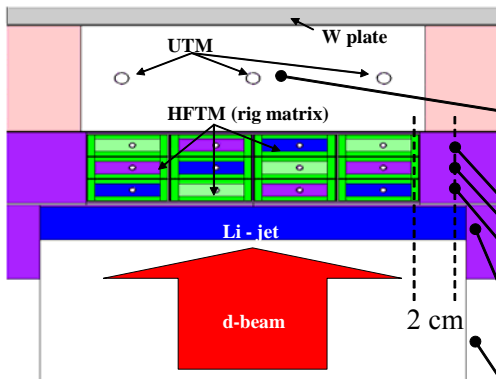


Fig. 1: Vertical cut of the PPCS fusion power reactor with HCLL blanket.

resentation of the fusion reactor radiation conditions one needs to have the gas production to dpa ratios 1.0 for hydrogen and 0.3 for helium. As Table 1 shows during irradiation near UTM rods these ratios will amount 20 and 1.3, hence 20 - 4 times exceeding the fusion levels.

Nuclear Responses: IFMIF vs. Fusion Reactor

IFMIF: HFTM, Reflector, UTM (plan view)



Location	Nuclear Responses		
	Damage rate [dpa/fpy]	H [appm] (Ratio H/dpa)	He [appm] (Ratio He/dpa)
PPCS Reactor with HCLL blanket, 4000 MW fusion power			
<i>Divertor</i>			
Outer W target plate	2.37	2.34 (1.0)	0.68 (0.29)
IFMIF, 40 MeV @ 250 mA			
<i>UTM</i>			
Push-pull samples	3.6	67 (19)	4.6 (1.3)
<i>HFTM</i>			
3 rd row rig	5.1	98 (19)	6.8 (1.3)
2 nd row rig	8.0	143 (18)	10.0 (1.3)
1 st row rig	10.7	183 (18)	12.9 (1.2)
<i>HFTM Lateral Reflector</i>			
3 rd row rig	2.2 - 1.9	36 - 31 (16)	2.5 - 2.3 (1.1)
2 nd row rig	2.6 - 2.1	40 - 32 (15)	2.9 - 2.3 (1.1)
1 st row rig	2.9 - 2.4	45 - 33 (16)	3.1 - 2.2 (1.1)
<i>Li-target Flange</i>			
X = 14, Z = -2cm	1.1	3.6 (3.3)	0.41 (0.37)
<i>Deuteron Beam Tube</i>			
X = 14, Z = -15cm	0.32	0.45 (1.4)	0.067 (0.21)

Fig. 2: Horizontal cut of the IFMIF test cell fragment: Li-jet, HFTM, neutron reflector, UTM and W plate.

Table 1: Tungsten nuclear responses in the divertor of fusion power reactor and at different locations inside IFMIF as indicated in Fig. 2.

In the HFTM, even higher tungsten atom displacement rates (5 to 11 dpa/fpy) could be reached depending on the rig and row housing the specimens. But the gas-to-dpa ratios will also exceed fusion level by same large factor as in UTM.

The reasons of that are the difference of energy neutron spectra inside the fusion and IFMIF facilities and sensitivity of gas production reactions to the high energy neutrons. The fusion neutron spectra cut off at 15 MeV, whereas IFMIF ones produced by d-Li reaction extends up to 55 MeV (Fig. 3). The gas productions cross sections on tungsten such as (n,xp) and (n,xα) have thresholds around 10 MeV and increases one-two orders of magnitude as neutron energy goes up from 14 to 55 MeV (Fig. 4). The dpa cross section increases only two times in this energy range, being the same time non threshold reactions.

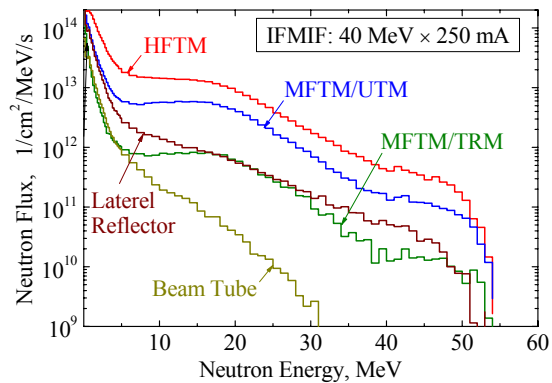


Fig. 3: Energy differential neutron flux in the HFTM, MFTM, HFTM Lateral reflector and deuteron beam tube.

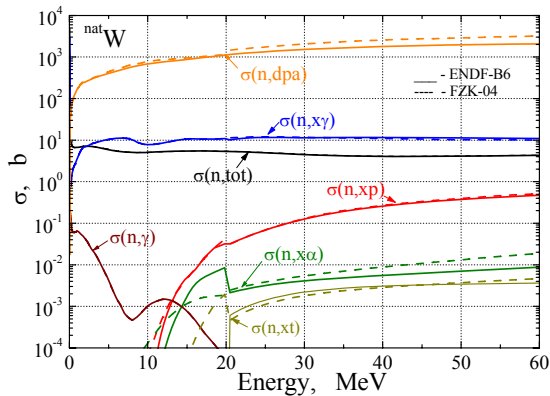


Fig. 4: Neutron reactions cross sections for natural tungsten from ENDF/B-VI (solid curves) and FZK-04 (dash curves) libraries.

Principally, for the reproduction the fusion gas-to-dpa ratios in the IFMIF the tungsten specimens should be shifted in side-ward or even backward directions relative to the deuteron beam direction, where the fraction of neutrons with energy more than 15 MeV essentially decreases (Fig. 3). We considered following geometrically possible spots for the samples as indicated in Fig. 2: the HFTM lateral reflector, lithium target flange and deuteron beam tube (inside the vacuum system). Results of calculations are summarized in Table 1: location of the tungsten specimens inside the HFTM lateral reflector gives the acceptable dpa rate but the gas-to-dpa ratio as large as in HFTM and UTM; practically

the same gas-to-dpa ratios as in the fusion reactor divertor could be achieved inside the deuteron beam tube, but at 0.3 dpa/fpy displacement rate which is 10 times less than fusion one; location of the W specimens in the flange of Li-target exhibits the intermediated option with dpa rate half of fusion one and gas-to-dpa ratios 3-2 times larger.

Further study is needed to clarify the possibility of the housing the tungsten specimens there regarding all engineering issues.

The results of estimation of nuclear responses in the tungsten depend on the neutron induced reactions cross section used in the calculations. As Fig. 4 shows, the agreement between ENDF/B-VI library and recent new evaluation FZK'04 [7] are quit reasonable up to 60 MeV. Nevertheless the differences for some specific reactions are visible and reach in the case of helium production even a factor of 5.

To estimate the influence of nuclear data base on final results we calculated tungsten nuclear responses with these two evaluations. The results show that dependence of W nuclear responses on nuclear data amounts 3 to 6% for the case of fusion reactor calculations and 5 to 40% for IFMIF. The largest difference appears for gas production in tungsten, that emphasizing the necessity for experimental validation of the relevant cross sections in the IFMIF energy range.

Optimization of the Tungsten spectral shifter for reproduction fusion irradiation conditions in Medium Flux Test Module

Previous Monte Carlo simulations has shown that for the properly selected geometry IFMIF irradiation conditions can perfectly meet helium, hydrogen and displacement production rates relevant for DEMO reactor. Additional spectral shifter allows also fitting primary recoil spectrum so that the fraction of damage produced by recoils with the energy greater than given is very close to that of DEMO reactor.

Spectral shifter materials should withstand significant radiation and thermal loads being able to effectively modify neutron spectrum. Tungsten was selected as a spectral shifter material due to its high melting temperature, good thermal conductivity as well as good neutronics properties such as high scattering ability. The further sections describe the selection of the optimal geometry of spectral shifter plates (position, width) with the aim to reproduce DEMO irradiation conditions at creep-fatigue testing machine and tritium release module as close as possible (details are available in [8]).

Various positions of spectral shifter plates

Two tungsten spectral shifter plates positioned in front and behind the creep-fatigue testing machine (CFTM) were proposed for the adjusting of the primary knock-on atom spectrum at in situ creep-fatigue samples. Previous neutronics calculations showed that an adjusted spectrum perfectly matches that of the DEMO reactor at the first wall position.

Later during preliminary engineering design it was recognized that two plates would require too much design efforts and space for their cooling and temperature monitoring. Therefore designers suggested placing one plate of double width behind the CFTM. This part of the task is aimed at the study of consequences of such disposition for the change of irradiation conditions at CFTM and tritium release module (TRM).

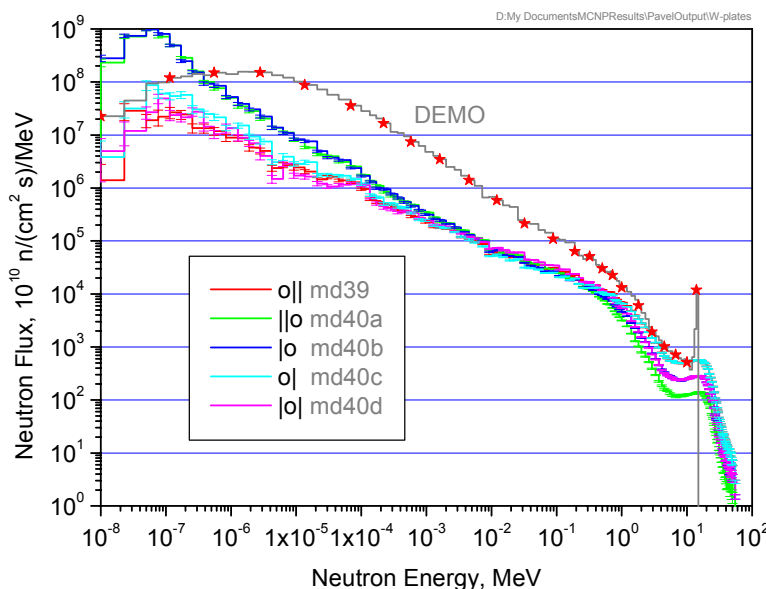
Table 2: Description of geometry variants.

Variant	Position relative to CFTM	Width, cm
md39	behind	6.4
md40a	in front	6.4
md40b	in front	3.2
md40c	behind	3.2
md40d	in front & behind	3.2

Several geometry variants differing by the width and placement of tungsten spectral shifter plates were considered (see Table 2).

Neutron spectra, damage and gas production at CFTM

Neutron transport calculations were performed using McDeLicious-05 code with an updated version of the evaluated d-Li reaction cross sections. The obtained neutron spectra for the discussed above IFMIF geometry variants and DEMO reactor are presented in Fig. 5. The effect of the width of the spectral shifter plate positioned in front of CFTM is clearly visible as a change of the shoulder height in the range 1 - 20 MeV. This part of the neutron spectrum is effectively shifted to the low neutron energy by the tungsten plate.



The plate placed behind the CFTM reflects neutrons back further decreasing neutron flux available at TRM. The efficiency of thermal neutron absorption slightly increases with the plate thickness (cf. md39 and md40c). Damage and gas production rates in iron located inside the central creep-fatigue specimen are collected in Table 3.

Fig. 5: Differential neutron spectra at CFTM position compared with the DEMO First Wall spectrum.

Table 3: Irradiation conditions for the central creep-fatigue specimen (cell 5021) at CFTM (Fe) and at the first row of TRM (Be).

Variant	the central creep-fatigue specimen, Fe				first row of TRM, Be	
	Flux, 10^{14} n/cm ² /s	Damage, dpa/fpy	He appm/fpy	H, appm/fpy	Flux, n/cm ² /s	Damage, dpa/fpy
md39	3.33	11.76	75.4	215.2	9.73×10^{13}	3.23
md40a	1.81	3.50	18.4	52.3	1.33×10^{14}	2.76
md40b	2.30	6.26	37.2	106.0	1.69×10^{14}	3.74
md40c	3.16	11.64	75.4	215.1	1.81×10^{14}	4.22
md40d	2.53	6.48	37.2	105.9	1.32×10^{14}	2.91

As could be expected very similar results were obtained for the variants with full (md39) and half-width (md40c) W-plates behind CFTM. The plates placed in front of the CFTM gradually decrease damage and gas production rates with increasing plate thickness. Qualitatively similar results were obtained during preliminary study performed before the availability of the global geometry IFMIF model [Report TW0-TTMI-003-D10, 2002]. The results of damage rate in beryllium placed at TRM are presented in Table 3.

Differential primary recoil spectra are qualitatively similar to that for DEMO First Wall (see Fig. 6). Considerable difference is observed only at energies lower than 300 eV.

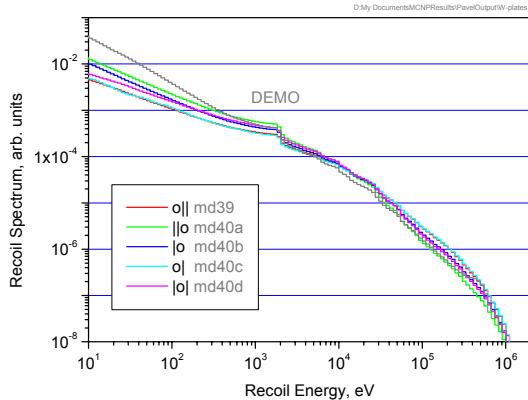


Fig. 6: Differential recoil spectra at CFTM position for various geometry configurations versus DEMO First Wall recoil spectrum.

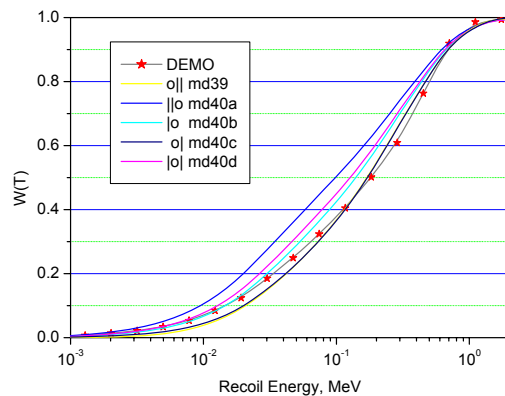


Fig. 7: Fraction of damage produced by recoil with energy greater than given for various geometry configurations.

However, even a small difference in the high-energy portion of the spectrum could result in substantial change of radiation damage rates. For example, damage produced at the central creep-fatigue sample varies in the range from 3.5 up to 11.8 dpa/fpy. It can be seen from Table 3 that maximum damage rate at CFTM is obtained for the variants (md39, md40c) where tungsten plates are placed behind CFTM. For the plate of full-width the damage rate is slightly larger than that for the half-width due to the more effective neutron backscattering from the thicker plate.

It is expected that damage at TRM decrease with the width of W-plates placed in front of TRM. Indeed, thick tungsten plate noticeably reduces damage rate at TRM (cf. 3.50 dpa/fpy for the full-width plate (md40a), 6.26 dpa/fpy for the half-width plate (md40b) and 11.64 dpa/fpy for the half-width plate placed behind CFTM (md40c)). In contrary, damage rate for

the variant with half-width plate behind CFTM (md40.c) is even slightly higher than for the variant without W-plates (fw21.6) from our previous study. It might be related to the presence of the extended carbon reflector in variants considered in the present report.

Fraction of damage produced by recoils with an energy greater than given energy T, so called W(T) function, is plotted in Fig. 7. It can be seen that good approximation to the DEMO curve is provided by the variants md39, md40c and md40b.

Conclusions

The nuclear responses in the tungsten under irradiation parameters for 4000 MW power reactor with helium cooled lithium lead blanket have been calculated. To reproduce them in the IFMIF facility the relevant calculations have been performed at several locations: inside the High Flux Test Module and its lateral neutron reflector, between the pull-push rods of the Universal Test Machine, in the lithium target flange and inside deuteron beam vacuum tube. The calculations have been performed by the McDeLicious code using a detailed 3-d geometrical model of the entire IFMIF test cell. In this approach the recently updated d-Li evaluated cross section data and high energy neutron transport cross sections from LA-150, ENDF/B-VI and FZK/INPE-50 libraries were employed.

The comparison of the tungsten nuclear responses has shown that the atom displacement damage rate (dpa) inside UTM and HFTM is 1.5 - 4.5 times higher than for the fusion power reactor divertor and is comparable in the cases of the HFTM lateral reflector. The gas-to-dpa production ratio for tungsten irradiated there, however, exceeds that of the fusion power reactor divertor by several times due to the IFMIF neutron spectrum which extends above 14 MeV. Desirable ratio could be obtained in deuteron beam tube, but dpa rate there drops by one order of magnitude below fusion one. Some kind of compromise could be reached in the lithium target flange, where dpa under- whereas gas-to-dpa ratio over-rate the fusion levels by factor of 2-3.

The comparison of the nuclear responses calculated with different evaluated cross sections files (ENDF/B-VI and FZK-04) reveals the spread of 3 - 40%.

If a degree of approximation of W(T) is considered to be the major criterion for recoil spectra optimization together with the damage rates at CFTM and TRM, than the variant with half-width tungsten plate located behind CFTM (md40c) seems to be the most preferable one. It provides similar damage level at CFTM as the variant with full-width plates and the highest damage rate in beryllium irradiated at TRM.

Staff:

U. Fischer
V. Heinzl
A. Möslang
S.P. Simakov
P. Vladimirov
F. Wasastjerna (TEKES, Finland)

Literature:

- [1] S.P. Simakov, U. Fischer, A. Möslang, P. Vladimirov, F. Wasastjerna, P. Wilson, Neutronics and activation characteristics of the International Fusion Material Irradiation Facility, Fus. Eng. Des. 75-79 (2005) 813-817.
- [2] Yu. Lizunov, A. Möslang, A. Ryazanov and P. Vladimirov, New evaluation of displacement damage and gas production for breeder ceramics under IFMIF fusion and fission neutron irradiation, Journ. Nucl. Materials 307-311 (2002) 1680-1685.

- [3] U. Fischer, Y. Chen, S.P. Simakov, P.P.H. Wilson, P. Vladimirov, F. Wasastjerna, Overview of recent progress in IFMIF neutronics, *Fus. Eng. Des.* 81 (2006) 1195-1202.
- [4] U. Fischer, P. Pereslavytsev, Neutronic Analyses for the Conceptual Design of a HCLL Reactor, Final report on the EFDA Task TW4-TRP-002, D.2a, Karlsruhe, March 2005.
- [5] S.P. Simakov, U. Fischer, U. von Möllendorff, I. Schmuck, A. Konobeev, P. Pereslavytsev, Advanced Monte Carlo Procedure for the D-Li Neutron Source Term Based on Evaluated Cross-Section Files, *J. Nucl. Mat.* 307-311 (2002) 1710-1714.
- [6] U. Fischer, M. Avrigeanu, P. Pereslavytsev, S.P. Simakov, I. Schmuck, Evaluation and Validation of D-Li Cross-Section Data for the IFMIF Neutron Source Term Simulation, *Proc. of ICFRM-12* (in print).
- [7] P. Pereslavytsev, U. Fischer, Evaluation of n + W cross section data up to 150 MeV neutron energy., *AIP Conference Proceedings* v. 769 (2005) 215.
- [8] S. Gordeev, V. Heinzl, A. Möslang, S. Simakov, E. Stratmanns, P. Vladimirov, IFMIF - Design study for the in situ creep fatigue tests, *Symposium on Fusion Technology (SOFT-24)*, Warsaw, September 2006

TW5-TTMI-003 D 9 Automatic Generation of a 3D Test Cell Model for MC Calculations from CAD Data

The objective of this task was to generate a detailed 3D geometry model of the IFMIF test cell for Monte Carlo transport calculations from available CAD design data using the CAD interface program McCad developed recently at FZK [1]. The use of CAD design models allows efficient and consistent geometry preparation for neutronics analyses. It requires, however, a preprocessing of the CAD model to adjust it to the needs of the Monte Carlo code as well as the conversion of the CAD data into a representation appropriate for the Monte Carlo code.

The interface program McCad provides a CAD interface for the Monte Carlo code MCNP. It is able to perform the conversion of the CAD data into MCNP geometry including the generation of voids, error analyses and model repair. It provides capabilities for the visualization, modelling, and exchange of geometry data and is also capable to generate CAD geometry models from available MCNP input decks.

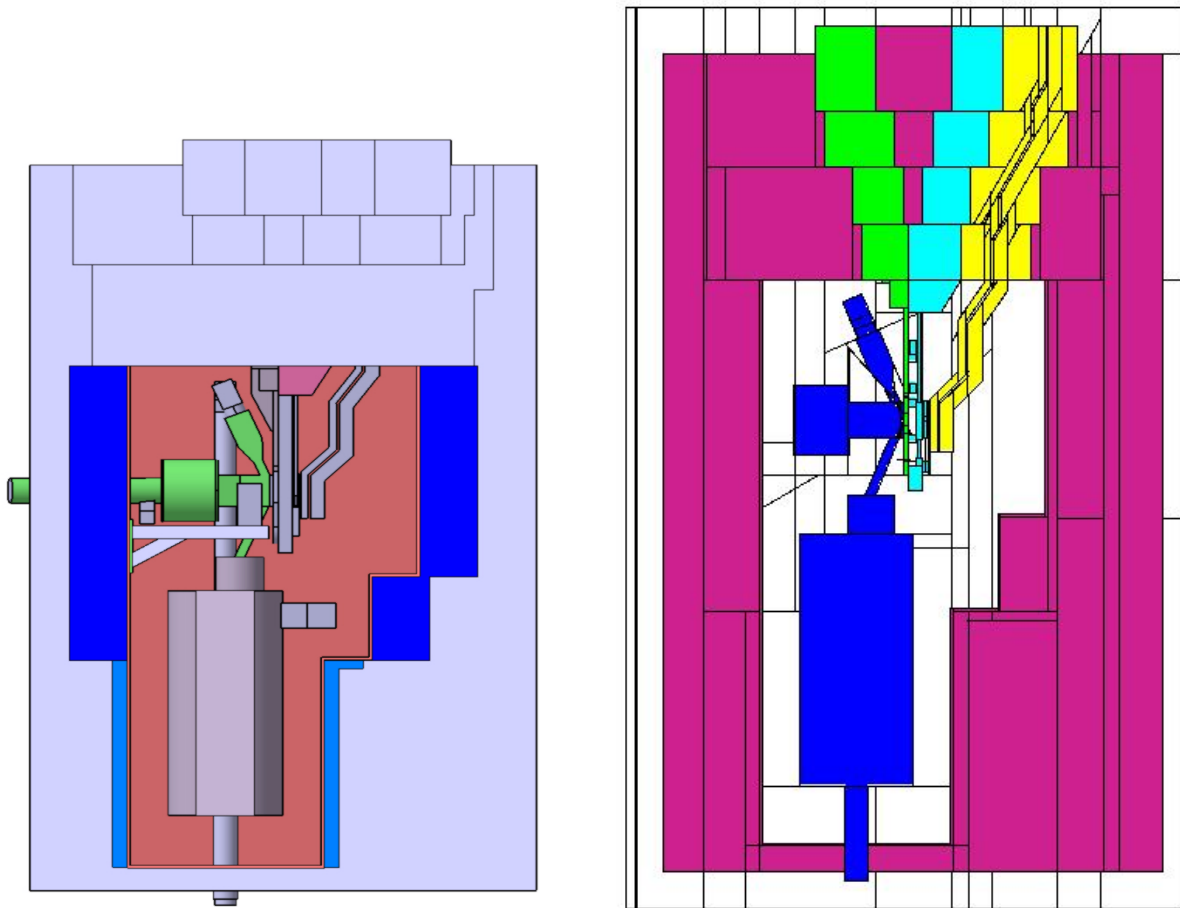


Fig. 1: Comparison of 3D geometry models of the IFMIF test cell. Left side: Engineering CAD model developed and visualised by CATIA V5. Right side: MCNP model converted by the McCAD interface programme and visualised by the MCNP plotter in a 2D cut

The most recent engineering CAD model of the IFMIF test cell has been used to generate a dedicated neutronics model which contains all sub-systems and components through detail suppression and geometric simplification. The latter step is necessary to remove free form surfaces of the geometry which can not be treated by MCNP. Analyses of the dedicated neutronics model were performed using McCad in order to check for modelling errors and to ensure its suitability for neutronics calculations. Subsequently, the model was converted into

MCNP geometry by McCad including the generation of voids. Since the conversion algorithm does not introduce approximations the generated MCNP model is fully equivalent to the underlying neutronics CAD model. Fig. 1 compares the engineering CAD model, constructed with the CATIA V5 software, and the converted MCNP model as produced in a 2D view by the MCNP plotter.

The converted geometry model has been validated through a stochastic calculation of the volumes by MCNP as well as through source neutron distribution calculations by the McDeLicious code. This model will serve as a reference model for upcoming neutronics analyses. It will be continuously updated to keep it consistent with the engineering design model.

Staff:

U. Fischer
S.P. Simakov
S. Stickel
H. Tsige-Tamirat

Literature:

- [1] H. Tsige-Tamirat, U. Fischer: CAD Interface for Monte Carlo Particle Transport Codes. The Monte Carlo Method: Versatility Unbounded in a Dynamic Computing World ; Proc.of the Conf., Chattanooga, Tenn., April 17-21, 2005 LaGrange Park, Ill. : ANS, 2005

TW6-TTMI-003 D 1

Manufacturing and Procurement of a Complete HFTM Compartment Including the Whole Set of Test Samples and the Qualification of Brazing Procedure for the Heating Systems

Background and Objectives

For the generation of a materials database, definition of engineering rules and verification of materials performance in future fusion power reactors the IFMIF d-Li neutron source is accepted as the most promising irradiation facility. With IFMIF a fusion relevant radiation environment with accelerated testing could be provided.

The design of the test facilities has been advanced significantly, comprising neutronics, thermal and mechanical analyses.

The objective of the subtask was to complete the manufacturing of a High Flux Test Module compartment with three fully equipped and instrumented irradiation rigs. The brazing technology of heater wires to the capsule shall be qualified to complete the fabrication route of the HFTM rigs. In addition, the NaK filling of narrow channels has to be demonstrated.

Manufacturing

The fabrication techniques developed and used for separate parts of the HFTM container and rigs will be applied to the manufacturing of 3 full rigs, constituting a complete HFTM compartment. Tolerances have to be qualified in advance, in particular the uniform brazing of heater elements. This will be performed by thermography using a state-of-the-art infrared camera and by supporting X-ray micro-tomography by the group of Ion Tiseanu, MedC Bucharest. The irradiation capsules will be filled by small scale irradiation specimens as foreseen in IFMIF. Three complete sets of specimens (3 capsules each about 90 specimens) have to be fabricated for this purpose.

NaK filling of narrow channels for improving 3d-heat transfer has to be demonstrated in glove boxes and will be checked afterwards by X-ray micro-tomography.

Two rig casings, made of AISI 316 (DIN 1.4301) and Eurofer steel, resp., have been produced already according to the detailed drawing in Fig. 1. The third one, again of AISI 316, is underway. They were manufactured by milling, stress-free annealing and spark erosion of the interior. The outside was directly spark eroded to form the rib structure on the surface. The manufacturing of the capsules started with the coarse and fine milling of the outside of the capsule casing from a massive slug. It followed the milling of the grooves by a 5-axes milling machine. For the embedding of the heater wires into the grooves a special clamping device was required to fix mechanically the wires at the long sides of the capsules. The wires were brazed to the capsule wall with help of the braze guidance box described above. The outer surface was ablated down to the original capsule surface by spark erosion. Finally the interior was spark eroded to obtain the specimen volume.

Additional parts for the irradiation rigs were produced according to the details given in Fig. 2. The lower plug cap for the capsule was milled and spark eroded similar to the other pieces. The upper axial reflector was milled from the outer side, holes for the thermocouple and for the two heater cold end ducts were drilled. The upper plug cap was manufactured quite similarly; the ducts have been attached by welding. As one rig will be tested in the single-rig compartment of ITHEX, an additional lower entrance part, resembling the HFTM lower reflector, has been produced as shown in Fig. 2. This piece will be welded to the bottom of the rig.

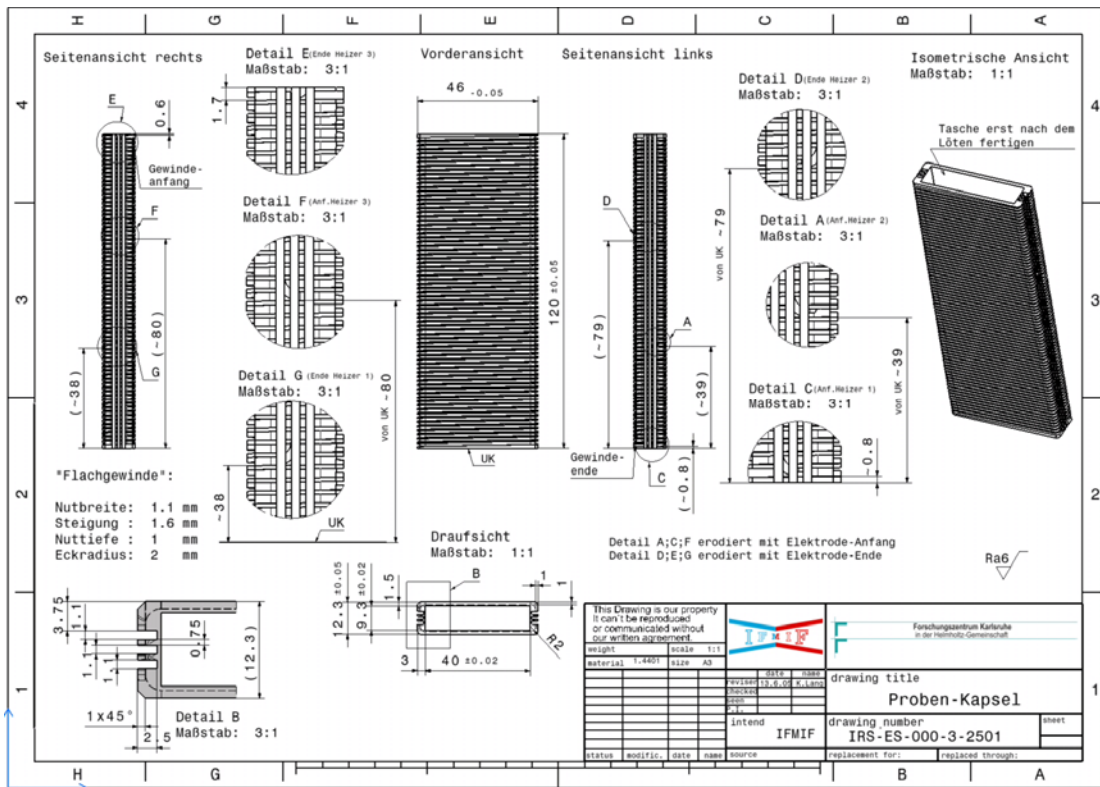
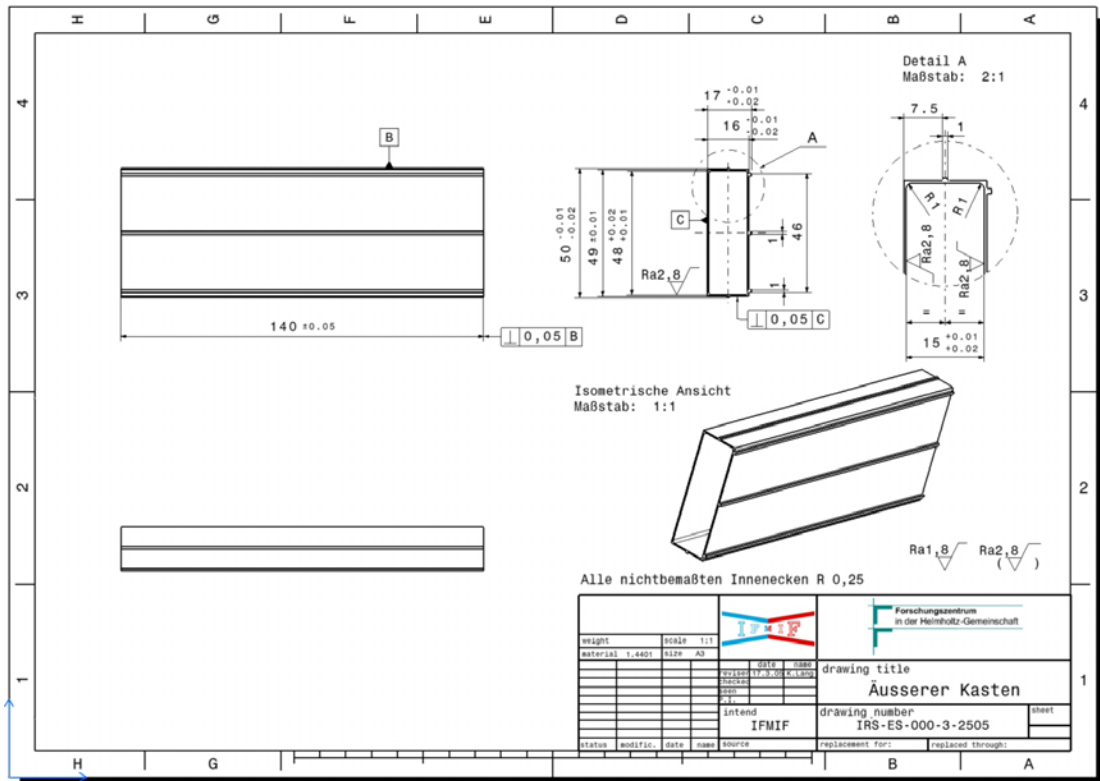


Fig. 1: Technical drawings for rig and capsule.

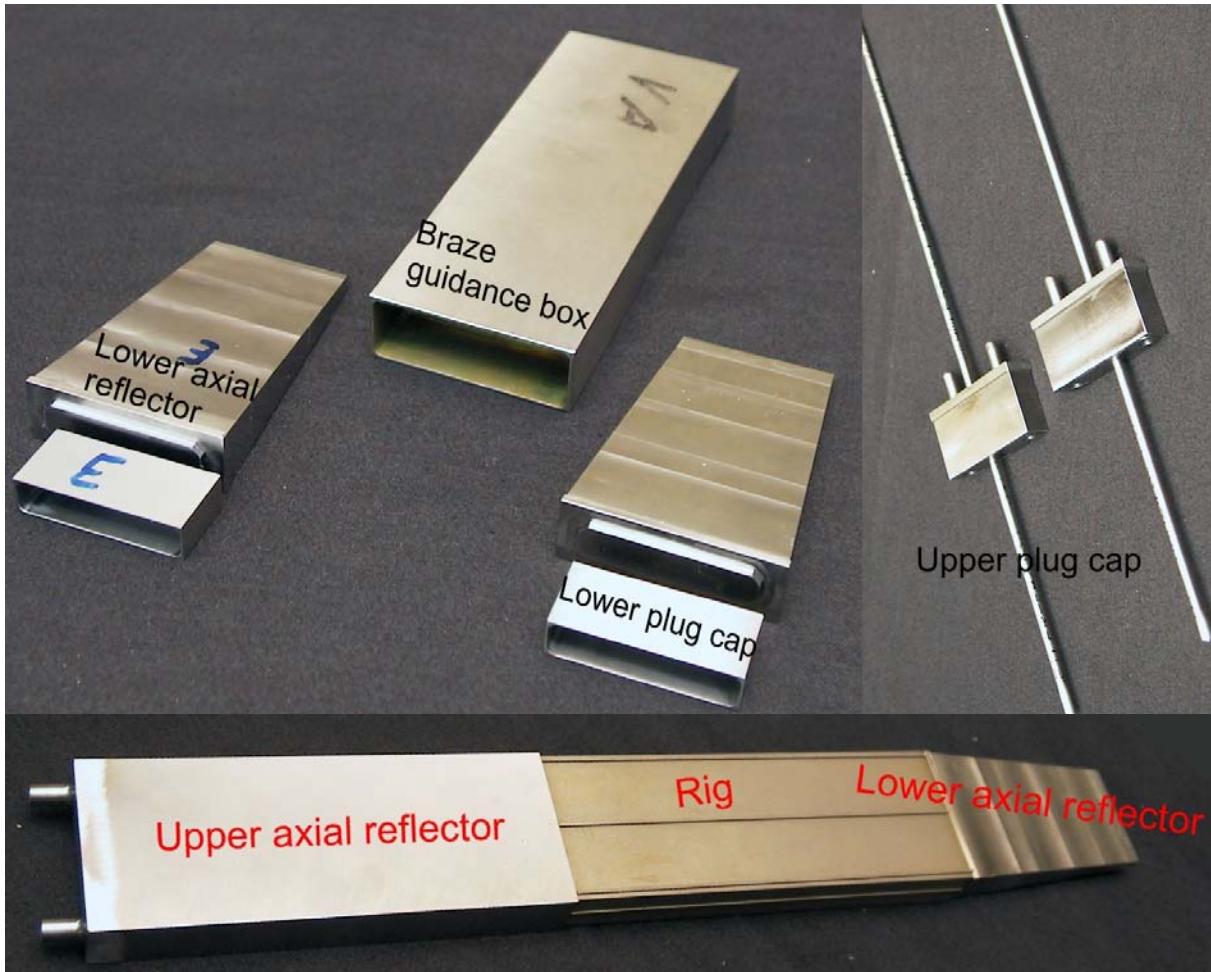


Fig. 2: Pieces of the full rigs ready for the final assembling.

The IFMIF specific small scale specimens have been produced from Eurofer for the three capsules. The reference specimen packing scheme has been used with two identical bundles of specimens per capsule. In total 36 pc. Fatigue (with holder), 72 pc. Tensile, 36 pc. Charpy bend-bar, 18 pc. Creep, 60 pc. Fracture Toughness, and 18 pc. Crack Growth specimens have been machined.

Since the suggested vacuum oven for the brazing procedure has shown large temperature deviations, the further manufacturing has been interrupted. In addition, specific braze samples (see Fig. 3) are prepared similar to the capsule design to test the braze procedure in probably two options. This will be performed soon. Similarly, a glove box for Na filling will be available for a test capsule (see Fig. 3), which is manufactured at the moment.

Conclusion and outlook

Although the manufacturing has been delayed due to lack of man-power, availability of tools and problems with the braze oven temperature, it is expected to proceed with braze and Na filling samples very soon. The results obtained should give confidence in the quality of the manufacturing route for the HFTM rigs. The final procurement of the three rigs is foreseen till April 2007.

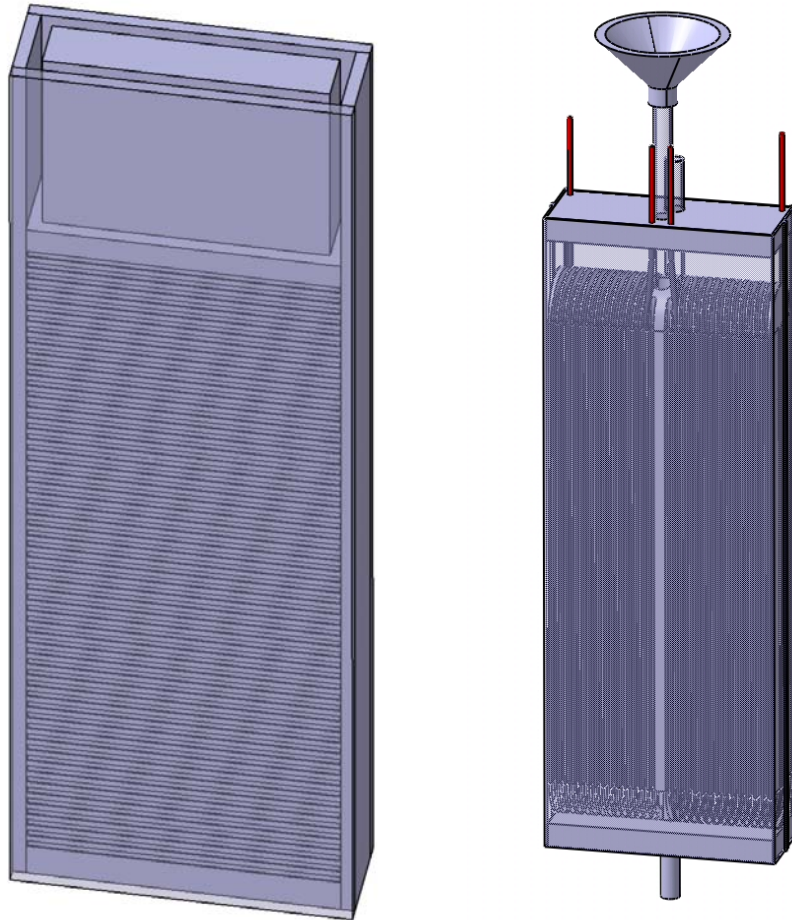


Fig. 3: Models of the braze sample (left) and NaK-filling sample (right).

Staff:

O. Albrecht
F. Arbeiter
V. Heinzel
D. Leichtle
E. Stratmanns

TW6-TTMI-003 D 3

Development of Activation Foils Dosimeters for the Determination of IFMIF-relevant Flux Spectra: Analytical Tools

The objective of the task is the development of analytical tools and procedures for the determination of neutron spectral fluxes in the IFMIF test cell by the dosimetry foil technique. This procedure also foresees the verification of the method at the NPI/Řež cyclotron in a white neutron spectrum extending up to 35 MeV (Task TW6-TTMI-003, Deliverable D 4).

Methodological approach

The International Fusion Material Irradiation Facility (IFMIF) will provide an accelerator based intense neutron source with a white spectrum extending up to 55 MeV for high fluence irradiations of fusion reactor candidate materials. Numerous computational efforts have been undertaken so far to simulate the IFMIF neutron source and to predict the spectral neutron fluxes and nuclear responses in the specimens and other components located inside the test cell, e.g., see [1]. During the IFMIF operation experimental methods will be needed to measure and monitor the neutron flux and to validate in such a way the computational tools and data developed for the neutronics predictions.

The IFMIF facility comprises two deuteron beams impinging on the Li-jet target. Just behind it the High, Medium and Low Flux Test Modules (HFTM, MFTM, LFTM) are located to house the specimens for long term irradiations. This equipment is located inside the concrete bunker (test cell) so the distance from the d-Li neutron source to the wall amounts 1.5 - 2 m. The neutron spectra calculated inside the HFTM, MFTM and at the surface of the front (d-beam downstream) test cell wall are shown in Fig. 1. These spectra have been calculated using the McDeLicious code [2] with recently evaluated d-Li cross section data [3] and a 3-d geometrical model of the test cell. As it is seen the spectra are smooth and decreasing functions of the neutron energy up to 55 MeV, do not contain a prominent 14 MeV peak due to (i) the angular smoothing of direct contribution from the volume d-Li neutron source even to the relatively small detector and (ii) the multiple scattering on bulk test modules and other surroundings. Such *a priori* information about the spectra structure is important for the unfolding procedure, for which the calculated energy differential fluxes could be used as a guess ones.

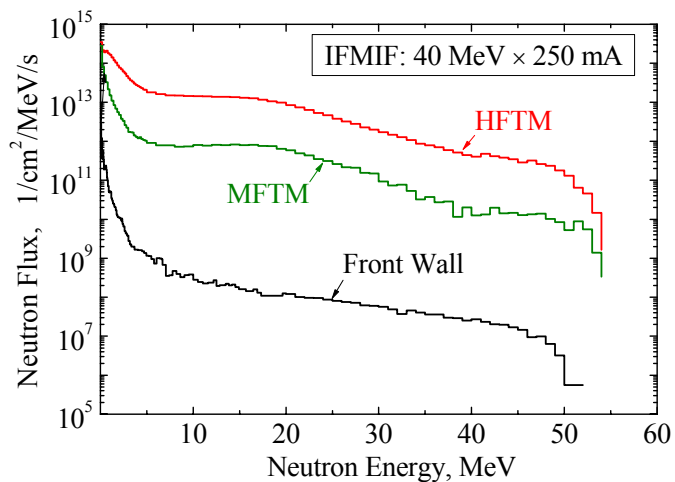


Fig. 1: Energy neutron flux calculated by the McDeLicious code for the IFMIF subsystems: inside the High Flux Test Module (HFTM), the Medium Flux Test Module (MFTM) and on the front wall of the test cell.

The dosimetry foil method makes it possible to reconstruct the neutron spectrum from γ -activities of the unstable nuclear produced by the neutron activation reactions in a set of the materials called dosimetry foils or detectors. For the reliable completion of this procedure a set of dosimetry reactions sensitive to the different energy ranges of the spectra are needed. Table 1 lists the elements and neutron reactions which may be suitable for this purpose. As a guide the international dosimetry reaction file IRDF-2002 [4] was taken since it contains the evaluated cross sections and its uncertainties based on numerous measurements (it is stan-

standard dosimetry library below 20 MeV). Above this energy, the evaluations are available in the European Activation File EAF-2005 [5] up to 55 MeV, ENDF/B-VI.8 [6] up to 30-150 MeV and the Intermediate Energy Activation File IEAF-2001 [7] up to 150 MeV. It seems reasonable to include in this list also other reactions on the same elements to have more dosimetry reactions with a minimum number of foils.

Table 1: Dosimetry reactions relevant for the white neutron spectrum determination up to 55 MeV with indication of pure target element melting temperature, decay half life of residual nuclei and energy range where cross section exceeds its half maximum. The upper energy limits of IRDF-2002 and ENDF/B-VI.8 libraries and available experimental data are listed. Reactions highlighted in grey were used for neutron spectrum determination at U120M cyclotron of NPI/Řež.

Dosimetry Reaction	Melting Temp., °C	Half Life T _{1/2}	Energy (σ > σ ^{max} /2) MeV	Upper Energy Limit, MeV		
				IRDF 2002	ENDF B-VI.8	Experim. Data
Reactions with maximum cross sections below 10 MeV						
⁹³ Nb(n,n') ^{93m} Nb	2477	16.1 y	2 – 10	< 20	< 150	< 15
¹⁰³ Rh(n,n') ^{103m} Rh	1964	0.94 h	2 – 11	< 20	< 20	< 17
¹¹⁵ In(n,n') ^{115m} In	156	4.49 h	2 – 11	< 20	< 20	< 20
Reactions with maximum cross sections between 10 and 20 MeV						
²⁷ Al(n,α+) ²⁴ Na	660	14.9 h	8 – 18	< 20	< 150	< 50
^{nat} Ti(n,x) ⁴⁸ Sc	1668	1.82 d	10 – 30	< 20	< 20	< 20
⁵⁵ Mn(n,2n) ⁵⁴ Mn	1246	312.3 d	14 – 25	< 20	< 20	< 40
^{nat} Fe(n,x) ⁵⁶ Mn	1538	2.58 h	8 - 18	< 20	< 150	< 15
⁵⁹ Co(n,α+) ⁵⁶ Mn	1495	2.58 h	10 - 18	< 20	< 20	< 20
⁵⁹ Co(n,p) ⁵⁹ Fe	1495	44.5 d	8 – 25	-	< 20	< 55
⁵⁹ Co(n,2n) ⁵⁸ Co	1495	70.9 d	13 - 27	< 20	< 20	< 75
^{nat} Ni(n,x) ⁵⁷ Co	1455	271.8 d	13 – 30	-	< 150	< 150
^{nat} Ni(n,x) ⁵⁸ Co	1455	70.86 d	3 – 15	< 20 ^b	< 150	< 150
^{nat} Ni(n,x) ⁶⁰ Co	1455	5.27 y	8 – 17	< 20 ^b	< 150	< 20
⁸⁹ Y(n,p) ⁸⁹ Sr	1552	50.5 d	10 – 30	-	< 20	< 20
⁸⁹ Y(n,2n) ⁸⁸ Y	1552	106.7 d	14 – 25	< 20	< 20	< 28
⁹⁰ Zr(n,2n) ⁸⁹ Zr	1855	3.2 d	9 – 20	< 20	< 20	< 28
⁹³ Nb(n,2n) ^{92m} Nb	2477	10.2 d	11 – 22	< 20	< 150	< 24
¹⁹⁷ Au(n,2n) ¹⁹⁶ Au	1064	6.18 d	10 – 20	< 20	< 30	< 38
¹⁶⁹ Tm(n,2n) ¹⁶⁸ Tm	1545	93.1 d	10 – 20	< 20	-	< 28
Reactions with maximum cross sections above 20 MeV						
^{nat} Fe(n,x) ⁵¹ Cr	1538	27.7 d	32 – 55 ^a	< 20	< 150	< 150
^{nat} Fe(n,x) ⁵⁴ Mn	1538	312.3 d	28 – 55 ^a	< 20	< 150	< 150
^{nat} Ti(n,x) ⁴⁶ Sc	1668	83.8 d	7 – 45	< 20	< 20	< 112
^{nat} Ti(n,x) ⁴⁷ Sc	1668	3.35 d	20 – 40	< 20	< 20	< 20
⁵⁹ Co(n,3n) ⁵⁷ Co	1495	271.8 d	25 - 45	-	-	< 80
^{nat} Ni(n,x) ⁵⁷ Ni	1455	1.48 d	15 – 45	< 20 ^b	< 150	< 110
¹⁶⁹ Tm(n,3n) ¹⁶⁷ Tm	1545	9.3 d	20 – 35	-	-	< 30
¹⁹⁷ Au(n,3n) ¹⁹⁵ Au	1064	186.1 d	20 – 30	-	< 30	< 28
¹⁹⁷ Au(n,4n) ¹⁹⁴ Au	1064	38.0 h	30 – 40	-	< 30	< 38
²⁰⁹ Bi(n,3n) ²⁰⁷ Bi	271	31.2 y	20 – 30	-	< 150	< 40
²⁰⁹ Bi(n,4n) ²⁰⁶ Bi	271	6.2 d	30 – 40	-	< 150	< 90
²⁰⁹ Bi(n,5n) ²⁰⁵ Bi	271	15.3 d	40 – 55	-	< 150	< 100
²⁰⁹ Bi(n,6n) ²⁰⁴ Bi	271	11.2 h	50 – 70	-	< 150	< 147

After comparison available evaluated activation cross section files with experimental data for all reactions preselected for the IFMIF neutron spectrum unfolding procedure we finally have chosen the EAF-2005 library covering all needed reactions in the whole IFMIF relevant energy range, agreeing with IRDF-2002 data below 20 MeV and reasonably representing experimental points above.

To unfold the neutron spectrum we used the SAND-II code in a modified version. Originally this code and the supplemented dosimetry cross sections library (640 groups format) were developed to adjust fission type neutron spectra to the measured reactions rates [8]. Later the main subroutine of this package was modified for input the cross sections in 80 group structure covering the energy range 0.1 to 1000 MeV [9]. Since both mentioned approaches do not optimally cover the IFMIF energy range, we modified this code further to enable the use of nuclear data from the EAF-2005 library having 211 groups and covering the energies from 0.1 eV to 55 MeV. Further modifications concern the calculations of the sensitivity energy domain of dosimetry detectors.

p-D₂O neutron source spectrum determination

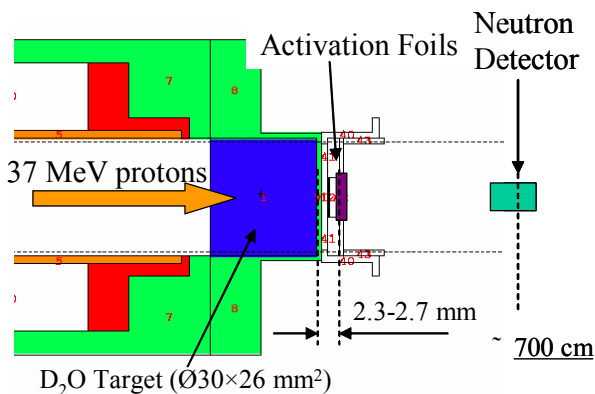


Fig. 2: Geometry (MCNPX model) of the p-D₂O neutron source at the U-120M cyclotron of NPI/Řež.

The neutron flux spectra determination by multiple foil activation method has been tested at the U120M cyclotron facility of the Nuclear Physics Institute at Řež.

A 37 MeV proton beam current of $\approx 12 \mu\text{A}$ bombarded the heavy water target, Fig. 2, and produced a white neutron spectrum which is similar to that of the IFMIF neutron source except it's cut-off at 35 MeV. This neutron source was used for the study of the activation of fusion materials [10]. This is why the spectrum at the distance 2-3 mm from the target bottom has to be known. In this experiment a stack of pure metallic foils of Al, Ti, Fe, Co, Ni, Y, Nb, Lu

and Au having a diameter of 12 mm and thicknesses ranging from 0.05 to 0.3 mm were irradiated during 9 to 12 hours in several runs. The mean proton beam current and total charge were recorded and used for the subsequent normalization of results obtained in different runs. The induced γ -ray activities were measured by high purity germanium detector (HPGe) at several cooling times from 1 h up to 100 days afterwards. These data were used to calculate specific nuclei activities at the end of the irradiation and then saturated ones A_{exp} , which could be reached during constant and infinitely long irradiation. Finally, 29 activation reactions highlighted in grey in the Table 1 and additionally $^{59}\text{Co}(n,\gamma)^{60}\text{Co}$, $^{89}\text{Y}(n,\gamma)^{90}\text{Y}$, $^{197}\text{Au}(n,\gamma)^{198}\text{Au}$ were employed for the neutron spectrum adjustment.

For the unfolding iterative procedure an initial guess neutron spectrum is needed. To get it, the spectrum at distance 700 cm was measured by with a scintillation detector having calibrated reaction recoils response function. This spectrum was renormalized to the foil stack position using $^{27}\text{Al}(n,\alpha)^{24}\text{Na}$ reaction rates measured at the different distances from the target. Below the detector threshold of 4 MeV, the spectrum was supplemented by MCNPX calculations simulating the neutron source, the target and the experimental hall.

The initial guess spectrum is shown in Fig. 3 (upper part), where the final spectrum obtained after the adjustment procedure is also displayed. The bottom part of Fig. 3 shows the ratios of calculated to measured saturated activities $A_{\text{cal}}/A_{\text{exp}}$ for all dosimetry reactions used in the present analyses. The abscissa data show the energy weighted with the product of the neutron flux and the corresponding cross section with the horizontal bars showing the mean square deviations. In such a way the sensitivity energy range for every reaction is clearly indicated. In particular one can notice that most of the used reactions are concentrated between 10 and 25 MeV, with a few at higher energy and no one between 3 and 10. To cover these energies high threshold reactions like $^{209}\text{Bi}(n,xn)$, $^{169}\text{Tm}(n,3n)$ and (n,n') reactions on ^{93}Nb , ^{103}Rh and ^{115}In (see Table 1) need to be included in the analyses.

As seen in Fig. 3 the adjustment procedure requires to decrease the initial spectrum by factor of 1.5 - 3 to bring the A_{cal}/A_{exp} ratios close to unity. On this way the iterative procedure converges after 5 - 10 iterations when the standard relative deviation between calculated and experimental activities summed over all 29 detectors reach its minimum of 7-8%.

The uncertainties of adjusted spectrum result from those of the measured activities ($\approx 4\%$) and dosimetry cross sections. Since the SAND-II code does not deal with this problem we estimated them as follows. In the energy range 10 to 25 MeV, where we have 21 dosimetry detectors, the uncertainties of the spectrum could be assessed as a mean square deviation of A_{cal}/A_{exp} ratios from unity, which amounts to 3%. Above 25 MeV, where only two reactions $^{59}\text{Co}(n,3n)^{57}\text{Co}$ and $^{197}\text{Au}(n,4n)^{196}\text{Au}$ were used in the adjustment procedure, a dominant contributor is the cross section uncertainty of these reactions. We estimate them at a level of 20 - 30% as mean deviations of EAF-2005 cross sections from measured ones. Further independent experimental validation of the unfolding procedure and its uncertainties by proton-recoil telescope technique is presently under way.

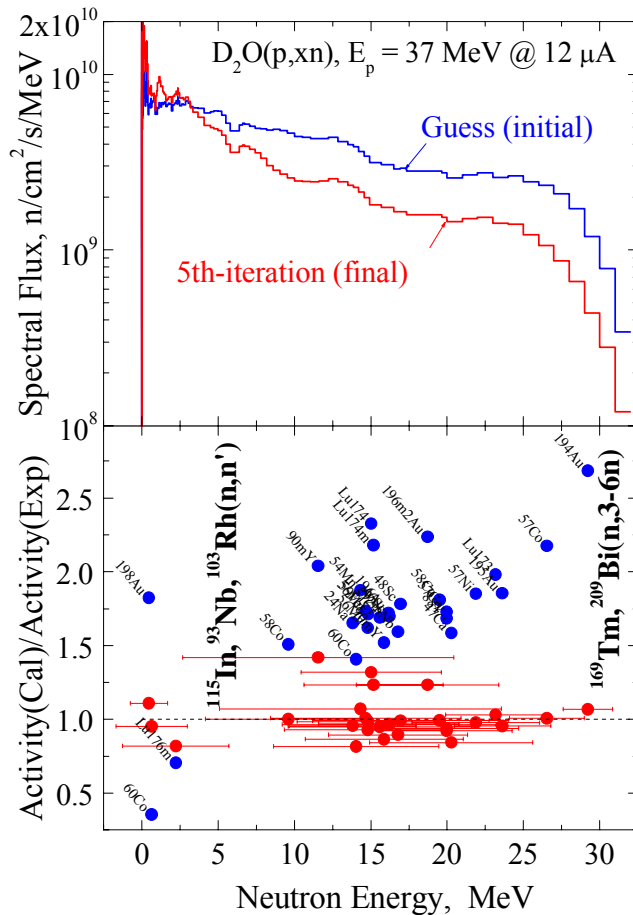


Fig. 3: Upper part - energy differential neutron fluxes at distance 3.2 mm from D_2O target: guess spectrum (dash histogram) and final one (solid) obtained by SAND-II code. Bottom part - corresponding calculation to experiment activities ratios for indicated radionuclides: before (open circles) and after (closed) adjustment procedure (the reactions to be sensitive to energy range 1 to 10 MeV and above 20 MeV are shown).

Dosimetry detectors for IFMIF neutronics

Applying this method for the neutron spectra determination in the IFMIF facility we have to consider its specific conditions such as high neutron fluxes, high temperatures and restricted space inside or between the test modules for allocation of dosimetry foils. One has to take into account rather long time for foil extractions from the IFMIF test cell and delivering them to the gamma detectors (we tentatively estimate it as a few hours).

As Table 2 shows, the highest temperature during IFMIF operations will be kept in the HFTM: up to 650°C for the ferritic-martensitic steel specimens and 1100°C for vanadium alloys, in the MFTM or LFTM up to 700°C for ceramic breeder materials and 900°C for Be alloys. The temperature near the IFMIF test cell walls should be kept below 80°C to avoid the concrete overheating. Comparing these data with the melting temperatures of dosimetry foils made of pure elements (Table 1) one can note that most of them will be in a solid state during irradiation inside the IFMIF test modules, whereas indium, bismuth and for some options the gold will be melted there. This means these materials have to be encapsulated in the thin cans, which being activated have not to produce the γ -lines of the same energies.

Table 2: Maximum temperatures, mean neutron fluxes and activities of the reaction products $^{115}\text{In}(n,n')^{115\text{m}}\text{In}$, $^{27}\text{Al}(n,n')^{24}\text{Na}$ and $^{197}\text{Au}(n,4n)^{194}\text{Au}$ after 10 hours irradiation of dosimetry detectors in the different IFMIF test cell components and close to the p-D₂O neutron source at U120M cyclotron.

Parameter	IFMIF (d-Li: 40 MeV @ 250 mA)			U120M (p-D ₂ O: 37 MeV @ 10 μA)
	HFTM	MFTM	Front Wall	
$T_{\text{max}}, ^\circ\text{C}$	650 - 1100	700 - 900	80	≈ 30
n-flux, n/cm ² /s	$7.3 \cdot 10^{14}$	$1.4 \cdot 10^{14}$	$1 \cdot 10^{12}$	$5 \cdot 10^{10}$
Activity, Bq/kg:				
$^{115\text{m}}\text{In}$	$5 \cdot 10^{14}$	$3 \cdot 10^{13}$	$4 \cdot 10^{11}$	$4 \cdot 10^{10}$ (calc.)
^{24}Na	$1 \cdot 10^{14}$	$7 \cdot 10^{12}$	$2 \cdot 10^9$	$2 \cdot 10^{10}$ (exp.)
^{194}Au	$8 \cdot 10^{12}$	$5 \cdot 10^{11}$	$3 \cdot 10^8$	$8 \cdot 10^8$ (exp.)

The high neutron flux in the IFMIF test modules will result in a high activity of the residual nuclei and hence a possible overloading of the γ -ray spectrometer. For the sake of assessment we calculated induced activities for the three dosimetry reactions $^{93}\text{Nb}(n,n')^{93\text{m}}\text{Nb}$, $^{27}\text{Al}(n,\alpha)^{24}\text{Na}$ and $^{197}\text{Au}(n,4n)^{194}\text{Au}$ (each sensitive to the different energy regions of the IFMIF spectra) after 10 h irradiation in HFTM, MFTM and on the front wall of the test cell. In Table 2 they are compared with those measured or calculated during irradiation close to the p-D₂O neutron source at the U120M/NPI facility. It shows that the same sizes and mass dosimetry foils can be used for the neutron spectrum determination in the vicinity of the IFMIF test cell walls. For the case of the medium and high flux test modules the foils size/mass can be reduced by 2 – 4 orders of magnitude, thus opening the possibility for allocation of the miniaturized dosimeter detectors at any point there.

The neutron spectrum determination procedure requires the knowledge of the time profile of d-Li neutron source intensity (ideally it should be constant) during the dosimetry foils irradiation. This means that detectors monitoring on-line the deuteron beam current and neutron intensity have to be integrated in the IFMIF facility.

The dosimetry foil method could be used for the measurement of the total neutron fluence (time integrated neutron intensity at the point of interest) during irradiation campaign. The basic condition for this is following: the half life of the residual isotope, $T_{1/2}$, has to exceed essentially the irradiation period. For example, $^{93}\text{Nb}(n,n')^{93\text{m}}\text{Nb}$ ($T_{1/2} = 16$ y) and $^{209}\text{Bi}(n,3n)^{207}\text{Bi}$ ($T_{1/2} = 31$ y) activation reactions are suitable monitors for the total neutron fluence measurements along 8 - 15 years irradiation period, being sensitive to the different energy domains of the IFMIF spectrum 2-10 MeV and 20-30 MeV, correspondingly. The Nb and Bi miniaturized foils could be easily integrated together with specimens under investigation inside the IFMIF test modules for the long term irradiation.

Conclusions

The activation foil method has been proposed for the neutron spectrum and neutron fluence measurements in the IFMIF facility. Suitable elements were selected with dosimetry reactions having thresholds and effective cross sections covering the whole IFMIF energy range. The available evaluated nuclear data libraries and experimental data were carefully screened. The EAF-2005 library with 211 energy group structure was selected representing all desirable dosimetry cross sections in the energies from thermal to 55 MeV. It was also shown that further measurements and evaluations of high threshold activation reactions such as (n,xn) with $x > 3$ on Co, Tm, Bi and Au are of high importance since their uncertainties are presently assessed at the level of dozen percents and directly propagate into the final neutron spectrum.

For the determination of the neutron spectra from the induced γ -activities the unfolding code SAND-II was applied after having it modified for the use of the selected dosimetry cross sections above 20 MeV.

Staff:

U. Fischer
S.P. Simakov

NPI/Řež, Czech Republic
P. Bém
V. Burjan
M. Götz
M. Honusek
V. Kroha
J. Novák
E. Šimečková

Literature:

- [1] S.P. Simakov, U. Fischer, A. Möslang, P. Vladimirov, F. Wasastjerna, P. Wilson, Neutronics and activation characteristics of the International Fusion Material Irradiation Facility, *Fus. Eng. Des.* 75-79 (2005) 813-817.
- [2] S.P. Simakov, U. Fischer, U. von Möllendorff, I. Schmuck, A. Konobeev, P. Pereslavl'tsev, Advanced Monte Carlo Procedure for the D-Li Neutron Source Term Based on Evaluated Cross-Section Files, *J. Nucl. Mat.* 307-311 (2002) 1710-1714.
- [3] U. Fischer, M. Avrigeanu, P. Pereslavl'tsev, S.P. Simakov, I. Schmuck, Evaluation and Validation of D-Li Cross-Section Data for the IFMIF Neutron Source Term Simulation, *Proc. of ICFRM-12* (in print).
- [4] International Reactor Dosimetry File – 2002. Technical Report TECDOC, IAEA Vienna 2006 (in print).
- [5] R.A. Forrest, J. Kopecky and J-Ch.Sublet, The European Activation File: EAF-2005 cross section library, Report UKAEA FUS 515, Culham, January 2005.
- [6] Evaluated Nuclear Data File (ENDF), available from the Web Site of Brookhaven National Nuclear Data Center <http://www.nndc.bnl.gov>.
- [7] U. Fischer, D. Leichtle, U. von Möllendorff, I. Schmuck et al., Intermediate Energy Activation File IEAF-2001, NEA Data Bank, Paris, NEA-1656/01 (2001), RSICC Oak Ridge, DLC-217/IEAF-2001 (2002).
- [8] "SAND-II-SNL Neutron Flux Spectra Determination by Multiple Foil Activation-iterative Method", RSICC Shielding Routine Collection PSR-345, Oak Ridge 1996.
- [9] F. Maekawa, U. von Möllendorff et al., *Fus. Eng. Des.* 51-52 (2000) 815-820.
- [10] P. Bém, V. Burjan, M. Götz, M. Honusek, U. Fischer, V. Kroha, U. von Möllendorff, J. Novák, S.P. Simakov, E. Šimečková, Activation of Eurofer in an IFMIF-like neutron field, *Fus. Eng. Des.*, 75-79 (2005) 829-833.

TW6-TTMI-003 D 5

Structural Materials Selection Guideline for In-Test-Cell Components

Introduction

This task is aimed at providing designers as soon as possible with basic Materials Selection Guidelines (MSG) and recommendations for material selection using existing experimental data. This MSG is presently considered to be a one-time action as long as the IFMIF material properties handbook (MPH) and dedicated structural design criteria (SDC) are not yet available.

After a compilation of all loading parameters and operation conditions for the major test cell components, an evaluation of the relative importance of these parameters will be made giving rise to a Materials Selection Guideline for each component. Based on it, a screening of potential suitable materials will be done. Using an evaluation of already available materials properties, statements will be made, what structural material should be used for

- Li target (back plate, nozzle, coolant tubes, beam line),
- HFTM (canister, rigs, capsules),
- MFTMs (specimen clamping, pulling rods, canister, frames....),
- Test cell liner, envelope of shielding components (concrete blocks of ceiling, etc).

In addition, listings will be made on which urgent materials the data are therefore missing.

The following steps will be performed

- Collection of existing materials database: From materials property handbooks (ITER, SNS) as well as from IFMIF MPH, if available on time, from materials design limit data collections and from various publications.
- Evaluation of loading parameters and materials data, based on long term experience in the development of structural materials for fission and fusion applications, producing a Materials Selection Guideline.
- Recommendations for the selection of IFMIF structural materials based on the evaluation.
- Request on missing irradiation data: Based on existing irradiation property data and moderate extrapolations.

Results

Presently data about operation conditions of IFMIF Test Cell components are collected using official IFMIF documents, publications and presentations at various IFMIF meetings. Data about mechanical behavior of irradiated austenitic and ferritic-martensitic steels are collected from the literature.

However, the results on mechanical properties of reduced activation steels after irradiation in the HFR, Petten (SPICE) and BOR60, Dimitrovgrad (ARBOR) are only partly available at present. Post irradiation experiments (PIE) on the samples irradiated in HFR are currently performed in the FZK hot cells. The results will be available in the next 2-3 month. Additional data for the samples irradiated in BOR60 (30-40 dpa) will be also available next year.

Conclusions

The work on the task was started, however due to the delay with PIE after irradiations performed at HFR and BOR60 the task completion is delayed by six months.

Staff:

A. Möslang
P. Vladimirov

EFDA/05-1291 (TW5-TTMI-003a) Preliminary Design Description Document for the IFMIF Test Facility

Background and Objectives

During the last few years a sound design of the different Facilities of IFMIF has been developed, with special European responsibility in the Test Facility. The scope of this work is to produce a preliminary Design Description Document (DDD) for the IFMIF Test Facility based on the design work already done so far for the IFMIF systems. This report will document and summarize the work already done in relation with the Test Facility and shall identify future R&D activities, if needed.

Preparation

The DDD of the IFMIF Test Facility comprises parts in the responsibility of UKAEA, IMF and IRS. IRS will be responsible for the final edition of the DDD document, which a clear distinction of the different contributions.

A first meeting on 20.06.2006 with participants from the contributing partners and EFDA has defined a common framework and a general agenda of the content. The DDD will consist of the following parts:

1. Introduction and general description: IFMIF and its mission, general user requirements (Test Facility)
2. Design requirements: operational, technical, remote handling, safety and maintainability requirements
3. Engineering Description: from overall system description to test modules and instrumentation
4. Performance Analyses: Nuclear, thermohydraulic, mechanical analyses and operational scenarios
5. Manufacturing and Assembly: mainly on the High Flux Test Module
6. Remote Handling Procedures
7. Safety requirements and waste management

In the meantime major parts have been prepared, especially to chapters 3 and 4. It has been realized that other parts may be collected from the documentations already published by the international IFMIF team.

Conclusions and Outlook

The document has been elaborated and in the course of a monitoring meeting in November 2006 the partners discussed the progress and identified pending issues. The final document will be prepared and edited with reviewing from the partners and EFDA by the end of January 2007.

Staff:

F. Arbeiter
B. Dolensky
U. Fischer
S. Gordeev
V. Heinzel
D. Leichtle

A. Möslang
S. Simakov
V. Slobodtchouk
E. Stratmanns
P. Vladimirov

TTMI-004 IFMIF – Design Integration

TW6-TTMI-004 D 2

Proton and Deuteron Induced Activation and Dose Rates of the EVEDA Accelerator Prototype, Including Beam Dump. Proposals for Operational Scenarios of Low Activation

The objective of this task is the assessment of the activation of the reference IFMIF-EVEDA prototype accelerator (including the beam dump) caused by deuteron and proton beam losses and calculation of the resulting γ -dose rates around the activated accelerator components. The radioactive inventories produced in the accelerator components (Al, Cu, Nb) and beam dump materials will be calculated by using available beam losses estimations and deuteron and proton induced activation reaction cross sections.

The results presented in this report are available in [1].

Methodological approach

The IFMIF facility comprises two deuteron accelerators. Each of them is designed as consisting of: (I) deuteron ion source – produces 140 mA D⁺ ions at energy 95 keV; (II) Low Energy Beam Transport - guides deuterons to accelerator; (III) Radio Frequency Quadrupole accelerator (RFQ) - bunches the beam and accelerates to 5 MeV; (IV) Drift Tube Linac – accelerates ions to 40 MeV energy; (V) High Energy Beam Transport – directs the beam to the Li-jet target.

The goal of the present task is assessment of the radioactivity induced in the RFQ accelerator during its operation. For this purpose we employed the European Activation System EASY-2007.0 consisting of the inventory code FISPACT-2007 and European Activation Library EAF-2007 for protons and deuterons up to 55 MeV [2].

At the first stage, the status of the relevant charged particle cross sections has been studied. As an example, Fig. 1 shows radioactive inventories produced by the 40 MeV deuterons in copper, the main structural element of accelerator. It is seen that primary attention has to be drawn to the reactions producing unstable residual nuclei, decaying with emission of high energy γ -rays and hence making dominant contribution to the radiation dose, such as $^{nat}\text{Cu}(d,x)^{62,65}\text{Zn}$ and $^{nat}\text{Cu}(d,x)^{62,64}\text{Cu}$.

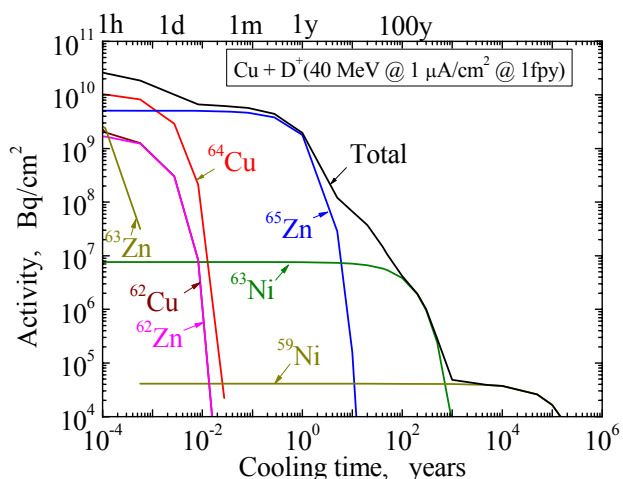


Fig. 1: Total and specific radioactive inventories produced by 40 MeV deuterons in the thick copper.

Fig. 2 shows available experimental cross sections (including the new ones recently received in NPI/Rez [3, 4]) and EAF-2005 and -2007 evaluations for the $^{nat}\text{Cu}(d,x)^{64}\text{Cu}$ reaction. In Fig. 3 these cross sections are validated against cumulative ^{64}Cu yield generated by the deuterons in the thick copper target. Regarding this results one can conclude that EAF-2007 library while reasonably reproducing the energy dependence still needs updating for the quantitative agreement with the measurements.

The activation of RFQ accelerator is caused by the losses of the charged particles occurring along the acceleration. These losses were calculated in the University of Frankfurt (task TW5-TTMI-001, Deliverable D3). Fig. 4 shows the dependence of the deuteron energy and current losses at different acceleration stages in RFQ. Using these data the radioactivity induced in the copper accelerating tubes was calculated by the EASY-2007 system. For this purpose, firstly the slowing down of deuterons in stopping material was calculated and then particle distribution along the track was converted to the energy spectrum.

The highest radioactive inventories are expected at the end of RFQ, where deuteron energy reaches the maximum of 5 MeV. For this point Fig. 5 shows decay curve for the induced radioactivity per every one meter of accelerating tubes after 1 fpy of RFQ operation. It is clearly seen that even there and even just after the beam shut down the radioactive inventory will be low the legal transport limit A2.

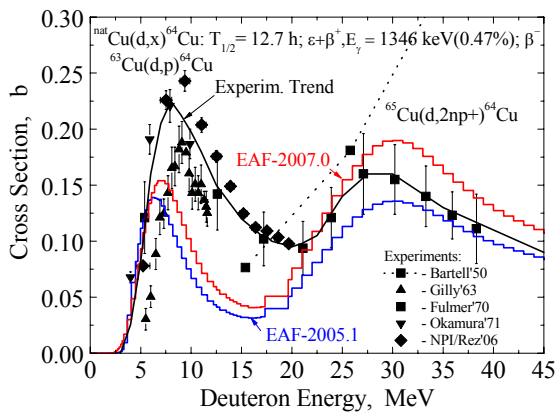


Fig. 2: ^{64}Cu production cross section in natural Cu: symbols – experimental data, histograms – EAF-2007.0 (red) and EAF-2005.1 evaluations.

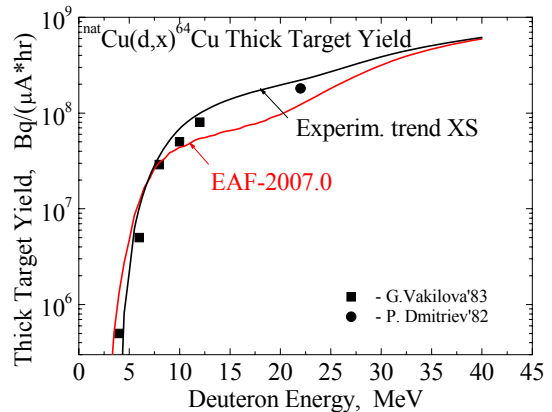


Fig. 3: ^{64}Cu production yield in the thick natural Cu target: symbols – experimental data, curves – calculated using experimental (black) or EAF-2007.0 (red) cross sections

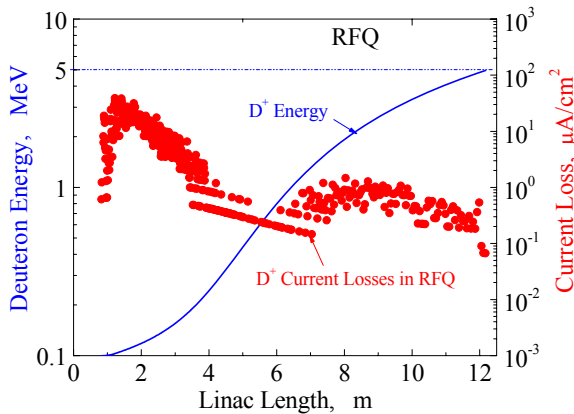


Fig. 4: Calculated deuteron energy (blue curve) and beam losses (red pints) versus RFQ accelerator length.

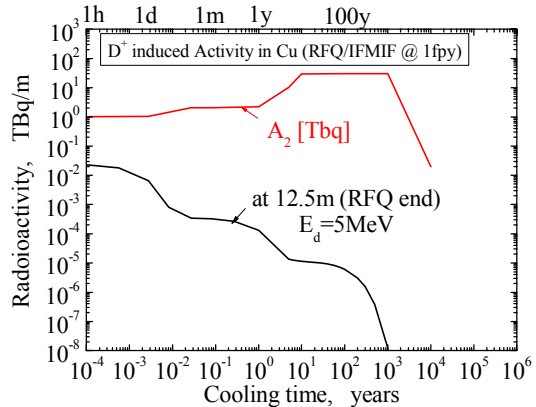


Fig. 5: Total Radioactivity generated in the copper fragments at the end of RFQ accelerator after 1 year operation (black curve) and legal transport limit A2 (red).

Conclusions

The proton and deuteron induced activation analysis has been performed for the RFQ accelerator, the first stage of the IFMIF linac, using the FISPACT/EAF-2007 activation system. The validation of EAF-2007 library against available differential cross sections and thick target

yields revealed the need of its updating. The assessed induced radioactive inventory in the RFQ fragments after 1 year operation was shown to be below the legal transport limit.

Staff:

U. Fischer
S.P. Simakov

Universität Frankfurt, Germany:
H. Klein
A. Sauer
R. Tiede

NPI/Řež, Czech Republic:
P. Bém
V. Burjan
M. Götz
M. Honusek
V. Kroha
J. Novák
E. Šimečková

UKAEA, Culham Science Centre, UK:
R. Forrest

Literature:

- [1] S.P. Simakov, P. Bém, V. Burjan, U. Fischer, R. Forrest, M. Götz, M. Honusek, H. Klein, V. Kroha, J. Novák, A. Sauer, E. Šimečková, R. Tiede. Deuteron Induced Radio-Activity in Copper. EFFDOC-998, EFF/EAF Monitoring Meeting, NEA Data bank, Paris, Nov. 2006
- [2] R. Forrest. Charged particle-induced reactions in EASY-2007. EAF-2007 Workshop, Prague, Oct. 2006
- [3] P. Bém, V. Burjan, M. Götz, M. Honusek, V. Kroha, J. Novák, E. Šimečková, U. Fischer, S.P. Simakov, R. Forrest, J. Kopecký. Activation cross section benchmarks at NPI cyclotron. EAF-2007 Workshop, Prague, Oct. 2006
- [4] E. Šimečková, M. Honusek, P. Bém, L. Bittmann, V. Burjan, M. Götz, V. Kroha, J. Novák, U. Fischer, S.P. Simakov. The activation of Cu and Al by deuterons at energies up to 20 MeV. EAF-2007 Workshop, Prague, Oct. 2006

Fuel Cycle Vacuum Pumping

TW3-TTFF-VP 35

Study of Cryopump Compatibility with Carbon Erosion Products

Predicting the amount and location of co-deposited hydrocarbon films is a major challenge for ITER. Recent studies have shown that only species with very small sticking probability may reach and stick along the inner surfaces of the pumping ducts. When the inner surfaces are covered with a thin amorphous film, the hydrogen recombination coefficient may be significantly reduced so that atomic hydrogen and/or methane radicals could reach the cryopump region. Charcoal is the working material for the sorption cryopumps in ITER [1]. For a proper design of these pumps two main questions have to be addressed. What products can be formed under charcoal interaction with atomic hydrogen? Will the absorbed atomic hydrogen and possible reaction products influence the charcoal ability to adsorb hydrogen isotopes at low temperatures?

This task was dedicated to the analysis of the possible interaction between H (or D) atoms or CH₃ (or CD₃) radicals and the ITER type activated charcoal sorbent in the cryopumps. It was organised in two stages. The experimental work with radicals themselves was performed in the Institute for Physical Chemistry of the Russian Academy of Sciences (IPC-RAS), Moscow (the future Institute for Physical Chemistry and Electrochemistry) and was accomplished the last year [2]. The tests involved a radio frequency plasma induced discharge in a hydrogen/hydrocarbon gas mixture as source for atoms, radicals and excited molecules in the order of ~ 0.1% in the exposed gas flow. The varied parameters included gas pre-loading of the charcoal sample and exposure time.

The main experimental results are summarized in the following. Under charcoal interaction with H(D)/H₂(D₂) mixtures (77K), methane or deuteromethane (CD₄) was found in the mass spectrum at heating of the samples up to 300K. The total number of methane molecules and hydrogen atoms adsorbed by the charcoal was found to be comparable. This means that the sticking coefficient of atomic hydrogen for the charcoal surface is close to unity at 77K. The charcoal adsorbed the most part of atomic hydrogen entering the tube cross-section and transformed into methane.

The methane yield increased with the exposure time; for the experiments with deuterium, the CD₄ yield slightly exceeded the CH₄ yield in similar experimental conditions. The rate of methane accumulation was not directly proportional to the involved sample mass. These facts allowed to suppose that the methane formation is a reaction with sequential steps of hydrogen atoms adding to "active" centres. It is possible that at one of the steps the absorbed molecular hydrogen also takes part in the reaction on the "active" centre. For the heavier charcoal samples (~50 mg) the effects of charcoal interaction with H atoms were shadowed by the effects of molecular hydrogen sorption because of the relative insufficiency of atomic hydrogen flow. To verify this assumption, the same total amount of charcoal mass (10 mg) was constituted from different numbers of granules with different sizes, by that varying the active surface/mass ratio. It was revealed that this size effect is clearly dominating the methane formation yield in such a way that it becomes less pronounced with increasing charcoal mass involved.

When scaling this effect to ITER, it becomes very obvious that the methane formation and associated carbon consumption problem is uncritical. For the radical tests, the ratios of hydrogen flow related to charcoal mass was in the order of 1 sccm/mg, whereas at ITER, this number is of the order of 4 sccm/g, more than 3 orders of magnitude lower.

It was also shown that the atomic hydrogen did not interact with previously adsorbed methane. H(D) atoms were captured by surface "active" centres regardless of the presence of considerable quantities of adsorbed methane in micropores. After increasing the temperature (up to 300K) the samples exposed in the H(D)/H₂(D₂) mixture remained hydrogenated. There was no indication of formation of higher hydrocarbons.

Remaing experiments in COOLSORP

The second stage of the task comprised measurements in the COOLSORP facility at FZK. This is a facility which allows to measure sorption isotherms of porous materials (sample sizes of about 1 g) at cryogenic, ITER relevant temperatures [3]. The aim was to check if the consumption of carbon atoms from the matrix during formation of methane within the radical-charcoal interaction process is associated with a loss of sorption capacity. The preliminary experiments in Russia (at a limited pressure range) revealed a certain decrease (in the range of few %), which however, would be completely within the experimental error bounds.

To validate this effect more closely, a batch of exposed charcoal was produced at IPC-RAS and shipped to FZK for characterisation in the COOLSORP facility. The batch contained 14 individual samples, sealed in a glass ampoule with argon, see Fig. 1.



Fig. 1: The radical exposed charcoal sample from IPC-RAS. *Left*: In the glass ampoule, as received; *middle*: The individual samples; *right*: The total sample inside the COOLSORP test cell.

Most samples were heated up to 300K to verify that methane has been formed and, consequently, carbon has been consumed, see Fig. 2.

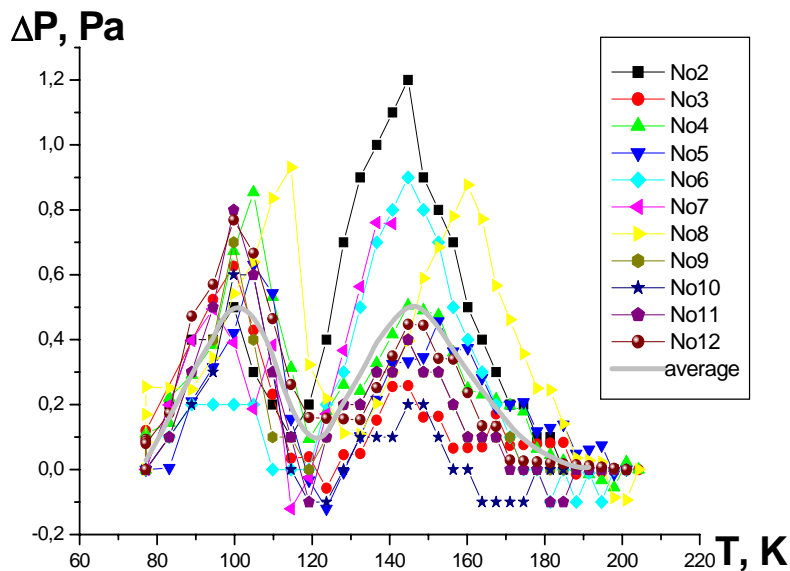


Fig. 2: Changing of pressure in the flow tube during desorption heating after charcoal exposure in H/H₂ gas mixture over 1 h (T=77K, P(H₂)=30-32 Pa, F=7 sccm) as a function of heating temperature. The peaks indicate the release of hydrogen (at about 100K) and methane (at about 150K).

The COOLSORP experimental programme is summarized in Table 1. For all conditions investigated with the exposed charcoal sample, there are data available at FZK for the standard non-exposed material for comparison. This allows for a very good comparison before and after the radical exposition.

Fig. 3 shows some comparison results. The revealed differences for the hydrogen isotopes are very marginal, for helium, the exposed charcoal features even higher sorption capacities, the reason of which is not really understood.

Table 1: List of all gas/temperature combinations investigated in COOLSORP with the H radical exposed charcoal sample.

Gas	Temperatures [K] measured in COOLSORP	IPC data for exposed material (for intercomparison)
He	4.2 10	- -
H ₂	20.4 77.4	- after H (12 to 120 mbar) after D (8 to 50 mbar)
D ₂	23.7 77.4	- -
N ₂	77.4	after H (100 to 500 mbar)
CH ₄	77.4	After H (qualitative) After D (qualitative)

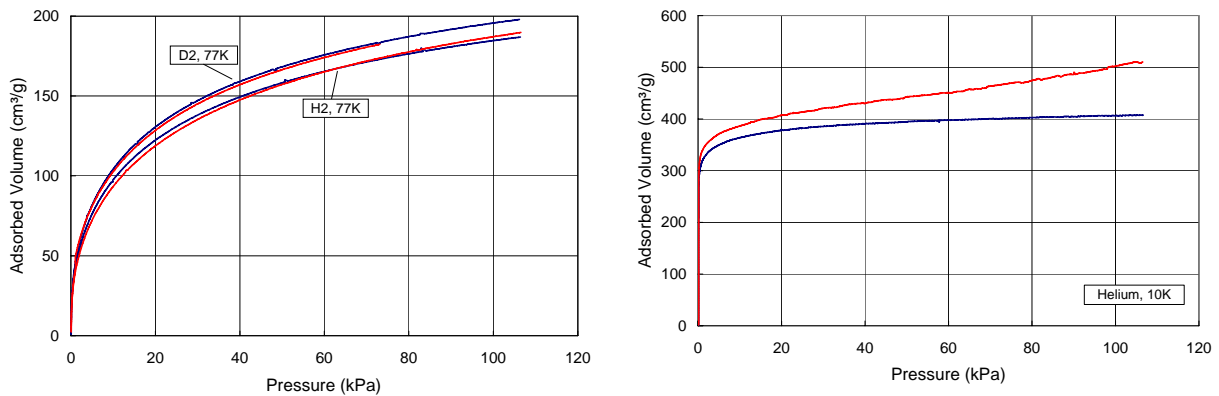


Fig. 3: Comparison of sorption isotherms before (blue colour) and after (red colour) the exposition to atomic hydrogen, for hydrogen and deuterium at 77K (left) and helium at 10K (right).

The task has been completed in 2006. No relevant deterioration of the ITER charcoal material due to hydrogen radical exposure has been identified.

Staff:

Chr. Day
V. Hauer

A.E. Gorodetsky
A.P. Zakharov (Institute of Physical Chemistry RAS, Moscow)

Literature:

[1] D. Murdoch, I. Cristescu, Chr. Day, M. Glugla, R. Lässer, A. Mack, EU fuel cycle development priorities for ITER, SOFT, Sept. 2006, Warsaw, Poland.

[2] A.E. Gorodetsky, S.P. Vnukov, R.K. Zalavutdinov, V.L. Bukhovetz, A.P. Zakharov, Chr. Day, G. Federici, Methane formation under charcoal interaction with atomic hydrogen and deuterium at 77 K, IAEA Fusion Energy Conference 2006, Chengdu, China, October 2006.

[3] Chr. Day, V. Hauer, W. Stautner, Low temperature characterization of two activated carbon materials, Carbon 2006, Aberdeen, UK, July 2006.

EFDA/04-1173 (TW4-TTFF-VP 41) Design and Procurement Specification for ITER Prototype Torus Exhaust Cryopump

Background and Objectives

The reference design of the ITER exhaust gas pumping includes 8 cryopumps to pump the torus via 4 ducts, see Fig. 1. The design of these cryopumps has to consider the different requirements for vacuum pumping, remote handling and safety, and provides strong interfaces to the surrounding environment of the installation port plugs of the ITER machine. The nominal target pumping speed of the individual cryopump to be implemented was derived in a flow and throughput analysis of the complete system using ITERVAC simulations [1].

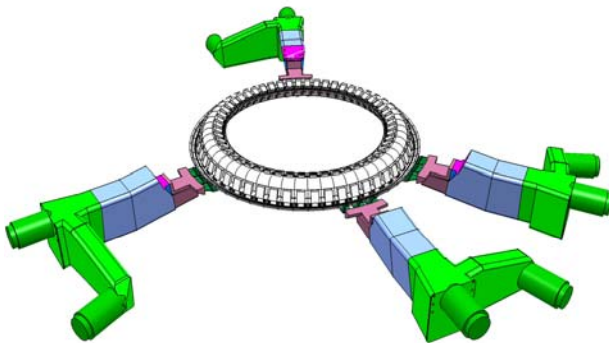


Fig. 1: ITER torus exhaust primary pumping system, showing the divertor system and the four duct connections towards the 8 cryopumps.

The aim of this task was the complete detailed design of the prototype torus exhaust cryopump (PTC), including the mechanical construction, the calculation of pumping speed and thermohydraulic properties, the definition of operational parameters and the assessment of all safety issues. The extensive data-base which has been achieved in the TIMO campaigns with the model cryopump has served as a very important reference. The basic concept of the cryosorption pumping philosophy realized in the PTC has been successfully validated in former test series at TIMO and JET as well as for NBI applications.

The PTC is a prototype device, which will be tested in the TIMO-2 facility at FZK. This test rig is an upgrade of the TIMO test bed which has already been used for the characterisation of the ITER model pump. It is anticipated that the serial pumps and the PTC will be alike, however some minor additional features have been introduced to the PTC design to ease defined testing.

ITER requirements on the torus cryopump

Pumping: The requirements on pumping are defined by the different operation modes. The key requirement in plasma operation is to maintain a typical divertor pressure between 1 Pa and 10 Pa against the high exhaust gas throughput of $153 \text{ (Pa}\cdot\text{m}^3\text{)/s}$. Different calculations showed that in combination with the limited conductance of the pumping ducts a pumping speed at the pump inlet of $50 \text{ m}^3\text{/s}$ (D_2 , 273K) per pump is reasonable. The pumping requirements for conditioning of the vessel as well as the dwell pumping between the burn pulses are depending on the preceding operation history, which determines the outgassing of the wall materials. For the dwell pumping mode at the end of the 1400 s dwell period (maximum repetition rate condition) a terminal base pressure of 0.5 mPa is required. To achieve this, the neutral beam cryopumps have to be used to assist the torus cryopumps [2]. In view of these challenging requirements, the chosen design philosophy for the individual torus cryopump was to optimise for maximum pumping speed in molecular flow regime.

Space and Remote Handling: The torus cryopump is classified as Remote Handling Class 2, which means that it does not have to be disassembled on a routine basis. The maximum possible outer cryopump diameter is 1780 mm. The available distance between the pump plug and the remote handling cask is limited to 550 mm. All parts having a length longer than that have to be designed such that they can be disassembled before starting any remote

handling operation. The pumping duct provides a maximum length of 2248 mm for the cryopump.

Safety: The maximum amount of pumped hydrogen isotopes is given by the limitation of the deflagration pressure which would result inside the cryopump under a LOVA (Loss of vacuum accident) event. The maximum allowed deflagration pressure in ITER is set to 0.2 MPa, the design pressure of the duct, leading to a maximum gas hydrogen inventory of 1.5 mol/m³ hydrogen isotopes. The ITER torus cryopump will have an open outer pump shell to reduce the hydrogen deflagration pressure by providing the larger volume of the port cell. Further, the maximum tritium inventory in all pumps open to the torus at each moment of time is set to the administration limit of 120 g. The pump plug is also working as a radiation shield that limits the radiation behind the bioshield to less than 10 mS/h. A pump plug thickness of 270 mm is therefore required.

Design description

The prototype torus cryopump is shown in Fig. 2 [3]. It is circular shaped with a maximum outer diameter of 1776 mm and a total length of about 2054 mm. The 4.5K charcoal coated pumping surface of 11.2 m² is roughly three times larger as was for the ITER model pump. The outer 80K shields and the louver baffle form an enclosure around the 4.5K pumping panels against the heat radiation from inside and outside the cryopump. The pumping speed can be varied by throttling the main valve, which opens towards the torus with a maximum stroke of 500 mm. The valve inlet diameter is 800 mm. The prototype torus cryopump can be separated into four main sub-assemblies: the pump outer shell including the pump plug, the 80K system, the 4.5K system and the pump inlet valve.

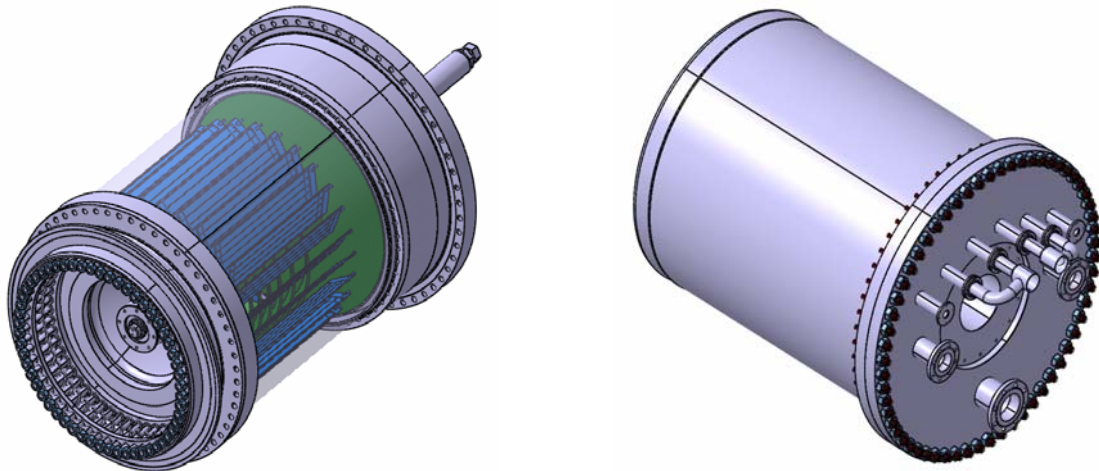


Fig. 2: Drawing of the prototype torus pump as single unit (left without outer 80K shield and housing).

Pump outer shell: The pump outer shell consists of the pump plug and the pump housing. The pump outer shell includes the gravity support of the valve and the 80K system. The shape is circular with an interior volume of about 3.1 m³. The maximum outer diameter of the pump housing is 1560 mm. The pump plug is connected with the pump housing by a double sealed flange with a connection to the service vacuum system in between to control the leak tightness of the seals. The outer diameter of the plug is 1776 mm. The pump plug includes the Johnston couplings and all vacuum flanges. The vacuum flanges are needed for the installation of the electrical feedthroughs and the forevacuum line. The pump housing and the pump plug can withstand a pressure of 0.2 MPa.

The 80K system: The 80K system (see Fig. 3) includes seven plain shields around the 4.5K panels which protect the panels from the heat radiation of the housing and the inner valve parts and the inner baffle structure. The baffle subassembly consists of 11 louver panels with

a 45° inclination for cooling the gas to be pumped and protecting the 4.5K panels against heat radiation through the pump inlet. The shields and baffles are cooled by a forced flow of gaseous helium (GHe) at a temperature of about 80K and a supply pressure of max. 1.8 MPa. Shields and baffles are connected in series to guarantee an uniform distribution of the coolant. All shields and baffles are made from hydroformed, 2 mm thick stainless steel sheets in spot-welded quilted design to exclude any plastic deformation caused by high pressures during operation.

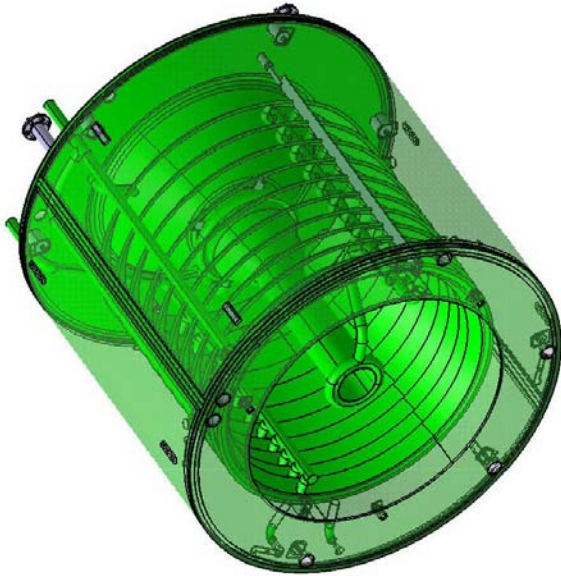


Fig. 3: 80K subassembly of the prototype cryopump.

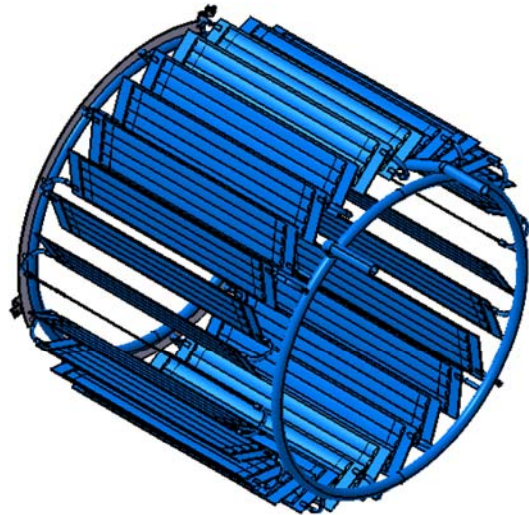


Fig. 4: The 28 panels of the prototype cryopump.

The 4.5K system: Fig. 4 shows the 28 rectangular panels of the 4.5K system which offer in total an effective pumping area of 11.2 m². This surface provides sufficient capacity for helium pumping at constant pumping speed during the complete pumping time of 600 s. The individual cryopanel is 1000 mm long and 200 mm wide. They are coated on both sides with activated carbon bound with an inorganic cement. An inclination of 45° is chosen to provide a two stage pumping, with the front side dedicated to pump gases with high sticking coefficients (e.g. hydrogen isotopes) and the back side to pump gasses with low sticking coefficients (e.g. helium), respectively. The cryopanel is cooled by a 200 g/s mass flow rate of supercritical helium at 4.5K and 0.4 MPa. The 4.5K circuit is designed in accordance with the ITER requirements for a maximum pressure drop of 0.035 MPa.

The panels arrangement consists of 4 parallel groups of 7 panels in series. Each panel will be made in line-welded quilted design with four parallel channels. The double wall panels will be manufactured from 2 mm thick stainless steel.

Inlet valve: The pumping speed can be varied by an integral inlet valve. It has a maximum stroke of 500 mm and consists of the valve disc, the valve shaft and the removable actuator assembly (see Fig. 5). It can be throttled over the complete range with an accuracy of 1 mm. The maximum time for complete opening or closing is 10 s. The valve disc is cooled by a helium flow at 300 K and 1.8 MPa. A double bellow and a double tube

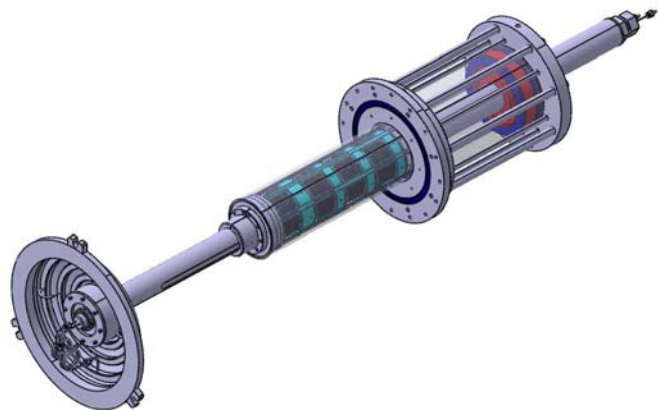


Fig. 5: Inlet valve subassembly.

structure enable to achieve the leak tightness and a double confinement around the valve shaft. All connections to outside are double sealed with a connection to the service vacuum system of ITER. The valve actuator as well as the outer part of the valve shaft can be removed to allow the remote handling of the pump.

Vacuum performance

The ITER torus cryopump is installed in connection with a duct double bellows (1350 mm ID, 1140 mm long). The pumping probabilities of the combination ITER torus pump and duct double bellows in the molecular flow regime have been calculated by Monte-Carlo simulations using the MOVAK3D-code. The results of the calculations are shown in Table 1. It must be noted that the influence of the sticking coefficient on the pumping speed (which shows a factor of 5 difference between helium and deuterium) could be effectively minimised, so that practically only the square root molecular mass influence is left. It can be estimated that the nominal pumping speed of the cryopump alone is about 50% higher than that of the cryopump and bellows combination.

Table 1: Pumping probabilities and effective pumping speeds of one ITER torus cryopump including the duct double bellows.

Gas	Pumping probabilities [%]	Effective pumping speed [m ³ /s]
Helium	12.0	51
Hydrogen	12.7	77
Deuterium	12.9	55
Tritium	12.9	45

Outlook

During 2006, a Technical Specification Document based on the design described above has been elaborated, with which EFDA has successfully carried out the call for tender procedure for manufacturing the PTC and associated fatigue testing on the actuated valve design [4]. The planned time until completion of the pump manufacturing and acceptance testing at the manufacturer's premises is 18 months. During that time, FZK will act as Technical Liaison Organisation for all technical aspects of the manufacturing [5]. After that, the PTC will be installed in TIMO-2 at FZK and parametrically tested for validation of the design and demonstration of the appropriateness of this design for the ITER series pumps.

Staff:

Chr. Day	H. Jensen
M. Dremel	A. Mack
H. Haas	R. Simon
V. Hauer	H. Strobel

Literature:

- [1] Chr. Day, A. Antipenkov, H. Haas, V. Hauer, A. Mack, D.K. Murdoch, M. Wykes, R&D and design for the mechanical and cryogenic vacuum pumping systems at ITER, European Vacuum Conference, Paris, France, April 2005, accepted for publication in *Vacuum*.
- [2] M. Wykes, P. Andrew, Chr. Day, G. Federici, Assessment of the ITER dwell pump down, Proc. 21st SOFE, Knoxville, TN, IEEE 2006.
- [3] V. Hauer, J.-C. Boissin, Chr. Day, H. Haas, A. Mack, D.K. Murdoch, R. Lässer, M. Wykes, Design of the ITER torus prototype cryopump, SOFT Conference, Warsaw, Poland, Sept. 2006.
- [4] D. Murdoch, I. Cristescu, Chr. Day, M. Glugla, R. Lässer, A. Mack, EU fuel cycle development priorities for ITER, SOFT, Sept. 2006, Warsaw, Poland.
- [5] H.S. Jensen, Chr. Day, QA efforts in manufacturing large cryopump systems for nuclear fusion application, ASEVA Summer School, June 2006, Salamanca, Spain.

TW4-TTFF-VP 45

Performance Assessment of Mechanical Pumps in Tritium Plant

The Tritium Plant of ITER requires many vacuum pumps and compressors to move tritium and other gases within the plant and to deliver gases to the fuelling subsystems of the torus, with defined mass flows during ITER pulses. Several manufacturers produce mechanical pumps suitable for tritium operation and candidate pumps for the use in the Tritium Plant have been identified and tested.

The objective of this task was to review the experience at tritium facilities, such as JET and TLK, and for selected pumps to be tested under representative conditions of the ITER Tritium Plant. Manufacturers' data for most pumps are either for discharge to atmospheric pressure (vacuum pumps) or for the inlet at atmosphere (compressors). The ITER Tritium Plant requires pumps that operate over conditions where the inlet and outlet pressures are variable and several pumps have been tested over these conditions. A further objective is to rationalise number of types of pump to as small a range as possible as this will bring benefits in operation, reliability and capital costs of the Tritium Plant.

Selected pumps from the manufacturers Thales and Metal Bellows have been tested to measure their pumping performance over a range of inlet and outlet pressures with both helium and nitrogen. On the basis of these tests and also the experience in operation and maintenance gained at TLK of these pumps, recommendations have been made with caveats for the use on the various types of pumps in ITER. The caveats note in particular the maintenance requirements and the complexity of such work inside a glove box. Replacement of a failed pump is likely to be the prime option on ITER for many pumps and this has implications for the design of glove boxes and the positioning of the pumps inside. None of the pumps selected are expected to survive the operational lifetime of ITER (20 years) if they are in continuous or near-continuous operation without either being repaired or replaced.

A draft final report was delivered in October 2006 to EFDA for comments.

Staff:

C. J. Caldwell-Nichols
S. Beloglazov
R. Wagner
S. Welte

TW5-TTFF-VP 51

Mechanical Tests and Post-operational Examination of TIMO

Background and Objectives

Following more than five years of successful performance testing of the (50% scale) ITER model torus exhaust cryopump in TIMO, the programme objective of advancing to the design, construction, installation and testing of a full scale ITER cryopump was being prepared. The activities included in the present task remained to be carried out on the existing TIMO facility before adaptation of the infrastructure to accommodate the 1:1 scale prototypical torus cryopump (PTC).

During 2006, the TIMO facility was opened, the pump was dismantled from the test vessel and undergoing multi-cycle tests of the inlet valve. Following that, the model pump was completely disassembled and all components thoroughly examined.

Evaluation of the cryogenic safety tests

The final experimental activities in TIMO focussed on the performance under a loss-of-vacuum accident (LOVA). In dedicated experiments a LOVA was simulated under various conditions with nitrogen as model inbreak gas, leading to rapid temperature increase of the normally cold pump structures, with the potential for overpressurisation of the supercritical helium (SCHe) circuits [1]. In order to design the pressure relief system in ITER properly, tests to determine the characteristics of the pressurisation (pressure level, pressure rise rate) were carried out in TIMO 2005, and evaluated in 2006. The investigated pressurisation rates were between 0.3 and 4.7 mbar/s and chosen such to simulate the ITER torus LOVA reference accident (pressurisation rate of 2.3 mbar/s) with the pump being cold. The experimental limit as given by TIMO was the 18 bar burst disc pressure of the SCHe loop (normal operation pressure is 4 bar), and the use of nitrogen instead of air.

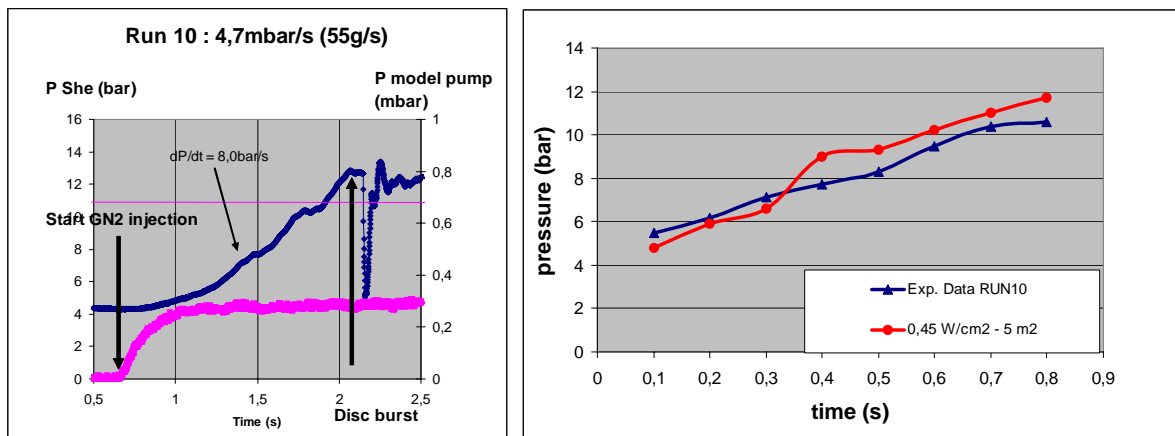


Fig. 1: Typical result of a cryogenic safety test simulating a LOVA event with a pressurisation rate of 4.7 mbar/s. The right plot correlates the measured SCHe pressure increase curves (blue curve) with a VINCENTA model calculation (red curve).

The aim was to quantify the heat loads under these conditions which can be very high (up to about 4 W/cm²) for non-insulated surfaces according to the literature. The high complexity of the cryopump interior structures which are partly blank and partly charcoal-coated, makes an a-priori modelling extremely difficult. By comparison of the experimental pressure rise curves with calculated ones using the VINCENTA code, which was recently adopted by CEA Grenoble, it was found that the best fit could be achieved for an integral averaged heat flux of ~ 0.5 W/cm², see Fig. 1 [2]. This value is of the typical low order for well defined superinsulated tanks, which can therefore be regarded as very positive result. With these tests the model pump assessment programme in TIMO was completed. The collaboration between

FZK and CEA on VINCENTA work will be continued with the aim to develop a stand-alone model.

Pump dismantling and external cycling tests of the inlet valve

The original plan to perform the multi-cycle test campaign of the inlet valve in-situ was abandoned at an early stage, after having identified a malfunction of the valve plate mounting. It was decided to first analyse this failure during the dismantling activities, before deciding on how to continue. In order to get access to the model pump itself, the cryogenic lines, the exhaust gas lines, the gas supply lines and the operation platforms in the surrounding of the pump plug had to be dismantled. Fig. 2 shows some photographs of the dismantling procedure of the actual cryopump from the test vessel.



Fig. 2: Steps of the ITER model pump dismantling from the test vessel.

The inspection of the inlet valve was the first step in the examination programme of the removed model pump. Within these activities the conjectures formulated in 2005 on the basis of a remote camera investigation could all be confirmed [3]; the examinations now clearly identified a broken tube in the cooling water loop, a damaged bellow of the inlet valve plate, but no serious damages on the sealing surface of the inlet valve seal. As the main reason for these failures in the surrounding of the valve plate, the assembled Belleville washers were identified, which were plastically deformed, probably due to a wrong material choice by the model pump main assembly manufacturer (see Fig. 3).

To check the feasibility for continuation of the multi-cycle test campaign, the leak rate of the metallic seal was measured. The results of the leak tests revealed that the sealing function of the inlet valve seal could still be provided. On the basis of this positive result it was decided to repair the damaged parts in the valve arrangement and to commence the inlet valve cycling tests.

A total of 30 000 cycles were performed. In the course of that, the tightness of the inlet valve was checked every 5 000 cycles. In addition to these leak rate measurements visual inspections at the critical parts like the Belleville washers, the bearings and the valve actuator were done. After completion, it could be shown that the metallic seal of the inlet valve can still fulfil the required tightness ($2 \cdot 10^{-2}$ mbarl/s at a pressure difference of 5 mbar).

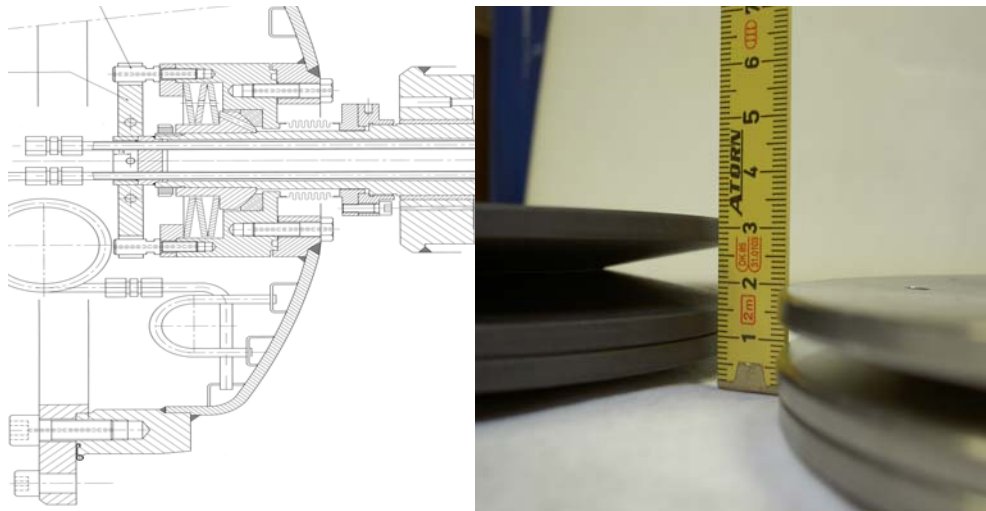


Fig. 3: Left: Drawing of the inlet valve with the construction details concerning the Belleville washers, cooling water tubes and valve plate bellows. Right: Photo showing the spring arrangements with the old Belleville washer set (right side) and the new one (left side).

However, significant wear was detected at the 5 mm sized bronze bearing (an abrasion of 1.6 mm over the total cycling time). On the valve shaft an increasing number of score marks were observed at the area of the bearing positions. And at the valve actuator side a high dust production was noticed as a result of the viton seal abrasion. Despite these mechanical damages, see Fig. 4, the functionality of the valve was always provided. Due to this lesson, special emphasis will be given to the question of friction and tribology of the valve shaft for the design and manufacturing of the 1:1 scale PTC.

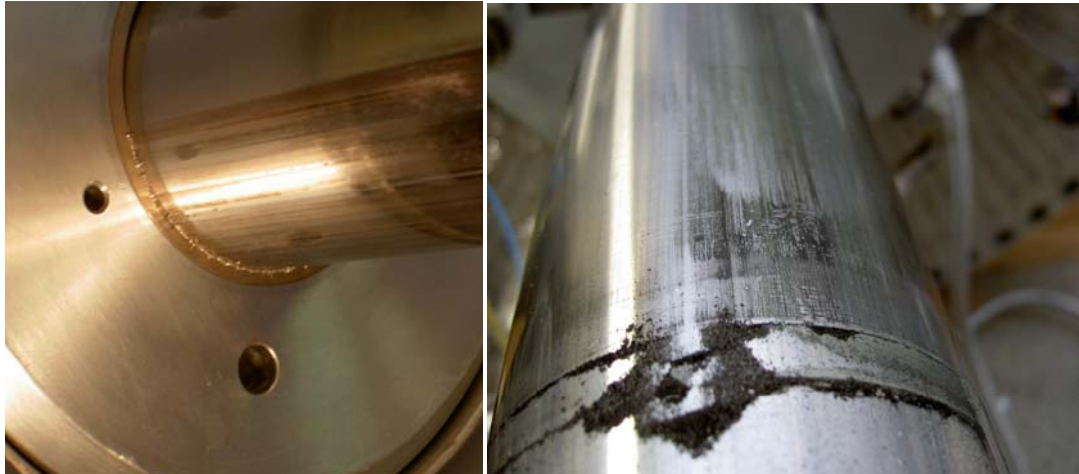


Fig. 4: The photos show the results of the valve shaft movement in the area of the inlet valve (left) and the dust at the valve actuator caused by the viton seal abrasion (right).

Post operational examination of TIMO

After the cycling test was finished, the disassembly of the model pump and the detailed examination of all parts was started. The examination programme included visual inspections, functional tests and leak tests, and comprised the following components:

- The valve actuator,
- The valve shaft bellow system,
- The inlet valve including the inlet valve bellow and the fixating devices,
- The valve shaft,

- The housing of the model pump,
- The 80K baffle rings,
- The 5K panel arrangement,
- The 80K housing including the 80K valve shaft shield and the 80 K conical shield, and
- The pump plug including the valve shaft bearings.

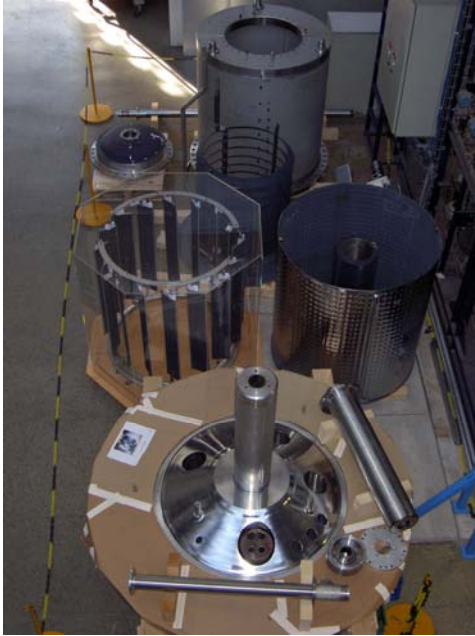


Fig. 5: Overview of the dismantled model pump parts.

Fig. 5 shows the individual pump parts, Fig. 6 illustrates the typical view of the charcoal coated cryopanel, which were in the past considered to be critical. The inspection results were very positive and did not reveal any weak points. The pump interior parts were shiny and clean, did not show aging or degradation in any respect and looked the same as during their first assembly in 1998.

About 50 g of loose solid substance was found in total in the test vessel as well as in the model pump, and was collected for further examination, chemical and elementary analysis of which is still ongoing. Most of that was wear from the valve shaft and bearing material produced during the valve cycling tests. It did also contain some small parts of the blackening coating which has fallen off.

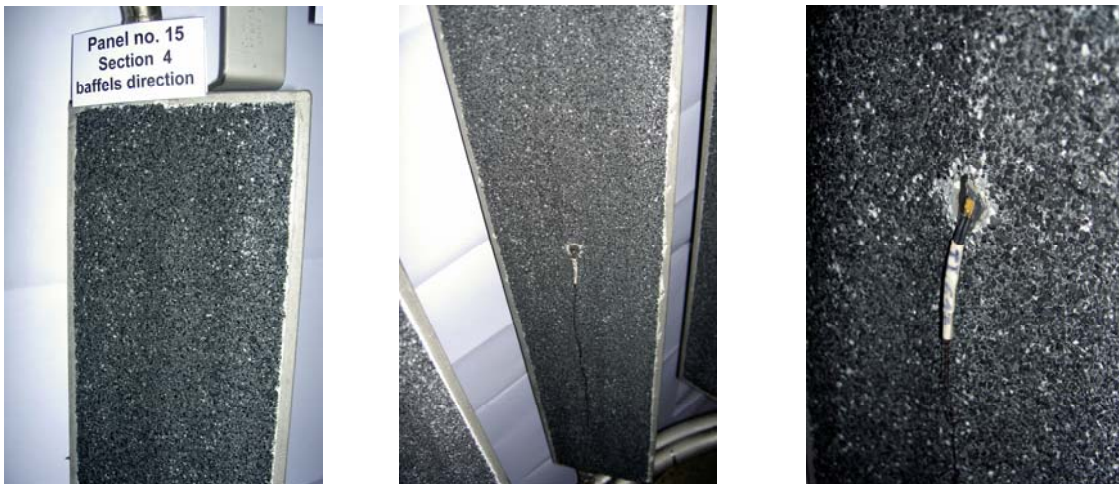


Fig. 6: The three photos exemplify the typical impression of the actual situation concerning the charcoal coating surface on the cryopanel.

To reveal any performance degradation which might have happened during the lifetime of the pump, a sample of the activated charcoal particles collected in the model pump will be subjected to sorption isotherm measurements at different temperature levels in the facility COOLSORP. The aim is to compare the test results of the used charcoal from the model pump with the results charcoal in the delivery status. This activity is planned for early 2007 and will finalize this task.

Staff:

Chr. Day
H. Haas
H. Jensen
P. Pfeil
H. Stump
R. Vallcorba (CEA Grenoble)
J. Weinhold
D. Zimmerlin

Literature:

- [1] H. Haas, A. Antipenkov, Chr. Day, M. Dremel, A. Mack, D.K. Murdoch, Experiences from the operation tests of the ITER model pump, in: L. Zhang (ed.), Proc of the ICEC-20, pp. 95-98, Elsevier, Amsterdam, 2006.
- [2] A. Girard, R. Vallcorba, Status of VINCENTA modelling, 12th ITER-EFDA-FZK Interface meeting, April 2006, ITER IDM ITER_D_24W9L9.
- [3] H. Haas, TIMO dismantling activities and preparation for TIMO-2, 12th ITER-EFDA-FZK Interface meeting, April 2006, ITER IDM ITER_D_24W9GB.

TW5-TTFF-VP 57 ITERVAC Validation Test

Background and objectives

The ITERVAC code developed at FZK has become an essential tool for the proper design of the ITER vacuum pumping systems which are at most locations characterised by very high throughputs and therefore being operated in transitional flow regime. Thus, the standard vacuum formulae and Monte Carlo codes are not applicable.

Because of the importance which is given to the calculation results of ITERVAC, the code must be extensively benchmarked. A theoretical benchmarking was done in the field of laminar and purely molecular flow, however, it has been found that literature data for (intermediate) transitional flow range, which is of major importance for the ITER conditions, are scarce and even not existing for geometries as complex as for the ITER vacuum pumping ducts. In order to validate proposed design modifications, such as to increase the conductance of the path from the divertor to the torus exhaust cryopumps, which have to be made while respecting other functions of the design (e. g. shielding, structural strength of the cassette), an experimental confirmation of the modelling results is required. One has therefore started to set-up a versatile test facility to provide a broad and relevant range of well defined experimental data which can be used to benchmark the code.

Set-up and commissioning of the TRANSFLOW test rig

The basic idea of the new TRANSFLOW test rig (Transitional Flow Experiments) is the measurement of the conductance of different channels in the transitional flow regime. The philosophy of this approach is not in first line to investigate directly a 1:1 model of the ITER duct, as this would necessitate a huge facility with expensive instrumentation. It is rather foreseen to use different interchangeable test pieces which would be modelled by ITERVAC and the measured results compared against predictions from the ITERVAC modelling calculations. For the start, a long cylindrical duct was used, for which there exist solutions for the whole range of rarefied gas flows [1]. This is also thought to validate the functionality of the facility. Following that, more exotic cross-sections will be investigated (conical, trapezoidal..).

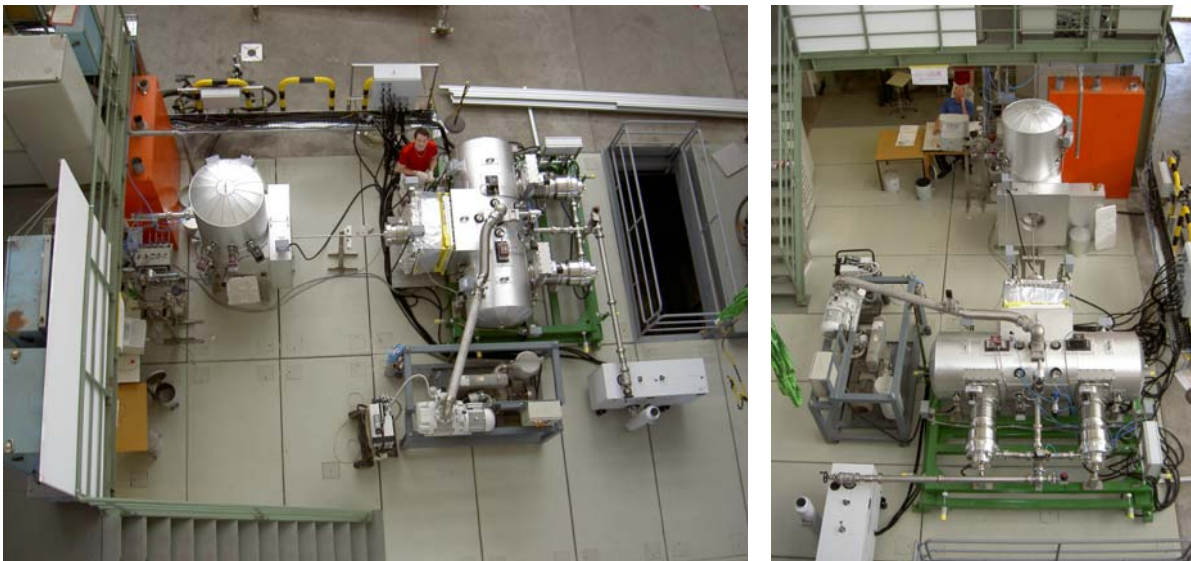


Fig. 1: Bird's eye views of the TRANSFLOW facility (commissioning at 17 July 2006).

For scale-up, the characterisation of the flow regime is done by the Knudsen number, which is between $Kn=0.5$ and 0.01 in transitional flow regime. Higher numbers indicate the molecu-

lar flow regime, lower ones the viscous flow regime. The soundness of a vacuum system in terms of gas throughput is characterised by the Mach number. Mach numbers close to unity indicate a potential bottleneck. Fig. 1 shows a bird's eye view of TRANSFLOW, with the long circular duct being installed (diameter 16 mm, length 1280 mm). The test rig can be separated into the dosing dome, two adapter flanges with the test channel in between and the pump dome. The dosing dome serves the purpose to produce an isothermal flow at a constant pressure difference through the test channel. The pump dome holds all pumps. The gas flow path comprises the first adapter flange, the test channel, the second adapter flange, the pump dome, and finally the turbomolecular pumps (2xLEYBOLD MAG 2800 l/s) with the forepumps (LEYBOLD Screw 250 m³/h). The 2 adjustable gate valves (VAT Switzerland) upstream the turbopumps can be used for reducing the pumping speed, and, by that, modifying the pressure and Kn range. Pressures and temperatures are measured in both domes. The measurements are taken at isothermal conditions. The gases helium and nitrogen are used. The typical pressure inside the TRANSFLOW test rig is in between 100 Pa and 10⁻⁶ Pa. The temperature range is in between 20°C and 200°C. For temperature regulation a heating system of both domes, the adapter flanges and the test channel is provided.

Fig. 2 shows the bare dosing dome and pump dome, respectively, during the acceptance tests at the manufacturer TRINOS, Germany (integral leak tightness better 1·10⁻⁸ (mbar·l)/s) and with the heating system being attached.



Fig. 2: Top: Photos of the dosing dome during the integral leak test at the manufacturer (*left*) and after the resistance heating system has been attached (*right*). Bottom: Correspondingly for the pump dome.

The dosing system, see Fig. 3, includes four commercial calibrated parallel thermal mass flow meters (10, 100, 1000, 10 000 sccm) and a choked flow orifice gas inlet for micro dosage below 1 sccm. The orifice device was developed in-house and especially calibrated using a vessel of known volume, see Fig. 4. The installation of the turbomolecular pumps completed the facility assembly, see Fig. 5.

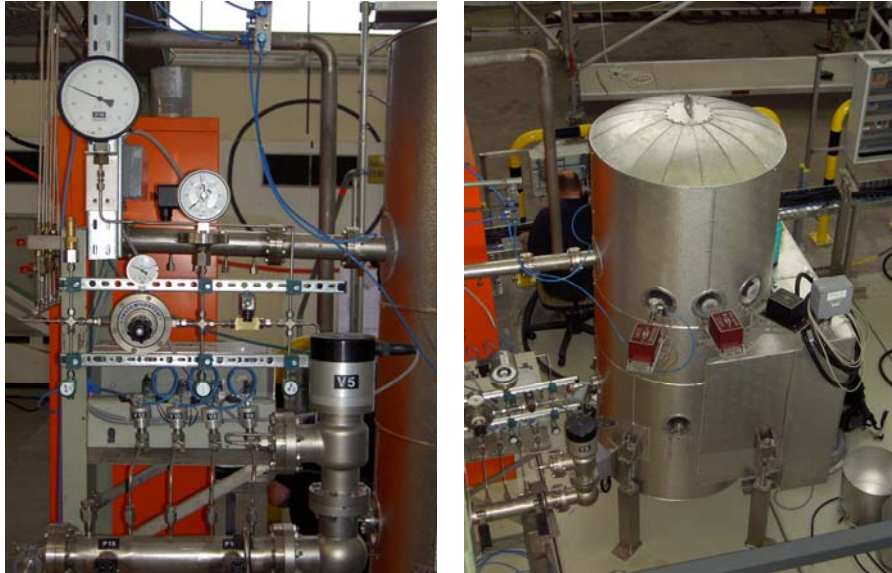


Fig. 3: *Left:* The gas dosing system, *right:* The dosing dome, fully thermally insulated, with the high precision vacuum gauges being installed.



Fig. 4: The orifice flow device for establishing very small flows, and the test set-up for its calibration.



Fig. 5: Mounting the big 2800 l/s turbomolecular pumps via the 250 CF gate valves onto the pump dome

The first operation phase of the facility was focussed on the long circular duct, followed by a square duct, see Fig. 6.



Fig. 6: Cross-sections of the first test channels: A long circular duct (diameter 16 mm), and a long square duct (hydraulic diameter 16 mm), with a length/diameter ratio of 80.

The measurements in TRANSFLOW produce an integral result of the throughput and associated pressure difference between dosing and pumping dome, where the pressure gauges are located. This result contains the influence of the domes, which is however considered to be small due to the very big size of the domes compared to the diameter of the duct, as well as of any unavoidable adapter pieces included in the flow path. The aim of the experiments is to derive the conductance of the single test channel. In order to get this, the whole TRANSFLOW facility was described in ITERVAC as a serial network of conductances, comprising 11 unit cells, according to the scheme shown in Fig. 7. Based on this model, the conductance of the actual test duct (element 5 in Fig. 7) can be deduced, which can then be compared with the values of theoretical models, if there exist any [1].

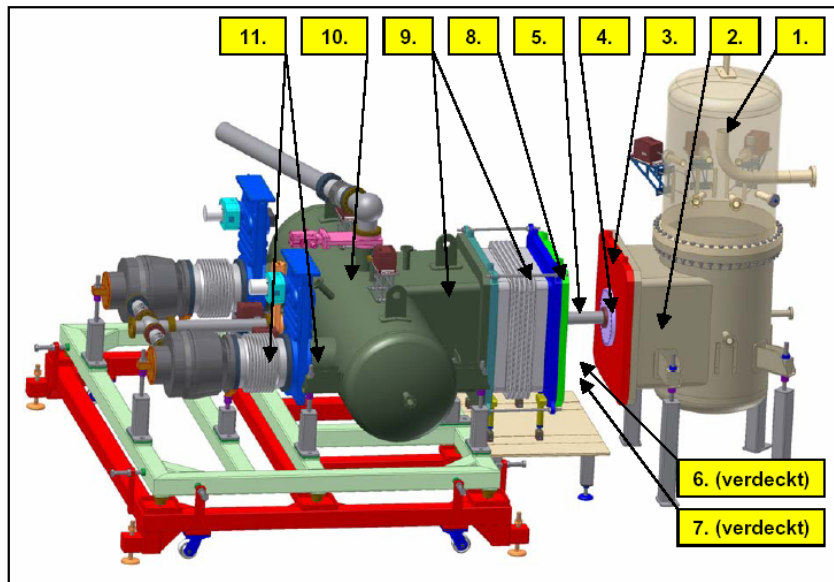


Fig. 7: Scheme for modelling the gas flow path in TRANSFLOW as a series of different unit cells for ITERVAC.

The experiments have shown good progress and some preliminary results have already been determined [2]. The experiments will be continued, thereby including other duct cross-sections, and a detailed comparison of the TRANSFLOW results with theoretical solutions will be elaborated. If evaluated positively, ITERVAC will not only be used to optimise the torus exhaust and NBI vacuum systems, but will also become an important design tool for the divertor flows, where it will be used to identify and optimise bypass leaks.

Staff:

Chr. Day
V. Hauer
H. Jensen
P. Lange (Diploma student)
R. Müller
P. Pfeil
H. Stump
St. Varoutis (Guest scientist, University Thessaly, Volos, Greece)
J. Weinhold
D. Zimmerlin

Literature:

- [1] Chr. Day, V. Hauer, G. Class, D. Valougeorgis, M. Wykes, Development of a simulation code for ITER vacuum flows, IAEA Fusion Energy Conference, Chengdu, China, Oct 2006.
- [2] P. Lange, Status TRANSFLOW and first results, 13th ITER-EFDA-FZK Interface meeting, Sept. 2006, ITER IDM ITER_D_24 ULZ6.

TW5-TTFF-VP 58 Upgrade of TIMO

Following successful completion of the testing of the 50% scale ITER model pump, a full scale ITER prototype torus cryopump (PTC) is being designed and manufactured which will be tested in the TIMO test bed at FZK [1]. Certain features of the TIMO infrastructure need to be upgraded to accommodate the larger ITER scale pump, and the scope of this task is to provide for the supply and installation of these features. The upgraded facility will be named TIMO-2. The extent of upgrading necessary has been minimised by former provision of the required additional capacity in the existing TIMO subsystems wherever possible.

Data acquisition system and PLC

In the reported year 2006 the replacement of the hardware components for the data acquisition system as well as the PLC on the basis of the Siemens PC-S7 was completed, see Fig. 1. Different sensors for flow and temperature measurement were ordered to replace existing ones which have failed (in some cases to provide redundancy).

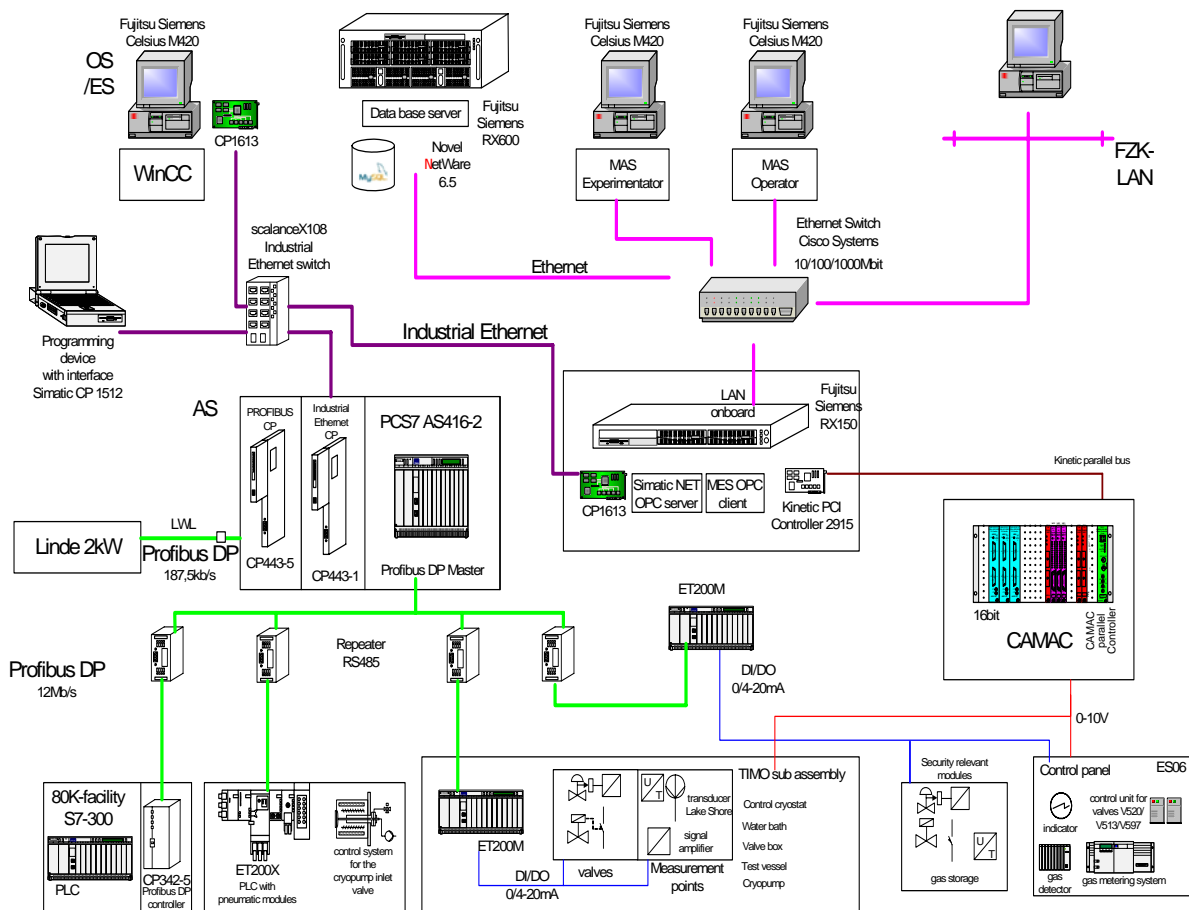


Fig. 1: Conceptual overview of the interactions between the new data acquisition, the PLC and the different parts of the test facility

The new data acquisition software based on MySQL was installed and the functional tests have started. One important issue was the transfer of all the measured data which were collected with the old system during the extended test campaigns with the ITER model pump into the new MySQL data base system. During these tests also the data transfer and communication between the PLC and MySQL were checked. A wiring plan was elaborated to prepare the hardware installation between the TIMO-2 data acquisition and PLC in the op-

eration room and the measurement points in the field of the facility subsystems. All necessary cabling and devices were specified and ordered.

Modifications of the facility subsystems

The 3000 l LHe control cryostat of the TIMO facility which provides the 4K supercritical helium was opened for refurbishment. The aim is to replace some faulty sensors and add sensors at critical points in the piping of the control cryostat to get redundant temperature measurement. All necessary sensors are procured and the installation work is in progress.

The design phase for a new ITER relevant transfer line between the valve box and the pump plug of the PTC has started. The line provides two flexibles for the supply and return of the cryogenes. This means in each line cryogenic helium at 4.5K and 80K will be transferred. In addition to these flexible lines a fixed part is foreseen at the connection to the valve box flange in which flow sensors will be integrated in the return line side.

The overall requirement for the TIMO upgrade work is to provide a test environment which allows to replicate ITER relevant conditions in all possible aspects [2]. One scaling parameter is the surface-related flowrate of the gases to be pumped. As the PTC features a pumping surface which is about three times larger than the one of the model pump, larger gas dosing and metering systems were procured. The new mass flow controller (flow range up to 50 l/min) can be included into the existing process gas metering piping system of TIMO-2.

To fulfil the ITER requirements concerning the regeneration pump down time (10 Pa cross-over pressure in 150 s) and to be consistent with the current ITER forepumping system design, it will be necessary to install a new vacuum pump system providing higher pumping speeds. The new regeneration pump train, which has to be especially certified for pumping hydrogen, is under procurement and will include a 2000 m³/h roots pump backed by a 250 m³/h rotary vane pump.

Staff:

H. Haas
H. Jensen
P. Pfeil
H. Strobel
H. Stump
J. Weinhold
D. Zimmerlin

Literature:

- [1] Chr. Day, A. Antipenkov, H. Haas, V. Hauer, A. Mack, D.K. Murdoch, M. Wykes, R&D and design for the mechanical and cryogenic vacuum pumping systems at ITER, European Vacuum Conference, Paris, France, April 2005, accepted for publication in *Vacuum*.
- [2] H. Haas, H. Strobel, Chr. Day, Status TIMO-2, 13th ITER-EFDA-FZK Interface meeting, Sept. 2006, ITER IDM ITER_D_24ULX7.

TW6-TTFF-VP 53

Tritium Test of Ferrofluidic Cartridge Seals for Roots Roughing Pump

Background and objectives

In accordance with the ITER vacuum requirements, the latest Fuel Cycle R&D results [1] and the results achieved in the previous R&D Task TW3-TTFF-VP34, the ITER forevacuum pumping system shall provide a unit pumping speed at its inlet of at least $1 \text{ m}^3/\text{s}$. The best pump type to meet this goal is a Roots pump. A tailor-made tritium-compatible pump of $250 \text{ m}^3/\text{h}$ was tested at FZK on helium in the frame of the EFDA Task TW3-TTF-VP12 [2].

To make a catalogue pump tritium-compatible, the following main modifications are needed: a stainless steel housing, metal stationary seals, and tight rotary shaft seals between the process and lubricant chambers. As technical solution for the latter requirement, FZK developed ferrofluidic rotary feedthroughs. The validation test results of the tailor-made tritium-compatible pump featuring such ferrofluidic seals were positive. In order to complete the qualification of this type of a rotary seal for tritium and to recommend the solutions applied in the $250 \text{ m}^3/\text{h}$ pump for the ITER-relevant size pumps, final tests of the seal with tritium remains to be performed. This problem will be solved in the present task.

Test programme

The test cartridge will be integrated into a test unit with two tight volumes separated with the seal. In one of these volumes a pre-defined amount of tritium (ca. 300 Ci) will be filled, in order to get ca.1 bar pressure. The second volume will be maintained at ca. 0.8 bar nitrogen and permanently monitored for tritium by an ionisation chamber. The rotation of the shaft will be provided by an electric motor; the tests will be performed at 1500 rpm for several months until a steady state leak rate is achieved. After completion of the tritium tests the seal performance on helium will be checked in order to discover if the seal has degraded. Then the seal will be dismantled, the ferrofluid will be sampled and examined by the scintillation method for the tritium uptake.

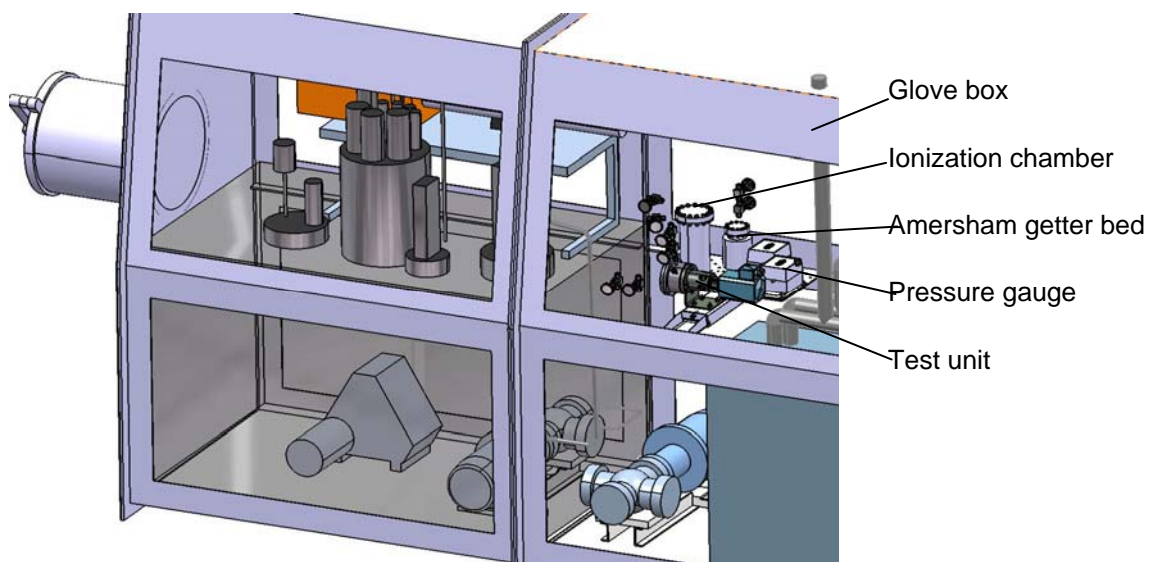


Fig. 1: FACT layout in the PETRA glove box.

The facility, named FACT (Ferrofluidic Advanced Cartridge Tritium experiment), was agreed to be located inside the existing glove box of the PETRA facility in TLK. It shall use existing vacuum transfer and nitrogen supply systems. The lay-out in the glove box is shown in Fig. 1; the flow diagram of FACT is given in Fig. 2.

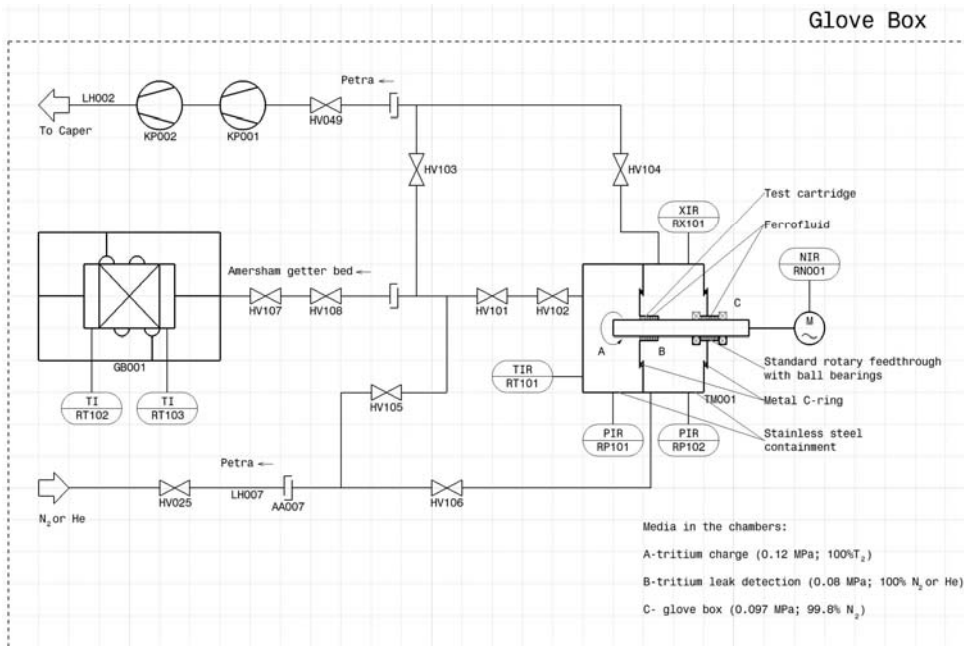


Fig. 2: FACT flow scheme.

Chamber A will be filled with pure tritium at 1.2 bar pressure, chamber B will be filled with nitrogen and connected to an ionisation chamber. The pressure in both chambers will be measured by precise calibrated diaphragm gauges (type BARATRON 690A) and continuously recorded together with the signal from the picoamperemeter of the ionisation chamber.

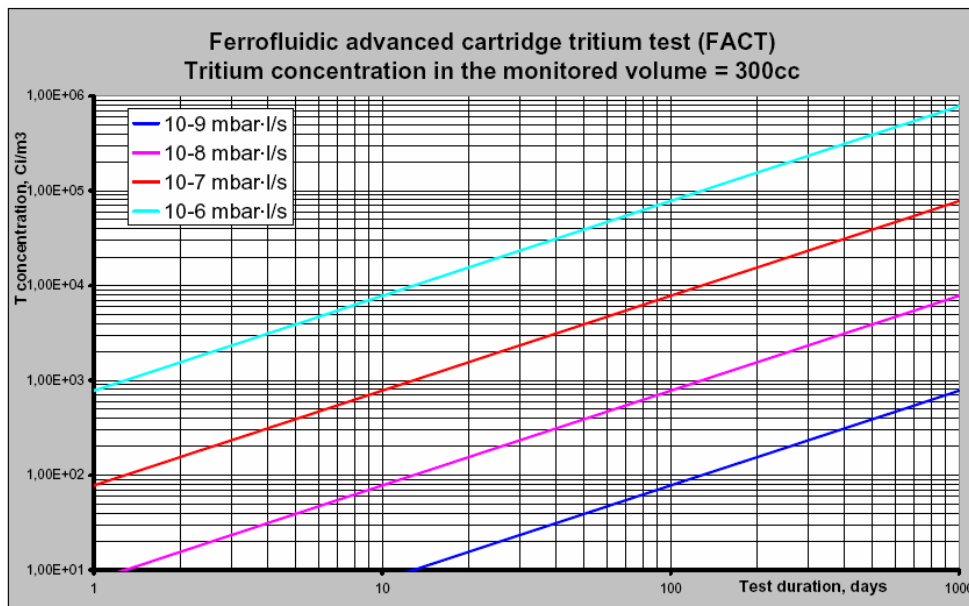


Fig. 3: Tritium concentration ranges forecasted in the monitored volume.

Fig. 3 presents an assessment of the tritium concentration for forecasted leak rates and shows the corresponding experimental times to be expected.

The design and manufacturing of the components and assembly of the facility is underway and expected to be completed in June 2007.

Staff:

A. Antipenkov
U. Besserer
Chr. Caldwell-Nichols
Chr. Day.

Literature:

- [1] M. Glugla, D.K. Murdoch, A. Antipenkov, S. Beloglazov, I. Cristescu, I.-R. Cristescu, C. Day, R. Laesser and A. Mack, ITER fuel cycle R&D: Consequences for the design, Fusion Engineering and Design 81 (2006) 1-7, 733-744.
- [2] A. Antipenkov, Test results with 250 m³/h Roots pump equipped with cartridge type ferrofluidic seals, 11th ITER-EFDA-FZK Interface meeting, Oct. 2005, ITER IDM ITER_D_24WHW4.

TW1-TTF/VP 13

Compatibility of Leak Localisation Tracers with Cryopanel

Background and Objectives

For ITER, a powerful and sensitive leak detection system is of utmost importance. Consequently, a multi-stage approach has been developed to meet the different leak detection requirements. One of the various strategies involved is for locating a leak in the cooling water circuits which is considered to be the most likely type of a leak into the vacuum vessel. Leak localisation will only be performed after a water leak has been noticed by poor plasma performance and confirmed.

A concept was proposed to add tracer substances at low concentrations which would be released in the gaseous phase in the event of a leak. These tracers would be pumped by the cryopumps and released during regeneration. They could then be detected by the global leak detection system located in the vacuum pump room which is connected to the torus roughing line and monitors the gases exhausted from the cryopumps. Due to the chemical species, the tracer substance will be released not after partial regeneration but after the less frequently performed (over night or over the weekend) regenerations at high temperature (470K). The use of the cryopump would ensure a high sensitivity even for very small leaks due to their accumulation effect over the pumping operational time in between the regenerations.

Any substance to be used as a tracer must be investigated for compatibility with the cryosorption pumping concept. In last year's programme, it was investigated what amounts of tracers accumulated to the panels can be accepted without leading to charcoal poisoning which would result in a deterioration of pumping performance [1]. Different tracers may be added to the different sub-loops so that one becomes able to pinpoint the leak down to the component level. Therefore, several tracers have been proposed, ranging from lighter hydrocarbons over alcohols to aromatics. The remaining experimental programme conducted in the present reporting period comprised the measurement of the release behaviour of the heavier candidate tracers. Only those which are compatible to the available 450K maximum regeneration temperature limit are acceptable.

Remaining experimental programme

The following candidate tracer substances have been investigated in TIMO [1] in this reporting period: 2-methyl-1-butanol, benzene, xylene, toluene and benzyl-alcohol. The release pattern of these species was monitored by high resolution quadrupole mass spectrometry as reference device, in many cases in parallel with a GC-MS [2]. Each reactivation test started from ambient regeneration, with deuterium from the preceding pumping test filling the closed pump volume to about 70 mbar. From this starting point, the temperature of the cryopanel system was increased in steps of about 30K, and the gas composition was analysed. After having reached 470K at all inner pump parts, the pressure was reduced by means of the forepumping system down to 10⁻¹ mbar with corresponding gas analysis to assess the effect of pressure reduction on gas release.

Fig. 1 shows the corresponding curves for benzene, toluene and 2-methyl-1-butanol. Benzene is released first, the other two species need temperatures above 150°C to get quantitatively released. All three species do not see a complete release, even after heating up to the maximum available temperature of 470K. However, if the temperature is maintained and the pump interior volume is being evacuated by the forepumps, a pressure-induced desorption is being initiated which leads to complete gas release. The 10⁻¹ mbar level which was adhered to in the TIMO experiments corresponds to the required cryopump cross-over pressure, the mechanical end vacuum provided by the ITER forepump trains.

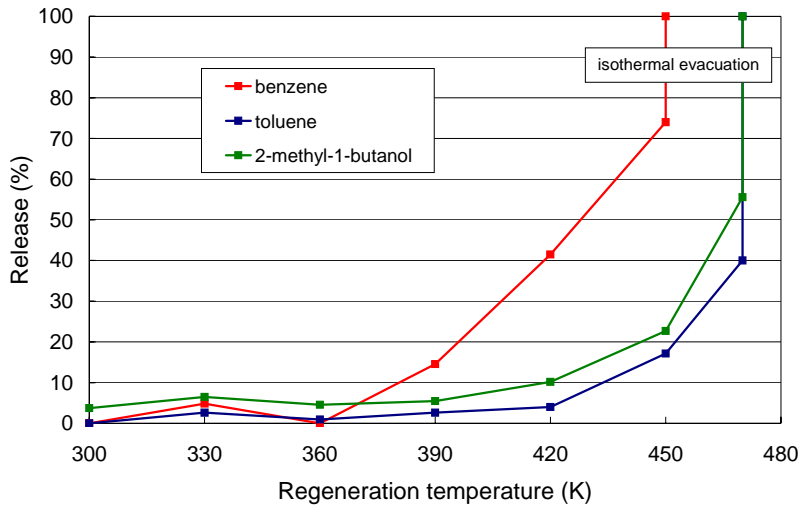


Fig. 1: Measured temperature- and pressure-induced regeneration curves.

Fig. 2 illustrates another interesting effect. Shown are the release curves of pure water and of water released from a panel that was pre-doped with a tracer material. The initial composition of the sorbed phase was (5 vol% 2-methyl-1-butanol)+(95 vol% water), and (50 vol% benzene)+(50 vol% water), respectively. Obviously, the regeneration pattern is very much different. This is probably due to the different chemical affinity in terms of electronegativity which is high between water and the hydroxyl group of the alcohol, and low for water and the totally symmetric benzene molecule. However, in all three cases, a complete regeneration is achieved under the condition of maximum temperature.

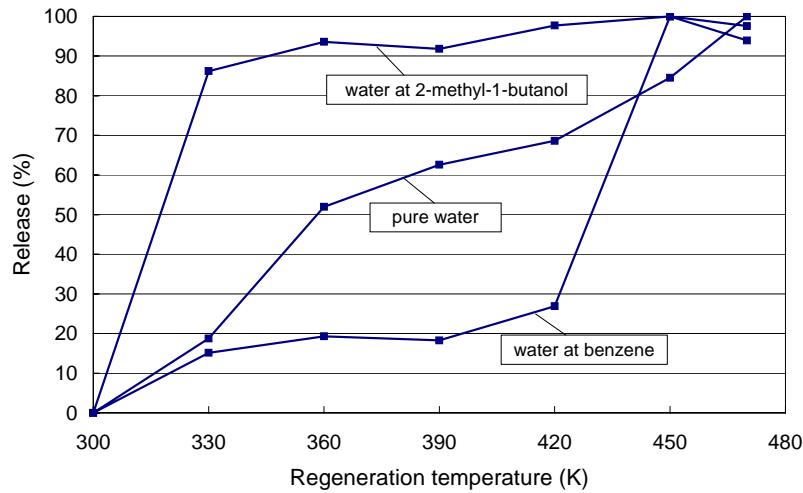


Fig. 2: Influence of the presence of tracers on the release behaviour of water.

The task has been closed. A fundamental understanding of the release and poisoning behaviour of potential tracer substances for leak-detection has been gained and potential analytical difficulties have been described. It has been shown that a broad variety of chemical species could be used for leak detection and localisation purposes. The next step is on the ITER cooling water experts to fix the substances, which also have to fulfil other requirements from water processing point of view. Following that, more detailed investigations for quantitative confirmation may have to be re-started.

Staff:

Chr. Caldwell-Nichols
Chr. Day
A. Edinger

Literature:

- [1] H. Haas, Chr. Caldwell-Nichols, Chr. Day, A. Mack, and D.K. Murdoch, Study of poisoning effects with the ITER model pump during relevant operation cycles, Fusion Engineering and Design 81 (2006) 845-850.
- [2] Chr. Caldwell-Nichols, Chr. Day, H. Haas, M. Glugla, D.K. Murdoch, M.E.P. Wykes, A leak localisation technique for ITER water cooling circuits, Knoxville, Proc. 21st SOFE 2005 (CD-ROM), IEEE, 2006.

Fuel Cycle Tritium Plant

Tokamak Exhaust Processing

TW1-TTF-TR 11

Gas Processing during in-situ Tritium Recovery from PFC's

TW3-TTFD-TR 31

Improvements to the Mechanical Design of the PERMCAT Component

TW4-TTFD-TR 41

Experimental Investigation of Undesired Side-reactions in PERMCAT

TW4-TTFD-TR 43

Comparison of Batch and Continuous Operation Modes for the Impurity Processing Stage of the Tokamak Exhaust Processing System

Introduction

The Tokamak Exhaust Processing (TEP) system is one of the key systems of the inner fuel cycle of the ITER Tritium Plant. Besides the exhaust gases from the vacuum vessel during the nominal burn and dwell D-T operation, many different sources will produce tritiated gaseous streams within the Tritium Plant, from which deuterium and tritium need to be recovered. Since ITER does not have a dedicated system for the treatment of gaseous wastes all the tritium therefore needs to be recovered primarily with the TEP system.

The decontamination factor required for the TEP system is defined for a short pulse of the D-T burn phase of ITER. It is based on the ratio of tritium-inlet to tritium-outlet flow rates, and is specified to be 10^8 . Taking the gas composition and flow rates during the burn phase into account this decontamination factor can be translated into a target outlet concentration of $\leq 10^{-4} \text{ gm}^{-3}$ (equivalent to $\leq 1 \text{ Ci m}^{-3}$ or $\leq 0.4 \text{ ppm}$ tritium). Off-gases from the TEP system shall be stacked via the Normal Vent Detritiation System (N-VDS) of ITER after intermittent storage for decay of γ -active species in dedicated tanks. The removal of tritium down to levels below 1 ppm from D-T streams containing also tritiated impurities such as water or hydrocarbons can only be achieved by multistage processes. Fig. 1 shows the principle of the 3 steps for the TEP system within the inner fuel cycle of ITER.

To experimentally investigate the individual steps of the TEP system and to demonstrate the overall process in an integral manner the so-called CAPER facility is operated at the Tritium Laboratory Karlsruhe (TLK) for more than one decade. CAPER is a versatile semi-technical test rig with a typical tritium inventory of about 3 to 5 g, and a team of about 4 persons is required for experiments; its modular set-up allows different routing of gases, and a large number of control loops along with the comprehensive instrumentation installed permit a proper characterization of the chemical processes and components. The latter is particularly important to scale the process to ITER capacity and throughputs. A mock-up section within the CAPER facility is available and employed for the preparation of gases with different compositions, particularly tritium and tritiated impurity contents, as they are expected to appear from the various modes of tokamak operation and from operation of other systems of ITER. The CAPER facility is also an essential and central system within the closed tritium cycle of the TLK. All primary gaseous wastes arising from experiments at TLK are detritiated in CAPER. The integral tritium operation of the facility can therefore be considered as representative for the TEP system within the Tritium Plant of ITER.

CAPER operated in TLK is a unique facility that covers integrally the 3 steps of the TEP system. As a general concept, it comprises palladium / silver membranes, which are highly selective for the permeation of hydrogen isotopes in the molecular form and allow recovering pure Q_2 (Q means H, D or T), and catalyst beds, which promote cracking or isotope ex-

change reactions that liberates tritium chemically locked in molecules such as water or hydrocarbons.

It employs a Pd/Ag permeator as a first step ('impurity separation') to recover the main part of un-burnt D-T mixture. The second step ('impurity processing') is carried out in a closed loop involving heterogeneously catalyzed cracking or conversion reactions combined with the permeation of hydrogen isotopes through another Pd/Ag permeator to liberate and recover tritium from tritiated hydrocarbons or tritiated water. The third step ('final clean-up') removes almost all of the residual tritium by counter current isotopic swamping and is based on a so called permeator catalyst (PERMCAT) reactor. The PERMCAT reactor is a direct combination of a Pd/Ag permeation membrane and a catalyst bed specifically developed for the final clean-up of gases containing up to about 1% of tritium in different chemical forms such as water, hydrocarbons or molecular hydrogen isotopes.

The first step of the CAPER process was particularly investigated in view of the influence of different inert gas loads and the ample results of the parametric study previously reported. To finalize the current tasks recent experimental work was mainly focused on the second and last stage.

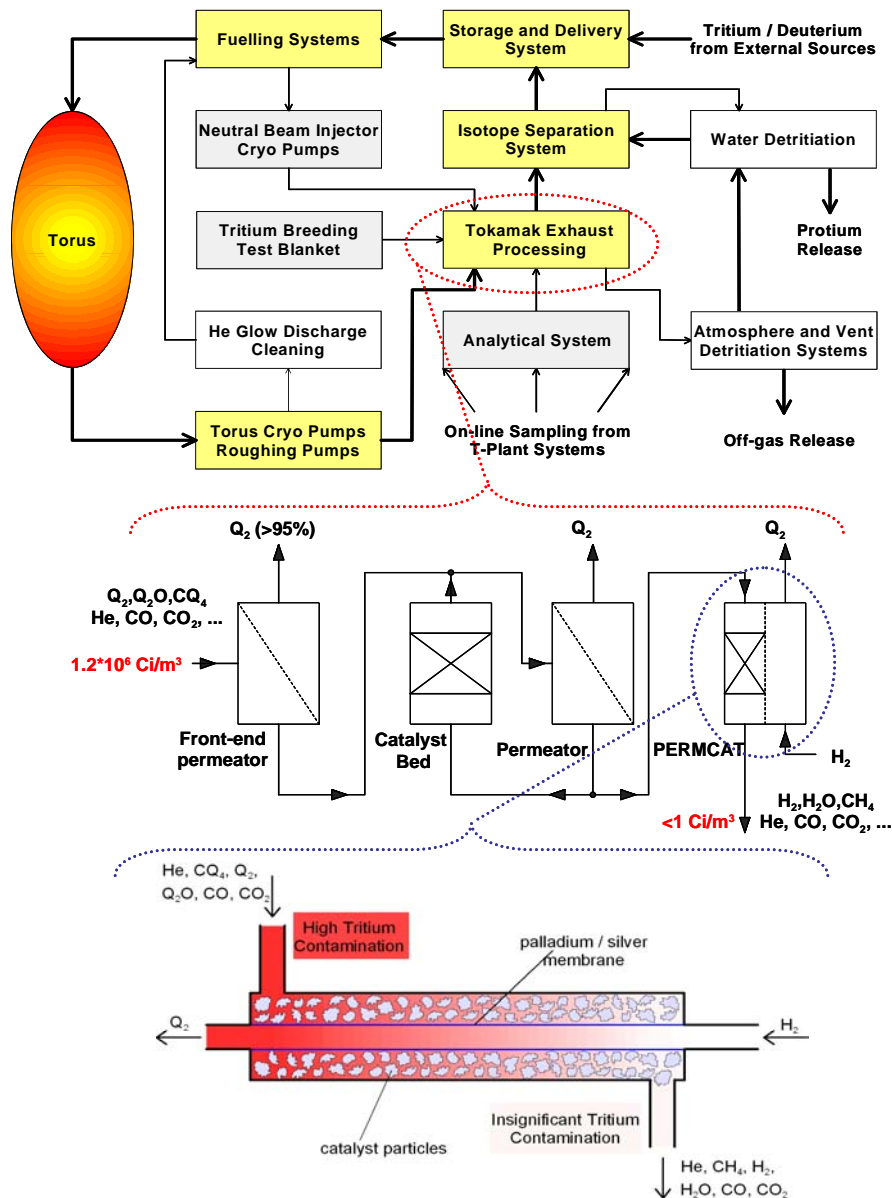


Fig. 1: The PERMACAT process is the final clean-up stage of the Tokamak Exhaust Processing system within the inner-fuel cycle of ITER (Q means H, D or T).

Gas processing during in-situ tritium recovery from PFC's

Since the amount of tritium in the torus shall not exceed the designed safety guideline of about 350 g, tritium recovery from Plasma Facing Components (PFC) is a key issue for the long term operation of ITER. The aim is to find an effective in-situ cleaning method that can cope with safety considerations. As a general concept, the physical processes avoiding the production of tritium oxide are preferred, since highly tritiated water in liquid form seems difficult to handle (stoichiometric DTO means 1.3×10^6 Ci/kg). For this purpose He and H₂/D₂ Glow Discharge Cleaning (GDC) are already considered in ITER operation, but other methods such as oxidative treatments and/or baking clean-up could also be engaged. Whatever the process(es) chosen, each and every resulting effluents shall be detritiated within the tritium plant, primarily with the TEP system.

Different extrapolations via calculations codes, considering the current PFC configuration for ITER (Be, W, CFC) and empirical data from other DT fusion machines, agree to predict for ITER a tritium retention between 2 to 5 grams per pulse (450 s), mainly in the divertor region. This means it will take only 70-175 pulses to reach the tritium inventory limit, which is far from the 3000 pulses predicted divertor lifetime if erosion only is of concern.

Many cleaning campaigns have been conducted in existing DT fusion machines, for example at JET and TFTR, and several issues can be pointed out. First, the removal rate required for ITER should be orders of magnitude faster than the ones achieved up to now. Another challenge is the removal of tritium deposited on the side of the tiles and in shadowed areas, where plasma or glow discharges are rather ineffective. Moreover the efficiency of these techniques is often limited in terms of residual tritium inventory. It is demonstrated that bake-out in presence of oxygen (thermo-oxidation) is one of the most effective and straightforward option to recover the residual tritium trapped in carbon co-deposited layers. Unfortunately it presents several limitations, mainly the final production to a large extent of highly contaminated water.

As far as carbon-based materials are used for PFC, hydrocarbons are likely the major tritiated species produced during in-situ cleaning phases. If oxygen is added to some extent while cleaning, tritiated water vapour will appear as well. Depending upon the gas composition, the first or even the first and second step of the TEP process shall be bypassed and the gas directly fed into the second or third step, respectively. Indeed, both tritiated gaseous species can be processed with either the 2nd loop or the final clean-up stage of the TEP system. However, the presence of carbon oxides could reduce the throughput because of side reactions.

The ability to recover tritium from gaseous mixtures containing high partial pressures of hydrocarbon has already been demonstrated, not only for the 2nd loop of the CAPER process, but also for the final clean-up stage. Indeed, a mixture containing up to 6% tritiated hydrocarbons plus 8% hydrogen isotopes with a total activity of about 200 kCi/m³ has been successfully processed with the PERMCAT unit. Originally it was foreseen to send this mixture in the 2nd loop of CAPER, but for technical reasons, it has been processed with PERMCAT; providing appropriate flow rates and pressures, an outlet activity below 1 Ci/m³ was achieved, thus satisfying the ITER requirements.

In addition, the process of gaseous mixtures containing high partial pressures of water vapour has been investigated with the PERMCAT unit of CAPER. The test run reported herein concerns a mixture containing in He: 1.6% of Q₂ (Q = H, D or T) with an activity of 22.5 kCi/m³ plus 1.9% of water vapour (D₂O is produced using a reference gas D₂ + O₂ passing through the "recombiner" reactor (20 g of Pd-based catalyst @ 220°C). The results in Fig. 2 indicate that the outlet activity remains all along the run under the limit of 1 Ci/m³, even with an impurity inlet of 100 ml/min. Given the inlet activity of 23 kCi/m³ and an outlet activity ranging from 0.25 to 1 Ci/m³, DF between 2×10^4 and 9×10^4 were achieved during this run,

completely satisfying the ITER requirements and demonstrating that PERMCAT can easily cope with up to 2% of water vapour in the impurity flow.

Above and beyond, if during the tritium recovery, the production of tritiated water vapour is more significant, two options can be envisaged. First it could be processed in the gaseous form, but then it would require a significant addition of an inert carrier gas to avoid condensation. Following, the gas load to the second (and third) step of the TEP system would be substantially higher than considered so far; then other than burn and dwell are likely to become design limiting cases. The alternative would be to process it in the liquid form. But then, neither the TEP system nor the Water Detritiation System (WDS) can cope with such stream within their current design, since the first cannot process high partial pressures of vapour and the latter is limited to 300 Ci/kg for the inlet activity.

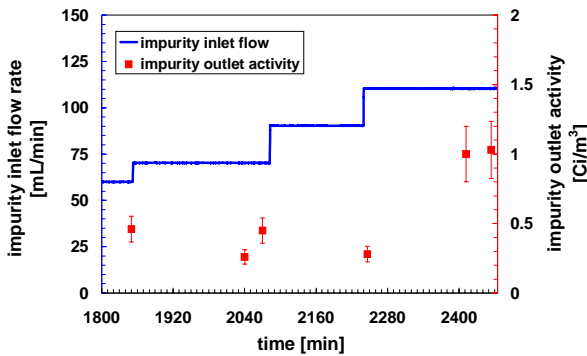


Fig. 2: Inlet impurity flow rate and activity at the impurity outlet of the PERMCAT reactor versus time.

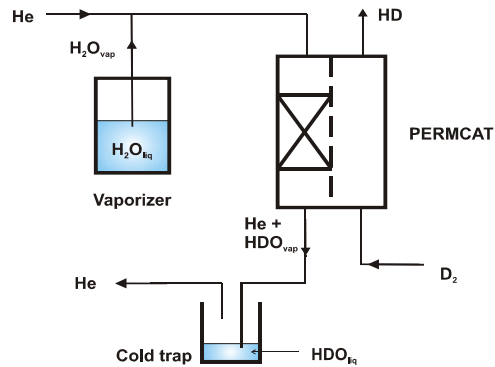


Fig. 3: Simplified illustration of the apparatus to process liquid water with a PERMCAT reactor.

The process of highly tritiated water using the PERMCAT process has been recently proposed. In fact, the principle of using a PERMCAT reactor to process liquid water has been established with “cold” experiments (without tritium) performed on single tube PERMCAT units using the apparatus described in Fig. 3. Fresh distilled water (H_2O) is heated up to $120^\circ C$ in a vaporizer to produce a water vapour flow mixed with a carrier gas (here He) and fed into the impurity side of the PERMCAT unit. At the same time pure D_2 is given in counter current in the purge side of the reactor. Each gas flow rate is regulated with a dedicated mass flow meter. Pressures are measured at the 4 inlets/outlets of the PERMCAT reactor and regulated with throttle valves. The processed water vapour is then collected at the reactor outlet in a trap cooled with liquid nitrogen. After about 8 hours of continuous operation a few grams of water are collected. The deuterium content in water is then measured off-line using FT-IR spectroscopy (stretching of D-O bond @ 2510 cm^{-1}) with an absolute precision of $\pm 2\%$. Each PERMCAT run is carried out with constant and predefined parameters. A parametric study on flow rates and pressures is done by repeating the experiment with changing a single parameter.

Table 1: Conversion between H_2O and D_2 with 2 single-tube PERMCAT units put in series.

Run	Flow rates [ml/min]			D in HDO [%]
	D_2	H_2O	He	
A	30	40	30	62
B	30	30	30	77
C	30	20	30	91
D	30	15	30	95

The results given in Table 1 are an example of a parametric study concerning flow rates: the water inlet flow is steeply decreased while maintaining constant the purge flow rate. In agreement with theoretical considerations, the highest D_2/H_2O flow rate ratio (run D) gives the best result with 95% of D in the water, but other runs also revealed conversions up to 99%. A parametric study of the He flow rate revealed that the optimal condition is a 1:1 ratio between carrier gas and water vapour. The aim for PERM-

CAT would be to detritiate stoichiometric liquid DTO down to an activity of 300 Ci/kg (DF of 4300) that would be compatible for blending with the WDS. Assuming that a single tube unit is able to process 15 ml/min of water vapour (15 µl/min of liquid), based on a continuous operation, 1 l of pure liquid DTO could be daily processed using a technical reactor comprising 46 tubes arranged in parallel. In comparison, the WDS in ITER has a very high throughput of 20 kg/h. However, considering the design value of 10 Ci/kg for the inlet activity during nominal operation, it would need 270 days to process 1 l of DTO because of the exorbitant dilution required.

In conclusion, the ability for the second loop of TEP to process impurity has already been demonstrated. Within these complementary investigations, it is now also demonstrated the high versatility of the PERMCAT process to deal with tritiated water either in gaseous or liquid phase. This is of great advantage for accommodating to any possible in-situ detritiation techniques of future DT fusion machines like ITER.

Improvements to the mechanical design of the PERMCAT component

The PERMCAT design must integrate the mechanical issue in order to overcome technical difficulties during operation. In fact, not only thermal expansion at the nominal operating temperature of 400°C but also lattice parameter increase of Pd/Ag due to hydrogen uptake by the membrane during permeation are both sources of mechanical constraints. Above and beyond nominal operational conditions that should engender limited mechanical stresses, off-normal events should also be considered since a large amount of hydrogen would be absorbed by the membrane in case of loss of heating during operation for example. It may provoke a global failure of the component or at least affect irreversibly the process efficiency since the geometrical arrangement has a crucial impact on the performances.

Indeed, significant lattice increases resulting in important membrane elongations (up to 2%) and/or deformations have been observed with a dedicated experiment involving a finger type Pd/Ag membrane submitted to different hydrogen partial pressures while varying the temperature.

Table 2: Comparative description of the different PERMCAT mechanical designs.

Type of Pd/Ag membrane	a) Finger-type	b) Tubular	c) Corrugated
Thickness (µm)	100	100	100
Length (mm)	530	400	280 ^{a)}
Outer Diameter (mm)	3.3	2.3	6.35 ^{a)}
Permeation area (cm ²)	53.3	27.6	55.0
Mass of catalyst (g)	6 ^{b)}	1.6 ^{c)}	9 ^{c)}

^{a)} before the production of convolutions, afterwards the apparent membrane length is shorter (about 220-230 mm) and the outer diameter varies between 6.35 to 8.05 mm

^{b)} catalyst bed hosted in the annulus part of the reactor

^{c)} catalyst bed hosted inside the Pd/Ag tube

Different PERMCAT mechanical designs (Fig. 4) have been proposed. The first one comprises a finger-type Pd/Ag membrane with an additional capillary tube; afterwards alternatives involving different kinds of bellows were introduced. Both new options are considered as upgrade designs since, firstly the global geometry is simplified (2 coaxial tubes instead of 3), and secondly they should be more robust, thus able to withstand to off-normal operation. Details on geometrical aspects of each type of PERMCAT component are given in Table 2. Each mechanical design has been submitted to experiments involving isotope exchange reactions between water vapour and deuterium. However, a direct and quantitative comparison between different reactors is not straightforward, since lengths, diameters of the membrane, as well as localisation and amount of

catalyst are specific to each type.

As expected from the noticeable differences between the reactors, contrasting processing aptitude are observed. An attempt for a quantitative comparison is given in Fig. 5. Two artifices are considered to account for the differences in geometry: the H₂O inlet flow rate is given per unit of permeation area; the performance expressed in term of decontamination factor is extrapolated at an equivalent and virtual length (1 m) assuming a logarithmic profile for concentrations along the axial direction of the reactor. The PERMCAT that includes the corrugated Pd/Ag membrane shows the best results. Finally the best performances are observed on the reactor that contains relatively to the permeation area the largest amount of catalyst, and gives the highest residence time of the water vapour.

Then, in collaboration with the main workshop of FZK, a new tritium compatible PERMCAT reactor using this Pd/Ag corrugated membrane design has been produced (Fig. 6). One of the main concerns for a tritium compatible PERMCAT unit, as commonly required for heated components, is the outer jacket that permits recovering tritium that would permeate out of the process. Homogeneous heating is ensured with two parallel copper plates that enclosed the PERMCAT tubes. A major improvement is done by using two single tube units placed in a row. It allows integrating in between an ionisation chamber, thus both improving the control and the comprehension of the process. Recently installed in the CAPER facility, first tests with tritium highlighted good detritiation ability. However up to now, the few results available do not allow yet a quantitative comparison between this new unit and the old one.

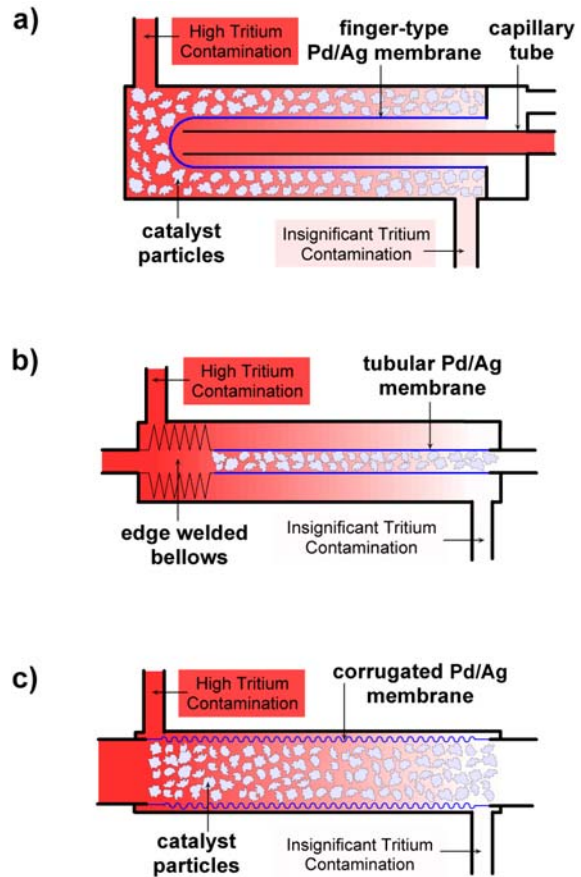


Fig. 4: Different mechanical designs of PERMCAT reactor developed and tested at TLK a) Finger-type membrane + capillary tube, b) Tubular membrane + edge welded bellows, c) Corrugated membrane.

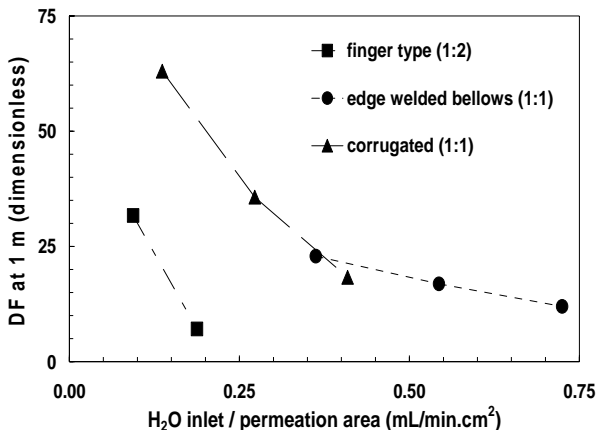


Fig. 5: Comparison between gas processing performances (DF = decontamination factor) of different designs at given swamping conditions (1:1 or 1:2 = H₂O/D₂ flow rate ratio).

In parallel, the design of a new multi-tube PERMCAT reactor has been engaged (Fig 7). It comprises a battery of 13 Pd/Ag finger type membranes that will be inserted in a common single catalyst bed. It includes also, like the first design, capillary tubes; one particularity of this reactor, it enables the exchange of the capillary tube set in order to study the influence of the capillary tube diameter. When an optimal configuration will be pointed out, this unit will be duplicated and 2 units in a row will be hosted in a common outer jacket.

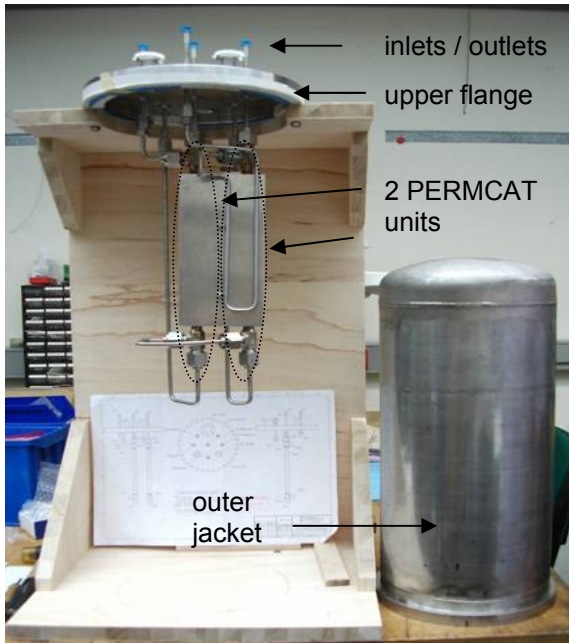


Fig. 6: View before the final assembly of the latest PERMCAT reactor installed in the CAPER facility, using 2 PERMCAT single tube units in series.

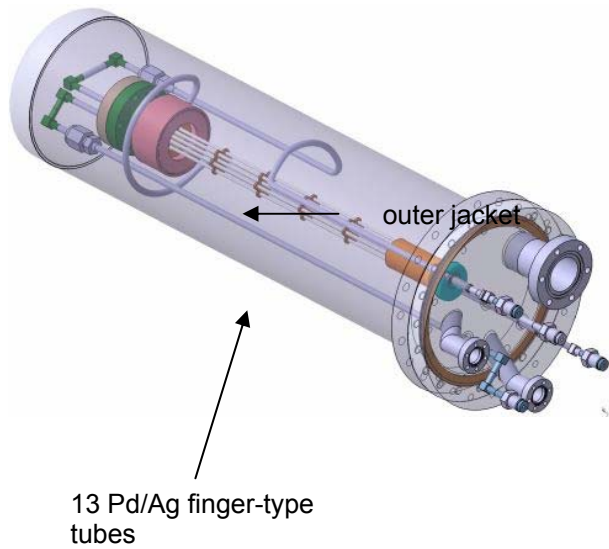


Fig. 7: Current 3D drawing of the next technical (multi-tube in a common single catalyst bed) PERMCAT reactor.

Beside experimental and design work, recent progresses concerning the numerical simulation of the PERMCAT process were achieved. By adding in the former 1 dimension simulation the axial and radial diffusion terms for the different gaseous species, it is now possible to perform calculations in order to improve and optimise the geometry of PERMCAT reactors, mainly in term of diameters and gap between each tube.

Experimental investigation of undesired side-reactions in PERMCAT

The PERMCAT process used catalyzed isotope exchange reactions to recover tritium from hydrocarbons or water (reaction 1 and 2). However, depending on the gas composition and the catalyst material, different unwanted side reactions can occur (3 and 4). The following reactions (non exhaustive list) are taking place simultaneously in the PERMCAT reactor:

- | | |
|--------------------------------------|--|
| (1) Isotope exchange reactions | $CQ_4 + 2 H_2 \leftrightarrow CH_4 + 2 Q_2$ |
| (2) Isotope exchange reactions | $Q_2O + H_2 \leftrightarrow H_2O + Q_2$ |
| (3) Inverse Water Gas Shift reaction | $CO_2 + Q_2 \leftrightarrow Q_2O + CO$ |
| (4) Methanation reaction a | $CO + 3 Q_2 \leftrightarrow CQ_4 + Q_2O$ |
| (5) Methanation reaction b | $CO_2 + 4 Q_2 \leftrightarrow CQ_4 + 2 Q_2O$ |

The main concern for the reactions (3) to (5) is the consumption of Q_2 either with CO or CO_2 and the following production of water and hydrocarbon. In fact Q_2 , instead of participating to the detritiation process via permeation and isotope exchange reactions, is chemically locked in molecules. Therefore it makes no doubt that either the throughput or the decontamination efficiency of the PERMCAT process is affected by the presence of carbon oxides in the impurity flow. In addition, depending on the significance of these undesired effects, the condensation of water in the bleed might occur. Therefore the importance of these side reactions shall be investigated experimentally.

The experimental study was conducted with the PERMCAT unit of the CAPER facility. Relevant gaseous mixtures containing different amount of carbon oxides were produced. For example, the PERMCAT run 4 was carried out with the following gas characteristics: tritiated species (Q_2 1.6%, CQ_4 0.43%, the corresponding activity is 4.2 and 4.5 kCi/m^3 respectively) in addition with a significant amount of CO and CO_2 , respectively 5.4 and 7.8%. For this experiment, a critical reduction of the decontamination factor was observed; measured to be 610, it is about two orders of magnitude lower than the one expected without carbon oxides.

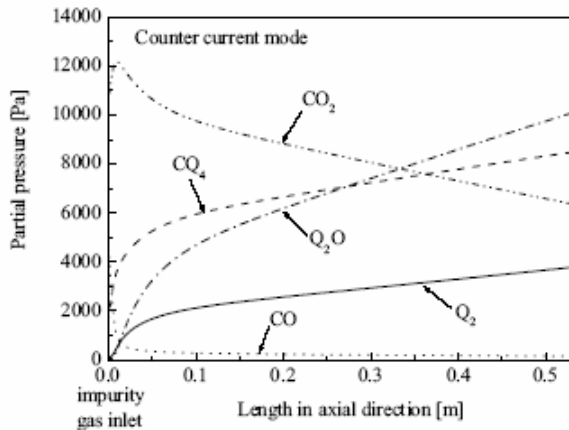


Fig 8: Simulated profile of the different chemical species along the axial direction of the PERMCAT reactor when a few percent of carbon oxides are present in the mixture.

In support to the experimental study, this typical PERMCAT run was simulated using the 1D calculation code. The main interest of the simulation is the computed profile of the chemical species along the axial direction of the reactor, as displayed in Fig 8. Two different behaviours are seen in the figure. On the one hand the CO and CQ_4 partial pressures strongly vary at the reactor entrance. The consumption of CO and the production of CQ_4 highlight the fact that methanation reactions are the most significant side reactions at the inlet of the process. On the other hand, the variation of CO_2 and Q_2O , which reveals the occurrence of the reverse WGS reaction, are less pronounced. However the linear behaviour observed would suggest that the

reverse WGS reaction may be the major part of side reactions taking place near the outlet of the reactor.

Comparison of batch and continuous operation modes for the Impurity Processing stage of the Tokamak Exhaust Processing system

In principle, the 2nd step of the CAPER (TEP) process being a closed loop comprising a catalyst reactor “Methane Cracker” and a palladium / silver “Permeator”, it can be operated in two different modes. In the straightforward batch mode (Fig. 9 a) the gas to be detritiated is filled into the loop from the “Storage Tank”, cycled for a certain time until the activity is sufficiently lowered; finally the loop is emptied into the “Collecting Tank”, ready for the next batch. Alternatively, in a continuous mode of operation (Fig. 9 b), the gas is continuously fed into the closed loop upstream of the “Permeator” at a flow rate much lower than the loop circulation flow rate. The pressure in the loop is kept constant by a simultaneous withdrawal of gas downstream.

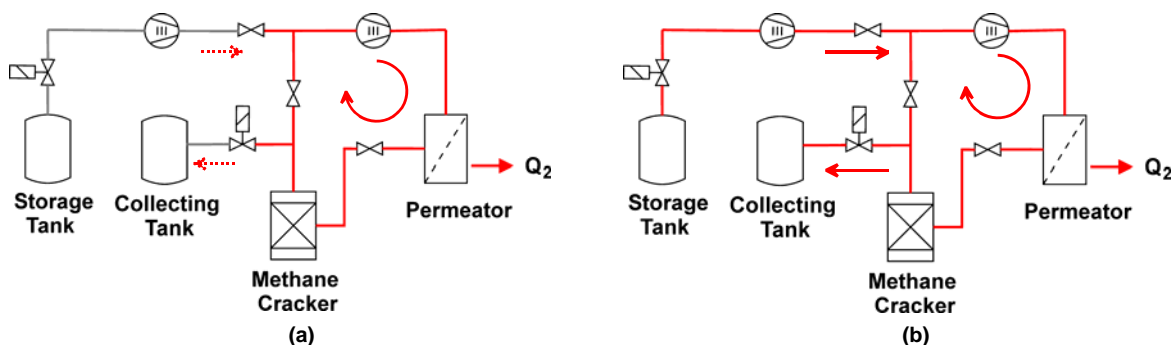


Fig. 9: Secondary loop of CAPER operated in a (a) batch mode or (b) continuous mode.

The batch mode is the regular operation mode of CAPER, mainly for the detritiation of waste gases produced within the facility. Very high decontamination factors are then achieved (up to 10^4) however the throughput is limited. Besides, the continuous mode has been largely studied with parametric test on inlet flow rates mainly. Such a mode seems to be easier to control, to have a higher throughput and also a reduced tritium inventory. It has been chosen as the reference mode for the 2nd of the TEP system in ITER.

However, during the study of the continuous mode operation, discouraging results (time constants, decontamination factors) have been observed from tests to tests, even if the starting gaseous mixture remains almost unchanged. A reason for this could be a temporary “poisoning” of the permeator, due to a carbon deposition on the Pd/Ag membrane resulting from the decomposition of methane at the surface. This affects the permeability, particularly at low hydrogen isotope partial pressures, when the permeation flux is governed by the dissociative adsorption rather than by the solubility of hydrogen. In fact, it has been experimentally observed that good and reproducible measurements are only achieved when the permeator is systematically regenerated prior to the test. In other words, the decontamination factor for the continuous operation mode is very sensitive to the temporary “poisoning” of the permeator. To restore the optimal conditions, the loop is filled with a He/O₂ mixture; carbon is then removed via the production of gaseous carbon dioxide. However, by processing gases containing significant amount of methane, the membrane will become soon poisoned again. Because of this sensitivity, the continuous operation mode for the 2nd loop is not to be the best choice for ITER.

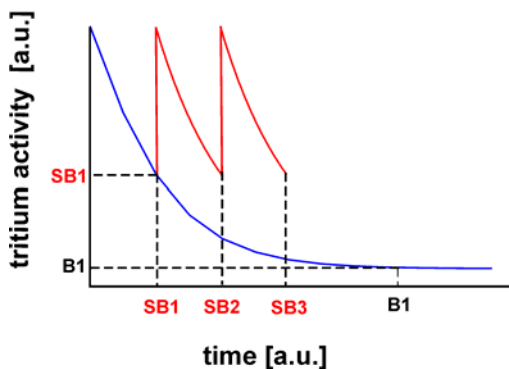


Fig. 10: Principle of the “short batch” mode operation for the 2nd loop of TEP.

A compromise between batch and continuous operation is the best solution. The so-called “short batch” mode would consist in feeding the loop with the gas to be processed at regular intervals (like a pulse mode). Starting like a batch mode, the loop is filled and the gas is processed for a while; assuming the activity in the loop is decreasing exponentially (blue line in Fig 10), this short batch mode takes advantage of the initial operation times, when the activity drops rapidly. Then, instead of waiting until the ultimate decontamination level is reached (like a batch), the loop is emptied as soon as the activity in the loop goes down to a certain threshold (e.g. SB1). Afterwards a new gas fraction is admitted into the loop and this cycle is repeated until all the gas is processed. Compared with the batch mode, the throughput is significantly increased while the decontamination factor is only slightly affected. The gain in throughput largely compensates the loss of decontamination factor. Also, the Pd/Ag membrane of the permeator is insensitive to partial poisoning by carbon deposition in this regime. Since the PERMCAT process can cope with higher inlet activity levels, this short batch mode should be the most suitable for the 2nd loop operation of TEP in ITER.

A parametric study on this particular operation mode has been completed. By varying the frequency of gas injection (between 3 and 10 min) and the intermediate processing time (between 3 and 10 min), it makes possible an optimisation of the process efficiency. The comparison of the achievable decontamination factor as a function of the throughput between short batch and continuous mode is given in Fig. 11. Considering that the secondary loop of CAPER was originally designed at the 1/8th scale of the throughput and off-gas composition of NET (the small European precursor of ITER), the alternative of the short batch mode for the 2nd loop seems now very attractive. In fact, the performances achieved are now almost half of the capacity required for ITER.

A compromise between batch and continuous operation is the best solution. The so-called “short batch” mode would consist in feeding the loop with the gas to be processed at regular intervals (like a pulse mode). Starting like a batch mode, the loop is filled and the gas is processed for a while; assuming the activity in the loop is decreasing exponentially (blue line in Fig 10), this short batch mode takes advantage of the initial operation times, when the activity drops rapidly. Then, instead of waiting until the ultimate decontamination level is reached (like a batch), the loop is emptied as soon as the activity in the loop goes down to a certain threshold (e.g. SB1). Afterwards a new gas fraction is

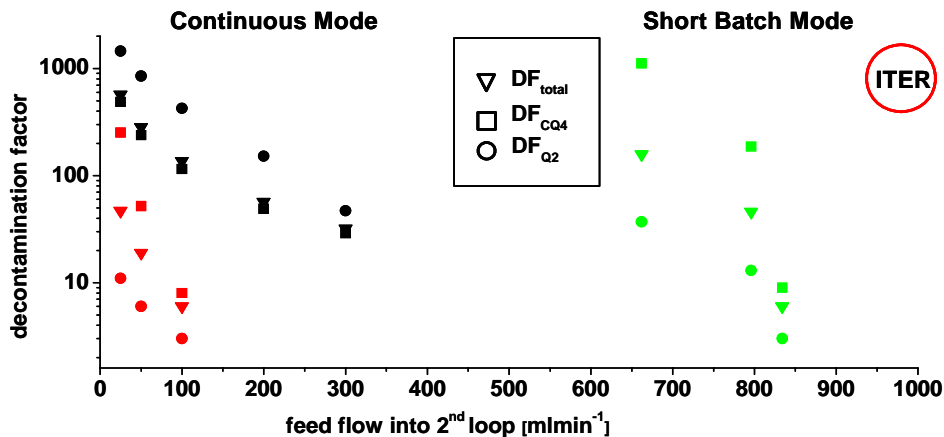


Fig. 11: Comparison between "short batch" and continuous operation mode for the 2nd loop of CAPER in terms of throughput and achievable decontamination factor (continuous mode: red \Rightarrow polluted permeator, black \Rightarrow cleaned permeator; short batch mode: green \Rightarrow cleaned permeator).

Conclusion

Since more than one decade, the TEP system of fusion machines like ITER is studied at TLK with the CAPER facility. Recent work focused on the operational mode of the second step; an alternative to the continuous mode is pointed out. The current studies mainly focus on the final clean-up stage. Mechanical design and production of technical multi-tube PERMCAT reactors validated with tritium experiments are the next steps. Besides, the process of liquid water with PERMCAT and progresses in the simulation code are the major ongoing tasks.

Staff:

B. Bornschein
 C. Corneli
D. Demange
 M. Glugla
 K. Guenther
 T.L. Le
 P. Schuster
 K.H Simon
 S. Welte
 R. Wagner

Literature:

- [1] M. Glugla et al. "ITER fuel cycle R&D: consequences for the design," *Fus. Eng. Design*, **81**, 733 (2006).
- [2] D. Demange, S. Welte, M. Glugla, "Experimental validation of upgraded designs for PERMCAT reactors considering mechanical behaviour of Pd/Ag membranes under H₂ atmosphere," presented at the 24th Symposium on Fusion Technology, Warsaw, 11-15 September 2006
- [3] B. Bornschein, D. Corneli, M. Glugla, K. Günther, T.L. Le, K.H. Simon, "Experimental validation of a method for performance monitoring of the Impurity Processing stage in the TEP system of ITER," presented at the 24th Symposium on Fusion Technology, Warsaw, 11-15 September 2006
- [4] D. Demange, B. Bornschein, D. Corneli, M. Glugla, K. Günther, T.L. Le, K.H. Simon, S. Welte, "The PERMCAT process for the decontamination of highly tritiated gaseous mixtures and liquid water produced during cleaning phases of fusion machines," presented at the 17th ANS Topical Meeting on the Technology of Fusion Energy, Albuquerque, 13-15 November 2006

TW1-TTF/TEP 13A

Self-assay, Fast Delivery Tritium Storage Bed Development

TW3-TTFD-TR 33

Determination of Isotopic Effect during Rapid Delivery from Storage Beds

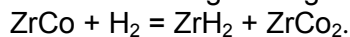
The storage of hydrogen isotopes as metal hydride is a technique chosen for the ITER Tritium Plant Storage and Delivery System (SDS). A prototype storage bed in 1:1 scale, has been intensively tested in the Tritium Laboratory addressing main performance parameters specified for the tritium storage beds foreseen for ITER.

The specification of the hydrogen storage bed can be summarized in the following way:

1. Storage capacity is 100 g of tritium and physically limited
2. High supply flow rate of hydrogen isotopes
3. Fully tritium compatible design
4. In-situ calorimetry with accuracy of 1 g i.e. 1% at level of 100 g of tritium.

At present the storage material ZrCo is used in the prototype bed. As a result of the several years of experiments storage beds have been characterized not only in view of supply, storage and accountancy performance, but also in view of the possible isotopic effects during rapid delivery and static isotopic effect.

Strong effect of disproportionation was obtained during testing. Disproportionation is a degradation of the gettering ability of the ZrCo due to the reaction:



As a result of this reaction the reversible storage capacity of the bed is reduced due to building up unusable tritium inventory in the bed. Once disproportionation occurred the initial properties of the bed can not be completely restored by reproporation, which is anyway a delicate process for a system serving reactor. In view of the fact that disproportionation is unavoidable within the operational procedures of the SDS ZrCo can not be applied in ITER. Depleted uranium as a reference getter material for the ITER SDS shall be considered.

Staff:

S. Beloglazov

E. Fanghänel

B. Kloppe

R. Wagner

TW4-TTFD-TR 44

Inactive Tests of Selected Composition Control Loop Performance under Typical ITER Operating Conditions

ITER will require various gas mixtures to be delivered to the torus subsystems, i.e. gas injection systems, pellet injectors and neutral beam injectors. The ITER Tritium Plant is to supply gas streams of hydrogen isotopes and impurity gases to these systems. For the neutral beam injectors only pure hydrogen or deuterium is required. For gas puffing and pellet injection gas mixtures are required and ITER will have gas valve boxes to produce and control the composition of the final mixtures required for plasma operations during each plasma pulse. 7 gas valve boxes are planned for gas puffing and 6 for pellet injection. These gas valve boxes will be located close to the torus or pellet injector and hence remote from the ITER Tritium Plant.

The original task assumed that the ITER fuelling systems would require specific gas mixtures to be supplied to them from the Storage and Delivery System of the ITER Tritium Plant. ITER has confirmed that the final mixing of gases will be performed at the gas valve boxes for gas puffing and pellet injectors and not in the Tritium Plant. The Tritium Plant is now required to supply basic mixtures of hydrogen isotopes and other gases to the gas valve boxes. The interface between the Tritium Plant and the gas valve boxes has to be fully defined, particularly the information of the gas compositions being supplied by the Tritium Plant.

The task will now concentrate in assessing information obtained from experimental rigs, particularly the CAPER facility at TLK, which use pumps, flowmeters and flow controllers to produce mixtures of hydrogen isotopes and other gases. The performance of these control systems in providing the required gas mixtures and the time profiles will be analysed to assist in the design of the control systems for the ITER gas valve boxes.

Staff:

C. J. Caldwell-Nichols

TW1-TTF/TR 16

Tritium Recovery from Ceramic Breeder Test Blanket Module

Tritium is produced in the Test Blanket Module (TBM) of ITER by nuclear reactions of the neutrons emitted from the plasma vessel with the lithium atoms (Li6) contained in the breeder material of the Helium Cooled Pebble Bed (HCPB). The tritium extraction is achieved with the help of a helium purge gas containing up to 0.1 % H_2 ; the addition of hydrogen is needed to facilitate the tritium release by isotopic exchange.

The tasks of the Tritium Extraction Subsystem (TES) are:

- Removal of tritium produced in the Test Blanket Module,
- Separation and intermediate storage of the two main chemical forms of tritium, i.e. HTO and HT,
- Purification and conditioning of the purge gas.

The TBM is also equipped with a Helium Cooling System, completed by a Coolant Purification System (CPS), needed to extract the tritium permeating into the coolant and to remove impurities that might concentrate in the helium.

Parametric studies of the main components of the TES i.e. Cryogenic Cold Trap (CT) and Cryogenic Molecular Sieve Bed (CMSB) were objectives of the task. Scalability of these components is discussed in the final report on deliverables D2, D3 presented in August 2006.

As far as the Cryogenic Cold Trap is concerned it was concluded that the present design can not be simply scaled to the full size of ITER TES. This is true for all other CTs tested and reported in the literature by other groups. Therefore either full scale tests need to be taken into account or alternative process options, such as water vapour adsorption at room temperature using a molecular sieve bed.

Cryogenic Molecular Sieve Bed (CMSB)

Based on the results of parametric testing the scale up of CMSB is suggested in order to meet the required throughput ($12 \text{ m}^3\text{h}^{-1}$). The size of the CMSB is optimized taking into account the regeneration pattern of the bed and the adsorbed hydrogen inventory. Results of the design studies are given in the table below.

Figure 1 shows the conceptual design of the 1:1 cryogenic molecular sieve for the TBM Tritium Extraction System. The intention of the drawing is to give the overall geometrical dimensions of the CMSB. Major difference of the 1:1 CMSB from the bed tested in FZK is the cooling principle. It is suggested to cool the adsorbent container by passing an 80K helium stream through the helical coil welded to the molecular sieve container surface.

Several arguments in favour of such an approach are listed as follows:

1. Heat of adsorption is not significant due to trace amounts of adsorbate (~1.5 W).
2. Simplified design of the CMSB due to no need in a LN_2 vessel. Only a vacuum isolation is required.
3. No need in an additional dewar for the LN_2 supply or storage after adsorption.
4. No need in evaporation of large amounts of LN_2 in order to heat up the CMSB for desorption.
5. Consistency with the ITER approach in providing cooling capacity for the users.

Design studies were supported by computer modelling of the adsorption brake through curves. The results of the calculations will be published in the proceedings of the SOFT-24 conference.

Adsorption time, day	5
H ₂ extraction rate, mol/day	13
Stoichiometric capacity of the bed, mol	65
MS-5A ads. Capacity mol/g	4.34×10^{-4}
Bed density	740
Stoichiometric adsorbent amount	150
Bed cross section area, m ²	0.245,
Superficial gas velocity, m/s	3.62×10^{-3}
Used bed length, m	0.83,
Unused bed length, m	0.07
Total bed length, m for the sake of spare space	0.90 0.95
Total bed volume, m ³	0.233
Adsorbent amount, kg (wet)	172
Adsorbent amount, kg (dry)	~ 170

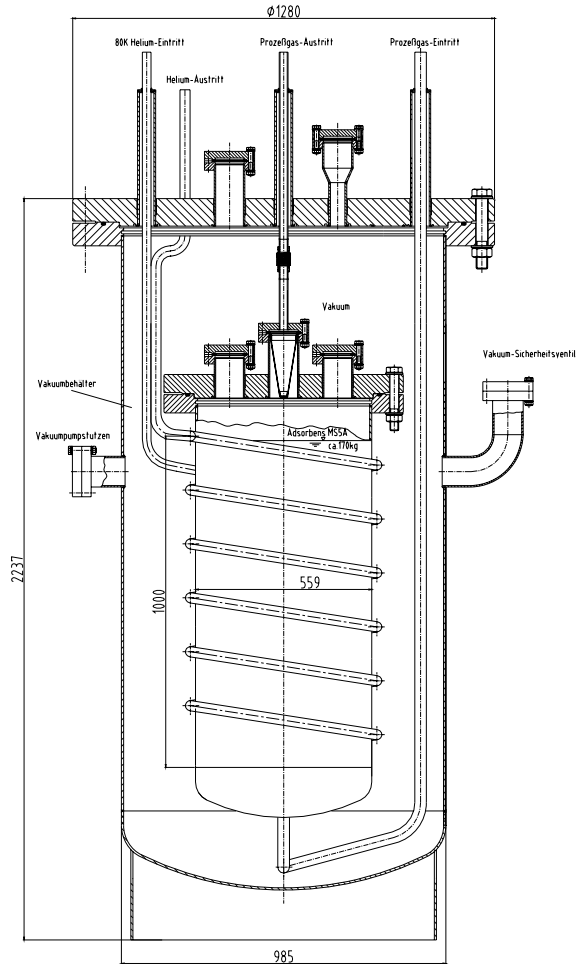


Fig. 1: 1:1 ITER TBM Cryogenic Molecular Sieve Bed

Staff:

S. Beloglazov
R.Wagner

Literature:

- [1] N. Bekris, C. Caldwell-Nichols, E. Hutter, "Cold trap and cryogenic molecular sieve adsorber: components for tritium extraction from purge gas of the HCPB-breeder blanket for ITER", Fusion Eng. Design, **69** (2003), 21-25
- [2] N. Bekris, E. Hutter, J. Rodolausse, "Parametric studies and scale-up of a cold trap in the tritium extraction loop of a HCPB breeder test blanket for ITER", Fusion Sci. Technology, **41** (2002), 1009-1013
- [3] N. Bekris, E. Hutter, H. Albrecht, R.-D. Penzhorn, D. Murdoch, "Cold trapping of traces of tritiated water from the helium loops of a fusion breeder blanket", Fusion Eng. Design, **58-59** (2001), 423-428

- [4] S. Beloglazov, N. Bekris, M. Glugla, R. Wagner, "Semi-technical cryogenic molecular sieve bed for the tritium extraction system of the test blanket module for ITER", Fusion science and technology vol. 48 (2005), 662-666
- [5] K. Munakata, S. Beloglazov, N. Bekris, M. Glugla, R. Wagner, E. Fanghaenel "Experimental and simulation study on adsorption of hydrogen isotopes on ms5a at 77K", Proceedings SOFT-24 (2006), to be published in Fusion Engineering and Design.

TW4-TTFD-TR 46 Design, Experimental Plan and Procurement of Cryogenic Distillation System for Isotope Separation Tests for ITER

The Water Detritiation System (WDS) of ITER is one of the key systems to control the tritium content in the effluents streams, to recover as much tritium as possible and consequently to minimize the impact on the environment. In order to mitigate the concern over tritium release into the environment during pulsed operation of the Torus, the WDS and Isotope Separation System (ISS) will operate in such way that WDS will be a final barrier for the processed protium waste gas stream discharged from ISS.

To support the research activities needed to characterize the performances of various components for WDS and ISS processes in various working conditions and configurations as needed for ITER design, an experimental facility called TRENTA based on the combination Combined Electrolysis Catalytic Exchange (CECE) – Cryogenic Distillation (CD), representative of the ITER WDS and ISS protium separation column, is under full commissioning at TLK.

The block diagram of the TRENTA facility is shown in Figure 1.

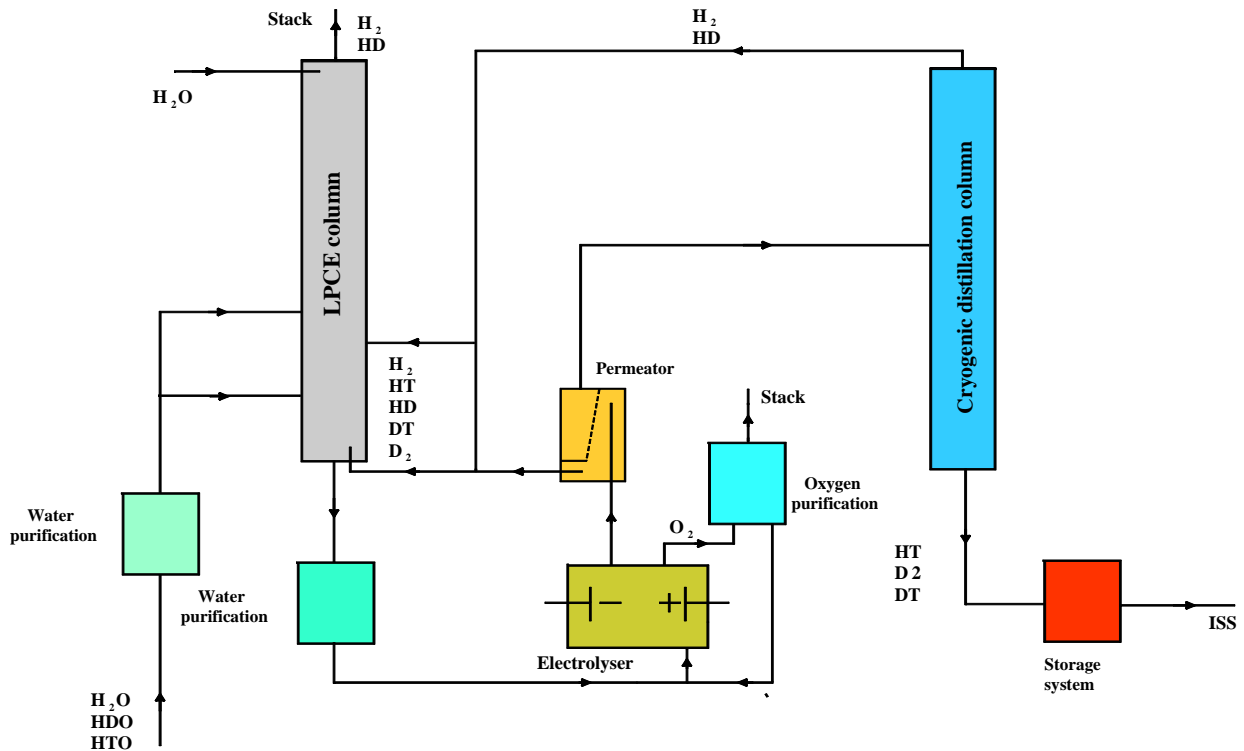


Fig. 1: Block diagram of the TRENTA facility.

The cryogenic distillation system which consists of refrigeration unit, cryogenic distillation cold-box including the cryogenic distillation column has been manufactured and installed in the Tritium Laboratory.

The refrigeration unit has been commissioned and the results are presented below. The scope of the commissioning of the refrigeration unit was to characterize the functioning of the compressor and gas purification unit and the cryogenic cycle when a certain heat load was introduced in the system by an electrical heater that simulates various loads from the condenser of the cryogenic distillation column. Two operational modes have been tested: full power mode and flexible power mode. In full load power mode, experiments can be carried out using the maximum cooling capacity of the plant at 16K. In the flexible power mode, a slow continuous adjustment of the plant capacity to the experimental requirements within the

capacity limits between 50 W and 250 W is possible. One of the requirements of the control system of the refrigeration unit was to control the lowest temperature of the helium stream provided to the cryogenic distillation column within a range less than 0.1K. The basis for this requirement is to allow performing investigations in the transitory regimes of the cryogenic distillation process due to thermal and composition fluctuations as expected within ITER ISS. The time evolution of the lowest temperature of the refrigeration unit during four hours of acceptance test is shown in Figure 2 (in between the two horizontal bars).

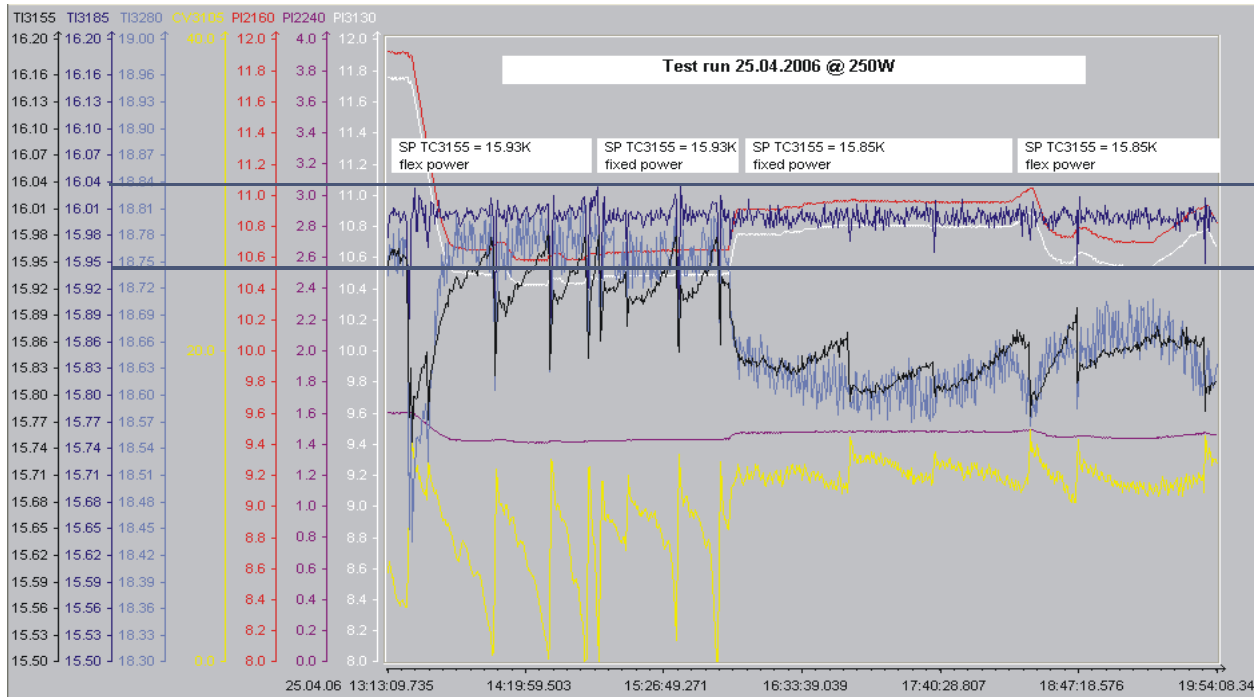


Fig. 2: The acceptance test of the TRENTA refrigeration unit.

The cryogenic distillation column, 2.7 m active length and 55 mm in diameter, has been manufactured and installed in the cryogenic distillation cold-box. The commissioning of the refrigeration unit with the cryogenic distillation column is ongoing. In 2007 investigations of two types of packing, Sulzer Ex and Helipack C with respect the separation performances and liquid hold-up are planned to be carried out.

Staff:

I. Cristescu
I. R. Cristescu
L. Dörr
S. Welte
W. Wurster

Literature:

I. Cristescu, Ioana R. Cristescu, L. Dörr, D. Murdoch; *Integrated tests of water detritiation and cryogenic distillation in view of ITER design*, TOFE - 2006, Albuquerque, submitted for publication in Fus. Eng. & Des.

TW4-TTFD-TR 47

Upgrading of LPCE (Liquid Phase Catalytic Exchange) Column for Trade-off Studies between WDS and ISS

The Combined Electrolysis Catalytic Exchange (CECE) process, based on Liquid Phase Catalytic Exchange (LPCE) column, developed in the TRENTA facility consists of two main units:

- A preparatory unit for the tritiated water to be fed into the electrolyzers and the LPCE column. This unit should receive the tritiated water from the TLK infrastructure and from the LPCE column and prepare the required composition of tritiated-deuteriated water for different operation conditions. It consists of several vessels, pumps and pipework.
- A tritium water processing unit, which basically consists of the LPCE column and the two enhanced electrolyzers for operation with tritium.

From the preparatory unit, the tritiated water can be sent both to the electrolyzers and to the LPCE column. The feeding location into the LPCE column depends on tritium and deuterium content of feed water to be established for each campaign of experiments. In the preparatory unit, the enriched water in deuterium and tritium withdrawn from the bottom of the LPCE column should be mixed with demineralised water in order to achieve the required tritium and deuterium content specific for each campaign. The deuterium content in the processed water will be in the range of 10^{-3} up to 10^{-4} deuterium atomic ratio and tritium content in the range of 5×10^8 Bqkg⁻¹ up to 5×10^{10} Bqkg⁻¹.

The LPCE column is filled with a mixture of catalyst/packing developed by TLK and ICIT Romania. The length of the LPCE column is 8 m and it is provided with feeding and sampling points at every 2 m. At the top of the LPCE column, demineralised water is supplied at different flow-rates in order to achieve inside the LPCE column specific ratios between gas and liquid. The vapours carried by the hydrogen stream at the top of the LPCE column are condensed and returned into the LPCE column. From the top of the LPCE column, the decontaminated hydrogen is released to the TLK stack via a flame arrester and a water seal pool.

The tritiated and deuteriated hydrogen to be fed into the bottom of the LPCE column is provided by two solid polymer electrolyzers (SPM) enhanced for tritium operation. The content of deuterium and tritium in the water fed into the electrolyzers should be kept as constant as possible during one campaign of experiments. Therefore, special procedures for water preparation are implemented.

The oxygen stream produced by water electrolysis is sent for decontamination to the oxygen stripping column. In the stripping column, the tritium and deuterium contained in the vapours carried by oxygen stream are transferred into demineralised water fed in at the top of the column. At the bottom of the stripping column, a catalyst bed is provided with the aim to convert to water the hydrogen that may be contained in the oxygen stream. From the bottom of the stripping column, the tritiated and deuteriated water is sent to the preparatory unit for further processing.

The installation and commissioning of all components of the CECE process have been completed.

The control system of the TRENTA facility consists of three main parts: over-pressure and over-temperature protection system, interlock system and process control. The process control was developed in order to provide the necessary control loops and measurements such that the mass balance around the TRENTA facility can be checked. During commissioning the over-pressure and over-temperature protection system have been verified. The pumps control system as function of various level indications has been proven. The functionality of

the sampling points on gas and liquid phase has been checked and preliminary results are already available. The associated analytics (Omegatron mass spectrometer, on-line Quadrupole mass spectrometer, Fourier transformed infrared spectrometer) have been individually calibrated and mass balance checks on steady-state overall experimental facility have been performed.

The temperature controllers of the heaters, namely the electrical heaters of boiler and the feeding streams have been adjusted in a narrow range of less than 1°C.

The operation control system of the CECE process of the TRENDA facility is shown in Fig. 1.

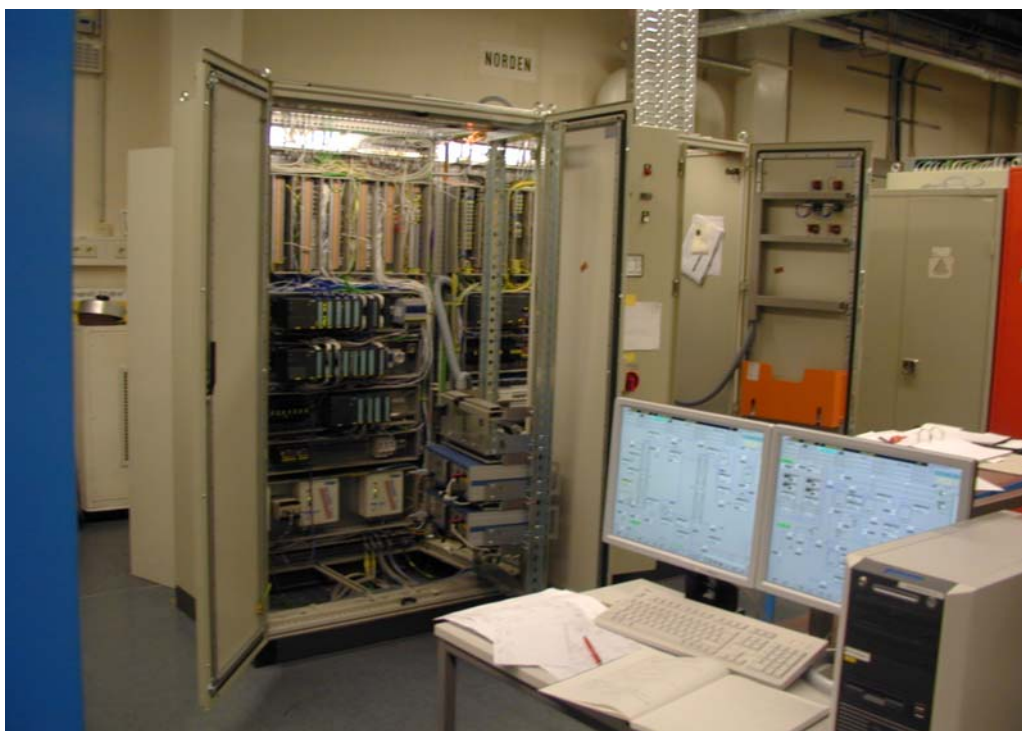


Fig. 1: The operation control system of CECE process.

In the actual configuration of the TRENDA facility, the tritiated water may contain tritium up to 10 Ci kg⁻¹, while for the deuterium content a wide range of concentration can be used and only administrative limits should be considered.

The trade-off studies between the CECE process and Cryogenic Distillation process will be focused on the following issues:

- Operation of the LPCE column with composition fluctuation in the stream returned from the CD column
- Operation of the CD column with composition and flow rate fluctuations in the feeding stream
- Operation in different dynamic modes in order to validate and benchmark the TRIMO code.

Staff:

I. Cristescu
I. R. Cristescu
L. Dörr
G. Hellriegel
R. Michling
P. Schäfer
S. Welte
W. Wurster

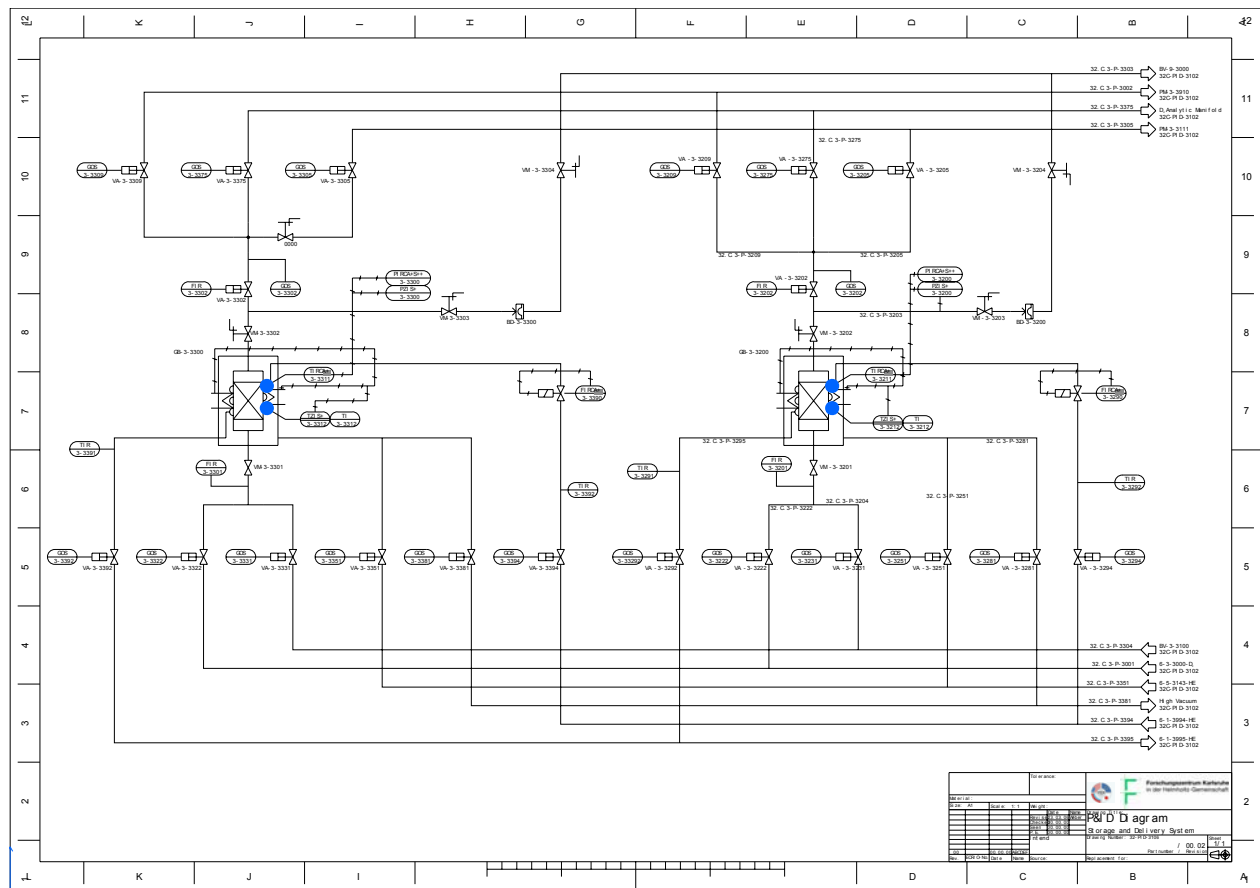
Literature:

I. Cristescu, Ioana R. Cristescu, L.Dörr, D. Murdoch, G. Hellriegel, P. Schäfer, S.Welte, W.Wurster; *Commissioning of water detritiation and cryogenic distillation systems at TLK in view of ITER design*; SOFT-2006, Warsaw, submitted for publication to Fus. Eng. & Des.

EFDA/05-1237 (TW5-TTFD-TPI 51) Development of ITER PRM and Standard Parts Catalogues in CATIA V5 for Tritium-containing System and Components

Introduction and objectives

Since the beginning of the ITER project CATIA software packages by Dassault Systemes have been the basic CAD tool. During the development of ITER the CAD system has developed from CATIA V4 to CATIA V5 supported by Project Management Systems ENOVIA VPM and ENOVIA LCA. Not only mechanical design but also circuit design was already produced in CATIA V4 AEC for the Tritium Plant HVAC ADS/VDS systems for FDR 2001. As the requirements for the system design increased, ITER IT surveyed the CATIA V5 Equipment and Systems design workbench (CATIA V5 E&S) together with ENOVIA LCA Project management system with a view to its application in design of piping, HVAC and other systems of ITER. Proof of Concept activities in the ITER DO have shown that CATIA V5 E&S CAD software will suit ITER requirements in the planned design disciplines.

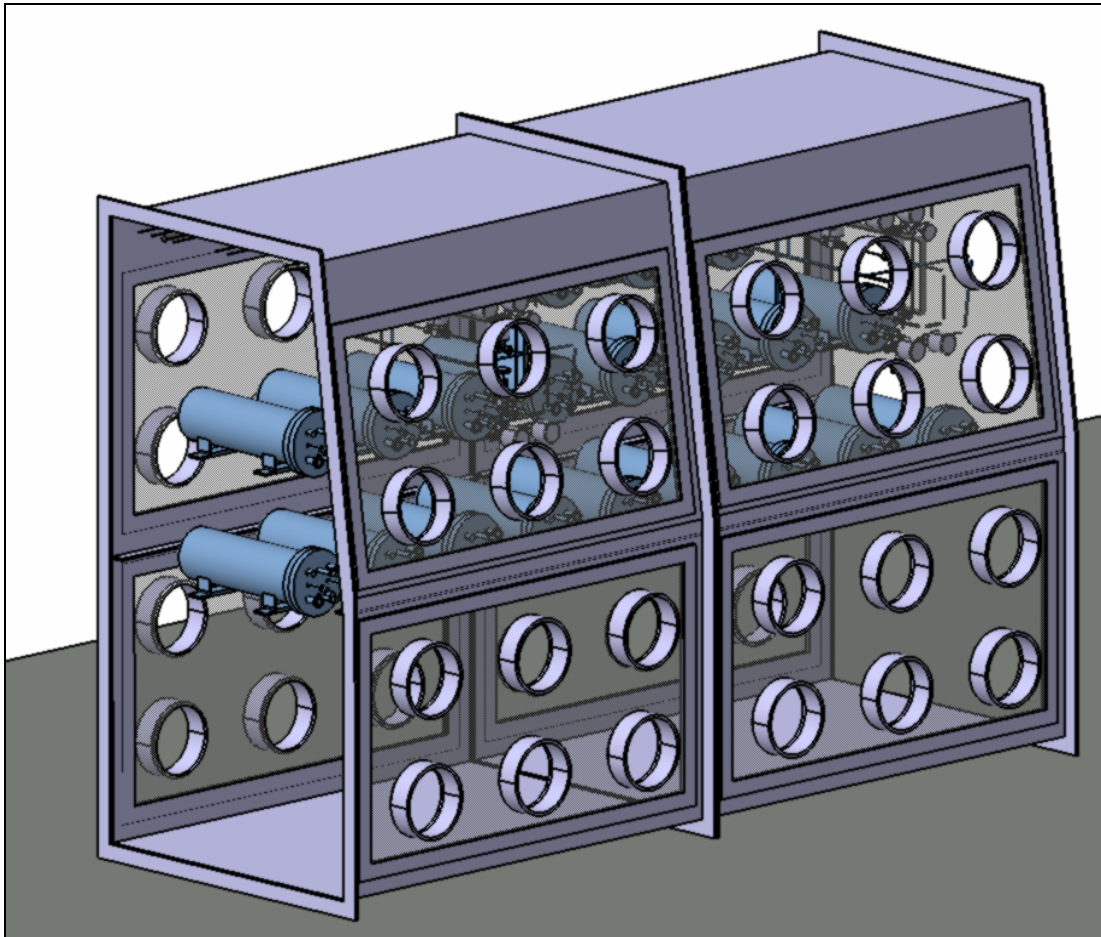


Example of the CATIA intelligent Piping and Instrumentation Diagram: part of SDS system of ITER Tritium Plant

CATIA V5 Equipment and Systems is a CAD system intended for design and integration of mechanical, electrical and fluid systems. The wide range of applications, such as Piping & Instrumentation Diagrams (P&ID), Heating, Ventilation and Air Conditioning (HVAC) Diagrams, Piping Design, Tubing Design, HVAC Design, and Equipment Arrangement provides the ability for the upstream design process from the functional 2D design (P&ID, HVAC diagrams) to the 3D detailed design. Intelligent P&ID are integrated with detailed 3D design giving the possibility to propagate design data and insure design consistency between the schematic 2D design – P&ID diagrams – and the detailed 3D design. One of the main part in the systems engineering is creating of the consistent and structured database containing all necessary information on systems components. Using CATIA V5 E&S software tools the

project database is filled with the required information simultaneously with production of P&IDs or 3D detailed design. In other words, in this case the CAD system serves as a graphical interface intended to automate the creating of the project database. However, one should understand that data structure in the project should be decided before the design process starts. Depending on the project, in most cases the project specific data structure is required. In addition, a number of other project specific requirements shall be implemented in the CAD system, such as components classification, identification system, project standards and specifications, design rules, drawing standards. In CATIA V5 E&S specific resources are implemented through the Project Resources Management system. The Project Resource Management (PRM) is a framework of the project which, on the one hand, gives a tool to customize the working environment. On the other hand it organizes the design process to ensure design compliance with established standards, specifications, standardization, industrial conventions, terminology and practice. Feature Dictionaries, Catalogues for components as well as for standards and specifications are main parts of the CATIA V5 PRM.

In addition to the CAD system the Project Data Management (PDM) system is necessary to be applied in order to allow data validation, product management, product life cycle, systems configuration. There are several PDM systems supporting CATIA V5: ENOVIA VPM, ENOVIA V5 LCA, SmarTeam.



Example of detailed 3D layout in CATIA V5 E&S

Scope of the task includes the development of the ITER PRM, in order to create 2D symbols catalogue in CATIA V5 and to create catalogues of 3D parts for the systems that compose the Tritium Plant. The elements of P&ID, pipes, piping parts and equipment will carry attribute information that is defined in the PRM.

Work performed

An intensive work was performed in collaboration with other groups in ITER collecting all required engineering data to be implemented in CATIA V5 E&S PRM: component classification, drawing standards, engineering standards, specifications. As a result a first version of PRM was composed and tested in FZK and supplied to the ITER CAD Office.

The draft report on all deliverables was presented in November 2006.

Staff:

S. Beloglazov
C. Caldwell-Nichols
M. Glugla
M. Lux
R. Wagner
V. Weber
A. Lazar (MEC Rumania)

EFDA/05-1239 (TW5-TTFD-TPI 52) Development of a Resource-loaded Schedule for the Overall ITER Tritium Plant Integration

The objective of the task is to develop the resource-loaded time schedule for the overall Tritium Plant Integration. The Tritium Plant design main activities will comprise designing of systems: Tokamak Exhaust Processing (TEP), Isotope Separation System (ISS), Water Detritiation System (WDS), Storage and Delivery System (SDS), Analytical System (ANS), Atmosphere Detritiation System (ADS), Vent Detritiation System (VDS) and auxiliary systems with high degree of integration, Automated Control System (ACS), Safety System (SS) and secondary containments. The task covers the development of an integrated overall resource-loaded time schedule for the ITER Tritium Plant, based on inputs from systems design tasks to be provided by the responsible Participating Teams PT's.

The required time schedule for Tritium Plant Design and Integration is made in conjunction with the over-all time schedule for ITER. Eventually this activity should extend up to including stand-alone system and integrated plant commissioning to co-ordinate installation and commissioning of the Tritium Plant systems with building construction, with infrastructure and with other interfaces. The main activities monitored in the resource-loaded time schedule for the Tritium Plant are presented in Figure 1.

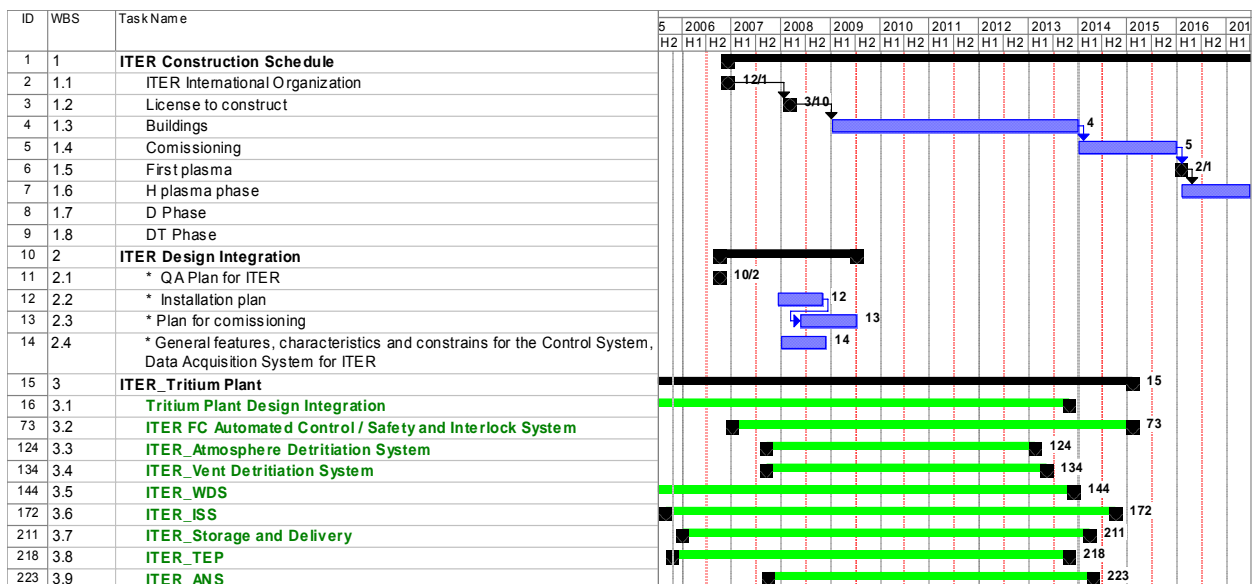


Fig. 1: Monitored activities for the Tritium Plant

A total number of approx. 220 tasks are currently monitored; the systems which are detailed more are the ones where EU-PT is responsible that are WDS and ISS. Considering on one hand the complexity of the Automated Control system and on the other hand the experience of EU related to this activity, this system was also thoroughly detailed.

In 2006 an evaluation of the tasks foreseen to start or develop in 2007-2008 have been done and the following priorities have been established:

- Establishing the process flow diagrams for the detritiation systems, ADS, VDS and WDS. Related to these systems, tasks (contracts) inside the EU-PT have been launched and the deadline agreed is within the dates established in the time schedule.
- Design work for the ISS (covered by the ITER task ITA 32- 07). As it is envisaged to combine WDS and ISS the detailed design of these systems will be covered by an EFDA task, and an agreement upon the content of this task and deadlines is already established. It is therefore considered that the current plans are in-line with the time schedule.

- The detailed design activity for the SDS should end December 2008, however no additional details related to planning, status or on-going activities inside the Korean PT is available.
- Related to the detailed design activity for TEP, this should also end December 2008 and the US participating team confirmed the initial planning without detailed specification upon WBS inside the US PT for this system.
- Urgent work is the work corresponding to the ACS-SS. A unified Automated Control System for the Tritium Plant is envisaged with a common Tritium Plant Process Control Room. Automated Control System and Safety System are independent from the operational point of view, however they have to be designed in conjunction. The design of the Tritium Plant ACS-SS needs as inputs P&ID's for the sub-systems (WDS, ISS, ANS, SDS, TEP, ADS, Tritium Extraction from Breeder Blanket Module). In Europe IEC 61508 standard is accepted for industrial plants (chemical, etc.), however the use of this standard for the tritium plant is not yet adopted. Until present no analyses into the consequences of adopting this standard or a hardwired solution for the SS have been done and it is considered of highest priority to make a decision due to implications related to the design/procurement for the subsystems, design integration issues and management of the Tritium Plant as a whole.
- Related to the ANS, for this system design activities were planned to start in 2007. As for the ACS-SS, this system is not allocated to PT's but covered by fund. Because of the R&D and design activities performed within the last year, it became more clear the necessity and importance of an accurate analytical system, for operation and for tritium inventory procedure (licensing).

The resource-loaded time schedule for the Tritium Plant activities show that the activity of the inactive commissioning of the Tritium Plant might end in 2015. At this moment in time the major uncertainties in the time assessment for sub-tasks are due to:

- If the IEC 61508 standard will be considered as unacceptable the tasks related to the Safety System will have to be re-evaluated;
- All the tasks related to installation and commissioning will have to be re-evaluated when the Installation plan and Commissioning plan will become available. However it is important to mention that the time schedule for design and manufacturing is considered to be rather accurate; therefore this information from the Tritium Plant can be used as input data for the Installation plan and Commissioning plan from ITER IT.

Recently, PRIMAVERA was adopted as the management software tool for both ITER IT and EU-DA planning. The present work done in Microsoft Project can be easily integrated in a PRIMAVERA project. As the design, installation and commissioning will advance permanently updates will be needed and it is highly recommended that the resource-loaded planning activity will be carried on by ITER-IT.

Staff:

I. R. Cristescu
I. Cristescu
G. Hellriegel
P. Schäfer

EFDA/05-1240 (TW5-TTFD-TPI 53)

Definition of Interfaces and Supply Limits between Tritium Plant and Torus Pumping, Fuelling, Neutral Beam and Wall Conditioning Systems

The evaluation of the interfaces have been made mainly related to the processing of different technological streams between vacuum pumping, fuelling, wall conditioning systems and the tritium plant. In some cases when data concerning the utilities have been available, the consequent interfaces with the tritium plant have been identified. However, it is considered that this issue will have to be further developed when detailed information of the equipment is available.

The tritium plant consists of the following subsystems:

- Tokamak Fuel Cycle Subsystems
- Confinement and Detritation Systems (ADS, Ventilation Detritation System, Glove box Detritation System, Water Detritation System)
- Room Depression Systems
- Tritium Monitoring Systems (Safety and Area Monitoring)
- Building Ventilation Systems (Tokamak, Tritium, Hot Cell, Radwaste)
- Utilities (Compressed air, Normal & Safety Chilled Water, Breathing Air)
- Contaminated drain collection and transfer system (Tokamak, Tritium, Hot Cell Bldg, etc.)
- Electric Power Supply Network (Class IV-A/B, III-A/B, II-A/B)
- Plant Operation Control and Interlock.

DDD's of 2001 have been used as reference for the development of this task. In some cases when the developments have been agreed between the parties responsible for the systems which have interfaces and if no major changes have been required, the results of R&D programs have been considered in the present definition of the interfaces.

The interfaces have been characterized with respect to time evolution of the flow-rates, pressures and gas stream compositions during burn, dwell phases and wall conditioning. A tree structure configuration has been implemented for the management of this task.

The main issues to be considered during the design activities of the systems analysed in the frame of the task are summarized below:

1. Interfaces between the fuelling system and the tritium plant

For the fuelling system, there are still on-going R&D activities and the results have to be considered for a detailed and improved quantification of the interfaces. As far as gas processed in the fuelling system is concerned and the potentially ablated and recovered gas from the pellet injector systems to be processed in the TEP and ISS, the actual configuration and size of the ISS will allow processing with an increase in the tritium inventory. Based on the available data from pellet injector operation strategy the impact on ITER ISS has been evaluated for the 8 typical fuelling cases:

An accurate evaluation of the tritium inventory within the ITER ISS can be done when the operation procedure within the fuelling system and the detailed design of TEP will be available to be implemented in the TRIMO code.

Typical Fuelling cases	1	2	3	4	5	6	7	8
T/D ratio	25/75	40/60	50/50	50/50	60/40	70/30	75/25	90/10
D2 flow rate	84	48	0	40	4	0	0	0
DT flow rate	6	42	120	30	66	50	30	0
Tritium flow rate	30	30	0	50	30	50	50	50
Total flow rate	120	120	120	120	100	100	80	50

2. Interfaces between vacuum pumping system and the tritium plant

As far as vacuum pumping is concerned, the data available in the DDD 3.1 give detailed information on the interfaces with the tritium plant. The proposal to design a single pumping train with the duty to lower the cryopump pressure down to 10 Pa and providing the feeding pressure of the front end permeators up to at least 0.25 MPa should be evaluated with respect to the simplicity of the process and easy operation.

3. Interfaces between wall conditioning systems and tritium plant

For the wall conditioning system, the P&ID has to be developed in order to define the utilities required. The processing route for the tritiated water recovered during regeneration of the molecular sieve beds is not defined. The proposal to collect the tritiated water from the wall conditioning system and the vacuum pumping system during high temperature regeneration has to be evaluated in more detail and a procedure to process the highly tritiated water to be implemented within the tritium plant.

In order to recover tritium from the deuterium stream used for glow discharge cleaning, an appropriate feeding location on ISS has to be considered in correlation with the ablated gas from the pellet injector.

4. Interfaces between neutral beam injectors and the tritium plant

FMEA studies related to the NBI injectors showed that water leaks from various water cooled components determine the functional availability of the system. Therefore, procedures for recovery of the water especially during high temperature regeneration have to be implemented. The water like impurities will be accumulated on the feed side of the permeator, and hence need to be removed in order to keep the permeation capacity and to avoid condensation during cool down of the permeator.

The interfaces with the Atmosphere Detritiation System during maintenance activity within the NBI box when fully opened to torus have to be considered with respect to tritium trapped on NBI cryopanel and tritium out-gassing from in-vessel components

Staff:

I. Cristescu
 I. R. Cristescu
 C. Day
 A. Antipenkov

EFDA/05-1251 (TW5-TTFD-TPI 54) Development of a Tritium Manual for ITER

A Tritium Manual is required for use by ITER designers and operators as the prime source of relevant information on tritium properties, tritium processes in ITER, tritium compatible components, tritium safety, QA procedures and design guidelines for ITER systems that handle tritium. It will be mandatory to use components and devices for ITER tritium systems recommended in the manual and to follow procedures laid down in the manual.

The initial objective of the task is to initiate the construction of the ITER Tritium Manual on the ITER Baseline website in a format similar to the existing ITER manuals using the ITER Document Management System. The list of topics is agreed and the information is now being assembled for inclusion in the Tritium Manual before approval. As the manual will need to be valid for up to 40 years the format will reflect this as far as can be foreseen, noting that over this period there will be many revisions and updates of the information and also that nature of information technology will change radically. The Manual will contain lists of recommended components from specific manufacturers that are to be used in the construction of ITER tritium systems. As further work on the design of the ITER Tritium Plant is anticipated over the next few years the manual will need to be updated to reflect these developments.

A draft report on deliverable 2 was presented in July 2006 and draft versions of volumes 1 and 2 posted in the ITER Document Management System (IDM) allowing them to be available for review by interested parties from the ITER project.

Staff:

C. J. Caldwell-Nichols
R.-D. Penzhorn

EFDA/05-1342 (TW5-TTF-TLK) Documentation of ITER-relevant Experience Gained from Operation of the Tritium Laboratory Karlsruhe (TLK) in 2005 and 2006

The Tritium Laboratory Karlsruhe (TLK) is a semi-technical facility which was founded with the aim of establishing tritium handling techniques in Europe and to develop the technologies for the fuel cycle of future fusion reactors. Now, the principal objective of the Tritium Laboratory Karlsruhe at FZK is the hosting of experiments operated to prepare for the procurement of components for the Tritium Plant of ITER. TLK now has a license to hold 40 g of tritium and has gained considerable experience in handling tritium since the first license was granted in 1993. In an experimental area of around 1000 m² there are glove boxes with a total volume of about 125 m³ which are available for the experimental R&D work at TLK. In addition, experience gained in the operation of the TLK infrastructure provides valuable contributions to the design and preparation of operating procedures for the ITER Tritium Plant. The objective of this task was to cover aspects of operation of TLK related to ITER Tritium Plant experiments and to provide for documentation of technical data on operation of the TLK infrastructure which are of relevance to ITER.

The TLK infrastructure, comprising the subsystems for tritium storage, a clean-up system for the recovery of tritium, a hydrogen isotope separation system, an analytical system and including confinement of tritium with tritium retention and monitoring, was operated continuously in 2006 [1]. The infrastructure supplied the tritium necessary for technical experiments, took back the tritium after the experiments were finished and processed the returned gases for reuse. The main emphasis was on the support of the experimental facility CAPER for the processing of simulated plasma exhaust gases expected from a fusion reactor. After the modification of the Isotope Separation System (ISS) in 2005 a comprehensive commissioning program was carried out for the active operation with tritium. Following successful cold commissioning, first runs with 30% and 70% tritium in the gas batches to be separated have been carried out. The ISS is now available again for the separation of all hydrogen mixtures arising at TLK and its operation has been greatly simplified.

More than 40 molecular sieve beds from the different Tritium Retention Systems (TRS) of the glove boxes have been regenerated using the AMOR facility up to the end of August 2006 and the collected tritiated water sent to the waste treatment department of FZK for disposal. Because of other research activities in TLK, the AMOR facility had to be relocated to another area of the laboratory. After a short commissioning phase the AMOR facility returned to full operation and the first regenerations of tritium loaded molecular sieve beds have been carried out successfully.

The programme to modify the original facilities and systems after more than 12 years of tritium operation continued throughout 2006. Parts of the tritium monitoring system for the room air and the atmosphere in the glove boxes have been replaced so that the preconditions for the operation of the system for the next 10 years are fulfilled.

As a result of destructive inspection work to determine the failure of experimental components, the repair glove box became heavily contaminated with tritium-containing dust; even the lines to the ionization chamber and the ionization chamber itself used to monitor the glove box atmosphere were contaminated. After an extensive decontamination programme the contamination in the repair box and in the connecting lines was cleared up to acceptable levels. The glove box is now in full operation again. The experience at TLK now makes it possible so that tasks, such as the replacement of a failed pump in the Central Tritium Retention System, is now a routine procedure for the TLK staff. Despite several interventions on tritium systems, no member of the TLK staff has received a recordable radiation dose in 2006 due to tritium.

Staff:

H.-D. Adami
U. Besserer
L. Dörr
H. Dittrich
M. Göckel
G. Hellriegel
F. Kramer
S. Krieger
K. Nolte
E. Porter
F. Rehlinghaus
P. Schäfer
P. Schuster
J. Wendel

Literature:

- [1] Dörr, L.; Besserer, U.; Glugla, M.; Hellriegel, G.; Hellriegel, W.; Schäfer, P.; Wendel, J.: The closed tritium cycle of the tritium laboratory Karlsruhe, Fusion Science and Technology, 48(2005) p. 262-67

Safety Analysis and Environmental Impact

TW5-TSS-SEA 3.5

In-vessel Safety: Mitigation of Hydrogen and Dust Explosions

Objectives

Risk studies for ITER have shown possibilities for the generation of reactive hydrogen-dust-air mixtures, which after ignition could result in potential pressure loads to the vacuum vessel and in the mobilization of tritium. This work aims at fundamental understanding and numerical modelling of hydrogen and dust explosions for ITER-typical gas and dust mixtures. The results will be used to derive effective mitigation measures against hydrogen/dust reactions in ITER.

To evaluate the dust explosion hazard in ITER, it is proposed to develop a semi-phenomenological code suitable for modelling the combustion/explosion process under ITER typical conditions for the whole variety of the accident scenarios. The main objective of this work is to complete the experimental data on ITER-relevant dusts to support the code development/validation. The effective dust burning rates necessary for the code combustion module are to be measured depending on the dust particle size, dust concentration, and turbulence level using the method of open-end combustion tubes. Another activity on this way is to support mitigation methods of the dust/hydrogen explosion hazard. To this aim, the Limiting Oxygen Concentrations of explosion atmospheres preventing the dust/H₂ explosions are to be measured.

Status

The investigations of the explosion behaviour of some ITER-relevant dusts have been performed in 2002-2005 using a standard method of a 20-l sphere. The explosion indices of fine graphite and tungsten dusts and their mixtures, and their dependences on dust particle size, have been measured. The tested dusts appeared to explode in wide concentration ranges generating overpressures about 5-7 bar; the minimum ignition energy was evaluated as 2 kJ. Further tests with 8 to 18 vol. % hydrogen added to graphite-dust/air mixtures showed the possibility of the cloud ignition by a weak electric spark, if the hydrogen content is higher than 10 vol. %. At hydrogen concentrations higher than 12 vol. % the combined hydrogen/dust/air explosion can generate rates of pressure rise higher than hydrogen/air alone. In case of a strong ignition source, the dust-fuel constituent increases the hydrogen-relevant maximum explosion overpressure at any of the tested concentrations.

In 2005 tests were performed to support an inerting method to mitigate the hydrogen/dust explosion hazard in ITER. The limiting oxygen concentrations were measured for 4-micron graphite dust using the 20-l sphere method. The oxygen content in the pre-explosion atmosphere was varied from normal 20.8 vol % to 10 vol. %. The tested mixtures were ignited by 2 or 10 kJ chemical igniters. It was shown that even a weak dilution of the dust-cloud atmospheres could reduce drastically the resulting pressure loads.

Another experimental technique has been developed to measure efficient burning velocities of the flame propagating in the quiescent dust/air mixture under concern. The velocity data are to be used in a semi-empirical code to model H₂/dust explosions in ITER. First tests were performed with 4 µm graphite dust in a 15 cm inner diameter 2 m long open combustion tube. The tests indicated the importance of the scale effect for the flame propagation in the tested clouds. For this reason, the preparation of a larger open combustion tube of 35 cm diameter and 3 m length for further tests was started.

Results

The Limiting Oxygen Concentration measurements have been continued in 2006 with 1 μm tungsten dust using the 20-l sphere method. The tests were performed at normal initial conditions. As a dilution gas nitrogen is used to reduce the oxygen concentration in the pre-explosion atmosphere. The mixtures were ignited by 5 kJ chemical igniters. Only one dust concentration of 3000 g/m^3 was tested. The results are presented in Fig. 1, where the maximum overpressure and rate of pressure rise are plotted versus oxygen content in air diluted with nitrogen. The explosion regimes observed seem to be exaggerated because of a too high ignition energy for a small combustion volume. However, the value of 14.5 vol. % O_2 can be considered as a conservative estimate for the Limiting Oxygen Concentration of 1 μm tungsten dust.

A large combustion tube of 35 cm inner diameter and 3 m length (PROFLAM II facility) has been completed to prepare for the tests with 4 μm graphite dust (see Fig. 2). A series of dispersion tests have been done to choose the proper dispersion pressure, dispersion reservoir volume, and dispersion timing. The best dust cloud homogeneity is obtained with the 300 l pressure reservoir pressurised to 20 bar. Typical high-speed shots of the dispersion process are shown in Fig. 3.

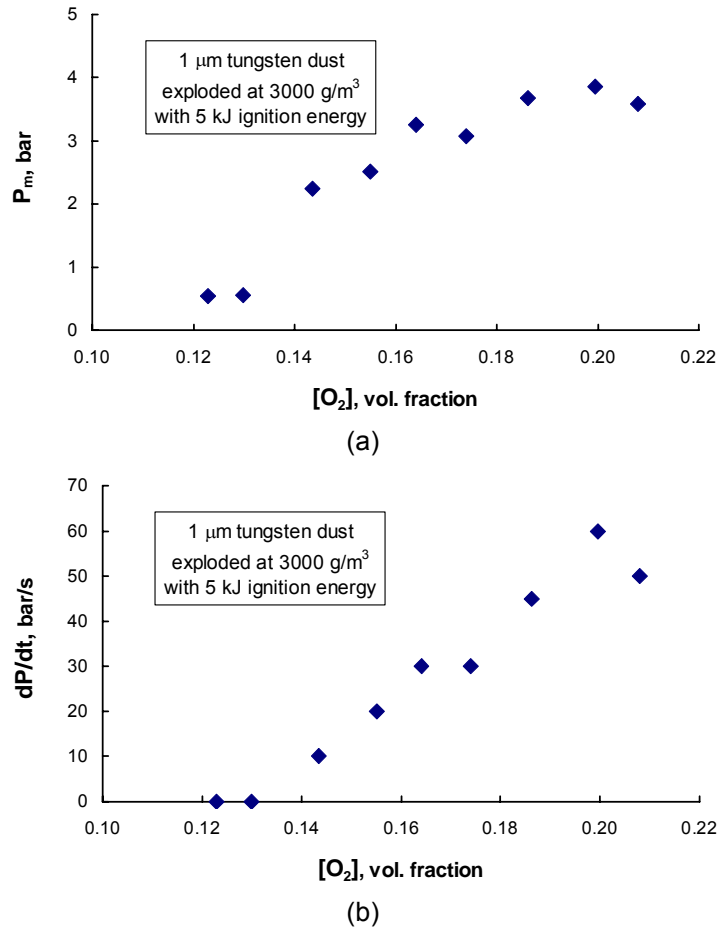


Fig. 1: Maximum overpressure (a) and rates of pressure rise (b) measured with 1 μm tungsten dust of 3000 g/m^3 cloud density in nitrogen-diluted air ignited by 5 kJ igniters versus oxygen content.

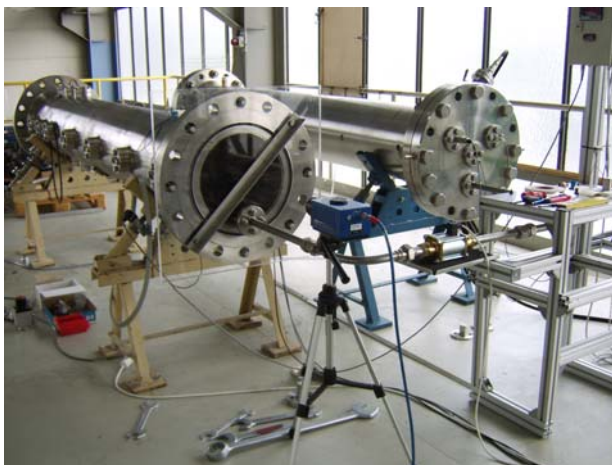


Fig. 2: PROFLAM II facility.

In order to establish the limits of flame propagation and to provide the dust cloud parameters for measuring the effective burning velocities, a series of flame propagation tests was performed. The tests were made in the closed tube varying the dust cloud density, dispersion process parameters, and the ignition energy. The dust clouds were ignited at one of the tube ends with chemical igniters of 10 to 30 kJ thermal energy. The dust cloud density ranged from 150 to 600 g/m³. The dispersion pressure was 5 and 20 bar. In all the tests no flame propagation was observed. The maximum overpressures were about 1.5 bar independent of dust density and dust cloud volume.

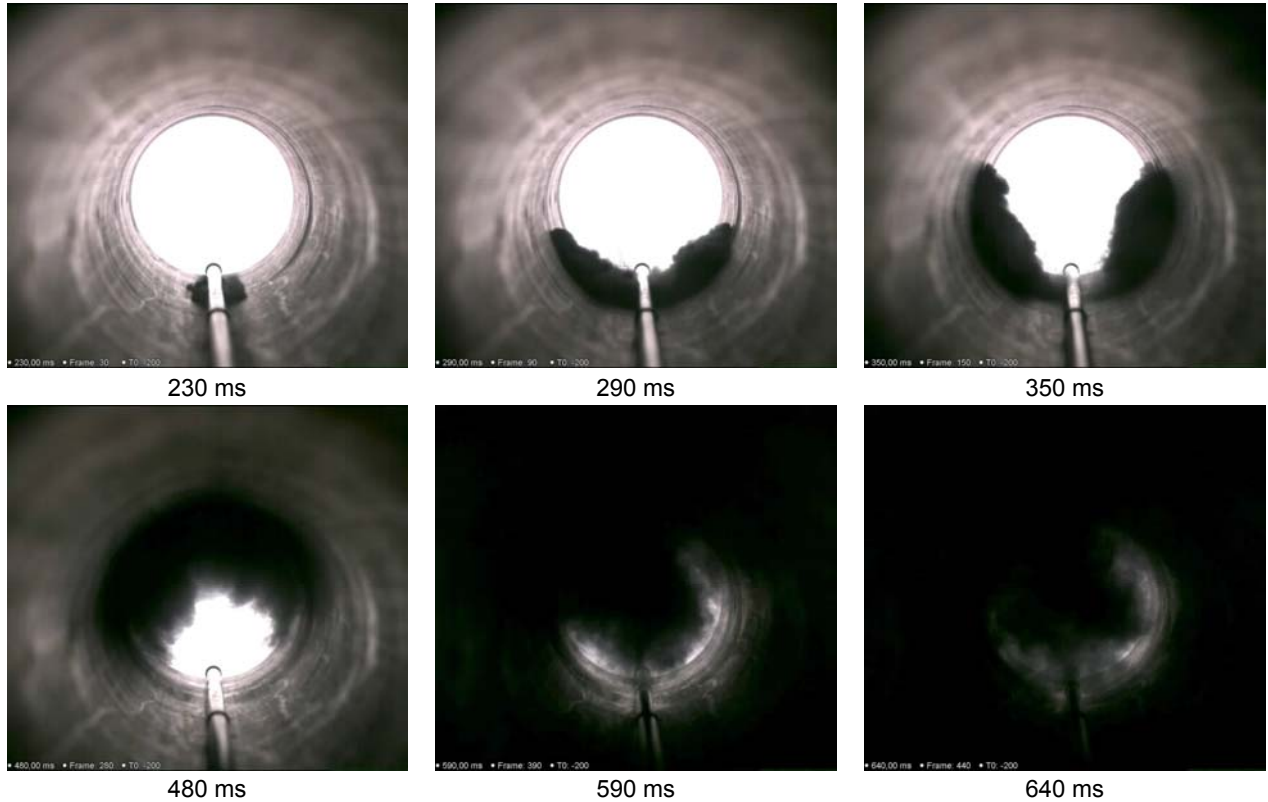


Fig. 3: Dispersion of 4 μm graphite dust in PEOFLAM II tube.

The results are in contradiction with the previous ones obtained in 20-l sphere. The possible reasons of the failure to ignite the dusts are considered including (i) poor dust dispersion in a bigger tube giving non-homogeneous dust clouds, (ii) lower level of turbulence provided by a weaker dispersion system; (iii) different particle size of the dust dispersed in the 20-l sphere by a powerful dispersion and in a larger volume with a weaker dispersion device, (iv) different initial conditions in the 20-l sphere and in larger volumes at the mo-



Fig. 4: PROFLAM I facility.

ment of ignition. Further tests are planned to clarify the issue: providing a more powerful dispersion regime to get higher dust spatial density distribution homogeneity and stronger turbulence level; use a finer dust; and some tests at elevated initial pressures.

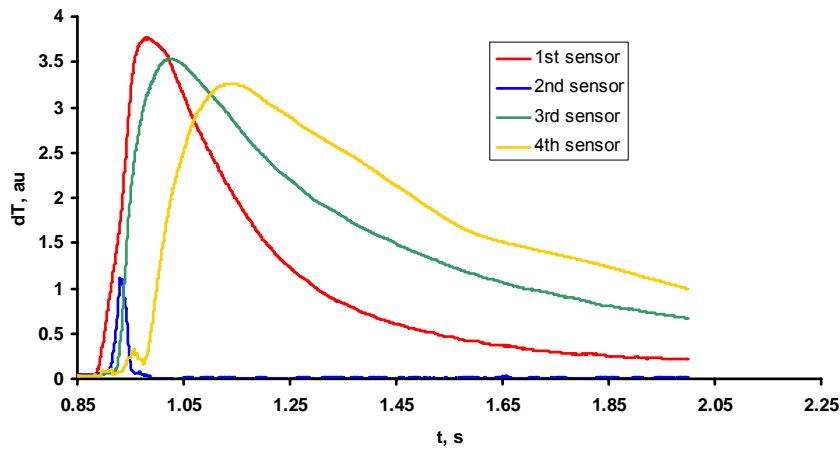


Fig. 5: Thermocouple signals in combined hydrogen/dust test.

The 15 cm inner diameter open combustion tube has been finally built up this year (PROFLAM I facility, see Fig. 4). It consists of a 3 m length metal tube with 40 measuring ports connected to a 11 m³ dump tank rated to 3 bar, and vacuum, dispersion, ignition, and measurement systems. Several tests have been performed with the tube charged with

the 4 μm graphite dust and some hydrogen added to the pre-dispersion atmosphere. The main purpose was to test the functionality of the facility and its systems and to get first results on detecting flame-arrival times with the thermocouples. Typical signals recorded from the thermocouples in a combined hydrogen/dust test of 15 vol. % of hydrogen and 200 g/m³ graphite dust ignited by a weak electric spark are shown in Fig. 5. The shape of the curve recorded by the farthest sensor even has two peaks that could reflect the two flame fronts coming to the sensor location, first the hydrogen, and second the dust flame fronts. One can see that the system can resolve even the fast propagation of hydrogen flame.

In all the tests the pressure recorded at the close end was stable about 1 bar with no significant variations. It means that in all the tests the flame propagated over a quiescent mixture.

Outlook

Measurements of LOC of tungsten/hydrogen/air mixtures in DUSTEX facility.

Further tests in PROFLAME II facility on flame propagation in fine graphite dusts.

Study of flame propagation in graphite clouds in hydrogen containing atmospheres (PROFLAME I facility).

Staff.:

S. Baur

A. Denkevits

B. Kaup

F. Prestel

A. Friedrich, ProcScience

K. Sempert, ProScience

G. Stern, ProScience

Literature:

[1] A. Denkevits and S. Dorofeev. Explosibility of fine graphite and tungsten dusts and their mixtures. Journal of Loss Prevention in the Process Industries, 19 (2006) 174-180.

[2] A. Denkevits. Explosibility of Hydrogen-Graphite Dust Hybrid Mixtures. Proc. of 6th Int. Symp. on Hazards, Prevention, and Mitigation of Industrial Explosions: Halifax, Nova Scotia, Canada, August 27 – September 1, 2006

EFDA/05-1369 (TW5-TSS-SEA 3.5) Development of a Dust Explosion Computer Model

Objectives

To understand and predict behaviors of tons of dust expected in the vacuum vessel in ITER, especially in case of Loss Of Vacuum Accidents (LOVA), fundamental studies about aerosol particle transport should be performed. Therefore, this task is devoted to developing numerical models of dust mobilization and to realising dust simulations based on the Computational Fluid Dynamics (CFD) computer code GASFLOW. In detail, three objectives are defined, (i) establishing of the governing equation system for particle transport and modeling of particle diffusion, suspension and deposition; (ii) reviewing the analytical and experimental data for benchmarking the numerical models; (iii) validating the dust models based on the theoretical solutions or data.

Main results

1. Numerical models

1.1 *Governing equations of particle transport*

A Lagrangian discrete particle transport model is established to describe the particle motion in a conveying gas flow. The equations are solved numerically in GASFLOW independently of solving the fluid dynamics equations. It is assumed that the dust cloud is diluted enough so that the presence of particles does not affect the accompanying gas flow at all. This assumption is especially suitable for the situation possibly taking place in ITER. The governing equations of particle motion are as follows,

$$\begin{aligned} \frac{dx_p}{dt} &= u_p \\ \frac{dy_p}{dt} &= v_p \\ \frac{dz_p}{dt} &= w_p \end{aligned} \tag{1-1}$$

$$\begin{aligned} \frac{du_p}{dt} &= \frac{3}{4} C_D \frac{\rho_g}{\rho_p} \frac{(\mathbf{u}_g - \mathbf{u}_p) |\bar{\mathbf{U}}_g - \bar{\mathbf{U}}_p|}{d_p} + \xi \frac{v_p^2}{x_p} + g_x \\ \frac{dv_p}{dt} &= \frac{3}{4} C_D \frac{\rho_g}{\rho_p} \frac{(\mathbf{v}_g - \mathbf{v}_p) |\bar{\mathbf{U}}_g - \bar{\mathbf{U}}_p|}{d_p} - \xi \frac{u_p v_p}{x_p} + g_y \\ \frac{dw_p}{dt} &= \frac{3}{4} C_D \frac{\rho_g}{\rho_p} \frac{(\mathbf{w}_g - \mathbf{w}_p) |\bar{\mathbf{U}}_g - \bar{\mathbf{U}}_p|}{d_p} + g_z \end{aligned} \tag{1-2}$$

where,

x_p, y_p, z_p the coordinates of particle location,

u_p, v_p, w_p the directional particle velocities,

u_g, v_g, w_g the directional fluid velocities,

$\bar{\mathbf{U}}_p, \bar{\mathbf{U}}_g$ the velocity vectors of particle and fluid, respectively,

ρ_p, ρ_g the density of particle and fluid, respectively,

d_p the diameter of particle,

g_x, g_y, g_z the directional gravities,

ξ the geometry factor (0 for Cartesian coordinates and 1 for cylindrical coordinates),

C_D the drag coefficient, defined as,

$$C_D = \begin{cases} \frac{24}{\mathbf{Re}_p} \left(1 + \frac{\mathbf{Re}_p^{\frac{2}{3}}}{6} \right), & \text{if } \mathbf{Re}_p < 905 \\ 0.44, & \text{if } \mathbf{Re}_p \geq 905 \end{cases} \quad (1-3)$$

\mathbf{Re}_p the particle Reynolds number, defined as,

$$\mathbf{Re}_p = \frac{d_p |\bar{\mathbf{U}}_g - \bar{\mathbf{U}}_p|}{\nu} \quad (1-4)$$

ν the fluid kinematic viscosity.

1.2 Particle turbulent dispersion model

The overall velocity of particle includes mean velocity and diffusion velocity, namely,

$$\begin{aligned} \mathbf{u}_p &= \bar{\mathbf{u}}_p + \mathbf{u}_{\text{diff}} = \bar{\mathbf{u}}_p \pm \sqrt{\frac{4\lambda}{\delta t}} \mathbf{erf}^{-1}(\zeta_1) \\ \mathbf{v}_p &= \bar{\mathbf{v}}_p + \mathbf{v}_{\text{diff}} = \bar{\mathbf{v}}_p \pm \sqrt{\frac{4\lambda}{\delta t}} \mathbf{erf}^{-1}(\zeta_2) \\ \mathbf{w}_p &= \bar{\mathbf{w}}_p + \mathbf{w}_{\text{diff}} = \bar{\mathbf{w}}_p \pm \sqrt{\frac{4\lambda}{\delta t}} \mathbf{erf}^{-1}(\zeta_3), \end{aligned} \quad (1-5)$$

where,

$\bar{\mathbf{u}}_p, \bar{\mathbf{v}}_p, \bar{\mathbf{w}}_p$ the directional mean velocities of particle,

λ the particle diffusion coefficient,

δt the time step of numerical scheme,

$\zeta_1, \zeta_2, \zeta_3$ the random numbers between zero and one.

The λ is determined by a turbulent dispersion model for particles. The model is formulated as,

$$\lambda = \frac{\mu_{\text{turb}}}{1 + \frac{\tau_p}{\tau_g} \rho_g \mathbf{Sc}_p}, \quad (1-6)$$

where,

μ_{turb} the turbulent dynamic viscosity,

\mathbf{Sc}_p the particle Schmidt number,

τ_p the particle relaxation time,

τ_g the fluid relaxation time.

2. Validation

2.1 Particle trajectory validation in case of Cartesian coordinate system

I. Without gravity

As shown in Figure 1, a uniform advection Stokes flow with velocity of \mathbf{u}_0 is contained in a 2D channel. The particles are injected into the gas flow with an initial velocity of \mathbf{V}_0 in the transverse direction. Then the particles are entrained to move.

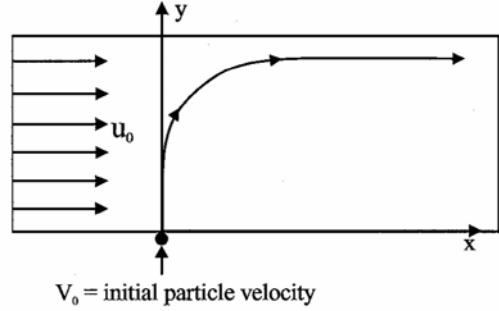


Fig. 1: Trajectory validation problem in a Cartesian system without gravity.

This problem is simulated by using the GASFLOW particle model. The simulated particle trajectory is shown in Figure 2. For comparison, the particle transport equation is solved directly in case of a small Reynolds number corresponding to Stokes flow. The theoretical solution describing the particle trajectory is obtained as,

$$\begin{aligned} x_p &= u_0 \left(t + \frac{\exp(-\Gamma t) - 1}{\Gamma} \right) \\ y_p &= -\frac{V_0}{\Gamma} (\exp(-\Gamma t) - 1), \end{aligned} \quad (2-1)$$

where, $\Gamma = 18 \frac{\mu_g}{d_p^2 \rho_p}$.

The equations of particle motion are solved by using a numerical scheme outside of GASFLOW, the trajectory of which is also shown in Figure 2 as the series of "Numerical". The comparison clearly demonstrates that the particle transport model of GASFLOW works in a proper way.

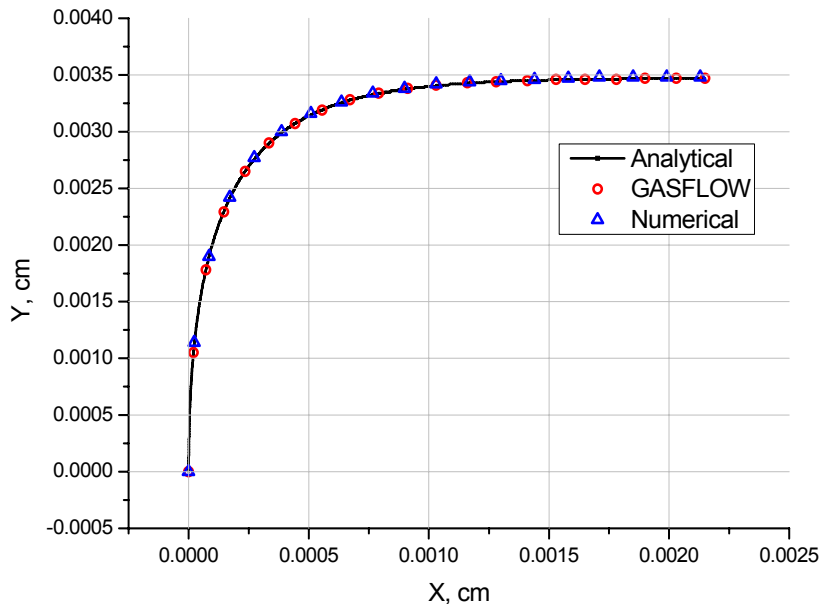


Fig. 2: Trajectory comparison in a Cartesian system without gravity.

II. With gravity

Based on the problem I, gravitational terms are considered. The problem and the results are shown in Figure 3 and Figure 4, respectively. In the case, the theoretical solution is as,

$$x_p = u_0 \left(t + \frac{\exp(-\Gamma t) - 1}{\Gamma} \right),$$

$$y_p = \left(\frac{g_y}{\Gamma^2} - \frac{V_0}{\Gamma} \right) (\exp(-\Gamma t) - 1) + \frac{g_y}{\Gamma} t. \quad (2-2)$$

It is obvious that gravity is treated in a right way in the particle model of GASFLOW.

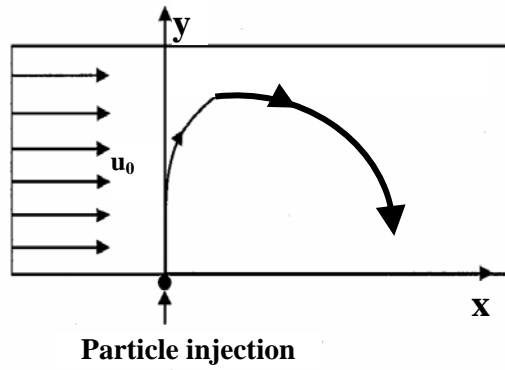


Fig. 3: Trajectory validation problem in a Cartesian system with gravity.

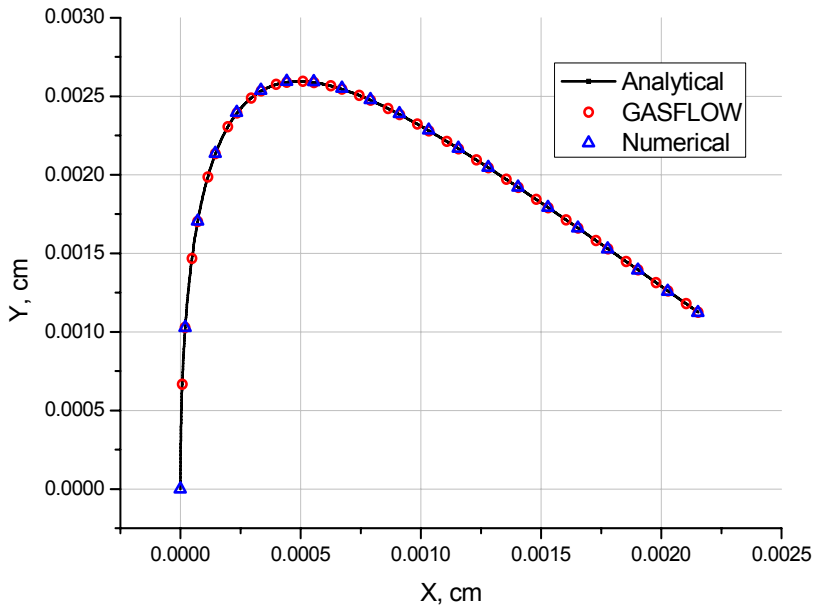


Fig. 4: Trajectory comparison in a Cartesian system with gravity.

2.2 Particle trajectory validation in case of cylindrical coordinate system

A Stokes flow contained in a 180 degree curved duct has a fluid velocity distribution, where the local velocity is proportional to the radial distance to the center of the duct, as shown in Figure 5. The particles are injected into the flow with an initial velocity equal to the local fluid velocity, i.e., 3 cm/s. In the Figure, the red circle line stands for the particle trajectory simulated by GASFLOW, the blue triangle line is the solution obtained by directly solving the particle motion equations outside of GASFLOW. The consistency between the two trajectories

manifests that the particle solver of GASFLOW works properly in case of cylindrical coordinate system.

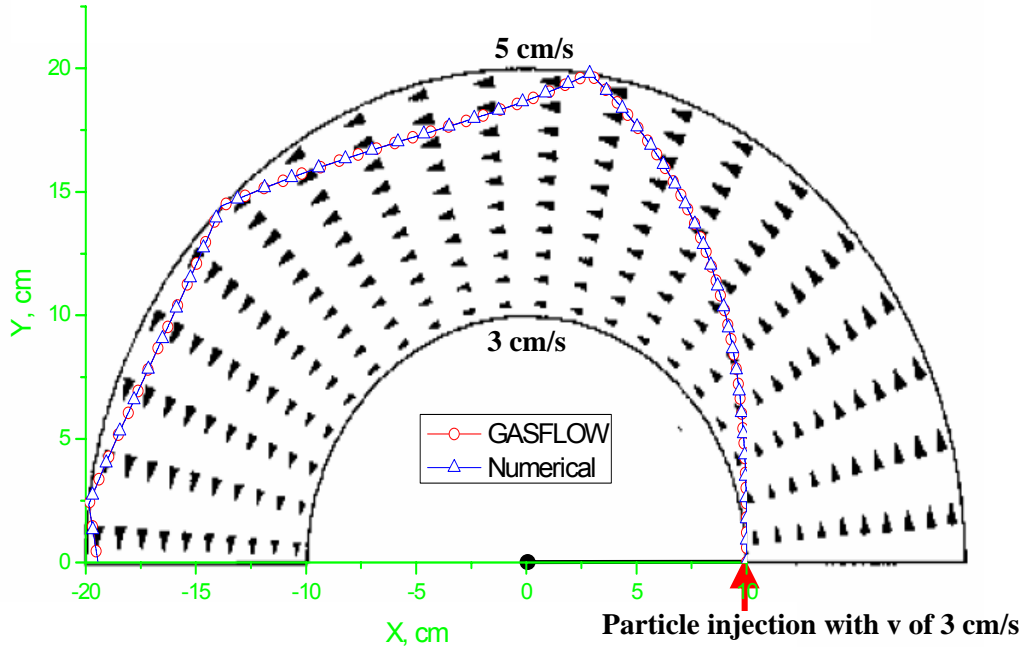


Fig. 5: Trajectory comparison in a cylindrical coordinate system.

2.3 Particle diffusion without advection

The diffusion model is validated in one-dimensional (1D), two-dimensional (2D) and three-dimensional (3D) cases, respectively. The problem is defined in a 1D pipe, or a 2D square box, or a 3D cube with stagnant flow (fluid is quiet). A point source of particle is released instantaneously at the very center of the domain. Then the particle concentrations at 1 second and 5 seconds after the release are recorded. The theoretical solution about the concentration distribution is formulated as,

$$C(\mathbf{r},t) = \frac{Q}{\sqrt{(4\pi\lambda t)^s}} \exp\left(-\frac{\mathbf{r}^2}{4\lambda t}\right), \quad (2-3)$$

where,

$C(\mathbf{r},t)$ the particle concentration at location of \mathbf{r} and the time t ,

Q the overall particle number being released,

λ the particle diffusion coefficient,

s dimension option, equal to 1 for 1D, 2 for 2D, and 3 for 3D.

The three cases of 1D, 2D and 3D diffusion problems are simulated by GASFLOW. Together with the analytical solutions, the particle concentration distributions along the distance to the position of release at 1 second and 5 second are shown in Figure 6, respectively. According to the figures, the GASFLOW simulations are almost perfect comparing to the analytical solutions in 1D and 2D cases. In the case of 3D, some random deviations are seen between the

simulation points and the theoretical lines. However this would be misleading because the deviations are completely statistical effects. If the number of released particle increases by, say, 10 times more, it is certain that the discrepancy between the simulating points and the solution line would get much smaller. Naturally it will take much longer CPU time to simulate.

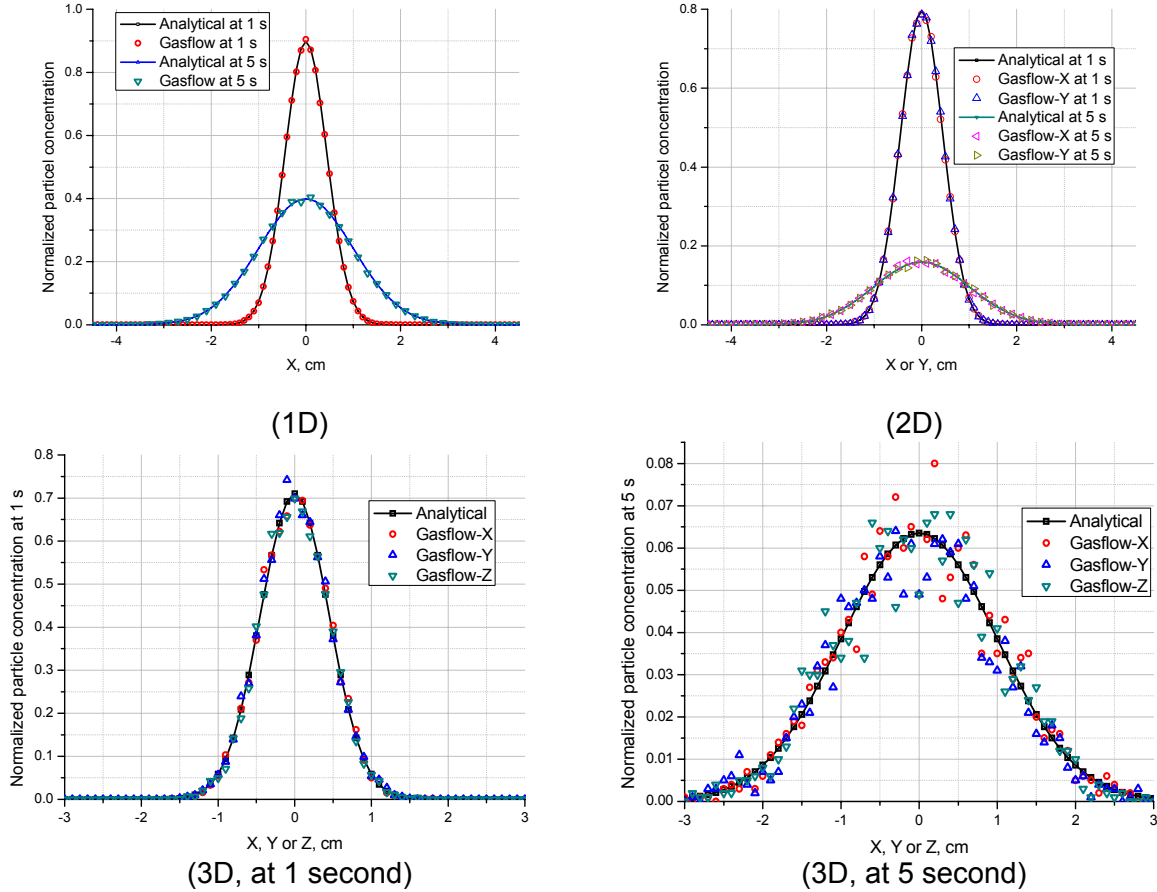


Fig. 6: Particle diffusion without advection in 1D, 2D and 3D.

2.4 Particle diffusion with advection

In order to validate further the diffusion model of GASFLOW, an advection diffusion problem is established, as shown in Figure 7. The advection flow in a straight channel has a velocity of \mathbf{V}_0 , an area source of particles are released continuously with an initial velocity of also \mathbf{V}_0 , from a square box of $[-0.5,0.5] \times [-0.5,0.5]$ in the $x-y$ plane. The particle concentration along the x -axis at 10 second is obtained by GASFLOW simulation, as shown in Fig. 8.

In Figure 8, the black solid line stands for the theoretical solution about the particle concentration derived by using Green's function method to solve the advection diffusion partial differential equations. The solution is formulated as,

$$C(x, y, t) := \frac{1}{4} \int_0^t q \cdot \left[\operatorname{erfc} \left[\frac{x - v \cdot \tau - x_0}{2 \cdot (D \cdot \tau)^{0.5}} \right] - \operatorname{erfc} \left[\frac{x - v \cdot \tau + x_0}{2 \cdot (D \cdot \tau)^{0.5}} \right] \right] \cdot \left[\operatorname{erfc} \left[\frac{y - y_0}{2 \cdot (D \cdot \tau)^{0.5}} \right] - \operatorname{erfc} \left[\frac{y + y_0}{2 \cdot (D \cdot \tau)^{0.5}} \right] \right] d\tau \quad (2-4)$$

where,

$C(x,y,t)$ the concentration at location of (x,y) and at time of t ,
 q the strength of particle source,
 v the advection velocity,
 D the diffusion coefficient,
 $x_0 = 0.5\text{cm}$,
 $y_0 = 0.5\text{cm}$.

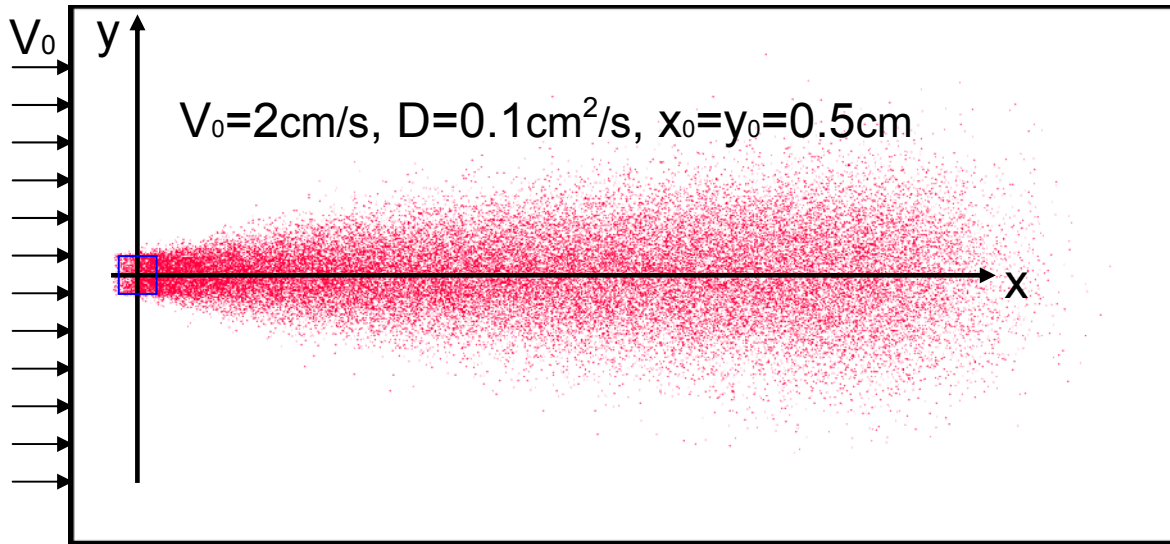


Fig. 7: Advection diffusion problem.

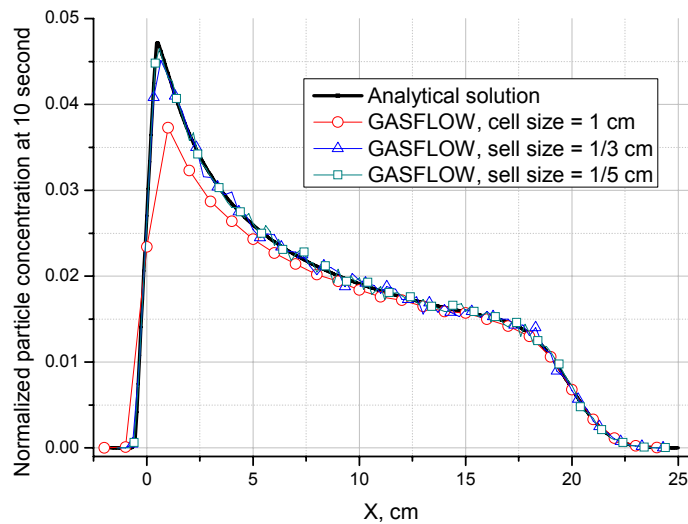


Fig. 8: Particle diffusion with advection, comparison of concentration.

In GASFLOW simulations, the grid size is set as 1 cm per cell for beginning, then decrease it to 1/3 cm, and then to 1/5 cm. According Figure 8, the numerical solution converges to the theoretical one from the coarse mesh to the refined mesh step by step. It is strongly verified that the particle diffusion model in GASFLOW can reproduce the physical phenomena correctly.

3. Conclusions and prospects

The numerical models of dust mobilization are established in GASFLOW. The functions of particle transport and particle diffusion are validated based on analytical solutions. In the next step, the turbulent dispersion model will hopefully be verified against experimental data from literature.

Staff:

W. Breitung
G. Necker
J.R. Travis
Z. Xu

Literature:

- [1] Z. Xu, J.R. Travis, G. Necker, J.R. Garcia-Cascales, H. Paillere, Review and Definition of 3D Dust Mobilization Equations: GASFLOW and CAST3M Models, FZK Internal Report, 2006
- [2] Z. Xu, J.R. Travis, G. Necker, J.R. Garcia-Cascales, H. Paillere, Review of Analytical and Experimental Test Cases for Dust Mobilization Modeling, FZK Internal Report, 2006

TW5-TSS-SEA 5.4 Busbar Arcs Behaviour and Consequences

TW5-TSS-SEA 5.4 D 2 - 4 Experimental Simulation in the VACARC Facility

High power arcs at the ITER magnet coils current leads (so-called busbars) are a possible threat for the cryostat wall which is part of the ITER safety containment. For licensing questions, this very improbable event must be investigated. Presently no suitable numerical models with reasonable accuracy are available. Model development turned out to be difficult due to low knowledge of arc propagation and destruction behaviour. This was the reason to set up a campaign of model experiments on high current arcs propagating along insulated conductors.

The VACARC experiments continue the experimental contribution to busbar arcs started with the MOVARC experiments in the frame of EFDA task TW3-TSS-SEA5.4. The VACARC results are not intended for direct extrapolation to ITER scale but will be used for the support of model development and model validation. In addition, VACARC also provides experimental practice for possible full scale experiments. The VACARC setup is based upon an available plasma spray device which had been taken out of service several years ago (Fig. 1). The VACARC vessel is designed for vacuum conditions which represent a more realistic simulation of the ITER cryostat conditions than the 1 bar argon atmosphere of MOVARC. The model conductor is a 10mm copper rod with a 1mm thick steel jacket covered with glass fiber insulation. With regard to a real ITER TF busbar, the scale is about 1:4. VACARC was completed and set into service in spring 2006.

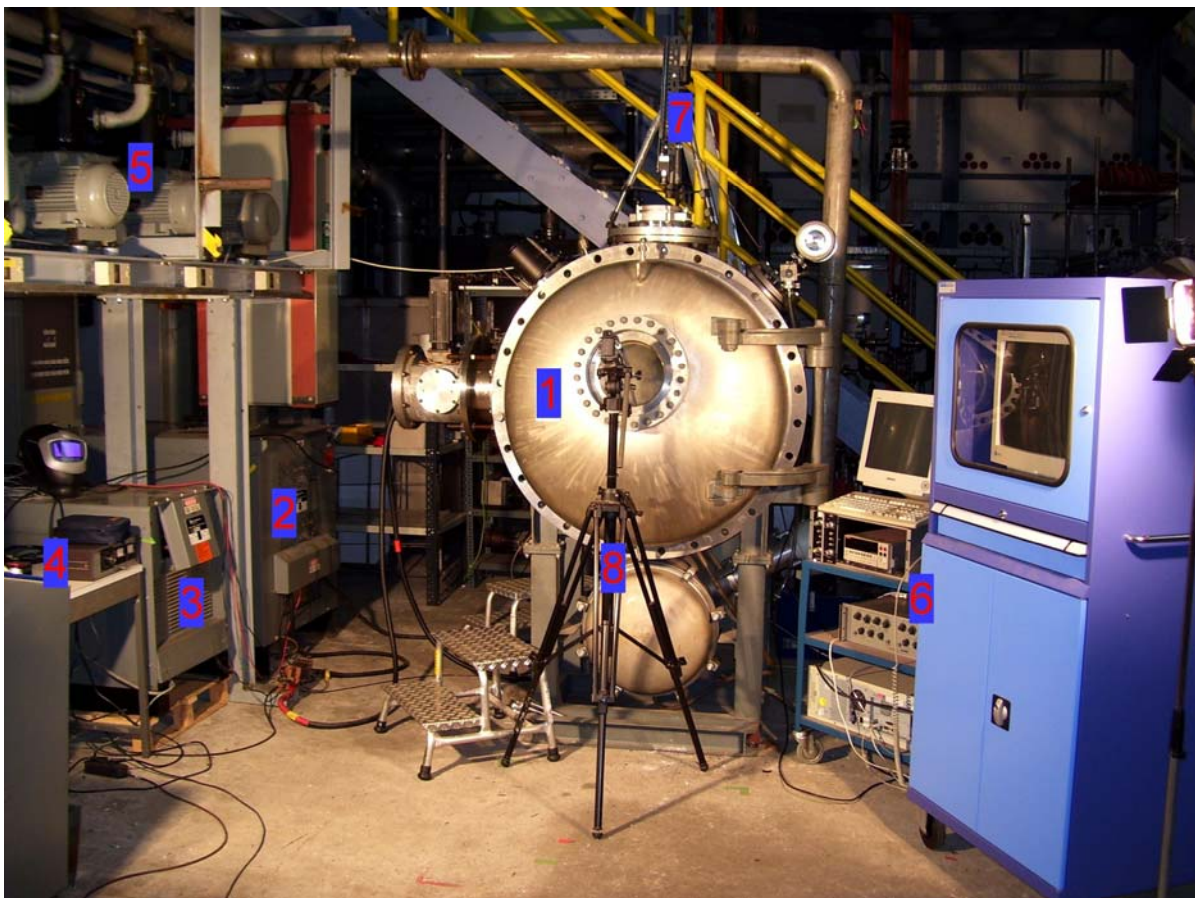


Fig. 1: Present setup of VACARC: 1. Vacuum vessel, 2. 120kW power converter, 3. 20kW power converter, 4. control unit for power converters, 5. vacuum pumps, 6. data acquisition devices, 7. high-speed camera, 8. video camcorder.

A first series of experiments was performed with the 20kW power converter which was used already in MOVARC. With identical experimental setup like in MOVARC but with vacuum conditions instead of 1bar protective argon atmosphere, the arcs turned out to burn more stable at a reduced propagation speed. The enhanced stability allowed for a wider range of accessible parameters including considerably higher gap widths. Moreover, now also backward experiments may be performed. While in forward mode the arc burns a gap into the insulation and the steel jacket, in backward mode the whole model conductor cross section is molten. As the increased melting volume consumes more power, the backward arcs were significantly slower which implied also a higher damage to the structure side which was represented by a 10mm thick steel ground rail. From the safety aspect, this backward mode is more dangerous with regard to possible penetration of vacuum barriers.

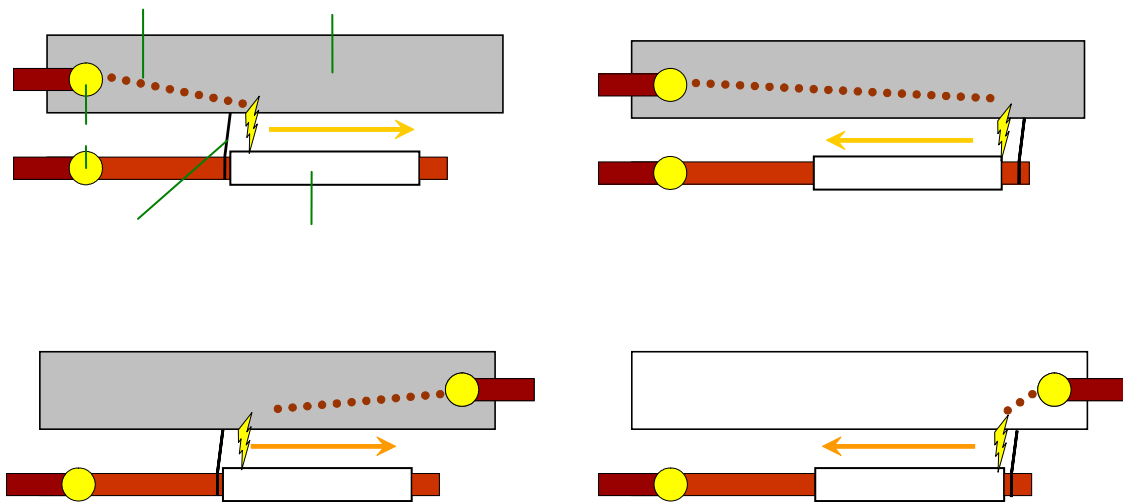


Fig. 2: The basic setup options (see text). The configurations "a)" and "d)" are preferential, because for currents above about 300A in the "b)" arrangement the arc extinguishes early, while for the "c)" setup arc movement does not start reliably.

Whether an arc moves forward or backward is decided by external forces like convection or magnet field. As in VACARC no background field is applied and the pressure is low ($< 1\text{mbar}$), the magnetic self-forces of the arc column are decisive. As their origin is a local field gradient that occurs at bent parts of the current path, the self-forces can be manipulated by the layout of the local current path through the model setup. A U-shaped current path gives maximum driving forces (in the closed side of the "U" direction) while in a Z-shaped setup the driving forces on both arc spots almost cancel out each other, see Fig. 2. Backward burning experiments were only possible with the Z-setup above about 300A, while for forward experiments the driving force provided by the U-setup turned out to be advantageous to avoid the arc getting stuck with subsequent melting through of the conductor.

Figs. 3-5 show examples out of the recent experimental campaign. The results of the forward experiments confirm the MOVARC findings of a close to linear dependence of the arc propagation speed on total arc power, while there are, however, still deviations due to an unpredictable, special burning behaviour like arc column bending, fluctuations or plasma jets. The enhanced stability of VACARC somewhat reduced these effects. Compared to the MOVARC results, the arc speed was about a factor of 0.5 lower at comparable setups but with low pressure instead of 1bar argon protective gas. For the backward experiments, the arcs propagated slower and surprisingly, their velocity was quite constant independent of the arc power or other parameters besides the model conductor dimensions. Maybe, a maximum of heat ingress at the arc spot is reached here, or the transition region between melting and vaporization is entered with the excess energy being used mainly for the second phase tran-

sition. In the latter case, a further increase of the arc power would cause higher arc speeds again.

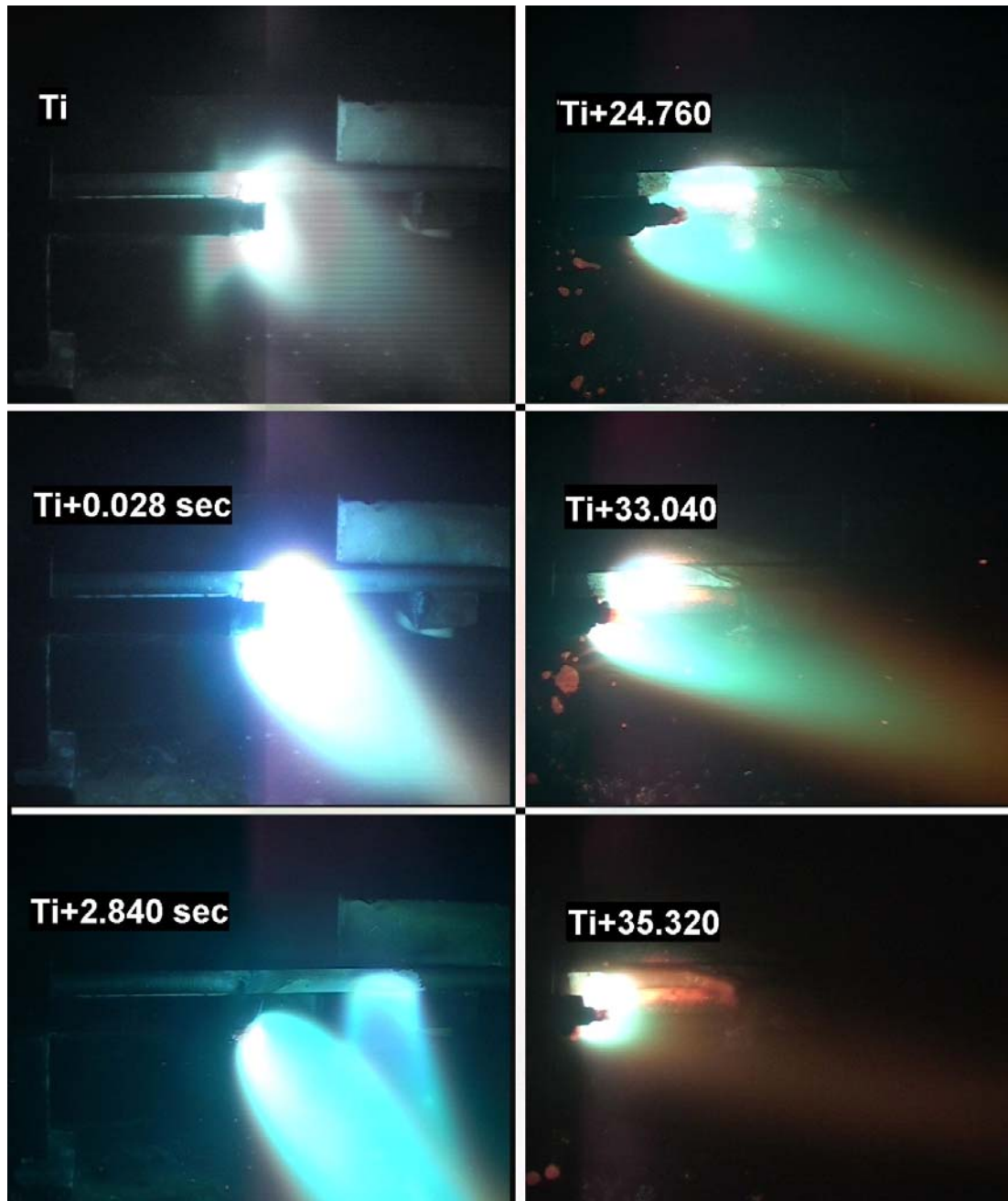


Fig. 3: Frame sequence during the (backward) experiment VA1005. The arc current is about 560A. It takes almost 10s for arc stabilization, however then the arc burns and propagates very stable for another 24s melting the whole conductor cross section.

The present limit for the arc current is about 750A with arc powers of up to 60kW. New main current leads and some changes with regard to reliability and safety will allow going to the limits of the 120kW power converter in the next step. The enhanced quality of the experimental results and the new option to perform backward experiments will allow progress in numerical modeling which is required to answer open busbar arc related safety questions for ITER.

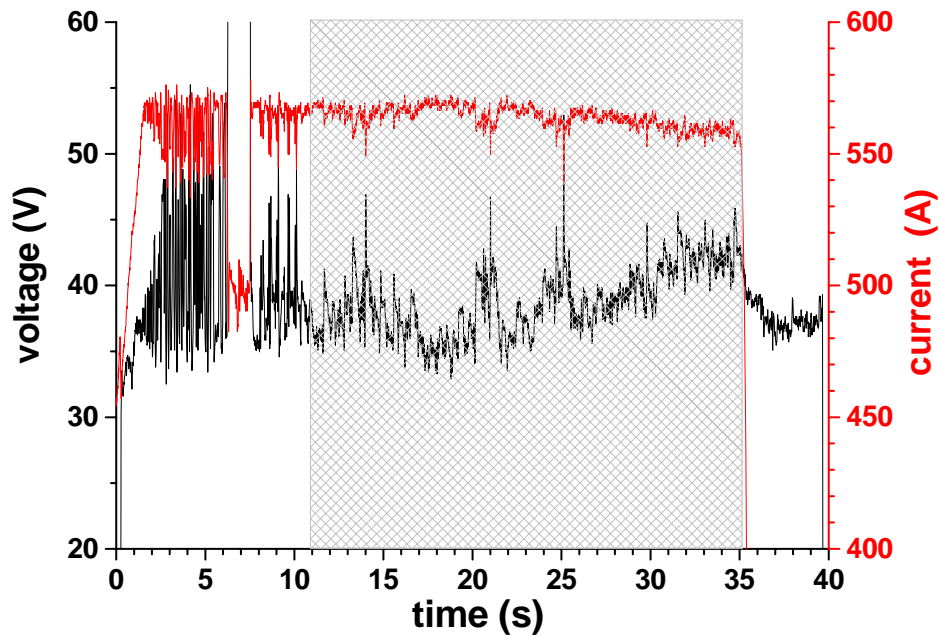


Fig. 4: Electrical data of the (backward) experiment VA1005 shown in the picture sequence above. In the first 10s strong fluctuations accompanied by arc bending and jumping occur, however then the arc stabilizes and propagates quite stable. The data in the stable, grey shaded time range can be used for further evaluation.



Fig. 5: Photographs taken after arc experiments. The left picture was taken after the backward experiment VA1005 (560A, 22kW). The conductor was completely molten and there is considerable damage to the ground rail. The right picture was taken after the forward experiment VA1010 (750A, 30kW). The conductor insulation and steel jacket are cut, however the copper core is mostly undamaged. The ground rail shows only slight burning traces although the arc power was about 50% higher than in VA1005. This means with regard to safety questions, the backward mode is obviously the more dangerous one.

Staff:

D. Klimenko
V. Pasler

Literature:

- [1] D. Klimenko, V. Pasler, Small experiments on busbar arcs: Final report on MOVARC experiments, TW3-TSS-SEA5.4/D4, December 2005.
- [2] D. Klimenko, V. Pasler, Report on preparation status of the VACARC experiments, TW5-TSS-SEA5.4/D2, December 2005.
- [3] D. Klimenko, V. Pasler, Interim report on VACARC experiments, TW5-TSS-SEA5.4/D3, June 2006.
- [4] D. Klimenko, V. Pasler, Final report on VACARC experimental results, TW5-TSS-SEA5.4/D4, to appear Dec. 2006.

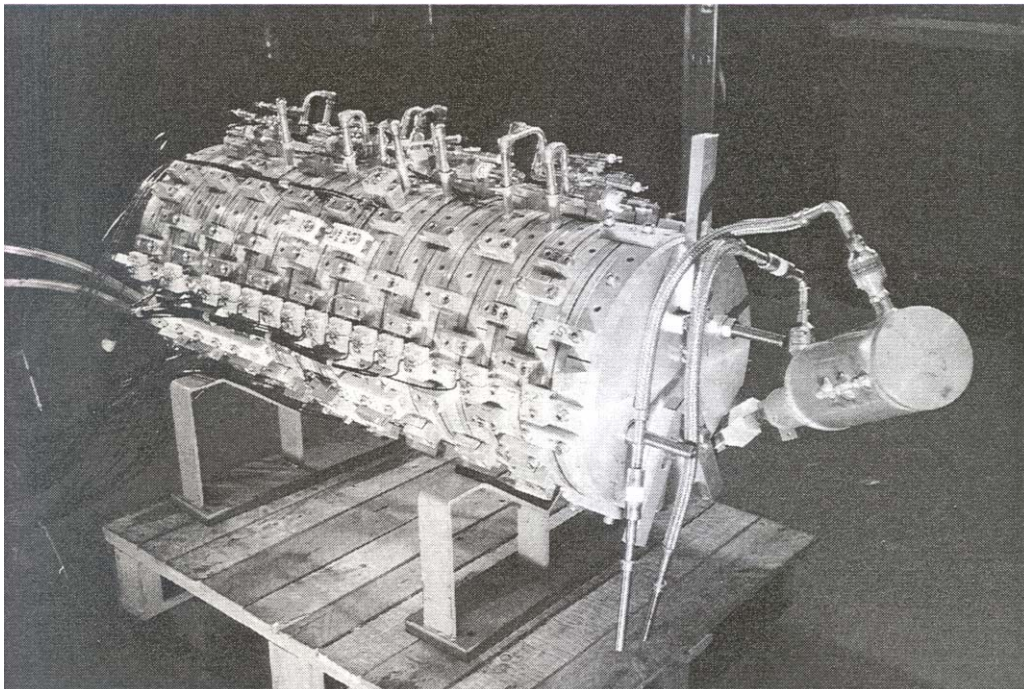
TW5-TSS-SEA 5.5

Validation of EU Safety Computer Codes and Models

TW5-TSS-SEA 5.5 D 5

Validation of MAGS: Quench Simulations for the Q3D Coil

Validation of numerical codes did become more important after the decision for Cadarache to host ITER. Validated numerical codes must be available to satisfy the requirements of the licensing authorities of ITER. The validation of the MAGS code is in progress since many years. The present approach is to calculate quench propagation using data from the Q3D experiments performed at FZK in the mid 1990's for comparison. This was done because an earlier MAGS approach showed several weaknesses which required clarification. Most of these problems could be solved.

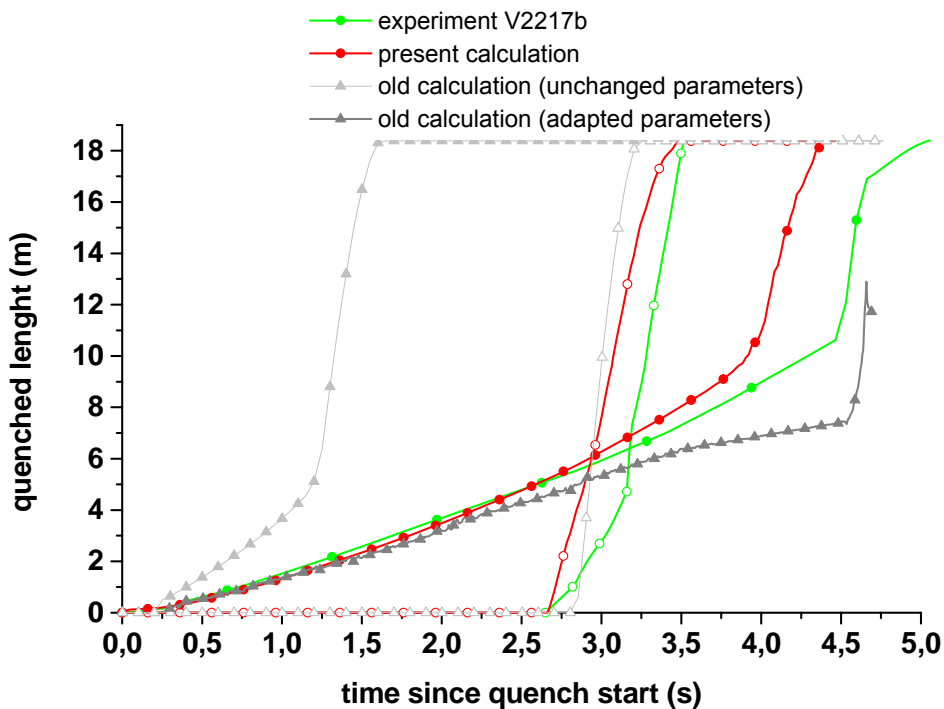


Photograph of the Q3D coil ready for installation in the cryostat. The coil length is about 1m. On the coil surface there are clamps that hold the windings in place. On the top of the coil there are the helium pressure and temperature sensors, the other cables are connecting the voltage taps and the thermometers. The photograph is taken from [1].

The Q3D coil is a single layer coil wound out of a prototype cable for the Wendelstein 7-X experiment. This conductor is a NbTi cable in an aluminum jacket cooled by forced flow of supercritical helium. The coil was wound in a bifilar arrangement with the current of the two subcoils in a serial arrangement but in opposite direction, and separate helium circuits for the subcoils. Quench propagation was investigated along and between the cables. The coil was instrumented for quench tracking with voltage taps and thermocouples, also several pressure sensors were placed along the cables.

In the first validation calculation using the Q3D experiments performed in 1998, a reduction of the circumferential thermal conductivity of the conductor cable copper matrix by a factor of 0.02 was required to hit the experimental quench propagation behaviour [1]. Although there is a justification due to the magnet field dependence of the thermal conductivity of copper for a reduction by a factor in the order of 0.5, a change of this extent puts a question mark to this validation effort. For this reason, a new calculation was initiated [2]. The enhanced modeling capability of the MAGS code with regard to helium to simulate heat transfer as well as a more appropriate mesh representation helped to improve the results without a questionable

manipulation of material properties data. With regard to the need to change material properties, the field dependence of the thermal conductivity of the copper matrix was taken into account by a factor of 0.5 which is realistic for the given RRR value of 226 at 4-5T. Another slight reduction by an additional factor of 0.84 came through the twisting of the strands inside the cable. Finally only the thermal conductivity of the Kapton(TM) insulation layer (which was also considerably adapted during the first approach) still turned out to be a factor of ten too high to describe the start of the second cable quench. A similar factor was already detected in calculations for the TFMC, which also has an insulation containing several Kapton(TM) layers [3]. In this case the result was confirmed by another group [4]. The Kapton(TM) properties however do not affect the longitudinal quench propagation in the initially quenching cable but play a role for the start of the quench of the second, parallel cable.



MAGS calculation for the quenched length over time for the experiment 2217b compared to experimental data. Solid symbols are for the first cable, open symbols indicate the second one. For comparison, also the results of the earlier MAGS approach [1] are shown. The improvement is also visible against the version of the first approach with strongly adapted parameters.

In summary, besides the still unclear Kapton(TM) issue, a successful and reasonable validation calculation could be performed that improved the validation status of MAGS with regard to the first approach.

Staff:

V. Pasler

Literature:

- [1] W. Kuhn, Experimentelle Untersuchung der dreidimensionalen Quenchausbreitung in zwangsgekühlten supraleitenden Spulen, FZK report No. FZKA 6086 (in German) Forschungszentrum Karlsruhe, Thesis, July 1998.
- [2] V. Pasler, Validation of MAGS: Quench simulations for the Q3D coil, TW5-TSS-SEA5.5/D5, to appear Dec. 2006.
- [3] Volker Pasler, Rainer Meyder, Gernot Schmitz, Effective thermal conductivity of the conductor insulation of the ITER toroidal field model coil at operation temperature, *Cryogenics* 43, 199–207, (2003).
- [4] S. Nicollet, J.L. Duchateau, P. Hertout, M. Rebai, Heat transfer from plates to conductors: from toroidal field model coil tests analysis to ITER model, *Cryogenics* 43, 209–214, (2003).

TW5-TSS-SEP 2

Doses to the Public and Validation of UFOTRI

Objectives

The objective of this task is to demonstrate the validation level of the computer codes used and to calculate on request by EFDA in a consistent way doses to the public for given source terms, for realistic meteorological and siting conditions, for ITER (European site) and for fusion power plants. This comprises the enhancement of the "Fusion-Release-Target-Scoping-Tool" by the ingestion dose criterion for an easy assessment of all types of release targets and validation of UFOTRI in the frame of the EMRAS (Environmental Modelling for RADIation Safety) international benchmark project including a comparison of concentration and dose criteria for the ingestion pathways.

Work performed

Having completed the scoping tool in the last reporting period, the main activities focused on the test and validation of UFOTRI in the frame of the EMRAS activity and on providing support of the ITER team in the licensing procedure.

The Tritium Working Group of the EMRAS project aims on improving models of OBT formation and translocation in plants, animals and fish. Up to now seven different scenarios were exercised. FZK contributed with the UFOTRI code to the soybean and the hypothetical scenario. The soybean scenario is based on experimental data collected at the Korean Atomic Energy Research Institute. Commercially available soybean was sown in May 2001 in 6 plastic pots (41cm x 33cm x 23cm high). Tritium exposure was carried out six times at different growth stages: July 2, July 13, July 30, August 9, August 24, and September 17. The pots were introduced into a glove box for the tritium exposure and the experiments were conducted under natural solar conditions, which resulted in high temperatures within the glove box. The surface of the soil was covered with vinyl paper so that uptake was only through the foliage. After exposure, the pots were placed in an open field among other soybean plants. UFOTRI performed well in the scenarios being the only model which provides simulation results within one order of magnitude around the measurements for all the 6 different exposure conditions.

The objective of the hypothetical scenario is to analyse the consequences of an acute atmospheric release of tritium, by considering various pathways in terms of activity in biosphere compartments and products, as well as the contribution of the various forms of tritium (HT, HTO and OBT) to the total exposure. The basic assumption is that 10 g of tritium are released over a period of 1 hr and the calculation period is 1 year. Results of the first predictions differed considerably and it was not possible to find consensus why model results diverged. Therefore, a new revised scenario was prepared to resolve the differences between the models. Nevertheless, the still existing huge variety in some of the results demonstrated the need for further refinement of the codes. It is important to note, that UFOTRI and the French code used also for the licensing efforts of ITER in France performed in a similar way. This strengthened the confidence in both codes to be further applied in the licensing procedure.

To support the licensing activities for ITER, calculations with COSYMA and UFOTRI were performed to determine doses to the public and activity concentrations in food products around the ITER site Cadarache. Source terms for ITER, defined for activated dust, activated corrosion products and tritium in form of tritium gas (HT) and tritiated water (HTO) were used as basis for the calculations. One weather condition was selected for the investigation. It is characterised by poor diffusion condition and a wind speed of 2 m/s and no rain. A release from a stack (60 m high, with building wake effects) and from a 10 m release point (without building wake effects) were assumed. Special dispersion parameters for France, the so

called Doury parametrisation scheme, were applied. Calculations were carried out for three age groups (adult, 10 year old child and one year old infant) for tritium and for two age groups (adults and one year old infant) for activation products.

Having released only one gram of the material, doses are in general low and do not reach any of the dose criteria for intervention. Maximum doses in the near range do not exceed one mSv for the release of one gram of tritium or activation products. Adults are in most cases the critical group as children consumed no milk products produced in the region around Cadarache. Activity levels in food products are far below any criteria selected for these calculations.

Further work

Calculations to support the siting of ITER at Cadarache will continue with an expanded spectrum of release conditions and a refined set of input parameters.

Staff:

F. Fischer
I. Hasemann
W. Raskob

Literature:

- [1] Neill P. Taylor and Wolfgang Raskob, UPDATED ACCIDENT CONSEQUENCE ANALYSES FOR ITER AT CADARACHE, 17th ANS topical meeting on the Technology of Fusion Energy (TOFE), ANS Winter Meeting in Albuquerque, 13 -15 November 2006

DEMO Conceptual Studies

**TRP-001
PPCS He-cooled Divertor Concepts**

TW5-TRP-001 D 1

TW6-TRP-001 D 1 + D 2

He-cooled Divertor Development: Conceptual Design, Analysis, and Tests

Introduction

Work carried out in 2006 (TW6-TRP-001) under cooperation with Efremov focused on the HHF He-loop experiments for 1-finger divertor mock-ups [1] which are based on the reference design HEMJ with jet impinging cooling and the backup solution HEMS [2] with a slot flow promoter. Preparatory work for the HHF tests [3] concerning technological investigation and manufacture of the mock-ups was carried out.

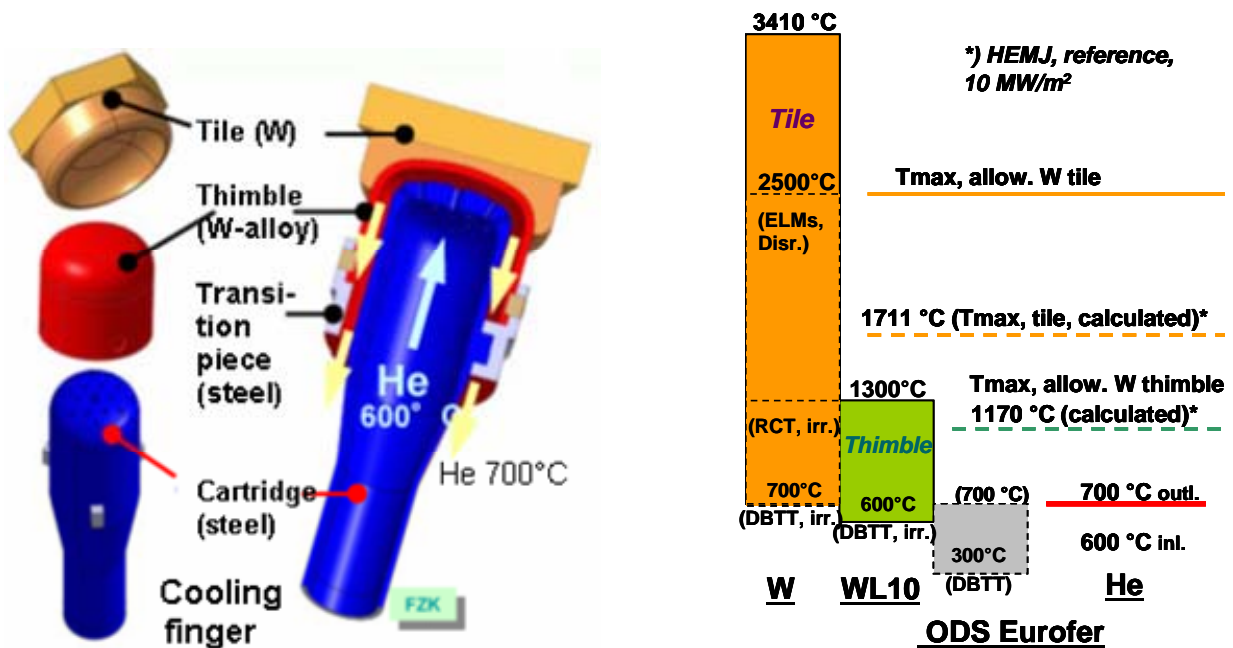


Fig. 1: He-cooled modular divertor designs HEMJ.

The reference design HEMJ [4] (Fig. 1, left) is based on the use of multiple-jet cooling. This design offers advantages in relatively simple construction and cheap production. It uses small hexagonal W tiles (18 mm width over flat) as a thermal shield and sacrificial layer (5 mm thickness). They are brazed to a pressure carrying thimble (Ø15 x 1 mm) made of WL10, thus forming a cooling finger. The working temperature window of the W divertor finger is estimated to be between 600°C and 1300°C (Fig. 1, right), the values dictated by the DBTT and RCT under fusion neutron irradiation. The W finger unit is connected to the supporting structure made of ODS steel (e.g. an advanced ODS EUROFER or a ferrite version of it). To compensate the large mismatch in the thermal expansion coefficients of W and steel, a transition piece is needed. The current transition piece design is based on Cu casting with a conical interlock. A steel cartridge carrying the jet holes is placed concentrically inside the thimble. The number, size (D), and arrangement of the jet holes as well as the jet-to-wall distance H are important parameters. The results of the CFD parametric study [5] of HEMJ show that – unlike the jet hole diameter – the jet-to-wall distance (within the design range of 0.6 – 1.2 mm) has no excessive influence on the divertor performance and the pressure losses. The following geometry of the type J1c (Table 1) was defined for the following high-heat-flux (HHF) tests: 24 holes Ø 0.6 mm and 1 centre hole Ø 1 mm, jet-to-wall spacing 0.9 mm.

Table 1: HEMJ design parameters.

	Jet hole diameter D (mm)	Jet-to-wall distance H (mm)
J1a	0.6	1.2
J1b	0.6	0.6
J1c	0.6	0.9
J1d	0.7	0.9
J1e	0.85	0.9

Helium loop construction

This He loop enables mock-up testing at a nominal helium inlet temperature of 600°C, an internal pressure of 10 MPa, and a pressure loss in the mock-up of up to 0.5 MPa. The flow-chart of the loop is shown in Fig. 2. Since the He loop is designed for operation together with the TSEFEY facility (Fig. 3, left) with its own water-cooled target system, all of its main units are placed on a vehicle moveable on railways (Fig. 3, right). In the first stage of the helium loop a stationary helium mass flow rate of 24 g/s was achieved by means of an oil-free membrane compressor.

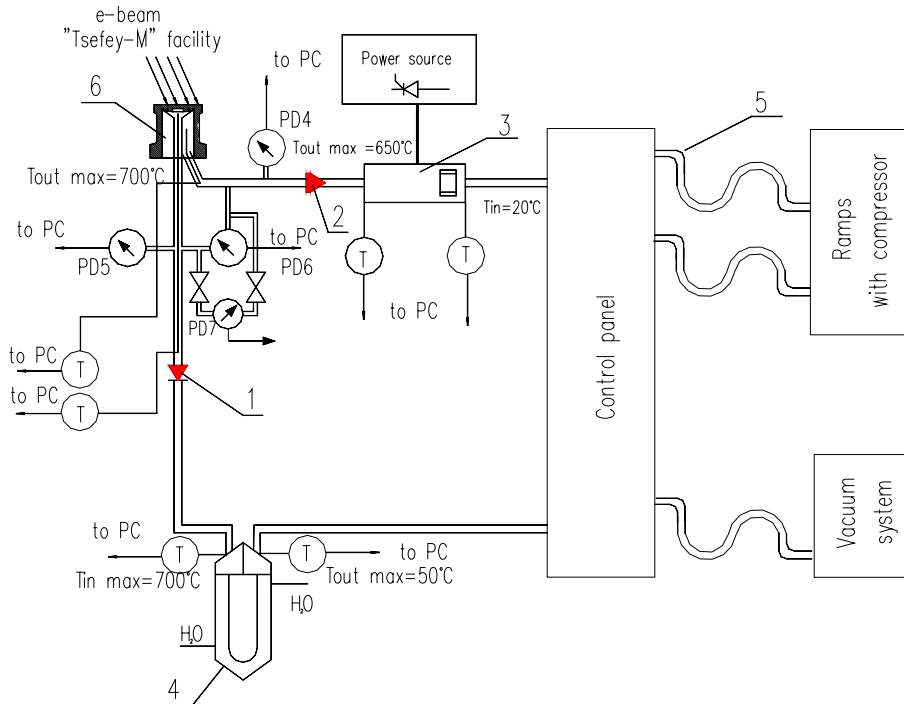


Fig. 2: Helium loop flowchart : 1, 2 – hot valves, 3 – flowing helium heater, 4 – flowing helium cooler, 5 -flexible high-pressure line.

The high-heat-flux tests

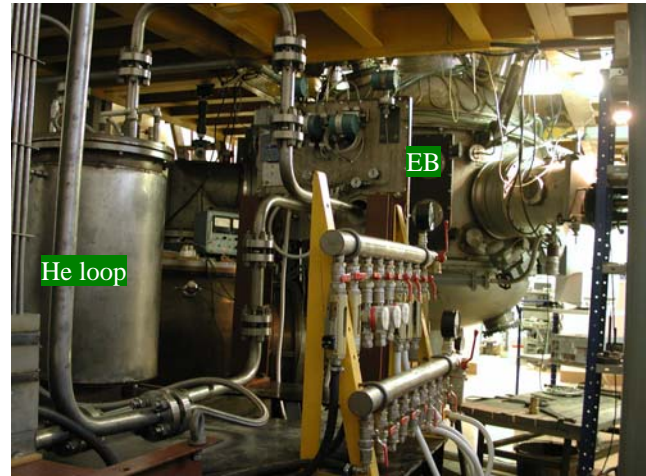
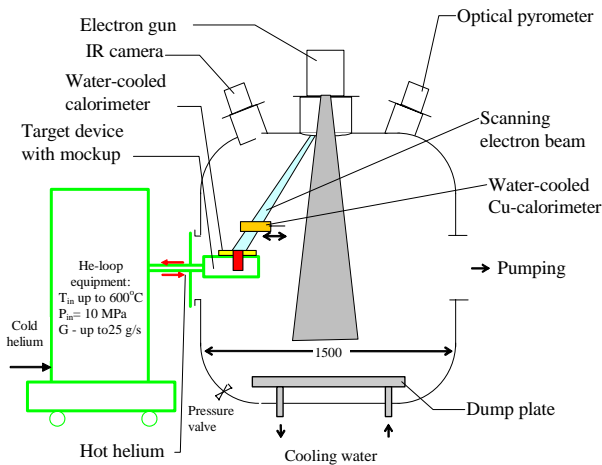
The HHF experiments are performed at the new test facility at Efremov which consists of the TSEFEY electron-beam testing machine and the He-loop facility (Fig. 3). This combined device provides for a steady-state surface-loading heat flux (with a total power of up to 60 kW at 27 keV beam energy) and a He coolant at a pressure of ~ 10 MPa, an inlet temperature of $\leq 600^{\circ}\text{C}$, and a mass flow rate of ≤ 50 g/s.

Based on the knowledge gained from the technological investigation, the reference W mock-up was defined for the high-heat-flux tests. The HEMJ version J1c (Table 1) was chosen as reference. The definition of the 1-finger mock-up is given in Table 2. The HEMJ jet cartridge and the holding structure of the mock-ups are made of Eurofer which differs from the designated ODS Eurofer material. As an alternative to the W/Eurofer joint by cast copper, a

brazed W/Eurofer joint using Co-based filler metal was considered for mock-up manufacture (mock-ups #5/HEMJ and #6/HEMS). Castellated and non-castellated W tiles were also investigated (mock-ups #1/HEMJ and #2/HEMS).

Table 2: Material and joining techniques defined for 1-finger mock-up manufacturing.

Materials	
W tile	PM pure tungsten
Thimble	WL10
Supported tube structure	Eurofer
Joining methods	
Tile/thimble	Brazing (STEMET [®] 1311) $T_{br} = 1100^{\circ}\text{C}$
Thimble/supported tube structure of Eurofer	Conic lock filled with cast copper



a)

b)

Fig. 3: The testing facility: a) TSEFEY, b) TSEFEY with He-loop integrated.

In the first test campaign six 1-finger mock-ups (Fig. 4), five of HEMJ and one of HEMS type, were fabricated. The manufacturing sequence was as follows:

- Machining of external surface of the W thimble (from WL10)
- Machining of cylindrical ring from Eurofer
- Machining of internal surface of the tile (manufactured from pure W)
- Brazing of W thimble to cylindrical ring (filler metal 71KHCP, $T_{br} = 1100^{\circ}\text{C}$)
- Brazing of W thimble to W tile (filler metal STEMET[®] 1311, $T_{br} = 1100^{\circ}\text{C}$)
- Machining of the internal surface of the W thimble
- Machining of the tile to the shape required

For HHF testing of the mock-ups manufactured at the TSEFEY facility, a special target device was designed and manufactured. This target device consists of two main parts, the manifold device and the water-cooled shielded mask. This mask (Fig. 3) has a hexagonal-shaped frame made of molybdenum.

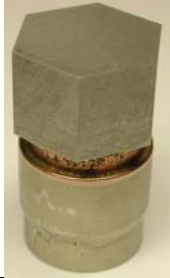
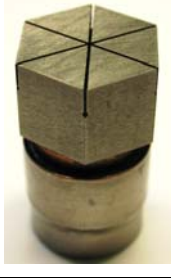




Exp. No. 1 (Mock-up #4)	Exp. No. 2 (Mock-up #2)	Exp. No. 3 (Mock-up #5)	Exp. No. 4 (Mock-up #3)	Exp. No. 5 (Mock-up #1)	Exp. No. 6 (Mock-up #6)
					
HEMJ					HEMS

Fig. 4: First series of W 1-finger mock-ups manufactured: Five HEMJ mock-ups (four – with Cu cast in thimble-steel conical lock, one - with Co brazing in thimble-steel conical lock) and one HEMS mock-up.

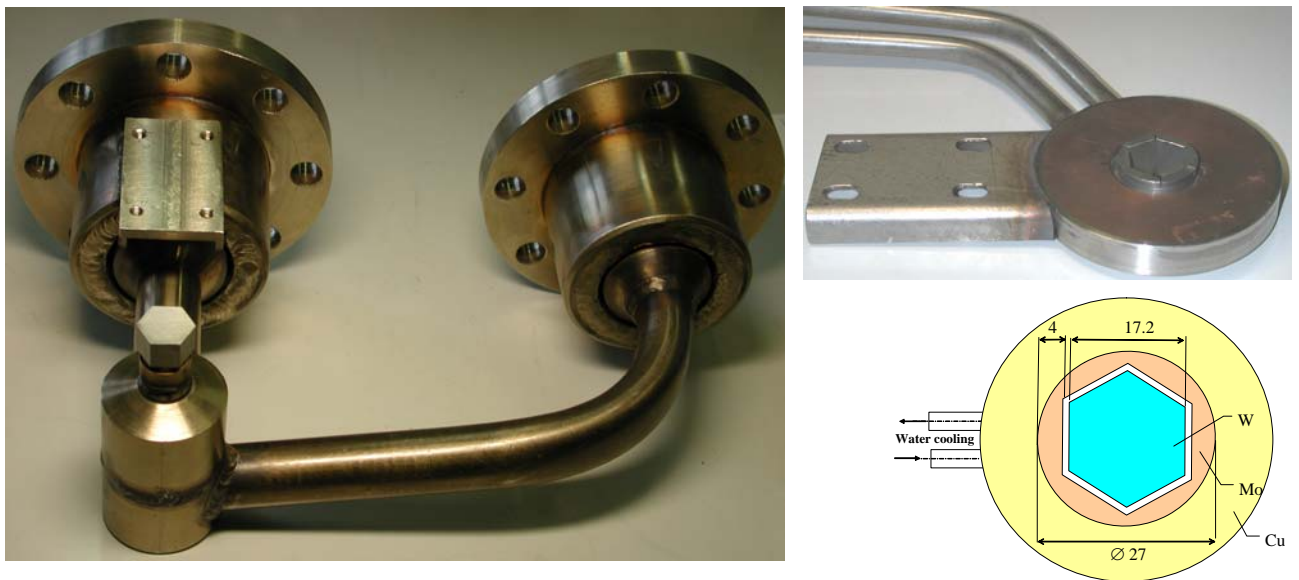


Fig. 5: Target device with mock-up holder and water-cooled shielded mask.

HHF experimental results

The first test campaign covered six mock-ups, the tiles of which were made of Russian tungsten. The mock-ups were tested within an HHF range of 5–13 MW/m². The heat flux is determined via the heat power absorbed in the helium. The helium cooling parameters are 10 MPa inlet pressure, ~ 500–600°C inlet temperature, and a varying mass flow rate in the range of ~ 5–15 g/s. The thermocyclic loading was simulated by means of switching the beam on and off (e.g. 60s/60s).

The experiments started with the mockup #4 with non-castellated W tile. It survived stepwise heat loads from 4 up to 11 MW/m² (Fig. 6) each with 10 temperature cycles (60s/60s) without any damages. It was then further tested at higher heat fluxes to find out the maximum heat load performance. After 6 cycles at 13 MW/m² the tile and thimble were partially detached, tile melting and cracking detected. The pressure carrying thimble and the loop remain intact. The following mockup #2 with castellated W tile also survived outstandingly up to 11.5 MW/m² (Fig. 7) under similar testing conditions. At a higher load of 12.5 MW/m² cracks in tile and thimble and gas leakage were detected. Crack propagation in thimble came from the inside. The mass flow rate of about 13.5 g/s was applied in these first two experiments. The respective pressure loss was measured about 0.3 MPa. This pressure loss is equivalent to about 0.08 MPa at the nominal mass flow rate of 6.8 g/s and is regarded optimistic compared

to the calculated value above. Mockup #5 (non-castellated): At 9 MW/m², no problem, after 100 cycles and 13 g/s; One crack in thimble close to joint was detected after 24 cycles at 9 MW/m² and 7 g/s (this mockup was the one with the Co joint, much harder than Cu). Mockup #3 (non-castellated): Tested only at 7 g/s, early cracks through tile and thimble even after limited number of tests. Mockup #1 (non-castellated): 9 g/s He flow rate, 10 cycles ok at 5, 6, and 8; failure after 2 tests at 10 MW/m². Mockup #6 (HEMS, Co-brazed thimble joint) survived perfectly 10 MW/m², 100 cycles, 10 g/s, without any damages and leaks. But, its pressure loss is about a factor of 3 higher than those of the HEMJ type. Altogether it can be said that the performance of the He-cooled divertor concepts (HEMJ and HEMS) of 10 MW/m² has been confirmed by the first experiment series. All mockups tested underwent destructive post-examinations.

W parts of some mockups in particular the thimble proved as pre-damaged, presumably getting micro cracks initiated during the fabrication processes. There was never a suddenly and/or completely broken mockup, i.e. no brittle failure. Also recrystallization of thimble was never observed on any mockup. For the next test series the mockup geometry has to be optimised by means of finite element analyses, the quality of the mockup fabrication to be improved.

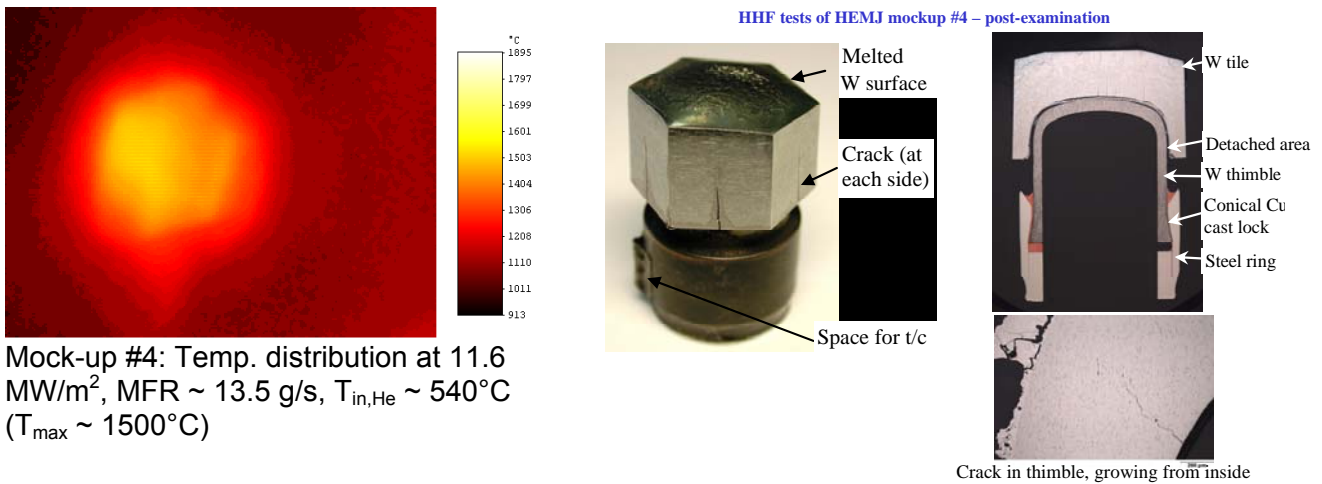


Fig. 6: HHF test of mock-up #4 (HEMJ, non-castellated): a) IR picture of temperature distribution (left), b) Post-examination (right) after the last power step (6 cycles at 13 MW/m²).

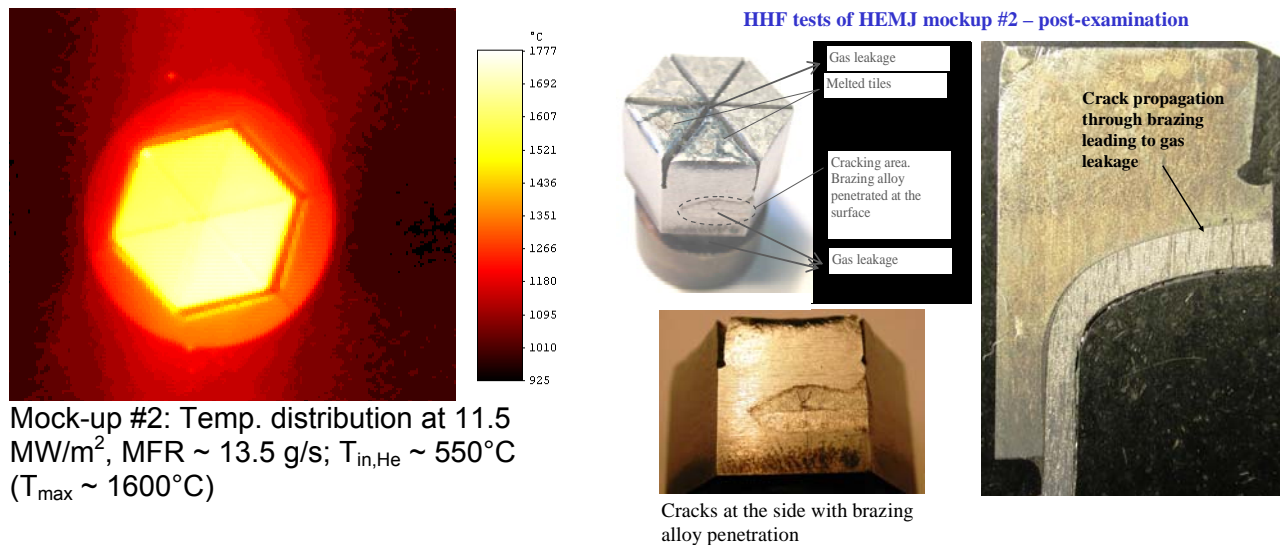


Fig. 7: HHF test of mock-up #2 (HEMJ, castellated): a) IR picture of temperature distribution (left), b) Post-examination (right) after the last power steps (max. 13.5 MW/m²).

The HEBLO experiments for CFD code validation

The results of post-calculations with CFD codes for the HEMS experiments show good agreements. Fig. 8 shows as an example the static pressure distribution along the slot length calculated with STAR-CD in comparison with the measured values. As evident from the illustration, the results - with the exception of the inlet and outlet positions - agree well with one another. In this case the RNG High Reynolds turbulence model was applied.

The 10:1 HEMJ mockup which contains a heating plate and various instrumentations was manufactured and installed into the HEBLO test section. After the pretests of all components several experiments were performed successfully under variation of parameters mass flow rate, helium temperature and the heat flux. Post-calculations and evaluations are underway.

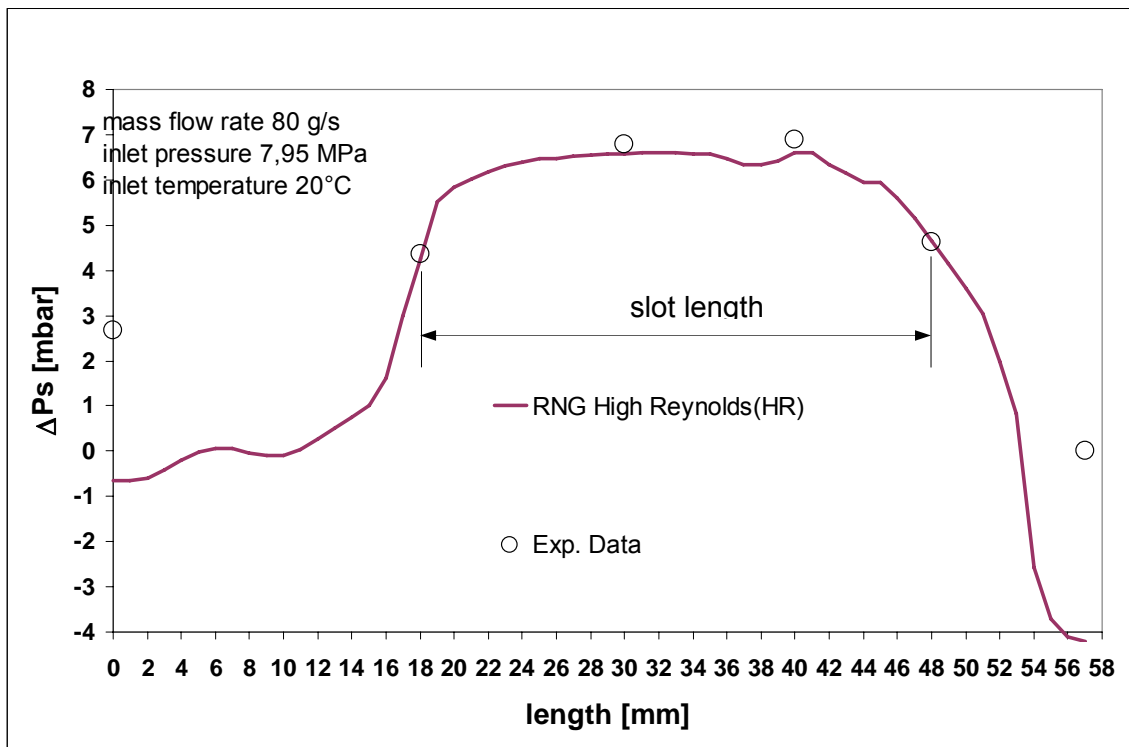


Fig. 8: Calculated and measured static pressures along the flow path in the slot (flow direction from the right to the left).

Progress of W structuring processes

Powder injection moulding (PIM) [6] is regarded a promising method for mass production of W and/or W alloy components. A complete PIM production process including feedstock formulation, injection moulding, debinding and thermal consolidation was established for tungsten components. To improve the PIM performance various W powders with a particle size between 0.7 μm FSSS and 3.0 μm FSSS have been tested regarding feedstock viscosity and sintering activity. This investigation was performed before and after powder deagglomeration by jet milling. Deagglomeration was found to be necessary for low feedstock viscosity at a powder loading $\geq 50\text{Vol.}\%$ as well as for enhanced sinter ability. For a low feedstock viscosity, a powder particle size $\geq 2.0 \mu\text{m}$ FSSS was found to be superior, while the sintering activity increases with decreasing particle size (Fig. 9). Thus further experiments were done, applying a powder with a particle size slightly below (1.2 μm FSSS) and above (2.5 μm FSSS) the optimised particle size of 2.0 μm FSSS. The powder particle properties of both powders are shown in Table 3.

Table 3: Powder particle properties of optimised tungsten powders for PIM.

FSSS [μm]	D20 [μm]	D50 [μm]	D90 [μm]	BET [m^2/g]
1,2	0,9	1,5	3,4	0,48
2,5	1,3	2,7	4,9	0,25

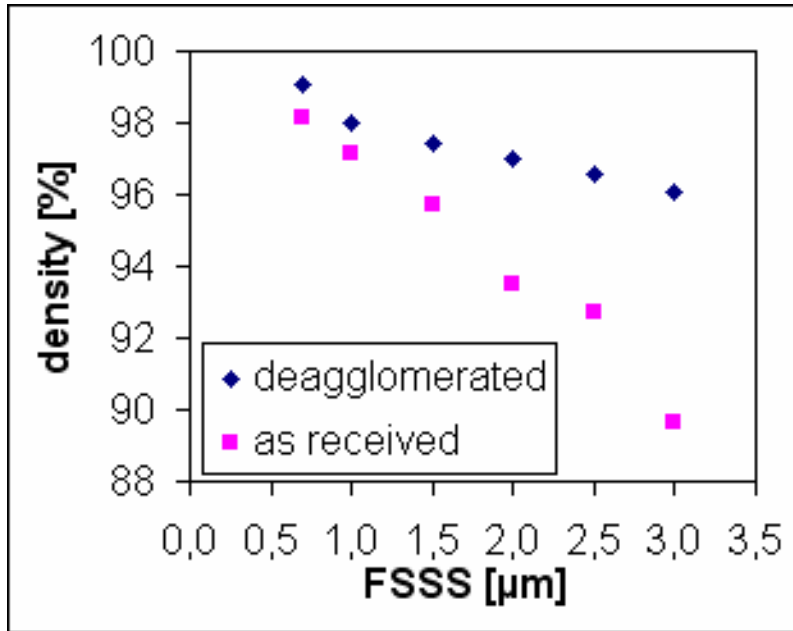


Fig. 9: Particle size dependent sintering ability of tungsten powders after deagglomeration as well in the as received state.

Micro cavities such as isolated gearwheels and gear housings as well as the fusion relevant Slot Array have been replicated successfully applying an optimised feedstock system. An example of an as sintered Slot Array prepared by PIM is shown in Fig. 10. Density measurements of tungsten components after sintering at a temperature $>2000^\circ\text{C}$ in H_2 show a density of 19.14 g/cm^3 for a powder with a particle size of $1.2\ \mu\text{m}$ FSSS and of 18.37 g/cm^3 for $2.5\ \mu\text{m}$ FSSS, respectively. Further on the hardness of these samples has been tested and a hardness comparable to recrystallized

tungsten was detected ($1.2\ \mu\text{m}$ FSSS: 357 HV10; $2.5\ \mu\text{m}$ FSSS: 324 HV10; recrystallized after Lassner& Schubert [7]: 300 HV30).

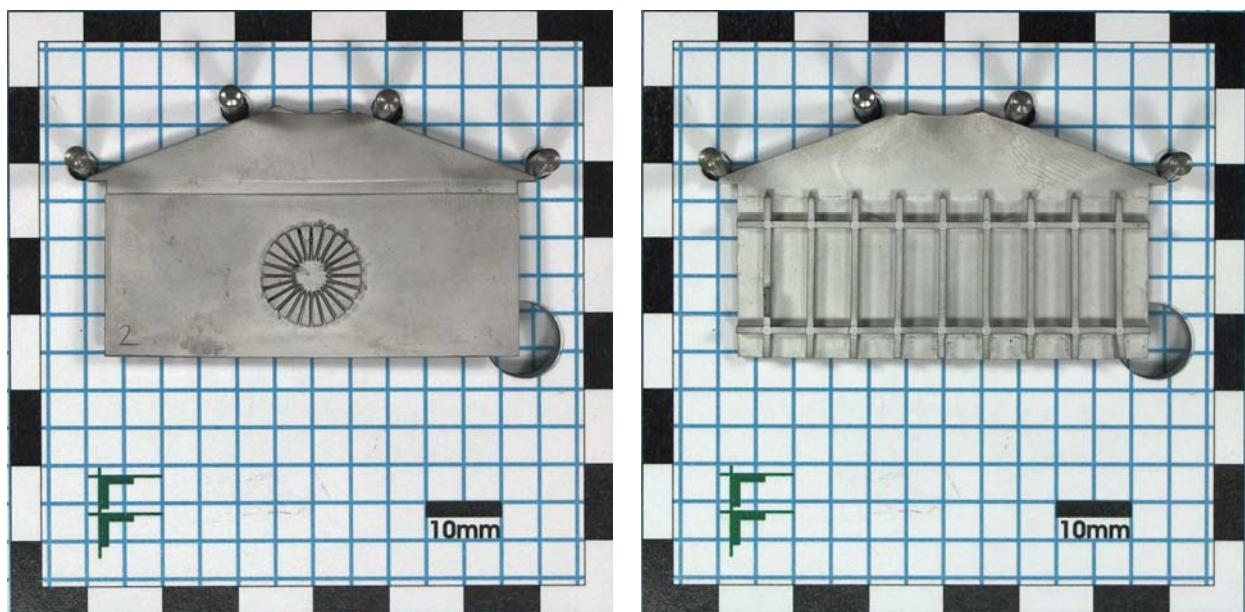


Fig. 10: As sintered slot array prepared by powder injection moulding with pure tungsten.

From the experience concerning the PIM-process for tungsten components, injection moulding of microstructured components has successfully been broadened to the tungsten alloys WL10, WCu, and WHA (W:Ni:Fe = 92.5:5:2.5).

A first future step in PIM of tungsten components for fusion applications has to be a design decision. Afterwards a suitable tool design will be developed and tested in injection moulding experiments. Further on performance tests have to be done for testing the ability of components prepared by PIM to meet the requirements of the application. For optimised material properties further optimisation of the thermal treatment related to the powder applied as well as alloy development might be necessary.

The electro chemical machining (ECM) has been commercially used since several years e.g. in steel die shaping with excellent surface qualities and exhibits large potential in shaping and finishing of parts made from W alloys. However, due to the extreme physical and chemical properties of W standard ECM can not be applied for structuring of W parts without basic and technological investigation. The ECM development on working of W showed that both electrolyte and equipment parameters have to be adapted to W properties to enable ECM for W shaping. The first and most important milestone in the ECM basic research was the development of a special electrolyte which allows region-selective dissolution of W and thus the proof that W can be structured by ECM. Two different electrochemical etching methods Mask-ECM (M-ECM) and Cathodic-ECM (C-ECM) were developed to structure tungsten bulk material with high processing rates. The region-selective structuring in the M-ECM method is achieved by lithographic manufactured resist masks. The working accuracy depends on several parameters e.g. the grain structure or the current type. Structures with electrochemically etched depths of 0.6 mm were achieved by M-ECM before a degradation of the used low quality resist Novolak was observed. Resists with higher stability e.g. SU-8 or metal masks promise larger depths, however, additional equipment is required for their application. Thus, the current focus is set on the investigation and development of the C-ECM method, for which a new constructed facility with micrometer step motor allows accurate shaping by three-dimensional cathode tools, which serve as negative moulds to be copied in to the tungsten metal. Here, the region-selective metal dissolution is also dependent on several parameters. The performed investigation series showed that an accurate controlled cathode-anode distance in the 10 μm range is essential followed by current and pulse type control or optimal electrolyte flow for numbering some of the parameters. In both ECM methods, high frequency pulse currents had led to enhanced structure accuracy.

Fig. 11 shows the step profile of an ECM worked W piece in dependence of the applied pulse frequency. Based on these basic results the technological process development is now orientated to application of μs -pulses and the demonstration of reproducibility. Beyond the micro-shaping technology surface finishing of 'larger' components e.g. thimbles is included into the

development line due to the fact that ECM is the single shaping process which will not introduce micro defects into W parts as usual e.g. in EDM working [8, 9].

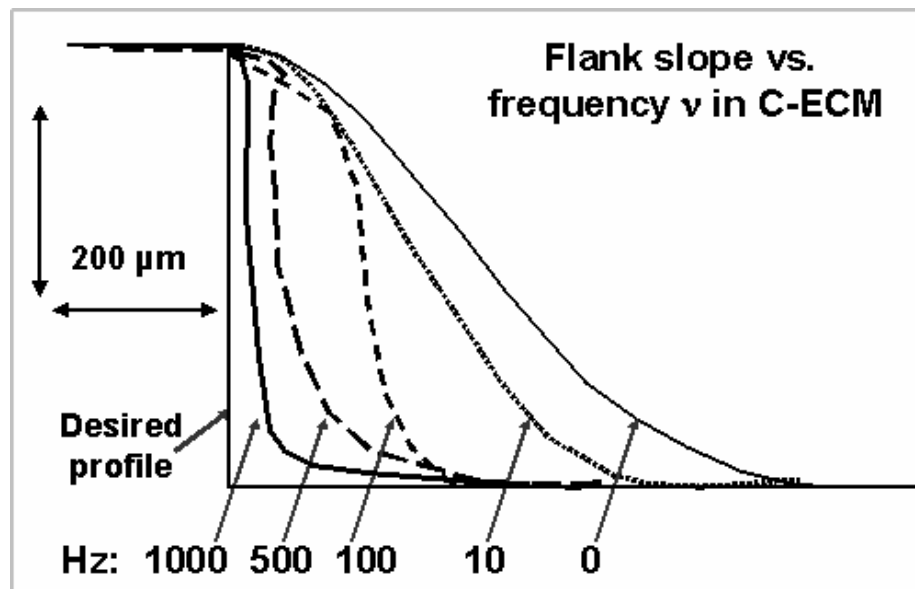


Fig. 11: Higher accuracy of bulk metal removal in C-ECM at increasing frequencies of pulsed currents; C-ECM groove worked with 1000 Hz.

Conclusions and outlook

The current phase of the divertor development is aimed at the construction and high-heat-flux tests of prototypical tungsten mock-ups to demonstrate their manufacturability and their performance. In cooperation with the Efremov Institute, comprehensive technological studies were performed on W/W and W/steel joints of the divertor parts. Based on these results, first series of W mock-ups were fabricated for high-heat-flux testing in a test facility, consisting of the Tsefey EB and a helium loop (10 MPa He, 600°C) built for this purpose to simulate the thermohydraulics conditions close to those of DEMO. The first HHF test campaign of six mock-ups was performed successfully. The tested mock-ups were subjected to destructive post-examinations. It turned out that W parts of some mock-ups, in particular the thimble, were pre-damaged, presumably by micro cracks initiated during the fabrication processes. There never was a suddenly and/or completely broken mock-up, i.e. no brittle failure. Nor was a recrystallisation of the thimble observed in any mock-up. Altogether, it can be said that the performance of the He-cooled divertor concepts (HEMJ and HEMS) of 10 MW/m² was confirmed by the first experiment series.

Prior to the next series of tests on 1-finger mock-ups, which is planned to start in the beginning of 2007, further improvement of the mock-ups has to be done as regards the design of the finger elements to reduce the thermal stresses at the joint interfaces as well as the manufacturing technique for the tile and thimble production. The rules for the manufacturing process are to be specified as a basis for the production of the following 9-finger module. The future steps will focus on the completion of the 9-finger mock-ups and their tests in the second stage of the helium loop construction, which shall provide for a sufficient mass flow rate for such tests.

Regarding the mass production process of W divertor components, PIM and ECM have been investigated and found to be suitable. A PIM process for fabricating microstructured tungsten parts has been successfully demonstrated. In ECM technique further progress can be expected by an optimized C-ECM test facility.

Staff:

S. Gordeev
N. Holstein
W. Krauss
R. Kruessmann
G. Messemer
V. Piotter
J. Reiser
P. Norajitra
R. Ruprecht
V. Widak
B. Zeep
K. Zinn

Literature:

- [1] P. Norajitra, A. Gervash, R. Giniyatulin, A. Kokoulin, A. Komarov, W. Krauss, R. Kruessmann, V. Kuznetsov, A. Makhankov, I. Mazul, I. Ovchinnikov, V. Smirnov, V. Widak, N. Yablokov, He-cooled Divertor Development – the Reference Design and High Heat Flux Tests of 1-finger Mock-ups, TW5-TRP-001, FZK internal report, August 2006.
- [2] P. Norajitra, T. Chehtov, A. Gervash, R. Giniyatulin, T. Ihli, R. Kruessmann, V. Kuznetsov, A. Makhankov, I. Mazul, I. Ovchinnikov, J. Weggen, B. Zeep, Status of He-cooled divertor development (PPCS Subtask TW4-TRP-001-D2), Wissenschaftliche Berichte, FZKA 7100, 2005.
- [3] Nuclear Fusion Programme, Annual Report of the Association Forschungszentrum Karlsruhe/EURATOM, January 2005 - December 2005, Wissenschaftliche Berichte, FZKA-7210 (April 2006) (EUR-22253-EN).

- [4] T. Ihli, R. Kruessmann, I. Ovchinnikov, P. Norajitra, V. Kuznetsov, and R. Giniyatulin, An advanced He-cooled divertor concept: Design, cooling technology, and thermohydraulic analyses with CFD, *Fusion Engineering and Design* 75–79 (2005) 371-375.
- [5] R. Kruessmann, Parametric study to evaluate the design options of the HEMJ divertor cooling concept by CFD simulations, FZK internal report, 2006.
- [6] B. Zeep, V. Piotter, M. Torge, P. Norajitra, R. Ruprecht, J. Haußelt, Powder injection molding of tungsten and tungsten alloys, *Proceedings of the EURO PM2006*, Ghent, Belgium, 2006, Vol. 2, pp. 85-90.
- [7] E. Lassner & W.-D. Schubert; „Tungsten: Properties, Chemistry, Technology of the Element, Alloys, and Chemical Compounds“; 1999; Kluwer Academic / Plenum Publishers, New York; ISBN 0-306-15053-4.
- [8] N. Holstein, W. Krauss, and J. Konys, Development and fabrication aspects regarding tungsten components for a He-cooled divertor, *Proceedings of the 23rd Symposium of Fusion Technology - SOFT 23*, Venedig, 20.-24.9.2004, *Fusion Engineering and Design*, Volumes 75-79, November 2005, 775-778.
- [9] W. Krauss, N. Holstein, J. Konys, Strategies in Electrochemical Machining of Tungsten for Divertor Application, *Proceedings of the 24rd Symposium of Fusion Technology - SOFT 24*, Warschau, 11.-15.9.2006.

TRP-002 DEMO Physics Studies

TW5-TRP-002 D 2 Analysis of Total Radiation in Tokamak Reactor Scenarios

1. Introduction

The aim of this task, terminated during 2006, was to develop a modelling capability, based on a 2D plasma edge code (B2-EIRENE) and a 1.5D core transport code (ICPS), which allows the radiation fraction in tokamak reactor scenarios to be analyzed and characterized in terms of edge and core plasma parameters, in particular to quantify the core impurity contamination associated with a given level of radiation. The task is carried out with the integrated modelling as described in more detail in [1] and in a separate contribution to this Annual report [2].

Ongoing work for that task and also for the DEMO simulations is described in more detail in [3]. The continuation of this work is described in [4] and connected work on startup is described in [5].

The geometric parameters chosen for the DEMO modelling task are similar to those of ITER as developed in the Conceptual Design Activity (1991) ($B=5.7T$, $R=8.1m$, $a=2.8m$, $\kappa=1.7$, $\delta=0.36$). Present modelling examines DEMO operation in ELMy H-mode with a $q\sim 4$ ($I=21$ MA) and a fusion power of ~ 3 GW.

The transport model uses MMM95 core transport and is as described in the separate contribution to this Annual Report [2].

Integrated core and edge/divertor modelling of a plasma prototypical of DEMO ELM'y H-mode has been performed in which medium- to high-Z impurity seeding was employed to reduce the power into the scrape-off layer (SOL) and thereby the divertor power load. The core plasma simulation is linked to the SOL and divertor plasma simulation via scaling relationships determined from extensive series of SOL simulations. The results of the task are described in more detail in [6] and key results are included in a publication [7].

2. Divertor Plasma Modelling

The scaling laws for the edge plasma parameters are derived from the 2D modelling in terms of a normalised divertor neutral pressure, as previously determined from simulations for ITER, JET, and ASDEX-UG, were extended and modified to apply to DEMO parameters. It

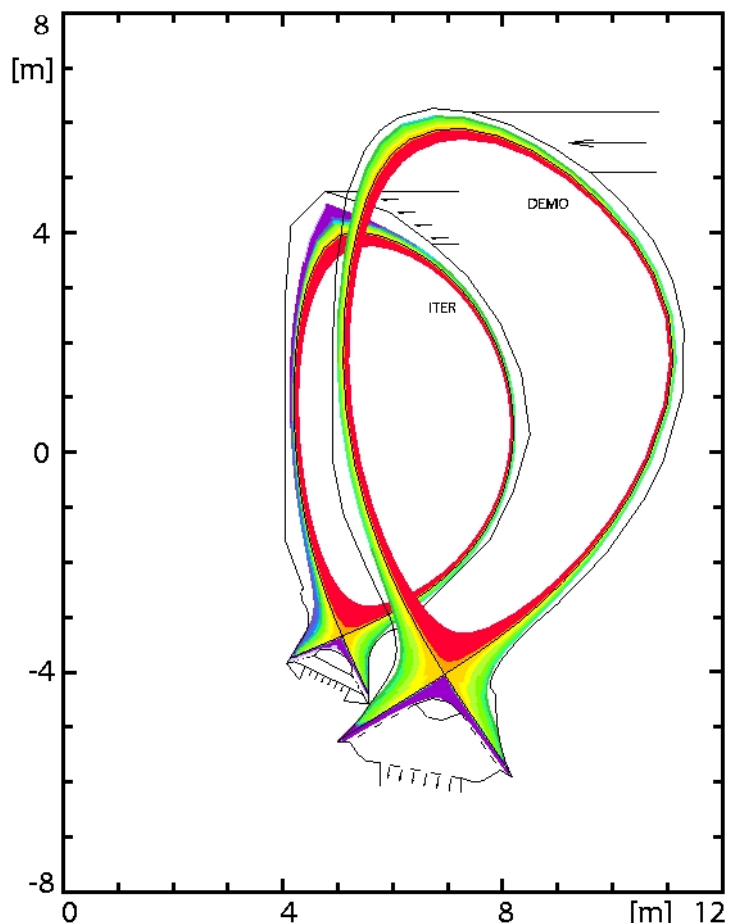


Fig. 1: Comparison of ITER and the larger prototypical DEMO geometry: Divertor and edge plasma is shown in colour.

was found that DEMO and ITER scalings can be superposed, provided that the power is included as a power density with respect to the device volume, and the pumping speed as a specific pumping speed relative to the device area, and a size scaling was introduced.

The normalised deuterium pressure in the private flux region was found in previous studies to be the key parameter to obtaining a scaling of the results. In the present study, this parameter was found to scale with size as the strike point radius to the power 1.21 (Fig. 2).

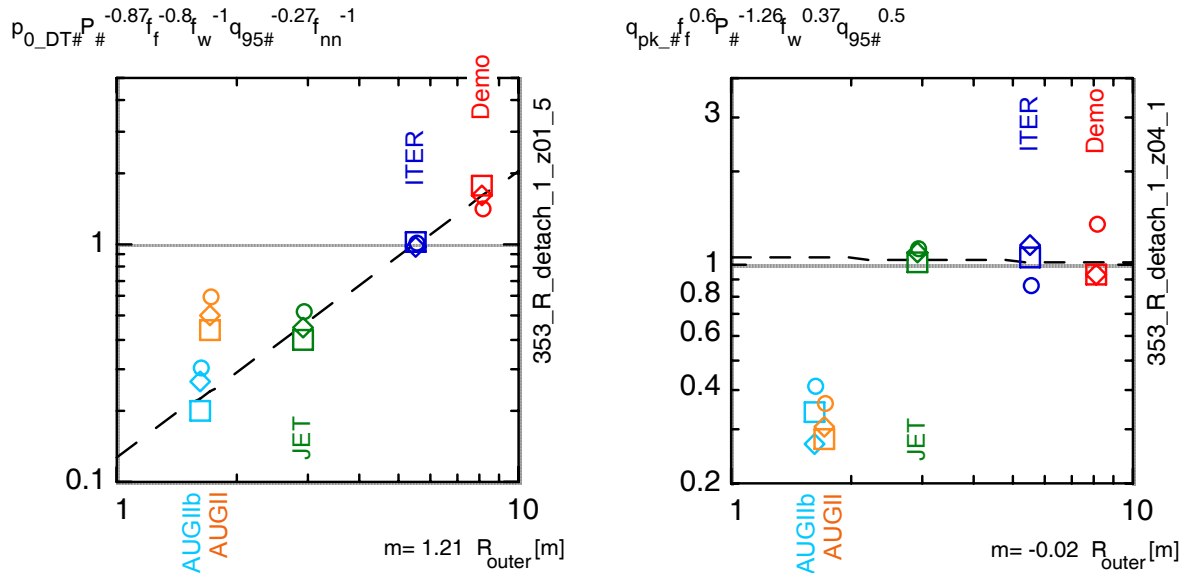


Fig. 2: a) Normalised divertor pressure versus radius of outer strike point R_{outer} at incipient detachment of the inner divertor, $\mu = 1$, and b) normalised peak power at the divertor plate, versus major radius of the outer strike point for devices indicated and for SOL powers from small (circle), medium (lozenge) to high (square). Powers are: AUG: 2,4,8 MW, JET: 8,16,24 MW, ITER: 86, 100, 130 MW, DEMO: 200, 400, 500 MW. Fit exponent is indicated on the figure for fit from ITER to DEMO.

Fig. 2 b) shows the positive result that the normalised peak power load per unit area at the detachment point remains practically constant from ITER to DEMO. The range covered in MW/m² for the range of ITER powers is the same as that for the range of DEMO powers, which are higher. Further details of the size scaling are not given here - they can be found as a table in [1], [5] and in published form in [7].

Specifically, for DEMO and ITER at comparable power density and specific pumping speed, and at the same operating point (same distance from the density limit given by incipient detachment of the

inner divertor), the scaled helium density remained approximately constant (Fig. 3a), the scaled helium flux decreased, and the peak power per unit area on the divertor plate remained constant Fig. 3b). The scaling of the results with parameters other than the size was preserved in going from ITER to DEMO.

When the sparse results available at present with the full neutral model are taken into account, it is found that the peak power is unchanged, but the helium density and flux should be reduced by a factor 0.33 from the scaling with the linear neutral model, as seen also in Fig. 3a. This result is very positive for ITER and DEMO.

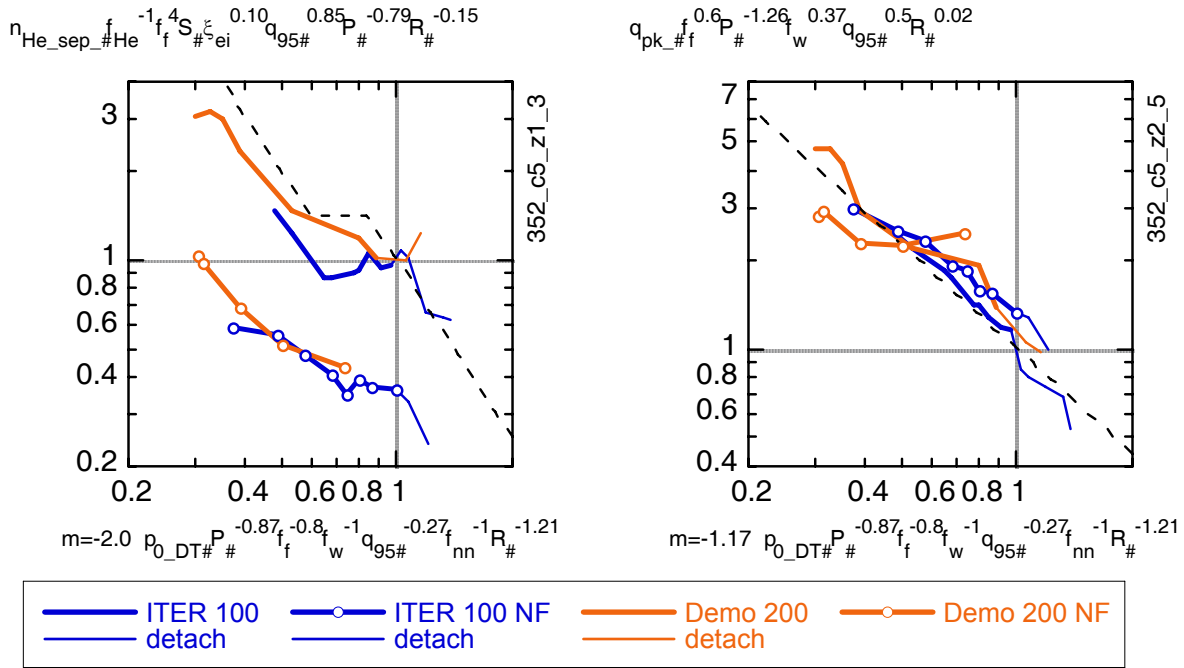


Fig. 3: a) Helium density at the separatrix (scaled)
 b) peak power load at the divertor plate (scaled) versus DT neutral pressure in the private flux region (scaled) for DEMO (200 MW) and ITER (100 MW) for linear neutral model and for more complete nonlinear neutral model including ion-ion and ion-molecule collisions (marked NF). 1 on the horizontal scale represents incipient detachment of the inner divertor. Other scaling parameters are explained in [1], [5], [7].

2. Core Plasma Modelling

For the core simulations, the transport model had previously been calibrated to JET and Asdex-UG experimental results and employed for the determination of the ITER operating space. The simulations for DEMO used the same reference transport model, with the addition of neoclassical transport for impurities. Very flat profiles resulted for electrons and seed impurities. As a sensitivity study, two variants were also investigated, one in which an anomalous diffusion and pinch term was added to all particle transport parameters resulting in moderately peaked profiles for all species, the other in which only impurity profiles were strongly peaked.

Impurity seeding was employed to reduce the power into the SOL and thereby the divertor power load while the fusion power was held at the desired value by adjusting the fuelling rate and thereby raising the plasma density as the impurity concentration increased. Three different seed impurities were investigated, representing typical medium-low, medium, and high Z seed impurities. Because of the smaller dilution, the density increase required is smaller as the impurity Z increases. Typical values of the plasma parameters as a function of the impurity concentration for Xenon are shown in Fig. 4.

The density required for the desired fusion power also depends on the transport model, with the lowest values for the peaked profile variant and the highest value for the peaked impurity profile variant. The reference model required approximately the Greenwald density with the highest Z seed impurity; corresponding densities for the transport variants are 0.9 and 1.4 of Greenwald density. However, all simulations are performed at the same fraction of the edge-based density limit.

Typical results are shown as a function of the injected impurity and the transport model in Fig. 5.

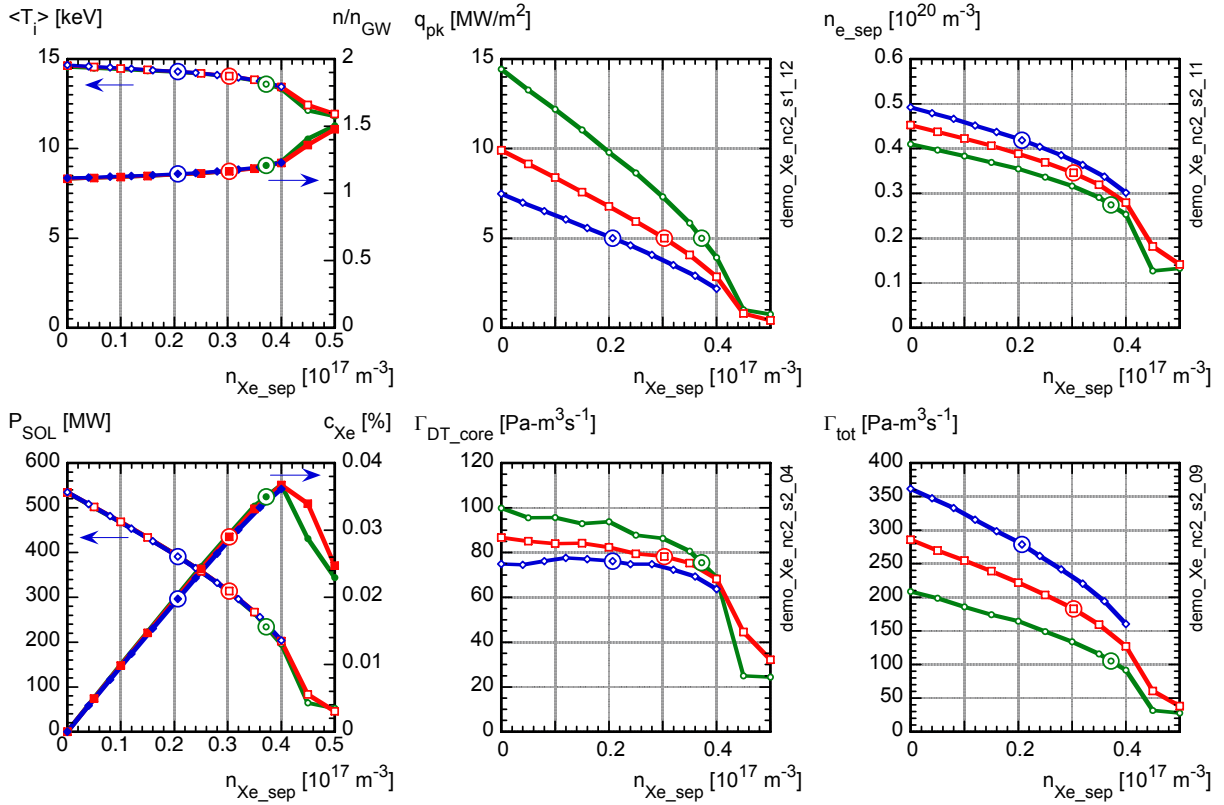


Fig. 4: Parameter variation as Xe edge density is raised for the reference model at different fractions of edge-density limit (green - 0.5, red - 0.7, blue - 0.9). Circles at $q_{pk} \sim 5 MW/m^2$.

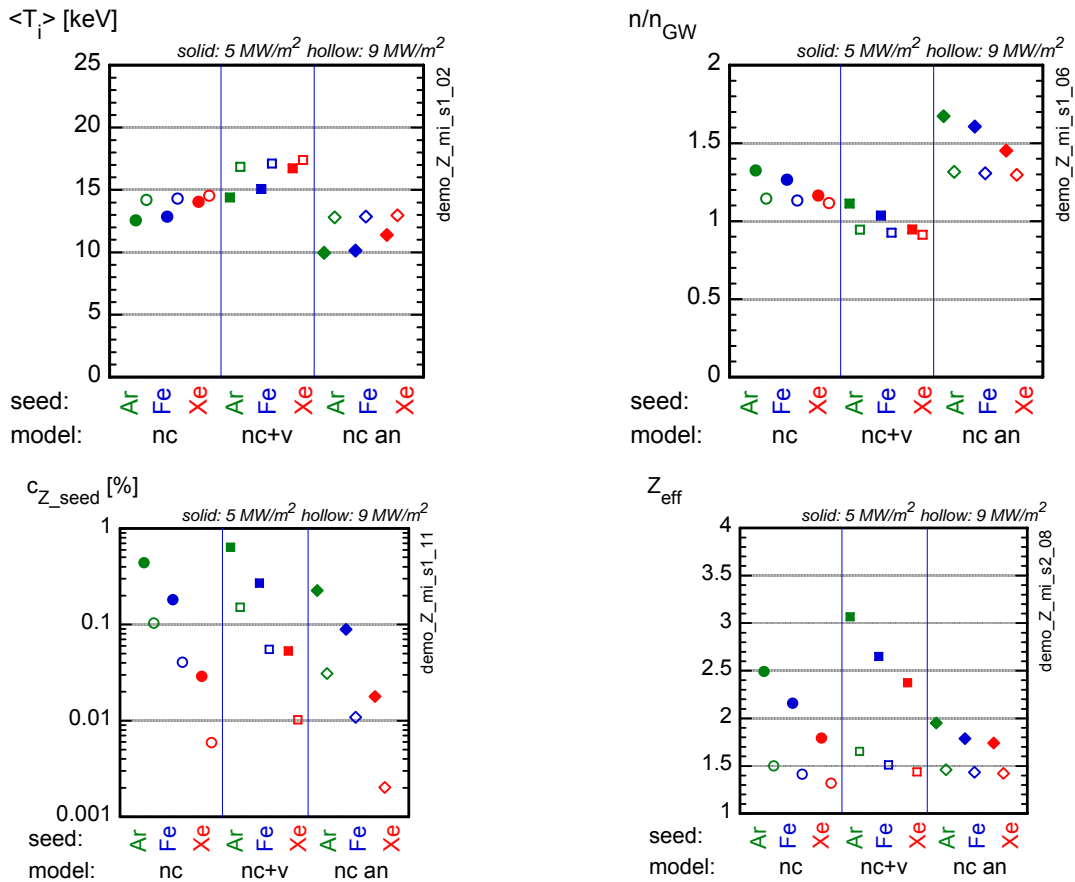


Fig. 5: Parameters at $q_{pk} = 9$ and $5 MW/m^2$ (hollow and filled symbols resp.) for three different seed impurities (Ar - green, Fe - blue, and Xe - red) and different particle transport models (reference - "nc" - left, variant A - "nc+v" - centre, variant B - "nc an" - right of each figure). All results at 70% of edge-based density limit ($\mu = 0.7$).

For all impurities and all transport models investigated, close to ignited operation ($Q=150$) was found feasible at a fusion power of 3 GW at 75% of the edge density limit based on divertor detachment with a peak divertor power load of 7 MW/m^2 , while the power entering the SOL ($\sim 300 \text{ MW}$) was still well above the LH threshold. Such impurity seeding is therefore consistent with the requirements of a helium-cooled divertor with the requirement that peak power be less than 10 MW/m^2 and allows a reasonable operating window.

3. Perspectives

Many caveats exist, and must be clarified by further simulations in subsequent tasks: a) the SOL simulations must be done over a wider range in power and density, b) the SOL scaling is for the moment based on full carbon walls rather than realistic mixed-material surfaces, c) the SOL scaling here does not yet include neutral-neutral collisions and the full molecular package, d) the SOL modelling must be extended to include the seed impurity. Further work in core plasma simulation includes e) validation of impurity and main ion particle transport, f) extension to longer pulse and hybrid scenarios leading to steady-state, and g) integration of the SOL/divertor results with seed impurities into core modelling. This last point is especially important because it introduces a new strong coupling effect between core plasma and divertor operation, which is presently absent in the coupled simulation. The successor to this task is task D3 [4].

Staff:

H. D. Pacher (INRS-EMT, Varennes, Québec, Canada)
G. W. Pacher (Hydro-Québec, Varennes, Québec, Canada)
A. S. Kukushkin (ITER International Team)
G. Janeschitz
I. Landman
S. Pestchanyi - with the collaboration of G. Pereverzev (IPP Garching).

Literature:

- [1] Pacher H.D., Pacher G.W., in collaboration with ITER IT Garching, FZ Karlsruhe, Max-Planck-Institut für Plasmaphysik Garching, EFDA CSU Garching, "Divertor and core plasma modelling for ITER - Final Report June 2006", INRS Energie, Mat. et Télécom. Report, INRS-EMT-029-0606, June, 2006
- [2] Pacher H.D., Pacher G.W., "Divertor and Core Plasma Modelling for ITER", this Annual Report (Physics Section)
- [3] Pacher H.D., Pacher G.W., in collaboration with ITER IT Garching, FZ Karlsruhe, Max-Planck-Institut für Plasmaphysik Garching, EFDA CSU Garching, "Divertor and core plasma modelling for ITER - Intermediate Report December 2006", INRS Energie, Mat. et Télécom. Report, INRS-EMT-033-1206, December, 2006, in preparation
- [4] Pacher H.D., Pacher G.W., "Task TW6-TRP-002.D3 DEMO Physics Studies, D3 - Development of an improved treatment of plasma radiation for medium- and high-Z impurities", this Annual Report (Systems Studies Section)
- [5] Pacher H.D., Pacher G.W., "Task TW6-TRP-012.D1b, Optimisation of fusion power plants for H2 production, D 1b - Optimisation of a 'start-up' scenario where the power is less than 100MW", this Annual Report (Systems Studies Section)
- [6] Janeschitz, G., Pacher H.D., Pacher G.W., Kukushkin, A.S. "Task TW5-TRP-002.D2 DEMO Physics Studies, D2 Analysis of total radiation in tokamak reactor scenarios", Final report Rev. A , April 2006, , revised May 2006, submitted to EFDA
- [7] Pacher, H.D., Kukushkin, A.S., Pacher, G.W., Janeschitz, G., Coster, D.P., Kotov, V., Reiter, D. "Effect of the tokamak size in edge transport modelling and implications for DEMO", presented at 17th International Conference on Plasma Surface Interactions in Controlled Fusion Devices, Hefei, China, accepted for pub. by J. Nucl. Mat. (2006)

TW6-TRP-002 D 3

Development of an Improved Treatment of Plasma Radiation for Medium- and High-Z Impurities

1. Introduction

The aim of this task is to extend the assessment of operation of a DEMO-sized tokamak at high core radiation using the current integrated 2D edge and 1.5 D core plasma model performed in EFDA Task TW5-TRP-002 [1] to include the effect of seed impurities on the SOL/divertor region and assess the additional coupling between core and edge thus introduced, as well as toward longer pulse operation. The task uses a 2D plasma edge code (B2-EIRENE) and a 1.5D core transport code (ICPS), which allows the radiation fraction in tokamak reactor scenarios to be analyzed and characterized in terms of edge and core plasma parameters, in particular to quantify the core impurity contamination associated with a given level of radiation. The task is carried out with the integrated modelling as described in more detail in [2] and in a separate contribution to this Annual report [3]. Ongoing work for that task and also for the DEMO simulations is described in more detail in [4] and connected work on startup is described in [5].

2. Core Plasma Modelling

The implications of impurity-seeding on long-pulse operation of DEMO were investigated using the reference model of [1], i.e. with neoclassical transport of particles in the absence of an anomalous pinch. Four different impurities were modelled ranging from medium-low to medium-high Z (neon to xenon). The additional heating power, which could also be used to drive current, was held fixed at 50 MW, while the fuelling was adjusted so as to obtain a fusion power of 3 GW, resulting in an essentially ignited plasma ($Q=60$). Power deposition profiles were either peaked near the mid-radius (at 0.4 minor radius) or far off-axis (at 0.7 minor radius). The effect of a modest decrease of plasma current from the nominal 21 MA to 18 MA was also investigated.

The gas puffing and impurity seeding were adjusted so as to operate at 70% of the edge-based pressure limit at a peak power load of 5 MW/m². The variation of plasma parameters for the different conditions investigated is shown in Fig. 1.

For the same fusion power, the normalized beta increases from 2.6 to a moderately optimistic value of 3.1. Whereas the ratio of density to Greenwald limit increases from 1.1 to 1.3, the density remains at 0.7 of the edge-based density limit.

The burn duration, assuming 100 Vs available for burn at 21 MA, is approximately 3000s in the absence of impurity seeding and current drive, and is reduced to 1800 s by neon seeding (the decrease is less for higher Z impurities). Reduction of the plasma current to 18 MA extends the burn duration with neon seeding to 4000s in the absence of current drive, 10000 s with near-axis current drive, and 25000 s with off-axis current drive. Increase of the Z of the seed impurity to xenon then yields a burn duration of ~50000 s at these conditions.

Further work is required in the following areas: the validation of impurity transport, the effect of ELM's on overall plasma resistance, and the effect of the seed impurity on the SOL/divertor region. This last effect introduces a new strong coupling between core plasma and divertor operation, which is not presently addressed in the coupled simulation.

3. Divertor Plasma Modelling

As reported in [1], [2], extensive modelling of DEMO with the linear neutral model was carried out and resulted in a series of scaling relations as a function of the size for use as edge boundary conditions of the 1D core transport code. Modelling of a number of cases for

DEMO with the more comprehensive nonlinear neutral model is underway. Initial results show significant effects: the neutral pressure at detachment is a factor 2 higher, the helium densities and fluxes are a factor 3 lower, and the DT neutral flux a factor 2 higher, than with the previous linear neutral model; other scalings are not changed strongly. It is therefore necessary to continue simulations with the more complete nonlinear neutral model.

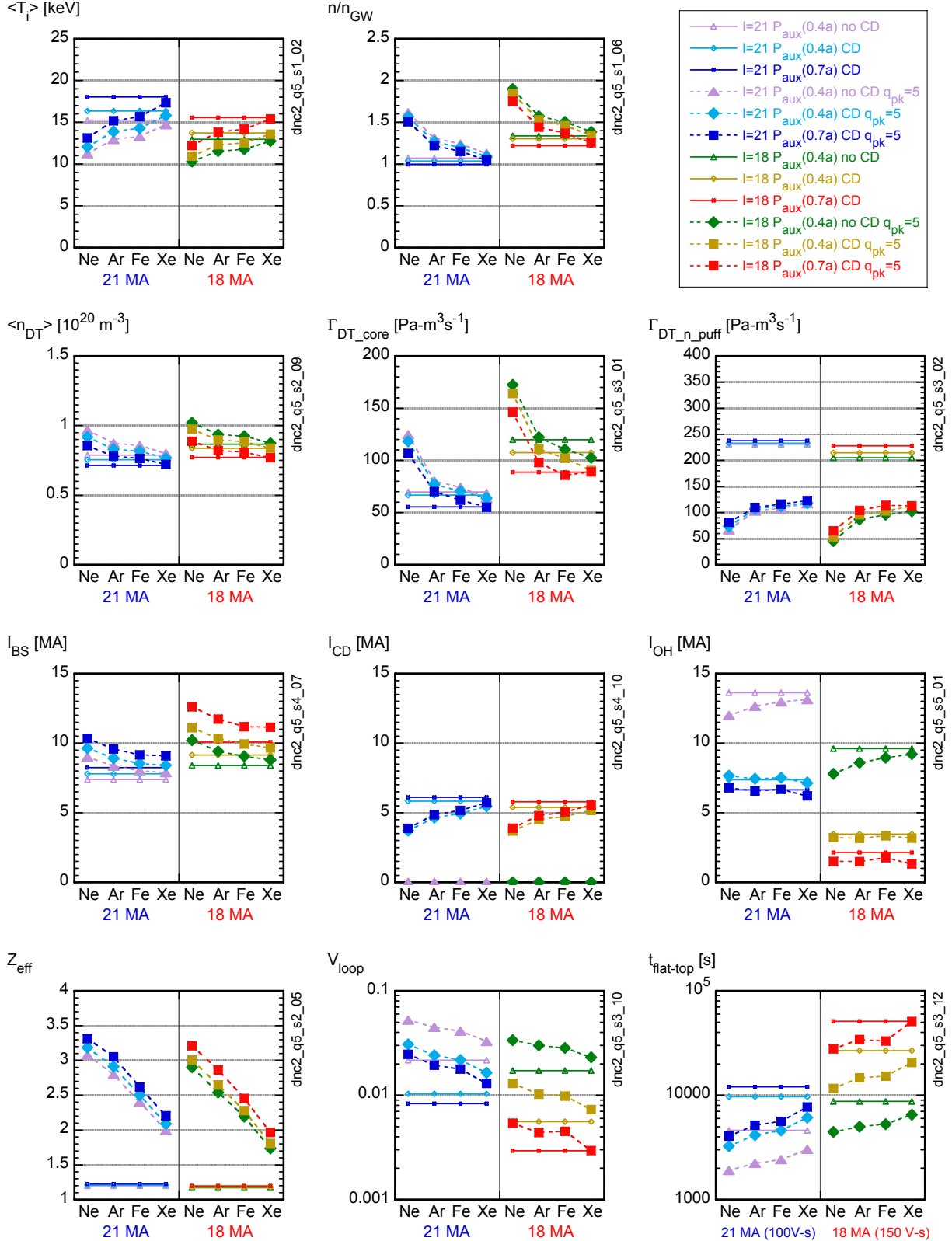


Fig. 1: Variation of plasma parameters at peak power load q_{pk} of 5 MW/m^2 with seed impurity species at 21 MA (left part of each plot) and 18 MA (right part). Parameters in the absence of impurity seeding are indicated by thin solid lines.

However, for DEMO conditions, modelling until convergence is reached requires much more time than it does for ITER so that at time of writing further comprehensive results are not yet available. It will probably be necessary to implement parallel Monte Carlo calculations to obtain more acceptable run times of individual cases for DEMO. We are starting to look into this. Initial edge/divertor modelling including seeded impurities (neon) has also started, but has not yet reached the point where the radiation from the additional impurities is significant. This work is ongoing.

4. Perspectives

The task has followed up on Task TW5-TRP-002.D2. The present task has been ongoing since September 2006. Further work is indicated in the two sections above.

Staff:

H. D. Pacher (INRS-EMT, Varennes, Québec, Canada)
G. W. Pacher (Hydro-Québec, Varennes, Québec, Canada)
A. S. Kukushkin (ITER International Team)
G. Janeschitz
I. Landman
S. Pestchanyi - with the collaboration of G. Pereverzev (IPP Garching).

Literature:

- [1] Pacher H.D., Pacher G.W., "Task TW5-TRP-002.D2 DEMO Physics Studies, D2 Analysis of total radiation in tokamak reactor scenarios", this Annual Report (Systems Studies Section)
- [2] Pacher H.D., Pacher G.W., in collaboration with ITER IT Garching, FZ Karlsruhe, Max-Planck-Institut für Plasmaphysik Garching, EFDA CSU Garching, "Divertor and core plasma modelling for ITER - Final Report June 2006", INRS Energie, Mat. et Télécom. Report, INRS-EMT-029-0606, June, 2006
- [3] Pacher H.D., Pacher G.W., "Divertor and Core Plasma Modelling for ITER", this Annual Report (Physics Section)
- [4] Pacher H.D., Pacher G.W., in collaboration with ITER IT Garching, FZ Karlsruhe, Max-Planck-Institut für Plasmaphysik Garching, EFDA CSU Garching, "Divertor and core plasma modelling for ITER - Intermediate Report December 2006", INRS Energie, Mat. et Télécom. Report, INRS-EMT-033-1206, December, 2006, in preparation
- [5] Pacher H.D., Pacher G.W., "Task TW6-TRP-012.D1b, Optimisation of fusion power plants for H2 production, D 1b - Optimisation of a 'start-up' scenario where the power is less than 100MW", this Annual Report (Systems Studies Section)

EFDA/05-1283 (TW5-TRP-003 D 1) Review of Blanket Segmentation and Maintenance

Large Module and Multi-Module Segment (MMS) Blanket Integration and Maintenance for DEMO

Objectives

The main lines in the European breeder blanket development are the ceramic breeder and the liquid metal breeder blanket. In both cases the breeder blankets are cooled by helium gas whilst the different breeder materials result in different Tritium extraction and circulation systems (purge gas for ceramic breeder and liquid metal for the liquid metal blanket). The Forschungszentrum Karlsruhe (FZK) breeder blanket development is predominantly focused on the ceramic breeder blanket, namely the HCPB (helium-cooled pebble bed) concept [TASK EFDA/05-1280 - TW5-TRP-005-D2-Part 1], but nevertheless also studies for the HCLL (helium-cooled lithium lead) concept were carried out. In addition in continuation of the long experience in the area of dual coolant blanket concept, which was developed at the FZK in the 1990th a new version of the concept is under investigation with special regard to the Multi-Module-Segment integration concept [EFDA/05-1280 - TW5-TRP-005-D2-Part 2]. Some years ago the engineering activities in the view on DEMO were substantially broadened towards overall reactor integration including the development of radial build and shielding concepts, mechanical layout and attachment systems, maintenance schemes, piping concepts and the development of the according remote handling systems as well as considerations on electrical power generation.

The objective of this completed task was to provide a conclusive review and comparison of possible blanket segmentation for the DEMO fusion reactor. Important aspects of this task accomplished in the scope of the DEMO conceptual studies were integration and maintenance. The large module review was to limit the total number of blanket modules in order to reduce the replacement time and to maximise the plant availability. The maximum size of the modules is limited by the opening of the equatorial ports. The size of the port is itself limited by the magnets arrangement. Only basic concepts for the handling devices have been developed during the previous European Power Plant Conceptual Study (PPCS) and there was limited detailed investigation on the hydraulic and mechanical connections of the modules. These preliminary conceptual studies had to be detailed and reviewed.

As a possible alternative the multi-module-segments (MMS) concept consisting of a "banana" back-plate supporting a number of smaller modules had to be analysed. The MMS can be handled through vertical ports. However, still it is feasible to give support or perform some specific maintenance tasks through the equatorial port like in ITER. In advance of the completion of the hereby described design work this concept was lacking of the necessary detailed information for a significant assessment.

Description of work

A fusion reactor integration and maintenance concept for a Helium cooled pebble bed blanket (HCPB) in separate modules was analyzed ("large modules"). The integration concept developed for the modular shield blanket in ITER and according technology was considered as a starting point for further developments. One important goal regarding the large module concept was to limit the total number of blanket modules. However, as a result of the investigation carried out in this DEMO scoping study several severe limitations in the possible blanket size were determined. The electromagnetic loads and thermal stresses during transient events scale with the module size and for rather large modules an unacceptably strong increase of transient loads causing unacceptable large poloidal and radial torques have to be expected. A module size of 4 m² front surface area was considered challenging but still a reasonable ambitious basic layout in regard on the complete set of boundary conditions. As

the resulting weight of the modules was estimated to be about 10 tons, the weight capacity of the in-vessel remote handling machine has to be doubled when compared to the ITER'98 machine (compare Figure 1). Due to the limited space available in the remote handling ports which are employed for inserting the rail and the manipulators of the in-vessel transporters, this was assumed as an upper boundary. Thus, the assumption of even higher load capacities was considered to be not reasonable.

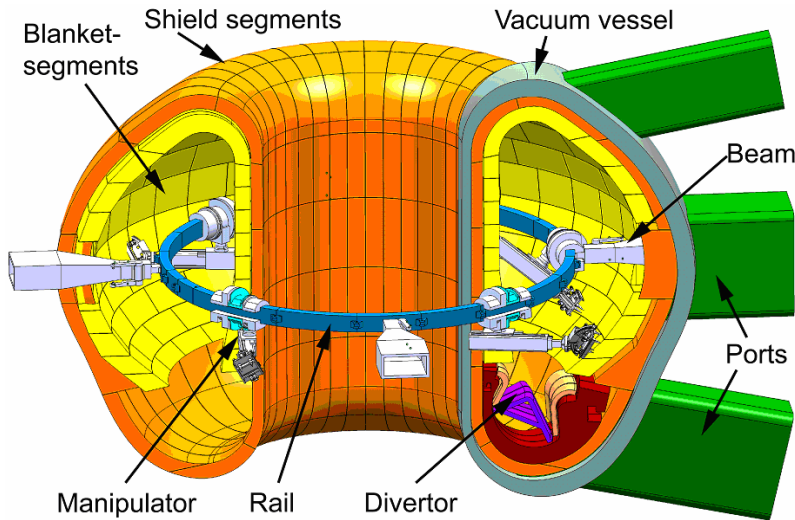


Fig. 1: Maintenance of Large Module Concept: ITER-like in-vessel remote handling machine modified for DEMO.

Especially the integration of a large number of Helium pipes (more than 800 in total) with an inner diameter of 150 mm at the inboard and 200 mm at the outboard turned out to be a challenging task. Detailed 3D CAD models had to be built to approach this topic. The thermal compensation system needed for Helium pipes to cope with the differential expansions of pipes and surrounding low temperature structure was investigated in detail and a high pressure multi-layer compensator system was

proposed to be applied. Although a technique for the cutting and re-welding of the pipes for blanket maintenance which is based on the use of in-bore tools was developed. The tools (cutting, welding and inspection tools) are inserted through the large Helium pipes. For a reasonable short maintenance time a parallelization of the in-bore procedures is necessary. The issue of neutron streaming in the Helium pipes could be successfully treated by an improved shielding concept including the use of neutron absorber plates in the bends of the hydraulic connection key of the blanket modules.

An alternative blanket maintenance concept for DEMO was developed involving a multi-module segment (MMS) blanket and vertical ports for inserting and removing of the MMS. Each MMS consists of a number of blanket modules which are connected to a strong vertical manifold structure by use of a flexible attachment system and likely concentric hydraulic connections in the zero point of the relative motion between blanket module and manifold (compare Figure 2).

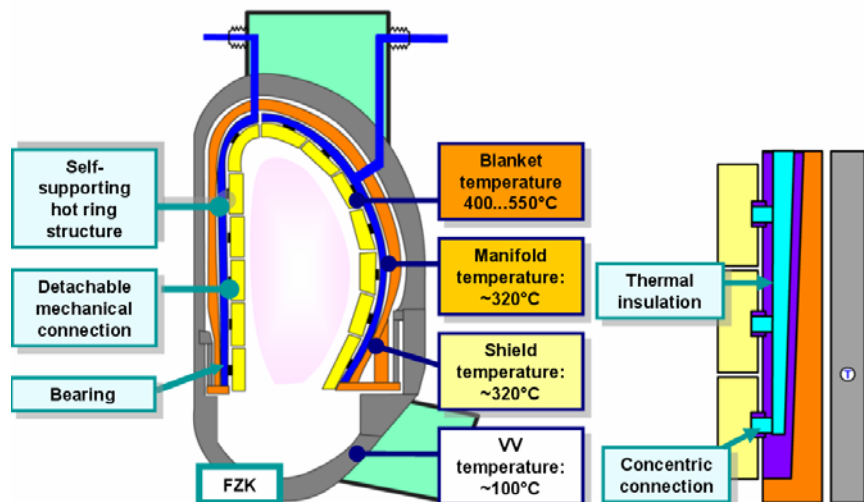


Fig. 2: Sketch of the MMS integration for a HCPB blanket.

The MMS are transported toroidally in the vacuum vessel by a remote handling transport machine located in the divertor region. The transport machine is equipped with sliding car-

riage systems for the movement of the inboard and outboard MMS in transverse radial/poloidal direction (compare Figure 3).

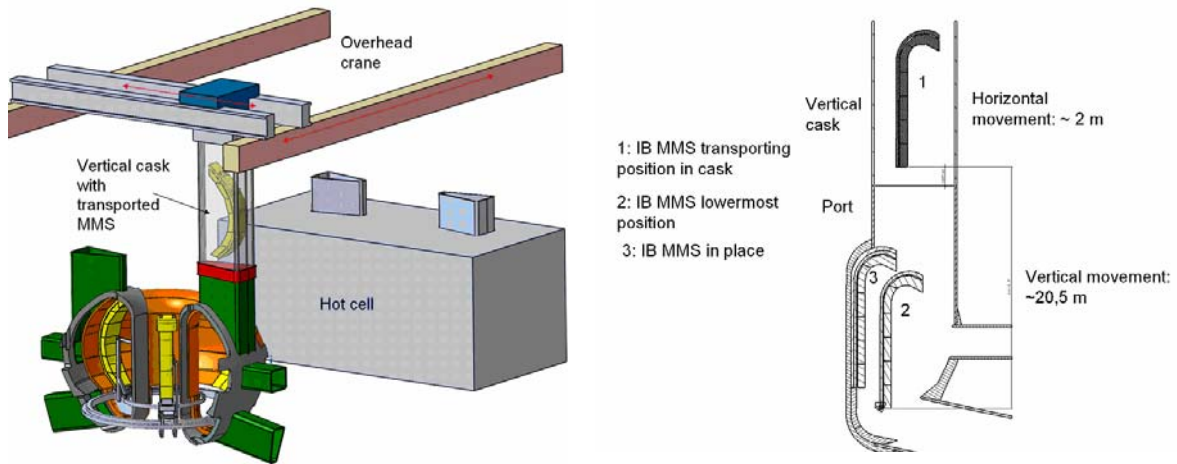


Fig. 3: Basic layout of transport system outside the vacuum vessel (left) and principle requirements for the range of the gripper / manipulator (right).

In the final position the MMS are bolted onto a permanent self-supporting shield structure, which is operated at nearly the same steady-state (medium) temperature as the MMS manifold structure. The shield structure is toroidally closed and can expand fairly unconstrained during heat up within the vacuum vessel. The actual segmentation in toroidal direction is based on acceptable total weight of the segments and the size and number of the maintenance ports. Figure 4 shows a possible segmentation and numbers the segments due to an exchange sequence employing only two maintenance ports.

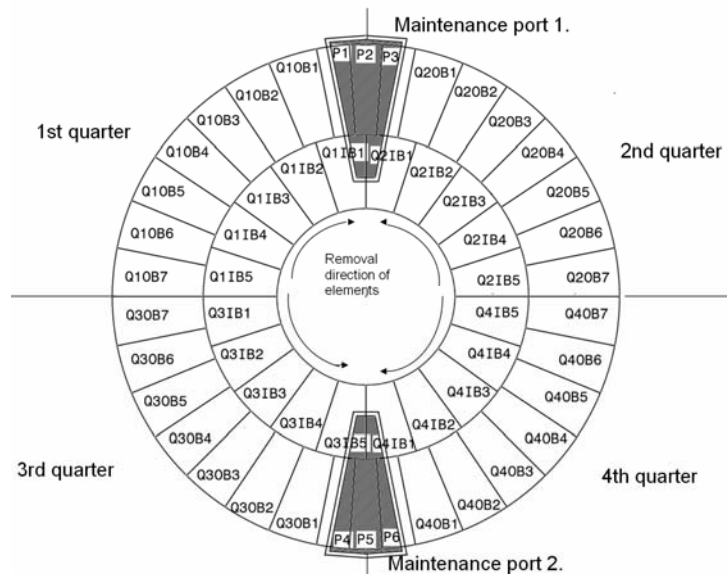


Fig. 4: Segmentation and exchange sequence employing two maintenance ports.

Advantages of this maintenance concept are:

- The maintenance time could be likely reduced in comparison to a separate module maintenance scheme.
- The flexible attachments and hydraulic connections between the blanket modules and the manifolds could be done outside the reactor (compare Figure 5).
- Large flexible attachment systems between vertical segments and cold components are not needed.
- Only a small (two/four) number of ports have to be opened for maintenance.
- Only relatively simple and low accuracy remote handling steps are necessary for the large components.

- A small number of independent units have to be handled.

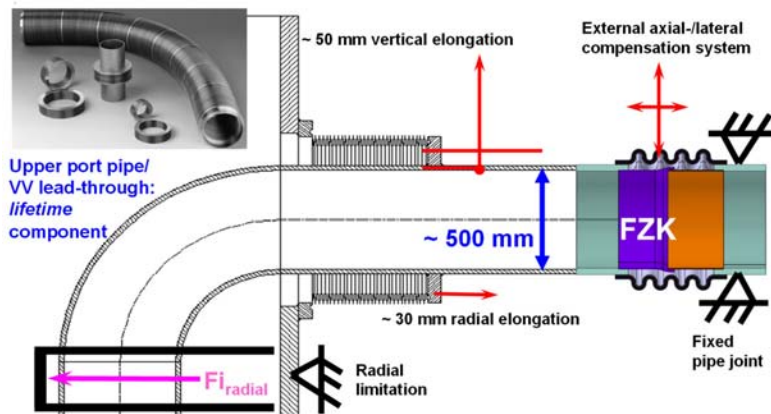


Fig. 5: Sketch of the lead through of the Helium pipes in the vertical ports.

A drawback of the MMS system might be the increased waste volume since the manifolds behind the blanket modules are likely not re-weldable due to helium production in the steel.

While a number of promising new approaches and proposals have been presented, further work will be necessary to develop more detailed design solutions and allow for final judgments on feasibility and

performance. This has to include additional thermo-mechanical analyses of the MMS and shield components especially under transient boundary conditions. Nevertheless, as a result from the hereby presented work in the frame of TW5, for the next phase in the DEMO conceptual studies MMS in combination with a vertical maintenance scheme is determined as default for further investigations with regards to reactor integration and maintenance.

Staff:

- D. Filsinger
- U. Fischer
- T. Ihli
- C. Köhly
- P. Pereslvtsev
- C. Polixa
- J. Rey

Nagy, D. (Visiting scholar at FZK from HAS, KFKI-Research Institute, Budapest, Hungary)

EFDA/05-1280 (TW5-TRP-005 D 2)

Review of Blanket Concepts for the DEMO Conceptual Study

Part 1 - Critical Review of the European DEMO Helium Cooled Pebble Bed (HCPB) Blanket Concept for the Large Module and Multi-Module Segment (MMS) Maintenance

Objective

The Helium Cooled Pebble Bed (HCPB) blanket has been a European DEMO reference concept for nearly a decade. The recent European Power Plant Conceptual Study (PPCS) confirmed that the HCPB built from the reduced-activation ferritic-martensitic steel Eurofer is an acceptable choice of a blanket relying only on limited technological extrapolation. Based on the outcome of the PPCS in the following years a modular blanket design for the HCPB was investigated in more detail. This approach was based on the assumption of a large module integration concept with modules in the range of four square meters First Wall surface being handled and replaced separately.

The main objective of the completed task was to provide a critical review of the European Helium Cooled Pebble Bed (HCPB) blanket concept for DEMO shown in Figure 1. Integration aspects as well as design aspects had to be covered. Attention had to be drawn on the blanket layout to facilitate fabrication and reliable manufacturing. The work in this task was based on results of former work carried out in the frame of the extensive long term technology R&D programme, the PPCS and the SEAFP and SEAL studies.

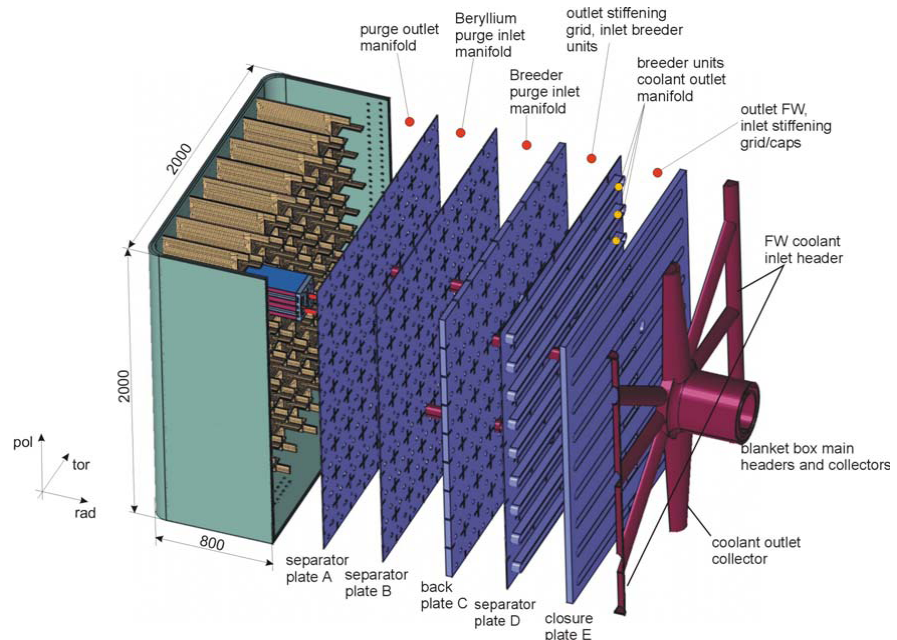


Fig. 1: Large module HCLL blanket box.

Description of work

The Helium Cooled Pebble Bed (HCPB) blanket design which mainly consists of a U-bend first wall with two-dimensional stiffening grid and multi-layer manifold at the radial back of the module is appropriate to build large modules and provides sufficient strength against pressurization accidents nearly independently from the overall size of the module. As a result of the review carried out in the present study it can be concluded, that the design is not yet completely optimized in terms of simplicity of fabrication and in terms of pressure drop. The fabrication of the foreseen structures with internal cooling channels and the assembly of the cooled plates, i.e. joining of the stiffening grid plates to the First Wall and the back walls need to be addressed carefully. The cooling plate design with meandering cooling channels that lead to asymmetric temperature distribution and lateral plate deflection could be optimized by either introducing a symmetric cooling channel design or adapting a newly proposed curved cooling plate design with straight internal cooling channels. The pressure drop in the large

modules is relatively large and could be improved to a certain extent. Not all of the optimization principles newly proposed for the MMS blanket sub modules are to be adapted easily due to the large size of the first wall and the modular design concept where a large number of breeder units have to be connected to common manifold layers which are placed behind each other at the radial back of the module (compare Figure 1). A strong feature of the large module design is the absence of toroidal or poloidally oriented manifolds in the breeding zone, which should be kept by any evolved design. It is self evident that the pressure drop and circulation power could be reduced significantly by increasing the helium pressure. This would lead to an increased amount of steel structure, eventually reduced tritium breeding and/or increased radial build. Increasing the helium pressure would necessitate a number of severe changes in the blanket design and in the layout of out of vessel systems like the cooling loop including the heat exchangers.

A large module attachment system that (i) can be opened and closed remotely during blanket replacement, (ii) allows for the differential thermal expansions of the large modules and the shield during all thermal load cases and (iii) provides enough strength against the electromagnetic loads during transient plasma events like disruptions is necessary for the large module concept. At the current state the feasibility of such a system has not been proven.

The neutronic performance of the large module HCPB blanket is very good. The tritium breeding ratio is sufficiently high and the needed radial build of the breeding zones is small, when compared to liquid metal blankets. Also the energy multiplication is very high due to the use of beryllium as a very efficient neutron multiplier and from this the plant efficiency is promising even when choosing moderate helium temperatures. The amount of beryllium in the HCPB blanket is relatively high, which also results in a good shielding capability of the blanket modules. The pebble bed filling strategy for the large modules needs to be developed in detail.

In regard on the multi module segments (MMS) integration concept (compare also TW05-TRP-003-D1) a large number of potential simplifications could be introduced and possible improvements in regard on the helium cooling technique could be applied. By means of heat transfer enhancement with a ribbed inside of the First Wall cooling channels illustrated in Figure 2 and a turned flow direction (poloidal instead of toroidal for the MMS 2 m x 1 m configuration) a significant reduction of the pressure drop and from this a better efficiency of the Helium cooled DEMO fusion power plant seems feasible.

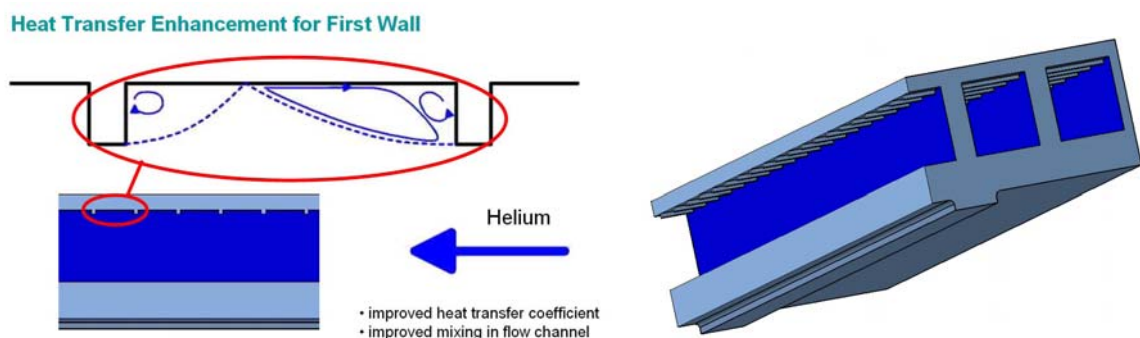


Fig. 2: First Wall concept with internal rib structure for heat transfer enhancement: Sketch of eddies occurring behind and in front of the cooling ribs (left); 3D CATIA model (right).

A new breeder cooling plate design with straight internal cooling could help significantly to simplify the fabrication process and removes the issue of lateral plate deflections. This design could also be used with the large module blanket. Additionally new design features in regard to the internal blanket box design could be applied. A reduced number of breeder units with only two breeder units placed on top of each other in poloidal direction could allow simplifying the manifold design and reducing the manifold pressure losses.

A newly proposed option for the blanket module attachment system is appropriate for taking advantage of the MMS system that deals with permanent connections between the MMS back plate and the modules and which gives more freedom in using smaller blanket sub-modules. This is only limited by the requirement to assure the tritium breeding self-sufficiency. A MMS configuration with 2 m wide (toroidal) and 1 m high (poloidal) modules can be attached by a welded concentric hydraulic connection and two welded bending plates in a promising way. Thermal stresses during transient thermal and electromagnetic events seem to be acceptable. An exemplary result of a calculation employing finite element methods can be seen in Figure 3.

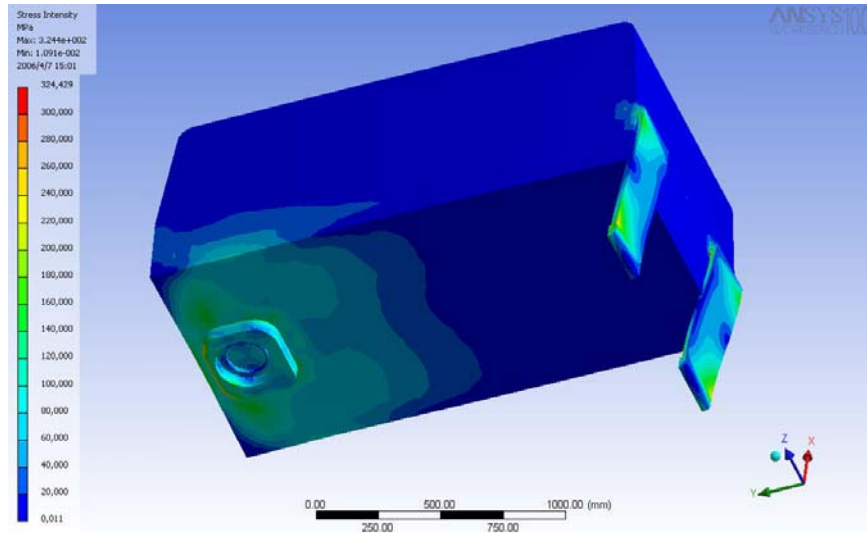


Fig. 3: Contour plot displaying an exemplary distribution of thermal stresses in the improved blanket box.

A number of promising new approaches and proposals in accordance with a more elongated module shape rather than a square shape have been proposed. A conceptual design is presented in Figure 4.

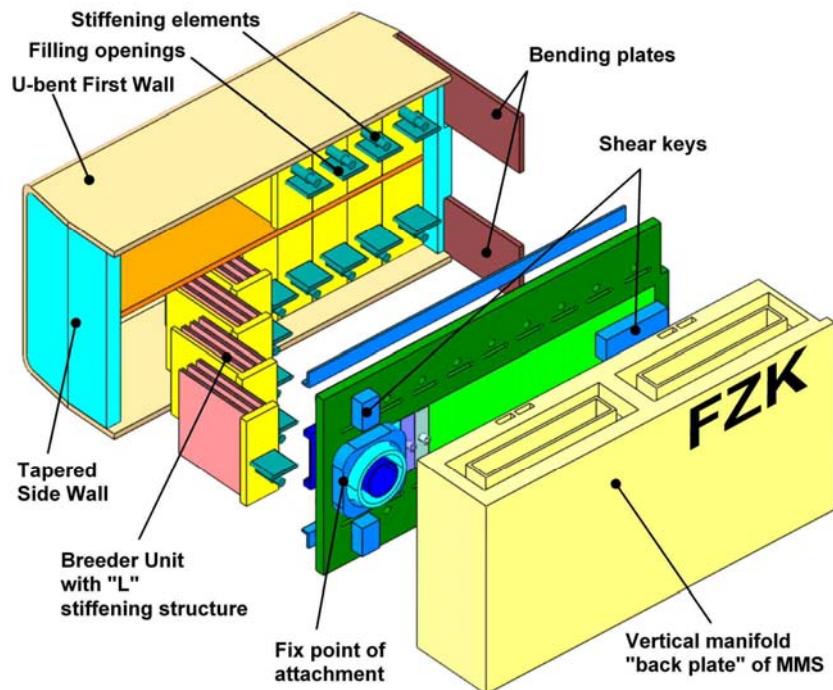


Fig. 4: Improved HCPB blanket box adapted for the MMS concept.

If the proposed features can be successfully realized, the main advantages of the MMS HCPB blanket will be:

- A simplified structure and fabrication (likely also results in better reliability).
- A simplified filling procedure.
- Feasibility of a flexible attachment of modules (remote handling is not required).
- A significant reduction of pressure drop and circulation power and therefore significantly increased plant efficiency.
- Integration into the MMS concept which deals with large handling units and shifting of most mechanical and hydraulic connection steps outside the vessel is possible. This most likely will result in both, reduced maintenance time and improved reliability.

Further improvements of a fusion reactor with HCPB blankets can be achieved by increasing the helium temperature and the helium pressure. Higher helium temperatures can be allowed when using improved structural materials (like ODS grades of ferritic steel) and using advanced beryllium multipliers.

While this completed work programme enabled to present a number of promising new approaches and proposals it is evident that further work will be necessary to develop detailed design solutions and allow for final judgments on the feasibility and actual performance. Further work in the scope of the next stage of the DEMO conceptual studies needs to focus on the confirmation of the presented approaches and requires further analysis of the attachment system and in particular a detailed design of the manifolds.

Staff:

D. Filsinger
T. Ihli
C. Köhly
J. Rey

Part 2 - Dual Coolant Lead Lithium (DCLL) Blanket Concept for the Multi-Module Segment (MMS) Maintenance and Magneto Hydrodynamic (MHD) Analysis

Objective

The Helium Cooled Pebble Bed (HCPB) and the Helium Cooled Lead Lithium (HCLL) blanket are the European reference concepts and therefore serve as a basis for the development of the European ITER test blanket modules (TBM). A drawback of both concepts on the long term might be the limited coolant exit temperature, which is defined by the need of keeping the coolant temperature below the acceptable structural material temperature. For this reason the helium exit temperature cannot exceed roughly 500°C in the case of a Eurofer made blanket. Some improvements could be expected for a partly or completely ODS-Eurofer made blanket structure, whereby a maximum exit temperature between 600°C and 650°C might be the upper limit to be expected from today's view.

However, a major step in achieving higher exit temperatures while using a common Eurofer made steel structure could be achieved if a thermal insulation between a liquid breeder circulated through the blanket and the structural material is applied. In this case the exit temperature of the liquid breeder can be chosen some hundred K higher than the allowable temperature of the structure. As the liquid breeder has to be pumped through the strong magnetic field inside the reactor although an electrical insulation is necessary between the breeder and the conducting steel structure to keep the magneto hydrodynamic (MHD) pressure drop reasonably low. These considerations led to the development of the Dual Coolant Lead Lithium (DCLL) blanket concept in the 1990th at the Forschungszentrum Karlsruhe. In the DCLL concept the liquid breeder is separated by flow channel inserts from the Helium cooled struc-

ture. The reference material for the flow channel inserts is silicon carbide fiber-reinforced silicon carbide (SiC_f/SiC). The DCLL blanket concept was the basis for the recent European Power Plant Conceptual Study (PPCS) model C and is considered a basis for the US TBM effort. The PPCS confirmed that a DCLL blanket built from the reduced-activation ferritic-martensitic steel Eurofer and some ODS-Eurofer used for the First Wall could be an attractive choice for an advanced future fusion power plant in terms of overall plant efficiency.

Description of work

Under this second part of the task the DCLL concept was reviewed in regard to DEMO and especially in regard on the DEMO multi module segments (MMS) integration concept (compare also TW5-TRP-003-D1). In the MMS concept a vertical row of blanket modules is mounted onto a common back plate which houses the helium coolant and breeder manifolds (compare Figure 1). The aim of this approach is combining the advantages of the DCLL blanket in terms of efficiency and high exit temperature with the advantage of a comparative fast blanket replacement procedure that allows achieving reasonable high plant availabilities.

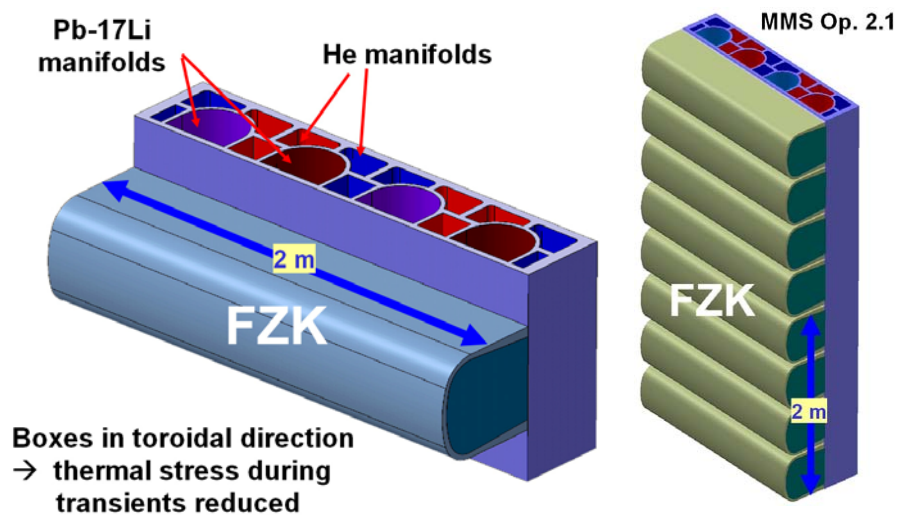


Fig. 1: DCLL blanket for the Multi-Module Segment (MMS) concept.

In the present investigation equivalent boundary conditions as used for the simultaneously performed DEMO MMS HCPB Blanket approach were taken into account. For example the helium coolant pressure was set to 8 MPa in contrast to the PPCD Model C where a pressure of 14 MPa along with artificial surface roughness in the flow channels was assumed.

In contrast to the MMS HCPB concept where a gap between the blanket sub-modules and the MMS manifold was foreseen, for the MMS DCLL configuration a rigid (welded) connection between the sub-modules and the manifold is considered more adequate. The underlying intention is the simplification of the breeder flow path with the aim of keeping the magneto hydrodynamic pressure drop small (compare Figure 2). Especially removing toroidally oriented liquid breeder manifolds and ensuring large breeder channel cross sections was considered important. The drawback of this MMS DCLL configuration compared to the MMS HCPB configuration which deals with a flexible connection between the blanket sub-module and the manifold is that the use of a toroidally closed supporting shield structure (hot ring shield) and a simple mechanical connection between MMS and shield is not applicable. The reason for this is that the entire DCLL MMS heats up during a relatively short time when the plasma is switched on and therefore a flexible attachment between the MMS and the shield is necessary to cope with the differential thermal expansions. Nevertheless, due to the reasons mentioned before and the relatively small amount of helium coolant present in the manifolds (keeping the temperature constant near the Helium inlet temperature is more compli-

cated as for entirely Helium cooled blankets) in the case of the DCLL the rigid module manifold connection was chosen in the present study.

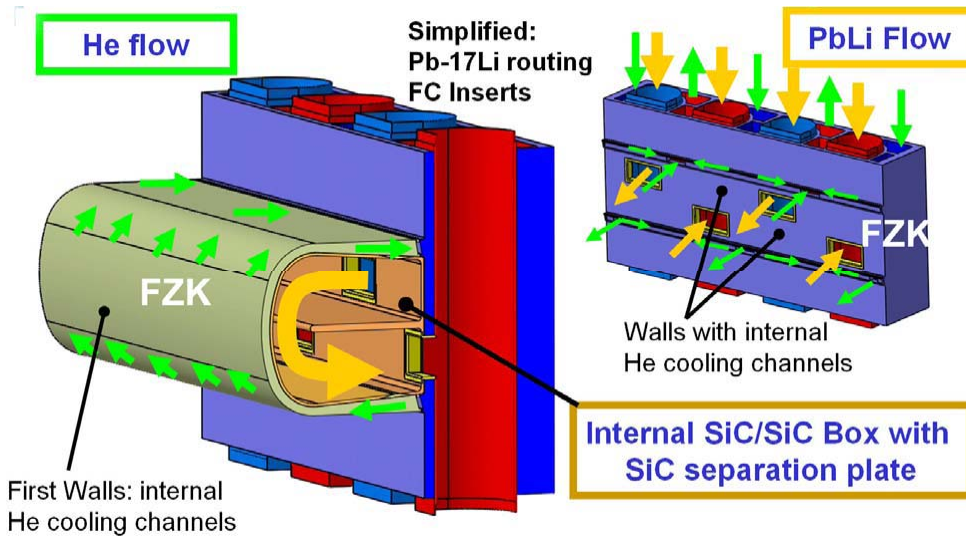


Fig. 2: Flow paths of helium und lead lithium in the DCLL blanket and manifold.

The main emphasis of the new MMS design for the DCLL blanket is simplification and adaptation to a vertical replacement strategy. The new design deals with a comparatively simple flow routing, a reduced amount of Helium cooled structures and simplified flow channel inserts made from SiC_r/SiC. Most of the power (up to 67%) is collected within the liquid breeder that leaves the multi-module blanket at 700°C. The vertical segment concept allows for simple draining by gravity force.

The concept seems to have the potential to fulfil the requirements in terms of mechanical strength and a promising hydraulic lay-out could be derived. Preliminary calculations to assess mechanical and thermal stresses have been performed (compare Figure 3).

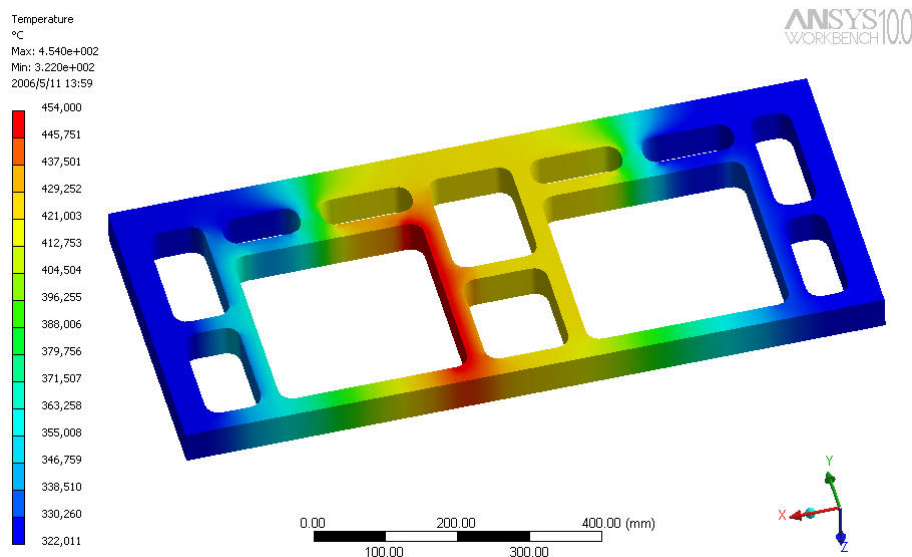


Fig. 3: Exemplary calculation of the temperature distribution in the DCLL manifold.

While a number of promising new approaches and proposals for the DCLL blanket are presented in this report it is evident that further work will be necessary to develop more detailed

design solutions and allow for final judgments on feasibility and performance. Open issues remain especially in the following areas:

- Behaviour of the flow channel inserts under operational conditions.
- Tritium extraction from the hot breeder stream.
- Tritium permeation into the Helium stream.
- Detailed MHD pressure loss in 3D geometries to be determined and adjusted.
- Integration of the MMS DCLL blanket into the reactor, especially providing a suitable attachment system.
- Need of advanced power conversion cycle (better than Helium Brayton cycle) to offer significant improvements over the HCPB equipped plant.

When compared to the optimized MMS HCPB concept which was analyzed in parallel (part 1 of the present task report) it turned out that the DCLL blanket should be combined with an advanced power conversion cycle to offer a better plant efficiency. As DEMO will be the first fusion reactor plant to be built it is unlikely that the risk will be taken to combine an extremely complex new fusion reactor as a heat source with a new power conversion system that has not been proven to work reliable over decades in other applications like coal or fission plants. Nevertheless, a DCLL based DEMO machine may offer additional potential for further increase in the maximum outlet temperature that could result in important advantages in the area of hydrogen production and efficiency, if advanced power conversion cycles become available. Due to the high temperature of the liquid metal and the need to extract both, tritium and heat from it, the technological challenge for the realization of the DCLL concept includes especially the out-of vessel systems like heat exchangers, pipes, valves and tritium extraction system. Evidently, concerning the feasibility and reliability of a DCLL based reactor important issues remain to be solved. The concept presented in this study may serve as basis for ongoing R&D on the DCLL concept including the fields of flow distribution, MHD effects, tritium breeding and neutronics, corrosion, tritium permeation, flow channel inserts, fabrication, tritium extraction system, liquid metal loop for high temperatures, flexible attachment system and remote handling.

Staff:

L. Bühler
D. Filsinger
T. Ihli
C. Köhly
C. Polixa
J. Rey

**TRP-005
Neutronic Analysis**

**TW6-TRP-005 D 2
TBR and Shielding Analyses for the HCPB DEMO Reactor**

The objectives of Task TW6-TTRP-005, Deliverable 2, are (i) to proof the capability of the HCPB blanket concept developed for DEMO to achieve tritium self-sufficiency, (ii) to proof the capability of the internal components and the vacuum vessel to provide sufficient shielding, and (iii) to provide the nuclear power generation data required for the thermal-hydraulic layout of the DEMO reactor(s).

This task has been started only recently. Prior to the development of a suitable reactor model and detailed design analyses it is required to define a proper set of reactor parameters. This is an iterative process starting with the definition of a suitable radial build which depends, among others, on the dimension of the shield system. The required shield dimension, in turn, depends on the shielding efficiency which is given by the assumed material composition of the shield and its geometrical configuration. The shield system must be designed in such a way that a sufficient protection of the super-conducting magnets is ensured. In this context the radiation design limits for the superconducting magnets have been critically reviewed and updated to the state-of-the-art. Table 1 summarizes these limits for ITER and DEMO.

First assessments of the shielding requirements were performed with the objective to reduce, as much as possible, the radial dimension of the shield system. The related shielding analyses were conducted on the basis of 3D shielding calculations performed with the MCNP code using a suitable modified PPCS reactor model. As a result of these analyses, a shield thickness of 30 cm was recommended assuming an efficient shielding mixture including tungsten carbide, water and steel.

Table: 1: Updated radiation design limits for the superconducting toroidal field coils.

	ITER		DEMO
Integral neutron fluence for epoxy insulator [m ⁻²]	1×10 ²²	~ 1×10 ⁷ Gray	2~3×10 ²²
Peak fast neutron fluence (E>0.1 MeV) to the Nb ₃ Sn superconductor [m ⁻²]	1×10 ²³		--
Peak fast neutron fluence to Nb ₃ Sn ternary superconductor [m ⁻²]	0.5~1×10 ²²		1×10 ²²
Peak displacement damage to copper stabiliser, or maximum neutron fluence, between TFC warm-ups [m ⁻²]	1~2×10 ²¹	Equivalent to 0.5~1×10 ⁴ dpa	1×10 ⁴ dpa between TFC warm-ups
Peak nuclear heating in winding pack [W/m ³]	1×10 ³		<5×10 ³

Staff:

U. Fischer
P. Pereslavytsev

**TRP-009
He-cooled Divertor Test Module for ITER**

**TW5-TRP-009 D 2
Testing suitable HEMS/HEMJ Prototypes in ITER**

The intermediate-term goal of the He-cooled divertor development [1] (TRP-001) is the completion of a test divertor module (TDM) which is envisaged to be tested in ITER from 2020 onward (Fig. 1). The objectives of the TDM are function tests and full validation of the divertor concept under real fusion boundary conditions to be aimed at future application in DEMO. For this purpose a suitable prototype for such tests in ITER are to be developed which has a similar approach as developing the test blanket module (TBM) for DEMO.

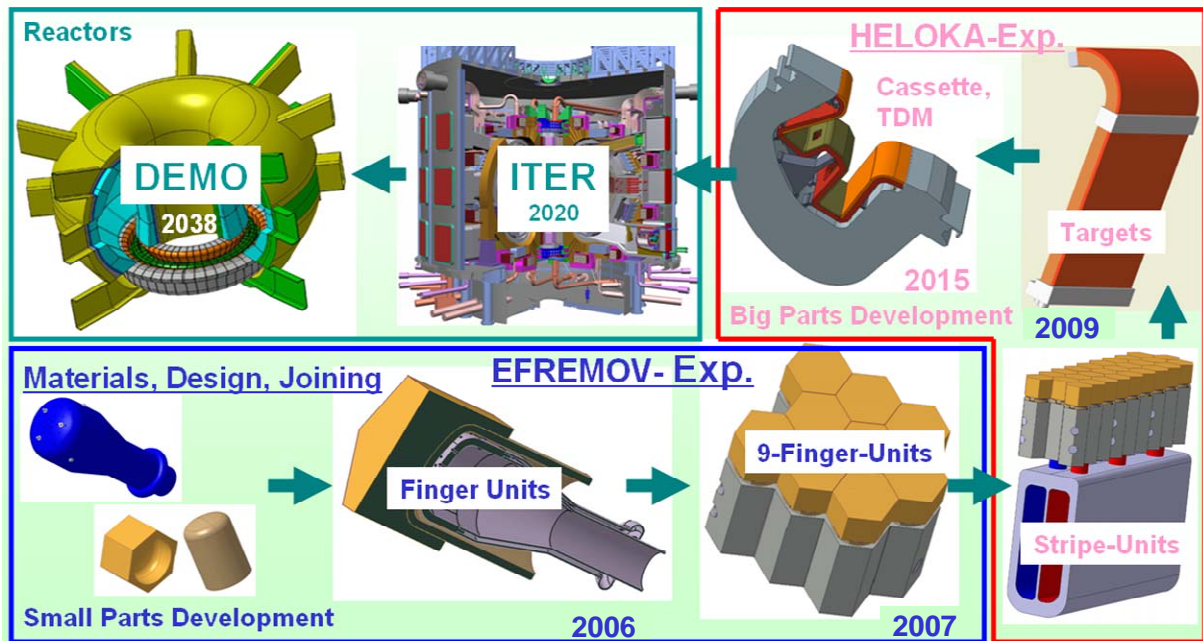


Fig. 1: Roadmap of the He-cooled divertor development.

Basis for the TDM investigations [2] are the CATIA designs of water cooled ITER divertor cassette received from ITER both a complete model in V4 version (Fig. 2) and incomplete model in V5 version with design being updated. The associated thermalhydraulic data are taken from the current ITER DDD report from the ITER IDM data base. The thermalhydraulic examination for our helium cooled divertor concept resulted in that the cooling of the entire cassette with helium is not possible for space reasons ($d_{h-He} \gg d_{h-water}$), therefore only the outer vertically target (OVT) will be cooled with helium. The inlet and outlet temperatures of the helium were chosen with 600°C and 650°C, respectively. Assuming a He speed of 70 m/s a necessary inner diameter of the main pipes resulted to 150 mm. Inconel 625 is chosen as material of the He main tubes, which allows a relatively high operating temperature of up to 750°C as well as a post-heat-treatment-free welding. The dimensioning of the tube wall thickness is based on the AD Merkblatt specifications resulting in a size ($d_a \times s$) of inlet and outlet tubes of 170 x 10 mm.

The ITER cassette types (i.e. standard, second and central cassettes), the possibilities for connecting He cooling tubes onto the ITER cassette body, as well as the ITER port types have been discussed. There are altogether three central cassettes each equipped with two second cassettes on the left and on the right building up to a tripel arrangement, which is positioned at the three existing maintenance ports (No. 2, 8, 14). The pipe connection position at the lower end the cassette has been found as suitable. The He pipes can be guided via the existing cut-out in the cassette body at this bottom zone of the central cas-

sette, which is normally occupied by the diagnostic block, and attached to the OVT. This attachment possibility exists only with central cartridges, which - unlike the standard and second cassettes being hung up and shifted into the rail system - are hung up into the toroidal ring as last one. Thus, sufficient space outward is given for the pipe connections. The maintenance port No. 2 (Fig. 3) has been found suitable for the TDM test, since the location of measuring instruments originally planned for this port could be omitted for the testing period for our TDM of about 6 months.

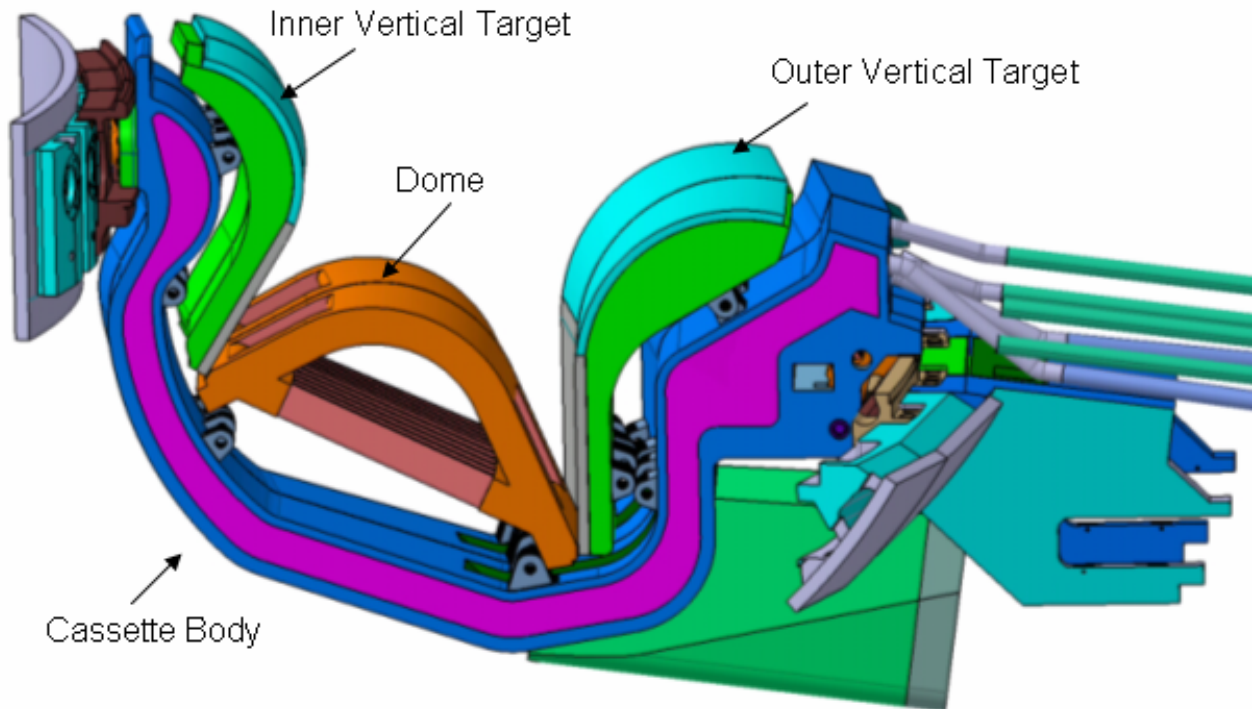


Fig. 2: ITER divertor cassette.

Staff:

R. Kruessmann
P. Norajitra
V. Widak
R. Ruprecht

Literature:

- [1] P. Norajitra, R. Giniyatulin, T. Ihli, G. Janeschitz, P. Karditsas, W. Krauss, R. Kruessmann, V. Kuznetsov, D. Maisonnier, I. Mazul, C. Nardi, I. Ovchinnikov, S. Papastergiou, A. Pizzuto, P. Sardain, European Development of He-cooled Divertors for Fusion Power Plants, Nucl. Fusion 45 (2005) 1271-1276.
- [2] V. Oberheide, L.V. Boccaccini, R. Kruessmann, P. Norajitra, S. Stickel, Assessment of He-cooled Test Divertor Module (TDM) for ITER, FZK internal report, 2006.

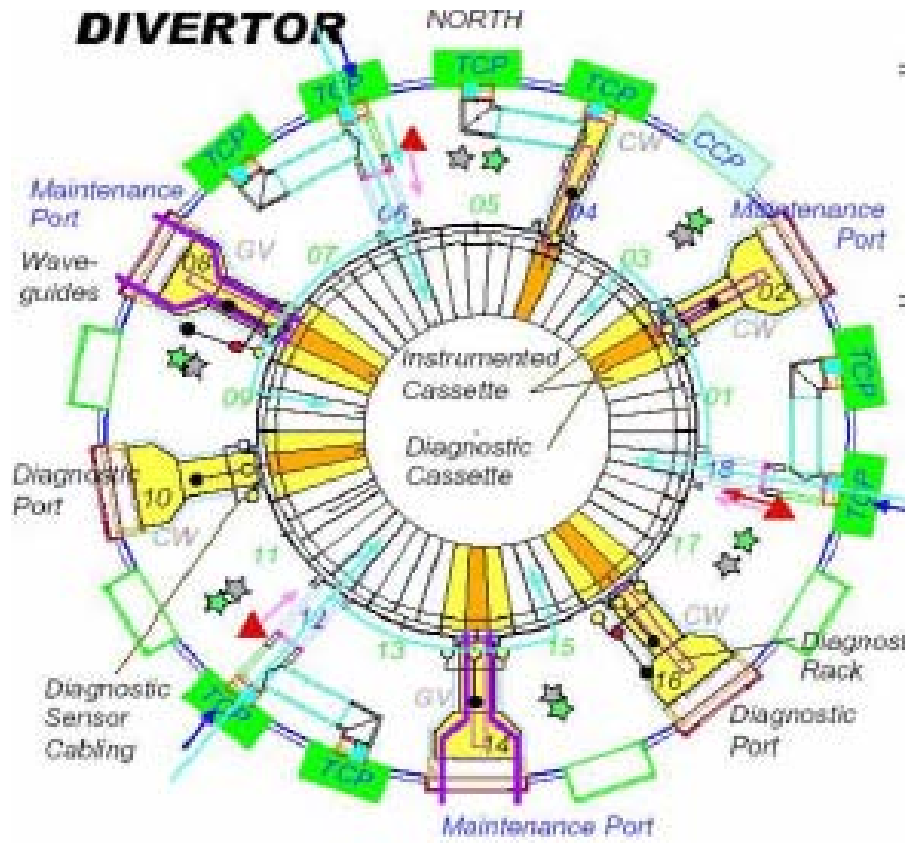


Fig. 3: Suitable TDM test position in ITER: Central cassette of maintenance port 2.

TRP-012

Optimisation of a Fusion Power Plants for the Production of Hydrogen

TW6-TRP-012 D 1b

Optimisation of a 'Start-up' Scenario where the Power is less than 100MW

1. Introduction

The aim of this task is to optimise the "start-up" of a DEMO-sized tokamak including the L- to H-mode transition with auxiliary power below 100 MW. The task is carried out with the integrated modelling based on a 2D plasma edge code (B2-EIRENE) and a 1.5D core transport code (ICPS), as described in more detail in [1] and in a separate contribution to this Annual report [2]. Ongoing work for that task is described in more detail in [3], and results concerning the steady state values of a highly radiating DEMO configuration are described in [4], [5]. The present task has just been active since the autumn of 2006.

2. Initial Plasma Modelling

The geometric parameters chosen for the DEMO modelling task are similar to those of ITER as developed in the Conceptual Design Activity (1991) ($B=5.7T$, $R=8.1m$, $a=2.8m$, $\kappa=1.7$, $\delta=0.36$). (see Figure in [4]).

The ICPS model for core plasma transport in the connected work described in [2], [4], [5] is a time-dependent model. However, in those studies, for reasons of computational efficiency, a number of accelerator algorithms were applied in several of the equations, since the interest there was in the quasi-steady-state results. Checks were performed to ascertain that the quasi-steady-state results were unaffected by these algorithms. The startup scenarios of the present study must, however, be determined in real time. At the present time, the code is being converted to real-time operation. This work is ongoing and initial results on real-time scenarios for DEMO are not yet available.

3. Perspectives

The task has just started. Once the code operates in real-time mode, the ramp-up of plasma current from ~5 MA onwards and the concurrent rampup of density and auxiliary power will be optimised using the ICPS model in ASTRA so as to obtain an L- to H-mode transition with an auxiliary power below 100 MW. Simplified boundary conditions will be used while the plasma is in the limiter configuration and the full integrated model for core and edge will be used after transition to the diverted geometry.

Staff:

H. D. Pacher (INRS-EMT, Varennes, Québec, Canada)

G. W. Pacher (Hydro-Québec, Varennes, Québec, Canada)

A. S. Kukushkin (ITER International Team)

G. Janeschitz

I. Landman

S. Pestchanyi - with the collaboration of G. Pereverzev (IPP Garching).

Literature:

- [1] Pacher H.D., Pacher G.W., in collaboration with ITER IT Garching, FZ Karlsruhe, Max-Planck-Institut für Plasmaphysik Garching, EFDA CSU Garching, "Divertor and core plasma modelling for ITER - Final Report June 2006", INRS Energie, Mat. et Télécom. Report, INRS-EMT-029-0606, June, 2006

- [2] Pacher H.D., Pacher G.W., "Divertor and Core Plasma Modelling for ITER", this Annual Report (Physics Section)
- [3] Pacher H.D., Pacher G.W., in collaboration with ITER IT Garching, FZ Karlsruhe, Max-Planck-Institut für Plasmaphysik Garching, EFDA CSU Garching, "Divertor and core plasma modelling for ITER - Intermediate Report December 2006", INRS Energie, Mat. et Télécom. Report, INRS-EMT-033-1206, December, 2006, in preparation
- [4] Pacher H.D., Pacher G.W., "Task TW5-TRP-002.D2 DEMO Physics Studies, D2 Analysis of total radiation in tokamak reactor scenarios", this Annual Report (Systems Studies Section)
- [5] Pacher H.D., Pacher G.W., "Task TW6-TRP-002.D3 DEMO Physics Studies, D3 - Development of an improved treatment of plasma radiation for medium- and high-Z impurities", this Annual Report (Systems Studies Section)

TW6-TRP-012 D 2

Assessment of the Impact of a Fusion Power Plant for H₂ Production on Internal Components

Objectives

Studies carried out in the EU on fusion power plants have focused so far on electricity production. Another important alternative is the production of hydrogen and exploitation of the role that fusion power can play in a developing hydrogen economy. Hydrogen is regarded as a major secondary energy carrier that will have a large market share for applications including heating and transportation. Previous studies [1, 2, 3] have concluded that fusion power can make a major contribution by providing the large quantities of energy required for sustainable hydrogen production and generating economic off-peak power in an integrated energy system. The objectives of the present study follows up a specific conclusion from an earlier study [1], that due to the important role fusion power plants can play in a hydrogen economy, consideration should be given to optimizing the design of a fusion plant for the production of hydrogen rather than electricity – a ‘Hydrogen Production Fusion Power Plant’ (HPFPP). The hydrogen production cycles described in the earlier study are to be considered as the basis for this study.

The scope of the work performed under this DEMO technology subtask comprises the following more or less independent aspects. Assessment of (i) the impact on the design of internal components of an HPFPP, including possible alternative blanket layouts, (ii) cooling fluid(s), in particular the possible use of CO₂ rather than He, and (iii) the impact of pulsed operation on the design of the mechanical structure.

Design of Internal Components

Breeding blankets are key components of fusion power plants and determine to a large degree their attractiveness. For this reason emphasis in the study about internal components is on blanket concepts. Regardless of other aspects, the key parameter to judge the attractiveness of a blanket concept is the prognoses of the achievable outlet temperature. The outlet temperature determines the choice of the most appropriate cycle for energy production and its efficiency. Therefore it also determines the most decisive value of a power plant, namely the cost of electricity. This is also true in the case of a HPFPP. The blanket outlet temperature determines the possible processes for hydrogen production from fusion power and it also determines the thermal-to-hydrogen conversion efficiency to be expected. This allows focusing on blanket outlet temperatures as an indicator to assess the impact of the prospective of a HPFPP on the design of internal components. Table 1 summarizes the main EU blanket concepts considered for a potential application in a conceptual power plant. Reflecting the EU philosophy for a fusion power plant the concepts with the highest development risks but also most promising attractiveness (highest outlet temperatures, e.g. TAURO or A-HCPB) have taken a back seat [4].

In comparison to this, relying on previous investigations [1, 2] an overview of applicable hydrogen production processes is given and their requirements on process temperature are specified. The presented processes were selected considering conceivable technical feasibility and sufficient efficiency. Due to this, plasma chemical methods aiming towards direct water splitting into hydrogen and oxygen as described in [2] are not considered.

Thermochemical water splitting is the conversion of water into hydrogen and oxygen by a series of thermally driven chemical reactions. Currently the leading alternatives for thermochemical hydrogen production are the Westinghouse hybrid sulphur process (WSP) and the sulphur-iodine process (SI). Other processes have also been suggested but are less developed and require process temperatures $>1000^{\circ}\text{C}$. Figure 1 shows a simple schematic of the coupling between the thermochemical water-splitting process and fusion reactor for hydrogen production. This sketch does not account for the fact that thermochemical water splitting is realized by a series of thermally driven chemical reactions. Especially the different levels of temperature required for the employed chemical reactions and the flow of different chemical compositions might lead to quite complex flow schemes [8].

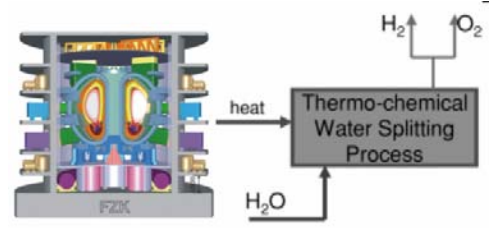


Fig. 1: Schematic of simple coupling of the thermochemical water-splitting process and fusion reactor for hydrogen production (adopted from [9]).

Table 1: Characteristic design parameters of the current EU blanket concepts for the conceptual power plant DEMO.

Blanket Concept	HCLL [5]	DCLL [6]	HCPB [7]
Application	DEMO	DEMO	DEMO
Tritium breeder	Pb-17Li	Pb-17Li	Li_4SiO_4
Neutron multiplier	Pb-17Li	Pb-17Li	Be
Fuel form	liquid	liquid	pebbles
Breeder $T_{\text{max,allowed}}$	500°C (average) $\sim 550^{\circ}\text{C}$ (peak)	700°C (average) $\sim 750^{\circ}\text{C}$ (peak)	Li_4SiO_4 : 950°C (peak) Be: 650°C (peak)
Structural material	EUROFER	EUROFER (SiC/SiC inserts)	EUROFER
Structure $T_{\text{max,allowed}}$	550°C	550°C	550°C
Interface $T_{\text{max,allowed}}$	480°C (Pb-17Li - steel)	480°C (Pb-17Li - steel) 700°C (Pb-17Li - SiC/SiC)	$>500^{\circ}\text{C}$ (Li_4SiO_4 - steel) $>500^{\circ}\text{C}$ (Be - steel)
Purge medium	Pb-17Li	Pb-17Li	He
Coolant: $T_{\text{in}} / T_{\text{out}}$	He: $300^{\circ}\text{C} / 500^{\circ}\text{C}$	He: $300^{\circ}\text{C} / 500^{\circ}\text{C}$ Pb-17Li: $460^{\circ}\text{C} / 700^{\circ}\text{C}$	He: $300^{\circ}\text{C} / 500^{\circ}\text{C}$
Coolant pressure	He: 8 MPa	He: 8 MPa Pb-17Li: 0.12 MPa	He: 8 MPa

There is a range in temperature allowing a utilization of these processes. This range is determined by the thermodynamic equilibrium of the specific chemical reactions and the associated production rates required. Thus, if accepting a change in efficiency, it is possible to adjust the process to the available heat source. Figures 2 and 3 taken from [10] illustrate the influence of temperature on the expected thermal-to-hydrogen efficiency. It has to be mentioned that compared to the values given in [1] the estimates of efficiencies in [10] seem to be rather optimistic. The estimates were performed with the aim of employing nuclear power from fission reactors to produce hydrogen and are dependant on the specific assumptions such as efficiencies of heat exchangers, recuperators and power conversion cycle. This has to be considered if assessing the given values. Especially in the case of the hybrid Westinghouse process, the efficiency of the power conversion cycle affects the thermal-to-hydrogen efficiency. It is shown that a significant (relative) increase in efficiency can be achieved with the help of higher process temperature. Furthermore, it can be assumed that power plants operating with a heat source powered by fusion should be able to reach very similar cycle efficiencies as fission power plants, powering a heat source operated at the same temperature level.

Figure 2 shows clearly that the SI process has only a limited value with a heat source at a temperature level below approximately 780°C (thermal-to-hydrogen efficiency <30%). Compared to this, the WSP as proved in Figure 3 is more tolerant. If providing a heat source at a temperature level higher than approximately 630°C a thermal-to-hydrogen efficiency higher than 30% is expected to be achieved.

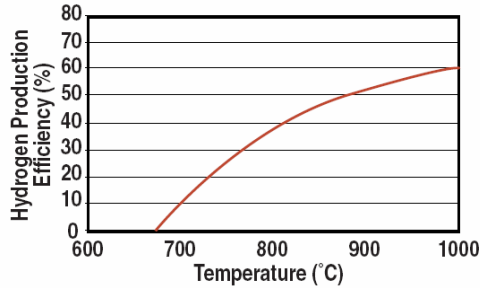


Fig. 2: Estimated SI cycle thermal-to-hydrogen efficiency versus peak process temperature [8].

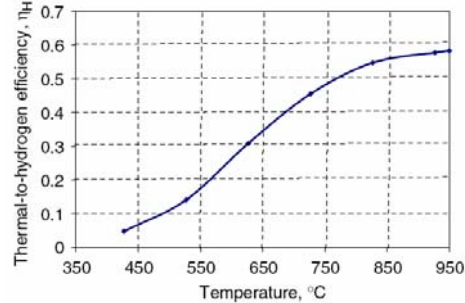


Fig. 3: Thermal-to-hydrogen efficiency for the hybrid WSP coupled to a gas turbine modular high temperature reactor [10].

Electrolysis is the reference for thermochemical processes. With 70% efficiency at the electrolyser and typical power conversion efficiencies between 35%-40% one may expect conversion efficiencies around 25%-28% for hydrogen production from electrolytic water-splitting. At first hand, this process does not entail any adaptation of the power plant due to hydrogen production. The efficiency of the power plant needs to be optimized for the production of electricity only. A significant gain in thermal-to-hydrogen conversion efficiency can be achieved if electrolysis of steam is operated at a higher temperature level (high temperature steam electrolysis: HTSE). Figure 4 shows the energy demand for water and steam electrolysis. The total energy demand (ΔH) for water and steam decomposition is the sum of the Gibbs energy (ΔG) and the heat energy ($T\Delta S$). The electrical energy demand, ΔG , decreases with increasing temperature as shown in the figure. The ratio of ΔG to ΔH is about 93% at 100°C and about 70% at 1000°C. This drives the increase of the thermal-to-hydrogen conversion efficiency with increasing temperature, even though the total energy demand ΔH slightly increases. Additionally, high temperature helps in reducing cathodic and anodic overvoltage, which cause the power loss of the electrolysis (a typical value is 10% overpotential of ideal potential). Thus, the HTSE can produce hydrogen with lower electric power than conventional water electrolysis [10, 11]. This process is particularly advantageous when coupled to high efficiency power cycles and can consequently yield very high overall thermal-to-hydrogen efficiencies. The overall efficiency value is driven by the operating temperature and the cycle efficiency. As the electrolysis temperature increases, ΔG and thermal losses decrease such that the overall thermal energy required for the electrolysis decreases. Therefore, the overall thermal-to-hydrogen energy efficiency increases with increasing operating temperature.

Of particular interest for the presented study is the process proposed in [9]. HTSE is coupled with an advanced gas cooled fission reactor (AGR). The HTSE average process temperature is 900°C, whereas the reactor exit temperature and the SCO_2 cycle turbine inlet temperature are: 550°C to 700°C. The 900°C at the HTSE unit, which is higher than the reactor exit temperature, is achieved with recuperative and electrical heating. With direct coupling between the power conversion cycle (supercritical CO_2 recompression Brayton cycle) and the reactor, the authors claim that the system can achieve 38.6% to 48.2% of net hydrogen production energy efficiency. This independency of the HTSE process temperature offers an alternative if the reactor exit temperature is limited due to technological requirements or limitations.

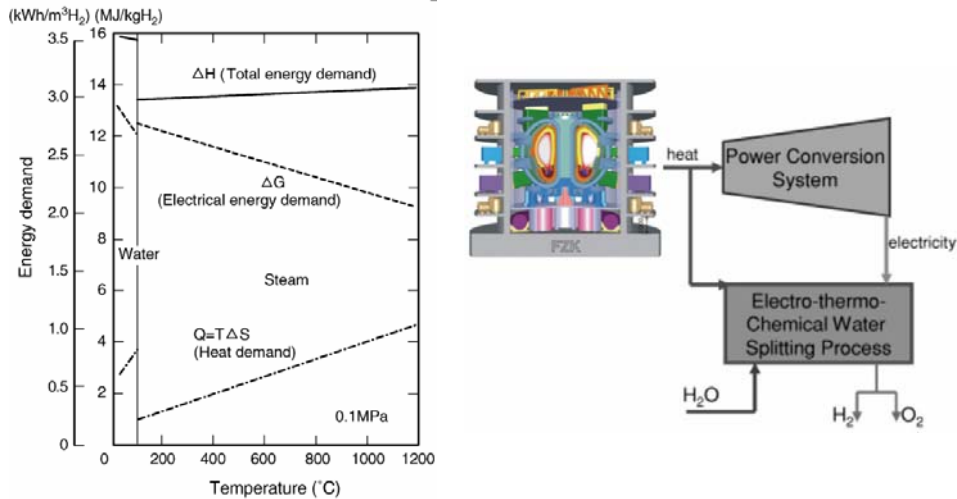


Fig. 4: Energy demand for water and steam electrolysis versus electrolysis temperature [11] (right) and simple schematic of the coupling of the electrothermochemical water-splitting process, fusion reactor and power conversion system for hydrogen production (adopted from [9]).

From all this, a very general and global statement describing the temperature requirements for effective hydrogen production processes which can also be recognized in the Generation IV fission reactor development trends could be “the higher temperature the better”. Promising for a HPPFP with limited outlet temperature is the HTSE process since this process can be adjusted to the available temperature level of the heat source. This process would be applicable for all current blanket concepts but would suffer from rather low net hydrogen production energy efficiency. An optimization might be possible if additional heating is applied. Studies in the scope of fission power plant development suggest that effective hydrogen production with either the SI, WSP or HTSE process is feasible with a heat source of approximately >700°C. Current EU fusion technology can only partly fulfil this demand when considering the heat delivered by the Pb-17Li coolant in the DCLL blanket concept (700°C) or the heat from the Helium cooled divertor (700°C).

In the next stage of the study a possible increase of outlet temperature of the different blanket concepts employing even more advanced materials [12] or by design changes needs to be addressed.

Cooling Fluid CO₂ instead of Helium

Helium is the current choice of coolant for DEMO, but because Helium is a relatively scarce resource, the decision to use it in large power plants will probably rest not only on thermodynamic considerations. For instance, a satisfactory solution of the practical problem of sealing the system at the high pressures is required. Experience with sealing high-pressure carbon dioxide in gas-cooled reactors has shown that leakage is substantial, and helium, being a lighter gas, will be even more difficult to contain.

Also required pumping power for the coolant is of high relevance since it directly reduces the achievable output power. To judge this issue it is important to provide meaningful comparisons with appropriate assumptions and sufficient significance. Also compatibility of CO₂ with structural materials especially under irradiation needs to be examined. All these aspects need to be approached in the next phase of this study [13, 14].

Impact of Pulsed Operation

Steady-state electricity production is an essential requirement of a fusion reactor, and it has generally been assumed that the most cost-effective approach to this goal involves steady-state plasma operation. The cost disadvantage associated with pulsed plasma operation may be acceptable if certain physics challenges involved in achieving steady-state plasma opera-

tion prove more difficult, or more expensive, to resolve than assumed. Therefore, more detailed comparisons between steady-state and pulsed tokamak operation, including physics as well as technological aspects, have to deliver essential input for future DEMO studies.

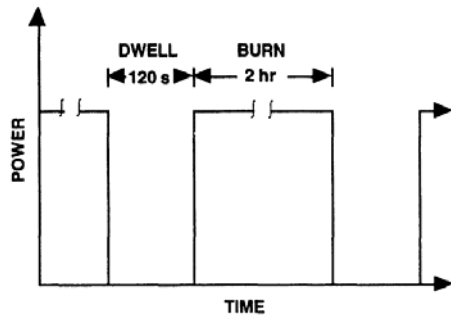


Fig. 5: Illustration of cyclic power output during burn time and associated dwell time of a pulsed tokamak [15].

Regarding technology aspects these comparisons need to comprise the transient operation of the internal components. As a first step the agreement about a representative pulsed scenario is necessary. Only limited information is available but former work in the scope of the DEMO studies and also the US PULSAR study can serve as starting point (compare Figure 5) [15].

From this an estimate of cyclic temperature and cyclic mechanical loads for the relevant reactor components needs to be provided.

Appropriate stress (strength) estimations need to be performed. Prospective life time analyses are required considering the expected number of cycles and, therefore, eventually low cycle fatigue of the adopted structural material [16]. Pulse length is more or less determined by the burn time and under consideration of the components life time dependant on radiation damage due to swelling and transmutation the minimum number of cycles to be tolerated can be determined. The necessary material data will have to be collected as far as the current state of material development allows [17, 18]. If the relevant data are not available meaningful assumptions will have to be established for an estimation of durability. All these issues will be approached in the next phase of the presented study.

Staff:

D. Filsinger

Literature:

- [1] Romero, M., Vidal, A., State-of-the-art high temperature innovative processes for H₂ production, Final report TW5-TRP-008 D1, CIEMAT, 2006.
- [2] Schiller, R., Feasibility of H₂ production by fusion power, Final report TW5-TRP-008 D2, HAS, 2006.
- [3] Hamacher, T., Fusion and Hydrogen: Some First Ideas about the Role of Fusion in a Hydrogen Economy, Final report TW5-TRP-008-D3, IPP Report, May 2006.
- [4] Malang und Fütterer, Macro-Task PPA-2 Blankets, Executive Summary, 1999.
- [5] Cachon, L., HCLL blanket concept for the DEMO conceptual study, Final report TW5-TRP-005-D1, 2006.
- [6] Ihli, T., Rey, J., Polixa, C., Bühler, L., Köhly, C., DCLL blanket concept for MMS: Maintenance and magneto hydrodynamic analysis, Final report TW5-TRP-005-D2 part 2, 2006.
- [7] Ihli, T., Köhly, C., Rey, J., Critical review of the European DEMO HCPB blanket concept for Large Module and MMS maintenance, Final report TW5-TRP-005-D2 part 1, 2006.
- [8] Schultz, K.R., Production of hydrogen by fusion energy: A review and perspective, Fusion Science and Technology, Vol. 44, pp. 393-399, 2003.
- [9] Yildiz, B., Hohnholt, K.J., Kazimi, M.S., Hydrogen production using high-temperature steam electrolysis supported by advanced gas reactors with supercritical CO₂ cycles, Nuclear Technology, Vol. 155, pp. 1-21, July 2006.

- [10] Yildiz, B., Kazimi, M.S., Efficiency of hydrogen production systems using alternative nuclear energy technologies, *International Journal of Hydrogen Energy*, 31, 99. 77-92, 2006.
- [11] Hino, R., Haga, K., Aita, H., Sekita, K., R&D on hydrogen production by high-temperature electrolysis of steam, *Nuclear Engineering and Design*, 233, pp. 363-375, 2004.
- [12] Zinkle, S.J., Advanced materials for fusion technology, *Fusion Engineering and Design*, 74, pp. 31-40, 2005.
- [13] Herrazti, B., Paule, A., Power conversion cycles, Final report TW5-TRP-006, CIEMAT, 2006.
- [14] Ward, D. J., Stainsby, R., Final report on the comparison between power conversion cycles for DEMO, Final report TW5-TRP-006, UKAEA, 2006.
- [15] Sager, G.T., Wong, C.P.C., Kapich, D.D., McDonald C.F., Schleicher, R.W., Limitations of power conversion systems under transient loads and impact on the pulsed Tokamak power reactor, 15th IEEE/NPSS Symposium on Fusion Engineering, Hyannis, MA, USA, October 11-15, 1993.
- [16] Crowell, J.A., Blanchard, J.P., Fatigue life of the plasma-facing components in PULSAR, *Fusion Engineering and Design*, 27, pp. 515-521, 1995.
- [17] Rieth, M., Schirra, M., Falkenstein, A., Graf, P., Heger, S., Kempe, H., Lindau, R., Zimmermann, H., EURO-FER 97 Tensile, Charpy, Creep and Structural Tests, *Wissenschaftliche Berichte, FZKA 6911*, 2003.
- [18] Schmitt, R., Petersen, C., Isothermal low cycle fatigue of reduced activation ferrite/martensite (RAF/M) materials, Final report TTMS-002 D-19, FZKA 6942, 2004.

Tritium Inventory Control

TW3-TI-VP 31 High Temperature Regeneration Tests of the ITER Model Torus Cryopump

Task Objective

The regeneration of the cryopumps is a key issue for the tritium inventory control for ITER [1]. To stay within the inventory limits, a multi-staged regeneration approach will be taken, comprising the regular regeneration stage at 100K to release the hydrogen isotopes themselves, a second stage at ambient temperatures to release air-likes and light hydrocarbons, and a high temperature reactivation stage at ~ 470K to release any strongly sorbed substances such as water and heavy hydrocarbons [2]. Especially the latter substances have a strong potential to build-up a high semi permanent tritium inventory in the cryopumps by isotope exchange. Although it could be shown that there will not result a significant poisoning effect from accumulated impurities (see task TW1-TTF-VP13), from inventory limitation point of view it is essential to have an effective regeneration procedure available. The objective of this task was therefore to show that the available maximum regeneration temperature limit at ITER is sufficient to release the accumulated impurities.

Release results

Within the present task, representative species which are known to be difficult to regenerate, such as water and heavy hydrocarbons were investigated quantitatively in the TIMO facility [3]. This was done in parallel to the water tracer substances programme (task TW1-TTF-VP13). The release pattern of these species was monitored by high resolution quadrupole mass spectrometry as reference device, in many cases in parallel with a GC-MS. Each reactivation test started from ambient regeneration, with deuterium from the preceding pumping test filling the closed pump volume to about 70 mbar. From this starting point, the temperature of the cryopanel system was increased in steps of about 30K up to 470K, and the gas composition was analysed. Fig. 1 shows some representative results for the release of water and i-octane after very high amounts of sorbed gas (of the order of 2 (mbar-l)/cm²). It is revealed that both species start to get released in a quantitative manner at a temperature range around 100°C. Both species are released completely within the stagewise regeneration heating until 470K. The experiments performed under this task confirmed clearly that the 470K upper temperature limit in ITER is sufficient.

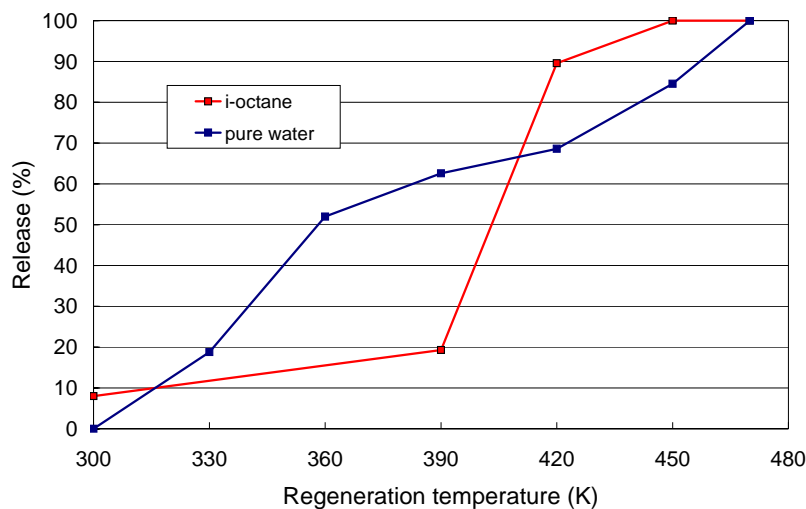


Fig. 1: Temperature-driven regeneration of the cryopump from pumped water and i-octane.

Staff:

Chr. Day
A. Edinger

Literature:

- [1] M. Glugla, D.K. Murdoch, A. Antipenkov, S. Beloglazov, I. Cristescu, I.-R. Cristescu, Chr. Day, R. Lässer, A. Mack, ITER fuel cycle R&D, Fusion Engineering and Design 81 (2006) 733-744.
- [2] Chr. Day, A. Antipenkov, I.R. Cristescu, M. Dremel, G. Federici, H. Haas, V. Hauer, A. Mack, D.K. Murdoch, M. Wykes, Hydrogen inventories in the vacuum pumping systems of ITER, Fusion Engineering and Design 81 (2006) 777-784.
- [3] H. Haas, C. Caldwell-Nichols, Chr. Day, A. Mack, and D.K. Murdoch, Study of poisoning effects with the ITER model pump during relevant operation cycles, Fusion Engineering and Design 81 (2006) 845-850.

Design Support and Procurement

EFDA/05-1279 (TW5-TDS-NSA3)
Nuclear Analyses Service: Part 1 – Enabling-Coordinating Activities

Deliverable 5
Version 1 of the CAD - MCNP Interface Programme and Manual of Use

The objective of this task was (i) to develop a full operational version of the CAD-MCNP interface programme McCad and make available a release version to ITER and other interested partners, (ii) to automatically generate a Monte Carlo geometry model on the basis of the 40° ITER torus sector CAD (CATIA) model provided by ITER, test and validate the model by means of MCNP calculations, and (iii) to evaluate the (automatic) CAD to MCNP conversion procedure against other available approaches.

McCad is an interface programme developed at FZK for the conversion of CAD geometry data into the semi-algebraic representation of the Monte Carlo code MCNP [1]. It provides a graphical user interface (GUI) with components for modelling, visualization, and data exchange. The CAD geometry data are imported via data files in the IGES (version 5.3) or STEP neutral format. In the frame of task TW5-TDS-NAS1, the development of McCad has been continued to complete different parts of the programme, enhance several features, add additional functionality and perform specific benchmark tests. The current version of McCad is capable to automatically generate an MCNP input deck from CAD data. It performs sequences of tests on CAD data to check their validity and neutronic suitability. It provides methods for the repair of CAD models and the completion of the final MCNP model by void spaces. The latter step is necessitated by the fact that the void space between parts is traditionally not available in CAD models whereas it is required by the MC codes for tracking the particles.

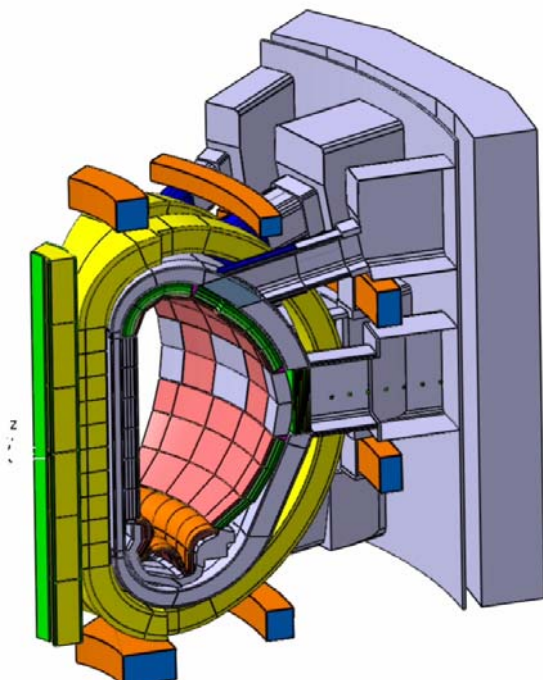


Fig. 1a: CAD model of ITER 40 ° torus sector (CATIA V5).

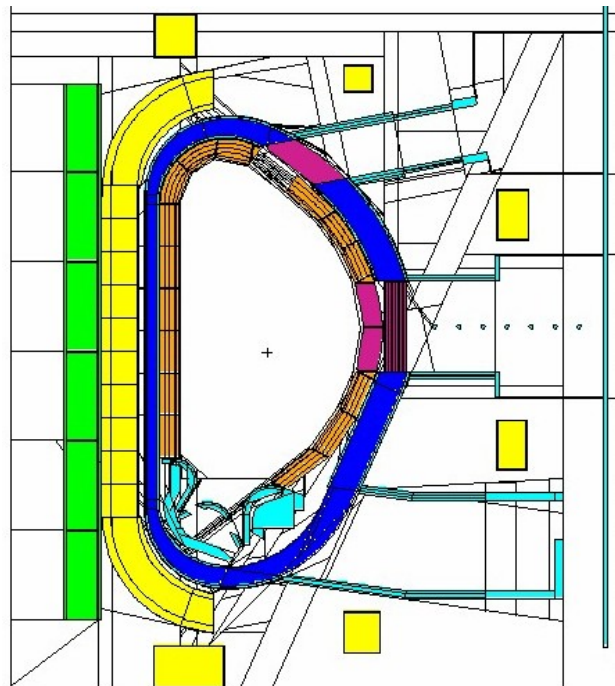


Fig. 1b: Converted MCNP model (2D vertical cut by MCNP plotter).

An essential part of the task TW5-TDS-NAS1 was devoted to test McCad for the automatic conversion of a complex ITER geometry model and verify that the generated model can be really used in MCNP calculations. A dedicated CAD neutronics model of a 40° ITER torus sector was generated to this end by the ITER drawing office. The model contains all signifi-

cant components although some details have been suppressed and geometric simplifications were applied in order to comply with the requirements for the use with MCNP calculations, see Fig. 1a. The CAD model was converted by McCad into an MCNP geometry representation through several (automated) steps including error detection and correction as well as the completion of the model by voids. The converted MCNP model, generated automatically by McCad, is shown in Fig. 1b in a vertical cut as provided by the MCNP geometry plotter. The conversion process was shown to introduce no approximations so that the resulting MCNP geometry is fully equivalent to the original CAD geometry.

The converted model has been validated first by means of stochastic volume calculations. Perfect agreement was obtained for the volumes of the geometry cells as calculated by MCNP using the converted model and the corresponding volumes provided by the CAD system.

MCNP transport calculations were then performed for specified nuclear responses (tallies) such as the neutron wall loading, the neutron fluxes at specified locations and the nuclear heating in specified components. Fig. 2 shows the calculated neutron wall loading distribution. The peaking values amount to 0.62 and 0.76 MW/m², inboard and outboard, respectively, while the poloidal average is at 0.54 MW/m². The corresponding values based on the standard ITER MCNP model are 0.60 and 0.77 MW/m² for the peaking values, and 0.55 MW/m² for the poloidal average.

The calculated responses also compare favourably to the results obtained by other approaches developed elsewhere for the use of CAD geometry data in MCNP calculations (ASIPP Hefei, China; University of Wisconsin, Madison, USA). It was concluded that the McCAD interface works properly and can be applied with confidence in future neutronics analyses for ITER. Thus, consistency of the engineering CAD models and the neutronics models applied in MCNP calculations will be ensured.

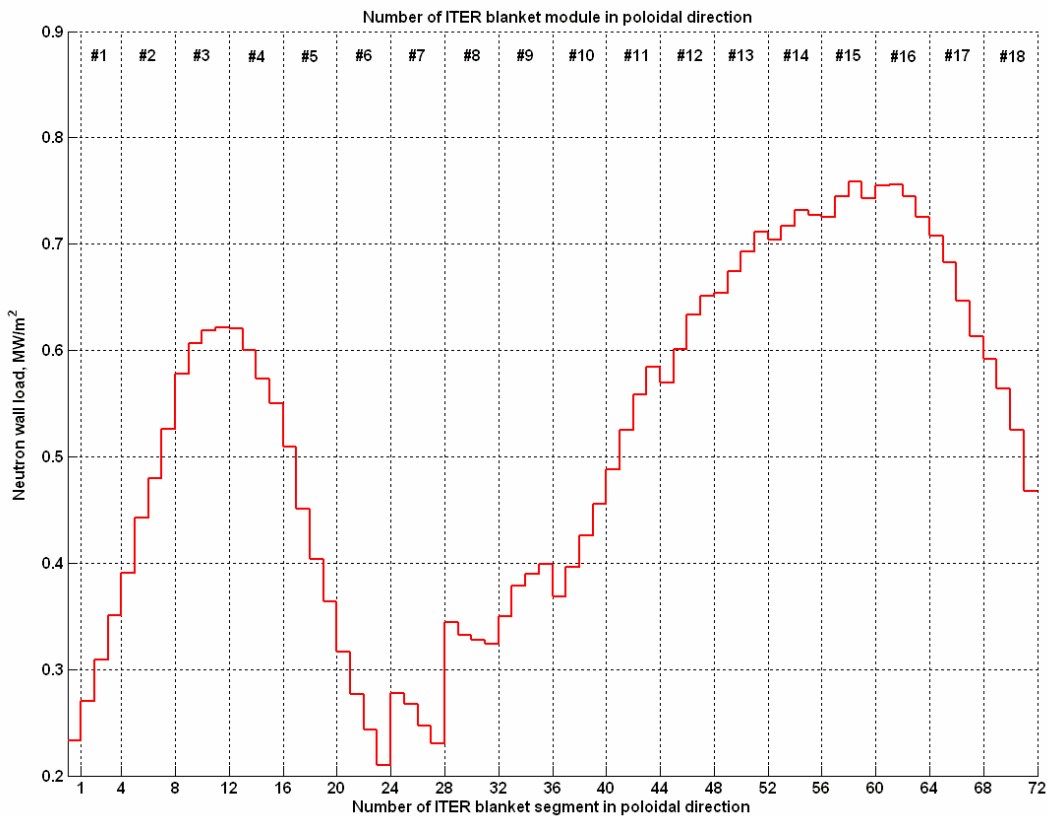


Fig. 2: Neutron wall loading distribution calculated by MCNP with the converted ITER model.

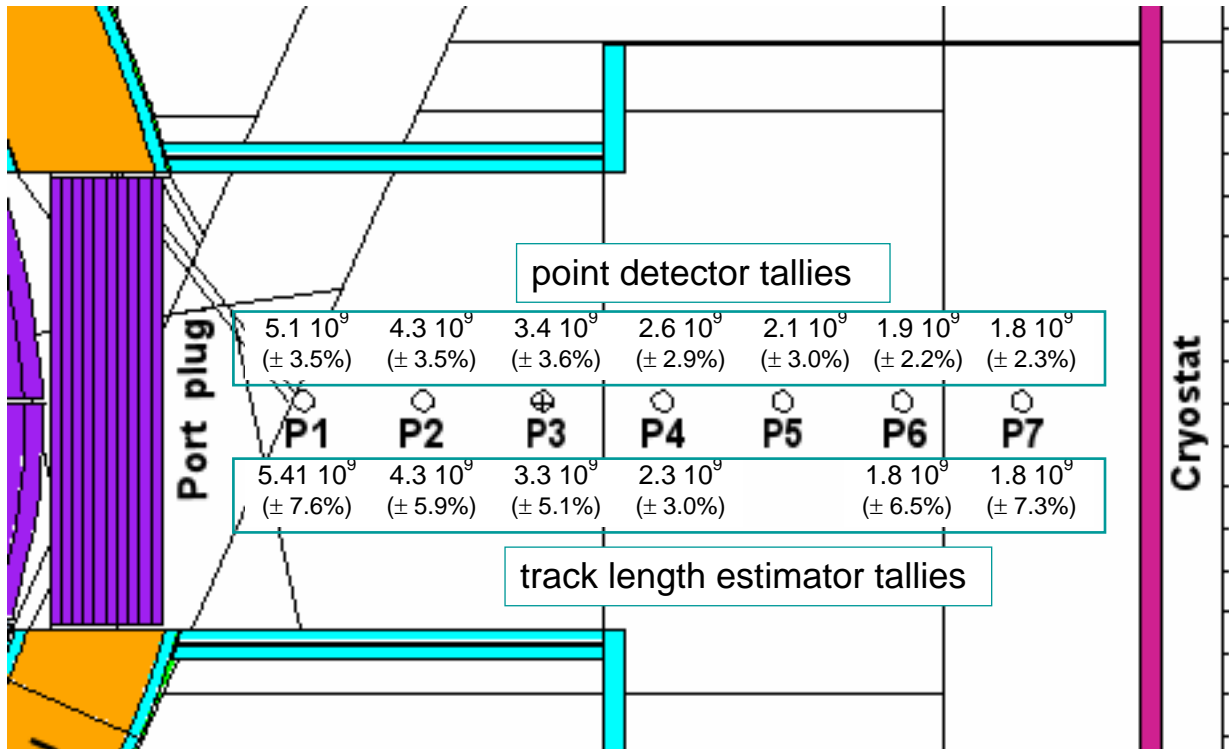


Fig. 3: Neutron fluxes calculated at the specified locations behind the test blanket port in the ITER midplane by the point detector and track length estimator tallies.

Staff:

U. Fischer
 A. Serikov
 S. Stickel
 H. Tsigé-Tamirat

Literature:

- [1] H. Tsigé-Tamirat, U. Fischer: CAD Interface for Monte Carlo Particle Transport Codes. The Monte Carlo Method: Versatility Unbounded in a Dynamic Computing World ; Proc.of the Conf., Chattanooga, Tenn., April 17-21, 2005 LaGrange Park, Ill. : ANS, 2005

EFDA/05-1331 (TW4-TDS-CLDES) Final Design of HTS Current Leads for ITER

Introduction

In line with ITA-11-62-EU the objective of this task is to perform a final design of ITER high temperature superconducting (HTS) current leads (CL), quantifying the issues associated with the lead cooling conditions. The results include confirmation of the lead size and orientation and the preferred cooling requirements.

The work will be done in collaboration with the Centre de Recherches en Physique des Plasmas (CRPP), Villigen, Switzerland. Forschungszentrum Karlsruhe will focus on the steady state 70 kA HTS CL for the Toroidal Field Coils and CRPP on the pulsed 45 kA HTS CL for the Central Solenoid and Poloidal Field Coils.

Background

High temperature superconductors have successfully demonstrated their considerable advantages over conventional materials and entered the market. Therefore, an R&D program was launched in Japan and EU in order to design and construct HTS components for ITER. As a result of this programme a 60 kA HTS current lead was successfully manufactured and tested in Japan in 2002. The EU 70 kA ITER prototype current lead using HTS was assembled in 2003 and tested in 2004 in nominal conditions. Afterwards, the 70 kA HTS current lead was successfully operated at a He inlet temperature of 80K and retested using LN2 as requested by the International Team. These tests confirmed the possibility of using the 80K cooling circuit foreseen in ITER for the thermal shields. For the first time, it was also demonstrated that LN2 cooling of a 70 kA HTS-CL is possible. This cooling method offers low power consumption and the possibility to adjust the time in case of a LOFA event by an appropriate size of the LN2 inventory. As a consequence, the International Team in agreement with the Participant Teams has decided to introduce HTS CL in ITER.

Since several years, Forschungszentrum Karlsruhe and CRPP Villigen have been involved in the development and construction of high amperage current leads including the European 70 kA HTS current lead for ITER.

Status of the Work

A. Operation of the 70 kA HTS current lead with helium and liquid nitrogen

The developed 70 kA HTS-CL was operated with 50K He (design operation) cooling up to 80 kA. The cooling power consumption at rated current was lowest for this operation. The 80K He operation is less optimal with respect to the cooling power consumption. However, it may be attractive for devices where 80K helium is already available for radiation shield cooling (e.g. for ITER). The safety margin in case of a LOFA event is much lower than for 50K He cooling. For ITER, a considerably larger amount of HTS material would be needed to increase the margin.

For the first time a 70 kA HTS-CL was operated up to 75 kA with LN2 cooling at both atmospheric and sub-atmospheric pressure in stable conditions. This cooling method requires a cooling power which is as low as for 50K He cooling. It offers the possibility to adjust the time to intervene in case of a LOFA event by an appropriate size of the LN2 inventory. A sub-atmospheric operation at 70K which would save a substantial amount of HTS material compared to 80K operation is possible but a failure of the pump unit has to be considered and a redundancy is required for a reliable system.

B. Operation of the HTS current lead under fault conditions

A linear ramp down of the TF coil current within 30 minutes in the presence of a loss of mass flow rate failure in the current lead supply has been simulated. The current lead will quench during the ramp down process about 7.5 minutes after LOFA start.

To judge the sensitivity of the electrical quench detection systems even during pulsed operation, the compensated panel and quench detection voltages were studied in both DC and pulsed operation. Both show a broader distribution during current operation than during stand-by but there is no difference between DC and pulsed operation. The inductive voltage signals during ramp up and down are much lower than 1 mV except for the clamp contact voltage which shows an inductive signal of 4.5 mV.

The electrical quench detection system used in the 70 kA HTS current lead is a stable and reliable system although the inductive component was not perfectly compensated. A detection level of 10 mV and a time delay of < 1 s should be enough to withstand the time of an exponential current decay with $\tau = 11$ s.

The top end HTS temperature may be used as a backup quench detection system with a temperature limit of 90K. On the other hand, the temperature measurement might be too slow if a quench of the HTS part has to be considered. In such a case, the electrical system is mandatory.

C. Thermodynamic optimisation of the 70 kA HTS current lead

A thermodynamic optimisation has been done using the numerical code CURLEAD. A set of simulation runs was performed using the He inlet temperature and the HTS top end temperature as parameters. For all parameter sets, the optimum He mass flow rate and heat exchanger length was evaluated. The temperature dependence of the amount of HTS material has been estimated by scaling the cross section according to the critical current dependence on temperature for a perpendicular field of 50 mT and an appropriate temperature margin. The amount of stainless steel has been scaled as the HTS tape cross section. No contact resistance between the HTS module and the heat exchanger has been assumed.

The result of the power consumption optimisation is as follows:

- The optimum He inlet temperature is 50K.
- The optimum HTS top end temperature is 70K, i.e. the temperature difference is 20K.
- There is a broad minimum concerning the temperature difference.

Staff:

R. Heller
R. Lietzow

Literature:

- [1] R. Wesche, R. Heller, P. Bruzzone, W.H. Fietz, R. Lietzow, A. Vostner, „Design of High Temperature Superconductor Current Leads for ITER”, presented at SOFT 2006, Warsaw, Poland

JET Technology

JW5-FT-3.11 Assessment of in-situ Detritiation in JET-OPL Tile Analysis

The tritium retention by the first wall materials is a very important issue for all carbon based fusion machines. Even though there are available many successful methods to detritiate such materials the most promising ones can only be used ex-situ. However, recently laboratory experiments have also shown that the use of detritiation methods based on photon-cleaning such as laser or flashlamps can be among the most promising techniques which can also be used in-situ. In this respect flashlamp photonic cleaning has been tested *in-situ* at the Beryllium Handling Facility (BeHF) at JET. Several OPL tiles have been exposed to numerous pulses with a maximum power density of 100 J.

To assess the efficiency of this detritiation method, four tiles, 1 graphite and 1 CFC and the adjacent untreated tiles were sent to TLK. The tritium depth profiles measured for all tiles have shown that the tritium surface activity for both types of tile is similar and depends on their relative location inside the vacuum vessel. Moreover, it has been also shown that the CFC tiles allow a better migration of molecular tritiated species, most likely between the CFC fibres, than graphite does. Concerning the surface tritium, the photon cleaning treatment (using 100 J per pulse) did not show any remarkable difference between the treated and the corresponding untreated tile. On the other hand, comparing the bulk tritium fraction for treated and the corresponding untreated tiles it is obvious that the photon-cleaning treatment did not have any noticeable effect. Indeed, the average tritium concentration for the 4 tiles, treated or untreated, remains remarkably constant.

In order to have a second estimation of the efficacy of the detritiation process, the combustion data obtained for the 4 OPL tiles were also compared to the results obtained by calorimetry. For such comparison the following assumptions have been taken into account:

- 1) For the calculations, it is easier to assess the tritium contained by the tiles by considering the tiles as been constituted by two parts; the plasma exposed part and the bulk.
- 2) The plasma exposed part is also divided in two parts; a) one part where there is an obvious co-deposited layer and b) the rest of the tile where there is no visible trace of co-deposition. The latter corresponds, not only to the larger part of the tile which is directly facing the plasma and where net erosion occurs but also, to the shaded zones of the tiles, mainly the region of both edges (see Fig.1).

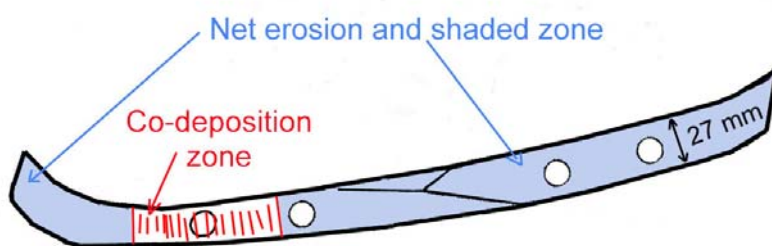


Fig. 1: Schematic illustration of a typical plasma exposed surface of an OPL tile.

Typically the plasma exposed surface of the OPL tile can be represented as a stripe having an average length of 34.3 ± 0.3 cm and 2.7 cm wide giving a total plasma exposed surface ranging between 91.7 cm^2 to 93.2 cm^2 per OPL tile. (Fig. 1).

The 4 tiles are very similar having almost the same geometrical dimensions and therefore, the total plasma exposed surface is approximately the same for all tiles. However, the dimension of the co-deposited zone is variable and is only estimated by visual inspection of the tile. Mostly, the co-deposit was found on the left part of the tile (see Fig.1) while the right side is much cleaner even though sometimes sharp coloured patterns can also be observed.

Based on the combustion data it is possible to give a rough estimation of the total tritium content of the tiles. The estimation is performed in two steps. Knowing the total surface of the tile available to the plasma and using the values of the tritium concentration for the plasma exposed samples (A1 samples) measured by combustion, it is possible to assess the total tritium amount present on the surface of the tiles whereas, using the bulk activities together with the tiles' density and weight we may estimate the tritium amount trapped into the bulk.

Estimation of the tritium content present in the plasma exposed surface of the OPL tiles

Table 1 gives an estimation of the total tritium surface activities for both zones (co-deposition and net erosion/shaded) calculated by the combustion data. The conversion of the triton atoms to Becquerel units (decays/s) is performed using the usual formula

$A = \lambda \cdot N$ where A represents the activity in Bq, N the number of tritons and λ is the radioactivity constant for tritium i.e. $\lambda = 1.78 \cdot 10^{-9} \text{ s}^{-1}$.

Table 1: Estimation of the tritium distribution on the surface of the 4 OPL tiles.

	Co-deposition zone	Total tritium in co-depos.	Net erosion and shaded zone	Total tritium on eros./ shad.	Total tritium on the tile surface
	(T cm ⁻²)	(T)	(T cm ⁻²)	(T)	(T / Bq)
CFC untr.	1.64 10 ¹⁶	1.51 10 ¹⁷	4.20 10 ¹⁵	3.53 10 ¹⁷	5.04 10 ¹⁷ / 9.02 10 ⁸
CFC treated	1.57 10 ¹⁵	4.38 10 ¹⁶	3.67 10 ¹⁵	2.36 10 ¹⁷	2.80 10 ¹⁷ / 4.98 10 ⁸
Graph. untr.	4.07 10 ¹⁵	7.04 10 ¹⁶	3.51 10 ¹⁴	2.64 10 ¹⁶	9.68 10 ¹⁶ / 1.72 10 ⁸
Graph. treated	5.70 10 ¹⁵	6.90 10 ¹⁶	3.52 10 ¹⁴	2.80 10 ¹⁶	9.70 10 ¹⁶ / 1.73 10 ⁸

The visual inspection performed before any treatment is very important as it can explain some discrepancies which may occur after the tritium analysis. Indeed, as it is illustrated in Table 1 compared to the untreated CFC tile, the treated CFC treatment exhibits still high tritium content even after treatment which is very comparable to the corresponding untreated CFC. This can be explained by the fact that the treated CFC had already before treatment a wider co-deposition zone.

Estimation of the tritium content present in the bulk of the OPL tiles

In a second step, the estimation of the bulk tritium activity is performed using the average tritium activities measured by combustion for the bulk samples associated with the density and weight of the tiles. From combustion measurement it is possible to obtain the average density of each tile, as the geometrical dimensions and weight of each disc were precisely measured.

From these measurements it appears that the graphite tiles are more dense (~12%) than the CFCs and this was also confirmed by the respective weight of the various tiles. The graphite tiles are weighting in average 935 g while the CFC are about 13% lighter averaging 815 g. Table 2 gives the average densities and weight for the 4 OPL tiles. Once again it is worth mentioning that the geometrical dimensions of the tiles are very similar.

Table 2 gives the average bulk activities measured by combustion for the 4 OPL tiles. As we can notice graphite tile is more dense than CFC and two independent measurements confirm this. Firstly, by the density values obtained by the combustion of the small discs which were weighed and their geometric dimensions measured (1mm thick for 7.8 mm diameter), secondly, by the weight of individual tiles.

Table 2: Density and weight measurements for the 4 OPL tiles.

	Density	Average	Weight	Average
	g cm ⁻³	g cm ⁻³	g	g
CFC untreated (2B12T-160)	1.41 ± 0.09	1.47 ± 0.09	800	815
CFC treated (2B12B-56)	1.48 ± 0.12		830	
Graphite untreated (2B15B-5882)	1.68 ± 0.10	1.68 ± 0.10	935	935
Graphite treated (2B16B-top)	1.68 ± 0.09		936	

Considering the density measurements the relative difference between the two type of tiles is $\{(1.68-1.47)/1.68\} * 100 = 12.5\%$. Considering now the weight of each tile (they have approximately the same dimensions, i.e. we assume that they have the same volume) then the relative difference is $\{(935-815)/935\} * 100 = 12.8\%$ which is in fairly good agreement with the density calculation given above.

By combining the data given in tables 1 and 2 and taking into account the combustion measurements obtained for the bulk samples, it is possible to estimate the total tritium amount trapped by the surface and the bulk of the tile. Table 3 reports these results.

Table 3: Calculation of the estimated total tritium activity for the 4 OPL tiles.

	Total tritium on the surface	Total tritium in to the bulk	Total tritium per OPL tile
	(Bq)	(Bq)	Bq / mCi
CFC untr.	9.02 10 ⁸	4.57 ± 0.43 10 ⁸	1.36 ± 0.43 10 ⁹ / 36.8
CFC treated	4.98 10 ⁸	3.95 ± 0.52 10 ⁸	8.93 ± 0.52 10 ⁸ / 24.1
Graph. untr.	1.72 10 ⁸	1.29 ± 0.60 10 ⁸	3.01 ± 0.60 10 ⁸ / 8.1
Graph. treated	1.73 10 ⁸	7.85 ± 0.55 10 ⁷	2.51 ± 0.55 10 ⁸ / 6.8

Finally, Table 4 compares the results obtained by calorimetry and full combustion. Calorimetry is providing values which are in average one order of magnitude higher than what combustion has given. However, taking into account the fact the above mentioned approximations concerning the estimation of co-deposition and erosion/shaded zones the agreement between the two techniques is reasonably good especially for the CFC tiles. For the graphite tiles, the deviation between both measurements is even higher probably because the tritium activity is very low (as combustion measurements shows) and therefore, the error committed by the calorimetric measurements is much higher. Indeed, the values to be measured are very close to the background or the sensitivity limit of the calorimeter.

Table 4: Comparison of the calorimetry and the combustion measurements for the 4 OPL tiles.

Tiles	Comparison	Total tritium per OPL tile measured by		Factor
		Calorimetry	Combustion	
		mCi	mCi	
CFC untreated (2B12T-160)		328	36.8	8.9
CFC treated (2B12B-56)		107	24.1	4.4
Graphite untreated (2B15B-5882)		175	8.1	21.9
Graphite treated (2B16B-top)		78	6.8	11.5

The efficacy of the flashlamp photonic cleaning has been assessed using full combustion technique on small samples and the calorimetric measurements of the complete tiles. As the density measurements have shown, the different open porosity characterising both tiles could also have an influence to the tritium migration into the bulk of the tile.

Comparing the tritium distribution throughout the tiles we may also notice the following; 1) comparing the CFC and graphite untreated tiles, surface activities do not vary that much. In general, CFC seems to have a bit more tritium on the surface than the graphite tile but this is most likely related to their relative location inside the vessel. 2) it is remarkable to see that on average the bulk tritium concentration for the CFC tiles is greater to the corresponding tritium fraction for the graphite tile by approximately factor five. This observation has been verified for the 4 tiles. It has been attributed to the different structure and density characterising both material and especially to the fibre structure of the CFC tiles which allows a better migration, of molecular tritium and “bigger” tritiated molecules such as methane, between the fibres than graphite does. Indeed, for steric reasons (*steric hindrance*)¹ the migration of molecular species is more difficult between the graphite reticular planes than it is between (or along) the carbon fibres.

Of course we can also imply the higher tritium concentration measured for the surface CFC samples which in a first sight could explain the higher tritium concentration found in the bulk of the CFCs. However, for 2 graphite samples (out of 5) the tritium surface activity was at least as high as the corresponding tritium activity measured for the CFC samples and nevertheless, both graphite cylinders exhibited a lower tritium concentration for the bulk samples. As at the same time the density of the graphite tiles was clearly higher than the CFC tiles we assumed that the lower tritium concentration found for the graphite tiles should be connected to the lower open porosity exhibited by this type of carbon tiles. Additional measurements are needed to support this conclusion.

Comparing the bulk tritium fraction for treated and the corresponding untreated tiles it is obvious that the photon-cleaning treatment at the energy of 100 J per pulse did not had any noticeable effect. The average tritium concentration for the 4 tiles, treated or untreated, remains remarkably constant.

Finally comparison of the calorimetric and combustion measurements showed a difference in the obtained value. The reasons for this difference require further investigation. However, the agreement is quite good when the tritium activity present in the tiles is sufficient enough and well above the sensitivity limit of the calorimeter.

Working with adjacent tiles makes very difficult to draw general conclusion about the efficiency of the detritiation process as adjacent tiles do not necessary have similar tritium concentrations. To have a better assessment and a more reliable comparison it will be much better to treat only partly one single tile, say along the poloidal or the toroidal direction and leave the other part untreated. Such a procedure has to be taken into account for future tile analysis.

Staff:

N. Bekris
B. Kloppe
R. Rolli
J. Ehrmann

Literature:

- [1] R.-D. Penzhorn, J.P. Coad, N. Bekris, L. Doerr, M. Friedrich, W. Pilz; Tritium in plasma facing components, Fusion Engineering and Design 56–57 (2001) 105–116.

¹ *Steric effects as referred to this report arise from the fact that the volume (molecular volume) required for an easy migration of a chemical compound is close to the available space left by the structural parameters of the material making such migration difficult if not impossible.*

JW5-FT-5.20 Shutdown Dose Rate at JET Tokamak – Code Benchmark

The objective of Task JW5-FT-5.20 is to validate the computational methods for shutdown dose rate calculations through the comparison with measured dose rates that will be recorded in a dedicated benchmark experiment on JET. The experiment, to be conducted by an experimental team of ENEA Frascati, has been further delayed and is now scheduled for mid 2007. The task schedule has been revised accordingly.

The task of FZK is to analyse the experiment by means of the rigorous 2-step (R2S) approach, developed at FZK for the Monte Carlo based calculation of shut-down dose rates in 3D geometry [1].

The related task deliverables are on the adaptation of the JET MCNP model to the R2S requirements and pre-analysis, on the R2S calculations for the benchmark experiment, and on the data analysis and comparison of D1S/R2S experimental results. Work on the adaptation of the JET MCNP model has been performed for a preliminary MCNP model of JET octant 1 provided by ENEA Frascati early 2006. It includes the Geiger-Mueller detector with updated surrounding for the out-of-vessel dose measurement and the TLD in the upper irradiation end for the in-vessel measurement. The related pre-analysis included R2S shutdown dose rate calculations for the original and the adapted model assuming a representative irradiation history. The calculations for the original model were performed to identify the decay gamma source cells contributing significantly to the shut-down doses at the specified detector positions in and out-of-vessel. These were shown to be in-vessel components such as the inner walls, limiters and the saddle coil. Accordingly, a fine spatial segmentation was applied to these geometry cells. This is required with the R2S-approach to achieve a sufficiently high accuracy when calculating the neutron flux and decay gamma source distribution.

Staff:

U. Fischer
P. Pereslavytsev

Literature:

- [1] Y. Chen, U. Fischer, "Rigorous MCNP based shutdown dose rate calculations: Computational scheme, verification calculations and applications to ITER", Fus. Eng. Des. 63-64 (2002), 107-114.

JW1-FT-6.1

Impact of Tritium on the Performance of a Prototype Cryosorption Pumping Panel

Background and Objectives

This task is an essential complement to the parallel assessment of the pump performance of the ITER torus model cryopump in FZK, where the tritium fractions have been replaced by deuterium. The central objective of this task, being performed within the Task Force Fusion Technology at JET [1], is to study the interaction of tritium and tritiated gas mixtures with the cryopanel, in terms of pumping performance and desorption characteristics.

Within this task, a Prototype Cryosorption Pump (PCP) was designed, manufactured and installed into an existing cryogenic forevacuum module of the Active Gas Handling System (AGHS) at JET. The PCP was first used in 2003 as regular pump during TTE, and then subjected to a parametric test programme [2]. The measured pumping behaviour was excellent.

Experiments in 2006

The experiments performed in this report's period were defined on the basis of the results achieved in the 2003/2004 campaigns. There, the pumping mechanism for tritium under ITER-relevant conditions was clearly found to be condensation/re-sublimation. This may cause problems in all competing pumping situations when gases being pumped by condensation (such as tritium) and gases being pumped by sorption (such as helium) are to be pumped concurrently: There is a potential risk that the build-up of layers of condensed tritium frost may block the charcoal pores, so that the pumping speed for mixtures with helium may be significantly worse than predicted from the pure gas pumping curves. It was therefore agreed to perform pumping speed tests with different compositions of the binary mixture He-T₂. The second experimental category which was defined in conjunction with the 2004 results was the investigation of a potential poisoning effect of hydrocarbons. In these tests, the cryopumping surface was doped with defined amounts of hydrocarbons prior to the actual pumping speed measurement. By comparison of the measured pumping speed with the one measured at a freshly reactivated panel one could derive any poisoning effect.

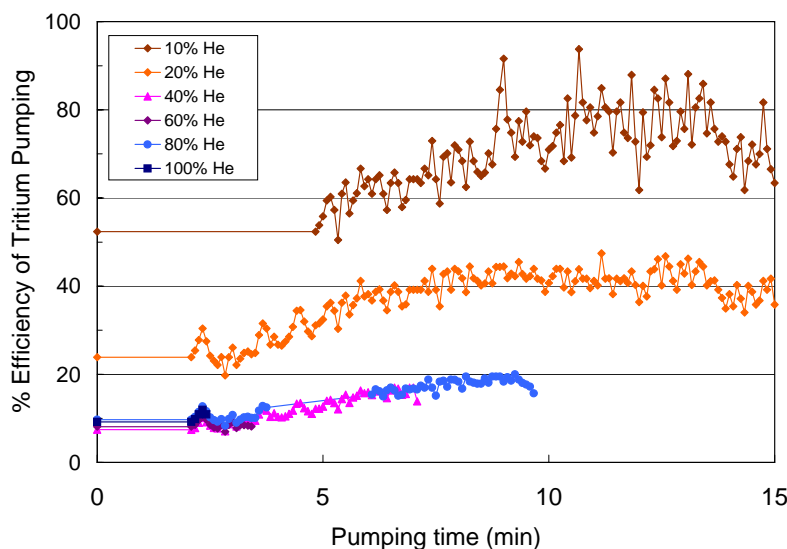


Fig. 1: Pumping of the He-T₂ binary at varied composition.

To assess the pore clogging effect, a parametric variation of the composition in the He-T₂ binary system was performed in terms of pumping and regeneration. The pumping results are plotted in Fig. 1, in a relative scale, related to the case of pure tritium which shows the largest pumping speeds.

It is clearly revealed that the decrease in pumping speed is more than proportional to the increasing helium content. Already at ~ 30% of helium, the overall pumping speed has dropped to the low level of pure helium. However, in no case, pumping speeds below the ones of pure helium have been measured. These results illustrate a competing pumping situation between tritium and helium, but do not indicate any pore clogging effects by the tritium frost [3].

It is known from previous studies that only light hydrocarbons have the possibility to pass the divertor and get transported into the cryopumps, or are being formed in situ by radical-charcoal interaction. Methane/ethane/propane were therefore used as representative hydrocarbons. The objective of the poisoning tests was to investigate the influence of these hydrocarbons on pumping of tritiated gases. Each test comprised two steps: First a defined pre-loading of the charcoal coated panels with the hydrocarbons in the order of ~ 0.1 (mbar·l)/cm² (here we prepared three binary mixtures with the following molar composition: CH₄/D₂=20/80, C₂H₆/D₂=15/85, C₃H₈/D₂=10/90), then the actual pumping speed test, which was done with a He/T₂=10/90 mixture (for reasons of ITER relevance). The performance of the pre-loading step is a critical procedure, which has to be done very carefully to ensure that all hydrocarbon ends up sorbed onto the charcoal of the panel. To achieve this, the hydrocarbon/D₂ mixture has to be processed from the high pressure supply bottle onto the panel in such a way that any composition change, especially by formation of liquid is excluded. Thermodynamically speaking, one has to stay above the dew point curve on the whole process path. In this step, deuterium acts only as a carrier gas which is pumped out after the loading step.

Fig. 2 shows the calculated curves (only possible for H₂) which were used for definition of the process parameters. The good part of the chart is the one below and to the right of the curves.

The pumping tests with hydrocarbon-doped cryopanel were all positive. The results did not show any deviation from the ones measured at the fresh panel [2].

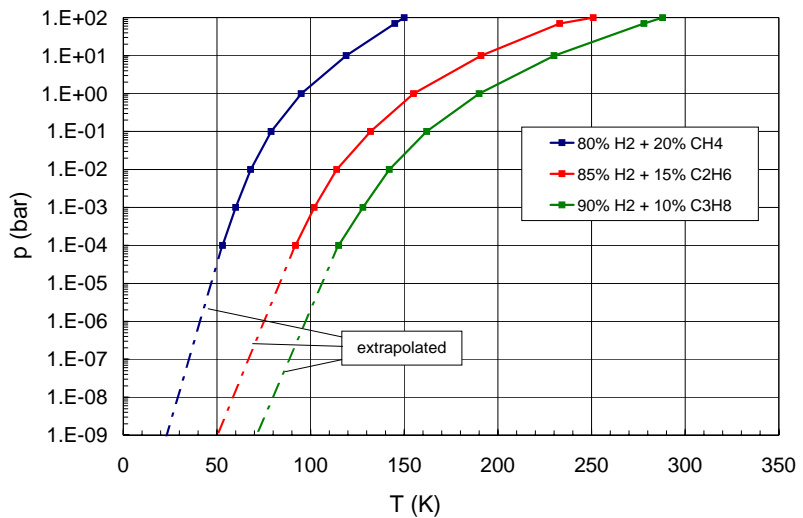


Fig. 2: Calculated dew point curves for three Hydrocarbon/hydrogen systems used.

Task summary

For the first time, a prototypical cryosorption pump in technical scale based on the design principle of the ITER cryopumping systems, has been operated and comprehensively characterized with tritium and tritiated gases. The tests were performed at JET using the AGHS as a versatile test bed. The PCP was first used as a regular pump during the TTE, and was then subjected to a parametric test programme. The measured pumping behaviour for tritium and tritium containing mixtures was excellent and the results form a reliable basis for the design of the ITER cryosorption pumping systems.

In spite of the experimental limitations, the scientific value and output of this task fully justified the decision to implement a technical scale test unit in a tritium plant in parallel to ongo-

ing physics work in the torus. It was the first good example to show how JET with its unique capabilities in tritium handling can be used to prepare operation of ITER.

The ITER cryosorption pumping concept could be fully validated. No severe design weaknesses have been identified. The processing of tritium did not cause any deterioration of the pump performance.

Table 1 summarizes again all relevant pump runs performed under this task, which is now closed. It is currently considered to keep the PCP installed in AGHS and do series of gas purging to reduce the tritium content inside the pump vessel. The residual amount of tritium retained on the pump could then be determined by a mass balance calculation, deducting the tritium recovered from the plant from that measured before. If being left in place, the pump will remain available for the next tritium campaign at JET.

Table 1: Record of the PCP operational history.

Run #	Gas	Date
TTE1	D ₂ pellet gas	24 Oct 2003
TTE2	Divertor gas (0.1% tritium)	28 Oct 2003
TTE3	NB gas (5.1% tritium)	29 Oct 2003
TTE4	Divertor gas (0.005% tritium)	30 Oct 2003
TTE5	Torus cleaning gas (average 0.03% tritium)	31 Oct to 12 Nov 2003
1	D ₂	18 August 2004
2	D ₂	18 August 2004
3	D ₂	19 August 2004
4	D ₂	19 August 2004
5	H ₂	20 August 2004
6	He	20 August 2004
7	D2-Base/He =90/10	21 August 2004
8	N ₂	21 August 2004
9	T ₂	23 August 2004
10	T ₂	24 August 2004
11	D ₂ /T ₂	25 August 2004
12	D ₂ /T ₂ /10%He	26 August 2004
13	H ₂	27 August 2004
14	D2-Base/He =90/10	27 August 2004
15	T ₂ /He=90/10	2 Dec 2005
16	T ₂ /He=80/20	5 Dec 2005
17	T ₂ /He=60/40	6 Dec 2005
18	T ₂ /He=40/60	7 Dec 2005
19	T ₂ /He=20/80	8 Dec 2005
20	T ₂ /He=10/90	9 Dec 2005
21	He	12 Dec 2005
22	T ₂ /He=90/10 (Panels with propane)	16-18 Jan 2006
23	T ₂ /He=90/10 (Panels with ethane/propane)	30-31 Jan 2006
24	T ₂ /He=90/10 (Panels with methane/ethane/propane)	31 Jan - 2 Feb 2006

Staff:

Chr. Day

S. Grünhagen (delegated to JET)
H. Jensen

UKAEA D. Brennan
 P. Camp
 S. Knipe
 A. Miller
 R. Stagg
 J. Yorkshades

Literature:

- [1] C. Grisolia, S. Rosanvallon, P. Coad, N. Bekris, J. Braet, D. Brennan, B. Brichard, G. Counsell, Chr. Day, J. Likonen, G. Piazza, C. Poletiko, M. Rubel, A. Semerok, JET contributions to ITER technology issues, Fusion Engineering and Design 81 (2006) 149-154.
- [2] Chr. Day, D. Brennan, P. Camp, H.S. Jensen, G. Jones, A. Mack, A. Miller, Performance of ITER-relevant cryopump panels for tritiated gases, Fusion Science and Technology 48 (2005) 29-34.
- [3] Chr. Day, D. Brennan, P. Camp, H.S. Jensen, Validation of the ITER cryosorption pumping concept under tritium, SOFT Proceedings, Warsaw, Poland, September 2006.

Heating Systems Technology Project

Coaxial Cavity Gyrotron and Test Facility

TW6-THHE-CCGDS4 D 1b

Design, Support to the Industrial Development and Preparation of Technical Specifications

TW6-THHE-CCGT1 D 1

Scientific Execution and Co-ordination of the Tests

In a cooperation of European research institutions (FZK Karlsruhe, CRPP Lausanne, TEKES, Helsinki) and European tube industry (Thales Electron Devices (TED), France) the development of a 2 MW, 170 GHz coaxial cavity gyrotron, suitable to be operated in continuous wave (CW) as could be used for ITER, is going on. In summer 2004, EFDA has placed a contract at TED for the fabrication of a first industrial prototype of such a gyrotron. Within the cooperation, the physical specifications and the design of the components for the industrial prototype are being contributed by the research institutions, and TED is responsible for the technological aspects of the tube.

2 MW, CW 170 GHz prototype of a coaxial cavity gyrotron for ITER

The first industrial prototype of the 2 MW, CW 170 GHz coaxial cavity gyrotron designed for operation in the $TE_{34,19}$ mode, has been fabricated and factory tests have been performed. The gyrotron has been delivered to CRPP Lausanne in December 2006 where a suitable gyrotron test facility has been constructed. A photography of the gyrotron is shown in Fig. 1. The fabrication by Ansaldo of a SC-magnet suitable for operation of the 170 GHz gyrotron is delayed by almost one year now. At present, a delivery of the magnet is expected for the end of January 2007. Thus, tests with the gyrotron could start earliest end of February 2007.

To prepare the tests, the procedure of alignment of the coaxial insert and of the outer cavity wall relative to the electron beam and the axis of the magnetic field has been simulated in order to obtain corresponding sets of operating parameters. For performing the experimental tests on the prototype gyrotron, in total a time of six months is foreseen. A planning of the experimental sequence has been done in cooperation with the partners.

In case that serious and unexpected problems with the SC-magnet should result in a further long delay of the delivery, the possibility has been investigated to use as a back up solution the existing SC-magnet at FZK for testing the industrial prototype gyrotron. As a result it has been found, that an operation of the prototype gyrotron in the FZK magnet is possible. It would require some minor modifications of mechanical fittings. Since the magnetic field value is lower than required for nominal conditions, the experimental operation would have to be performed at reduced parameters (B-field, velocity ratio). However, according to the simulations, it is expected that the $TE_{34,19}$ mode at 170 GHz could be excited in single mode operation at reduced power and efficiency. Nevertheless, useful information concerning the performance of the gyrotron could be obtained.

170 GHz experimental pre-prototype coaxial cavity gyrotron

In parallel to the work on the industrial prototype, experimental investigations with the pre-prototype 170 GHz coaxial cavity gyrotron have been continued at FZK. The experiments performed and the results obtained are summarized as follows:

- Parasitic low frequency oscillations:

As already reported in the last annual report, strong parasitic low frequency (LF) oscillations mainly around 260 MHz have been excited in the gyrotron. Based on experimental observations and on results of simulations with the electromagnetic 3D-code "CST microwave studio", some geometrical modifications on the coaxial insert of the prototype tube have been suggested in order to suppress the excitation of the parasitic LF-oscillations. To verify the success of the modifications made, tests will be performed on the experimental pre-prototype gyrotron. For this purpose, a dedicated coaxial insert has been fabricated.

- Cavity and RF generation:

In experiments it has been shown that an increase of the level of microwave stray radiation in the gyrotron resulted in a decrease of both the single mode operating range and the efficiency. A Brewster window has been prepared for further experiments with reduced stray losses and in particular with reduced reflections from the window into the competing modes. In addition, theoretical investigations of the RF-generation have been continued and a new cavity design is under consideration in cooperation with TEKES, Finland.

- Quasi-optical (q.o.) RF output system:

The (q.o.) RF output system - launcher and mirrors - fabricated for the industrial prototype gyrotron has been tested successfully in low power ("cold") measurements before installation inside the tube. The RF beam distribution measured has been found to be in agreement with the design calculations.

A new, more sophisticated code has been used for optimization of the launcher. Unfortunately, the optimization procedure of this code did not result in a satisfactory design. A modified optimization procedure for designing the launcher for the $TE_{34,19}$ mode with a Gaussian content $\geq 95\%$ is in progress. In the meantime, as a first step the Gaussian content of the RF output system is going to be increased to a value $> 85\%$ by a new launcher designed with the coupled-mode method used so far. A test with that system is in preparation.

- Measurements with the CNR microwave load:

The performance of an un-cooled version of the spherical 2 MW microwave load designed and fabricated at CNR Milano and foreseen to be used for testing the prototype gyrotron has been investigated on the experimental 170 GHz pre-prototype gyrotron. The goal was (1) to measure the power distribution (hot spots) along the wall of the load and (2) to determine the amount of microwave power reflected from the load and from a pre-load back into the gyro-



Fig. 1: Photography of the first industrial prototype of the 2 MW, CW, 170 GHz coaxial cavity gyrotron (fabricated by TED).

tron. As a result it has been found that about 3% of the RF output power is reflected, mainly by the pre-load, back into the gyrotron. The distribution of the RF power along the wall was found to be sufficiently uniform for absorption of the envisaged RF power (2 MW).

Summary and outlook

The fabrication of the first prototype of the 2 MW, 170 GHz coaxial cavity gyrotron has been accomplished and the tube is ready for delivery. Due to the delayed delivery of the SC-magnet, the testing of the prototype can be performed at earliest in the time between March and September 2007. In case of an additional delay of the SC-magnet, operation of the prototype gyrotron could be performed under restricted conditions in the SC-magnet existing at FZK.

The influence of the level of stray radiation on the gyrotron performance has been investigated with the experimental pre-prototype coaxial gyrotron. The pre-prototype tube has been used to study the microwave performance of an un-cooled version of the microwave load designed and fabricated by CNR Milano. The design work on an RF-output system with a Gaussian content >95% is going on.

Staff:

A. Arnold
G. Dammertz
J. Flamm (Uni K'he)
G. Gantenbein
S. Illy
J. Jin
W. Leonhardt
D. Mellein
B. Piosczyk
O. Prinz
T. Rzesnicki
M. Schmid
W. Spiess
J. Szczesny
M. Thumm
R. Vincon

Literature:

- [1] B. Piosczyk, S. Alberti, D. Bariou, P. Benin, T. Bonicelli, G. Dammertz, O. Dumbrajs et al., "170 GHz, 2 MW, CW Coaxial Cavity Gyrotron for ITER – Status and Results obtained on a Pre-prototype Tube"; 14th Joint Workshop on Electron Cyclotron Resonance Heating (EC14); Santorini, Greece, May 2006; to be published, <http://www.hellasfusion.gr/englishver/ec14conference.php>.
- [2] B. Piosczyk, S. Alberti, D. Bariou, P. Benin, T. Bonicelli, G. Dammertz, O. Dumbrajs et al., "170 GHz, 2 MW, CW Coaxial Cavity Gyrotron for ITER – Status and Results obtained on a Pre-prototype Tube", IRMMW -THz 2006, September 18 – 22, Shanghai, China
- [3] O. Loukscha, B. Piosczyk, G. Sominski, M. Thumm, D. Samsonov, "On Potentials of Gyrotron Efficiency Enhancement: Measurements and Simulations on a 4 mm Gyrotron", IEEE Trans. Plasma Science, vol. 34,3 502-511, June 2006.
- [4] B. Piosczyk, S. Alberti, D. Bariou, P. Benin, T. Bonicelli, G. Dammertz, O. Dumbrajs, et al., "170 GHz, 2 MW, CW Coaxial Cavity Gyrotron for ITER – Status and Results obtained on a Pre-prototype Tube", 21st Fusion Energy Conference, 15 – 21 October 2006, Chengdu, China; <http://www-pub.iaea.org/MTCD/Meetings/announcements.asp?ConfID=149>;
- [5] T. Rzesnicki, J. Jin, B. Piosczyk, M. Thumm, G. Michel, D. Wagner, „170 GHz, 2 MW Coaxial Cavity Gyrotron – Design Verification of the New RF Output System”, International Journal of Infrared and Millimeter Waves, 27(2006), pp.1-11

- [6] J. Jin, B. Piosczyk, M. Thumm, T. Rzesnicki, S. Zhang, "Quasi-optical Mode Converter/Mirror System for a High-Power Coaxial Cavity Gyrotron". IEEE Transactions on Plasma Science, 34(2006) pp.1508-15
- [7] J. Jin, M. Thumm, B. Piosczyk, T. Rzesnicki, "Theoretical Investigation of an Advanced Launcher for a 2 MW 170 GHz $TE_{34, 19}$ Coaxial Cavity Gyrotron." IEEE Transactions on Microwave Theory and Techniques, 54(2006) pp.1139-45
- [8] G. Michel, O. Prinz, T. Rzesnicki, "A Design Scheme for Quasi-Optical Mode Converters of Coaxial Cavity Gyrotrons." Litvak, A.G. [Hrsg.] Strong Microwaves in Plasmas : Proc. of the Internat. Workshop, Nizhny Novgorod, Russia, July 25 - August 1, 2005
- [9] T. Rzesnicki, J. Jin, B. Piosczyk, M. Thumm, G. Michel, D. Wagner, "Low Power Verification of a New RF Output System for a 170 GHz, 2 MW Coaxial Cavity Gyrotron.", Wiesbeck, W. [Hrsg.] German Microwave Conf. (GeMIC 2006), Karlsruhe, March 28-30, 2006 Proc. on CD-ROM
- [10] T. Bonicelli, S. Alberti, S. Cirant, O. Dormicchi, D. Fasel, JP. Hogge, S. Illy et al., "EC Power Sources: European Technological Developments towards ITER" 24th SOFT - 11-15 September 2006 - Warsaw, Poland, Paper ID 510

EFDA/04-1185 (TW4-THHN-IITF2) The First ITER NB Injector and the ITER NB Test Facility: Progress in the Design

Summary of the design work in 2006

Within this task, a complete detailed design of the cylindrical Neutral Beam Injector (NBI) cryopump was elaborated. The final report of the present task included the detailed CATIA-V5 drawings of the design of the cryopump as well as the thermo-hydraulic calculations of the pipe routings of the cryogenic circuits. Complementary mechanical analysis (ANSYS FEM) was performed as well. In parallel, recommendations for the conventional mechanical and turbomolecular pumping systems for the Neutral Beam Test Facility (NBTF) were given and performance calculations for the different operational modes of the NBI were made.

However, the design of the NBI system to be used in ITER has been changed at the end of this task in February 2006 towards a rectangular shaped beam line vessel including a top lid to enable a vertical access to the beam line components. This design change of the ITER facility makes the use of a cylindrical shaped cryopump no longer possible and requires a re-design of the entire cryopumping system [1]. The task TW4-THHN-IITF2 has been closed in March 2006 and it has been agreed with EFDA to consider the new design changes and their consequences in a separate future EFDA task (TW6-THHN-NBD1, under launch). Nevertheless, certain preparative studies in view of the future task have been performed in the course of 2006 [2].

Hydrogen pumping experience

Valuable operational experience was gained with the NBI cryosorption pumps manufactured by FZK for the negative ion source testbed at IPP Garching [3]. One important result was the confirmation of the pumping speed dependence on pumped gas amount, see Fig. 1.

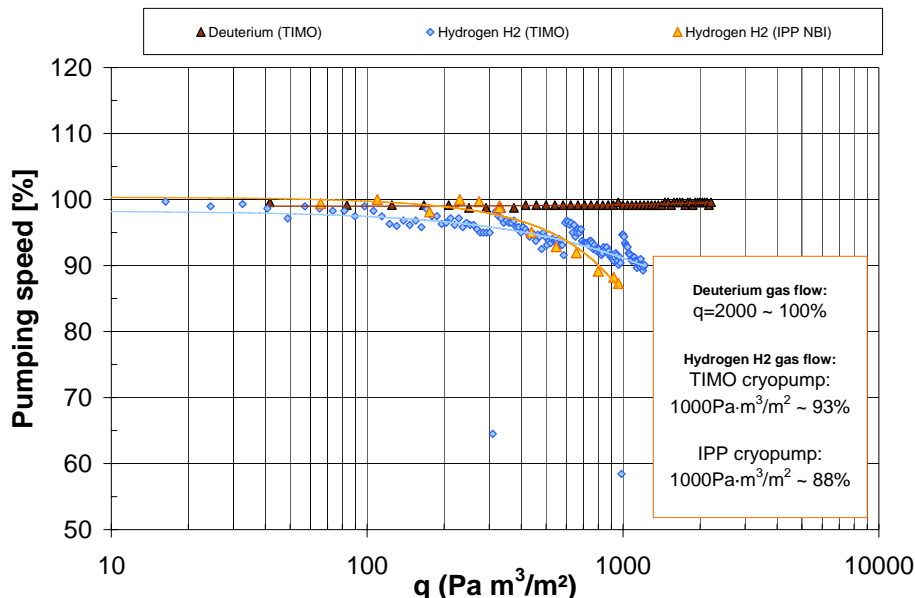


Fig. 1: Illustration of the pumping speed evolution with increasing pumped gas amount. In the case of D₂, the pumping speed is constant; in the case of H₂, it decreases.

It was found, for the IPP cryopump as well as for the TIMO cryopump, that for hydrogen (H₂) pumping, there results a continuous decrease in pumping speed beginning from the start of

the operation, which is not the case for deuterium pumping. This is attributed to the different pumping mechanisms. At a surface-related accumulated gas load of $\sim 1000 \text{ (Pa}\cdot\text{m}^3\text{)/m}^2$, the H_2 pumping speed decrease is about 10%. If the NBI cryopump shall be able to pump over 3000 s, and the pumping speed shall decrease less than 10%, then the new cryopump will have to provide very large charcoal coated surfaces. Moreover, new calculations of the needed gas throughputs for the beam line operation resulted in an increase of the hydrogen gas flow by 40%, which further challenges the requirement on the hydrogen capacity significantly.

Outlook

The detailed design work on the NBI cryopump will restart in 2007 under a new EFDA task. Recently, first discussions about the new challenging requirements and their consequences on the cryoplant have started in the Neutral Beam Group meetings of CCNB and with Consorzio RFX, the Association in charge for the ITER Neutral Beam Test Facility.

Staff:

A. Antipenkov
Chr. Day
M. Dremel
R. Simon
H. Strobel

Literature:

- [1] T. Bonicelli et al., Review of the EU activities in preparation of ITER in the field of EC power sources and NB system, Fusion Energy Conference, Chengdu, China, Oct 2006.
- [2] M. Dremel, Base design investigations of a rectangular shaped cryopump for ITER NBI, 13th ITER-EFDA-FZK Interface meeting, ITER IDM ITER_D_24UM4L.
- [3] M. Dremel, A. Mack, Chr. Day, H. Jensen, Cryosorption pumps for a Neutral Beam Injector test facility, Adv. Cryogenic Engng. 51 (2006) 583-590.

EFDA/05-1352 (TW5-THHN-MONRF)

Monitoring the EU/RF Collaborative Tasks on the First ITER NB Injector and the ITER NB Test Facility

Background and Objectives

The central work of this task is related to gas flow and density calculations for the Neutral Beam Test Facility (NBTF) and the ITER Neutral Beam Injector (NBI). The Kurchatov Institute of the Russian Federation (KIAE) is performing calculations using the three codes: PDP (Power Deposition Profiles), MC-GF (Monte Carlo - Gas Flow) and BTR (Beam Transport and Reionisation), developed in KIAE for ITER NBI and similar tasks. These codes describe different substantial features of the NB systems and also serve for different kinds of studies on the proposed or chosen set of injector parameters. The present task with FZK has defined the input parameters from the cryopump point of view, which acts as the dominant gas sink, having a strong influence on the gas profile along the entire beam line and, thus, on the re-ionisation processes and the efficiency of the machine.

The aim of the task is to set up a user-friendly interface for the input data of these codes and to adapt them to the present design of the ITER NB and NBTF as well as to carry out computations of power deposition, power balance, gas flow and density profiles in the NB line components.

Preliminary cryopump design

It was agreed to use the new beam line vessel conceptual design distributed by ITER in February 2006 as a basis for this task. The new vessel design includes an upper flange for assembling the neutralizer, the residual ion dump and the calorimeters from top. Consequently, the cylindrically shaped cryopump investigated in detail in previous studies (EFDA-Task TW4-THHN-IITF2) [1], which would close the top access cannot be used anymore. Therefore, FZK has proposed a new draft cryopump adopted to the new vessel geometry. It is based on two rectangular shaped cryopumps, which are placed to the left and the right of the beam line components and can be assembled and disassembled through the top flange, see Fig. 1.

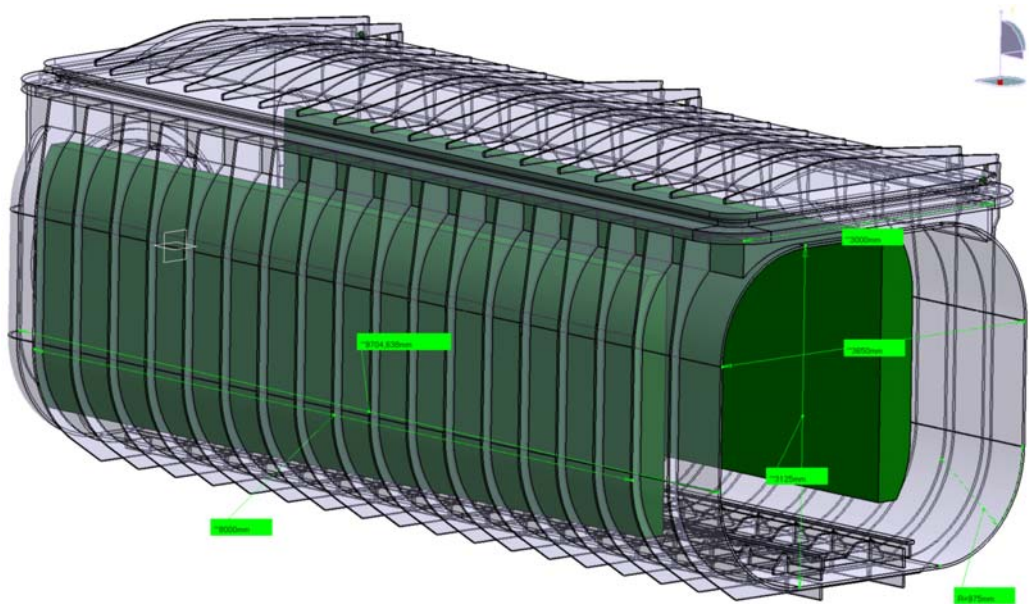


Fig. 1: 3D model of the beam line vessel (transparent) with the proposed cryopump design (in green colour). The beam source vessel has been blanked for better overview.

The design of the cryopump was driven by maximisation of pumping speed combined with a quantitative assessment of the pumping capacity. The present input parameters for the gas throughputs were taken from the previous NBI design task TW4-THHN-IITF2; there, a gas throughput of 520 (mbar.l)/s was given for hydrogen, and a value of 300 (mbar.l)/s for deuterium, both of which higher than given in the underlying ITER baseline design. The pulse duration was assumed to be 3000 s, as given in the ITER documentation. The draft FZK cryopump design was handed over to KIAE as input to their calculations [2].

Training week on using the codes

The MC-GF code includes the interaction of the gas molecules with the surfaces of the beam line components and needs a proper description of the surface temperatures and the expected accommodation coefficients. These values are subject to change during the design evolution. Therefore, the idea was to list the input parameters in a separate file to be as flexible as possible. The development of an interface for how to handle that file was one of the objectives in the present task.

In 2006, the cryopump input from FZK has been used by KIAE to set up a user interface based on an EXCEL sheet listing all necessary input parameters to start the calculations. Underway is the proper integration of the beam source and the neutralizer. The overall gas distribution profile is strongly influenced by the choice of the beam source design (for which there currently exist four different alternatives), the choice of the residual ion dump (magnetically or electrically) and finally the operation mode of the calorimeter. To cover all combinations of the different designs, the EXCEL sheet includes up to 107 input parameters. During a training week together with the persons in charge of the codes from KIAE and the European Associations CEA and Consorzio RFX the background of the codes and the use of all three codes was trained.

Future Activities

Based on the experience gained in the training week, the codes and the input file for the codes will be improved and the beta-versions of the codes will be distributed. After having tested the codes and especially the EXCEL interface for the input of the parameters, a final version shall be elaborated and used in future tasks to advance the NBI design.

FZK will especially benchmark the MC-GF computer code produced by KIAE against the ITERVAC computer code available at FZK, which covers gas flow calculations for arbitrary Knudsen numbers and geometries. This will be done for the new ITER beam line design considering two rectangular cryopumps in a beam line vessel with top access. The results of this task will become an important input for the detailed design of the ITER NBI cryopump expected to start in a parallel task in 2007 (TW6-THHN-NBD1).

Staff:

M. Dremel
V. Hauer
X. Luo
H. Strobel

Literature:

- [1] M. Dremel, Chr. Day, A. Mack, H. Haas, V. Hauer, E. Speth, H.D. Falter, R. Riedl, B. Graviil, Design and manufacturing of cryosorption pumps for testbeds of ITER relevant neutral beam injectors, in: L. Zhang (ed.), Proc of the ICEC-20, pp. 461-464, Elsevier, Amsterdam, 2006.
- [2] M. Dremel, V. Hauer, H. Strobel, Chr. Day, NBI Cryopumps; results and changes, 12th ITER-EFDA-FZK Interface meeting, April 2006, ITER IDM ITER_D_24W9KQI

Physics

ECR Heating and Current Drive – Step-Tunable Gyrotron Development

1. Introduction

Magnetohydrodynamic (MHD) instabilities are one of the main reasons for the limit of plasma confinement [1]. The stability is to a large extent determined by the distribution of the plasma currents, and driving localized currents in a plasma is a very important tool to suppress current-driven instabilities and thus to optimize the performance of tokamaks. The suppression of plasma pressure limiting MHD instabilities (so called 'Neoclassical Tearing Modes') has been demonstrated successfully by localized electron cyclotron current drive (ECCD) at ASDEX-Upgrade, DIII-D and JT-60U.

The absorption of RF-waves with the angular frequency ω is dependent on the resonance condition $\omega - k_z v_z = \omega_c$. Thus, the driving currents can be counteracted by an external current drive at different localizations either by changing the injection angle (e.g. with steerable mirrors) or the RF-frequency.

For experiments on plasma stabilization at ASDEX-Upgrade (IPP Garching) with advanced electron-cyclotron-resonance heating (ECRH) and ECCD, multi-frequency tunable 1-MW long-pulse gyrotrons are highly needed. Two gyrotrons have been ordered by IPP Garching from "Gycom" in Russia. The first gyrotron operates as a two-frequency gyrotron at 105 GHz and 140 GHz (the thickness of the single disk window is matched to these frequencies), the second one operates as a multi-frequency gyrotron with different frequencies between 105 GHz and 140 GHz. As operating mode, the TE_{22,8}-mode was chosen at 140 GHz. The frequency of 105 GHz corresponds to the TE_{17,6}-mode [2,3].

2. Gyrotron cavity

The TE_{22,6}-gyrotron, existing at FZK, has been modified to operate in the TE_{22,8}-mode like the industrial gyrotron. This choice has been made in order to compare the results with those from the industrial gyrotrons. With the short-pulse gyrotron from FZK, fast step-tunability within 1 s in a range of 15 GHz had been proven very successfully. Beam tunnel, collector and the superconducting magnet system of the TE_{22,6} gyrotron are used in the new experiment. The resonator, the quasi-optical mode converter and the output window had to be modified.

The behaviour of a new resonator including uptaper was calculated and optimized with regard to broadband behaviour for modes between 105 GHz and 143 GHz [4].

3. Quasi-optical mode converter

The quasi-optical mode converter of the gyrotron consists of a dimpled-wall antenna and a beam-forming mirror system optimized for nine modes from TE_{17,6} to TE_{23,8}. With the help of a new code, more complex wall structures of the waveguide antenna can be calculated. Thus it was possible to find an optimised new design where the field amplitude near the cut is strongly decreased. This reduces the losses and the stray radiation considerably [5,6].

There are two key parameters, which have to be chosen before the mirror optimisation: the window position and the waist size of the output beam. The central point of the CVD-diamond Brewster window (see below) is set to the position 325 mm from the gyrotron axis. In order to match the requirement of small window aperture, the optimised waist size of the reference fundamental Gaussian beam at the output window is chosen to 10.4 mm.

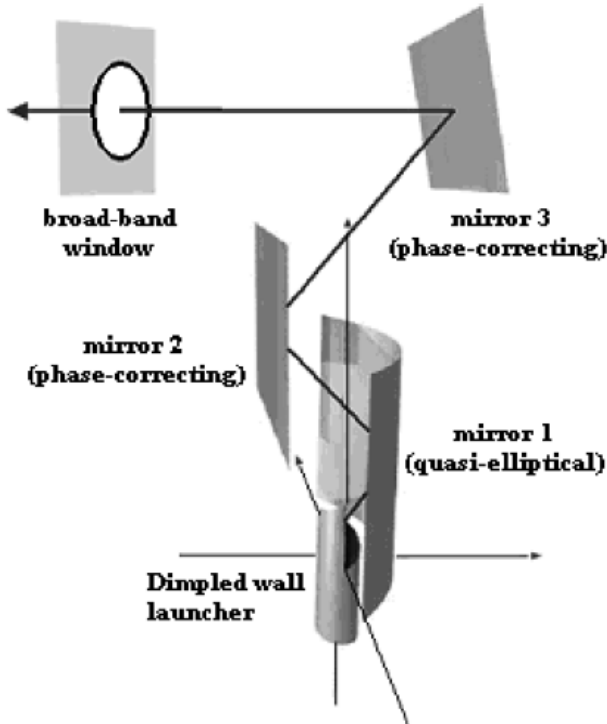


Fig. 1: Scheme of an internal quasi-optical mode converter.

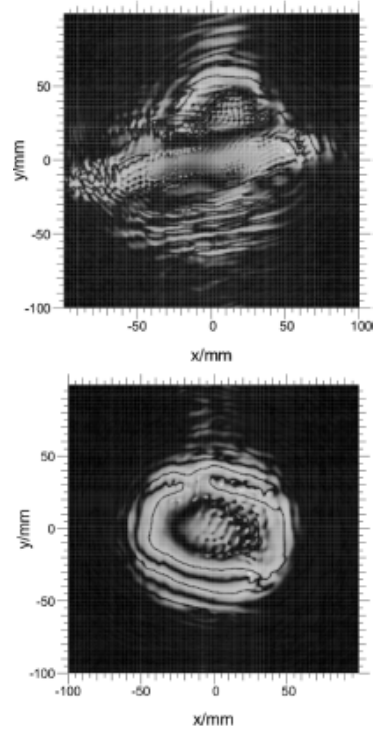


Fig. 2: Calculated surface contour map of mirror 2 (top) and mirror 3 (bottom).

The first mirror is a large, quasi-elliptical one, which was taken from the previous design. Its main purpose is to focus the divergent beams radiated from the launcher. The second and the third mirrors are adapted phase-correcting ones with a complicated nonquadratic shape function of the surface. There are small variations of the surfaces of these phase-forming mirrors, which modify the phase of the local plane wave (see figure 2).

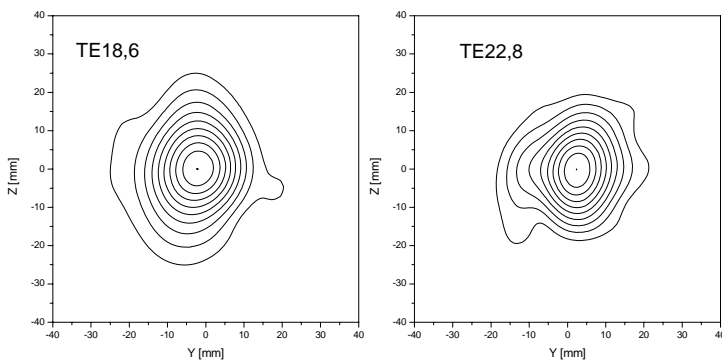


Fig. 3: Calculated power density distribution at 325 mm from gyrotron axis. Normalised power contours are shown in linear scale with 0.1 relative decrements.

For this design, the calculations predict that the efficiency for converting the high order mode into the fundamental Gaussian beam should exceed 90 % for all modes under consideration. As an example, the calculated beam pattern for $TE_{18,6}$ and $TE_{22,8}$ are given in figure 3.

It is planned to perform low power measurements of the quasi-optical output system using a vector network analyser with a high dynamic range. Results of such a measurement are necessary for interpretation of and comparison with the high power experiments (see 5).

4. CVD-diamond Brewster window

Efficient operation for the large number of operating modes at different frequencies is only possible by using a broadband diamond Brewster window fabricated by chemical vapor deposition (CVD). Due to the large Brewster angle, the diameter of the disk also has to be rather large in order to have a sufficiently large aperture for the RF beam. One disk with a

thickness of 1.7 mm and a diameter of 140 mm was developed by Element Six and already delivered. This disk can be used for the elliptic shape of a Brewster window with an effective aperture of 50 mm.

Because of the elliptic shape, the stresses during the brazing procedure are different from those of circular disks. These stresses were calculated to be increased by a factor of 1.3. To investigate whether a diamond disk will sustain these stresses, brazing tests were ordered from Thales with a quartz disk and a small diamond disk for which the stresses are increased compared to the circular one. In case of successful brazing tests, the 140 mm diamond disk will be brazed with copper cuffs, so that it will be possible to cool the disk at the edge.

However, the first brazing of a ceram disk failed and leaks occurred. After refined FEM calculations of the brazing tool to localise positions of high mechanical stresses, a new attempt will be made to braze a vacuum tight disk.

For the experiments in 2006 the gyrotron was equipped with a quartz glas Brewster window with an aperture of 85 mm.

5. Experimental results

Experiments have been performed with the short pulse step tunable gyrotron in order to measure the output beam of the modes under consideration ($TE_{17,6}$ at 105.2 GHz up to $TE_{23,8}$ at 143.5 GHz) and to compare these results with theoretical calculations. Since no special efforts have been made to operate the tube at optimised parameters for each mode, the output power was between 300

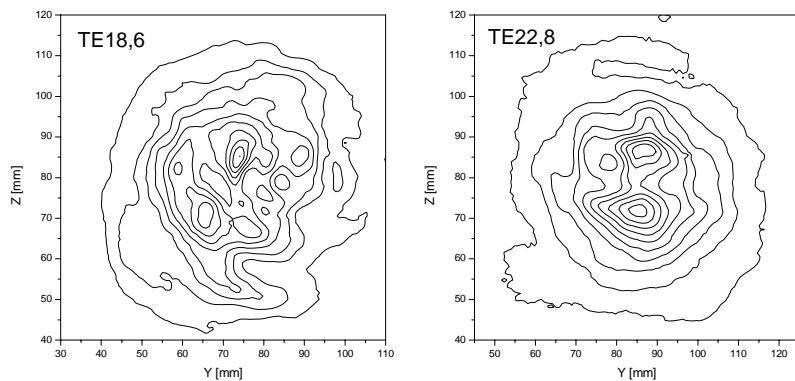


Fig. 4: Measured power distribution of the gyrotron output beam at 635 mm (left) and 665 mm (right) from the axis.

and 600 kW for single mode operation. The analysis of the measured beams yielded a Gaussian mode content of 77 – 88 % and a higher waist radius then expected from the calculations for all modes. Typical beam pattern of the modes $TE_{18,6}$ and $TE_{22,8}$ are given in figure 4. Note that the position of the pattern along the axis of propagation is different from those of figure 3. These results suggests that the launcher and mirror system should be optimised to increase the Gaussian content and to adapt the beam radius to the planned window aperture.

Staff:

A. Arnold
G. Dammertz
I. Danilov
J. Flamm (Uni Karlsruhe)
G. Gantenbein
R. Heindinger
S. Illy
W. Leonhardt

D. Mellein
B. Piosczyk
O. Prinz
M. Schmid
W. Spieß
J. Szczesny
M. Thumm
X. Yang

Literature:

- [1] Zohm, H., M. Thumm: On the use of step-tuneable gyrotrons in ITER, *Journal of Physics: Conference Series*, 25, 274-282, 2005.
- [2] Leuterer, F.; Wagner, D.; Manini, A.; Monaco, F.; München, M.; Ryter, F.; Schütz, H.; Zohm, H.; Franke, T.; Thumm, M.; Heidinger, R.; Gantenbein, G.; Kasperek, W.; Litvak, A.G.; Popov, L.G.; Nichiporenko, V.O.; Myasnikov, V.E.; Denisov, G.G.; Tai, E.M.; Solyanova, E.A.; Malygin, S.A. First tests of the new multi-frequency ECRH system at ASDEX upgrade. 33rd IEEE Internat.Conf.on Plasma Science (ICOPS 2006), Traverse City, Mich., June 4-8, 2006 Book of Abstracts S.190 report from ECRH system at AUG
- [3] Wagner, D.; Leuterer, F.; Manini, A.; Monaco, F.; München, M.; Ryter, F.; Schutz, H.; Zohm, H.; Franke, T.; Heidinger, R.; Thumm, M.; Kasperek, W.; Gantenbein, G.; Litvak, A.G.; Popov, L.G.; Nichiporenko, V.O.; Myasnikov, V.E.; Denisov, G.G.; Tai, E.M.; Solyanova, E.A.; Malygin, S.A. New frequency step tunable ECRH system for ASDEX upgrade. *International Journal of Infrared and Millimeter Waves*, 27(2006) S.173-82
- [4] Borie, E. Drumm, O., Illy, S., Koppenburg, K., Kartikeyan, M.V., Piosczyk, B., Wagner, D., Yang, X., Dammertz, G., Thumm, M., Possibilities for multifrequency operation of a gyrotron at FZK. *IEEE Transactions on Plasma Science*, **30**, 828-835, 2002.
- [5] Yang, X., Arnold, A., Dammertz, G., Koppenburg, K., Piosczyk, B., Wagner, D., Thumm, M. Improved beam-forming mirror system for a multi-frequency gyrotron at FZK. 2006 IEEE Internat.Vacuum Electronics Conf.held jointly with the 2006 IEEE Internat.Vacuum Electron Sources Conf. (IVEC/IVESC 2006), Monterey, Calif., April 25-27, 2006 New York, N.Y. : IEEE, 2006 S.411-12 ISBN 1-4244-0108-9
- [6] Yang, X., Thumm, M., Arnold, A., Borie, E., Dammertz, G., Drumm, O., Koppenburg, K., Wagner, D., Progress toward optimization of phase-correcting mirrors for a multifrequency 1-MW gyrotron. *IEEE Transactions on Plasma Science*, **34**, 652-658, 2006.

Microwave Heating for Wendelstein 7-X

Introduction

Electron Cyclotron Resonance Heating (ECRH) has an inherent capability for plasma start up, localised heating and current drive and is of particular importance for stellarators. ECRH is thus foreseen as a basic heating system in the first operation stage of W7-X with 10 MW heating power at 140 GHz in continuous wave (CW) operation [1]. The complete ECRH-system for W7-X will be provided by FZK, which in 1998 established the 'Projekt Mikrowellenheizung für W7-X' (PMW). The responsibility covers the design, development, construction, installation and integrated tests of all components required for stationary plasma heating on site at IPP Greifswald. PMW also coordinates the contributions from IPF Stuttgart, which is responsible for the microwave transmission system and part of the HV-system, and from the team at IPP Greifswald, which is responsible for the in-vessel components and for the in-house auxiliary systems. In particular, a European collaboration had been established between the Forschungszentrum Karlsruhe, the Centre de Recherche de Physique des Plasmas (CRPP) Lausanne, the Institut für Plasmaforschung (IPF) of the University of Stuttgart, the Commissariat à l'Énergie Atomique (CEA) in Cadarache and Thales Electron Devices (TED) in Vélizy, to develop and build a prototype gyrotron for W7-X with an output power of 1 MW for CW operation at 140 GHz.

A contract between CRPP Lausanne, FZK Karlsruhe and Thales Electron Devices (TED), Vélizy, had been settled to develop and build these continuously operated gyrotrons. The development phase was finished successfully, and seven series tubes were ordered at the industrial company Thales Electron Devices (TED). Including the pre-prototype tube, the prototype tube and the 140-GHz CPI-tube now operated at IPP Greifswald, ten gyrotrons will be available for Wendelstein 7-X. To be able to operate these gyrotrons, eight more superconducting magnetic systems are necessary and have been delivered by Cryomagnetics, Oak Ridge, USA.

Series Gyrotrons

The tests of series gyrotron #1 at Forschungszentrum Karlsruhe were reported earlier [2-4]. After these successful tests, the tube was delivered to IPP Greifswald for tests at highest output power and pulse lengths of 30 minutes. A directed output power of 865 kW was measured inside the load, and a total tube output power of about 920 kW was estimated taking into account the losses in the transmission line [5,6]. It passed successfully the "Site Acceptance Test" and is sealed now in order to avoid the initialisation of the guaranteed lifetime.

The second series tube [5-8] was delivered to Forschungszentrum Karlsruhe in February 2006 (Fig. 1).

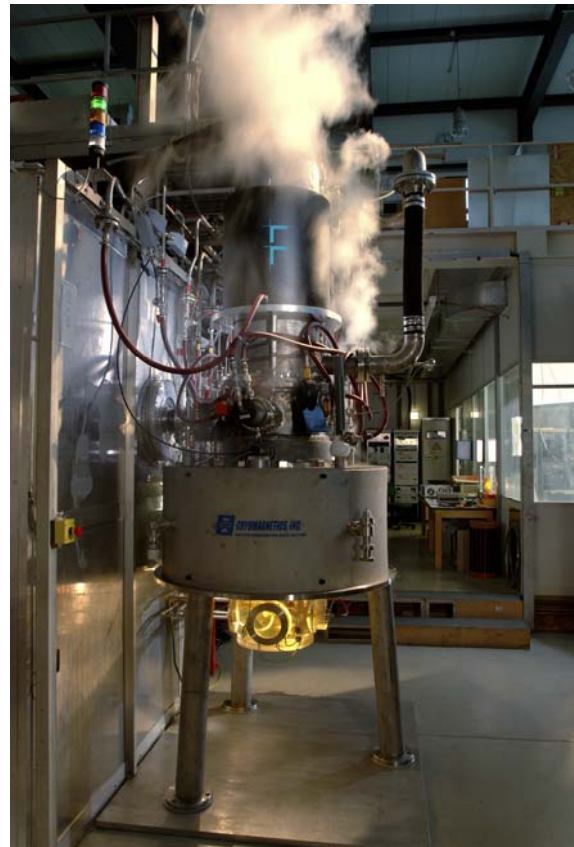


Fig. 1: The 2nd series tube at the test facility of FZK. The fog is caused by evaporating liquid nitrogen.

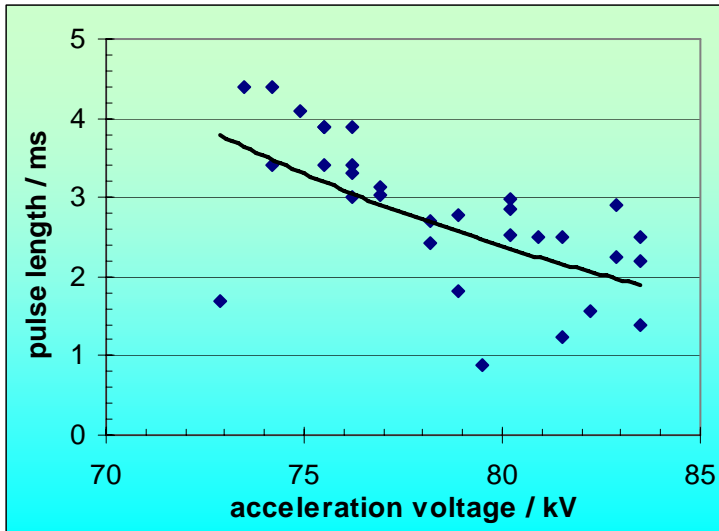


Fig. 2: Output power of tube #2 for different accelerating voltages at a beam current of 50 A.

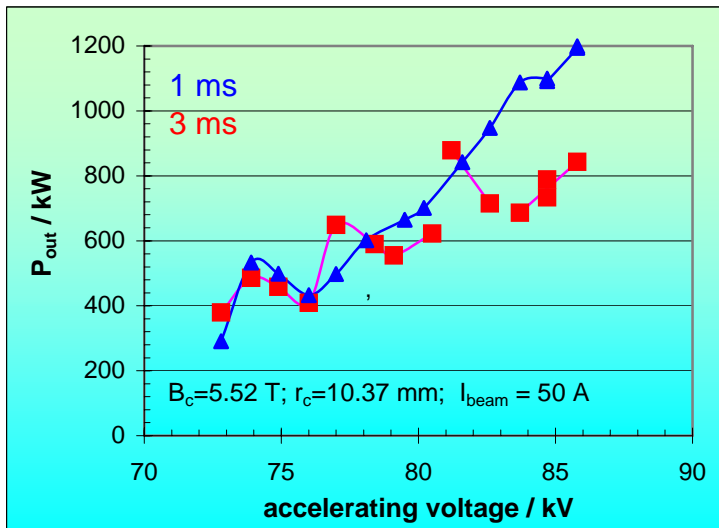


Fig. 3: Accessible pulse length for the correct mode versus accelerating voltages at $I_{\text{beam}} = 40 \text{ A}$ for tube #2. The line gives an exponential least square fit to the measured data.

At a pulse length of one millisecond an output power of 970 kW was measured at a beam current of 40 A with an efficiency of 27%. At a beam current of 50 A an output power of almost 1200 kW was obtained. When increasing the pulse length, severe mode hopping to the neighbouring mode ($\text{TE}_{27,8}$ mode) was observed. It was not possible to increase the pulse length to values exceeding 2-3 ms at accelerating voltages of more than 80 kV. Figure 2 shows the output voltage at a beam current of 50 A for pulse lengths of 1 ms and of 3 ms. At accelerating voltages exceeding 81 kV the output power (averaged over the pulse length) is reduced. The reason is caused by the fact that the neighbouring mode is excited with reduced power. Figure 3 shows the possible pulse length for which the correct mode, that is the $\text{TE}_{28,8}$ mode, can oscillate.

To avoid mode hopping at even higher pulse lengths, also the accelerating voltage had to be decreased stronger. At 50 ms pulse length the accelerating voltage had to be reduced to values as low as 74 kV this reducing the output power to less than 500 kW.

In order to eliminate the influence of possible external problems, measurements on the quality of the test stand at FZK were performed: The stability of the body and accelerating voltage, the tube pressure (neutralisation), the alignment between gyrotron and the magnetic axes, stability and homogeneity of the electron beam, low frequency oscillations and so on were investigated. No indications for any irregularities could be found.

A comparison between the frequency behaviour for series tube #1 and tube #2 which might give an indication of problems with the cavity did not show any differences between the tubes. The time constant for the thermal expansion was very similar (160 ms) and also the frequency shift in long pulse operation turned out to be almost the same when extrapolating to the same power.

The tube has been sent back to TED for a visual inspection. A severe damage was found in the beam tunnel which is caused by an overheating of the copper disks and maybe also due to overheating of the BeO / SiC-ceramics. A clear connection between the damage and the bad behaviour of the tube needs further investigation.

The third series gyrotron [5-8] has been delivered to FZK during April 2006. In short pulse operation, the behaviour of the output power has been examined. The dependence on the electron beam current was similar to what had been found for the prototype after the exchange of the cathode emitter. At about 42 A, a power of about 1 MW could be achieved. Figure 4 shows the result of the optimization procedure for different combinations of main magnetic field and electron beam radius inside the cavity. The dependence of the output power as function of the electron beam current does not show the expected almost linear dependence. The decrease of output power for electron currents exceeding 40 A is seen in poor optimization of parameters due to the short experimental time. (It was more important to investigate the behavior of the tube in long pulse operation than to optimize in short pulse operation). However, it is clearly seen that at a current of 42 A an output power of 1 MW could be achieved with an efficiency of 32 %. This is in agreement with the values obtained with series tube #1.

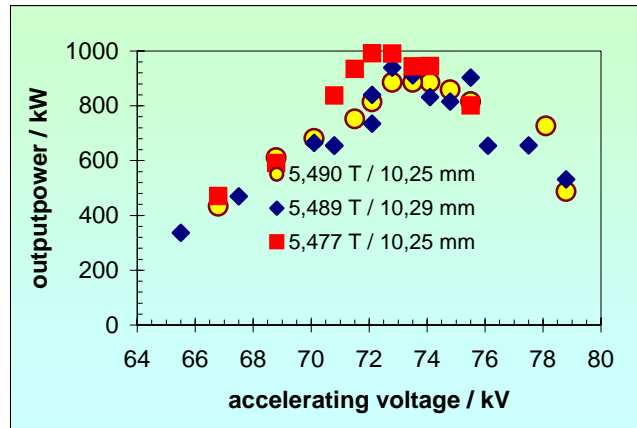


Fig. 4: Output power (tube #3) for different magnetic field combinations, that is for different magnetic fields and electron beam radii (see legend).

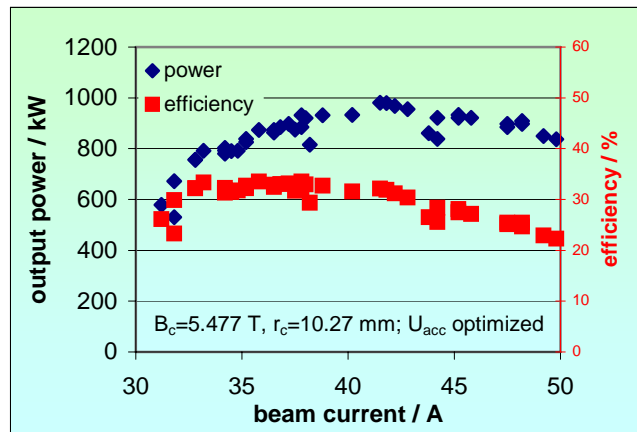


Fig. 5: Output power and efficiency (without energy recovery) versus beam current for tube #3.

In long pulse operation, the parameters as for example magnetic fields in the cavity- and gun-regions are different compared to short pulse operation due to neutralisation and expansion of the cavity. The optimisation procedure for finding the operating parameters at high output power in long pulse operation was performed in 1s-pulses assuming that the instantaneous power is well described by the frequency difference between the initial frequency and the instantaneous frequency (after one second). For tube #1 the output power increased slightly with increasing magnetic field (see straight line in Fig. 6). For tube #3 a different behaviour was found. The output power decreased with increasing magnetic field due to the fact that the accelerating voltage could not be increased correspondingly. This behaviour is shown in the Figure 6. The frequency shift (being assumed to be proportional to the power) is plotted as function of the accelerating voltage for different currents in the main coil that is for different magnetic field values. The gun coil current was changed as well but with almost no effect. Increasing the accelerating voltage to higher values than shown in Fig. 6 led in most cases to arcing inside the tube. Sometimes, this effect was accompanied by a strong increase in body current.

So, even for pulse lengths of 1 s the power of the series tube #3 dropped to values of only 750 kW. For longer pulses the power dropped even further, to about 650 kW at 180 s. The reason is not understood.

To eliminate possible malfunctions in the experimental set-up (e.g. HV power supply etc.) the tube was sent to Greifswald for long pulse operation. No difference could be found. The output power was limited to about 600 kW for long pulse operation. The tube did not pass the

acceptance tests. It is assumed that a similar problem as for tube #2 could be the reason, but further investigation seems to be necessary.

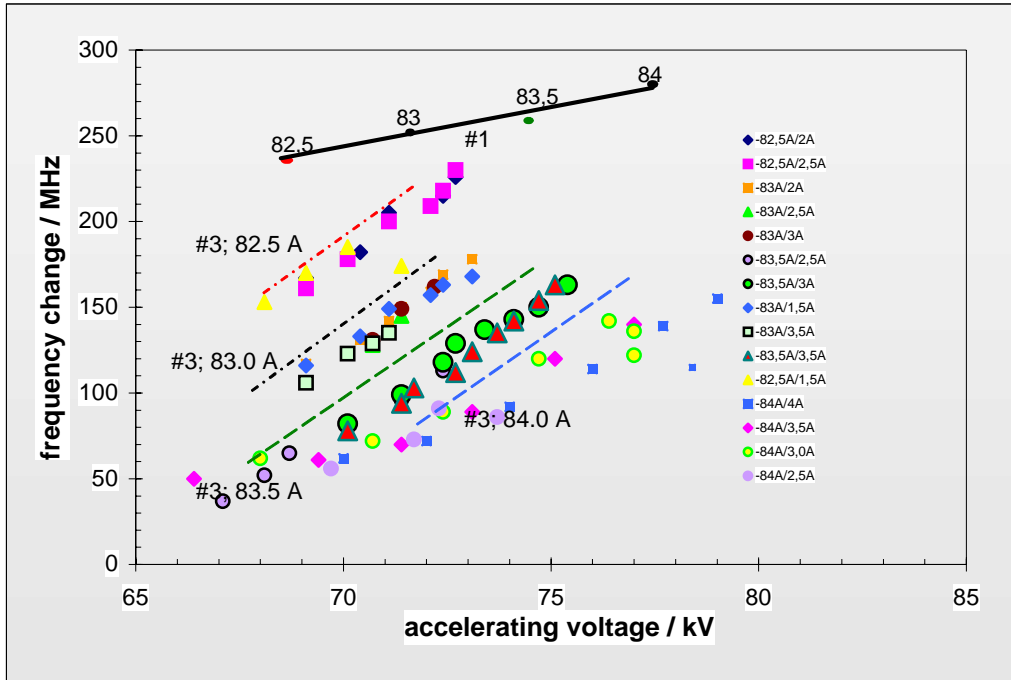


Fig. 6: Change of resonance frequency for a pulse length of 1 s for tube #3. (The straight line shows the results of tube #1.) The numbers give the current for the main magnetic coils.

All the tubes deliver similar output mode purity. Table 1 summarizes the determined parameters of the output RF-beams of the prototype tube and the series gyrotrons. The variation of the beam parameters, the lower beam waist compared to the design value and the elliptical shape of the beams are probably due to fabrication and alignment tolerances. The similarity of the Gaussian content for all tubes also indicates that the quasi-optical mode converter works well for all the gyrotrons.

Table 1: Parameters of the output beam for the different gyrotrons. Given are the values for the waist w_{0x} / w_{0y} , the distance of the waist from the window z_{0x} / z_{0y} and the mode purity of the gyrotron output RF-beam.

	w_{0x} / w_{0y} [mm]	z_{0x} / z_{0y} [mm]	TEM ₀₀ [%]
Prototype	18,6 / 21,3	202 / 71	97
Series tube #1	17,7 / 21,6	127 / 126	97.5
Series tube #2	20,2 / 22,5	104 / 40	97
Series tube #3	17,5 / 20,6	130 / 90	97

The electron beam sweeping system for reducing the density of the collector loading by the electron beam was investigated thoroughly. At Forschungszentrum Karlsruhe, the radial sweeping system was proven to operate similar to the existing axial sweeping system. At IPP Greifswald, both systems were used simultaneously. Thus the spread electron beam was moved up and down on the collector surface with a reduced frequency of 7 Hz. With this system of combined radial (50 Hz) and axial (7 Hz) sweeping the loading density of the collector could be reduced by almost a factor of two. This would allow the gyrotron to be operated at higher electron beam currents leading also to higher output power. (Up to now the collector loading was the limiting factor for the output power). This behaviour is also very important for gyrotrons with higher output power as for example the 2-MW coaxial cavity 170-GHz gyrotron being developed for ITER.

Because of the problems with tube #2 and #3, the delivery of tube #4 to Forschungszentrum Karlsruhe has been postponed to February of 2007 in order to avoid the problems mentioned.

Transmission line

The transmission line consists of single-beam waveguide (SBWG) and multi-beam waveguide (MBWG) elements (Fig. 7). For each gyrotron, a beam conditioning assembly of five single-beam mirrors is used. Two of these mirrors (M1, M2) match the gyrotron output to a Gaussian beam with the correct beam parameters, two others (P1, P2) are used to set the appropriate polarisation needed for optimum absorption of the radiation in the plasma. A fifth mirror (M3) directs the beam to a plane mirror array (beam combining optics: BCO), which is situated at the input plane of a multi-beam wave guide. This MBWG is designed to transmit up to seven beams (five 140-GHz beams, one 70-GHz beam plus an additional spare channel) from the gyrotron area (entrance plane) to the stellarator hall (exit plane). At the output plane of the MBWG, a mirror array separates the beams again and distributes them via CVD-diamond (chemical vapor deposited diamond) vacuum barrier windows to individually movable antennas (launchers) in the torus. To transmit the power of all gyrotrons, two symmetrically arranged MBWGs are used.

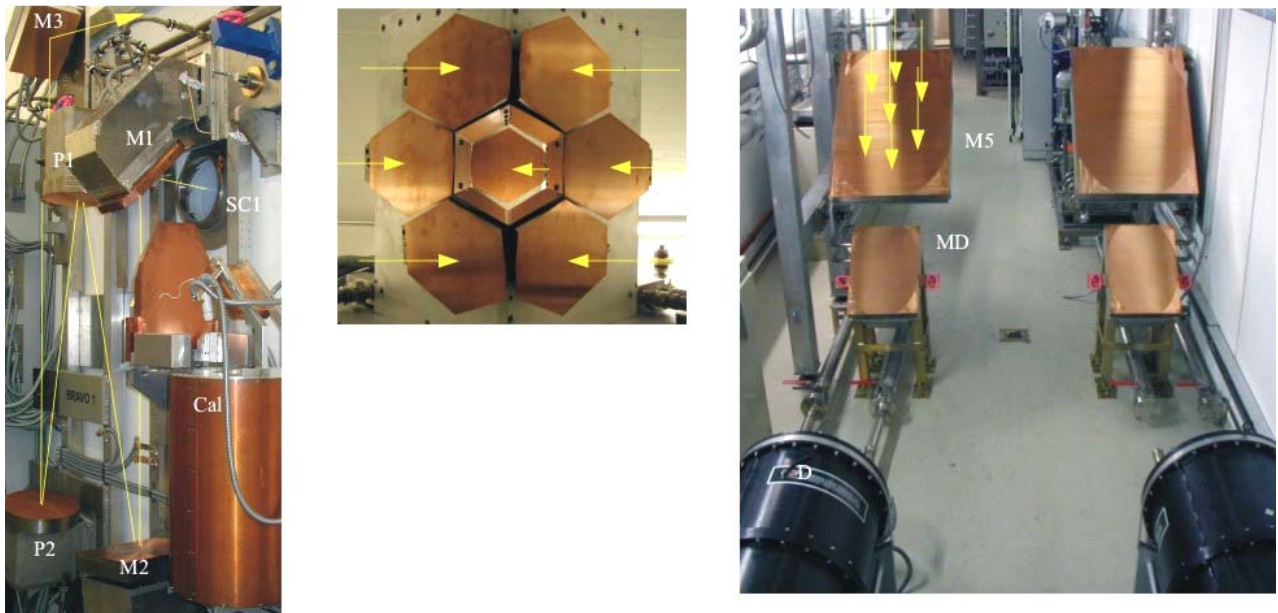


Fig. 7: View into the transmission duct of the ECRH system on W7-X. The left picture shows the matching optics M1, M2, and polarizers P1, P2, as well as M3, switch mirror SC1 and short-pulse calorimeter Cal for one gyrotron. In the middle, the beam combining optics (BCO) as seen from the first MBWG mirror M5 is displayed. Individual beams coming from M3 are impinging on the plane mirrors from left and right and are directed onto M5 of the MBWG system. The right picture shows a view into the beam duct with two large multi-beam mirrors M5 and the mirrors MD which can focus one selected beam into one of the CCR dummy loads D seen in the foreground.

All mirrors for the transmission system up to the torus hall are now installed, including calorimeters, absorbers for stray radiation and retro-reflectors. These devices can be used to test the MBWG in a double transit, and to measure the transmission efficiency with the stationary RF-loads; high-power tests are in preparation. The design of the mirrors near to the torus as well as their support and shielding structure is completed for the major parts, and calls for tender for fabrication were launched. The design of the transmission system in front of the torus as well as the beam optimization in the launcher were done, yielding broad-band transmission characteristics. A mock-up of this part of the transmission line was tested with respect to break-down problems; no arcing has been detected up to twice the maximum power density. In the following the specifications for the mirror surfaces M13 and M14 (inside the torus hall) were completed, and the mirrors are under fabrication. For the gyrotrons in-

stalled in 2006, matching mirrors were designed and fabricated on the basis of thermographically recorded beam profiles and subsequent phase retrieval.

During the acceptance tests of gyrotrons, precise frequency modulation experiments have been performed. The results will be used in the development of a fast high-power millimeter wave switch, which consists of a diplexer and a tiny frequency-shift keying of the gyrotron [9]. Such a device is prepared for test in the transmission duct. Note that due to easy access to all components, the W7-X ECRH system is well suited as a test bed [10]. Therefore the system could be used for investigation of several devices like in-vessel mirrors, dummy loads and an ITER launcher mock-up.

A new ECRH-power diagnostic based on fast bolometers was developed during a diploma thesis in collaboration with the University of Applied Science in Stralsund. About 0.1 ‰ of the ECRH power was coupled out of the main beam by a corrugation on the first mirror's surface. This power was focused on the 1 cm² surface of the bolometer foil, which was coated by a microwave absorbing dye. The bolometer signal yielded a very good linearity over a power variation from 50 kW to 800 kW. With a matched analogue electronic compensation of the internal bolometer transfer function, a rise-time of about 15 ms could be achieved. Furthermore, the signal showed a good long term stability.

HV-systems

For the operation of the gyrotron with depressed collector, a precise control of the beam acceleration voltage is necessary, which is provided by the body voltage modulator. The beam current of the gyrotrons is controlled by the cathode heater supply, which is on cathode potential (about -55 kV). In case of arcing inside the gyrotron, a thyatron crowbar protects the tubes from being damaged. Details can be found in [10] and [12].



Fig. 8: HV control system for the W7-X gyrotrons: Modulator, crowbar and ignition coil (left) and thyatron tube with new external circuitry for protection of the gyrotron (right).

The fabrication of the body voltage modulators and the heating and tube protection units by IPF Stuttgart is ongoing. Initial problems with voltage break-down of the thyatron crowbars have been solved by a redesign of the external circuits of the thyatron (Fig. 8; right). The corresponding modifications have been implemented in all Crowbar-heater-units, followed by successful tests. By the end of 2006, eight complete systems have been delivered to IPP Greifswald and were put into operation. Figure 8 (left) shows a complete HV system.

In-vessel-components

The motor driven movable prototype ECRH antenna was tested for reliability under vacuum conditions and with microwave stray radiation loading in the MISTRAL test chamber. The antenna was equipped with spiral tubes in order to provide the cooling water supply for the movable mirror. No arcing or damage was found at a microwave loading of up to 450 kW/m^2 in peak, which was already above the expected stray radiation level in W7-X. During the full range motion cycling tests in vacuum two ball joints of the same type were broken after approximately 1000 cycles. The joints were redesigned and the stainless steel ball was replaced by a ceramic ball. With the new joints the prototype antenna has passed the 10000 cycles test in vacuum successfully and the design was released for the serial ECRH antennas. Most parts of the serial antennas are already designed. The manufacturing of the in-vessel mirrors has started. The motor drives were ordered and have been delivered already.

Microwave radiation is strongly absorbed by the standard sealing o-rings used, made from Viton. The ECRH-antennas have to be equipped with vacuum shutters, which are build in between the vacuum vessel and the diamond disc barrier windows. In these shutters, the Viton o-rings have to be replaced by such made of low-absorbing material. After a first pre-selection, one shutter was equipped with an o-ring of the material Isolast J9505 and tested at IPP-Greifswald with a high power beam simulating the conditions as expected for W7-X. In the test, a temperature increase of 62° was found for steady state conditions. This qualifies the o-ring material for the application in W7-X.

For the heating scenarios with the second harmonic ordinary mode (O2) and the third harmonic extraordinary mode (X3), the expected single pass absorption is between 40% and 80%. This would lead to a thermal overloading of the inner wall armour graphite tiles by the non-absorbed part of the microwave beams. Therefore, in special positions the graphite tiles can be replaced by TZM (titanium, zirconium, molybdenum alloy) reflector tiles. With a large number of ray-tracing calculations the tile positions were optimised for every beam in such a way, that the beams are reflected back through the plasma center in a controlled way, with a high second pass absorption. A prototype tile was build and tested with an equivalent high power microwave beam at IPP Greifswald. Even though the maximum temperature increase was about 70% higher than in first ANSYS heat transport calculations, the use of the TZM-tiles seems to be feasible. In a next step, the thermal contact of the tile to the cooling base will be improved and the tile will be polished in order to minimise the microwave absorption.

Auxiliary systems

The water cooling system for the mirrors inside the torus have been installed as far as possible.

The controlling system and the visualization has been designed and installed. The visualization for the gyrotron operation has been improved. It has been adapted to the individual gyrotron boxes. The control and regulation system has for the first time been integrated into the main control system and was tested successfully.

Staff:

IHM / FZK	IPF (University of Stuttgart)	IPP (Greifswald/Garching)
A. Arnold	P. Brand	B. Berndt
<u>G. Dammertz</u>	C. Lechte	H. Braune
G. Gantenbein	M. Grünert	V. Erckmann (PMW)
R. Heidinger (IMF I)	W. Kasperek	F. Hollmann
S. Illy	H. Kumric	L. Jonitz
H. Kunkel	M. Krämer	H. Laqua
K. Koppenburg	R. Munk	G. Michel
W. Leonhardt	F. Müller	M. Nitz
D. Mellein	B. Plaum	F. Noke
G. Neffe	P. Salzmann	F. Purps
B. Piosczyk	K.H. Schlüter	T. Schulz
H. O. Prinz	D. Wimmer	P. Uhren
U. Saller		M. Weißgerber
M. Schmid		
W. Spiess		
M. Stoner		
J. Szczesny		
<u>M. Thumm</u>		
R. Vincon		
J. Wiegand		
C. Zöller		

Literature:

- [1] T. C. Luce, "Applications of High-Power Millimeterwaves in Fusion Energy Research," IEEE Trans. Plasma Science **30** (2002) 734-754
- [2] G. Dammertz, S. Alberti, A. Arnold, D. Bariou, E. Borie, P. Brand, H. Braune, V. Erckmann, G. Gantenbein, E. Giguët, R. Heidinger, J. P. Hogge, S. Illy, W. Kasperek, K. Koppenburg, H. Laqua, F. Legrand, W. Leonhardt, C. Liévin, G. Michel, G. Müller, G. Neffe, B. Piosczyk, M. Schmid, M. Thumm, and M. Q. Tran, "Experimental results on the 140 GHz, 1 MW, CW gyrotrons for the stellarator W7-X", Joint 30th Int. Conf. on Infrared and Millimeter Waves and 13th Int. Conf. on Terahertz Electronics, Williamsburg, Sept. 19-23, 2005, 235-236
- [3] G. Dammertz, S. Alberti, A. Arnold, D. Bariou, P. Brand, H. Braune, V. Erckmann, O. Dumbrajs, G. Gantenbein, E. Giguët, R. Heidinger, J. P. Hogge, S. Illy, J. Jin, W. Kasperek, K. Koppenburg, H. P. Laqua, F. Legrand, W. Leonhardt, C. Liévin, G. Michel, G. Neffe, B. Piosczyk, H. O. Prinz, T. Rzesnicki, M. Schmid, M. Thumm, M. Q. Tran, X. Yang, I. Yovchev, "High Power Gyrotron Development at Forschungszentrum Karlsruhe for Fusion Applications", IEEE Trans. Plasma Science **34** (2006), pp. 173-186
- [4] G. Dammertz, A. Arnold, D. Bariou, E. Giguët, R. Heidinger, S. Illy, J. Jin, F. Legrand, W. Leonhardt, C. Liévin, G. Neffe, B. Piosczyk, T. Rzesnicki, M. Schmid, M. Thumm, "Gyrotron Research at Forschungszentrum Karlsruhe", German Microwave Conf., Karlsruhe, March 2006, (CD-ROM).
- [5] G. Dammertz, S. Alberti, A. Arnold, V. Erckmann, G. Gantenbein, E. Giguët, R. Heidinger, J. P. Hogge, S. Illy, W. Kasperek, K. Koppenburg, H. P. Laqua, F. Legrand, W. Leonhardt, C. Liévin, G. Michel, G. Neffe, B. Piosczyk, M. Schmid, M. Thumm, M. Q. Tran, "Status of the Series Production of 1-MW, 140-GHz, CW Gyrotrons for W7-X"; Conf. Digest of the 2006 Joint 31st Int. Conf. on Infrared and Millimeterwaves and 14th Int. Conf. on Terahertz Electronics; Shanghai, China, September 2006, p. 21
- [6] G. Dammertz, S. Alberti, A. Arnold, V. Erckmann, G. Gantenbein, E. Giguët, R. Heidinger, J. P. Hogge, S. Illy, W. Kasperek, K. Koppenburg, H. P. Laqua, F. Legrand, W. Leonhardt, C. Liévin, R. Magne, G. Michel, G. Neffe, B. Piosczyk, M. Schmid, M. Thumm, M. Q. Tran, "Recent Results of the 1-MW, 140 GHz, CW Gyrotrons for the Stellarator W7-X", 14th Joint Workshop on Electron Cyclotron Resonance Heating (EC14); Santorini, Greece, May 2006, p. 90; to be published, <http://www.hellasfusion.gr/englishver/ec14conference.php>.
- [7] M. Thumm, A. Arnold, G. Dammertz, G. Gantenbein, R. Heidinger, S. Illy, W. Leonhardt, G. Neffe, B. Piosczyk, M. Schmid, S. Alberti, J. P. Hogge, M. Q. Tran, H. Braune, V. Erckmann, H. P. Laqua, G. Michel, W. Kasperek, R. Magne, E. Giguët, F. Legrand, C. Liévin, "EU megawatt-class 140 GHz CW gyrotron", 33rd IEEE Int. Conf. on Plasma Science, Traverse City, Michigan, June 2006, p. 374.

- [8] G. Gantenbein, S. Alberti, A. Arnold, G. Dammertz, V. Erckmann, E. Giguet, R. Heidinger, J. P. Hogge, S. Illy, W. Kasperek, H. P. Laqua, F. Legrand, E. Leonhardt, C. Liévin, G. Michel, G. Neffe, B. Piosczyk, M. Schmid, M. Thumm, M. Q. Tran, "Experimental Results of the 1-MW, 140-GHz, CW Gyrotron for W7-X", 21st IAEA Fusion Energy Conf., Chengdu, China, Oct. 2006; <http://www-pub.iaea.org/MTCD/Meetings/announcements.asp?ConfID=149>; to be published
- [9] W. Kasperek, M. Petelin, V. Erckmann, D. Shchegolkov, A. Bruschi, S. Cirant, M. Thumm, B. Plaum, M. Grünert, M. Malthaner, W7-X ECRH Teams at IPP, FZK and IPF, "Fast switching of high-power millimetre waves between two launchers: concepts, numerical investigations and first experiments", 14th Joint Workshop on Electron Cyclotron Emission and Electron Cyclotron Resonance Heating (EC 14), Santorini, Greece, May 9-12, 2006, Book of Abstracts p.7; <http://www.hellasfusion.gr/englishver/ec14conference.php>.
- [10] V. Erckmann, P. Brand, H. Braune, G. Dammertz, G. Gantenbein, W. Kasperek, H.P. Laqua, G. Michel, M. Thumm, M. Weissgerber, W7-X ECRH Teams at IPP, FZK and IPF, "The 140 GHz, 10 MW, CW ECRH plant for W7-X: a training field for ITER", 21st IAEA Fusion Energy Conf., Chengdu, China, October 16-21, 2006 (see. Ref. [8])
- [11] B. Plaum, G. Gantenbein, W. Kasperek, K. Schwörer, M. Grünert, H. Braune, V. Erckmann, F. Hollmann, L. Jonitz, H.P. Laqua, G. Michel, F. Noke, F. Purps, A. Bruschi, S. Cirant, F. Gandini, A.G.A. Verhoeven, ECRH groups, "High-power tests of a remote-steering antenna at 140 GHz". Fusion Science and Technology, **50**(2006) pp.1-14
- [12] H. Braune, P. Brand, V. Erckmann, W. Leonhardt, D. Mellein, G. Michel, G. Müller, K.H. Schlüter, M. Winkler, "Architecture of central control system for the 10 MW ECRH - plant at W7-X", 24th Symp. on Fusion Technology (SOFT 2006), Warszawa

Underlying Technology

Underlying Technology

Operation of the Fusion Materials Laboratory (FML)

The Fusion Materials Laboratory (FML) provides the infrastructure for the performance of tasks defined in the EFDA workprogramme related to the characterisation and testing of irradiated and non-irradiated fusion materials. Methods such as optical and electron microscopy, tritium adsorption and desorption, He pycnometry and Hg porosimetry, crush load, micro hardness, creep, Charpy impact and tensile tests as well as long-time annealing tests are applied. The work includes Post Irradiation Examinations (PIE) of Reduced Activation Ferritic Martensitic (RAFM) steels (reference material for DEMO and ITER-TBMs), investigations on materials relevant for the HCPB blanket (ceramic breeder materials, beryllium) and Plasma Facing Materials (tiles) from tokamaks (JET, TFTR).

PIE on selected samples from the HFR Ib and HFR IIb experiments were carried out. For this purpose Charpy impact and tensile tests were performed and tested specimens' small cuts for light optical, scanning and transmission electron microscopy were prepared and examined. The aim of the investigations was to study the irradiation effects on the mechanical and structural properties of these materials.

The investigation of blanket materials was continued with the characterisation of materials. Lithium orthosilicate pebbles were investigated by light optical microscopy and their porosity and deformation hardness were determined. Different batches of materials were characterised with respect to the influence of parameters of the fabrication process on the mechanical and structural properties. Adsorption and desorption experiments were done with irradiated beryllium pebbles to study the influence of the surface structure on the tritium kinetics. The characterization of pebbles from a uniaxially compressed metallic pebble bed for the determination of the mechanical parameters and the thermal conductivity of the metallic pebble bed was continued.

Further samples from ASDEX, JET and TFTR carbon tiles were prepared for the investigation of tritium retention in these materials. In the TLK these samples were analysed. The irradiation experiments on Tritium flakes from JET with the radiation of a Co60-source to study the effect of the gamma-radiation on the desorption properties of the adsorbed tritium were continued.

Detailed results and consecutive analysis of the measurements are reported in the respective chapters of this report.

For the PIE the following equipment was used:

- Charpy impact and tensile testing devices;
- Light optical, scanning electron and transmission electron microscopes;
- Desorption device with high temperature furnace for tritium and helium release measurements;
- He-pycnometer and Hg-porosimeter;
- Sphere crush and creep testing apparatus.

In the frame of the laboratory upgrading programme, an indentation device was set into hot operation inside a newly installed lead-shielded hot cell. The specification for a new remotely operated light optical microscope was set up and distributed among possible tenderers.



Remotely controlled indenter during mounting into FML box no. 4

Future activities:

Continuation of measurements as referred to above:

- PIE of the HFR II B irradiation phase: some 180 samples of steel, 15 dpa;
- Characterization of tiles;
- Characterization of new batches of ceramic breeder materials and beryllium.

Staff:

P. Barié
J. Ehrmann
A. Erbe
M. Gilpert
M. Holzer
H. Jackisch
S. Lautensack
P. Lauterbach
G. Mangei
W. Nägele
H. Ries
R. Rolli
G. Rösch
R. Schmidt
H.-C. Schneider
H. Steinle

Literature:

- [1] M. Matsuyama, Y. Torikai, N. Bekris, M. Glugla, A. Erbe, W. Naegele, N. Noda, V. Philipps, P. Coad and K. Watanabe, "Applicability of β -ray-induced X-ray spectrometry to in-situ measurements of tritium retention in plasma-facing materials in ITER", Fusion Engineering and Design, Vol. 81 (2006), pages 163 - 168
- [2] J. Reimann, R.A. Pieritz, R. Rolli, "Topology of compressed pebble beds", Fusion Engineering and Design, Vol. 81 (2006), pages 653 - 658
- [3] E. Lucon, P. Benoit, P. Jacquet, E. Diegele, R. Lässer, A. Alamo, R. Coppola, F. Gillemot, P. Jung, A. Lind, S. Messoloras, P. Novosad, R. Lindau, D. Preininger, M. Klimiankou, C. Petersen, M. Rieth, E. Materna-Morris, H.-C. Schneider, J.-W. Rensman, B. van der Schaaf, B.K. Singh and P. Spaetig, "The European effort towards the development of a DEMO structural material: Irradiation behaviour of the European reference RAFM steel EUROFER", Fusion Engineering and Design, Vol. 81 (2006), pages 917 – 923
- [4] Gaganidze, E., Schneider, H.-C., Dafferner, B., Aktaa, J., "High-dose neutron irradiation embrittlement of RAFM steels", Journal of Nuclear Materials, 355 (2006), pages 83 - 88

Appendix I: FZK Departments Contributing to the Fusion Programme

FZK Department	FZK Institut/Abteilung	Director	Ext.
Institute for Materials Research	Institut für Materialforschung (IMF)	I. Prof. Dr. K.-H. Zum Gahr	3897
		II. Prof. Dr. O. Kraft	4815
		III. Prof. Dr. H. Haußelt	2518
Institute for Pulsed Power and Microwave Technology	Institut für Hochleistungsimpuls- und Mikrowellentechnik (IHM)	Prof. Dr. M. Thumm	2440
Institute for Nuclear and Energy Technology	Institut für Kern- und Energietechnik (IKET)	Prof. Dr. T. Schulenberg	3450
Institute for Reactor Safety	Institut für Reaktorsicherheit (IRS)	Prof. Dr. V. Heinzel (Acting Head)	2550
Institute for Technical Physics	Institut für Technische Physik (ITP)	Prof. Dr. M. Noe	3500
- Tritium Laboratory Karlsruhe	- Tritiumlabor Karlsruhe (TLK)	Dr. M. Glugla	3226
Institute for Data Processing and Electronics	Institut für Prozessdatenverarbeitung und Elektronik (IPE)	Prof. Dr. H. Gemmeke	5635

Contributing:

Institute for Nuclear and Particle Physics, Technical University of Dresden	Institut für Kern- und Teilchenphysik Technischen Universität Dresden	Prof. Dr. H. Freiesleben	+ 49 351/4635461
Institute for Applied Physics University of Frankfurt	Institut für Angewandte Physik J.W. Goethe-Universität Frankfurt	Prof. Dr. H. Klein	+ 49 69/7982 3489
Institut für Strahlwerkzeuge University of Stuttgart	Institut für Strahlwerkzeuge Universität Stuttgart	Prof. Dr. T. Graf	+ 49 711/6856841

Appendix II: Fusion Programme Management Staff

Head of the Research Unit	Dr. G. Janeschitz	ext. 5460 e-mail: guenter.janeschitz@fusion.fzk.de
Assistant:	Mrs. M. Winkelmann	ext. 5461 e-mail: miriam.winkelmann@fusion.fzk.de
Secretariat:	Mrs. C. Hermsmeyer	ext. 5466 e-mail: carmen.hermsmeyer@fusion.fzk.de
Program Budget, Administration, Reports, EU-Affairs	BW. M. Henn	ext. 5547 e-mail: michael.henn@fusion.fzk.de
	Mrs. V. Lallemand	ext. 6461 e-mail: vera.lallemand@fusion.fzk.de
	Mrs. I. Pleli	ext. 8292 e-mail: ingrid.pleli@fusion.fzk.de
Blanket and Divertor Development, HELOKA, IFMIF, Public Relations	DI. W. Bahm	ext. 5465 e-mail: werner.bahm@fusion.fzk.de
Quality Management	DI. P. Freiner	ext. 4194 e-mail: peter.freiner@fusion.fzk.de
Fuel Cycle, Structural Materials, Superconducting Magnets, CAD-Office	DI. S. Gross	ext. 5468 e-mail: sigurd.gross@fusion.fzk.de
Plasma Heating Technology, Safety Studies, Neutronics	Dr. K. Hesch	ext. 5462 e-mail: klaus.hesch@fusion.fzk.de
Resource Loaded Planning, Physics, DEMO Divertor	Dr. M. Ionescu-Bujor	ext. 8325 e-mail: mihaela.ionescu-bujor@fusion.fzk.de

Address:

**Forschungszentrum Karlsruhe GmbH
Nuclear Fusion Programme Management
Post Office Box 3640, D - 76021 Karlsruhe / Germany**

Telephone No:

07247-82- Extensions

Telefax No:

07247-82-5467

world wide web:

<http://www.fzk.de/fusion>

Appendix III: Glossary

3D	Three-dimensional
3PB	3 Point Bending FM Probe, cf. SE(B)
AC	Alternating Current
ACP	Activated Corrosion Products
ACS	Automated Control System
ADS	Atomosphere Detritiation System
AGHS	Active Gas Handling System
AGR	Advanced Gas Cooled Fission Reactor
A-HCPB	Advanced Helium Cooled Pebble Bed
AISI 316L	Austenitic Steel
ALTAIR	Fast Reactor Irradiation from CEA in BOR 60
ANS	Analytical System
AP	Activated Dust
ARBOR-1	Fast Reactor Irradiation from FZK in BOR 60
ARBOR-2	Fast Reactor Irradiation from FZK and CEA in BOR 60
ASDEX	Axial-symmetrisches Divertor-EXperiment
ASIPP	(Chinese) Academy of Sciences, Institute for Plasma Physics, Hefei
ASTM	American Society for Testing and Materials
BB	Blanket Box
BCO	Beam Combining Optics
BD	Brittle Destruction
BET	Brunauer-Emmett-Teller (specific surface)
BIXS	Beta-Induced X-ray Spectrometry
BOR 60	Fast Reactor at SSC RF RIAR, Dimitrovgrad, Russia
BSCCO	$\text{Bi}_2\text{Sr}_2\text{Ca}_2\text{Cu}_2\text{O}_x$
BSM	Blanket Shield Module
BU	Breeding Unit
C(T)	Compact Tension FM Probe
CAD	Computer Aided Design
CATIA V5	CAD Software CATIA, Version 5
CC	Coated Conductor
CCNB	Coordinative Committee of Neutral Beams
CD	Cryogenic Distillation
CEA	Commissariat à l'Energy Atomique
CECE	Combined Electrolysis Catalytic Exchange

CFC	Carbon Fibre Composite
CFD	Computational Fluid Dynamic
CFTM	Creep Fatigue Test Module
CH-structure	Crossbar H-mode Structure
CICC	Cable in Conduit Conductor
CIEMAT	Centro de Investigaciones Energeticas Medioambientales y Tecnologicas (CIEMAT), Madrid ,Spain
CL	Current Lead
CMSB	Cryogenic Molecular Sieve Bed
COSYMA	Code System Maria
CP	Cooling Plata
CPC	Crack Propagation Criterion
CPS	Coolant Purification System
CRPP	Centre de Recherches en Physique des Plasmas
CS	Central Solenoid
CT	Compact Tension
CT	Cryogenic Cold Trap
Cu	Copper
CVD	Chemical Vapour Deposition
CW	Continuous Wave
D1S	Direct one-step method for shut-down dose rate calculations
DACS	Data Acquisition and Control System
DBTT	Ductile-to-Brittle Transition Temperature
DCLL	Dual Coolant Lead Lithium
DDD	Design Description Document
DEMO	Demonstration Power Station
dpa	Displacement per atom
DT	Deuterium Tritium
DTL	Drift Tube Linac
EAF-2005	European Activation File, Version 2005
EB	Electron Beam
ECCD	Electron Cyclotron Current Drive
ECH&CD	Electron Cyclotron Heating and Current Drive
ECM	Electro Chemical Machining
...C-ECM	Cathodic-ECM
M-ECM	Mask-ECM
ECOTAP	Energy Compensated Optical Tomography Atomic Probe
ECRH	Electron Cyclotron Resonance Heating
EDM	Electron Discharge Method

EDX	Energy Dispersive X-Ray
EFDA	European Fusion Development Agreement
EFF	European Fusion File
ELM	Edge Localized Mode
EM	Electro Magnetic
EMRAS	Environmental Modelling for Radiation Safety
ENDF/B-VI	American Evaluated Nuclear Data File B, Version VI
ENEA	Ente per le Nuove tecnologie, l'Energia e l'Ambiente, Italy
EPL	Enhanced Performance Launcher
EUROFER 97	European RAF/M Steel
F82H mod.	Japanese RAF/M Steel
FE	Finite Element
FEM	Finite Element Method
FISPACT	Fusion Inventory Code
FM	Fracture Mechanics
FPSS	Fixed Principal Axis for Stresses and Strains
FSSS	Fisher Sub-sieve Sizer
FTTT	Fracture Toughness Transition Temperature
FW	First Wall
FZK-04	Forschungszentrum Karlsruhe Evaluated Data File for W
GC-MS	Gas Chromatography Mass Spectrometry Unit
GDC	Glow Discharge Cleaning
Gricaman Mock up	Mock up for validation of mass flow in GRId, CAp and MANifold
GTN	Gurson-Tvergaard-Needleman
H	Helium
HAZ	Heat Affected Zone
HCLL	Helium Cooled Lithium-Lead
HCPB	Helium Cooled Pebble Bed
HCS	Helium Cooling System
HEBLO	HElium BLOwer (Helium facility at FZK)
HELICA	Helium-FUS3 Lithium Cassette
HELOKA	Helium Loop Karlsruhe
HEMJ	Helium-cooled Divertor Concept with Multiple JET Cooling
HEMS	Helium-cooled Modular Divertor Concept with Integrated Slot Array
HETRA Mock up	Mock up for Validation of HEat TRAnsfer Coefficient
HEXCALIBER	Helium-Fus3 Experimental Cassette of Lithium, Beryllium Pebble Beds

HFIR	High Flux Isotope Reactor, ORNL
HFR	High Flux Reactor
HFTM	High Flux Test Module
HHF	High Heat Flux
HIP	Hot Isostatic Pressing
HMI	Hahn-Meitner Institute
HP	High Pressure
HPFPP	Hydrogen Production Fusion Power Plant
HRTEM	High Resolution Transmission Electron Microscope
HT	High Temperature
HT	Tritiated Gas
HTO	Tritiated Water Vapour
HTS	High Temperature Superconducting
HTSE	High Temperature Steam Electrolysis
HV30	Vickers Hardness at 30 kp Load
HX	Heat Exchanger
IB	Focussed Ion Beam
I_c	Critical Current
ICT	Initial Crack Tip
IFMIF	International Fusion Material Irradiation Facility
IGES, STEP	Neutral Format for the Exchange of CAD Geometry Data
IPF	Institut für Plasmaforschung, Universität Stuttgart
IPP	Max-Planck-Institute for Plasma Physics, Garching
IRDF-2002	International Reactor Dosimetry File, Version 2002
ISO	International Organization for Standardization
ISS	Isotope Separation System
ISTC	International Science and Technology Center
ITER	International Thermonuclear Experimental Reactor
ITERVAC	Code for vacuum gas flows
J_c	Critical Current Density
JET	Joint European Torus
JETT	J-Evaluation on Tensile Test
JRC	Joint Research Center
KLST	Kleinstprobe (Small Specimen for Charpy-V Impact Tests)
kN	kilo Newton
Kn	Knudsen number

LCF	Low Cycle Fatigue
LHe	Liquid Helium
LOFA	Loss of flow accident
LOVA	Loss of Vacuum Accident
LPCE	Liquid Phase Catalytic Exchange
LSE	Lower Shelf Energy
L-T	Longitudinal-Transverse
LTS	Low Temperature Superconducting
LVDT	Linear Variable Differential Transducer
M5, M8 and M12	Thread diameter 5 mm, 8 mm and 12 mm
Ma	Mach number
MANET	Conventional 12 % Cr steel
Mat-DB	Materials Data Bank
MBWG	Multi-beam Waveguide
MC	Master Curve
McCad	Interface Programme for converting CAD geometry data to the semi-algebraic representation of the MCNP code
McDeLicious	Monte Carlo Code for D-Li Neutron Generation and Transport
MCNP	Monte Carlo Neutron Photon (code for particle transport simulations)
MEKKA	Magneto-Hydrodynamic Experiments in Sodium und Potassium Karlsruhe
MFTM	Medium Flux Test Module
MHD	Magneto Hydrodynamic
MMS	Multi-Module Segment
MOCVD	Metal-organic Chemical Vapour Deposition
MOD	Metal-organic Deposition (wet solution)
MOVAK3D	Monte Carlo Code for vacuum applications
MPa	Mega Pascal
NB	Neutral Beam
NBI	Neutral Beam Injector
NBTF	Neutral Beam Test Facility
N_f	Number of Cycles to Failure
NRG	Nuclear Research and Consultancy Group, National Nuclear Research Institute of the Netherlands, located in Petten
NTM	Neoclassical Tearing Modes
N-VDS	Normal Vent Detritiation System
OBT	Organically Bound Tritium
ODIN	Online Data & Information Network for Energy of JRC
ODS	Oxygen Dispersion Strengthened

OPL	Outer Poloidal Limiter
OPTIFER IVc	German RAF/M Steel
OST	Oxford Superconducting Technology
PAN-fibers	The NB31 fibers parallel to the surface
PCCV	Pre-Cracked Charpy V
PCP	Prototype Cryosorption Pump
PFC	Plasma Facing Components
PI	Plant Integration
PICCOLO	Pb-Li Corrosion Loop
PIE	Post Irradiation Examination
PLC	Programmable Logic Control
PMW	Projekt Microwellenheizung for W7-X
PPCS	Power Plant Conceptual Study
PTC	Prototype Torus Cryopump
Pt-PtRh-TC	Platinum Rhodium-Thermocouples
PWHT	Post Weld Heat Treatment
QSPA MK-200UG	Name of a Plasma Gun in TRINTI, Troitsk
R2S	Rigorous two-step method for shut-down dose rate calculations
RAFM	Reduced Activation Ferritic Martensitic
RCT	Recrystallisation Temperature
ReBCO	Re = Rare Earth Component
REM	Raster Electron Microscope
RF	Radio Frequency
RFQ	Radio Frequency Quadrupole
RPSS	Rotating Principal Stresses and Strains
RS	Remote Steering
RT	Room Temperature
SBWG	Single-beam Waveguide
SC	Single Crystal
SCHe	Supercritical Helium
SCK	StudieCentrum voor Kernenergie, National Nuclear Research Institute of the Netherlands, located in Petten
SDS	Storage and Delivery System
SE(B)	Single Edge Bending FM Probe, cf. 3PB
SEAFP	Safety and Environmental Assessment of Fusion Power
SEM	Scanning Electron Microscopy
SI	Sulphur-Iodine Process

SOL	Scrape-off Layer
SPICE	Sample Holder for Irradiation of Miniaturised Steel Specimens Simultaneously at Different Temperatures
SPM	Solid Polymer Electrolyser
SS	Safety System
SSC RF RIAR	State Scientific Centre of Russian Federation Research Institute of Atomic Reactors
TAP	Tomography Atomic Probe
TBM	Test Blanket Module
T_{Br}	Brazing Temperature
TDL	Thermo-luminescence Dosimeter
TDM	Test Divertor Module
TED	Thales Electron Devices, Vélizy
TEM	Transmission Electron Microscope
TEP	Tokamak Exhaust Processing
TES	Tritium Extraction Subsystem
TF	Toroïdal Field
TFTR	Tokamak Fusion Test Reactor (Princeton)
TIG	Tungsten Inert Gas
TIMO	Test Facility for ITER Model Pump
TLK	Tritium Laboratory Karlsruhe
TMF	Thermal Mechanical Fatigue
TPR	Tritium Production Rates
TRIMO	Tritium Inventory Modelling
TRM	Tritium Release Module
TRS	Tritium Retention System
TSEFEY	Electron Beam Facility
TTE	Trace Tritium Campaign at JET
UFOTRI	U nfall f olgen m odel T ritium
U_{LL}	Load Line Displacement
UMAT	User Material
USE	Upper Shelf Energy
VAMAS	The Versailles Project on Advanced Materials and Standards
VDS	Vent Detritiation System
VV	Vacuum Vessel
VVF	Voids Volume Fraction
W	Tungsten
WDS	Water Detritiation System

WHA	Tungsten Heavy Alloy
WL10	Tungsten, Dispersion Strengthened with 1 wt.% La ₂ O ₃ Particles
W-La ₂ O ₃	Tungsten Lanthanum Oxide Alloy
WSP	Westinghouse Hybrid Sulphur Process
WTZ	Wissenschaftlich-Technische Zusammenarbeit 01/577
XRD	X-ray Diffraction
YBCO	YBa ₂ Cu ₃ O _x
ϵ_{tot}	total strain range